J. Leszczynski
M. Shukla (Eds.)
European Academy of Sciences

Practical Aspects of Computational Chemistry

Methods, Concepts and Applications

Springer

Practical Aspects of Computational Chemistry

Jerzy Leszczynski • Manoj K. Shukla
Editors

Practical Aspects of Computational Chemistry

Methods, Concepts and Applications

Springer

Editors
Prof. Jerzy Leszczynski
Jackson State University
Department of Chemistry
and Biochemistry
1325 J. R. Lynch St.
Jackson MS 39217
USA
jerzy@icnanotox.org

Dr. Manoj K. Shukla
Jackson State University
Department of Chemistry
and Biochemistry
1325 J. R. Lynch St.
Jackson MS 39217
USA
mshukla@icnanotox.org

ISBN 978-90-481-2686-6 e-ISBN 978-90-481-2687-3
DOI: 10.1007/978-90-481-2687-3
Springer Heidelberg Dordrecht London New York

Library of Congress Control Number: 2009926517

Cover design: WMXDesign GmbH Heidelberg

Printed on acid-free paper

Springer is part of Springer Science+Business Media (www.springer.com)

Preface

Very few areas of science enjoy such a fast progress as has been witnessed in the last quarter of the 20th century for computational chemistry (CC). An access to increasingly faster and more powerful computers in parallel with continuous developments of more efficient computational programs and methods contributed toward employment of the CC approaches in both basic science as well as commercial applications. As a result, the investigated molecules are larger than ever and can be studied not only in vacuum but also in different solvent environments or in a crystal. Such remarkable progress has not been unnoticed by scientific community. In fact, the chemical and physical societies celebrated the great event of the 1998 Nobel prize in chemistry that was awarded to two leading theoretical chemists/physicists: Walter Kohn and John A. Pople for their seminal contributions to the development of efficient computational methods for quantum chemistry. Owing to the meticulous and continuous efforts, the computational chemistry methods have become complementary to the costly and time-consuming experiments and in many cases they provide the only reliable information when experiment is not possible or investigated species exhibit a health hazard to the investigators.

The methods and applications of the CC are the topics of the current book entitled *"Practical Aspects of Computational Chemistry: Methods, Concepts, and Applications. Special Issue of Annals–The European Academy of Sciences"*. It was not our goal to collect specialized contributions aimed at a narrow group of experts. Instead, we asked all authors to provide more general reviews, focusing toward general interests of the affiliates of the academy and members of scientific society. Though, it is not possible to cover all topics related to the CC in one volume, we hope that the collected contributions adequately highlight this important scientific area.

This book encompasses 23 contributions on different aspects of CC applied to a large arena of research field. The first contribution by Flores-Moreno and Ortiz deals with the theoretical formulation of electron propagator methods developed to compute accurate ionization potentials and electron affinity of system of different sizes. This review describes recent implementations that can be used for more challenging system without compromising the accuracy of the results. In the next

contribution, Cammi et al. have reviewed the implementation of Polarizable Continuum Model to describe the effect of different solvents on ground and excited state structural properties of variety of systems. Alkorta and Elguero have reviewed the chiral recognition from a theoretical perspective in the next contribution where a meticulous theoretical and experimental analysis is presented. Multiscale modeling is key for more accurate simulations of solid materials. In the following contribution, Horstemeyer has reviewed different aspects of computational mulisscale modeling, its successes, limitations, current challenges, and possible ways for improvement. The multiple minima problem is connected to all applications of theory to structural chemistry. Protein folding as an example of multiple minima problem is discussed by Piela in the next contribution.

σ-Hole bonding is defined as a highly directional noncovalent interaction between a positive region on a covalently-bonded Group V – VII atom and a negative site on another molecule, e.g. a lone pair of a Lewis base. Politzer and Murray have discussed an overview of σ-hole bonding in variety of system in their contribution. And this contribution is followed by the discussion of σ- and π-bonds in the main group and transition metal complexes by Pathak et al. In this contribution, authors have described possible mechanisms related to the phenomena where σ-bonds prevent π-bonds from adopting their optimal shorter distances. We collected three contributions discussing the structure-activity relationships. Two of them – one written by Benfenati and other by Puzyn et al. are devoted to the description of the REACH programs of the European Union for chemical regulatory purpose. The possibility of application of this new regulation to nanomaterials is also discussed. The third contribution by Vogt et al. discusses the structure-activity relationships in nitroaromatic compounds to predict their physicochemical properties.

In the next contribution, Lipkowski and Suwińska have discussed the different complications that may crop up in solving molecular structures using X-ray crystallography. These authors have described how molecular modeling methods can work as an auxiliary method in solving and refining such problems. Dihydrogen bonds are considered as a special type of hydrogen bond and are formed when two hydrogen atoms, one of them is negatively while other is positively charged, are usually closer than the sum of their van der Waals radii. Grabowski and Leszczynski have reviewed the novelty of dihydrogen bonds in the next contribution. And this is followed by a contribution from Michalkova and Leszczynski who have summarized the results of theoretical and experimental studies on organophosphorus systems, which may be used to develop theoretical models in explaining and predicting how clay minerals and metal oxides can affect the adsorption and decomposition of selected organophosphorus compounds. Clean energy resources is currently a major thrust area of fundamental and applied research. Dinadayalane and Leszczynski have discussed the mechanism toward the hydrogen storage in single-walled carbon nanotube via the chemisorption mechanism in the next contribution.

There are four contributions based on Monte Carlo (MC) simulations of different systems. These contributions include lucid discussion of the fundamentals of MC methods used in electronic structure calculations by Lester, the MC simulation, and

quantum mechanical calculations to compute the static dipole polarizability and the related dielectric constant of atomic argon in the liquid phase by Coutinho and Canuto and the application of free energy perturbation/MC simulations in molecular mechanics parameterization of CO_2(aq) for use in CO_2 sequestration modeling studies and that of similar investigations of liquid and solid phases of water to determine the melting temperature of several popular 3- and 4-site water models by Dick et al. In the next contribution, Latajka and Sobczyk have reviewed the low-barrier hydrogen bond problem in protonated naphthalene proton sponges. Experimental data related to the infra-red and NMR spectra and contemporary theoretical approaches to the barrier height for the proton transfer are also discussed.

The last four contributions are devoted to the structures and properties of nucleic acid fragments. Czyżnikowska et al. have discussed the most accurate and reliable framework for the analysis of intermolecular interactions in nucleic acid bases by the quantum chemical method. Shishkin et al. have reviewed the recent results of the conformational flexibility of nucleic acid bases and model systems. Such conformational flexibility arises from the high deformability of the pyrimidine ring where transition from a planar equilibrium conformation to a sofa configuration results in an increase of energy by less than 1.5 kcal/mol. DNA is constantly attacked by a large number of endogenous and exogenous reactive oxygen species (ROS), reactive nitrogen oxide species (RNOS), and alkylating agents. As a result of these interactions several lesions are produced and some of them are implicated in several lethal diseases. In the next contribution, Shukla and Mishra have reviewed recent results of interaction of ROS and RNOS with guanine. Nucleic acids can form complex structures that consist of more than two strands. Recent investigations of the polyads of the nucleic acid bases strongly suggest that all of the NABs can form stable tetrad structure in cyclic form through the H-bonding between the neighboring bases. The last contribution of this special issue is provided by Gu et al. where authors have reviewed the results of recent studies on structural properties of nucleic acid tetrads and role of metal ions in such formation.

With great pleasure, we take this opportunity to thank all the authors for devoting their time and hard work in enabling us to complete this book. We are grateful to the excellent support from the President of the EAS, Editor in Chief of the Annals, as well as the editors at Springer. Many thanks go to our families and friends without whom the realization of this book is not possible.

MS, USA Jerzy Leszczynski and Manoj K. Shukla

Contents

Contributors

Ibon Alkorta
Instituto de Química Médica (CSIC), Juan de la Cierva 3, E-28006 Madrid, Spain ibon@iqm.csic.es

Emilio Benfenati
Istituto di Ricerche Farmacologiche "Mario Negri," Via Giuseppe La Masa 19, 20156 Milano, Italy, benfenati@marionegri.it

R. Cammi
Dipartimento di Chimica G.I.A.F., Università di Parma, Parco Area delle Scienze, I-43100 Parma, Italy, chifi@unipr.it

Sylvio Canuto
Instituto de Física, Universidade de São Paulo, CP 66318, 05315-970 São Paulo, SP, Brazil, canuto@if.usp.br

C. Cappelli
Dipartimento di Chimica e Chimica Industriale, Università di Pisa, Via Risorgimento 35, I-56126 Pisa, Italy

Kaline Coutinho
Instituto de Física, Universidade de São Paulo, CP 66318, 05315-970 São Paulo, SP, Brazil, kaline@if.usp.br

C.E. Crespo-Hernández
Department of Chemistry, Case Western Reserve University, 10900 Euclid Avenue, Cleveland, OH 44106, USA, carlos.crespo@case.edu

Żaneta Czyżnikowska
Institute of Organic and Pharmaceutical Chemistry, The National Hellenic Research Foundation, 48 Vas. Constantinou Avenue, 11635 Athens, Greece

Thomas J. Dick
Department of Chemistry and Physics, Carlow University, 3333 Fifth Ave., Pittsburgh, PA 15213, USA

T.C. Dinadayalane
NSF CREST Interdisciplinary Nanotoxicity Center, Department of Chemistry and Biochemistry, Jackson State University, Jackson, Mississippi 39217, USA

José Elguero
Instituto de Química Médica (CSIC), Juan de la Cierva 3, E-28006 Madrid, Spain

Roberto Flores-Moreno
Facultad de Química, Universidad de Guanajuato, Noria Alta s/n, Guanajuato, Gto. 36050, México, rflores@quijote.ugto.mx

Leonid Gorb
NSF CREST Interdisciplinary Nanotoxicity Center, Department of Chemistry and Biochemistry Jackson State University, P.O. Box 17910, Jackson, MS 39217, USA

Department of Molecular Biophysics, Institute of Molecular Biology and Genetics, National Academy of Science of Ukraine, 150 Zabolotnogo St., Kyiv 03143, Ukraine

Sławomir J. Grabowski
NSF CREST Interdisciplinary Nanotoxicity Center, Department of Chemistry and Biochemistry Jackson State University, Jackson, MS 39217, USA

Department of Chemistry, University of Łódź, 90-236 Łódź, ul.Pomorska 149/153, Poland

Jiande Gu
NSF CREST Interdisciplinary Nanotoxicity Center, Department of Chemistry and Biochemistry, Jackson State University, Jackson, MS 39217, USA

M.F. Horstemeyer
Department of Mechanical Engineering, Mississippi State University, MS 39760, USA, mfhorst@cavs.msstate.edu

Eluvathingal D. Jemmis
Department of Inorganic and Physical Chemistry, Indian Institute of Science, Bangalore 560-012, India, jemmis@ipc.iisc.ernet.in

Z. Latajka
Faculty of Chemistry, University of Wrocław, Joliot-Curie 14, 50-383 Wrocław, Poland

William A. Lester, Jr.
Kenneth S. Pitzer Center for Theoretical Chemistry, Department of Chemistry, University of California, Berkeley, CA 94720-1460, USA

Chemical Sciences Division, Lawrence Berkeley National Laboratory, Berkeley, CA 94720, USA, walester@lbl.gov

Danuta Leszczynska
NSF CREST Interdisciplinary Nanotoxicity Center, Department of Chemistry and Biochemistry, Jackson State University, 1325 Lynch St, Jackson, MS 39217-0510, USA

Department of Civil and Environmental Engineering, Jackson State University, 1325 Lynch St, Jackson, MS 39217-0510, USA, danuta@icnanotox.org

Jerzy Leszczynski
NSF CREST Interdisciplinary Nanotoxicity Center, Department of Chemistry and Biochemistry, Jackson State University, 1325 Lynch St, Jackson, MS 39217-0510, USA, jerzy@icnanotox.org

Janusz Lipkowski
Institute of Physical Chemistry, Polish Academy of Sciences, Kasprzaka 44/52, Warszawa 01 224, Poland, janusz.lipkowski@wp.pl

Jeffry D. Madura
Center for Computational Sciences, Department of Chemistry and Biochemistry, Duquesne University, 600 Forbes Ave., Pittsburgh, PA 15282, USA

B. Mennucci
Dipartimento di Chimica e Chimica Industriale, Università di Pisa, Via Risorgimento 35, I-56126 Pisa, Italy

A. Michalkova
NSF CREST Interdisciplinary Nanotoxicity Center, Department of Chemistry and Biochemistry, Jackson State University, Jackson, MS 39217, USA

P.C. Mishra
Department of Physics, Banaras Hindu University, Varanasi 221 005, India
pcmishra@bhu.ac.in

Jane S. Murray
Department of Chemistry, University of New Orleans, New Orleans, LA 70148, USA

Department of Chemistry, Cleveland State University, Cleveland, OH 44115, USA

J.V. Ortiz
Department of Chemistry and Biochemistry, Auburn University, Auburn, AL 36849, USA, ortiz@auburn.edu

Manthos G. Papadopoulos
Institute of Organic and Pharmaceutical Chemistry, The National Hellenic Research Foundation, 48 Vas. Constantinou Avenue, 11635 Athens, Greece
mpapad@eie.gr

Biswarup Pathak
Department of Inorganic and Physical Chemistry, Indian Institute of Science, Bangalore 560-012, India

Lucjan Piela
Department of Chemistry, University of Warsaw, Pasteura 1, 02-093 Warsaw, Poland, piela@tiger.chem.uw.edu.pl

Peter Politzer
Department of Chemistry, University of New Orleans, New Orleans, LA 70148, USA

Department of Chemistry, Cleveland State University, Cleveland, OH 44115, USA, ppolitze@uno.edu

Tomasz Puzyn
NSF CREST Interdisciplinary Nanotoxicity Center, Department of Chemistry and Biochemistry, Jackson State University, 1325 Lynch St, Jackson, MS 39217-0510, USA

Laboratory of Environmental Chemometrics, Faculty of Chemistry, University of Gdańsk, Sobieskiego 18, 80-952 Gdańsk, Poland

S. Rahman
Department of Chemistry, Case Western Reserve University, 10900 Euclid Avenue, Cleveland, OH 44106, USA

Oleg V. Shishkin
STC “Institute for Single Crystals,” National Academy of Science of Ukraine, 60 Lenina Ave., Kharkiv 61001, Ukraine

NSF CREST Interdisciplinary Nanotoxicity Center, Department of Chemistry and Biochemistry, Jackson State University, P.O. Box 17910, Jackson, MS 39217, USA

P.K. Shukla
Department of Physics, Banaras Hindu University, Varanasi 221 005, India

L. Sobczyk
Faculty of Chemistry, University of Wrocław, Joliot-Curie 14, 50-383 Wrocław, Poland, sobczyk@chem.uni.wroc

Kinga Suwińska
Institute of Physical Chemistry, Polish Academy of Sciences, Kasprzaka 44/52, 01 224 Warszawa, Poland

J. Tomasi
Dipartimento di Chimica e Chimica Industriale, Università di Pisa, Via Risorgimento 35, I-56126 Pisa, Italy

Muthaiah Umayal
Department of Inorganic and Physical Chemistry, Indian Institute of Science, Bangalore 560-012, India

R.A. Vogt
Department of Chemistry, Case Western Reserve University, 10900 Euclid Avenue, Cleveland, OH 44106, USA

Jing Wang
NSF CREST Interdisciplinary Nanotoxicity Center, Department of Chemistry and Biochemistry, Jackson State University, Jackson, MS 39217, USA

Andrzej Wierzbicki
Department of Chemistry, University of South Alabama, Mobile, AL 36688, USA

Robert Zaleśny
Institute of Organic and Pharmaceutical Chemistry, The National Hellenic Research Foundation, 48 Vas. Constantinou Avenue, 11635 Athens, Greece

Chapter 1
Efficient and Accurate Electron Propagator Methods and Algorithms

Roberto Flores-Moreno and J.V. Ortiz

Abstract Recent developments in electron propagator methods that employ the quasiparticle approximation can facilitate calculations on molecules of unprecedented size. Reductions of arithmetic and storage requirements are considered. New and reliable approximations that offer a better compromise of accuracy and feasibility are proposed. Transition operator orbitals, in combination with the second-order self-energy, provide reliable predictions for valence and core electron binding energies with algorithms that are comparable in efficiency to their counterparts that employ ordinary Hartree–Fock orbitals. Quasiparticle virtual orbitals enable accurate evaluation of third-order self-energy contributions, while significantly reducing storage and arithmetic requirements. Algorithms that employ the resolution-of-the-identity approach to the evaluation of electron repulsion integrals require less memory but retain the accuracy of ordinary calculations. Numerical tests confirm the promise of these new approaches.

1.1 Introduction

Several methods of electron propagator theory (EPT) [1–4], or the one-electron Green's function [5, 6] approach, are now well established techniques [4, 7–16] for the theoretical description of molecular photoelectron spectra. Quasiparticle approximations in EPT can be viewed as correlated corrections to Koopmans's theorem (KT) results for electron attachment or detachment energies (EADEs). Systematic improvements in electron propagator approximations produce better results for ionization energies and electron affinities. However, these improvements may require lengthy calculations or large quantities of memory [11]. The diagonal, third order approximation (and therefore, the outer valence Green's function (OVGF) methods [6] as well) requires a step with ov^4 arithmetic scaling (where o and v are the

R. Flores-Moreno[1] and J.V. Ortiz[2] (✉)
[1]Facultad de Química, Universidad de Guanajuato, Noria Alta s/n, Guanajuato, Gto. 36050, México; [2]Department of Chemistry and Biochemistry, Auburn University, Auburn, AL 36849, USA
e-mail: Ortiz@auburn.edu; rflores@quijote.ugto.mx

J. Leszczynski and M.K. Shukla (eds.), *Practical Aspects of Computational Chemistry*,
DOI 10.1007/978-90-481-2687-3_1,

number of occupied and virtual spin-orbitals, respectively), and its self-energy formulae depend on the full set of transformed two-electron repulsion integrals [11]. Even the diagonal, partial third order method (P3) for ionization energies has an o^2v^3 step and calls for transformed integrals with one occupied and three virtual indices in its rate-limiting contraction [9]. The second order approximation (EP2) has a much better scaling behavior: for a single EADE calculation, the rate limiting contraction scales as ov^2. This step is even faster than a conventional, self-consistent field [17,18] iteration in the calculation of the reference Hartree–Fock [19,20] state. Unfortunately, the reliability of results from EP2 calculations is very poor compared to P3 or OVGF. The following order of reliability has been found:

$$\text{P3, OVGF} > \text{EP2} > \text{KT}.$$

This hierarchy of approximations constitutes a guide for judging the quality of the methods discussed below that aim to improve the efficiency of quasiparticle electron propagator calculations.

Even with efficient, modern implementations [21,22] of the P3 and OVGF quasiparticle approximations, only medium size systems [12–15] can be treated with average computer resources. A new set of approximations that may enable treatment of larger molecular systems using quasiparticle electron propagator methods has been introduced. This set includes the use of transition operator orbitals [23–25] in the second-order self-energy [26], reduction of the virtual orbital space for higher order quasiparticle electron propagator calculations [27] and use of the resolution-of-the-identity (RI) technique [28].

This paper is organized as follows. In Sect. 1.2, the superoperator formulation of EPT is outlined to introduce nonspecialist readers to the terminology that is used to discuss various approximations. In Sect. 1.3, approximations proposed for the treatment of large molecules are described. The benefits of these techniques and the reliability of their results are discussed in Sect. 1.4. Concluding remarks are made in Sect. 1.5.

1.2 Superoperator Formulation

The superoperator formalism that has been used in previous publications is outlined here [2, 9, 29]. The alternative diagrammatic and algebraic-diagrammatic representations can be found in other works [6].

After Fourier transformation, the time domain of the Green's function is translated to frequency dependency. We start with the resulting spectral representation of the one-electron propagator

$$G_{pq}(\omega) = \lim_{\eta\to 0} \sum_n \frac{\langle N|a_p|N+1,n\rangle\langle N+1,n|a_q^\dagger|N\rangle}{\omega - E_n(N+1) + E_0(N) + i\eta} + \lim_{\eta\to 0} \sum_n \frac{\langle N|a_q^\dagger|N-1,n\rangle\langle N-1,n|a_p|N\rangle}{\omega + E_n(N-1) - E_0(N) - i\eta}, \tag{1.1}$$

where $E_0(N)$ is the energy of the reference state with N electrons, $|N\rangle$, and $E_n(N \pm 1)$ is the energy of the nth state of the system with $N \pm 1$ electrons, $|N \pm 1, n\rangle$. Creation and annihilation operators for the pth canonical molecular orbital (MO) of the reference system are symbolized, respectively, by $a_p^\dagger$ and a_p. From this expression, it is obvious that poles of the electron propagator correspond to EADEs. When Hartree–Fock reference states are used, the following expansion is employed:

$$|N\rangle = W\left\{1 + \sum_{ia} \kappa_i^a a_a^\dagger a_i + \sum_{i>j,a>b} \kappa_{ij}^{ab} a_a^\dagger a_b^\dagger a_i\, a_j + \cdots\right\}|HF\rangle \tag{1.2}$$

where W is a normalization constant and $|HF\rangle$ is the Hartree–Fock approximation to the wavefunction. The correlation coefficients, κ, are obtained from Rayleigh–Schrödinger perturbation theory [30]. Occupied MOs are labeled with i or j, and virtual MOs with a or b.

In the superoperator approach, an abstract linear space is introduced [2]. The elements of this space are fermion operators generally expressed as linear combinations of products of creation or annihilation operators,

$$\{a_s, a_q^\dagger a_s a_t (s<t), a_p^\dagger a_q^\dagger a_s a_t a_u (p<q, s<t<u), \ldots\}, \tag{1.3}$$

where the limits of the indices avoid double counting. Here, p, q, s, t, and u are general MO indices. If Y and Z are two arbitrary operators, i.e., linear combinations of products of creation or annihilation operators, the identity superoperator, $\hat{I}$, is defined by

$$\hat{I}Y = Y \tag{1.4}$$

and the Hamiltonian superoperator, $\hat{H}$, by

$$\hat{H}Y = [Y, H]_- = YH - HY. \tag{1.5}$$

H is the Hamiltonian operator expressed in the language of second quantization,

$$H = \sum_{p,q} h_{pq} a_p^\dagger a_q + \frac{1}{4}\sum_{p,q,s,t} \langle pq||st\rangle a_p^\dagger a_q^\dagger a_t\, a_s, \tag{1.6}$$

where h_{pq} is a matrix element of the one-electron contributions including kinetic energy and external potentials acting on the electrons, such as the electrostatic nuclear attraction. $\langle pq||st\rangle$ is an antisymmetrized electron repulsion integral in Dirac notation. The superoperator linear space is defined in terms of the following rule for the inner product

$$(Y|Z) = \langle N|[Y^\dagger, Z]_+|N\rangle = \langle N|Y^\dagger Z + ZY^\dagger|N\rangle. \tag{1.7}$$

This rule associates a complex number to each pair of operators. The value of this number depends on the reference state used and the truncation of the perturbation series,

$$(Y|Z) = (Y|Z)^{(0)} + (Y|Z)^{(1)} + (Y|Z)^{(2)} + \cdots, \tag{1.8}$$

where orders are defined with respect to the fluctuation potential operator, i.e., the partitioning of Møller and Plesset [31] applies.

Using superoperators in combination with (1.1), we get the electron propagator matrix

$$\mathbf{G}(\omega) = (\mathbf{a}|(\omega\hat{I} - \hat{H})^{-1}|\mathbf{a}), \tag{1.9}$$

where $\mathbf{a}$ is the set of simple field operators, $\{a_p\}$. By applying Löwdin's inner projection technique [32], the inversion of an operator is avoided. Therefore, only a matrix must be inverted according to

$$\mathbf{G}(\omega) = (\mathbf{a}|\mathbf{h})(\mathbf{h}|\omega\hat{I} - \hat{H}|\mathbf{h})^{-1}(\mathbf{h}|\mathbf{a}), \tag{1.10}$$

where the projection space, $\mathbf{h}$, is composed of elements of the superoperator linear space of (1.3). When the set $\mathbf{h}$ contains the complete space, there is no approximation.

From (1.10), it follows that eigenvalues of the Hamiltonian superoperator correspond to poles of the Green's function, and therefore, to EADEs. Thus, we are faced with an eigenvalue problem [33, 34],

$$\hat{\mathbf{H}}\mathbf{C} = (\mathbf{h}|\hat{H}|\mathbf{h})\,\mathbf{C} = \omega\,\mathbf{C}. \tag{1.11}$$

The projection space can be decomposed for convenience into a primary space, $\mathbf{a}$, and a complementary space, $\mathbf{f}$. The latter space contains operators associated with ionizations coupled to excitations: triple products (two-hole particle, $2hp$, and two-particle hole, $2ph$, subspaces), quintuple products, heptuple products and so on. With this partition of the projection space, the eigenvalue problem can be rewritten as

$$\begin{pmatrix} (\mathbf{a}|\hat{H}|\mathbf{a}) & (\mathbf{a}|\hat{H}|\mathbf{f}) \\ (\mathbf{f}|\hat{H}|\mathbf{a}) & (\mathbf{f}|\hat{H}|\mathbf{f}) \end{pmatrix} \begin{pmatrix} \mathbf{C}_a \\ \mathbf{C}_f \end{pmatrix} = \omega \begin{pmatrix} \mathbf{C}_a \\ \mathbf{C}_f \end{pmatrix}. \tag{1.12}$$

The principal part of the eigenvectors, $\mathbf{C}_a$, contains the combination of coefficients that is required to build Feynman–Dyson amplitudes (Dyson orbitals) from the reference Hartree–Fock orbitals. Dyson orbitals as they result from (1.12) are not normalized, i.e., the sum

$$P_p = \sum_q |C_{qp}|^2 \tag{1.13}$$

is, in general, different from 1. P_p is known as the pole strength for the pth Dyson orbital. A larger pole strength reflects an attachment or detachment process that is well represented by an orbital. Small pole strengths correspond to correlation final states where orbital descriptions are invalid. If we are interested only in the solutions that are described chiefly by the principal space, the partitioning technique introduced by Löwdin [32] allows us to reduce considerably the size of the system of equations. The resulting system has an implicit dependence on the poles of the electron propagator matrix,

$$\left\{(\mathbf{a}|\hat{H}|\mathbf{a}) - (\mathbf{a}|\hat{H}|\mathbf{f})\left[\omega\mathbf{I} - (\mathbf{f}|\hat{H}|\mathbf{f})\right]^{-1}(\mathbf{f}|\hat{H}|\mathbf{a})\right\}\mathbf{C}_a = \omega\mathbf{C}_a. \tag{1.14}$$

Equation (1.14) is generally presented in the following, alternative form:

$$[\varepsilon - \Sigma(\omega)]\mathbf{C}_a = \omega\mathbf{C}_a, \tag{1.15}$$

where ε is a diagonal matrix containing Hartree–Fock canonical orbital energies as its nonzero entries and, $\Sigma(\omega)$ is known as the self-energy matrix. In actual calculations, the self-energy matrix is approximated to a certain order in the perturbation series. The order of this matrix defines the order of the electron propagator calculation. The first nonzero contribution occurs at second order, where

$$\Sigma^{(2)}_{pq}(\omega) = \sum_{a,i<j} \frac{\langle pa||ij\rangle\langle ji||aq\rangle}{\omega + \varepsilon_a - \varepsilon_i - \varepsilon_j} + \sum_{i,a<b} \frac{\langle pi||ab\rangle\langle ba||iq\rangle}{\omega + \varepsilon_i - \varepsilon_a - \varepsilon_b}. \tag{1.16}$$

Because second order is the first nonvanishing contribution, zero and first order electron propagator calculations correspond to KT results. In the diagonal, P3 self-energy, terms with three virtual indices, such as

$$\frac{1}{4}\sum_{a,i,j} \frac{\langle pa||ij\rangle}{\omega + \varepsilon_a - \varepsilon_i - \varepsilon_j} \sum_{b,c} \frac{\langle bc||qa\rangle\langle ij||bc\rangle}{\varepsilon_i + \varepsilon_j - \varepsilon_b - \varepsilon_c} + \cdots \tag{1.17}$$

occur. In OVGF calculations, a term with four virtual indices must be evaluated:

$$\frac{1}{4}\sum_{i,a,b} \frac{\langle pi||ab\rangle}{E + \varepsilon_i - \varepsilon_a - \varepsilon_b} \sum_{c,d} \frac{\langle ab||cd\rangle\langle cd||pi\rangle}{E + \varepsilon_i - \varepsilon_c - \varepsilon_d}. \tag{1.18}$$

The evaluation of such terms imposes a greater arithmetic burden than that encountered in second order calculations.

1.3 Quasiparticle Methods

Neglecting off-diagonal elements of the self-energy matrix in the canonical Hartree–Fock basis in (1.15) constitutes the quasiparticle approximation. With this approximation, the calculation of EADEs is simplified, for each KT result may be improved with many-body corrections that reside in a diagonal element of the self-energy matrix.

The quasiparticle approximation has succeeded in the description of valence ionization spectra of many systems. Recently, it has been shown that reliable results also can be obtained for core electron binding energies [26]. In this section, we will describe some recent developments that have been realized with the quasiparticle approximation.

The proposals found here can be seen as the result of a two-way strategy for the treatment of large molecules. First, we improve on the accuracy of the very efficient second order approximation. In addition, we introduce approximations that lower considerably the required computer resources for the use of higher-order approximations to the electron propagator within the quasiparticle approach.

1.3.1 Transition Operator Method

The transition operator method combined with the second-order quasiparticle electron propagator (TOEP2) may be used to calculate valence and core electron binding energies [26]. Because this approach adds relaxation corrections to second order electron propagator calculations, the accuracy of the results is consistently improved. For valence ionization energies, well known methods that include third-order terms achieve higher accuracy, but only with much more difficult computations. TOEP2 is proposed for the calculation of valence electron binding energies in large molecules where third-order methods are infeasible. For core-electron binding energies, TOEP2 results are more accurate than those obtained with the perturbative methods that have been applied extensively to valence ionization energies and electron affinities, such as P3 or OVGF [26].

Instead of the standard Hartree–Fock reference calculation, a grand-canonical Hartree–Fock calculation [35] is used with the occupation number of a single spin-orbital (i.e., the transition spin-orbital) set to 0.5. Upon convergence, appreciable corrections to the relaxation energy are included in the transition spin-orbital's energy [23, 24]. Usually a very close agreement with the ΔSCF method [36] is obtained [26]. The second order electron propagator is applied to the ensemble

reference state. After taking fractional occupation numbers into account [26,37–40], the Dyson equation in the quasiparticle approximation reads

$$\omega_p = \varepsilon_p + \sum_{a,i<j} \frac{|\langle pa||ij\rangle|^2 n_i n_j}{\omega_p + \varepsilon_a - \varepsilon_i - \varepsilon_j} + \sum_{i,a<b} \frac{|\langle pi||ab\rangle|^2}{\omega_p + \varepsilon_i - \varepsilon_a - \varepsilon_b} + \sum_{a,i} \frac{|\langle pi||pa\rangle|^2 (1 - n_p)}{\omega_p + \varepsilon_i - \varepsilon_p - \varepsilon_a}, \tag{1.19}$$

where p is the transition spin-orbital with an occupation number of 0.5. Occupation numbers are designated by n. Such calculations [26] have been performed recently with a modified version of the Gaussian 03 [36] suite of programs.

1.3.2 Reduction of Virtual Space

Electron density difference matrices that correspond to the transition energies in the EP2 approximation may be used to obtain a virtual orbital space of reduced rank [27] that introduces only minor deviations with respect to results produced with the full, original set of virtual orbitals. This quasiparticle virtual orbital selection (QVOS) process provides an improved choice of a reduced virtual space for a given EADE and can be used to speed up computations with higher order approximations, such as P3 or OVGF. Numerical tests show the superior accuracy and efficiency of this approach compared to the usual practice of omission of virtual orbitals with the highest energies [27].

For the pth EADE, the first-order, density-difference matrix in the virtual–virtual subspace [27, 29, 42], where

$$D_{ab} = \delta_{ap}\delta_{bp} - \sum_{i<j} \frac{\langle pa||ij\rangle}{(\omega_p + \varepsilon_a - \varepsilon_i - \varepsilon_j)} \frac{\langle pb||ij\rangle}{(\omega_p + \varepsilon_b - \varepsilon_i - \varepsilon_j)} + \sum_{i,c} \frac{\langle pi||ac\rangle}{(\omega_p + \varepsilon_i - \varepsilon_a - \varepsilon_c)} \frac{\langle pi||bc\rangle}{(\omega_p + \varepsilon_i - \varepsilon_b - \varepsilon_c)}, \tag{1.20}$$

is used to select an EADE-specific, reduced virtual space [27]. The computational procedure has three stages. First, an EP2 calculation is performed. In the second step, the density difference matrix of (1.20) is constructed and diagonalized. Eigenvectors that correspond to eigenvalues with the lowest absolute values are discarded and the Fock matrix is reconstructed and diagonalized in the reduced virtual orbital space. Finally, higher order calculations are performed with a new, smaller set of canonical virtual orbitals. Higher-order calculations proceed with the same algorithm as in ordinary, all-virtual calculations.

1.3.3 Resolution of Identity

RI methods also can be applied to electron propagator calculations in the quasi-particle approximation [28]. Savings in storage are dramatic. When compared to semi-direct algorithms [21, 22], the pre-factor for RI results in a considerable speed-up. The implementation is also much simpler. Test calculations with different approximations and basis sets show the reliability of this approach.

The RI approximation is based on the evaluation of individual electron repulsion integrals according to

$$(ps|qt) = \sum_{KL} (ps|K) G^{-1}_{KL} (L|qt) \tag{1.21}$$

with

$$(ps|qt) = \int\int \frac{\varphi^*_p(\mathbf{r})\varphi^*_q(\mathbf{r}')\varphi_s(\mathbf{r})\varphi_t(\mathbf{r}')}{|\mathbf{r}-\mathbf{r}'|} \mathrm{d}\mathbf{r}\,\mathrm{d}\mathbf{r}', \tag{1.22}$$

$$(ps|K) = \int\int \frac{\varphi^*_p(\mathbf{r})\varphi_s(\mathbf{r})K(\mathbf{r}')}{|\mathbf{r}-\mathbf{r}'|} \mathrm{d}\mathbf{r}\,\mathrm{d}\mathbf{r}', \tag{1.23}$$

$$G_{KL} = \int\int \frac{K(\mathbf{r}')L(\mathbf{r})}{|\mathbf{r}-\mathbf{r}'|} \mathrm{d}\mathbf{r}\,\mathrm{d}\mathbf{r}', \tag{1.24}$$

where $\varphi_p(\mathbf{r})$ is any canonical MO, and K and L are auxiliary basis functions. We have employed Cartesian Hermite Gaussian functions [43] for the auxiliary basis. The use of RI [44–48] can be seen as expansion of orbital products in terms of linear combinations of auxiliary functions.

The formulation used here corresponds to the use of RI with the Coulomb norm [47]. Although there are other formulations of the RI [48, 49], we will not use them here. Because we need the matrix $\mathbf{G}^{-1}$ only at this level of the calculation, its absorption into three-index quantities can be exploited [50] as follows:

$$T^q_{Kt} \equiv \sum_L G^{-1/2}_{KL} (L|qt). \tag{1.25}$$

Thus, four center integrals may be obtained as simple matrix multiplications of the three-index fields. This allows one to combine RI with most approximations without needing major modifications to existing algorithms and codes.

Considerable savings in storage can be made. Using RI as described here, the conventional implementation can be used, but with much less demand for disk storage. Furthermore, the transformation from atomic to MO bases can be realized for the three-index matrices with a formal gain of one order in the scaling of this task [28].

Note that the method described here does not use RI for the SCF solution of the reference system. Such an approximation would result in an approximate

description of the pole structure because the orbital energies would be affected [51]. We have not yet tested the combination of such an approximation with the approach proposed here.

If the Kohn–Sham orbitals [52] of density functional theory (DFT) [53] are used instead of Hartree–Fock orbitals in the reference state [54], the RI can become essential for the realization of electron propagator calculations. Modern implementations of Kohn–Sham DFT [55] use the variational approximation of the Coulomb potential [45,46] (which is mathematically equivalent to the RI as presented above), and four-index integrals are not used at all. A very interesting example of this combination is the use of the GW approximation [56] for molecular systems [54].

The RI can be combined with any of the methods presented here, including TOEP2 and QVOS. We do not recommend combining it with second-order approximations, such as EP2 and TOEP2, because they can be equally efficient without the RI if properly implemented.

1.4 Performance

The approximations discussed here are all ab initio. The performance of these approximations is analyzed in terms of mean absolute deviations obtained from calculations on many small molecules.

1.4.1 Transition Operator Method

Tables 1.1–1.6 show ionization energies of atoms of the second and third row of the periodic table, some valence ionization energies of molecules and a number of core electron-binding energies (CEBEs) of molecules for the 1*s* core orbital of C, N, O, and F, respectively. Comparison to experiment [57, 58] is provided in all these tables and is quantified in terms of mean absolute deviations in the last row. TOEP2 results are compared with other quasi-particle methods. In all these calculations, the transition spin-orbital occupation number was set to 0.5 electrons. The cc-pVTZ [59] basis set was used. From these tables, one may conclude that TOEP2 always improves over EP2. In Table 1.2, it is observed that for valence ionization energies of molecules, the more computationally demanding P3 and OVGF methods are clearly more accurate than TOEP2. For CEBEs, TOEP2 is the best method, being the most accurate and almost as fast as EP2.

Unlike EP2, TOEP2 is reliable enough in the calculation of valence EADEs and can be used as a very efficient alternative for the treatment of large molecular systems. For valence EADEs, the following reliability ordering is obtained:

$$\text{P3, OVGF} > \text{TOEP2} > \text{EP2} > \text{KT}.$$

Table 1.1 Ionization energies of atoms (eV)

Atom	Ionization	KT	EP2	TOEP2	P3	OVGF	Expt.[a]
Li	$^2S \rightarrow {}^1S$	5.34	5.35	5.35	5.35	5.35	5.39
Be	$^1S \rightarrow {}^2S$	8.42	8.89	8.89	8.84	9.23	9.32
B	$^2P \rightarrow {}^1S$	8.65	8.40	8.36	8.22	8.50	8.30
C	$^3P \rightarrow {}^2P$	11.91	11.30	11.25	11.10	11.35	11.26
N	$^4S \rightarrow {}^3P$	15.48	14.44	14.48	14.31	14.58	14.53
O	$^3P \rightarrow {}^4S$	14.15	12.93	13.04	13.07	13.39	13.62
F	$^2P \rightarrow {}^3P$	18.40	16.37	16.85	16.92	17.14	17.42
Ne	$^1S \rightarrow {}^2P$	23.00	20.12	21.03	21.21	21.44	21.56
Na	$^2S \rightarrow {}^1S$	4.96	4.98	4.98	4.98	5.00	5.14
Mg	$^1S \rightarrow {}^2S$	6.89	7.34	7.34	7.30	7.55	7.65
Al	$^2P \rightarrow {}^1S$	5.93	5.91	5.90	5.81	5.93	5.98
Si	$^3P \rightarrow {}^2P$	8.18	8.10	8.08	7.98	8.11	8.15
P	$^4S \rightarrow {}^3P$	10.65	10.49	10.49	10.35	10.48	10.49
S	$^3P \rightarrow {}^4S$	11.00	10.83	10.03	10.77	10.95	10.36
Cl	$^2P \rightarrow {}^3P$	13.05	12.58	12.70	12.58	12.74	12.97
Ar	$^1S \rightarrow {}^2P$	16.06	15.39	15.61	15.49	15.60	15.76
Av. $\lvert\Delta\rvert$		0.50	0.36	0.23	0.28	0.15	

[a] See [57]

Table 1.2 Valence ionization energies of molecules (eV)

Molecule	Orbital	KT	EP2	TOEP2	P3	OVGF	Expt.[a]
B_2H_6	$1b_{3g}$	12.85	12.21	12.30	12.14	12.36	11.9
CH_4	$1t_2$	14.80	14.07	14.34	14.22	14.32	14.40
C_2H_4	$1b_{3u}$	10.24	10.33	10.65	10.55	10.48	10.51
	$1b_{3g}$	13.77	12.75	13.00	12.98	13.06	12.85
	$3a_g$	15.94	14.48	14.94	14.89	14.77	14.66
	$1b_{2u}$	17.48	15.89	16.25	16.11	16.17	15.87
	$2b_{1u}$	21.52	19.34	19.69	19.44	19.61	19.23
HCN	1π	13.49	13.68	14.00	13.96	13.61	13.61
HNC	1π	14.13	13.74	14.11	14.11	14.02	12.55
NH_3	$3a_1$	11.60	10.17	10.65	10.73	10.74	10.8
N_2	$1\pi_u$	16.47	17.05	17.38	17.18	16.63	16.98
	$3\sigma_g$	17.17	15.02	15.47	15.93	15.35	15.60
	$2\sigma_u$	21.30	18.20	18.59	19.30	19.08	18.78
CO	5σ	15.09	14.06	14.13	14.27	13.85	14.01
	1π	17.28	16.37	16.88	17.04	17.07	16.91
H_2CO	$2b_2$	11.99	9.94	10.38	10.90	11.04	10.9
H_2O	$1b_1$	13.73	11.50	12.29	12.49	12.61	12.78
	$3a_1$	15.76	13.86	14.56	14.77	14.91	14.74
	$1b_2$	19.21	18.08	18.68	18.74	18.87	18.51
HF	1π	17.50	14.70	15.66	15.94	16.02	16.19
	3σ	20.68	18.94	19.64	19.84	19.84	20.00
F_2	$1\pi_g$	18.05	14.20	14.89	15.62	15.58	15.83
	$3\sigma_g$	20.46	20.46	21.06	21.04	21.00	21.1
	$1\pi_u$	22.05	17.35	18.10	18.89	19.01	18.8
Av. $\lvert\Delta\rvert$		1.17	0.62	0.36	0.25	0.25	

[a] See [9, 60] for geometry details and experimental values

Table 1.3 C 1*s* electron binding energies (eV)

Molecule	KT	EP2	TOEP2	P3	OVGF	Expt. [58]
C_2H_4	305.64	291.81	292.19	292.74	293.42	290.79
CH_4	304.92	291.59	291.15	292.35	292.94	290.86
C_2H_2	305.90	291.99	292.14	293.32	293.91	291.17
CH_3Cl	307.21	293.48	292.94	294.38	295.01	292.4
HCN	307.23	294.35	293.32	294.90	295.48	293.5
CH_3F	307.70	294.82	294.12	295.20	295.65	293.65
$HCONH_2$	308.91	296.14	294.99	296.65	296.74	294.45
H_2CO	308.54	295.97	295.31	296.35	296.57	294.47
ONCN	308.71	295.27	294.32	297.68	296.71	294.52
OCS	311.20	297.68	297.40	298.46	298.16	295.2
CO	309.11	297.97	297.33	298.24	298.02	296.13
CH_2F_2	310.26	297.84	297.05	293.93	298.16	296.40
Cl_2CO	312.20	298.26	297.36	300.46	299.84	296.75
CO_2	311.79	299.91	299.76	300.23	299.67	297.66
Av.$\lvert\Delta\rvert$	14.38	1.37	0.87	2.28	2.38	

Table 1.4 N 1*s* electron binding energies (eV)

Molecule	KT	EP2	TOEP2	P3	OVGF	Expt. [58]
HCN	424.44	406.22	406.52	409.77	410.49	406.36
ClCN	424.63	406.04	406.76	409.67	412.75	406.45
ONCN*	425.51	406.99	406.98	410.68	411.45	407.26
N*NO	427.12	408.95	409.10	412.56	412.44	408.66
N_2	426.59	409.64	409.63	412.35	412.83	409.83
ON*CN	429.76	412.18	411.19	417.89	415.74	411.05
ClNO	431.40	413.68	412.67	416.93	415.58	411.48
NN*O	431.12	413.32	414.33	416.40	416.01	412.57
NF_3	432.76	415.81	415.05	416.79	416.83	414.2
Av. $\lvert\Delta\rvert$	18.39	0.78	0.59	3.91	4.03	

*The asterisk designates the atom in which the 1*s* orbital is found

Comparison to full configuration interaction results also supports this ordering [26].

1.4.2 Reduction of Virtual Space

Table 1.7 shows quasi-particle calculations with a virtual space whose dimension has been reduced by the use of the QVOS procedure. As much as 50% of the virtual space's dimension was eliminated in these calculations, and errors of only 0.1 eV were introduced. With the larger, cc-pVQZ basis set, the errors that are introduced are smaller. In general, a larger basis set will result in a larger virtual space, and therefore, a larger reduction (in percentages) is possible. In P3 calculations on the larger molecules, benzene and borazine, similar errors were found [27].

The combination of P3 or OVGF methods with the QVOS approximation procedure ranks as follows with respect to accuracy when a 50% reduction of the virtual orbital space is performed:

Table 1.5 O 1*s* electron binding energies (eV)

Molecule	KT	EP2	TOEP2	P3	OVGF	Expt. [58]
$HCONH_2$	558.45	535.69	536.83	541.67	543.28	537.74
H_2CO	559.86	537.40	538.50	543.06	544.61	539.48
Cl_2CO	561.11	538.24	539.12	544.14	545.74	539.72
SO_2	561.12	537.74	540.54	544.79	545.86	539.84
H_2O	559.33	537.88	539.48	542.54	543.68	539.86
OCS	562.14	539.00	540.04	545.64	546.92	540.3
F_2CO	561.06	538.96	540.25	544.25	545.60	540.77
CO_2	561.89	539.44	541.40	545.50	546.66	541.19
O*OO	563.43	540.27	541.81	547.35	547.78	541.5
H_2O_2	561.32	539.44	540.92	543.97	545.12	541.8
CO	562.35	540.17	541.86	546.15	547.79	542.39
ClNO	564.78	542.06	542.45	548.13	549.53	542.65
ONCN	563.66	541.36	541.73	546.51	547.40	543.43
OF_2	566.60	545.10	545.83	548.88	549.26	545.33
OO*O	569.21	546.19	546.22	552.16	551.46	546.2
Av. $\|\Delta\|$	20.94	1.55	0.58	4.17	5.23	

*The asterisk designates the atom in which the 1*s* orbital is found

Table 1.6 F 1*s* electron binding energies (eV)

Molecule	KT	EP2	TOEP2	P3	OVGF	Expt. [58]
ClF_3(ax)[a]	715.72	689.24	692.51	697.49	699.08	692.22
CH_3F	714.87	689.71	691.68	696.33	698.16	692.66
SF_4(ax)[a]	715.88	689.87	693.04	697.55	699.14	692.88
CH_2F_2	715.88	690.82	693.54	697.36	699.10	693.65
PF_3	716.73	691.32	694.20	698.43	700.01	694.15
HF	715.30	690.74	693.20	697.16	698.64	694.18
ClF	717.12	691.34	693.06	698.55	700.25	694.44
NF_3	718.04	692.82	695.54	699.19	700.81	694.45
SiF_4	716.70	691.62	694.55	698.52	700.03	694.70
ClF_3(eq)[a]	718.99	693.41	694.80	700.18	701.47	694.76
OF_2	718.35	693.05	696.15	699.28	700.92	695.07
SF_4(eq)[a]	718.61	693.17	695.01	700.06	701.45	695.26
F_2CO	718.08	693.03	695.91	699.61	701.06	695.43
F_2	719.21	694.27	695.41	700.18	701.41	696.69
Av. $\|\Delta\|$	22.78	2.58	0.59	4.24	5.78	

[a]For the case of axial (ax) and equatorial (eq) fluorine atoms, each is evaluated separately

$$\text{P3, OVGF} > \text{QVOS-P3, QVOS-OVGF} > \text{TOEP2} > \text{EP2} > \text{KT.}$$

Retention of a larger number of virtual orbitals will improve the QVOS results with respect to the ordinary P3 and OVGF results.

Table 1.7 cc-pVTZ ionization energies (eV) with 50% virtual orbital space reduction

Molecule	Orbital	EP2	P3	OVGF	Expt.[a]
HF	1π	14.60	15.83	15.97	16.19
	3σ	18.84	19.71	19.79	20.00
N_2	$1\pi_u$	16.90	17.03	16.52	16.98
	$3\sigma_g$	14.85	15.75	15.36	15.60
	$2\sigma_u$	18.06	19.13	18.98	18.78
CO	5σ	13.99	14.15	13.76	14.01
	1π	16.26	16.90	16.98	16.91
	4σ	18.32	20.01	20.11	19.72
F_2	$1\pi_g$	14.02	15.38	15.46	15.83
	$3\sigma_g$	20.28	20.78	20.91	21.1
	$1\pi_u$	17.26	18.71	18.90	18.8
H_2O	$1b_1$	11.44	12.43	12.53	12.78
	$3a_1$	13.79	14.68	14.80	14.74
	$1b_2$	18.00	18.62	18.54	18.51
C_2H_4	$1b_{3u}$	10.30	10.52	10.42	10.51
	$1b_{3g}$	12.61	12.82	12.91	12.85
	$3a_g$	14.40	14.80	14.62	14.66
	$1b_{2u}$	15.80	16.00	16.07	15.87
	$2b_{1u}$	19.26	19.36	19.54	19.23
Av. $\lvert\Delta_{\text{exp}}\rvert$		0.74	0.18	0.20	
Av. $\lvert\Delta_{100}\rvert$		0.11	0.13	0.10[b]	

[a] See [9]

[b] When using cc-pVQZ, mean absolute deviations from the all–virtual calculations are 0.07 for EP2, 0.08 for P3 and 0.06 for OVGF

1.4.3 Resolution of the Identity

Table 1.8 shows calculated valence ionization energies in small molecules using P3 and RI-P3 (See [9,60] for geometry and reference details.). The cc-pVTZ [59] basis was employed. Auxiliary basis was automatically generated according to GEN-A2* specifications [61,62] in the deMon2k [55] program. The average absolute deviation of RI-P3 results with respect to ordinary P3 values is only 0.02 eV. This error is small compared to the errors that are inherent in the choice of typical basis sets. The RI-P3 procedure appears to be as applicable as the usual P3 method. The resulting reliability order is as follows:

$$\begin{aligned}\text{P3, OVGF} &> \text{RI-P3, RI-OVGF} > \text{QVOS-P3, QVOS-OVGF} \\ &> \text{RI-QVOS-P3, RI-QVOS-OVGF} > \text{TOEP2} > \text{EP2} > \text{KT.}\end{aligned}$$

Comparison of this conclusion with the ordering given in the introduction indicates that there are now many more options for the calculation of EADEs with quasi-particle electron propagator methods. Furthermore, the accuracy gap between EP2 and P3 or OVGF methods has been filled and better compromises for accuracy and computer resources are available for large molecules. In particular, the QVOS

Table 1.8 P3 Ionization energies (eV) calculated with and without resolution of the identity techniques

Molecule	Orbital	RI-P3	P3	Expt.[a]
B_2H_6	$1b_{3g}$	12.797	12.797	11.9
CH_4	$1t_2$	14.225	14.225	14.40
C_2H_4	$1b_{3u}$	10.567	10.552	10.51
	$1b_{3g}$	12.977	12.976	12.85
	$3a_g$	14.898	14.886	14.66
	$1b_{2u}$	16.113	16.107	15.87
	$2b_{1u}$	19.444	19.438	19.23
HCN	1π	13.968	13.955	13.61
HNC	1π	14.127	14.110	12.55
NH_3	$3a_1$	10.755	10.729	10.8
N_2	$1\pi_u$	17.203	17.183	16.98
	$3\sigma_g$	15.960	15.929	15.60
	$2\sigma_u$	19.338	19.303	18.78
CO	5σ	14.283	14.271	14.01
	1π	17.052	17.039	16.91
H_2CO	$2b_2$	10.910	10.903	10.9
H_2O	$1b_1$	12.526	12.491	12.78
	$3a_1$	14.805	14.770	14.74
	$1b_2$	18.766	18.741	18.51
HF	1π	15.978	15.935	16.19
	3σ	19.872	19.836	20.00
F_2	$1\pi_g$	15.641	15.619	15.83
	$3\sigma_g$	21.059	21.036	21.1
	$1\pi_u$	18.908	18.886	18.8
Av. $\lvert\Delta\rvert$		0.281	0.278	

[a] See [9, 60] for geometry and reference details

procedure can be tuned for speed or reliability depending on the dimension of the reduced virtual orbital space.

1.5 Conclusions

Judicious use of the approximations discussed here has the potential to facilitate accurate quasiparticle calculations on molecular systems of unprecedented size. These techniques provide a number of new options for the calculation of EADEs with advantageous compromises between computational cost and reliability.

TOEP2 can be used effectively for larger systems. Its errors are smaller than those of EP2, but the corresponding algorithms have very similar arithmetic and storage demands. TOEP2 is relatively easy to implement. However, special care must be taken in the procurement of the reference orbitals [26].

Reduction of the virtual orbital space with the QVOS procedure enables calculations with accurate methods, such as P3 and OVGF, at much less cost without jeopardizing the quality of the calculations. A reduction of the rank of the virtual

orbital space by 50% leads to deviations of about 0.1 eV with respect to calculations that employ the full set of virtual orbitals. Such errors are less than those that are usually inherent in the choice of an atomic basis set. Arithmetic operation and data storage requirements for results of a given quality may be substantially diminished by the QVOS procedure.

The use of RI is another practical way to realize calculations on larger systems. Dramatic reduction of disk requirements and improved efficiency can be achieved.

The approximations discussed here are based on FORTRAN code that communicates with the Gaussian 03 [36] suite of programs and the Kohn–Sham DFT program deMon2k [55]. These programs have been used for a large number of molecules. The mean absolute deviations presented in the tables illustrate the reliability of these techniques.

Acknowledgments The National Science Foundation (USA) provided support for this research through grant CHE-0451810 to Auburn University. R.F.-M. would like to thank CONACyT (México) for postdoctoral funding at the University of Guanajuato, and the Mexican National System of Researchers (Sistema Nacional de Investigadores) for support.

References

1. J. Linderberg, Y. Öhrn, *Propagators in Quantum Chemistry*, 2nd edn. (Wiley, Hoboken, 2004)
2. B.T. Pickup, O. Goscinski, Direct calculation of ionization energies. Mol. Phys. **26**, 1013–1035 (1973)
3. Y. Öhrn, G. Born, Molecular electron propagator theory and calculations. Adv. Quantum Chem. **13**, 1–88 (1981)
4. J.V. Ortiz, Toward an exact one-electron picture of chemical bonding. Adv. Quantum Chem. **35**, 33–52 (1999)
5. L.S. Cederbaum, W. Domcke, Theoretical aspects of ionization potentials of photoelectron spectroscopy: A many-body approach, Adv. Chem. Phys. **36**, 205–344 (1977)
6. W. von Niessen et al., Computational methods for the one-particle Green's function. Comp. Phys. Rep. **1**, 57–125 (1984)
7. J. Simons, in Theoretical Studies of Negative Molecular Ions, ed. by H. Eyring and D. Henderson *Theoretical Chemistry: Advances and Perspectives*, Vol. 3 (Academic, New York, 1978)
8. M.F. Herman et al., Theoretical studies of the equations of motion – Green's function methods and configuration interaction methods: Analysis of methods and applications. Adv. Chem. Phys. **48**, 1–69 (1981)
9. J.V. Ortiz, Partial third order quasiparticle theory: Comparisons for closed-shell ionization energies and an application to the borazine photoelectron spectrum. J. Chem. Phys. **104**, 7599–7605 (1996)
10. A.M. Ferreira et al., in Application and Testing of Diagonal, Partial Third-Order Electron Propagator Approximations, ed. by J. Cioslowski *Understanding Chemical Reactivity*, Vol. 22, Quantum–Mechanical Prediction of Thermochemical Data (Kluwer, Dordrecht, 2001), pp. 131–160
11. J.V. Ortiz, in The electron propagator picture of molecular electronic structure, ed. by J. Leszczynski *Computational Chemistry: Reviews of Current Trends*, Vol. 2 (World Scientific, Singapore, 1997), pp. 1–61
12. V.V. Zakjevskii et al., Base and phosphate electron detachment energies of deoxyribonucleotide anions. J. Am. Chem. Soc. **128**, 13350–13351 (2006)

13. V.V. Zakjevskii et al., Electron propagator studies of vertical electron detachment energies and isomerism in purinic deoxyribonucleotides. Int. J. Quantum Chem. **107**, 2266–2273 (2007)
14. O. Dolgounitcheva et al., Electron propagator calculations show that alkyl substituents alter porphyrin ionization energies. J. Am. Chem. Soc. **127**, 8240–8241 (2005)
15. O. Dolgounitcheva et al., Ab initio electron propagator calculations on the ionization energies of free base porphyrin, magnesium porphyrin and zinc porphyrin. J. Phys. Chem. **109**, 11596–11601 (2005)
16. J.V. Ortiz et al., in One-Electron Pictures of Electronic Structure: Propagator Calculations on Photoelectron Spectra of Aromatic Molecules, ed. by J.-L. Calais, E. Kryachko *Conceptual Perspectives in Quantum Chemistry*, Vol. 3 (Kluwer, Dordrecht, 1997), pp. 465–517
17. C.C.J. Roothaan, Self-consistent field theory for open-shells of electronic systems. Rev. Mod. Phys. **32**, 179–185 (1960)
18. G.G. Hall, The molecular orbital theory of chemical valency. VIII-A method of calculating ionization potentials. Proc. Roy. Soc. Ser. A **205**, 541–552 (1951)
19. D.R. Hartree, *The Calculation of Atomic Structures*. (Wiley, London, 1957)
20. V.A. Fock, Näherungsmethode zur Lösung des quantenmechanischen Mehrkörperproblems. Z. Phys. **61**, 126–148 (1930)
21. V.G. Zakrzewski, J.V. Ortiz, Semidirect algorithms in electron propagator calculations. Int. J. Quantum Chem. Symp. **28**, 23–27 (1994)
22. V.G. Zakrzewski, J.V. Ortiz, Semidirect algorithms for third order electron propagator calculations. Int. J. Quantum Chem. **53**, 583–590 (1995)
23. J.C. Slater, J.H. Wood, Statistical exchange and the total energy of a crystal. Int. J. Quantum Chem. (Suppl.) **4**, 3–34 (1971)
24. J.C. Slater, Statistical exchange-correlation in the self-consistent field. Adv. Quantum Chem. **6**, 1–91 (1972)
25. J.F. Janak, Proof that $\partial E/\partial n_i = \varepsilon_i$ in density-functional theory. Phys. Rev. B **18**, 7165–7168 (1978)
26. R. Flores-Moreno et al., Assessment of transition operator reference states in electron propagator calculations. J. Chem. Phys. **127**, 134106/1–8 (2007)
27. R. Flores-Moreno, J.V. Ortiz, Quasiparticle virtual orbitals in electron propagator calculations, J. Chem. Phys. **128**, 164105/1–6 (2008)
28. R. Flores-Moreno, J.V. Ortiz, Resolution of the identity for electron propagator calculations. unpublished results.
29. J.V. Ortiz, Energy gradients and effective density differences in electron propagator theory. J. Chem. Phys. **112**, 56–68 (2000)
30. P.-O. Löwdin, Studies in perturbation theory. IX. Connection between various approaches in the recent development-evaluation of upper bounds to energy eigenvalues in Schrödinger's perturbation theory. J. Math. Phys. **6**, 1341–1353 (1965)
31. C. Møller, M.S. Plesset, Note on an approximation treatment for many-electron systems. Phys. Rev. **46**, 618–622 (1934)
32. P.-O. Löwdin, Studies in perturbation theory. X. Lower bounds to energy eigenvalues in perturbation-theory ground state. Phys. Rev. **139**, A357–A372 (1965)
33. J.V. Ortiz, Improved electron propagator methods: An investigation of C_4, C_4^-, and C_4^+. J. Chem. Phys. **99**, 6716–6726 (1993)
34. J. Baker, B.T. Pickup, A molecular method for ionization potentials. Chem. Phys. Lett. **76**, 537–541 (1980)
35. S.F. Abdulnur et al., Atomic central-field models for open shells with application to transition metals. Phys. Rev. A **6**, 889–898 (1972)
36. P. Bagus, Self-consistent-field wave functions for hole states of some Ne-like and Ar-like ions. Phys. Rev. **139**, A619–634 (1965)
37. G.D. Purvis, Y. Öhrn, The transition state, the electron propagator, and the equation of motion method. J. Chem. Phys. **65**, 917–922 (1976)
38. G. Born et al., Elementary finite order perturbation theory for vertical ionization energies. J. Chem. Phys. **68**, 74–85 (1978)

39. G. Born et al., On the calculation of electron binding energies. J. Chem. Phys. **69**, 1162–1167 (1978)
40. J.V. Ortiz et al., Electron propagator calculations with a transition operator reference state. Chem. Phys. Lett. **103**, 29–34 (1983)
36. M.J. Frisch et al., *Gaussian 2003* (Gaussian, Inc., Pittsburgh, PA, 2003)
42. J. Cioslowski, J.V. Ortiz, One-electron density matrices and energy gradients in second-order electron propagator theory. J. Chem. Phys. **96**, 8379–8389 (1992)
43. A. Köster, Hermite gaussian auxiliary functions for the variational fitting of the Coulomb potential in density functional methods. J. Chem. Phys. **118**, 9943–9951 (2003)
44. N.H.F. Beebe, J. Linderberg, Simplifications in the generation and transformation of two-electron integrals in molecular calculations. Int. J. Quantum Chem. **12**, 683–705 (1977)
45. B.I. Dunlap et al., On some approximations in applications of Xα theory. J. Chem. Phys. **71**, 3396–3402 (1979)
46. J.W. Mintmire, B.I. Dunlap, Fitting the Coulomb potential variationally in linear-combination-of-atomic-orbitals density-functional calculations. Phys. Rev. A **25**, 88–95 (1982)
47. O. Vahtras et al., Integral approximations for LCAO-SCF calculations. Chem. Phys. Lett. **213**, 514–518 (1993)
48. E.J. Baerends et al., Self-consistent molecular Hartree–Fock–Slater calculations I. The computational procedure. Chem. Phys. **2**, 41–51 (1973)
49. C.-K. Skylaris et al., On the resolution of identity Coulomb energy approximation in density functional theory. J. Mol. Struct.: Theochem. **501**, 229–239 (2000)
50. A.P. Rendell, T.J. Lee, Coupled-cluster theory employing approximate integrals: An approach to avoid the input/output and storage bottlenecks. J. Chem. Phys. **101**, 400–408 (1994)
51. S. Hamel et al., Assessment of the quality of orbital energies in resolution-of-the-identity Hartree–Fock calculations using deMon auxiliary basis sets. J. Chem. Phys. **114**, 7342–7350 (2001)
52. W. Kohn, L.J. Sham, Quantum density oscillations in an inhomogeneous electron gas. Phys. Rev. **137**, A1697–A1705 (1965)
53. P. Hohenberg, W. Kohn, Inhomogeneous electron gas. Phys. Rev. **136**, B864–B871 (1964)
54. Y. Shigeta et al., Electron propagator calculations with Kohn–Sham reference states. Int. J. Quantum. Chem. **85**, 411–420 (2001)
55. A.M. Köster et al., deMon developers, (2006), http://www.demon-software.com
56. L. Hedin, New method for calculating the one-particle Green's function with application to the electron-gas problem. Phys. Rev. **139**, A796–A823 (1965)
57. Ionization potentials for atoms were taken from NIST tables (2007), http://physics.nist.gov/PhysRefData/IonEnergy/tblNew.html
58. W.L. Jolly et al., Core-electron binding energies for gaseous atoms and molecules. At. Data Nucl. Data Tables **31**, 433–493 (1984)
59. T.H. Dunning, Gaussian basis sets for use in correlated molecular calculations. I. The atoms boron through neon and hydrogen. J. Chem. Phys. **90**, 1007–1023 (1989)
60. R.C. Morrison, G. Liu, Extended Koopmans' theorem: Approximate ionization energies from MSCF wave functions. J. Comput. Chem. **13**, 1004–1010 (1992)
61. P. Calaminici et al., A density functional study of structures and vibrations of Ta_3O and Ta_3O^-. Comput. Lett. **1**, 164–171 (2005)
62. P. Calaminici et al., Density functional theory optimized basis sets for gradient corrected functionals: 3d transition metal systems. J. Chem. Phys. **126**, 044108/1–10 (2007)

Chapter 2
Properties of Excited States of Molecules in Solution Described with Continuum Solvation Models

R. Cammi, C. Cappelli, B. Mennucci, and J. Tomasi

Abstract The computational study of excited states of molecular systems in the condensed phase implies additional complications with respect to analogous studies on isolated molecules. Some of them can be faced by a computational modeling based on a continuum (i.e., implicit) description of the solvent. Among this class of methods, the polarizable continuum model (PCM) has widely been used in its basic formulation to study ground state properties of molecular solutes. The consideration of molecular properties of excited states has led to the elaboration of numerous additional features not present in the PCM basic version. Nonequilibrium effects, state-specific versus linear response quantum mechanical description, analytical gradients, and electronic coupling between solvated chromophores are reviewed in the present contribution. The presentation of some selected computational results shows the potentialities of the approach.

2.1 Introduction

We shall present in this contribution to the Annals a survey of some recent advancements in the description of the properties of molecules in solution obtained by using a continuum representation of the solvent [1]. The exposition will be kept at a relatively low formal level, our intention being to give a contribution not addressed to specialists in the field. In this introduction, we will report some comments to make the understanding of the approach easier.

There is no need to recall the role of properties of electronic excited states in chemistry, biology, material science, and other scientific fields, but it is worth remarking that in all the above quoted disciplines, what really matters is to gain detailed and reliable descriptions of the phenomena under scrutiny for material systems of considerable complexity, which are usually not isolated but interacting with a surrounding medium.

R. Cammi[1] (✉), C. Cappelli[2], B. Mennucci[2], and J. Tomasi[2]
[1]Dipartimento di Chimica G.I.A.F, Università di Parma, Parco Area delle Scienze, I-43100, Parma, Italy; [2]Dipartimento di Chimica e Chimica Industriale, Università di Pisa, Via Risorgimento 35, I-56126 Pisa, Italy
e-mail: chifi@unipr.it

J. Leszczynski and M.K. Shukla (eds.), *Practical Aspects of Computational Chemistry*,
DOI 10.1007/978-90-481-2687-3_2,

The complexity of the problem rules out the most advanced computational models elaborated by theoreticians as their computational cost is too high. A balance between accuracy and computational cost must be found, and this is made even more difficult by the need of describing at a comparable degree of accuracy, the ground and excited states, allowing in both cases, geometry optimizations and potential energy scans. In this contribution, our approach to these problems is reported, although this is a subject for which computational improvements are possible.

The remark on the medium opens the way to other problems. In the title of the contribution, we have indicated "continuum solvent models" as keyword, but this expression is too generic and it is worth to make more comments.

Solvation models were originally conceived for a single solute molecule in a homogeneous solvent, simply addressing solvation energy in the ground electronic state. Discrete and continuum models were possible, and both were implemented. The discrete models require a thermodynamic average of the solvent molecules, and this is done with Monte Carlo (MC) and molecular dynamics (MD) simulations. Continuum models do not need such an averaging.

As we are interested in problems in which different electronic states play a role, attention must be limited to models in which at least the solute is described at the quantum level.

This restriction rules out all discrete models exclusively based on semiempirical force fields, leaving among the discrete models the MC/QM and the MD/QM procedures, in which the second part of the acronyms indicates that the solute is described at the quantum mechanical (QM) level, as well as the full ab initio MD description, and some mixed procedures that derive the position of some solvent molecules from semiclassical simulations, replace the semiclassical description with the QM one, and repeat the calculation on these small supermolecular clusters. The final stage is to perform an average on the results obtained with these clusters. These methods can be used also to describe electronic excitation processes, but at present, their use is limited to simple cases, such as vertical excitations of organic molecules of small or moderate size. This limitation is due to the cost of computations, and there is a progressive trend toward calculations for larger systems.

Continuum models do not suffer from these limitations and the cost of calculations is similar to that experienced for isolated molecules, and all the levels of ab initio QM calculations are in principle accessible.

This feature of the continuum solvation approach is present in several widely distributed computational codes. We shall, however, make reference in the following portion to the codes we have developed, collectively indicated with the acronym PCM (polarizable continuum model), because we have used PCM in the calculations reported in the following section and as PCM contains the richest collection of procedures useful for the study of photophysical and photochemical phenomena [1].

PCM originated as a method to describe solvent effects on ground state molecules [2], but the extension to excited states was realized only after the original presentation, with a model [3], which introduced nonequilibrium effects in the solvent response for the optical processes of photon absorption and emission. The nonequilibrium solvation regime has later been applied to vibrational spectroscopies

(IR, Raman and related phenomena) to describe with a static approach the salient aspects of phenomena, which are essentially of a dynamical nature [1]. This regime was later shown to be essential for a correct description of the photophysical phenomena. It introduces in the QM formalism aspects that are not present in the standard formulation, particularly, that the excited states activated by the excitation process are not orthogonal to the fundamental one (a similar effect is present in the emission process). The orthogonality among states is a basic tenet of the standard formulation, and the selection rules are based on this property. The description obtained with this model is more realistic than the standard one, when the chromophore is immersed into a responsive medium. Discrete solvent simulation methods could hardly describe these effects.

Other features of PCM deserve a mention, having been employed in photophysical studies and being subjects of forthcoming developments of the model.

Photophysical phenomena can occur in isotropic liquid media, but analogous phenomena occurring in media not amenable to a uniform infinite fluid are of analogous, and perhaps of larger interest. Let us rapidly present some cases.

Molecules at the surface of a liquid, confined in capillary pores, and at the surfaces of a massive body all share the characteristics of having the solvent molecules immediately near to the chromophore in an averaged distribution differing from that of the bulk liquid. These local nonhomogeneities influence some properties of the system, including the spectral properties. We have tested the description of the local nonhomogeneity introduced in PCM with fairly good results, which have opened the possibility of studying a large number of interesting phenomena [4–8].

When the phase boundary of a liquid is given by a metal, other phenomena occur. We have so far examined the case of specimens with the metal in a nanoparticle aggregation, with the opportune morphology of the metal subsystem (noble metals are more appropriate): Surface enhancement effects on the spectroscopic property of a chromophore have been evidenced, in agreement with the available experimental findings (especially for SERS, but also for other spectroscopic signals) [9]. In some experiments of this type, the metal is covered by a substance with a dielectric response differing from that of the bulk liquid, Which has also been introduced in PCM [9].

Much work on these composite systems has to be done, For example, we have not considered yet the study of phenomena occurring at the surface of an electrified metal; the version of PCM for ionic solutions [10] has been available for a long-time, but the modeling of the electric double layer has not been done yet (every new modeling requires considerable intellectual and computational efforts).

Above, we have rapidly presented a few types of applications of continuum solvent models to the study of phenomena involving molecular excited states. Others could be mentioned as the case of chromophore inserted into a polymeric matrix or in organic crystals and the case of liquid systems experiencing a large external pressure. These are cases for which the computational version of PCM has been elaborated and tested [1, 11, 12], but many other phenomena have not been considered yet. There are big expectations for the future, and we are confident that within few years, the collective efforts of the laboratories working on these

subjects will considerably extend the number of phenomena for which an accurate QM description is possible.

The examples shown in this chapter are a partial testimony of the state-of-the-art in a field that progresses quite rapidly.

2.2 The Basic PCM

As reported in the Introduction, the basic PCM model has been proposed for describing solvent effects on molecules in the ground state. More specifically, the basic model has the following characteristics [1]:

1. The molecular solute is described at the QM level.
2. The solute–solvent interactions are limited to those of electrostatic origin.
3. The model system is composed by a single solute molecule.
4. The solvent is described as an isotropic polarizable dielectric medium at equilibrium at a given pressure and temperature.
5. Only the electronic ground state of the solute is considered.
6. No dynamical effects are considered in the basic models.

The essence of the basic model is then to describe the process of mutual solute–solvent interaction, and to extract from the final solute wavefunction, all the information regarding solvent effects.

The mutual polarization process between the solute and the polarizable medium is obtained by solving a system of two coupled equations, i.e., the QM Schrödinger equation for the solute in presence of the polarized dielectric, and the electrostatic Poisson equation for the dielectric medium in presence of the charge distribution (electrons and nuclei) of the solute. The solute occupies a molecular shaped cavity within the dielectric continuum, whose polarization is represented by an apparent surface charge (ASC) density spread on the cavity surface. The solute–solvent interaction is then represented by a QM operator, the solvent reaction potential operator, $\hat{V}_\sigma$, corresponding to the electrostatic interaction of the solute electrons and nuclei with the ASC density of the solvent.

In the computational practice, the ASC density is discretized into a collection of point charges $\{q_k\}$, spread on the cavity surface. The apparent charges are then determined by solving the electrostatic Poisson equation using a Boundary Element Method scheme (BEM) [1]. Many BEM schemes have been proposed, being the most general one known as integral equation formalism (IEFPCM) [10].

The PCM basic energetic quantity is directly connected with the solvation free energy of the solute, and it is given by the following free energy functional:

$$\mathcal{G} = \langle \Psi \left| \hat{H}^0 + \hat{V}_\sigma \right| \Psi \rangle - \frac{1}{2} \langle \Psi \left| \hat{V}_\sigma \right| \Psi \rangle \tag{2.1}$$

where $\hat{H}^0$ is the Hamiltonian for the isolated system. This specific functional form of $\mathcal{G}$ takes into account the nonlinearity of the quantum chemical problem, since the solute–solvent interaction operator V_σ depends on the electronic charge distribution of the solvent. The wavefunction of the solute is obtained by solving the following effective Schrödinger equation:

$$\hat{H}_{\text{eff}} |\Psi\rangle = \left[\hat{H}^0 + \hat{V}_\sigma\right] |\Psi\rangle = E^{\text{GS}} |\Psi\rangle \tag{2.2}$$

where H_{eff} is the effective Hamiltonian for the solute, and $|\Psi\rangle$ is the ground state wavefunction, containing all the relevant information about the solvent effect on the solute.

2.3 The PCM for Excited States

To apply the PCM model to the description of excited electronic states and processes of molecules in solution, several extensions have to be introduced into the basic model, in particular the accounting of dynamical effects and a proper QM evaluation of the excited electronic state. These extensions will be described in the following subsections.

2.3.1 Equilibrium vs. Nonequilibrium Solvation

In this section, we will describe the extension of the basic model necessary to properly describe the dynamically different solute–solvent interaction regimes, which can arise in processes involving excited electronic states [1].

The presence of different solvation regimes is due to the time dependence of the solvent polarization response to sudden changes ($\approx 10^{-13}$ s) in the solute charge distribution. In most cases, the solvent polarization response may be decomposed into two terms, one describing a fast (electronic) response and the other a slow (orientational) response. Here, fast indicates the part of the solvent response that is instantaneously equilibrated to the dynamical change of the solute charge distribution, while the slow refers to the remaining inertial component.

Such a splitting in the medium response gives rise to the so-called nonequilibrium solvation regime. In the case of a vertical electronic transition (from the GS to an excited state for absorption, or from an excited state to the GS for emission), the arrival state feels a nonequilibrium solvation regime as the characteristic time of the electronic transition is much shorter than the response time of the inertial components of the solvent, *and this component remains equilibrated with the initial electronic state*. The arrival state reaches an equilibrium solvation regime only if its life time is enough to allow for a complete relaxation of the slow (inertial) polarization of the solvent.

By using such a partition of the polarization, the free energy of the vertical excited state, $\mathcal{G}_{\mathrm{K}}^{\mathrm{neq}}$, can be obtained. The vertical transition energy K may then be obtained by subtracting the ground state free energy $\mathcal{G}_{\mathrm{GS}}$ to $\mathcal{G}_{\mathrm{K}}^{\mathrm{neq}}$. In the computational practice, it is convenient to consider the vertical excitation as a two-step process, in which the first step corresponds to a hypothetic vertical excitation in presence of the frozen ground state solvent polarization, while the second step corresponds to the relaxation of the solvent polarization.

At a given computational level, the solvent relaxation contribution to the excitation energy may be approximated by using two basically different methods, the state-specific method (SS) and the linear response method (LR), depending on the QM methodology used. This directly involves the problem of extending the PCM basic model to a QM description proper for excited states.

2.3.2 *The QM Description of the Excited States: State Specific vs. LR*

The SS approach uses a different effective Hamiltonian $\hat{H}_{\mathrm{eff}}$ (2.2) for each electronic excited state by calculating $\hat{V}_\sigma$ with the corresponding electron density (i.e., density matrix). The nonlinear character of $\hat{V}_\sigma$ is solved through an iterative procedure [13, 14], in which at each iteration, the solvent-induced component of the effective Hamiltonian is computed with the apparent charges determined from the standard ASC-BEM equation by exploiting the first order density matrix of the preceding step.

By contrast, the alternative PCM-LR approach [15–17] determines in a single step calculation the excitation energies for a whole manifold of excited states. This general theory may be combined with the Time-Dependent Density Functional Theory (TDDFT) as QM level for the solute. Within the PCM-TDDFT formalism, the excitation energies are obtained by proper diagonalization of the free energy functional Hessian.

The difference between the SS and LR approaches can be analyzed in terms of the two-step process introduced in the previous section [18, 19] to model the excitation process of solvated systems. The two approaches equally describe the first step, in which the solvent degrees of freedom are frozen. However the two theories diverge in the second step of the excitation process, in which the fast degrees of freedom of the solvent rearrange to equilibrate with the charge density of the solute excited state; in fact, the energy variation accompanying this relaxation is not explicitly accounted for in the LR framework. Instead, LR accounts for a correction which, originating from dynamic solute–solvent interactions, might be classified as a part of the dispersion interaction. However, we can obtain the first-order approximation to the State Specific free energy of the excited state by using a LR scheme. This is what we have called "corrected" Linear Response approach (cLR) in previous chapters [20]. The same scheme has been successively generalized to include higher order effects [21].

2.3.3 Excited State Properties Calculated as Energy Analytical Gradients

A further extension of the PCM basic model to treat excited states considers the calculation of their properties. A basic result of the QM shows that first order properties of isolated molecules can be expressed as derivatives of the energy with respect to a proper perturbation. The same statement can be generalized to molecules in solution, considering the derivatives of the basic energetic functional ($\mathcal{G}_{\mathcal{K}}$). Within this scheme, the properties of excited states may be evaluated for both the QM approaches described in the previous section, i.e., SS and LR. Here, we will focus on the evaluation of the properties by using the PCM-LR approach.

Within the PCM-LR method, the free energy gradient of the excited states is computed as sum of two derivative contributions. The first contribution is the derivative of the free energy of the reference state (usually the ground state) [22], from which excited states are activated by the excitation process. The second contribution is the derivative of the excitation vertical energy. The evaluation of analytical derivatives of the PCM-TDDFT excitation energy ω with respect to the generic parameter ξ (e.g., a nuclear coordinate) has been proposed by Scalmani et al. [23], as a generalization of the analogous derivative for the PCM-CIS excitation energies [24].

The geometrical derivatives of the PCM-TDDFT excitation energy of a given excited state can be used to obtain the equilibrium geometry of that state. From this equilibrium geometry the excited state can reach the ground state by a vertical emission process whose emission energy can be determined by a proper application of the non-equilibrium scheme presented in the previous section.

2.3.4 Electronic Coupling Between Chromophores in Solution

In this section, we will consider the extension of the basic PCM to describe the process of excitation energy transfer from a solvated chromophore (the donor, D) to another chromophore (the acceptor, A). This transfer process is known as "electronic energy transfer" (EET), and has extensively been studied as it plays a key role in the light energy capture and conversion, both in natural and artificial systems [25].

The dynamics of the EET process is expressed in terms of a rate constant, k, which depends on several factors: spectral properties of the D/A molecules, electron coupling between them, and the account of the screening effect of the solvent as a dielectric medium. In the so called weak coupling regime, the rate constant is predicted by the following Förster equation:

$$k = \frac{2\pi}{\hbar}|sV_s|^2 J \tag{2.3}$$

where J is a parameter depending on the spectral properties of D and A, the electronic coupling between the D/A is V_s and s is the solvent screening. Recently, the

PCM method has been extended to compute both the electronic coupling V_s and the screening factor s.

This extension of the PCM is described in detail in [26]. Here, it is sufficient to say that such an extension is an application of a nonequilibrium scheme within a QM perturbative linear response (PCM-LR) approach. The total electronic coupling, V_{total}, is obtained as a sum of two terms, the direct (or Coulombic-exchange) coupling, implicitly modified by the medium (V_s), and the contribution involving the explicit solvent effect (V_{explicit}):

$$V_{\text{tot}} = V_s + V_{\text{explicit}} \tag{2.4}$$

The effect of the medium denoted here as *implicit* reflects the influence of the solvent on the transition densities (i.e., spectral properties) of the D/A units, which determine the direct coupling V_s. The solvent explicitly enters into the definition of the coupling through the term V_{explicit} in (2.4), which describes an interaction between the two chromophores mediated by the medium, that generally leads to an overall reduction (i.e., a *screening*) of the D/A coupling.

Within this framework, the solvent screening factor in Förster's model can be obtained as ratio between the total coupling and the direct coupling $s = V_{\text{tot}}/V_s$.

The perturbative IEFPCM-LR model has been applied to study EET between molecules in liquid solutions [26–28] and at liquid/gas interfaces [29], and to the exciton splitting in conjugated molecular materials [30].

2.4 Numerical Examples

Limitations of space prompt us to reduce the display of numerical applications. Our selection of examples is focused on two cases: (1) the absorption/emission of solvated chromophores and (2) the energy transfer between chromophores in homogeneous and heterogeneous environment. In both cases, the emphasis will be on the analysis of the effects of the environment on each process with clear connections to theoretical and modelistic aspects discussed in the previous section. The details of the calculations will be omitted as they can be found in the quoted literature.

2.4.1 Absorption/Emission in Homogeneous and Heterogeneous Environments

Here, we summarize a recent study we have done on the effect of the environment on the electronic absorption and emission of 6-Propionyl-2-(*N*,*N*-dimethyl)aminonaphthalene (PRODAN) [8]. This system has widely been used as a fluorescence probe since it was introduced by Weber and Farris [31]. The effect of polar solvents on the absorption and more effectively, on the fluorescence spectra of PRODAN is large,

Table 2.1 Absorption and emission energies (eV) calculated at TDB3LYP/6-31+G(d,p) level in cyclohexane, acetonitrile and water

	Cyclohexane		Acetonitrile		Water	
	Abs	Emis	Abs	Emis	Abs	Emis
Exp.	3.62	3.18	3.51 (−0.11)	2.71 (−0.47)	3.46 (−0.16)	2.36 (−0.82)
PCM	3.35	3.09	3.26 (−0.09)	2.79 (−0.30)	3.26 (−0.09)	2.77 (−0.32)

For acetonitrile and water shifts with respect to cyclohexane are also reported in parentheses. The reported experimental data are taken from [34]

leading to significant shifts of the main bands: The experimental solvatochromic shift passing from cyclohexane to water is 1260 cm^{-1} for absorption and 6620 cm^{-1} for emission. Due to this large sensitivity to solvation, PRODAN has also been employed to probe the microenvironment in experiments on biomembranes, vesicles and reverse micelles [32–35].

Observed absorption and emission bands are assigned to transitions involving an intramolecular charge transfer corresponding to a $\pi \rightarrow \pi^*$ transition, in which the electronic charge density moves from the amino group toward the propionyl group through the whole central naphthalene structure.

In Table 2.1, we report the absorption and emission energies in cyclohexane, acetonitrile and water computed at TDB3LYP/6-31+G(d,p) level. All values have been obtained reoptimizing the geometries in each solvent and performing single point calculations by using the cLR formalism described in the previous section [20] as implemented in a local version of the Gaussian code [36]. We recall that for polar solvents, the transition energies have been calculated assuming a nonequilibrium solvation.

Before analyzing the agreement of PCM results with experiments, we would like to comment about the higher solvent sensitivity of emission energies with respect to absorption energies. This is a interesting consequence of nonequilibrium solvation. In fact, the ground state (S_0) will be differently stabilized by the apolar and the polar solvent. On excitation, a large dipole moment appears due to the charge transfer character of the excited state (S_1); this should induce a larger stabilization in the polar solvent with respect to the apolar one. However, this effect is reduced due to the nonequilibrium solvation in the polar solvent. Only when we let the polar solvent to completely relax, the different stabilization of S_1 in the two solvents becomes evident (the energy change from the vertical nonequilibrium to the completely relaxed state is the well-known reorganization energy). It is in this new equilibrium situation that the emission takes place, immediately after the transition; however, only in the case of cyclohexane, we have completely recovered the initial picture, while in water, a new nonequilibrium (this time on the S_0 potential energy surface) is reached. The combination of the different solvation in the equilibrated S_1 and the vertical S_0 in cyclohexane and water gives origin to the calculated red shift in the emission energy, which is more than three times larger than what found in the absorption.

Moving now to the comparison with experiments, it is more correct to analyze the solvent induced shifts instead of the absolute energies; in such a way, the analysis

Table 2.2 Absorption and emission data of PRODAN+2water in gas-phase and bulkwater

	Abs	Emis
Exp	3.46 (−0.16)	2.36 (−0.82)
Gas	3.39 (+0.04)	3.02 (−0.07)
PCM	3.13 (−0.22)	2.61 (−0.48)

Transition energies are in eV and in parentheses the shift with respect to the cyclohexane is shown

is not significantly affected by the possible intrinsic error due to the QM level. From Table 2.1, we see that PCM calculations lead to a red shift of the absorption energies with increasing solvent polarity. This correctly reproduces the observed behavior. Also for emission, PCM provides a correct description of the red-shift. The calculated shift for acetonitrile well correlates with experiments, even though the agreement is worse than for absorption. The different quality in the description of absorption and emission energies can be related to the lower accuracy of TDDFT in describing excited states with respect to DFT in describing ground states.

A final general comment about the PCM data is that, even though they correctly reproduce the observed shifts in the various solvents, the results in acetonitrile and in water give very similar results while experiments show a further red-shift moving from the first to the second, which can be explained in terms of a missing effect (e.g., hydrogen bonding) in the PCM description of water. PRODAN can in fact form H-bonds with water molecules. In order to properly account for such a specific effect, a good strategy is to introduce a "solvated supermolecule". This means to extend the concept of "solute" to PRODAN plus few H-bonded water molecules (i.e., those belonging to the first solvent shell) and to embed such a system within an external PCM continuum so to keep the effects of the outer shells (i.e., the so-called bulk effect) [37–39]. The results obtained using such a strategy are reported in Table 2.2.

The first result to comment about is the evidently different description obtained for the isolated and the solvated supermolecules. In absorption, the result obtained in the isolated supermolecule is even blue-shifted with respect to cyclohexane, while in emission, the red-shift is recovered, but is very small. Only by adding the effect of the bulk with the PCM, the correct behavior is obtained with a net red-shift both in absorption and emission. On the emission, however, the correction introduced with the two explicit water molecules is not sufficient to get a real quantitative agreement with the experiments. Once again, a possible source of inaccuracy is the TDB3LYP description of the excited state geometry, which is here complicated by the presence of the H-bonded water molecules.

We consider now the changes in PRODAN absorption and emission energies when immersed in heterogeneous environments, such as unilamellar vesicles and other membranes' mimickers. This analysis is obtained using, the extension of the IEFPCM to gas–liquid and liquid–liquid interfaces developed in our group [4–7]. Within this framework, the interface is modeled in terms of static (and dynamic) permittivity varying smoothly in the interfacial region. The use of such a diffuse region, whose width can be tuned, allows the method to better mimic the changes

in the dielectric properties of the bilayer representing the unilamellar vesicles. The bulk permittivities used to represent the partition of PRODAN between vesicles and water are those of cyclohexane and water.

A parameter to fix in the calculation at interfaces is the molecular orientation and position with respect to the interface. Different orientations have been tested, among which the most stable one is the one in which both polar heads of the molecule are within the diffuse region (see Fig. 2.1). Such an orientation presents a high sensitivity to different entrance directions due to the vicinity of the propionyl group to the interface: Apparently the situation in which PRODAN enters in water with the propionyl group should be more favorable, however, the use of a diffuse interface makes the two directions almost equivalent with respect to the solvation of the propionyl group, while this is not the case for the other polar group which is more efficiently solvated only if we assume that it first enters into water (see Fig 2.1).

Now that we have identified a preferential entrance position and direction, we can move to analyze the effects of the interface on absorption and emission energies.

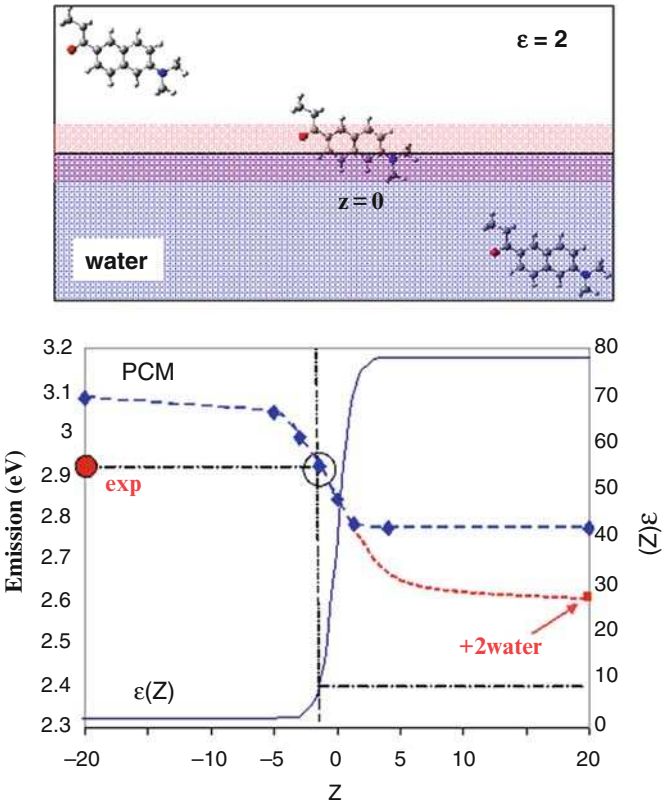

Fig. 2.1 Calculated emission energies of PRODAN as a function of its position with respect the cyclohexane/water interface. z is the coordinate perpendicular to the interface. The position-dependent value of the dielectric constant is also reported

The results are reported in Fig. 2.1 in which z is the coordinate perpendicular to the interface. The limit values ($z \to \pm\infty$) refer to bulk cyclohexane and bulk water; in the latter case, the result obtained for the solvated supermolecule is also reported (in red). In the same graph, we also report the position-dependent value of the dielectric constant used to mimic the diffuse interface.

In a recent paper by Moyano et al. [34], it is shown that the emission spectra of PRODAN is given in large unilamellar phospholipidic vesicles (LUVs). In such a study, the emission spectra were measured by increasing the concentration of the phospholipid, with respect to PRODAN in water, a shift in the band toward higher energies was found together with the appearance of a shoulder. The shift of the band was assigned to PRODAN moving from bulk water toward the interface near the water, and the shoulder to PRODAN in a less polar environment more inside the phospholipid tails. Experimentally, the position of PRODAN in LUV that gives origin to the observed shoulder is not known. According to what suggested in the above quoted paper [34], this should correspond to PRODAN located in the less polar region formed by the phospholipid tails. As it can be seen from the graph, such a value in the emission energy is obtained at $z = -1.5$: This indeed corresponds to PRODAN almost completely inside the $\varepsilon = 2$ region corresponding to a dielectric with effective permittivity of 7.5. This result well agrees with the analysis reported in that paper in terms of the well-known polarity parameter $E_{T(30)}$ [40]: For the band that corresponds to PRODAN in the less polar part of the bilayer, the $E_{T(30)}$ value found is similar to those in homogeneous tetrahydrofuran, i.e., a solvent with permittivity around 7.

2.4.2 How Solvent Controls EET and Light Harvesting

In two recent papers [41,42], we have applied the PCM-EET methodology described in Sect. 2.3.4, to compute the solvent screening factor s and the direct electronic coupling V_s for more than 100 pairs of molecules in four different photosynthetic proteins (PE545, PC645, PSII and LHII) for which structural models are available (in Fig. 2.2, we report an example of the arrangement of the interacting molecules for PE545).

The protein medium, intrinsic water, and surrounding medium were collectively modeled as a dielectric continuum with a relative static dielectric constant of 15 and optical dielectric constant of 2.29. Two contributions to the electronic coupling are calculated, as described in Sect. 3.4: The direct coupling, implicitly modified by the medium (V_s), and a contribution to the coupling involving the explicit solvent effect (V_{explicit}). Conceptually, the oscillating transition density of the D drives a response in the polarizable medium, which in turn, affects the oscillation of the A (and vice versa). This response of the medium to an electronic transition is here calculated introducing an apparent charge density on a cavity enclosing the molecule.

The computed screening factors $s = (V_s + V_{\text{explicit}})/V_s$ are shown in Fig. 2.3 for all the chromophores pairs, as a function of the D/A separation.

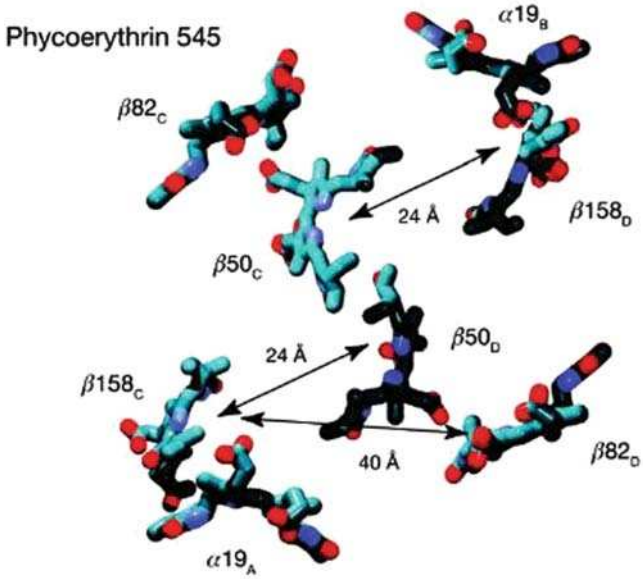

Fig. 2.2 Light-absorbing molecules in Phyconerythrin 545 (PE545) light-arvesting antenna from cryptophyte alage *Rhodomonas CS24*. Typical interchromophore (centre-to-centre) separation are indicated

Despite the range of sizes, shapes, and orientations of the D/A molecules, a trend is evident in the solvent screening factor s, which has been fitted by the functional form

$$s = s_0 + A\exp(-\beta R)$$

The D/A separation R enters this expression via the exponentially decaying contribution. The pre-exponential function is $A = 2.68$, indicating that $s = 1$ at a separation $R = 6.6$ and $\beta = 0.27^{-1}$ is the attenuation factor at close interchromophore separations. It is reasonable that at $R \sim 6.6$ the screening is negligible, since at that separation, the molecules share a cavity in the medium; hence, there is little or no intervening solvent. At large distances, s reaches an asymptotic value $s_0 = 0.54$. This result is intermediate within the limiting cases of screening between (infinitely thin) point dipoles, $s_0 \approx 1/n^2 = 0.5$ (commonly used in applications of Forster theory) and the prediction of Onsager theory, where the two transition dipoles are assumed to be contained in spherical cavities, $s_0 \approx 3/(2n^2 + 1) = 0.6$. The use of the screening factor s, therefore, makes a significant correction to calculate EET rates which have particular importance for the quantitative application and testing of EET models.

A clear understanding of why s depends on R is offered by the computational results for a chlorophyll dimer of LHCII as function of a systematic increase in the chlorophyll-a center-to-center separation, as reported in Fig. 2.4.

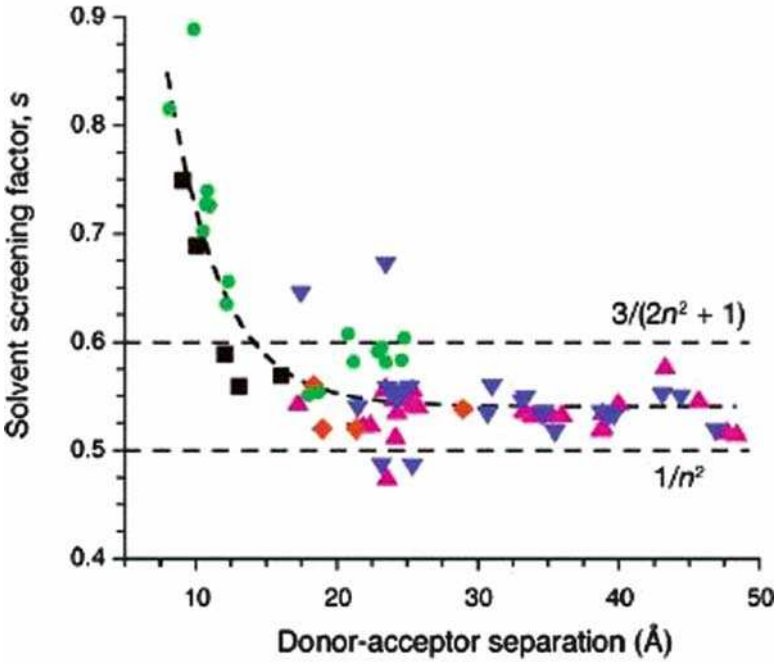

Fig. 2.3 Solvent screening of electronic couplings between chromophores in the four photosyntletic proteins: PE545 (pink triangles), PC645 (blue inverted triangles), PSII/LHCII (green circles). The protein medium is modeled as a dielectric continuum medium with a relative static constant of $\epsilon_{stat} = 15$ and optical dielectric constant of $n^2 = 2$. Calculated values for the solvent screening factor s for the various chromophores pairs. The Forster value $1/n^2$ and the Onsager value $3(2n^2 + 1)$ are indicated by the horizontal line

This figure shows that the calculated electronic coupling (V_{tot}) is reduced relative to the direct interaction between transition densities (V_s) by the additional coupling of the transition densities through the ASCs that represent the effect of medium polarization, V_{explicit}. In the case of large D/A distances, the ASCs representing the medium polarization on one cavity are not influenced by the presence of the second cavity. The effect of the solvent is, therefore, independent of the separation $s = s_0$. In this range, in addition, the location of the solvent between the chromophores leads to a reduction of the total coupling, as V_{explicit} necessarily decreases the direct V_s interaction. As the molecules approach each other, the screening is partially reduced ($s > s_0$). This trend starts to show up as the chromophores begin to share a common cavity. In this process, the solvent apparent charges induced by the D are progressively spread over the A microenvironment, thereby leading to a gradual decrease of the screening. When the two molecules are sufficiently close, the ASCs are spread over one large cavity enclosing the dimer, and their screening effect is significantly reduced. In this case, s approaches unity as $V_s \gg |V_{\text{explicit}}|$.

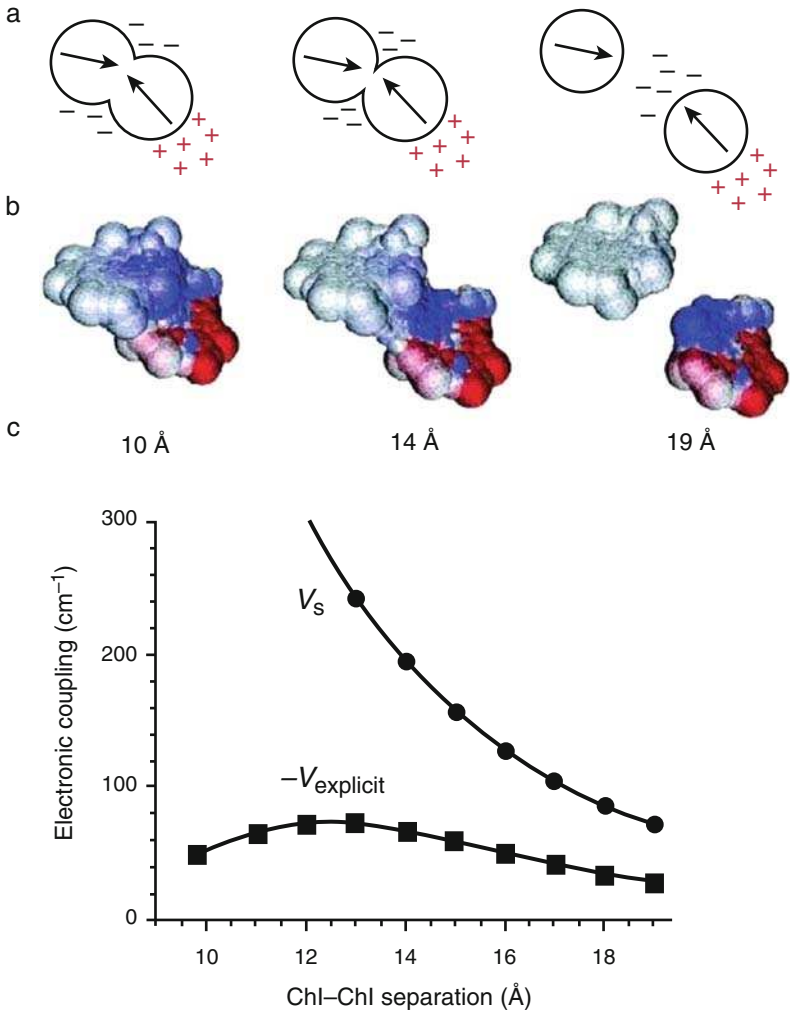

Fig. 2.4 The dependence of s on separation between Chl_{602} and Chl_{607} molecules in LHCII is explained by the formation of a common cavity: (**a**) schematic depiction of the interaction between two transition dipoles (arrows) immersed within cavities in a polarizable medium, (**b**) the apparent surface charges of the donor spread on the acceptor microenvironment, and (**c**) the spread of the surface charge over the cavities changes the magnitude and functional form of the electronic coupling

2.5 Conclusions

We have presented a survey of the methodological advancements in the description of properties of excited states of molecules in solution obtained with the models we have developed in the years and collectively indicated with the acronym PCM

(Polarizable Continuum Model). The potentialities of these new PCM tools for excited states have been shown by some numerical applications selected as partial testimony of the state-of-the-art in a field which progresses quite rapidly.

We end our contribution to this editorial initiative of the European Academy of Science by recalling the leading role played by the European quantum chemistry community in the development of quantum mechanical (QM) solvation models. We cite, as an example, the first quantum chemistry continuum solvation code developed by Rivail's group in Nancy in 1973 [43]. However, this initiative to address the solvation problem from a QM point of view was not entirely "out-of-the-blue." It was, on the contrary, a response to the challenges stimulated by a limited number of scientists working in France and in Italy (Paris, Nancy, Pisa), with strong contact, in competition and also in collaboration to each others [44]. More than 30 years later, the European quantum chemistry community is still at the forefront in the development of QM continuum solvation models, and we hope that the present contribution can be considered as a testimony of this activity.

Acknowledgments Many people, both from our group in Pisa and other groups, have collaborated to the development of the PCM method for excited states: M. Caricato, S. Corni, C. Curutchet, L. Frediani, C. Pomelli, G. Scalmani and G.D. Scholes. They are here collectively acknowledged.

References

1. J. Tomasi, B. Mennucci, R. Cammi, Quantum mechanical continuum solvation models. Chem. Rev. **105**, 2999 (2005)
2. S. Miertuš, E. Scrocco, J. Tomasi, Electrostatic interaction of a solute with a continuum. Chem. Phys. **55**, 117 (1981)
3. R. Bonaccorsi, E. Cimiraglia, J. Tomasi, On the free energy changes of a solution in light absorption or emission processes. Chem. Phys. Lett. **99**, 77 (1983)
4. L. Frediani, R. Cammi, S. Corni, J. Tomasi, A polarizable continuum model for molecules at diffuse interfaces, J. Chem. Phys. **120**, 3893 (2004)
5. L. Frediani, B. Mennucci, R. Cammi, Quantum-mechanical continuum solvation study of the polarizability of halides at the water/air interface. J. Phys. Chem. B **108**, 13796 (2004)
6. L. Bondesson, L. Frediani, H. Ågren, B. Mennucci, Solvation of N3- at the water surface: The polarizable continuum model approach. J. Phys. Chem. B **110**, 11361 (2006)
7. C. Curutchet, R. Cammi, B. Mennucci, S. Corni, Self-consistent quantum mechanical model for the description of excitation energy transfers in molecules at interfaces. J. Chem. Phys. **125**, 054710 (2006)
8. B. Mennucci, M. Caricato, F. Ingrosso, C. Cappelli, R. Cammi, J. Tomasi, G. Scalmani, M.J. Frisch, How the environment controls absorption and fluorescence spectra of PRODAN: A quantum-mechanical study in homogeneous and heterogeneous media. J. Phys. Chem. A **112**, 414 (2008)
9. S. Corni, J. Tomasi, Excitation energies of a molecule close to a metal surface, J. Chem. Phys. **117**, 7266 (2002)
10. B. Mennucci, E. Cancès, J. Tomasi, Evaluation of solvent effects in isotropic and anisotropic dielectrics, and in ionic solutions with a unified integral equation method: Theoretical bases, computational implementation and numerical applications. J. Phys. Chem. B **101**, 10506–10517 (1997).

11. B. Mennucci, R. Cammi, (eds.) *Continuum Solvation Methods in Chemical Physics: From Theory to Application*. (Wiley, Chichester, 2007)
12. R. Cammi, B. Mennucci, Structure and properties of molecular solutes in electronic excited states: A polarizable continuum model approach based on the time-dependent density functional theory, in *Radiation Induced Molecular Phenomena in Nucleic Acids: A Comprehensive Theoretical and Experimental Analysis*, ed. by M.K. Shukla, J. Leszczynski. Series: Challenges and Advances in Computational Chemistry and Physics, vol 5 (Springer, Netherlands 2008)
13. B. Mennucci, R. Cammi, J. Tomasi, Excited states and solvatochromic shifts within a nonequlibrium solvation approach: A new formulation of the integral equation formalism method at the self-consistent, configurational interaction, and multiconfiguration self-consistent level. J. Chem. Phys. **109**, 2798 (1998)
14. R. Cammi, B. Mennucci, K. Ruud, L. Frediani, K.V. Mikkelsen, J. Tomasi, A second order, quadratically convergent multiconfigurational self-consistent field polarizable continuum model for equilibrium and nonequilibrium solvation. J. Chem. Phys. **117**, 13 (2002)
15. R. Cammi, B. Mennucci, Linear response theory for the polarizable continuum model B. J. Chem. Phys. **110**, 9877 (1999)
16. M. Cossi, V. Barone, Time-dependent density functional theory for molecules in liquid solutions. J. Chem. Phys. **115**, 4708 (2001)
17. R. Cammi, L. Frediani, B. Mennucci, K. Ruud, Multiconfigurational self-consistent field linear response for the polarizable continuum model: Theory and application to ground and excited-state polarizabilities of para-nitroaniline in solution. J. Chem. Phys. **119**, 5818 (2003)
18. R. Cammi, S. Corni, B. Mennucci, J. Tomasi, Electronic excitation energies of molecules in solution: State specific and linear response methods for nonequilibrium continuum solvation models. J. Chem. Phys. **122**, 104513 (2005)
19. S. Corni, R. Cammi, B. Mennucci, J. Tomasi, Electronic excitation energies of molecules in solution within continuum solvation models: Investigating the discrepancy between state-specific and linear-response methods, Formation and relaxation of excited states in solution: A new time dependent polarizable continuum model based on time dependent density functional theory. J. Chem. Phys. **123**, 134512 (2005)
20. M. Caricato, B. Mennucci, J. Tomasi, F. Ingrosso, R. Cammi, S. Corni, G. Scalmani, Formation and relaxation of excited states in solution: A new time dependent polarizable continuum model based on time dependent density functional theory. J. Chem. Phys. **124**, 124520 (2006)
21. R. Improta, V. Barone, G. Scalmani, M.J. Frisch, A state-specific polarizable continuum model time dependent density functional theory method for excited state calculations in solution. J. Chem. Phys. **125**, 054103 (2006)
22. M. Cossi, G. Scalmani, N. Rega, V. Barone, New developments in the polarizable continuum model for quantum mechanical and classical calculations on molecules in solution. J. Chem. Phys. **117**, 43 (2002)
23. G. Scalmani, M.J. Frisch, B. Mennucci, J. Tomasi, R. Cammi, V. Barone, Geometries and properties of excited states in the gas phase and in solution: Theory and application of a time-dependent density functional theory polarizable continuum model. J. Chem. Phys. **124**, 094107 (2006)
24. R. Cammi, B. Mennucci, J. Tomasi, Fast evaluation of geometries and properties of excited molecules in solution: A Tamm-Dancoff Model with application to 4-dimethylaminobenzonitrile. J. Phys. Chem. A **104**, 5631 (2000)
25. G.D. Scholes, Long-range resonance energy transfer in molecular systems, Ann. Rev. Phys. Chem. A **54**, 57 (2003)
26. F. Iozzi, B. Mennucci, J. Tomasi, R. Cammi, Excitation energy transfer (EET) between molecules in condensed matter: A novel application of the polarizable continuum model (PCM). J. Chem. Phys. **120**, 7029 (2004)
27. C. Curutchet, B. Mennucci, Toward a molecular scale interpretation of excitation energy transfer in solvated bichromophoric systems. J. Am. Chem. Soc. **127**, 6978 (2005)
28. V. Russo, C. Curutchet, B. Mennucci, Towards a molecular scale interpretation of excitation energy transfer in solvated bichromophoric systems. II. The Through-Bond Contribution. J. Phys. Chem. B **111**, 853 (2007)

29. C. Curutchet, R. Cammi, B. Mennucci, S. Corni, Self-consistent quantum mechanical model for the description of excitation energy transfers in molecules at interfaces, J. Chem. Phys. **125**, 054710 (2006)
30. B. Mennucci, J. Tomasi, R. Cammi, Excitonic splitting in conjugated molecular materials: âĂČA quantum mechanical model including interchain interactions and dielectric effects. Phys. Rev. B **70**, 205212 (2004)
31. G. Weber, J. F. Farris, Synthesis and spectral properties of a hydrophobic fluorescent probe: 6-propionyl-2-(dimethylamino)naphthalene. Biochemistry **18**, 3075 (1979)
32. T. Parasassi, E.K. Krasnowska, L. Bagatolli, E. Gratton, Laurdan and prodan as polarity-sensitive fluorescent membrane probes. J. Fluor. **8**, 365 (1998)
33. E.K. Krasnowska, E. Gratton, T. Parasassi, Prodan as a membrane surface fluorescence probe: Partitioning between water and phospholipid phases. Biophys. J. **74**, 1984 (1998)
34. F. Moyano, M.A. Biasutti, J.J. Silber, N.M., Correa, New insights on the behavior of PRODAN in homogeneous media and in large unilamellar vesicles. J. Phys. Chem. B **110**, 11838 (2006).
35. M. Novaira M.A. Biasutti, J.J. Silber N.M., Correa, New insights on the photophysical behavior of PRODAN in anionic and cationic reverse micelles: From which state or states does it emit? J. Phys. Chem. B **111**, 748 (2007)
36. M.J. Frisch, G.W. Trucks, H.B. Schlegel, G.E. Scuseria, M.A. Robb, J.R. Cheeseman, J.A. Montgomery, Jr., T. Vreven, K.N. Kudin, J.C. Burant, J.M. Millam, S.S. Iyengar, J. Tomasi, V. Barone, B. Mennucci, M. Cossi, G. Scalmani, N. Rega, G.A. Petersson, H. Nakatsuji, M. Hada, M. Ehara, K. Toyota, R. Fukuda, J. Hasegawa, M. Ishida, T. Nakajima, Y. Honda, O. Kitao, H. Nakai, M. Klene, X. Li, J.E. Knox, H.P. Hratchian, J.B. Cross, V. Bakken, C. Adamo, J. Jaramillo, R. Gomperts, R.E. Stratmann, O. Yazyev, A.J. Austin, R. Cammi, C. Pomelli, J.W. Ochterski, P.Y. Ayala, K. Morokuma, G.A. Voth, P. Salvador, J.J. Dannenberg, V.G. Zakrzewski, S. Dapprich, A.D. Daniels, M.C. Strain, O. Farkas, D.K. Malick, A.D. Rabuck, K. Raghavachari, J.B. Foresman, J.V. Ortiz, Q. Cui, A.G. Baboul, S. Clifford, J. Cioslowski, B.B. Stefanov, G. Liu, A. Liashenko, P. Piskorz, I. Komaromi, R.L. Martin, D.J. Fox, T. Keith, M.A. Al-Laham, C.Y. Peng, A. Nanayakkara, M. Challacombe, P.M.W. Gill, Johnson, B.W. Chen, M.W. Wong, C. Gonzalez, J.A. Pople, Gaussian 03, Revision C.02, Gaussian, Inc., (Wallingford CT, 2004)
37. B. Mennucci, Hydrogen bond versus polar effects: An ab initio analysis on n * absorption spectra and N nuclear shieldings of diazines in solution. J. Am. Chem. Soc. **124**, 1506 (2002)
38. C. Cappelli B. Mennucci, S. Monti, Environmental effects on the spectroscopic properties of gallic acid: A combined classical and quantum mechanical study. J. Phys. Chem. A **109**, 1933 (2005)
39. B. Mennucci J.M. Martinez, How to model solvation of peptides? Insights from a quantum mechanical and molecular dynamics study of N-methylacetamide. 2. 15N and 17O nuclear shielding in water and in acetone. J. Phys. Chem. B, **109**, 9818, 9830 (2005)
40. C. Reichardt, *Solvents and Solvent Effects in Organic Chemistry*, (Wiley-VCH: Weinheim, 1990)
41. D.G. Scholes, C. Curutchet, B. Mennucci, R. Cammi, J. Tomasi, How solvent controls electronic energy transfer and light harvesting. J. Phys. Chem. B **111**, 6978 (2007)
42. C. Curutchet, D.G. Scholes, B. Mennucci, R. Cammi. How solvent controls electronic energy transfer and light harvesting: Toward a quantum-mechanical description of reaction field and screening effects. J. Phys. Chem. B **111**, 13253 (2007)
43. D. Rinaldi, J.L. Rivail, Polarisabilites molÃl'culaires et effet diÃl'lectrique de milieu Ãă l'Ãl' tat liquide. ÃL'tude thÃl'orique de la molÃl' cule d'eau et de ses dimÃl'res. Theor. Chim. Acta **32**, 57 (1973)
44. J. Tomasi, Thirty years of continuum solvation chemistry: A review, and prospects for the near future. Theor. Chem. Account **112**, 184 (2004)

Chapter 3
Chirality and Chiral Recognition

Ibon Alkorta and José Elguero

Abstract This review summarizes the literature survey on chiral recognition from a theoretical view point. Nevertheless, experimental results in the gas phase are reported when they are relevant for the theoretical calculations. The review is divided into the following sections: general considerations; experiment vs. theory; pure theoretical results; solvent effects; metals as glue; optical rotatory power; and conclusions.

3.1 Introduction

Chirality is so embedded in chemists' minds that they tend to commit two opposite errors. On one hand, they think that this notion is so evident that other professionals share it with them. On the other, they think that chirality is an exclusive characteristic of chemistry. At the most, while explaining chirality to students, they use the analogy of the hands (χειρ = hand), although both hands of a person are not perfect enantiomers.

"I call any geometrical figure, or group of points, chiral, and say it has chirality, if its image in a plane mirror, ideally realized, cannot be brought to coincide with itself." This is the celebrated definition stated by Lord Kelvin in 1904, in his Baltimore Lectures on Molecular Dynamics and the Wave Theory of Light.

3.1.1 Chiral Objects

In Fig. 3.1, we have represented a comparison of chiral objects based on their sizes. If we define an object whose mirror image is nonsuperposable with it as chiral, almost all objects of our life are chiral; a perfect macroscopic achiral object does not exist. But usually, we use the term chiral in the sense that its mirror image

I. Alkorta (✉) and J. Elguero
Instituto de Química Médica (CSIC), Juan de la Cierva 3, 28006, Madrid, Spain
e-mail: ibon Alkortaibon@iqm.csic.es

J. Leszczynski and M.K. Shukla (eds.), *Practical Aspects of Computational Chemistry*,
DOI: 10.1007/978-90-481-2687-3_3,

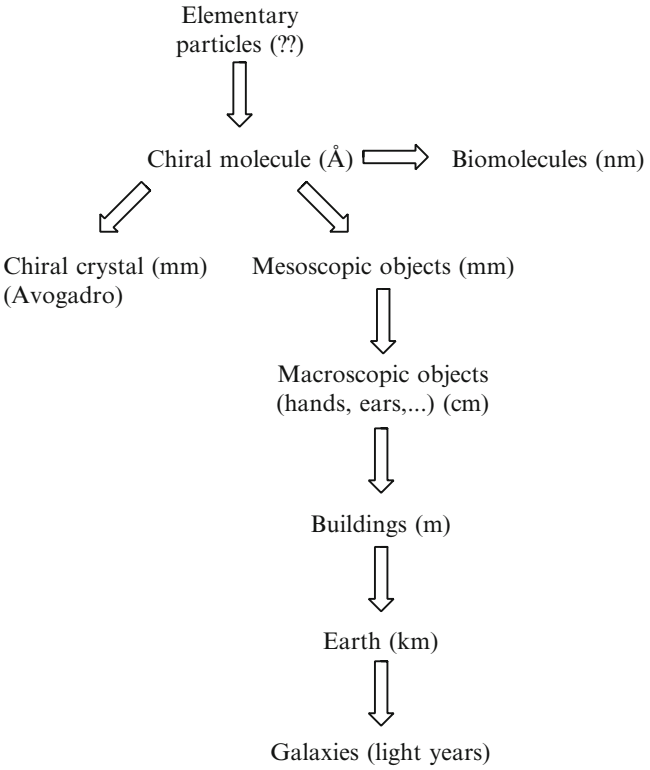

Fig. 3.1 Chiral objects

is either known or attainable. For instance, in the molecular world, a natural compound like proline has existed for millions of years as one enantiomer (the S one), until chemists prepared the R one (or a mixture of both, the R and the S).

The preceding discussion is somewhat related to Ernst Ruch's extraordinarily fruitful idea to classify chiral objects in two classes: shoes and potatoes (Fig. 3.2): "If asked to put our left shoes into one box and our right shoes into a second box we could accomplish the task without mental difficulty, in spite of the fact that the right shoes belonging to different people may be quite different in color, shape, and size, and although, probably, there is not a single pair of shoes which are precise mirror images of each other. If asked to solve the same problem with potatoes, we must capitulate. Of course, it is possible that by chance we find an antipodal pair. It is then clear that we must separate them, but for other potatoes different in shape, we have to make new arbitrary decisions each time. Any classification would be very artificial" [1–3].

There is some information about neutrinos that though they have no mass, they are chiral [4]. The Å domain (10^{-10} m) is a domain of chemistry, and since it is the subject of this chapter, only a comment. When chiral molecules assemble in a crystal, the crystal also becomes chiral [5], and its size could attain meters

Fig. 3.2 A pair of shoes and a potato

Fig. 3.3 A chiral quartz crystal

(Fig. 3.3). This related to the Avogadro's number ($6.02214199 \times 10^{23}$ mol^{-1} atoms per mol); a mol of quartz (60 g, $d = 2.65$ gcm^{-3}, 22.6 cm^3) contains 6×10^{23} molecules of SiO_2. It must be noted that a crystal is a collection of molecules, and not a supermolecule.

A second way to change the scale of molecules is to build up a large molecule from fragments. Nature does this and obtains, for instance, chiral DNA (if stretched out, would form very thin thread about 2 m long). Chemists prepare synthetic polymers that can be chiral and be measured in meters – fabric – or in km – tethered space elevators.

In the domain of mesoscopic objects (a few nm), there are also chiral representatives [6], for instance, the related problems studied by Whitesides [7]. Leaving aside

Fig. 3.4 Staircases and buildings

human beings, there are human constructs that are chiral: helical staircases, buildings, etc (Fig. 3.4). In general, they are considered chiral only when both enantiomers are present.

The Earth's orbital chirality (EOC) is mainly created by both the Earth's right-handed helical rotation around its spin axis and the Earth's right-handed helical revolution around the Sun [8]. Finally, spiral galaxies show axial symmetry and an intrinsic 2D chirality [9].

3.1.2 Chirality in Chemistry

Lets us introduce here some definitions from the IUPAC Gold Book [10] that will be useful for our presentation:

Chirality

Chirality is the geometric property of a rigid object (or spatial arrangement of points or atoms), which is nonsuperposable on its mirror image; such an object has no symmetry elements of the second kind (a mirror plane, a center of inversion, a rotation-reflection axis, ...). If the object is superposable on its mirror image, the object is described as being achiral.

Chiral

Chiral refers to the property of chirality. As applied to a molecule, the term has been used differently by different workers. Some apply it exclusively to the whole molecule, whereas others apply it to parts of a molecule. For example, according to the latter view, a meso compound is considered to be composed of two chiral parts of opposite chirality sense; this usage is to be discouraged. See: enantiomorph

In its application to an assembly of molecules, some restrict the term to an assembly in which all of the molecules have the same chirality sense, which is better called enantiopure. Others extend it to a racemic assembly, which is better just called as racemate. The use of the term chiral to describe molecular assemblies should be avoided.

Enantiomer

Enantiomer is one of a pair of molecular entities, which are mirror images of each other and nonsuperposable. See also: enantiomorph

Enantiomorph

Enantiomorph is one of a pair of chiral objects or models that are nonsuperposable mirror images of each other. The adjective enantiomorphic is also applied to mirror image-related groups within a molecular entity.

Superposability

Superposability is the ability to bring two particular stereochemical formulae (or models) into coincidence (or to be exactly superposable in space, and for the corresponding molecular entities or objects to become exact replicas of each other) by nothing more than translation and rigid rotation.

Since chirality is a geometrical property, all serious discussions on this topic require a mathematical treatment that is much out of this review. Note, however, that if you cut by the middle of a Klein bottle (an achiral object having a plane of symmetry), you obtain two Möbius strips both chiral and mutually enantiomorph (Fig. 3.5). This pure mathematical result is closely related to the situation of meso compounds described above [11].

In a static situation, many molecules exist in two perfect enantiomers, either "indefinitely" stable (sparteine) or interconverting (amines).

In a dynamic real case, the situation is very different. This analysis may be extended to formally achiral molecules that are composed of four or more atoms. The motions in such polyatomic molecules are restricted by the restoring forces imposed by bonding, and here, stochastic achirality is the result of internal vibrations. Thus, for example, molecular deformations in some vibrational states impart

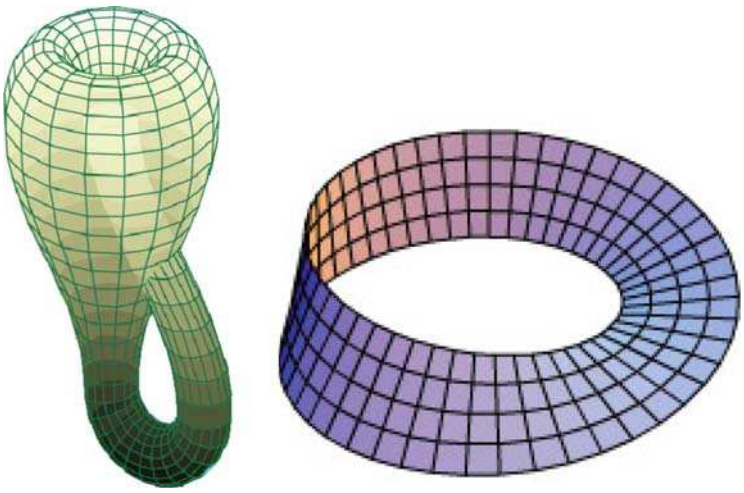

Fig. 3.5 Klein bottle and Möbius strip (or band)

chirality to the methane molecule, but the sense of chirality averages to zero under the conditions of measurement. As this discussion makes clear, the conventional Td symmetry of methane is a property solely of the model.

Of course, the probability is small that at any instant, the enantiomeric mixture at equilibrium is exactly equimolar; the absence of observable chirality phenomena, such as optical activity, is the result of rapid cancelations of random statistical fluctuations of activity in the time domain of observation. In other words, although, at any instant, the mixture (with a high degree of probability) has an excess of one enantiomer or the other, under measurement conditions, it effectively contains an equal number of enantiomeric molecules. When 10,000,000 dissymmetric [i.e., chiral] molecules are produced under conditions which favor neither enantiomorph, there is an even chance that the product will contain an excess of more than 0.021% of one enantiomorph or the other. It is practically impossible for the product to be absolutely optically inactive [12].

3.1.3 The Chirality of Biomolecules

In our previous discussion of the case of shoes and potatoes, we were aware of the fact that even if we find a potato that is the perfect mirror image of our sample, it will be fundamentally different to the point that the most different potatoes we can find, in size, form, color, are much more alike than the potato we would obtain by a mirror reflection because all the biomolecules – glucose – will be "unnatural." The same will happen with a RNA virus: its image will have all the sugars – riboses – with inverted configuration. Such a virus could not survive in our Earth.

The reason why biomolecules are composed of only one class of enantiomers, is very simple: biomolecules formed by repetition or combination of achiral molecules will not have enough recognition properties, and are not formed by natural evolution of live organisms. Those formed from racemic mixtures will be messy mixtures (2^n, n = number of monomers), incompatible with the extremely fine attuning of life.

This leaves open the question why one enantiomer is preferred to the other, which is one of the greatest problems of science. "One of the most fascinating endeavors of chemical research is to discover the origin of molecular handedness. Few topics as the search for the enantiomeric homogeneity of nature have surpassed the purely chemical threshold, interlocking the physical and life sciences and attracting the interest of their scientists over generations" [13]. There is a large bibliography on this topic [14–16], including the parity violation topic, that we will not discuss further.

A final comment about the relationship between chirality and electromagnetic radiation. In 1994, Breitmaier et al. published one of the major blunders of chemistry in the modern times! [17]. We [18, 19], and some others [20–23], published corrections and the original paper was withdrawn. However, what was called "the organic chemistry's version of the cold fusion," has a strong negative impact on further studies dealing with the effects of radiations.

3.2 General Considerations

In this review, we will report the results we obtained [5, 24–41] in the theoretical study on chiral recognition, together with the most relevant literature publications on the same topic (for a recent issue of a journal on Molecular Recognition see [42]). If we consider the simplest case of interaction, the bimolecular one, we must realize that although intimately related, the cases of chiral recognition (a chiral molecule A* discriminates between the chiral forms, R and S, of a molecule B) and chiral self-recognition (two enantiomers of the same molecule A, either the same – true self-recognition – or different) are to be distinguished. We will use the terms "homochiral" for a RR (or SS) dimer and "heterochiral" for an RS (or SR) dimer, but considering both examples of self-recognition.

When discussing chiral recognition, one must take into account two aspects: the quantitative and the qualitative. The first refers to the magnitude, and the second, to the sign (in the general case, what enantiomer of B, the R or the S is preferred, and in self-recognition what of the homo- or the heterodimer is most stable, Scheme 3.1).

This bimodal logic could be avoided by considering only three states (Scheme 3.2). Note that the interaction RR(SS) vs. RS(SR) being diastereomeric, the difference in energy could be very weak, but never null. It is easier to discuss the problem by means of Scheme 3.1, but when discussing the sign, we will consider only the situations where the effects are large.

3.2.1 Magnitude (Large vs. Small Effects)

The magnitude depends:

1. On the proximity of the two moieties. It is obvious that the progressive removal of the two halves will decrease the chiral discrimination, most likely in an exponential decay.

2. The absolute chirality of each moiety. It is evident that a methyl group (–CHDT) will be less efficient in inducing recognition than a substituent with

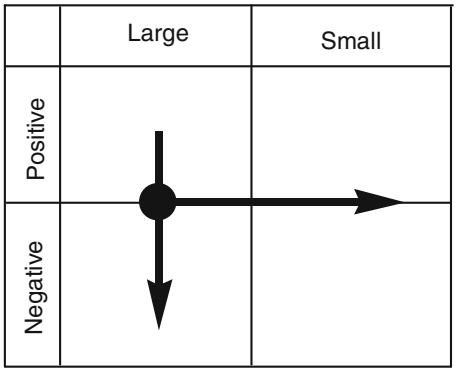

Scheme 3.1 The four possible situations

Scheme 3.2 The three-level classification

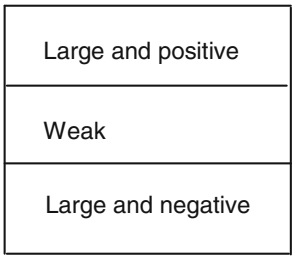

heteroatoms. The problem of quantifying chirality is the subject of many studies; we will counsel the reader interested in this problem to refer to Le Guennec's papers (and references cited therein) [43–48].

3. The rigidity of the complex. This aspect is not relevant in calculations since the minimum is rigid by definition, but experimentally, this is related to the number, 1, 2 or 3, of interactions linking the molecules in the simplest case of a chiral sp^3 carbon center.

3.2.2 Phase Effects

All these are true only for the gas phase; even if the experimental results corresponding to the gas phase are accessible using different techniques, they are much less common than the solution or solid state results. In condensed phases, the problem has one additional dimension: the environment. In the solid state, 26 identical boxes that influence the stabilities of the RR and RS complexes (self-recognition) surround the unit cell containing the complex. In solution, the polarity of the solvent should favor the more polar complex, usually the RR since the RS has, in general, an inversion center and thus, is devoid of dipole moment (self-recognition) [49]. This is true for general solvent effects (Onsager). For specific effects, like hydrogen bonds (HBs), between the complex and the solvent, it is expected that the relative energy ($\Delta E = E_{RR} - E_{RS}$) will be modified, either increased or decreased. Let us consider the following two cases: (a) Nonchiral solvents, e.g., methanol. The solvent can modify the geometry of the complex and this, in turn, the enantiodifferentiation. (b) Chiral solvents. They can be used either as the racemic mixture or as a pure enantiomer. For an example of the latter, see Scheme 3.3.

3.2.3 Sign (Positive vs. Negative)

To simplify the problem, let us consider the case of self-recognition (homo vs. heterochiral): why is it so difficult to predict (or explain) the sign of the interaction? The stability of the complex is the sum of a series of terms relating both enantiomers: steric, electronic, and orbital effects. These effects are transmitted either through

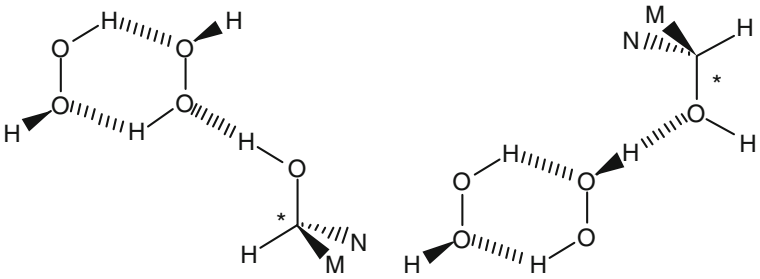

Scheme 3.3 Hydrogen peroxide dimer solvated by a chiral alcohol

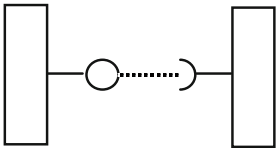

Scheme 3.4 Hydrogen bond (·····) between an HBD (–O) and an HBA ( )–)

space, or through bonds (covalent as well as hydrogen bonds or metal bonds). The forces that determine the molecular structures can be classified into covalent, metallic, and noncovalent, which, with some overlapping, correspond to strong, medium, and weak, or to situations found in organic, coordination, and supramolecular chemistry, respectively. All have the same importance for chemistry and for life, but the weaker they are, the more difficult is it to study and characterize.

Concerning noncovalent interactions, it is important to consider, besides their strength, the fact that there are two possibilities: either the groups that interact are complementary (the most common case) or identical. Identical groups that show attractive effects are found only in π-stacking and van der Waals interactions (possible also for two different groups). A metallic center can bring together two identical ligands, such as two phosphines, two cyclopentadienyl rings, two benzenes, etc. One of the strongest of the weak interactions, the HB, always occurs between two complementary groups (Scheme 3.4).

This assertion needs to be clarified. Two, or more water molecules are associated through HBs (Scheme 3.5). But, the two molecules are different: one acts as a HB donor (HBD), and the other as a HB acceptor (HBA). The same applies to all HBs between identical molecules.

When two neutral molecules, a charged and a neutral molecule, or two molecules of opposite charges approach each other, a bimolecular equilibrium structure is formed. If both molecules are chiral (this is the most common case but it is not a necessary condition) [50], two supramolecular complexes that differ in energy can be formed. This phenomenon is called chiral recognition; the name becomes self-recognition if the two molecules are identical. We assume that self-recognition corresponds both to the RR(SS) and the RS(SR) cases, although only in the first case, both molecules are identical. In the simple case of a tetrahedral sp^3 carbon, the recognition could involve three, two or one interaction (see Scheme 3.6); in more

Scheme 3.5 Water dimer

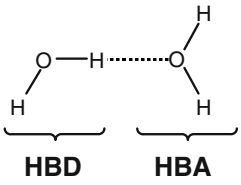

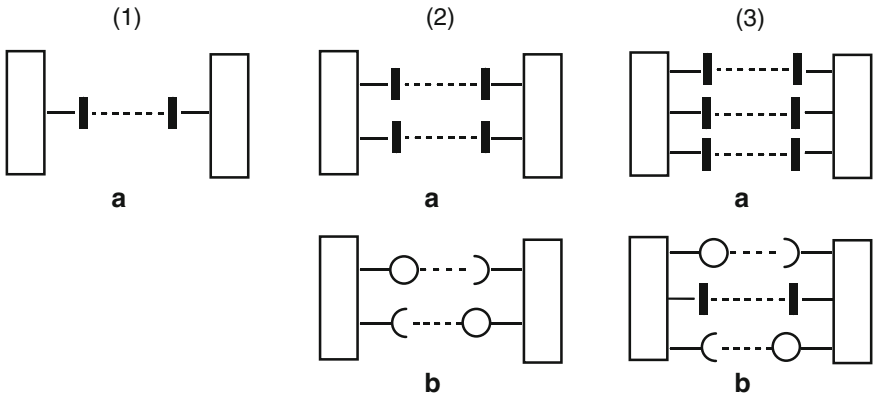

Scheme 3.6 Bimolecular complexes between identical molecules

complex cases, for instance in proteins, the recognition involves hundreds of contacts. From simple parity considerations, if three-centered HBs are excluded, self-recognition using HBs is only possible in the case of two interactions (see Scheme 3.6, Complex 2b). One interaction needs identical groups (Complex 1a) and three interaction need one (Complex 3b) or three identical groups (a rather improbable situation unless metallic centers are involved).

Bifurcated (three-centered) HBs [51] destroy the 1:1 parity and three interactions between two identical molecules are possible (Scheme 3.7).

There are molecules containing two sp^3 carbon atoms where four contacts are possible. Consider, for instance, a cyclopropane ring bearing two fluorine (black circles) and two hydroxy substituents (white circles) and consider the formation of O–H···F hydrogen bonds. There are two possible isomers, the meso and the d, l (Scheme 3.8), the second one being of C_2 symmetry.

Obviously, the meso compound will lead to a unique dimer devoid of chirality. In the case of the d,l isomer, the homochiral complex should be much more stable than the heterochiral one (with four repulsive F/F and OH/OH interactions). This assumption arises from a misunderstanding of these LEGO-like compounds where a 90° rotated solution is possible for the heterochiral situation (Scheme 3.9). This is due to the "square" disposition of the four anchoring points (Scheme 3.10).

To destroy the last possibility (twisted dd dimer with four HBs), it will suffice to transform the square into a rectangle (Scheme 3.11). Note that these rectangular

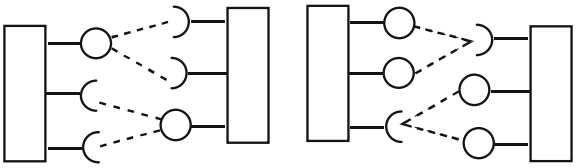

Scheme 3.7 Bimolecular complexes involving three-centered hydrogen bonds

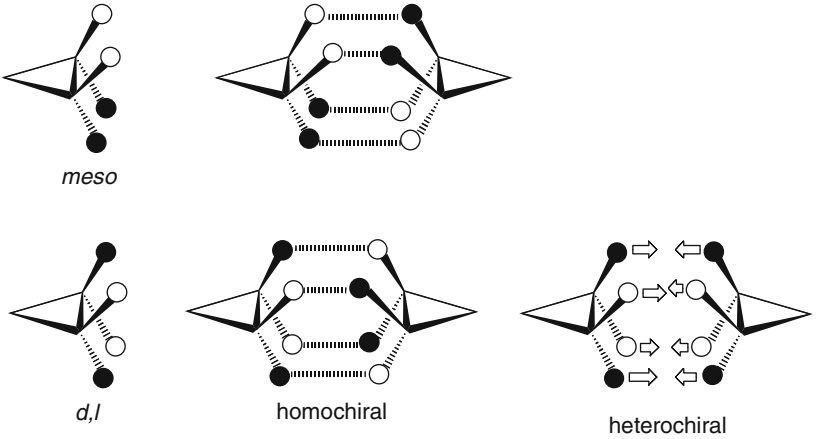

Scheme 3.8 Bimolecular complexes involving four hydrogen-bonds.

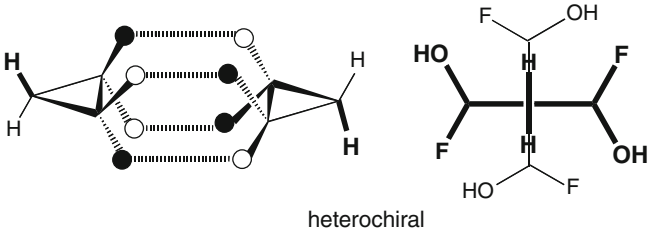

Scheme 3.9 90° twisted heterochiral complex involving four hydrogen bonds

molecules could form two HBs in the case of the heterochiral dimer, but this is a much poorer solution.

3.3 Discussion

All the experimental data and most of the calculations would correspond to gas-phase results and examples of chiral self-recognition. Only exceptionally, condensed phase results of chiral self-recognition or gas-phase results of classical

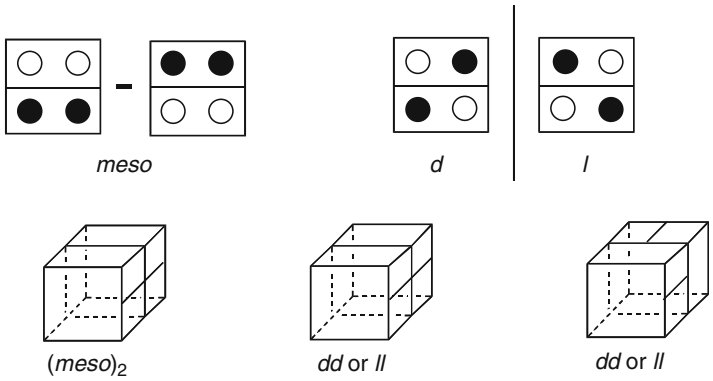

Scheme 3.10 The possible disposition of LEGO-like molecules

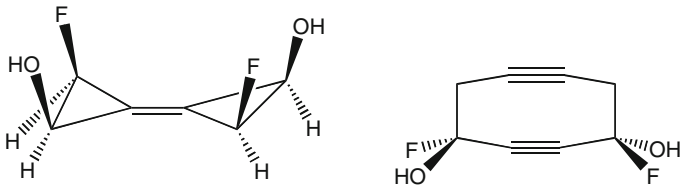

Scheme 3.11 Rectangular molecules: four HBs are only possible for the homochiral dimer

chiral recognition will be reported. We will follow the given order: a) experimental and theoretical results, where the publications describe both experimental data and the corresponding calculations; b) pure theoretical studies; c) solvent effects on chiral recognition; d) the use of metals to bring together the two chiral moieties, and e) optical rotatory power studies.

3.3.1 Experimental and Theoretical Results

The use of different methods based on mass spectrometry to analyze enantiomeric mixtures is much developed [52, 53]. Although outside this review, due to the obvious connection with our topic, some references deserved to be reported here. As expected, one of the main conclusions of these studies is that the chiral recognition of AR and AS by B* is much dependent on B*, which should be optimized empirically. The main contributions are due to Cooks [54–67], Sawada [68–79], Speranza [80–84], Fales [85], Leary [86, 87], and some others [88–97].

One of the most complete studies of chiral self-recognition concerns serine. The experimental studies carried out on hydrogen-bonded gas phase clusters, provide useful data to be compared with theoretical results, as in general, the latter are

performed in "gas phase" not taking into account solvent effects. Thus, both techniques help each other to get a better idea of the actual behavior of the systems involved.

Schalley and Weis [98] revised the results obtained by several studies on hydrogen bonded serine dimers. Those have reported the formation of unusually stable protonated serine octamers, with a clear preference for homochirality [99–103]. Mixed L- and D-serine clusters show up in a small ratio vs. the homochiral ones.

The protonated serine octamer (Ser)8H^+ is exceptionally stable, with a magic number effect of more than 20. The magic number effect M can be obtained from the mass spectra, by the abundance ratio of the n unit cluster compared with the $n-1$ and $n+1$ unit cluster, by the relationship $M=2I_n/(I_{n-1}+I_{n+1})$. Electrospray mass ionization experiments [98], performed on 0.1 M solutions of L-serine and D-[[13]C] Serine, show a strong preference toward the formation of homochiral protonated clusters (L-Ser)8H^+ and (D-[^{13}C]Ser)8H^+ instead of the heterochiral analogs (L-Ser)n (D-[^{13}C]Ser)$8-nH^+$ ($n=1-7$). The same trends are obtained in deuterium-labeling experiments mixing L-[D_3]-Serine and D-serine [98], and in soft-landing experiments of mass-selected protonated serine octamers starting from nonracemic solutions [104].

Upon fragmentation on MS experiments [99, 100], the octamers break into a protonated hexamer and a neutral dimer. Subsequently, the hexamer fragments into a protonated tetramer and a neutral dimer, and so on. The only fragment with a remarkable relative abundance (apart from the octamers) is the dimer, and the fragmentation pattern with loss of dimeric subunits, suggests that the dimers are the building blocks of the serine octamers. There is controversy about the structure of the serine octamer. Schalley and Weis [98], and Schalley [105] propose a structure where the aminoacids are in zwitterionic form, so that electrostatic interactions (Fig. 3.6) keep the octamer together, more than 30 hydrogen bonds being responsible for the geometry of the cluster.

The preference shown for homochirality would come from the hydrogen bonds between side –OH groups and the carboxylate oxygen atom in the next serine molecule (Fig. 3.7).

If we introduce heterochiral units in a homochiral octamer, the number of such hydrogen bonds would be diminished, with an increase in the energy of the cluster. Additionally, the homochiral octamer shows an alternate pattern of ammonium and carboxylate groups, being an eight point contact surface, which would be disrupted by introducing heterochiral units, decreasing the number of contact points.

The authors performed DFT/BP86 calculations on the serine monomer and octamer. According to their calculations, the zwitterionic serine monomer is less stable than the neutral species by 128 kJ mol^{-1}. For eight serine molecules, this means a destabilization of 1,024 kJ mol^{-1}. However, calculations show the zwitterionic serine octamer is 1,018 kJ mol^{-1} more stable than eight isolated neutral serine molecules, which is a result of the stabilization by solvation of charges in the cluster.

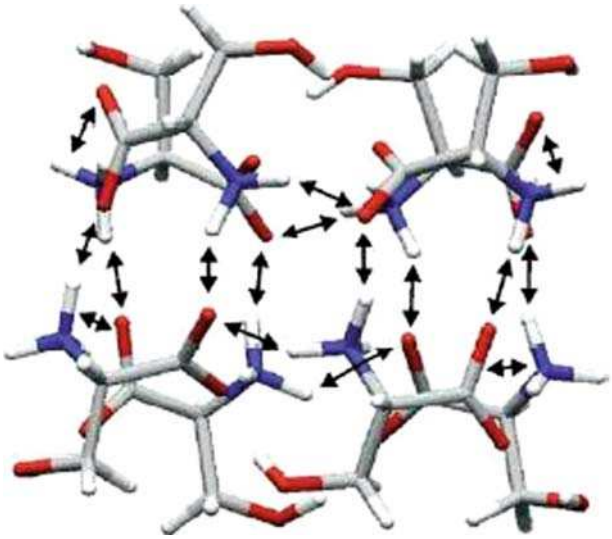

Fig. 3.6 Electrostatic interactions in serine octamer between zwitterionic-aminoacid units keep the cluster together

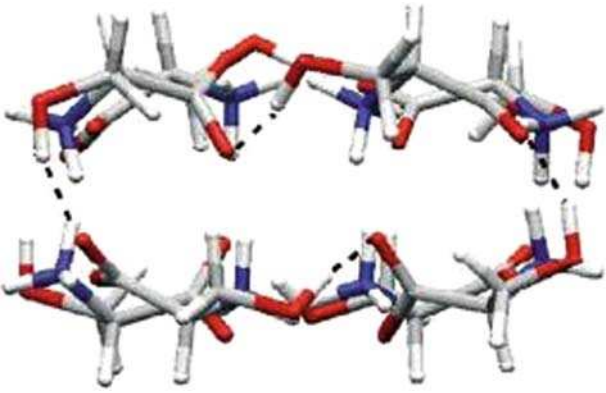

Fig. 3.7 Hydrogen bonds keep the cluster in shape

Shum et al. [106] carried out supersonic jet FTIR experiments on the chiral discrimination of neutral glycidol dimers (Fig. 3.8).

They found the main –OH stretching band placed at 3,492 cm^{-1} for the homochiral dimer and 3,488 cm^{-1} for the heterochiral one. The authors propose two main hydrogen-bonding behaviors. One possibility is the association by –O···H–O– bonds between the oxiranic oxygen of one glycidol molecule and the hydroxyl group of the other, being dimers with two hydrogen bonds. The other mode of association is a chelate, where both the oxirane and the hydroxyl group of one glycidol molecule are HB acceptors toward the hydroxyl group of the other molecule.

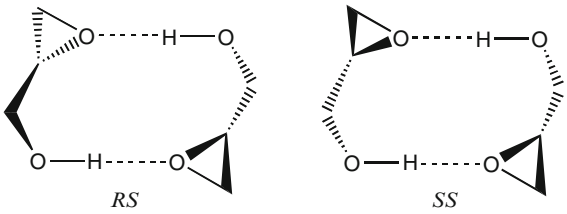

Fig. 3.8 Glycidol dimers

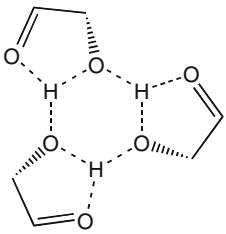

Fig. 3.9 Lactate trimers

Ab initio calculations at the B3LYP/6-31+G* level, show a higher stability for the dimer with two hydrogen bonds, and favor the chiral selectivity toward the homochiral dimer. The same group [107] studied the self-organization of methyl lactate in gas phase following the same experimental method. Again, the authors propose two association patterns by two C=O···H–O– bonds, or as a OH···OH···O=C chelate. In this case, the chelate dimers are 5 kJ mol^{-1} more stable than the doubly bonded dimers at the B3LYP/6-31+G* level, and 10 kJ mol^{-1} by MP2/6-31+G* methods. The chiral discrimination is in the 0–3 kJ mol^{-1} range. The spectral band analysis of the dimers shows several conformations, though in the presence of argon, the –OH stretching band shifts to a unique band, not affected by the change of the alkyl ester group (methyl, ethyl or isopropyl lactates). Another band, unaffected by the presence of argon in the experiment, is assigned to a homochiral trimer, where the hydrogen bonded carbonyl and hydroxyl groups are protected inside the cluster structure (Fig. 3.9).

The authors doubt this kind of processes being found on solution, due to the competition of solvation phenomena with the formation of complexes. Additionally, the solvation would make more difficult the study of chiral selectivity by FTIR, as there would be a broadening of the –OH stretching bands. However, they propose the study of the interactions of methyl lactate with several solvents, using the same gas phase technique.

Speranza [108] has developed a methodology to establish the enantiomeric discrimination of chiral monoalcohols and monoamines by mass spectroscopy. The method is based on the generation of supersonically expanded complexes formed by the alcohol or amine and chromophores as either R-(+)-1-phenyl-etanol or R-(+)-1-phenyl-1-propanol. The complexes thus formed, are ionized by R2PI (resonance 2-photon ionization spectroscopy) and their fragmentation studied by time of flight spectroscopy. It is possible to evaluate the enantiomeric discrimination

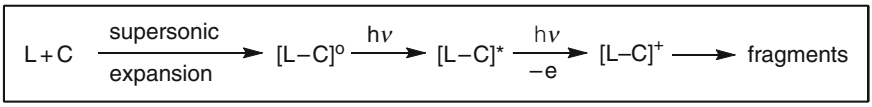

Scheme 3.12 A typical R2PI experiment

by following the shift on the bands of the free and complexed chromophore. There is also a different fragmentation in the diastereomeric complexes. The compounds used for the study are 2-butanol, 2-pentanol and 2-butyl amine, by complexation with R-(+)-1-phenyl-etanol or R-(+)-1-phenyl-1-propanol. The process can be described as shown in Scheme 3.12.

The binding energy of the [L–C]° and [L–C]* adducts depends on the nature and configuration of the functional groups in such a way that each complex is defined by a different resonant absorption ν, thereby allowing the specific ionization of an adduct in a mixture, even in the presence of the diastereomeric form. The analysis of the resonance frequencies for the complex transition between the fundamental and the first excited states shows a higher red shift in the heterochiral complexes vs. their homochiral analogs. This means a higher binding energy increase in the former than the latter during the first excitation. The authors point out that configuration issues are important, stating that the shift differences may be determined by the length of the side chain in the complexation agent (ethyl vs. propyl). The ligand conformation can have an influence as well, as an opposite shift has been found in the complexes of 2-pentanol with R-(+)-1-phenyl-1-propanol, due to steric congestion in the heterochiral complex [2-(S)-pentanol] which may modify the orientation of the –OH groups or even invert the HB donor–acceptor character of the groups.

Homochiral 2-butyl amine complexes show a higher fragmentation degree in the mass spectra vs. the heterochiral ones. For 2-butanol adducts, this behavior is inverted being higher the fragmentation for the heterochiral complexes in about 13–15%, even though the ionization provides a higher energy to the homochiral pairs. This is explained in terms of repulsive interactions operating on the heterochiral adducts, which are reduced in the case of the homochiral ones, with less hindrance.

The same group [109] has carried out another R2PI study on the chiral discrimination between R-(+)-1-phenylethan-1-ol and solvent molecules as S-(+)-butan-2-ol and R-(−)-butan-2-ol, and also with water (no chiral discrimination) to compare the contribution of dispersive forces vs. electrostatic interactions in the hydrogen bond. In the case of water, dispersive forces are reduced to the minimum, thereby making water a good reference. In the R2PI spectra of R-(+)-1-phenylethan-1-ol with S-(+)-butan-2-ol and R-(−)-butan-2-ol, there is a red shift of the chromophore band with respect to the free molecule. This implies that the chromophore acts as a HB donor, and the binding energy of both adducts is higher in the excited than in the fundamental one. This red shift is 12 cm^{-1} higher in the heterochiral complex than in the homochiral one, which means there is greater increase in the binding energy

of the former. The binding energy of the adduct in the fundamental state can be derived from the difference between the dissociative ionization limit of the adduct and the ionization limit of the free alcohol. In this case, the binding energy of the homochiral adduct is superior to that of the heterochiral one. The adducts of R-(+)-1-phenylethan-1-ol with water show two blue shifted peaks with respect to the noncomplexed chromophore, assigned by the authors to two electronic states, excited and fundamental.

Ab initio calculations at the B3LYP/6-31+G** level show the existence of only one conformation for the adduct. The blue shifted band assigned to the adduct indicates a –OH···π interaction between water and the chromophore [110–112]. The calculations made by these authors show two alternative structures. The more stable is the one with the alcohol as HB donor, and one of the water hydrogens placed at a distance of 1.98 Å with respect to the mass center of the aromatic ring in the alcohol molecule (Fig. 3.10). This –OH···π interaction is responsible for the two blue shifted chromophore bands. The less stable structure has the alcohol as HB acceptor, and no –OH···π interaction.

The authors explain that there is a slight equilibrium between attractive (electrostatic and dispersive) and repulsive (steric) forces in the fundamental and excited state of the adducts, depending on solvent configuration and the chromophore structure. The homochiral complexes have been found to be more stable than their heterochiral counterparts. Another R2PI study by Speranza [113] used R-(+)-1-phenyl-1-propanol as model, to study the interaction with several solvents as methanol, ethanol, 1-propanol, 2-propanol, 1-butanol, S-(+)-2-butanol, R-(−)-2-butanol, 1-pentanol, S-(+)-2-pentanol, R-(−)-2-pentanol, and 3-pentanol. The experimental results had the support of theoretical calculations at the B3LYP/6-31G level. In all cases studied, the homochiral complexes were found to be more stable than the heterochiral ones, both in fundamental and excited states, as well as for the corresponding ionic adducts.

Le Barbu et al. [114] have studied the chiral discrimination between 2-naphtyl-1-ethanol and propanol, 2-methyl-1-butanol, 2-butanol, and 2-pentanol by gas-phase fluorescence experiments in helium supersonic expansion, using laser controlled excitation. As the model compound chosen, 2-naphthyl-1-ethanol, has both a hydroxyl and a naphthyl group, a balance between HB and dispersive–repulsive forces with the solvent molecule can be attained. As a support, ab initio calculations at the MP2/6-31G** have been carried out. After studying the complex

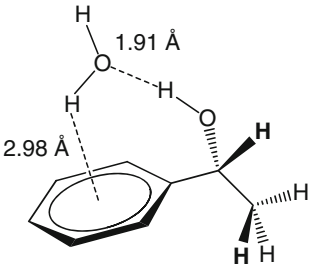

Fig. 3.10 Complexes of *R*-(+)-1-phenylethan-1-ol with water

formed, and taking into account the different conformations of the alcohol in the adducts, the important role of dispersive forces has been found. Depending on the chirality of the complex (homo- or heterochiral) and the aliphatic alcohol conformation (anti- or gauche-isomers), the hydrocarbon chain in the solvent has a different interaction with the naphthyl ring, with a change in the force balance determining the chiral discrimination in the complex.

The S0–S1 transition of the π electrons in the naphthalene ring does not substantially modify the electronic distribution of the hydroxy group in the chromophore. This is confirmed by the small energy difference of the transition from fundamental to excited state between 2-naphthyl-1-ethanol and 2-methyl naphthalene. Thus, the authors singled out dispersive forces as responsible for the stabilization of the excited complex vs. the fundamental state. In a recent article, these authors [115] use the same technique to study the complex formed by 2-aminoethanol and 2-naphthyl-1-ethanol, identifying several hydrogen binding modes through the amine and hydroxyl groups in the aminoalcohol.

King et al. [116] have studied the dimer of 2-butanol by microwave spectroscopy, using MP2/6-311G* calculations as support. The authors take into account conformational aspects, choosing previously to the spectroscopic analysis those dimers formed by the alcohol in the lowest energy configuration. Four different complexes are distinguished, two homochiral and two heterochiral, considering that both lone pairs in the oxygen atom may participate in hydrogen bonding. The calculations show one of the heterochiral complexes as the most stable, followed by the two homochiral complexes, and finally the other heterochiral adduct. By comparison with the rotational spectra of an enantiomerically pure sample, it has been possible to assign the spectral bands belonging to the heterochiral complex, showing a good agreement with the results obtained by ab initio calculations. The model indicates that the complexes tend to place the alkyl groups as far as possible, in order to minimize steric repulsion. This is accomplished by a rotation of the monomers along the oxygen–oxygen axis in the hydrogen bond.

Su, Borho and Xu have applied rotational spectroscopic and high-level ab initio studies to the 1:1 chiral molecular adduct of propylene oxide dimer [117]. Six homochiral and six heterochiral conformers were predicted to be the most stable configurations where each monomer acts as a proton acceptor and a donor simultaneously, forming two 6- or 5-membered intermolecular hydrogen-bonded rings. Rotational spectra of six, that is, three homochiral and heterochiral conformer pairs, out of the eight conformers that were predicted to have sufficiently large permanent electric dipole moments were measured and analyzed.

3.3.2 Pure Theoretical Studies

Leutwyler et al. [118] studied the degree of discrimination between hydrogen peroxide (HOOH) as HB donor and derivatives of 2-methyloxirane as HB acceptor at the MP2/6-311++G** computational level to optimize the structures, and with

the aug-cc-pVDZ, aug-cc-pVTZ, and aug-cc-PVQZ basis sets for the evaluation of the energies. The authors distinguish between the diastereofacial contribution that controls the face of the acceptor that forms the HB and the contribution between the two enantiomers of the donor on the same face of the acceptor. Two diastereomeric dimers can be obtained between HOOH and (R,R)-2,3-dimethyloxirane. The complex with the (P)–HOOH is favored over the (M)–HOOH by 1.5 kJ mol^{-1}.

In the case of dimers between HOOH and (R)-2-methyloxirane, four diastereomeric complexes are obtained (Fig. 3.11). The largest diastereomeric discrimination corresponds to the complexes in the syn face (−1.9 kJ mol^{-1}), which is the most stable dimer with the (P)–HOOH molecule. The chiral discrimination represents about 6% of the HB interaction energy.

The energetic, geometric, and electronic differences of the meso and chiral form of oxirane **1** and cyclobutene **2** derivatives were studied using DFT methods (Fig. 3.12) [34]. The partition of several molecular characteristics (energy, charge, and volume) into atomic contributions was carried out within the AIM framework. The energetic analysis shows that the main contribution to the energy differences came from the chiral carbon atom where the substituents X are attached. The molecular volume differences can be explained based on the results obtained for the substituents in both dispositions.

Partition methodologies have been classically used in which charge densities are concerned; however, their application to other properties such as energy and volume, is less common. In the paper [33], we describe how the differences in these atomic contributions shed light in the relative properties of diastereomeric molecules.

The chiral self-discrimination of twelve molecules showing axial chirality (Scheme 3.13), has been studied by means of DFT (B3LYP/6-31+G**) and ab initio (MP2/6-31+G** and MP2/6-311++G**) methods [25]. The interaction energy of the complexes was corrected with the inherent basis set superposition error (BSSE) and the zero point energy (ZPE). The results show similar qualitative tendencies for the three methods considered.

The interaction energies of the dimers, E_I, range between −27.2 and −77.4 kJ mol^{-1} while the corrected $E_{I(corr)}$ ones are between −11.3 and −52.3 kJ mol^{-1}. Regarding the relative energy of the homo vs. the heterochiral complex, the preferences are equally divided. The energetic distortion of the monomers within the

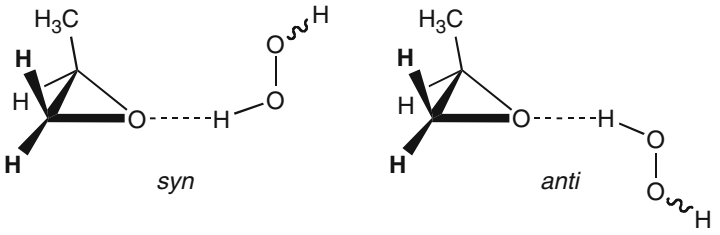

Fig. 3.11 Schematic representation of the *syn* and *anti* dimer of HOOH with (*R*)-methyloxirane

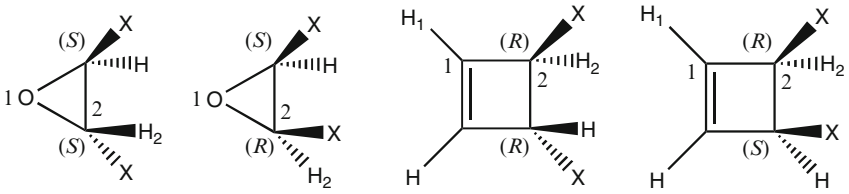

1 *(chiral)* **1** *(meso)* **2** *(chiral)* **2** *(meso)*

X = F, Cl, Br, CH_3, CN, CCH, CF_3, SiH_3

Fig. 3.12 Oxiranes and cyclobutenes

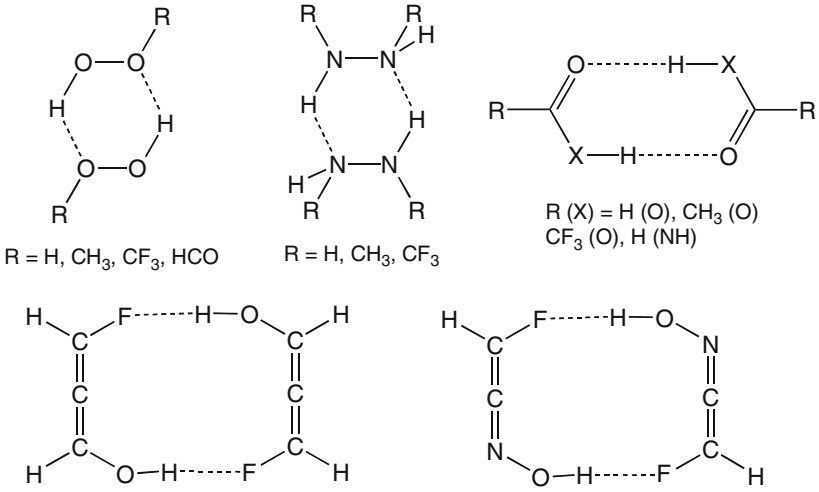

Scheme 3.13 Molecules with axial chirality

dimers is not able to explain the relative energy of the latter ones. The energetic differences found between monomers account up to 10% of the relative energy of the dimers and, in general, have opposite signs. Thus, the most stable dimers are formed with the less stable monomers.

The electron density analysis within the AIM methodology shows the presence of bond critical points due to the formation of the HB and, in some homochiral dimers, also between oxygen atoms of different molecules (Fig. 3.13). The presence of the latter bcps is associated to those complexes where the homochiral complex is more stable than the heterochiral one.

We carried out a theoretical study of the hydrogen peroxide clusters, (HOOH)n, from 2 to 10 monomers, using DFT/B3LYP and MP2 ab initio methods (Fig. 3.14) [35]. The results show that for n=2 and 3, the cluster with mixed chirality is preferred, while for larger clusters, the homochiral cluster is favored. The optical

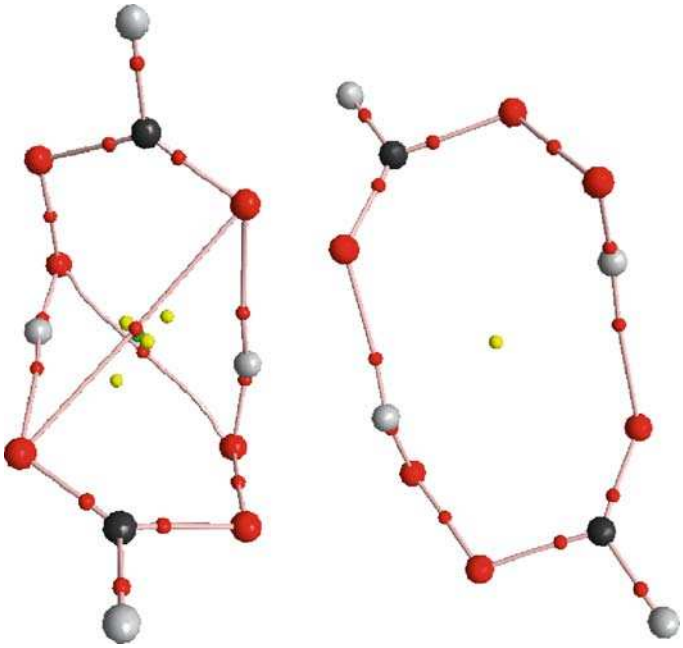

Fig. 3.13 Molecular graphs of the dimer of formic peroxyacid. Bond, ring, and cage critical points are represented with *red*, *yellow,* and *green dots*, respectively

rotatory power and vibrational circular dichroism spectra of some of the systems were also calculated and analyzed.

The final aim of this work is to encourage the experimental study of these complexes and understand the importance of the chiral effect of the different monomers within the final clusters as has been shown in the experimental study of hydrazine and lactate clusters. Another report on the different motifs of hydrogen peroxide clusters has also been published that shows similar energetic trends to the ones found in our work, but without considering their implications in the chiral recognition processes [119].

The electron density and its Laplacian have been correlated exponentially with the HB distance. These results are in agreement with other reports that show the generality of this rule [120–122]. The dimers of a series of chiral and nonchiral α-aminoalcohols were studied by means of DFT methods (B3LYP/6-311++G**) (Scheme 3.14). Due to the flexibility of the molecules, twelve possible complexes can be proposed in the case of the chiral molecules. Half of them are mirror image of the other half, and thus, only six where considered. The six unique configurations studied for each dimer (Scheme 3.15) correspond to three homochiral dimers (RR or SS) and three heterochiral ones (RS or SR), and can be grouped in three chairs, C1–3, and three boats, B1–3, respectively.

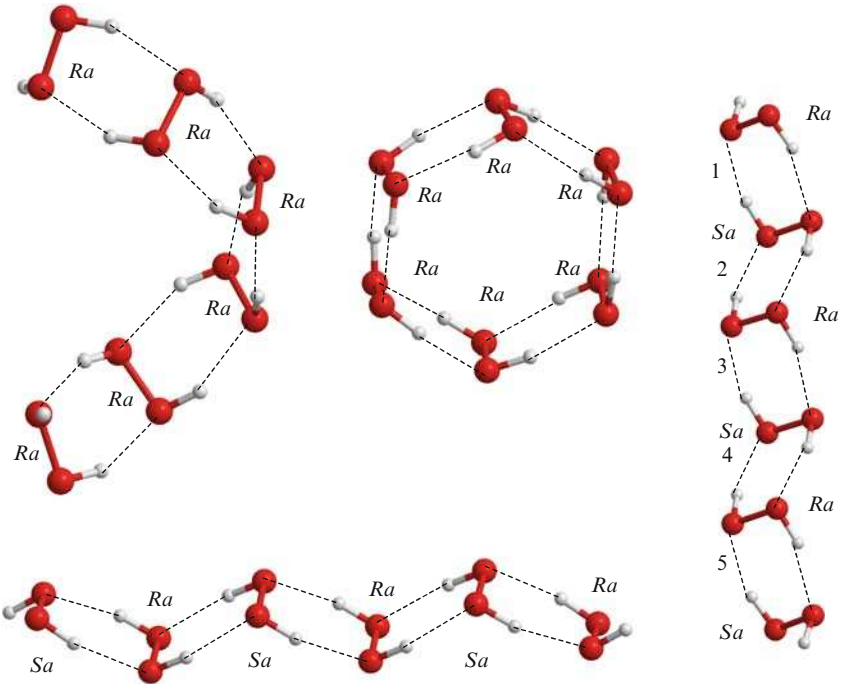

Fig. 3.14 Optimized geometries of the noncyclic homochiral, cyclic homochiral and noncyclic alternant chiral hexamers

The BSSE corrected interaction energy of the dimers ranges between −29 and −50 kJ mol^{-1}. If the contribution of each HB can be considered as independent, an average value of 25 kJ mol^{-1} will result which is similar to the HB formed in the water dimer (22.2 kJ mol^{-1}). The HB distance varies between 1.83 and 1.97 Å, and the HB angles are close to linear (>160°). In all the cases, the shorter HB corresponds to the most stable dimer. In addition, a linear correlation between the interaction energy of the dimer and the average HB distance can be established (Fig.3.15), as indication that the HB is the main interaction stabilizing the dimers.

In gas phase, the most stable conformation always corresponds to a heterochiral one in a chair disposition and the worse one to a homochiral one in a boat disposition. The largest difference between these two extremes is 17 kJ mol^{-1}. An estimation of the solvation effect has been carried using the PCM model and water as solvent. The ΔGsol range between −17 kJ mol^{-1} for the dimer of X/Y = CF_3 to −19 for X/Y = F/H. What is more important is the effect on the relative energy of the different configurations. Thus, in three of the cases studied

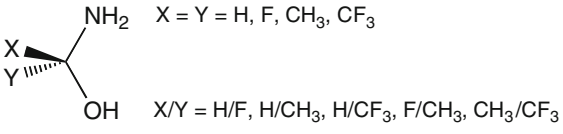

Scheme 3.14 Chiral and nonchiral α-aminoalcohols

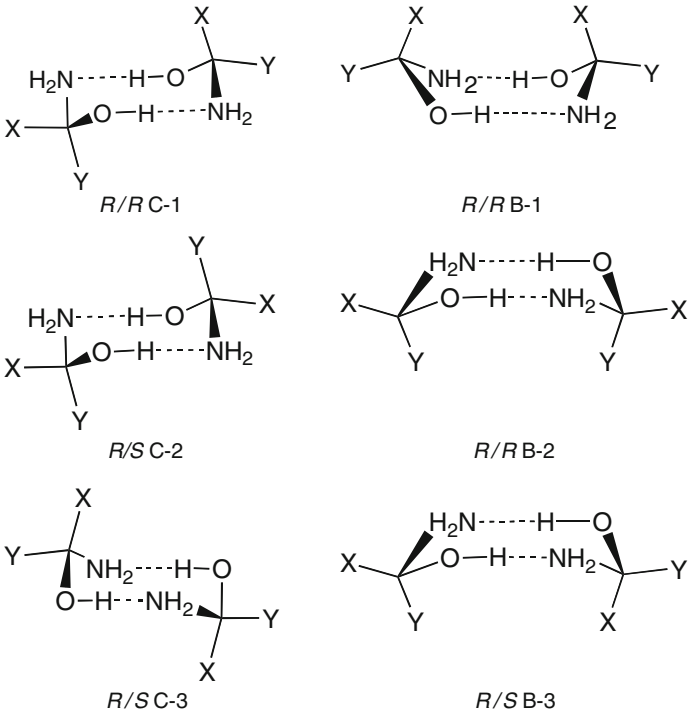

Scheme 3.15 Schematic representation of the configurations considered (B stands for pseudo-boat conformation and C for pseudo-chair)

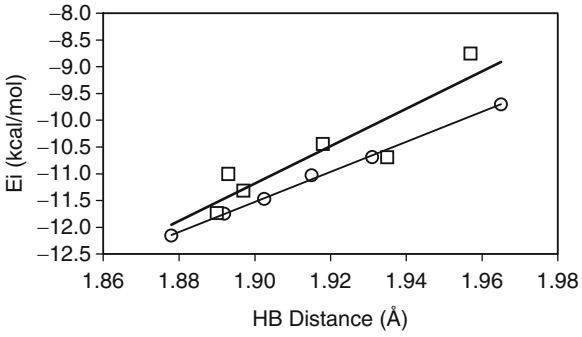

Fig. 3.15 Interaction energy vs. average HB distance for the dimers of X/Y=H/CH_3 (*circles*) and CF_3/CH_3 (*squares*). The corresponding linear relationships represented show correlation coefficients of 0.999 and 0.91, respectively. For the rest of the cases the correlation coefficients are 0.93, 0.97, and 0.93 for X/Y=H/F, H/CF_3, and F/CH_3, respectively

(X/Y=H/CH_3, H/CF_3, F/CH_3), the inclusion of the solvation energy results in that one of the homochiral configurations became the most stable, in contrast with the gas phase results.

Scheme 3.16 1H-1,6a-dihydropirrolo[2,3-b]pyrrole derivatives

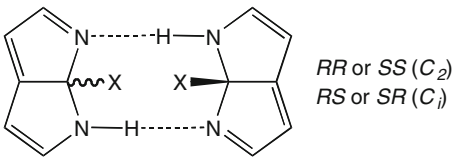

The homo- and heterochiral self-association of 1H-1,6a-dihydropirrolo[2,3-b] pyrrole derivatives has been studied using density functional theory (DFT) (B3LYP/6-31+G**) and ab initio (MP2/6-311+G**) methods [26]. The selected pyrrolo–pyrrole structure (Scheme 3.16) has a unique disposition of the NH group situated in cis to the substituent in position 6a. This simplifies the study, reducing the potential number of conformations, and also maximizes the interaction of the 6a position X groups in the homochiral complexes, as they are forced to point each other.

The complexes presenting two simultaneous hydrogen bonds may be found as homochiral dimers, where the groups in 6a position are above the average plane of the molecule skeleton, whereas in the heterochiral complexes, these groups are at opposite sides of the average molecular plane. The geometries of the complexes are C_2 and C_i for the homo- and heterochiral complexes, respectively. For the parent compound where X = H, the spatial disposition of the dimers favors the heterochiral complex in about 1.8 kJ mol^{-1}. The results obtained for several substituents are summarized in Table 3.1, where it can be observed that there is an increase in the chiral discrimination as the size and electrostatic repulsion of the X groups increase. The highest found value is −17 kJ mol^{-1} for the trichlorosilyl derivative (see Fig. 3.16).

When amphiprotic groups as NH_2 and OH are placed in 6a position, the possibility of a third hydrogen bond appears, and as a result, the tendency is reversed, the homochiral complexes being more stable than their heterochiral counterparts, due to the third hydrogen bond formed in the homodimer. In the amino substituted compound, the discrimination energy favors the homochiral complex in 11.3 kJ mol^{-1}.

Table 3.1 Chiral discrimination (kJ mol^{-1}) calculated at the B3LYP/6-31+G**and MP2/6-311+G** (in parenthesis). Negative values indicate that the heterochiral dimers are more stable

X	Chiral discrimination
H	−1.76 (−1.51)
F	−2.55 (−2.55)
Cl	−5.31 (−5.31)
CH_3	−6.61 (−8.28)
CN	−9.58 (−7.70)
CCH	−4.06
CF_3	−8.83
CCl_3	−13.68
$C(CH_3)_3$	−7.87
$Si(CH_3)_3$	−11.80
SiF_3	−11.09
$SiCl_3$	−16.90

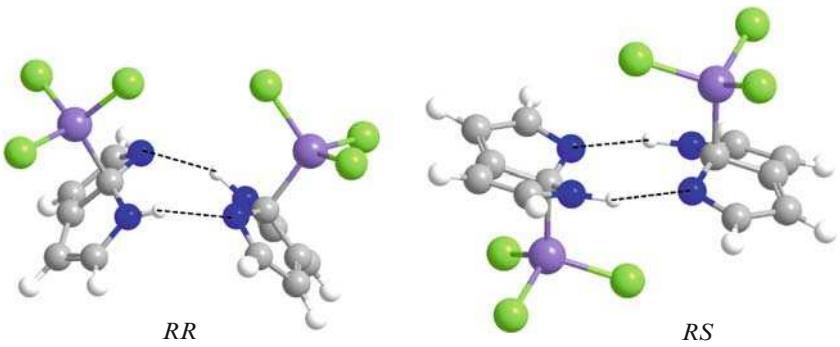

Fig. 3.16 Optimized structures of the homo and heterochiral dimers of trichlorosilyl derivatives

Two different proton transfer mechanisms, concerted and nonconcerted, have been studied (Scheme 3.17).

The nonconcerted TS presents a unique imaginary frequency, as indication of true TS. The results obtained in the MP2 calculations for the calculated transition states are slightly higher than the DFT values obtained, in agreement with previous reports showing DFT calculations underestimate TS barriers [98].

During the proton transfer process, a compression of the complexes is found to lower the energetic barrier [99]. In the cases studied here, the compression of the N···N distance is about 0.4 and 0.35 Å for the concerted and nonconcerted TS structures, respectively. Due to this compression in the TS, the chiral discrimination is larger than in the corresponding minima, up to 6.3 kJ mol^{-1}.

A similar study has been carried out for the self-association of 1,8a-dihydro-1,8-naphthyridine derivatives using DFT methods (B3LYP/6-31+G** and B3LYP/6-311++G**) [28]. Two possible dimers can be obtained from chiral 1,8a-dihydro-1,8-naphthyridine derivatives homochiral C_2 dimers and heterochiral C_i symmetry

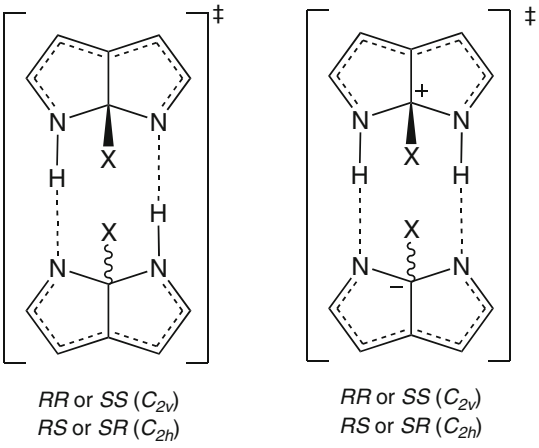

Scheme 3.17 Schematic representation of the proton transfer processes studied. On the left, the concerned transition state and on the right the nonconcerned one are shown

dimers (Scheme 3.18). The corrected interaction energies and the relative energies of the complexes studied are gathered in Table 3.2.

The energy results obtained with the two basis sets are very similar. In the cases treated, the heterochiral dimers (RS or SR) are always more stable than the homochiral ones (RR or SS). The largest relative energy is observed in the CF_3 dimers, probably due to the combination of the steric hindrance and electronic repulsion in the homochiral dimer. The *t*-butyl dimers that present mainly steric hindrance show smaller relative energies.

The proton transfer within the isolated monomers and in the dimers has been studied. The TS structure in the isolated monomer shows a C_s symmetry and produces an inversion in the chirality of the C8a center (Scheme 3.19). This intramolecular process presents high energy barriers (>113 kJ mol^{-1}), in analogy with similar processes in other heterocycles [123].

For the intermolecular proton transfer in the dimers, similar behavior and structures as in the previously described pyrrolo–pyrroles are found, being the nonconcerted TS the true states, with only one imaginary frequency, and C_s symmetry. The proton transfer energy barriers of the dimers range between 59

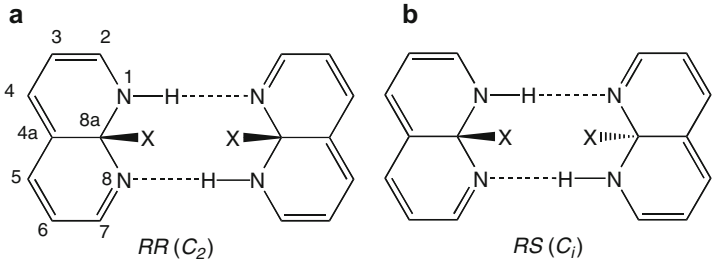

Scheme 3.18 Representation of the homochiral (**a**) and heterochiral dimers (**b**)

Table 3.2 Corrected interaction energy and relative energy (kJ mol^{-1}) of the homo vs. heterochiral dimers calculated at the B3LYP/6-31+G** and B3LYP/6-311++G** levels of theory

X	Chirality	B3LYP/6-31+G**		B3LYP/6-311++G**	
		$E_{I(corr)}$	E_{rel}	$E_{I(corr)}$	E_{rel}
H	RR	−49.0	0.0	−49.7	0.0
H	RS	−49.7	−0.5	−50.5	−0.6
F	RR	−49.9	0.0	−50.8	0.0
F	RS	−55.0	−5.1	−54.9	−4.6
CH_3	RR	−46.1	0.0	−46.5	0.0
CH_3	RS	−48.9	−3.0	−49.0	−3.0
CN	RR	−44.1	0.0	−44.4	0.0
CN	RS	−49.7	−5.6	−50.6	−5.8
CCH	RR	−45.2	0.0	−46.9	0.0
CCH	RS	−48.7	−3.5	−49.9	−3.6
CF_3	RR	−41.5	0.0	−42.9	0.0
CF_3	RS	−49.2	−7.7	−51.0	−7.9
t-Bu	RR	−37.1	0.0	−38.4	0.0
t-Bu	RS	−42.9	−6.2	−44.3	−5.9

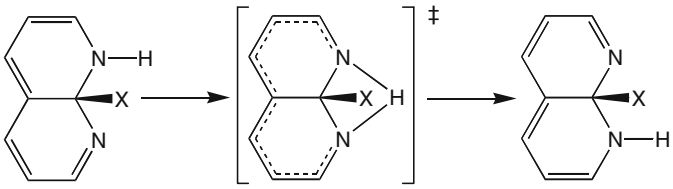

Scheme 3.19 Representation of the proton transfer within the isolated 1,8a-dihydro-1,8-naphthyridine derivatives

and 42 kJ mol^{-1} these values being about 84 kJ mol^{-1} smaller than the corresponding proton transfer in the isolated compounds. This indicates that the dimer formation considerably favors the proton transfer processes. Again, the chiral discrimination within the TS structures is larger than in the corresponding minima due to a closer proximity of the X groups within the homochiral dimers, which produces an additional penalty for those complexes.

The geometrical characteristic of the minima and transition states of the 1H-1,6a-dihydropirrolo[2,3-b]pyrrole and 1,8a-dihydro-1,8-naphthyridine derivatives have been analyzed using a Steiner–Limbach relationship [124–127]. This model is based on the assumption that the total valence of the hydrogen atom involved in the HB is equal to 1 (3.1). The r_1 and r_2 distances are defined in Fig.3.17 (right), and r_0 corresponds to the N–H distance for the isolated case (for the definition of r_1 and r_2 see [128]. The reformulation of (1) provides (2) that is expressed as a function of (r_1+r_2) and (r_1-r_2), which in lineal systems, corresponds to the distance between the heavy atoms and the relative position of the hydrogen, respectively. As shown in Fig. 3.17, all the geometries nicely fit in the same equation.

$$e^{(r_0-r_1)/b} + e^{(r_0-r_2)/b} = 1 \tag{3.1}$$

$$(r_1 + r_2) = 2r_0 + 2b\ln\left(1 + e^{-(r_1-r_2)/b}\right). \tag{3.2}$$

The chiral discrimination in the self-association of chiral 1,3a,4,6a-tetrahydroimidazo[4,5-d]imidazoles **3** has been studied using density functional theory methods [37], (Scheme 3.20). Clusters from dimers to heptamers have been considered. The heterochiral dimers (RR:SS or SS:RR) are more stable than the homochiral ones (RR:RR or SS:SS) with energy differences up to 17.5 kJ mol^{-1}. Besides, in larger clusters, the presence of two adjacent homochiral molecules imposes an energetic penalty when compared to alternated chiral systems (RR:SS:RR:SS...). The differences in interaction energy within the dimers of the different derivatives have been analyzed based on the atomic energy partition carried out within the AIM framework. The mechanism of proton transfer in the homo- and heterochiral dimers shows large transition-state barriers, except in those cases where a third additional molecule is involved in the transfer. The optical rotatory power of several clusters of the parent compound has been calculated and rationalized based on the number of homochiral interactions and the number of monomers of each enantiomer within the complexes.

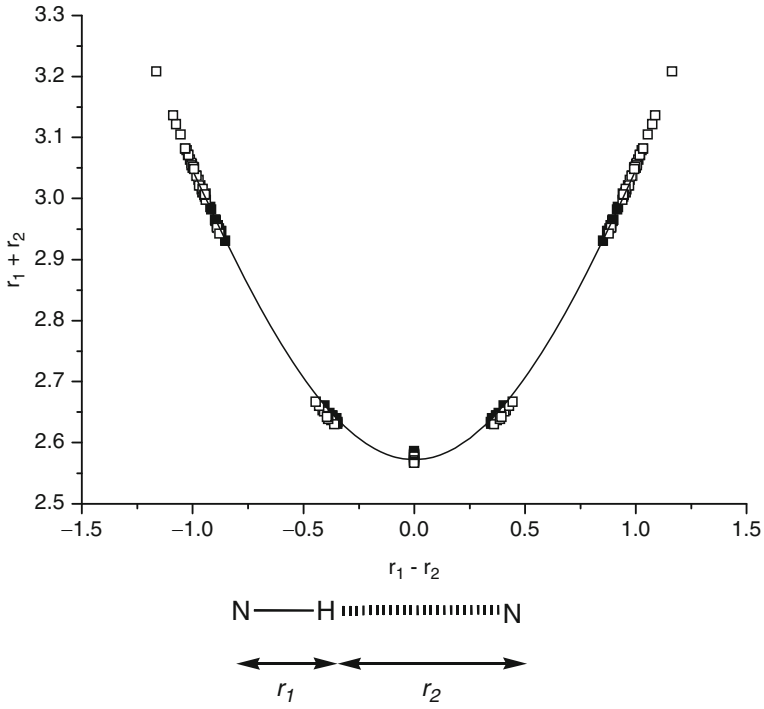

Fig. 3.17 r_1+r_2 vs. r_1-r_2 parameters for the calculated dimers structures of 1,8-naphthyridines in *black* and pyrrolo[2,3-*c*]pyrrolines in *white*. The fitted Steiner–Limbach relationship corresponds to $(r_1+r_2)=2*r_0+(r_1-r_2)+2*b*\mathrm{In}[1+\exp(-(r_1-r_2)/b)]$, with $r_0=0.985\pm0.001$, $b=0.429\pm0.002$, $r^2=0.999$, $n=154$

Again the limiting step corresponds to the transfer of the external proton; once this is achieved, the rest of the TS and the intermediate are below this barrier indicating that the proton will be transferred freely generating a barrierless racemization along the chain in a wavelike expansion [37] (Scheme 3.20).

Two mechanisms of transformation of one of the enantiomers into the mirror image one have been explored. The first one consists of the inversion of the carbon atoms evolving through a planar eight-membered ring into the other enantiomer. The second one corresponds to the simultaneous transfer of the two protons attached to the nitrogen of these molecules. In this case, the monomer and the two dimers have been studied both isolated and in the presence of one and two water molecules. The involvement of an additional molecule, water or another imidazoimidazole, reduces significantly the proton-transfer barrier. The chiral discrimination in the TS and intermediates studied for the dimers is larger than in the most stable dimer due to the higher energy values of the homochiral derivatives when compared to the heterochiral ones. Finally, the optical rotatory power of some of the derivatives has been computed. A small value has been obtained for the isolated monomer, but the formation of clusters increases significantly the values obtained. The ORP values

Scheme 3.20 1,3a,4,6a-Tetrahydroimidazo[4,5-d] imidazoles **3**

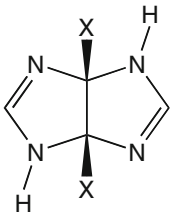

have been correlated with the number of homochiral interactions and the number of monomers of each enantiomeric form within the cluster.

Chiral recognition in complexes, linked by hydrogen bonds, has been studied experimentally and theoretically. In some cases, chiral systems can aggregate and form long chains or helix shape structures. The subsequent chemical processes along the chains can invert the chirality of the molecules producing what we have called racemization waves [37]. The control and rationalization of these processes are of the utmost importance in the development of novel molecules designed as switches.

A study of the chiral discrimination in diaziridine clusters has been carried out using DFT computational methods [38]. The most stable neutral structure corresponds to that with the monomers in alternated chirality. The proton transfer within the neutral diaziridine chain proceeds with high TS barriers. The protonation of the fist diaziridine of the chain tends to produce a spontaneous proton transfer from the first monomer to the second (Fig. 3.18). The studied processes of proton transfer in the charged system show small barriers. The proton transfer in the neutral or protonated systems produces an inversion of the chirality of the monomers as the process evolves along the chain producing chirality waves. Finally, the calculated ORP of the clusters is very dependent on the cluster size, cyclic or helix shape, and on the number of monomers that form the cluster.

The chiral discrimination in cyclic dimers and trimers of mono-substituted sulfoxides and thioperoxides (Scheme 3.21) has been studied by means of DFT (B3LYP/6-31+G**) and ab initio (MP2/6-311+G**) calculations [5]. In addition, the inter- and intramolecular proton transfer processes that interconvert these two classes of compounds have been considered for the isolated molecules and the clusters. These two classes of compounds present different kinds of chirality, while the sulfoxides show a stereogenic sulfur atom, the thioperoxides present axial chirality.

In all the cases considered, the thioperoxide isomer is more stable than the corresponding sulfoxide. The energy differences ranged between 33 kJ mol^{-1} for the fluorine derivative up to 134 kJ mol^{-1} for the SiH_3 substituted compound. The calculated TS barrier for the transformation of the isolated sulfoxide into the corresponding thioperoxide has been found to correlate with Taft's mesomeric constants, σ_R (3.3).

$$\mathrm{MP2} \cdot E_{\mathrm{rel}}\,(\mathrm{kJ\ mol^{-1}}) = 100 + 186\,\sigma_{\mathrm{R}}, \quad n = 8, r = 0.997. \tag{3.3}$$

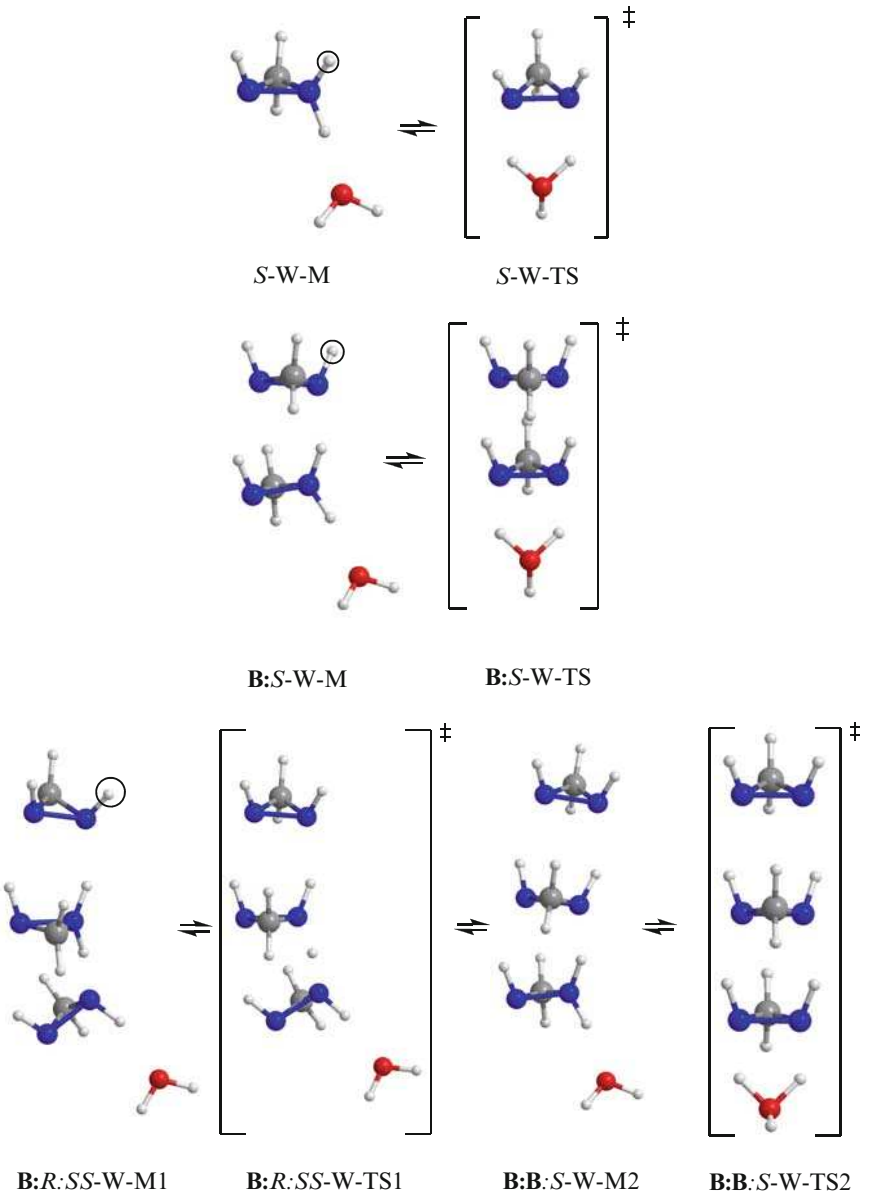

Fig. 3.18 Proton Transfer process in the presence of a water molecule. The circled hydrogen atom corresponds to the proton added to the molecules

The dimers studied present two simultaneous hydrogen bonds as indicated in Scheme 3.22 for the homochiral system. The interaction energies of the sulfoxide dimers range between −36.4 and −69.9 kJ mol^{-1}, while the range for the thioperoxides dimers is from −15.5 to −37.2 kJ mol^{-1}. These differences can be explained

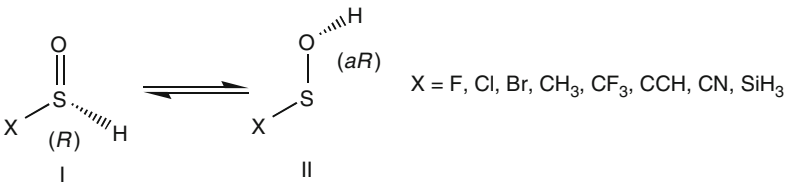

Scheme 3.21 Schematic representation of the monomers considered

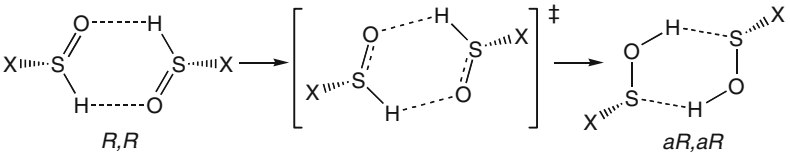

Scheme 3.22 Representation of the minima and TS of the homochiral dimers

since the S–H···O interactions are stronger than the O–H···S ones as shown in model complexes.

The relative energies between the two tautomeric complexes are almost twice the size of the corresponding monomer with a minor correction due to the stronger interaction energy of the sulfoxides vs. the thioperoxides dimers. The TS barriers range between 125 and 238 kJ mol^{-1}, which represent a reduction of 50–113 kJ mol^{-1} to those of the corresponding monomers. This is due to the presence of a second molecule that intervenes in the process and relaxes the geometrical structure disposition of the TS. Good linear relationships were found between the relative energy and the TS barrier vs. the Taft's mesomeric constants.

The chiral discrimination found in the minima and TS structures of these dimers are gathered in Table 3.3. Herein, no clear tendency was observed with a relatively large number of homochiral dimers (R,R or SS) being more stable than its corresponding heterochiral ones. Attempts to explain these results based on secondary interactions using the AIM methodology resulted in poor correlations with steric parameters such as Taft's E_S, an indication that a more complex mechanism controls these energetic differences.

Only three of thioperoxides studied present stable sulfoxides (X = F, Cl, and Br), and do not transform spontaneously to the corresponding thioperoxides. The interaction energies obtained follow the same tendency observed for the dimer with larger values due to a clear cooperative effect.

The chiral discrimination of the trimers (Table 3.4) shows that in all cases, the heterochiral trimer is more stable than the homochiral one, with the exception of the fluorine derivative of the sulfoxide and the TS of the chlorine one where both give almost identical energies.

The analysis of the geometries of all the minima and transition state of this study shows an excellent Steiner–Limbach correlation [128] for the 88 S···H····O interactions.

Table 3.3 Chiral discrimination (kJ mol^{-1}) calculated at the MP2/6-311+G** level[a]

X	Sulfoxides	Thioperoxides	TS	ES (Taft)
	Chiral discrimination	Chiral discrimination	Chiral discrimination	
Br	−1.72	1.00	4.23	−1.16
CF_3	1.26	−2.05	−5.65	−1.90
CH_3	−1.67	−2.68	−1.17	−0.12
Cl	−2.34	0.59	3.89	−0.97
CN	−0.59	−1.26	5.10	−0.51
F	−2.13	−2.47	1.09	−0.55
HCC	1.55	1.80	7.28	–
SiH_3	−2.26	0.59	−2.76	–

[a]Negative values indicate that the heterochiral dimer (RS) is more stable than the corresponding homochiral one (RR)

Table 3.4 Chiral discrimination (kJ mol^{-1}) calculated at the MP2/6-311+G** level[a]

X	Sulfoxides	Thioperoxides	TS
	Chiral discrimination	Chiral discrimination	Chiral discrimination
Br	−1.13	−4.10	−0.25
Cl	−1.80	−3.93	0.00
F	3.31	−2.93	−1.97

[a]Negative values indicate that the heterochiral trimer (RRS)is more stable than the corresponding homochiral one (RRR)

We have published a theoretical study of peptide model dimers in what homo- vs. heterochiral recognition is concerned for For–Gly–NH_2, For–Ala–NH_2, and four of their fluoro substituted derivatives using DFT methods (B3LYP/6-31+G** and B3LYP/6-311+G**) [27]. This is related to the work of Kojo and Tanaka [129], and Kojo et al. [130] that experimentally studies the cocrystallization of asparagine with other aminoacid.

Initially, the conformational minima for each isolated monomer were calculated by rotating the φ and ψ angles (Scheme 3.23). The number of minima found range between 3 and 4 for the nonchiral cases, and between 5 and 6 for the chiral ones. The results obtained at the two computational levels considered here are almost identical. The βL conformation is the most stable one for all cases except for glycine and alanine where it shows a relative energy of 0.4 and 3.6 kJ mol^{-1}, respectively. The presence of fluorine atoms as X1 or X2 substituents tends to destabilize the γ and δ conformations and favors the presence of ε and α ones that are absent in the rest of the cases. The intramolecular HB formed in each case is responsible for these tendencies. While the γ and δ conformations present an intramolecular HB that is disrupted by the presence of fluorine atoms at X1 and X2, new HBs are formed in the ε and α conformation, stabilizing their relative energies.

All the possible homo and heterochiral dimers as a combination of the different conformations of the monomers were built. Since the barriers between conformers within the monomers are small, in the process of optimization of the dimers, those

Scheme 3.23 Compounds studied and definition of the φ and ψ angles

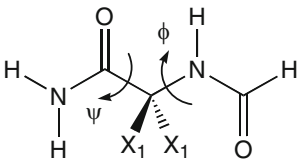

X_1	X_2
H	H
F	F
F	H
CH_3	H
CH_3	F
CF_3	H

corresponding to high-energy monomers disappear, due to the driving force of the HBs formed in the process. Thus, the number of minima found for the dimers ranges from 4 to 7 considering only the homochiral dimers, and can be twice if the homo and heterochiral ones are taken into account. A total number of 45 unique dimers were obtained for the six systems studied.

The interaction energy of the dimers shows that the g conformers are the most suitable to form two simultaneous HBs with interaction energies of -58 kJ mol^{-1} approximately for the dimers calculated. In contrast, the β conformers are the ones with the lowest interaction energies with only -29 kJ mol^{-1} approximately. Thus, the relative stability of the dimers is a balance between those of the starting monomers and the interaction energy. Considering independently the homo and heterochiral dimers in six cases, the most stable dimers are formed by γ monomers, in two cases by ε ones and in one case a mixture of γ and ε, and in another one by a dimer of β monomers. In general, the most stable dimers correspond to those in which analogous groups are located above and below the average plane formed by the HBs. Thus, in the homodimers, the most stable configuration corresponds in several cases to γL/γD configurations, while in heterodimers, it is formed by the same configuration with opposite chirality as L-γL/D-γL.

The heterochiral dimers are favored over the homo chiral ones in three of the four chiral cases. The only case where the homochiral disposition is favored corresponds to the α-fluoroalanine derivative ($X_1/X_2 = CH_3/F$) where an additional stabilizing interaction is observed between the π-clouds of the formylamino groups at the opposite ends of both monomers.

The differences in energy found for the heterochiral dimers vs. the homochiral ones (between 2.9 and 10.1 kJ mol^{-1}) should lead to very different populations of the given dimers; thus, it should be possible to observe these differences with a variety of standard techniques. In this sense, the homo and heterochiral dimers of *N*-acetylvaline *t*-butyl ester [131] and dihydroquinones [132] have been observed by NMR spectroscopy.

The calculation of the NMR shielding of the monomers shows a clustering of the values as a function of the conformation of the aminoacids, as has been shown previously by Perczel and Császár [133]. In the dimers, the formation of the HBs produces a shielding of the oxygen that acts as HB acceptor and a deshielding in the hydrogen atom up to 42 and -4 ppm, respectively. In addition, a deshielding of all the nuclei of the peptide backbone is observed in the complexes, with the exception of the Cα carbons, which show positive and negative variations. In the case of homo

vs. heterochiral complexes, the differences are large enough, even for those cases where the same conformers are involved, to be able to differentiate the two possible complexes experimentally.

Interesting correlations have been found between geometrical aspects of the dimers and energetic and electronic properties of the dimers. Thus, a clear relationship is obtained between the HB distance and angle (Fig. 3.19). The shorter HB corresponds to the more linear interaction. Other relationship involves a linear correlation between the HB distance and interaction energy, and an exponential relationship between the electron density and its Laplacian with the HB distance.

The dimers of phosphinic acid derivatives are one of the strongest HB complexes found in gas phase [134–137]. The chirality of the phosphinic acids relies on the presence of two nonidentical substituents on the phosphorus atom and the position of the hydrogen bonded to one of the two oxygens linked to the phosphorus. The chiral recognition in the minimum and proton transfer transition state structures of fifteen pairs of chiral phosphinic acid dimers (Scheme 3.24) has been carried out using DFT and MP2 methods, up to MP2/6-311++G(3df,2p) level [30].

The values of the interaction energy, between −93 and −106 kJ mol^{-1}, and the O···H distance of the HB formed, 1.59 Å in average, obtained at the MP2/6-311++G (3df,2p)//MP2/6-311+G** computational level, indicate the strength of the complex formed. In the same direction, the energy of the proton transfer barrier is very small (between 14 and 20 kJ mol^{-1}).

Even though the strength of the complexes is large, small chiral discrimination energies are obtained ranging from −0.67 to 0.37 kJ mol^{-1} at the MP2/6-311++G (3df,2p)//MP2/6-311+G** level. The small chiral discrimination found in the dimers studied could be associated to the tetrahedral disposition of the phosphorus atom that keeps far apart the nonoxygen substituents reducing the possibility of interaction between them, both in the homo and the heterochiral complexes. In order to confirm this hypothesis, calculations, where the substituents are in closer proximity within the dimers (Scheme 3.25), have been carried out. In these new

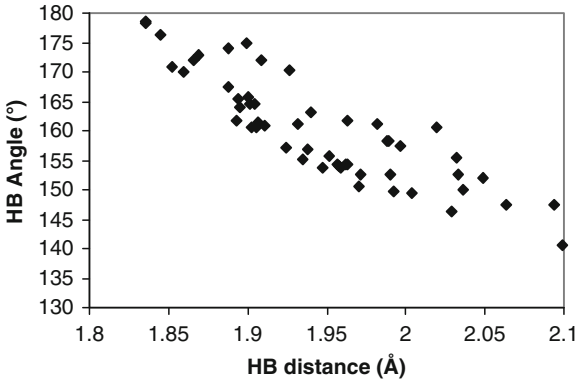

Fig. 3.19 NH···O angle vs. H···O distance in the HB formed

Scheme 3.24 Dimers of chiral phosphinic acids

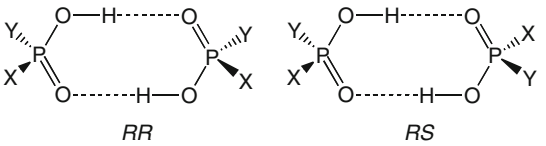

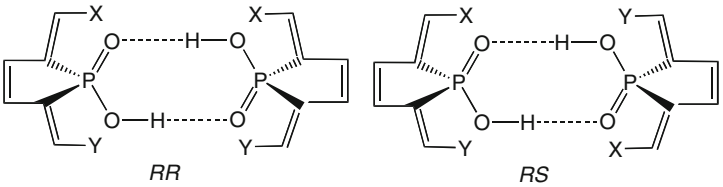

Scheme 3.25 Model of congested phosphinic acid dimers,

Scheme 3.26 Representation of the cyclic α-hydroxy carbonyl compounds

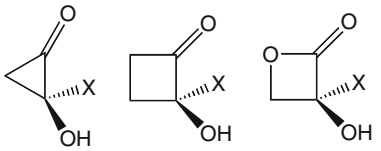

cases, energetic differences up to 9.2 kJ mol^{-1} have been obtained for X/Y = CF_3/H, favoring the heterochiral complex.

A study on the chiral complexation preferences of three series of cyclic α-hydroxy carbonyl compounds (Scheme 3.26) has been carried out using DFT and MP2 calculations. The dimer formation study has been preceded by a conformational exploration of the isolated monomers of the parent compounds. In addition, three possible dimers have been considered initially in the dimers of the parent compound, discarding those with the highest energies for the rest of the derivatives.

The energy results show a general preference for the heterochiral complexes, especially in the B3LYP/6-31+G** calculations. These results have been rationalized based on both the orbital interaction between the monomers and the distortion energy. In addition, a good linear relationship between the [O(lone pair) → OH (σ*)] and the HB distance (Fig. 3.20) has been found.

The conformational minima of a series of chiral ethers have been studied by means of DFT (B3LYP/6-31+G**) and ab initio (MP2/6-311+G**) methods [40]. The protonation of these compounds produces diasteromeric systems depending on the protonated lone pair. The relative energy of the conformers has been analyzed using the QTAIM and NBO methods (Fig. 3.21).

The effect of the hyperconjugation has been explored by evaluating the relative energy of the conformers removing all the hyperconjugation within the molecules or only the geminal or vicinal terms. The results have shown that the removal of the

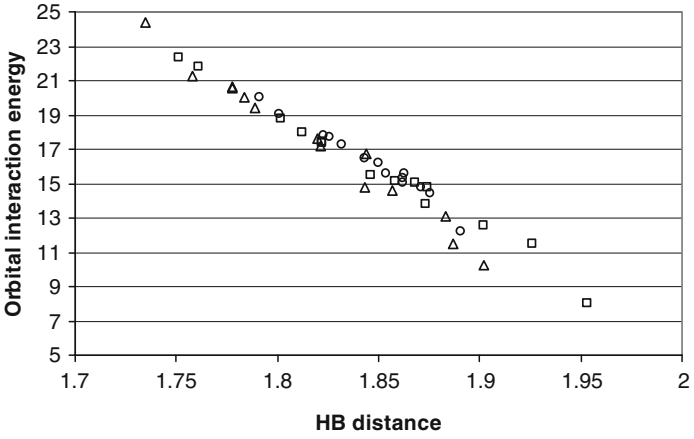

Fig. 3.20 Orbital interaction [O(lone pair)→OH (σ*)] (kJ mol^{-1}) vs. HB distance (Å)

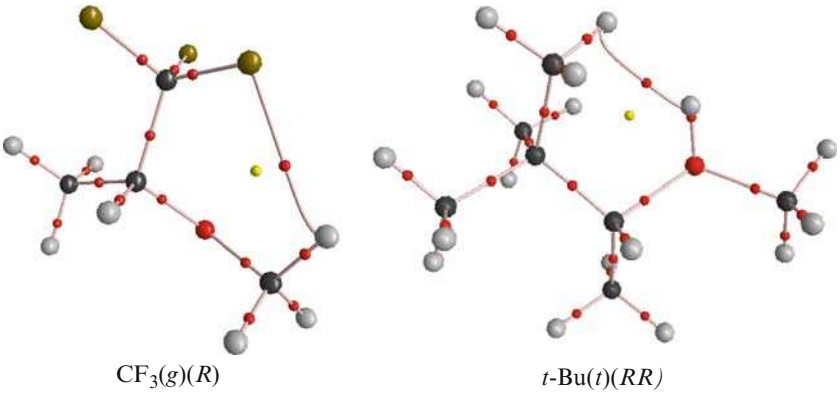

Fig. 3.21 Molecular graph with the atoms, bond critical points (*red*), ring critical points (*yellow*), and bond paths of two conformers of the CF_3 and *t*-Bu derivatives

geminal hyperconjugation has little effect on the relative stability of the different conformers, while the vicinal hyperconjugation is mostly responsible for the observed trend.

The most stable conformers of the protonated chiral ether correspond, in all the examples considered in the present article, to a RS chirality (R in the carbon atom and S in the oxygen one). The analysis of the atomic energies within the QTAIM method has been able to attribute the influence of the difference molecular groups to the stability of the RS configuration vs. the corresponding RR one.

The calculated volume has been shown to suffer a significant contraction due to the protonation. This effect is mainly attributed to a reduction in the size of the hydrogen atoms of the methyl groups.

3.3.3 Solvent Effects on Chiral Recognition

Only two articles considered the effect of solvation on the chiral recognition. The first one, already discussed in the previous section, checks the effect of water as solvent in the relative stability of a dimer of α-aminoalcohols [32]. While in the gas phase, one of the heterochiral dimers is always the more stable one, the inclusion of the water solvation effect provides, as the most stable configuration, a homochiral one in three of the four systems studied.

A more systematic work has been carried out by Zhou et al. in the hydrogen bonded dimers of hydrogen peroxide and its methyl derivative using B3LYP and MP2 methods, and the PCM solvation model for CCl_4, $CHCl_3$, acetone, methanol, and water solvent [49]. For each compound, two homochiral and two heterochiral configurations have been considered (Scheme 3.27). In the two systems considered, the configuration where the HBs generated a six membered ring (A in Scheme 3.27) is preferred over the one with the five-membered ring (B in Scheme 3.27) in gas phase. In addition, the heterochiral complex is more stable than the homochiral one.

However, the solvent effect tends to stabilize the more polar configurations that, in the case of the configuration A, correspond to the homochiral dimer. This effect is larger as the polarity of the solvent increases. In the two systems studied, the more stable dimer corresponds to a homochiral one.

3.3.4 The Use of Metals to Bring Together the Chiral Entities

According to a longstanding precept of chiral recognition, at least three points of contact should exist between the two chiral ligands within the metal-bound complexes in order to bring about the desired chiral recognition. There are numerous examples of chiral recognition in the case of helicates [138–140].

Speranza et al. [141] have studied the complexes of α-aminophosphonic acids with group I metallic cations by means of mass spectroscopy. The complexes had the structures $[MASB2]^+$ and $[MARB2]^+$ where M = (H, Li, Na, K), and AS and AR are enantiomers of an acid A, and B is a reference α-aminophosponic acid with a known configuration. After an inducted fragmentation process, the abundance ratio between the species $[MAB]^+$ and [MB2], which depends on the ligand configuration, is studied and the different stability of the diastereomeric complexes in gas phase assigned. Molecular mechanics MM2 calculations are used as support.

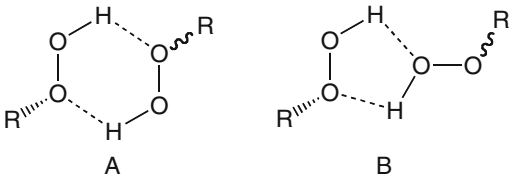

Scheme 3.27 Representation AU20 of the configuration considered (R=H, CH_3)

Scheme 3.28
Bisdiphenylborates and related compounds

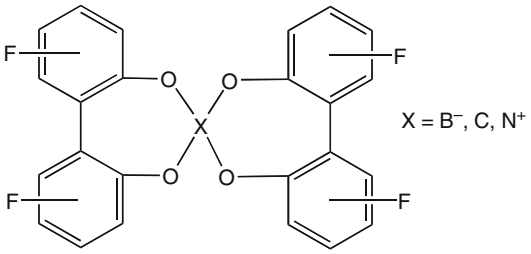

Table 3.5 Coefficients of a presence/absence equation to explain the E_{rel} (kJ mol^{-1})

Parameter	Coefficient	Standard error
X=B$^-$	2.47	0.54
X=C	−4.94	0.54
X=N$^+$	−11.97	0.54
3F	5.61	0.59
5F	−1.09	0.59
6F	−1.34	0.59

From the abundance ratio, the enantiodifferentiation energy of the clusters is obtained, having found seven cases in which the heterochiral complexes are more stable than the corresponding homochiral, while only four cases of the homochiral complex are more stable. A chiral recognition of between −1.8 kJ mol^{-1} and +2.3 kJ mol^{-1} has been found depending on the metallic center.

Our group has devoted two articles for the study of systems where the chiral subunits are bonded to a boron or to a metallic atom (Scheme 3.28). In both cases, the weakness of the bonds formed can be easily broken. In the first case, a series of bisdiphenylborates and the effect of the fluoro substitution on the relative stability of the homo vs. heterochiral complexes have been studied by means of DFT calculations (B3LYP/6-31G*) [29]. In addition, the corresponding isoelectronic structures, in which the boron has been substituted by a carbon or a positively charged nitrogen, have been considered. In all the cases, the homo and heterochiral complexes present D_2 and S_4 symmetries, respectively.

The effect of the central atom as well as the fluoro substitution in the different positions of the aromatic ring in the relative energy of the homo vs. the heterochiral complexes have been correlated assuming an additive scheme. The results obtained for the coefficients of the presence/absence equation (square fitting coefficient (r^2 of 0.98, and a standard deviation of 1.2 kJ mol^{-1}) are given in Table 3.5. The coefficient of the 4F substitution is not significant; thus, it has been removed from the equation.

This equation predicts the relative energy as a sum of the characteristics present on a given complex, for instance, the relative energy of the complex with X=B$^-$ and fluorine atoms in position 3 (2, 3F) is predicted to be 2.47+5.60=8.07 kJ mol^{-1} than compared with the DFT calculations (7.75 kJ mol^{-1}). These results indicate that the X=B$^-$ and the fluoro substitution in position 3 (3F) favor energetically the homochiral complex.

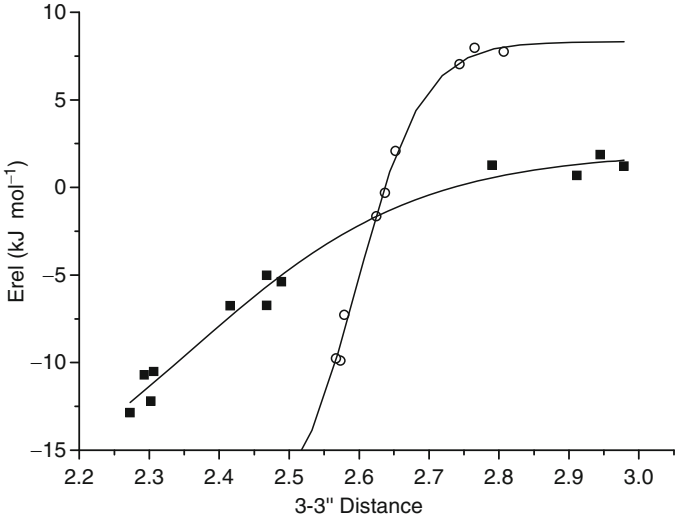

Fig. 3.22 E_{rel} (kJ mol^{-1}) vs. distance of the substituents in 3–3″ (Å) in the homochiral complex. In *open circles* are indicated the 3F substituted complexes and in black squares the 3H ones

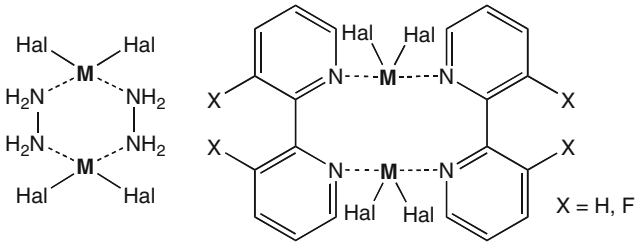

Scheme 3.29 Representation of the square planar organometallic

Another relationship found in this article corresponds to that for the relative energy and the distance between the atoms in positions 3–3″ (Fig. 3.22). This figure shows that complexes fluorinated in position 3 favor more rapidly the heterochiral complex (negative E_{rel}) as the distance becomes shorter than those with hydrogen in these positions. This is expected because of the different steric and electronic characteristics of these two atoms.

The square planar organometallic complexes formed by two ligand molecules (hydrazine, 2,2′-bipyridine, and 3,3′-difluoro-2,2′-bipyridine) and two M-Hal2 (M=Ni, Pd and Pt and Hal=F, Cl, and Br) fragments have been carried out using the B3LYP/ LANL2DZ computational level (Scheme 3.29) [29].

In all the hydrazine complexes, the heterochiral are more stable than the corresponding homochiral ones. In one of the 3,3′-difluoro-2,2′-bipyridine complexes, the homodimer is more stable than the heterodimer, and finally, half of the homochiral bipyridine complexes are more stable than the corresponding

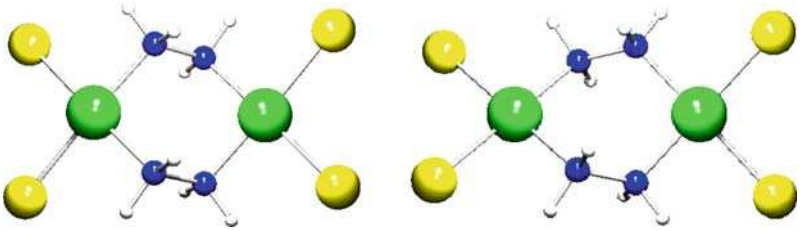

Fig. 3.23 The RS (*left*) and RR (*right*) diasteromers of binuclear metal complexes formed by hydrazine molecules and halogen atoms (*metal green, nitrogen blue,* and *halogen yellow*)

heterochiral ones. For the three families of complexes, a series of correlations has been found between the presence/absence of each metal and halogen atom, and the relative energy of the homo–heterochiral pairs.

Chiral discrimination in binuclear homo- and heterochiral complexes formed by hydrazine (Fig. 3.23), a metal atom of group 10 (Ni, Pd, Pt), and halogen atoms (F, Cl, Br, I), depends on the electronic properties arising from the metal atoms and the ligand atoms attached to them [36]. The complexes were studied by quantum chemical methods by applying DFT methods at the B3LYP/LANL2DZ level of theory.

To conclude, the relative energies of the optimized complexes are correlated with the electronegativity values of the metals and the halogens. Both have their influence also on the metal–nitrogen bonds, which is seen in the distances of the bond critical points in the M–N bonds. Furthermore, chiral discrimination is clearly correlated with the trans effect arising from the charge transfer from an electron lone pair of nitrogen to an opposite M–X antibonding orbital.

The 1:1 and 2:1 complexes of chiral bis(5H-pyrroles) and bis(oxazolines) with the lithium cation were studied by means of DFT methods (B3LYP/6-31G* and B3LYP/6-311+G**); also, the energetic, geometric, electronic, and orbital properties of the complexes were analyzed. To perform such a study, we have calculated first the isolated molecules and the 1:1 complexes [33].

The chiral discrimination in the 2:1 complexes (homo vs. heterochiral ones) indicates that, in all the cases, the heterochiral complexes are more stable than the homochiral ones, except for the *tert*-butyl derivatives. The chiral discrimination energies were discussed on the basis of different parameters related to the lithium atom, such as the N–Li distance, the orbital interaction between the lone pair of the nitrogen and an empty orbital of the lithium, and its atomic contribution to the total energy of the complexes.

A theoretical study of the chiral recognition of the bis(amino(phenyl)methanol) chromium(0) complexes and chiral discrimination of the dimers of amino(phenyl) methanol linked by HB has been carried out by means of a DFT method, the B3LYP/6-31+G**. The results (Fig. 3.24) show that in the chromium complexes, the homochiral one is preferred over the heterochiral one, while the opposite

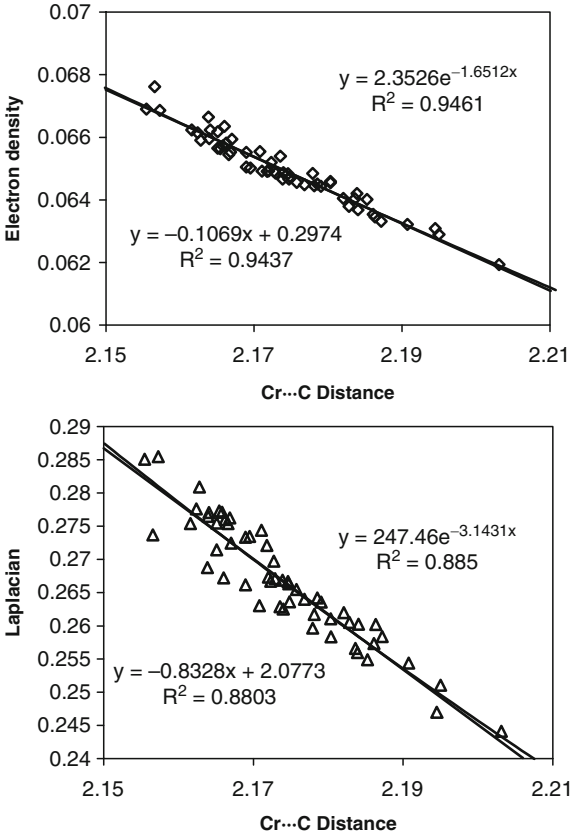

Fig. 3.24 Electron density and Laplacian at the bcp (a.u.) of the Cr···C interactions vs. the interatomic distance (Å)

happened in the HB dimers. Thus, the presence/absence of the chromium atom can be used to favor one or the other type of complex [39].

3.3.5 Optical Rotatory Power Studies

The measurement of the optical rotatory power of chiral substances has been of major importance in the characterization of the enantiomeric purity. A number of computational techniques have been developed in the last year to evaluate this property. A recent review [142] shows in detail the advances in this field. Application of the new implementation of the evaluation of the optical rotatory power has allowed to the study of the conformational [143–146] and solvent effects [147, 148] on the magnitude and sign of the optical rotation power.

Scheme 3.30
Chlorofluoroiodoacetic acid and chlorofluoroiodomethane

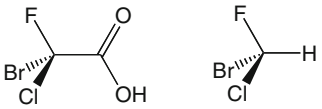

Scheme 3.31 Pantolactone (**4**)

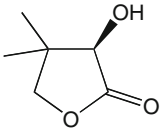

Two groups have developed methodologies to partition the calculated values in atomic contributions. Kondru et al. described the first order changes in the ground state in terms of perturbations to the molecule's occupied molecular orbitals (cn) by the electric (E) and magnetic (B) fields using coupled-perturbed Hartree–Fock methods, and analyzing the results using a method analogous to Mulliken population analysis [149]. This method has been applied to a series of oxirane derivatives and 2,7,8-trioxabicyclo[3.2.1] octanes. Later on, it has been used to analyze the effect of the conformational dependence of the optical rotation angle in the (R)-indoline molecule [150].

Ferraro and coll. used canonical transformation of the Hamiltonian to resolve the average optical rotatory power of a molecule into atomic contributions, based on the acceleration gauge for the electric dipole, and/or the torque formalism [151]. This method has been applied to the study of the conformational profile of the optical rotatory poser of hydrogen peroxide and hydrazine [152].

Two articles have addressed the variation of the optical rotatory power upon dimerization. In the first one, the different conformation accessible monomers and dimers of chlorofluoroiodoacetic acid (Scheme 3.30) have been theoretically calculated [153]. Using these results, the population weighted rotations for the (S)-monomer (11.9, 12.6, 14.5, and 28.2, respectively, at 589, 577, 546, and 435 nm) and (S)-dimers (10.1, 10.7, 12.4, and 24.2 at the same wave lengths, respectively) have been predicted at the B3LYP/aug-cc-pVDZ level. These results, together with the calculated optical rotation of the chlorofluoroiodomethane (5.8, 6.2, 7.5, and 19.3, respectively, at 589, 577, 546, and 435 nm at the B3LYP/DGDZVP level), have come up with the absolute configuration of this molecule as being (S)-(+) and (R)-(−).

In contrast, a study of the effect of the aggregation of the pantolactone (**4**) (Scheme 3.31) shows important differences between the rotatory power of the monomer and dimers [154]. The calculations show that while the monomer presents an almost null optical rotatory power (−1), the value of the dimer is very large (−200). These results are in agreement with the experimental variation of this parameter as a function of the concentration. The atomic partition indicates the important contribution of the hydrogen atom involved in the hydrogen bond to the rotatory power that is not observed within the monomer.

Scheme 3.32 MHP (**5**)

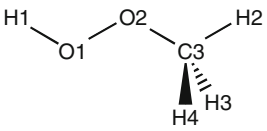

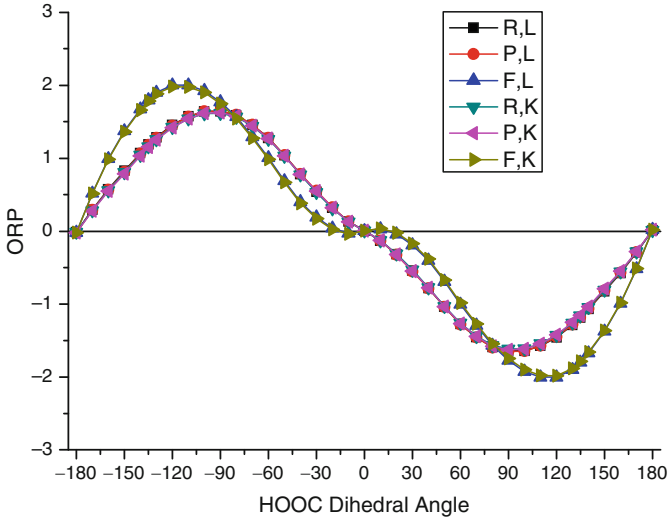

Fig. 3.25 The average rotatory power of **5** in various formalisms as function of the HO_1O_2C dihedral angle

We applied a methodology capable of resolving the optical rotatory power into atomic contributions [41] to a derivative of oxygen peroxide. The individual atomic contributions to the optical rotatory power and molecular chirality of the methylhydroperoxide **5** (MHP, also called hydroperoxymethane, Scheme 3.32) are obtained via a canonical transformation of the Hamiltonian by which the electric dipolar moment operator is transformed to the acceleration gauge formalism, and the magnetic dipolar moment operator to the torque formalism. The gross atomic isotropic contributions have been evaluated for the carbon, the nonequivalent oxygen, and the nonequivalent hydrogen atoms of methylhydroperoxide, employing a very large Gaussian basis set which is close to the Hartree–Fock limit (Fig. 3.25).

3.4 Conclusions

The survey of the literature that we have carried out demonstrates that chiral discrimination is a widespread phenomenon whose incidence is rapidly growing. Although the energetic differences are small in the chiral discrimination processes

(a few kJ mol^{-1} at utmost), there are a number of experimental techniques capable of measuring it. The power and accuracy of the theoretical methods allow the exploration of a large number of situations. It is expected that, in the incoming years, much more complex situations will be within the reach of calculations, progressively advancing the case of biomolecules.

Acknowledgments This work was carried out with financial support from the Ministerio de Educación y Ciencia (Project No. CTQ2006-14487-C02-01/BQU) and Comunidad Autónoma de Madrid (Project MADRISOLAR, ref. S-0505/PPQ/0225). Thanks are given to the CTI (CSIC) for the allocation of computer time.

References

1. E. Ruch, Algebraic aspects of the chirality phenomenon in chemistry. Acc. Chem. Res. **5**, 49–56 (1972)
2. P.W. Fowler, Quantification of chirality: Attempting the impossible. Symmetry Cult. Sci. **16**, 321–334 (2003)
3. R.B. King, Chirality and handedness: The Ruch "shoe-potato" dichotomy in the right-left classification problem. Ann. N.Y. Acad. Sci. **988**, 158–170 (2003)
4. E. Witten, High-energy physics: The mass question. Nature **415**, 969–971 (2002)
5. R.G. Kostyanovsky, Louis Pasteur did it for us especially. Mendeleev Commun. **13**, 85–90 (2003)
6. J. Zhang et al., Chiral nanotechnology. Chirality **17**, 404–420 (2005)
7. B.A. Grzybowski, G.M. Whitesides, Dynamic aggregation of chiral spinners. Science **296**, 718–721 (2002)
8. Y.J. He et al., Effect of earth's orbital chirality on elementary particles and unification of chiral asymmetries in life on different levels. Med. Hypotheses **54**, 783–785 (2000)
9. S. Capozziello, A. Lattanzi, Spiral galaxies as chiral objects, astrophys. Space Sci. **301**, 189–193 (2006)
10. IUPAC Gold Book. http://goldbook.iupac.org/index-alpha.html
11. J.F. LeMaréchal, Can a non-chiral object be made of two identical chiral moieties? J. Chem. Ed. **85**, 433–435 (2008)
12. K. Mislow, Fuzzy Restrictions and Inherent Uncertainties in Chiral Studies, in *Fuzzy Logic in Chemistry*, ed. by D.H. Rouvray (Academic, San Diego, 1997), pp. 65–90
13. M. Avalos et al., Absolute asymmetric synthesis under physical fields: Facts and fictions. Chem. Rev. **98**, 2391–2404 (1998)
14. S.F. Mason, Biomolecular homochirality. Chem. Soc. Rev. **17**, 347–359 (1988)
15. M. Avalos et al., Chiral autocatalysis: Where stereochemistry meets the origin of life. Chem. Commun. **11**, 887–892 (2000)
16. M. Avalos et al., From parity to chirality: Chemical implications revisited. Tetrahedron Asymm. **11**, 2845–2874 (2000)
17. G. Zadel et al., Absolute asymmetric syntheses in a static magnetic field. Angew. Chem. Int. Ed. **33**, 454–456 (1994)
18. C. Foces-Foces et al., Complete energy profile of a chiral propeller compound: Tris-(2′-methylbenzimidazol-1′-yl)methane. Tetrahedron Asymm. **1**, 65–86 (1990)
19. J. Elguero et al., Failed attempt to induce chirality using a magnetic field: The case of chiral helicity of tris(2-methylbenzimidazol-1-yl) methane. Heterocycl. Commun. **1**, 102–103 (1994)

20. B.L. Feringa et al., Attempts to carry out enantioselective reactions in a static magnetic field. Angew. Chem. Int. Ed. Engl. **33**, 1458–1459 (1994)
21. G. Kaupp, T. Marquardt, Absolute asymmetric synthesis solely under the influence of a static homogeneous magnetic field? Angew. Chem. Int. Ed. Engl. **33**, 1459–1461 (1994)
22. L.D. Barron, Can a magnetic field induce absolute asymmetric synthesis? Science **266**, 1491–1492 (1994)
23. W.H.-P. Thiemann, Homochirality of the evolution of biospheres. Biol. Sci. Space **12**, 73–77 (1998)
24. I. Alkorta, J. Elguero, Self-discrimination of enantiomers in hydrogen-bonded dimers. J. Am. Chem. Soc. **124**, 1488–1493 (2002)
25. I. Alkorta, J. Elguero, Discrimination of hydrogen-bonded complexes with axial chirality. J. Chem. Phys. **117**, 6463–6468 (2002)
26. O. Picazo et al., Large chiral recognition in hydrogen-bonded complexes and proton transfer in pyrrolo[2, 3-b]pyrrole dimers as model compounds. J. Org. Chem. **68**, 7485–7489 (2003)
27. I. Alkorta, J. Elguero, Theoretical study of peptide model dimers. Homo versus heterochiral complexes. Theochem **680**, 191–198 (2004)
28. O. Picazo et al., Dimers of 1, 8a-dihydro-1, 8-naphthyridine derivatives as models of chiral self-recognition. Struct. Chem. **16**, 339–345 (2005)
29. O. Picazo et al., Bonding properties related with chiral discrimination in dinuclear metal complexes of group 10. Eur. J. Inorg. Chem. **2**, 324–332 (2007)
30. O. Picazo et al., Chiral recognition in phosphinic acids dimers. J. Phys. Org. Chem. **18**, 491–497 (2005)
31. I. Alkorta et al., Effect of fluoro substituents and central atom nature on chiral derivatives of bisdiphenylborates and isoelectronic structures. Tetrahedron. Asymm. **16**, 755–760 (2005)
32. I. Alkorta et al., Chiral recognition in cyclic α-hydroxy carbonyl compounds: A theoretical study. J. Phys. Chem. A **109**, 3262–3266 (2005)
33. I. Alkorta et al., Chiral discrimination in lithium complexes of bis(5H-pyrroles) and bis (oxazolines). J. Phys. Chem. A **109**, 9573–9577 (2005)
34. I. Alkorta, J. Elguero, An atoms in molecules analysis of the differences between meso and chiral forms of oxirane and cyclobutene derivatives. Chem. Phys. Lett. **417**, 367–370 (2006)
35. I. Alkorta et al., Self-aggregation as a source of chiral discrimination. Chem. Phys. Lett. **427**, 289–294 (2006)
36. I. Alkorta et al., Chiral discrimination in binuclear square planar metal complexes of group 10. Inorg. Chem. Commun. **9**, 712–715 (2006)
37. I. Alkorta et al., Chiral recognition in self-complexes of tetrahydroimidazo[4, 5-d]imidazole derivatives: From dimers to heptamers. J. Phys. Chem. A **110**, 2259–2268 (2006)
38. I. Alkorta et al., Chiral recognition in diaziridine clusters and the problem of racemization waves. J. Phys. Chem. A **111**, 1096–1103 (2007)
39. K. Zborowski et al., A theoretical study of chiral recognition in bis[amino (phenyl) methanol] chromium(0) complexes. Pol. J. Chem. **81**, 621–629 (2007)
40. K. Zborowski et al., Enantiodifferentiation in protonation processes: A theoretical study. J. Mol. Struct. Theochem **811**, 37–44 (2007)
41. M. Sánchez et al., Atomic partition of the optical rotatory power of methylhydroperoxide. J. Chem. Phys. **128**, 064318-1–064318-8 (2008)
42. M. Suhm (ed.), Spectroscopic probes of molecular recognition. Phys. Chem. Chem. Phys. **9** (32), 4443 (2007)
43. P. Le Guennec, On the concept of chirality. J. Math. Chem. **23**, 429–439 (1998)
44. P. Guennec, Towards a theory of molecular recognition. Theor. Chem. Acc. **101**, 151–158 (1999)
45. P. Le Guennec, Two-dimensional theory of chirality. I. Absolute chirality. J. Math. Phys. **41**, 5954–5985 (2000)
46. P. Le Guennec, Two-dimensional theory of chirality. II. Relative chirality and the chirality of complex fields. J. Math. Phys. **41**, 5986–6006 (2000)

47. S. Capozziello, A. Lattanzi, Algebraic structure of central molecular chirality starting from Fischer projections. Chirality **15**, 466–471 (2003)
48. M. Petitjean, Chirality and symmetry measures: A transdisciplinary review. Entropy **5**, 271–312 (2003)
49. D.M. Du et al., Chiral discrimination in the hydrogen bonding complexes of the R–OOH (R=H and CH_3) dimer. Chem. Phys. Lett. **392**, 162–167 (2004)
50. M.A. Mateos-Timoneda et al., Supramolecular chirality of self-assembled systems in solution. Chem. Soc. Rev. **33**, 363–372 (2004)
51. I. Rozas et al., Bifurcated hydrogen bonds: Three-centered interactions. J. Phys. Chem. A **102**, 9925–9932 (1998)
52. M. Speranza, Chiral clusters in the gas phase. Adv. Phys. Org. Chem. **29**, 147–281 (2004)
53. M. Spereanza et al., Chiral recognition by mass-resolved laser spectroscopy. Mass Spectrom. Rev. **24**, 588–610 (2005)
54. W.A. Tao et al., Rapid enantiomeric determination of α-hydroxy acids by electrospray ionization tandem mass spectrometry. Chem. Commun. **20**, 2023–2024 (2000)
55. W.A. Tao et al., Copper(II)-assisted enantiomeric analysis of D, L-amino acids using the kinetic method: Chiral recognition and quantification in the gas phase. J. Am. Chem. Soc. **122**, 10598–10609 (2000)
56. W.A. Tao et al., Mass spectrometric quantitation of chiral drugs by the kinetic method. Anal. Chem. **73**, 1692–1698 (2001)
57. W.A. Tao, R.G. Cooks, Parallel reactions for enantiomeric quantification of peptides by mass spectrometry. Angew. Chem. Int. Ed. **40**, 757–760 (2001)
58. D. Zhang et al., Chiral resolution of D, L-amino acids by tandem mass spectrometry of Ni(II)-bound trimeric complexes. Int. J. Mass Spectrom. **204**, 159–169 (2001)
59. W.A. Tao et al., Rapid enantiomeric quantification of an antiviral nucleoside agent (D, L-FMAU, 2′-fluoro-5-methyl-, D, L-arabinofuranosyluracil) by mass spectrometry. J. Med. Chem. **44**, 3541–3544 (2001)
60. D.V. Augusti et al., Rapid quantitative chiral analysis of sugars by electrospray ionization tandem mass spectrometry using modified amino acids as chiral reference compounds. Anal. Chem. **74**, 3458–3462 (2002)
61. W.A. Tao et al., Quotient ratio method for quantitative enantiomeric determination by mass spectrometry. Anal. Chem. **74**, 3783–3789 (2002)
62. L. Wu et al., Ligand and metal-ion effects in metal-ion clusters used for chiral analysis of a-hydroxy acids by the kinetic method. Anal. Bioanal. Chem. **373**, 618–627 (2002)
63. D.V. Augusti et al., Chiral analysis using the kinetic method with optimized fixed ligands: Applications to some antibiotics. Chem. Commun. **75**, 2242–2243 (2002)
64. L. Wu et al., Chiral quantification of D-, L-, and meso-tartaric acid mixtures using a three-point calibration kinetic method. Chem. Commun. **137**, 136–137 (2003)
65. W.A. Tao, R.G. Cooks, Chiral analysis by mass spectrometry. Anal. Chem. **75**, 25A–31A (2003)
66. L. Wu, R.G. Cooks, Chiral analysis using the kinetic method with optimized fixed ligands: Application to some antibiotics. Anal. Chem. **75**, 678–684 (2003)
67. L. Wu et al., Kinetic method for simultaneous enantiomeric determination of amino acid mixtures. J. Mass Spectrom. **38**, 386–393 (2003)
68. M. Sawada et al., Enantioselectivity in fast-atom bombardment (FAB) mass spectrometry. J. Am. Chem. Soc. **114**, 4405–4406 (1992)
69. M. Sawada et al., Enantioselective complexation of carbohydrate or crown ether hosts with organic ammonium ion guests detected by FAB mass spectrometry. J. Am. Chem. Soc. **115**, 7381–7388 (1993)
70. M. Sawada et al., Cross-chiral examinations of molecular enantioselective recognition by fast atom bombardment mass spectrometry: Host–guest complexations between chiral crown ethers and chiral organic ammonium ions. Org. Mass Spectrom. **28**, 1525–1528 (1993)

71. M. Sawada, Chiral Mass Spectrometry, in *Biological Mass Spectrometry: Present and Future*, ed. by T. Matsuo et al. (Wiley, New York, 1994)
72. M. Sawada et al., Chiral recognition in molecular complexation for the crown ether–amino ester system. A facile FAB mass spectrometric approach. Chem. Commun. **21**, 2497–2498 (1994)
73. M. Sawada et al., Chiral recognition in host–guest complexation determined by the enantiomer-labeled guest method using fast atom bombardment mass spectrometry. J. Am. Chem. Soc. **117**, 7726–7736 (1995)
74. M. Sawada, Chiral recognition detected by fast atom bombardment mass spectrometry. Mass Spectrom. Rev. **16**, 73–90 (1997)
75. Sawada, M. et al., Determination of enantiomeric excess for amino acid ester salts using FAB mass spectrometry. Chem. Commun. 1569–1570 (1998)
76. M. Sawada et al., Chiral amino acid recognition detected by electrospray ionization (ESI) and fast atom bombardment (FAB) mass spectrometry (MS) coupled with the enantiomer-labelled (EL) guest method. J. Chem. Soc. Perkin Trans. **2**, 701–710 (1998)
77. M. Sawada, Development of quantitative chiral recognition mass spectrometry. J. Mass Spectrom. Soc. Jpn. **50**, 311–329 (2002)
78. M. Sawada et al., Depression of the apparent chiral recognition ability obtained in the host–guest complexation systems by electrospray and nano-electrospray ionization mass spectrometry. Eur. J. Mass Spectrom. **10**, 27–37 (2004)
79. M. Sawada, in *The Encyclopedia of Mass Spectrometry*, vol. 4, ed. by N.M.M. Nibbering, (Elsevier, Amsterdam, 2004), pp. 740–748
80. A. Filippi et al., Gas-phase enantioselectivity. Int. J. Mass Spectrom. **198**, 137–163 (2000)
81. B. Botta et al., Enantioselective guest exchange in a chiral resorcin[4]arene cavity. J. Am. Chem. Soc. **124**, 7658–7659 (2002)
82. D. Catone et al., Homolytic Cα–Cβ bond cleavage in a chiral alkylarene radical cation: Effects of asymmetric microsolvation. Angew. Chem. Int. Ed. **43**, 1868–1871 (2004)
83. A. Filippi, M. Speranza, Gas-phase activation and reaction dynamics of chiral ion-dipole complexes. Chem. Eur. J. **9**, 5274–5282 (2003)
84. G. Fago et al., Chiral recognition of o-phospho-serine by mass spectrometry. Angew. Chem. Int. Ed. **40**, 4051–4054 (2001)
85. H.M. Fales, G.J. Wright, Detection of chirality with the chemical ionization mass spectrometer. "Meso" ions in the gas phase. J. Am. Chem. Soc. **99**, 2339–2340 (1977)
86. G. Hofmeister, J.A. Leary, Chiral recognition of lithium-coordinated diols using tandem mass spectrometry. Org. Mass Spectrom. **26**, 811–812 (1991)
87. T.T. Dang et al., Chiral recognition in the gas phase: mass spectrometric studies of diastereomeric cobalt complexes. J. Am. Soc. Mass Spectrom. **5**, 452–459 (1994)
88. H. Suming et al., Stereochemical effects in mass spectrometry. 3-Detection of chirality by chemical ionization mass spectrometry. Org. Mass Spectrom. **21**, 7–10 (1986)
89. M.A. Baldwin et al., Identification of chiral isomers by fast atom bombardment mass-spectrometry – dialkyl tartrates. Biomed. Environ. Mass Spectrom. **16**, 357–360 (1988)
90. Y.-Z. Chu et al., Stereochemical effects in mass spectrometry. 7. Determination of absolute configuration of some organic molecules by reaction mass spectrometry. Org. Mass Spectrom. **23**, 821–824 (1988)
91. H.J. Yang, Y.-Z. Chen, Stereochemical effects in mass spectrometry. XIII-Determination of absolute configuration by fast atom bombardment mass spectrometry. Org. Mass Spectrom. **27**, 736–740 (1992)
92. N.M. Sellier et al., Ion/molecule reactions in the gas phase: Comparison of the enantioselectivity of two chiral gases. Rapid Commun. Mass Spectrom. **8**, 891–894 (1994)
93. A.K. Ghosh et al., C2-Symmetric chiral bis(oxazoline)-metal complexes in catalytic asymmetric synthesis. Tetrahedron Asymm. **9**, 1–45 (1998)
94. J. Guo et al., Measurement of enantiomeric excess by kinetic resolution and mass spectrometry. Angew. Chem. Int. Ed. **38**, 1755–1758 (1999)

95. H.C. Aspinall, H.C. Aspinall, Chiral lanthanide complexes: Coordination chemistry and applications. Chem. Rev. **102**, 1807–1850 (2002)
96. Z.P. Yao et al., Chiral analysis by electrospray ionization mass spectrometry/mass spectrometry. 1. Chiral recognition of 19 common amino acids. Anal. Chem. **72**, 5383–5393 (2000)
97. T. Hamada et al., Catalytic asymmetric aldol reactions in aqueous media using chiral bis-pyridino-18-crown-6-rare earth metal triflate complexes. J. Am. Chem. Soc. **125**, 2989–2996 (2003)
98. C.A. Schalley, P. Weis, Unusually stable magic number clusters of serine with a surprising preference for homochirality. Int. J. Mass Spectrom. **221**, 9–19 (2002)
99. R.G. Cooks et al., Chiroselective self-directed octamerization of serine: Implications for homochirogenesis. Anal. Chem. **73**, 3646–3655 (2001)
100. R.R. Julian et al., Nanocrystalline aggregation of serine detected by electrospray ionization mass spectrometry: Origin of the stable homochiral gas-phase serine octamer. J. Phys. Chem. B **106**, 1219–1228 (2002)
101. A.E. Counterman, D.E. Clemmer, Magic number clusters of serine in the gas phase. J. Phys. Chem. B **105**, 8092–8096 (2001)
102. K.J. Koch et al., Serine octamer metaclusters: Formation, structure elucidation and implications for homochiral polymerization. Chem. Commun. **18**, 1854–1855 (2001)
103. K.J. Koch et al., Chiral transmission between amino acids: Chirally selective amino acid substitution in the serine octamer as a possible step in homochirogenesis. Angew. Chem. Int. Ed. **41**, 1721–1724 (2002)
104. S.C. Nanita et al., Chiral enrichment of serine via formation, dissociation and soft-landing of octameric cluster ions. J. Am. Soc. Mass Spectrom. **15**, 1360–1365 (2004)
105. C.A. Schalley, Supramolecular chemistry goes gas phase: The mass spectrometric examination of non-covalent interactions in host–guest chemistry and molecular recognition. Int. J. Mass Spectrom. **11**, 11–39 (2000)
106. N. Borho et al., Chiral self-recognition in the gas phase: The case of glycidol dimers. Phys. Chem. Chem. Phys. **3**, 1945–1948 (2001)
107. N. Borho, M. Suhm, Self-organization of lactates in the gas phase. Org. Biomol. Chem. **1**, 4351–4358 (2003)
108. A. Filippi et al., Chiral discrimination of monofunctional alcohols and amines in the gas phase. Int. J. Mass. Spectrom. **210**, 483–488 (2001)
109. A. Giardini et al., Chirality and intermolecular forces: Studies using R2PI experiments in supersonic beams. Phys. Chem. Chem. Phys. **2**, 4139–4142 (2000)
110. A. Garrett, T. Zwier, Multiphoton ionization studies of clusters of immiscible liquids. II. C_6H_6–(H_2O)n, n=3–8 and $(C_6H_6)_2$–(H_2O)1,2. J. Chem. Phys. **96**, 3402–3410 (1992)
111. M.R. Topp, Dynamics and structure of aromatic molecular van der Waals complexes. Int. Rev. Phys. Chem. **12**, 149–204 (1993)
112. M. Satta et al., Energetics of monohydrated chiral R(+)-1-phenyl-1-propanol: supersonic beam experiments and density functional calculations. Chem. Phys. Lett. **316**, 94–100 (2000)
113. A. Latini et al., Short range interactions within molecular complexes formed in supersonic beams: Structural effects and chiral discrimination. Chem. Eur. J. **6**, 1042–1049 (2000)
114. K. Le Barbu et al., An experimental and theoretical study of jet-cooled complexes of chiral molecules: The role of dispersive forces in chiral discrimination. J. Phys. Chem. A **102**, 128–137 (1998)
115. N. Seurre et al., Structural study of hydrogen-bonded complexes between 2-aminoethanol derivatives and a chiral aromatic alcohol. J. Mol. Struct. **692**, 127–137 (2004)
116. A. King, B. Howard, A microwave study of the hetero-chiral dimer of butan-2-ol. Chem. Phys. Lett. **348**, 343–349 (2001)
117. Z. Su et al., Chiral self-recognition: Direct spectroscopic detection of the homochiral and heterochiral dimers of propylene oxide in the gas phase. J. Am. Chem. Soc. **128**, 17126–17131 (2006)

118. S. Portmann et al., Chiral discimination in hydrogen-bonded complexes. J. Chem. Phys. **113**, 9577–9585 (2000)
119. M. Elango et al., Hydrogen peroxide clusters: The role of open book motif in cage and helical structures. J. Phys. Chem. A **110**, 6294–6300 (2006)
120. I. Alkorta et al., Bond length-electron density relationships: From covalent bonds to hydrogen bond interactions. Struct. Chem. **9**, 243–247 (1998)
121. I. Alkorta et al., Comparison of models to correlate electron density at the bond critical point and bond distance. Theochem **496**, 131–137 (2000)
122. E. Espinosa et al., From weak to strong interactions: A comparative analysis of the topological and energetic properties of the electron density distribution involving X–F···F–Y systems. J. Chem. Phys. **117**, 5529–5543 (2001)
123. J. Catalán et al., Etude de la tautomerie annulaire du pyrrole, de l'imidazole et du pyrazole. Bull. Soc. Chim. Fr. **3**, 429–435 (1986)
124. T. Steiner, W. Saenger, Lengthening of the covalent O–H bond in O–HO hydrogen bonds re-examined from low-temperature neutron diffraction data of organic compounds. Acta Crystallogr. Sect. B **B50**, 348–357 (1994)
125. T. Steiner, Lengthening of the N–H bond in N–H N hydrogen bonds. Preliminary structural data and implications of the bond valence concept. Chem. Commun. **13**, 1331–1332 (1995)
126. M. Ramos et al., A theoretical study of the influence of electric fields on hydrogen bonded acid–base complexes. J. Phys. Chem. A **101**, 9791–9800 (1997)
127. I.D. Brown, Chemical and steric constraints in inorganic solids. Acta Crystallogr. Sect. B **B48**, 553–572 (1992)
128. J.T. Hynes et al. (eds), *Hydrogen-Transfer Reactions* (Wiley, Weinheim, Germany, 2007), p. 1393
129. S. Kojo, K. Tanaka, Enantioselective crystallization of D, L-amino acids induced by spontaneous asymmetric resolution of D, L-asparagine. Chem. Commun. **19**, 1980–1981 (2001)
130. S. Kojo et al., Racemic D,L-asparagine causes enantiomeric excess of other coexisting racemic D,L-amino acids during recrystallization: A hypothesis accounting for the origin of L-amino acids in the biosphere. Chem. Commun. **19**, 2146–2147 (2004)
131. A. Dobashi et al., Self-induced nonequivalence in the association of D- and L-amino acid derivatives. J. Am. Chem. Soc. **108**, 307–308 (1986)
132. T. Williams et al., Diastereomeric solute-solute interactions of enantiomers in achiral solvents. Nonequivalence of the nuclear magnetic resonance spectra of racemic and optically active dihydroquinine. J. Am. Chem. Soc. **91**, 1871–1872 (1969)
133. A. Perczel, A.G. Császár, Toward direct determination of conformations of protein building units from multidimensional NMR experiments I. A theoretical case study of For-Gly–NH_2 and For–L-Ala–NH_2. J. Comput. Chem. **21**, 882–900 (2000)
134. G.S. Denisov, K.G. Tokhadze, Ultrastrong hydrogen bond in gas phase. Dimer of dimethylphosphinic acid. Dokl. Phys. Chem. **337**, 117–119 (1994)
135. K.G. Tokhadze et al., First example of the ABC ν(OH) absorption structure for both gaseous and crystalline phase: Infrared studies of dimethylphosphinic acid. J. Mol. Struct. **404**, 55–62 (1997)
136. L. González et al., Very strong hydrogen bonds in neutral molecules: The phosphinic acid dimers. J. Chem. Phys. **109**, 2685–2693 (1998)
137. O. Mó et al., Spontaneous self-ionization in the gas phase: A theoretical prediction. Chem. Phys. Chem. **7**, 465–467 (2001)
138. O. Mamula et al., Helicates of chiragen-type ligands and their aptitude for chiral self-recognition. Chem. Eur. J. **11**, 3049–3057 (2005)
139. S.J. George et al., Helicity induction and amplification in an oligo(*p*-phenylenevinylene) assembly through hydrogen-bonded chiral acids. Angew. Chem. Int. Ed. **46**, 8206–8211 (2007)
140. M. Lama et al., Lanthanide class of a trinuclear enantiopure helical architecture containing chiral ligands: Synthesis, structure, and properties. Chem. Eur. J. **13**, 7358–7373 (2007)

141. A. Paladini et al., Enantiodiscrimination of chiral alpha-aminophosphonic acids by mass spectrometry. Chirality **13**, 707–711 (2001)
142. P.L. Polavarapu, Optical rotation: Recent advances in determining the absolute configuration. Chirality **14**, 768–781 (2002)
143. K. Ruud, T. Helgaker, Optical rotation studied by density-functional and coupled-cluster methods. Chem. Phys. Lett. **352**, 533–539 (2002)
144. P.J. Stephens et al., Ab initio prediction of optical rotation: A comparison of density functional theory and Hartree–Fock methods for three 2,7,8-trioxabicyclo[3.2.1] octanes. Chirality **14**, 288–296 (2002)
145. P.J. Stephens et al., Determination of absolute configuration using optical rotation calculated using density functional theory. Org. Lett. **4**, 4595–4598 (2002)
146. K.B. Wiberg et al., Conformational effects on optical rotation. 3-substitued 1-butenes. J. Am. Chem. Soc. **125**, 1888–1889 (2003)
147. P.J. Stephens et al., Prediction of optical rotation using density functional theory: 6,8-Dioxabicyclo[3.2.1]octanes. Tetrahedron Asymm. **11**, 2443–2448 (2000)
148. B. Mennucci et al., Polarizable continuum model (PCM) calculations of solvent effects on optical rotations of chiral molecules. J. Phys. Chem. A **106**, 6102–6113 (2002)
149. R.K. Kondru et al., Atomic contributions to the optical rotation angle as a quantitative probe of molecular chirality. Science **282**, 2247–2250 (1998)
150. R.K. Kondru et al., Structural and conformational dependence of optical rotation angles. J. Phys. Chem. A **103**, 6603–6611 (1999)
151. A. Ligabue et al., On the resolution of the optical rotatory power of chiral molecules into atomic terms. A study of hydrogen peroxide. J. Chem. Phys. **116**, 6427–6434 (2002)
152. M.P. Béccar Varela et al., Rationalization of the optical rotatory power of chiral molecules into atomic terms: A study of N_2H_4. Theor. Chem. Acc. **110**, 428–433 (2003)
153. J. Crassous et al., Preparation of (+)-chloro fluoroiodo-methane, determination of its enantiomeric excess and of its absolute configuration. Tetrahedron Asymm. **15**, 1995–2001 (2004)
154. M.R. Goldsmith et al., Optical rotation of noncovalent aggregates. J. Am. Chem. Soc. **125**, 15696–15697 (2003)

Chapter 4
Multiscale Modeling: A Review

M.F. Horstemeyer

Abstract This review of multiscale modeling covers a brief history of various multiscale methodologies related to solid materials and the associated experimental influences, the various influence of multiscale modeling on different disciplines, and some examples of multiscale modeling in the design of structural components. Although computational multiscale modeling methodologies have been developed in the late twentieth century, the fundamental notions of multiscale modeling have been around since da Vinci studied different sizes of ropes. The recent rapid growth in multiscale modeling is the result of the confluence of parallel computing power, experimental capabilities to characterize structure-property relations down to the atomic level, and theories that admit multiple length scales. The ubiquitous research that focus on multiscale modeling has broached different disciplines (solid mechanics, fluid mechanics, materials science, physics, mathematics, biological, and chemistry), different regions of the world (most continents), and different length scales (from atoms to autos).

4.1 Introduction

The recent surge of multiscale modeling related to solid mechanics, which has now grown into an international multidisciplinary activity and broached almost every industry, was originated from an unlikely source. As the US Department of Energy (DOE) national labs started to reduce underground nuclear tests in the mid 1980s, with the last one in 1992, the idea of a simulation-based design and analysis concepts were emerged, and multiscale modeling became a key in garnering more precise and accurate predictive tool. In essence, the number of large scale

M.F. Horstemeyer (✉)
Department of Mechanical Engineering, Mississippi State University, MS 39760, USA
e-mail: mfhorst@cavs.msstate.edu

J. Leszczynski and M.K. Shukla (eds.), *Practical Aspects of Computational Chemistry*,
DOI: 10.1007/978-90-481-2687-3_4,

systems level tests that were previously used to validate a design was reduced to nothing, thereby, warranting the increase in simulation results of the complex systems for design verification and validation purposes.

Essentially, the idea of filling the space of system level "tests" was then proposed to be filled by simulation results. After the Comprehensive Test Ban Treaty of 1996, in which many countries pledged to discontinue all systems level nuclear testing, programs such as the Advanced Strategic Computing Initiative (ASCI) were developed within the Department of Energy (DOE) and managed by the national labs within the US. Within ASCI, the basic recognized premise was to provide more accurate and precise simulation- based design and analysis tools. Because of the requirements for greater complexity in the simulations, parallel computing and multiscale modeling became the major challenges which needed to be addressed. With this perspective, the idea of experiments shifted from the large scale complex tests to multiscale experiments that provided material models with validation at different length scales. If the simulations were physically based and less empirical, a predictive capability could be realized. As such, various multiscale modeling methodologies were independently being created at the DOE national labs: Los Alamos National Lab (LANL), Lawrence Livermore National Laboratory (LLNL), Sandia National Laboratories (SNL), and Oak Ridge National Laboratory (ORNL). In addition, personnel from these national labs encouraged, funded, and managed academic research related to multiscale modeling. Hence, the creation of different methodologies and computational algorithms for parallel environments gave rise to different emphases regarding multiscale modeling and the associated multiscale experiments.

The advent of parallel computing also contributed to the development of multiscale modeling. Since more degrees of freedom could be resolved by parallel computing environments, more accurate and precise algorithmic formulations could be admitted. This thought also drove the political leaders to encourage the simulation-based design concepts.

At LANL, LLNL, and ORNL, the multiscale modeling efforts were driven by the materials science and physics communities with a bottom-up approach. Each had different programs that tried to unify computational efforts, materials science information, and applied mechanics algorithms with different levels of success. Multiple scientific articles were written, and the multiscale activities took different lives of their own. At SNL, the multiscale modeling effort was an engineering top-down approach starting from continuum mechanics perspective, which was already rich with a computational paradigm. SNL tried to merge the materials science community into the continuum mechanics community to address the lower length scale issues that could help solve engineering problems in practice.

Once this management infrastructure and associated funding were in place at various DOE institutions, different academic research projects were started, initiating various satellite networks of multiscale modeling research. This technological transfer also started in other labs within the Department of Defense and industrial research communities.

The growth of multiscale modeling in the industrial sector was primarily due to financial motivations. From the DOE national labs' perspective, the shift from large scale systems experiments mentality occurred because of the 1996 Nuclear Ban Treaty. Once the industry realized that the notions of multiscale modeling and simulation-based design were invariant to the type of product, and that effective multiscale simulations could in fact lead to design optimization, a paradigm shift began to occur in various measures within different industries as cost savings and accuracy in product warranty estimates were rationalized. For designing an automobile, airplane, building, or any structural system for that matter, large scale systems tests were (and are) expensive, and cost models showed that a physics-based design can give a great return on investment. The advantages include the following:

1. Multiscale modeling can reduce the product development time by alleviating costly trial and error iterations.
2. Multiscale modeling can reduce product costs through innovations in material, product, and process designs.
3. Multiscale modeling can reduce the number of costly large systems scale experiments.
4. Multiscale modeling can increase product quality and performance by providing more accurate predictions of response to design loads.
5. Multiscale modeling can help develop new materials.
6. Multiscale modeling can help medical practice in making diagnostic and prognostic evaluations related to the human body.

Hence, the market drivers for such an explosion of multiscale modeling into various industrial sectors are being realized.

4.2 Multiscale modeling publications

On the basis of the recent ISI Web of Knowledge (http://www.isiwebofknowledge.com/), Fig. 4.1 illustrates the increasing trend of articles that have been published with "Multiscale Modeling" as the title. Certainly, a multiscale modeling article does not need to have these two particular words in the title of the article, but this trend illustrates the rapid growth in the area.

Although the nature of multiscale modeling is really interdisciplinary, these articles have been distributed in particular disciplines. The ISI Web of Knowledge shows that the largest number of multiscale modeling articles arose from the Materials Science community followed by the Meteorological and Atmospheric community. The next two disciplines are the Mechanics and Mathematics communities followed by Physics, Electrical Engineering, and Chemistry (and chemical engineering). Other disciplines have produced multiscale modeling articles, but to a much lesser degree.

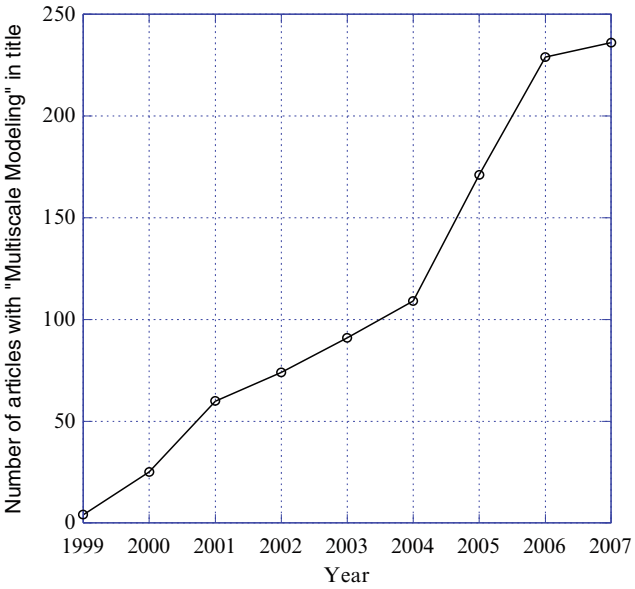

Fig. 4.1 Number of journal articles published with "Multiscale Modeling" in the title. Note the recent trend since 1999 shows a large growth rate

Because of the interdisciplinary nature of multiscale modeling, several new journals have been started to allow a platform of presentation that has historically not been a focus of stovepiped disciplines. One journal is the *Multiscale Modeling and Simulation: A SIAM Interdisciplinary Journal* (http://www.siam.org/journals/mms.php), which has given attention to communication bridges between mathematics, chemistry, physics, engineering, computer science, and environmental sciences. Another recent journal is the *International Journal for Multiscale Computational Engineering* (http://www.begellhouse.com/journals/61fd1b191cf7e96f.html), which focuses mainly on algorithm developments, though other multiscale issues have been addressed. In 1998, *Physical Mesomechanica* began in Russia to address multilevel issues related to plastic flow [1]. A recent journal is the International *Journal of Theoretical International Journal of Theoretical and Applied Multiscale Mechanics* (http://www.inderscience.com/browse/index.php?journalCODE=ijtamm), which focuses on constitutive modeling issues between size scales and domains. Earlier, although journals carried articles on multiscale modeling, the reviews were typically critical as no appreciation of bridging methodologies were given much credence.

Although multiscale modeling has broached many disciplines, this review will focus on solid materials as described below. As a former manager of the computational fluids dynamic group at Sandia National Labs, the author readily recognizes many areas where multiscale modeling has affected fluids, for example, in polymer flows, turbulence modeling, weather analysis, etc. However, for brevity's sake the focus here will be on multiscale modeling of solids.

4.3 Bridging Between Scales: A Difference of Disciplines

Synergy/systems thinking and interdisciplinary thinking bring about the whole being greater than the sum of the parts. Multiscale modeling requires that several disciplines' interaction, which has led to miscommunications and misunderstandings between communities about what multiscale modeling really is, particularly when one discusses the bridging methodology between length scales.

Clearly, one key in multiscale modeling is the notion of the bridging. Without officially stating the bridging methodology, each discipline has developed its own methods. Before we discuss each discipline's bridging paradigm, let us consider an analogy of the Brooklyn Bridge in New York versus the Golden Gate Bridge in San Francisco. If one were to just translate the Brooklyn Bridge to San Francisco and call it the Golden Gate Bridge, one would find that the old adage of a "square peg in a round hole" fits. The Golden Gate Bridge required a different design than the Brooklyn Bridge because of the different requirements on each side of the bridge and the environments that must be sustained. In other words, the boundary conditions played a major role in the design of the bridge. The same notion needs to be considered when developing bridges for multiscale modeling between different length scales. However, the different research disciplines (materials science, applied mechanics, atmospheric sciences, etc.) tend to focus on the research at each pertinent length scale and not so much the bridge. In fact, modern computational tools at each length scale were just recently published in Yip's [2] Handbook of Materials Modeling, which provides a thorough review of a wide variety of current tools; however, this work did not really deal with bridging methodologies.

In the next sections, the multiscale modeling methods are presented from the different disciplines perspectives. Clearly one could argue that overlaps occur, but the idea here is to present the multiscale methods from the paradigm from which they started. For example, the solid mechanics internal state variable theory includes mathematics, materials science, and numerical methods. However, it clearly started from a solid mechanics perspective and the starting point for mathematics, materials science, and numerical methods has led to other different multiscale methods.

4.3.1 Solid Mechanics Bridging (Hierarchical Methods)

Inherent within the idea of multiscale modeling is the bridging methodology and the associated length scale of the feature that is required to gain the accurate physics required for the engineering problem [3]. To decide on the pertinent length scale feature of importance, one must consider that in modern solid mechanics, continuum theories are driven by the conservation laws (mass, momentum, and energy); however, there are too many unknowns than the number of equations, so constitutive relations (sometimes erroneously called "laws") are required to solve

the set of differential equations for finite element or finite difference analysis (most modern solid mechanics tools employ finite element analysis). When developing a multiscale modeling methodology for the constitutive relations, the kinetics, kinematics, and thermodynamics need to be consistent in the formulation. There are also certain classical postulates in continuum theory that guide the development of the constitutive theory (objectivity, physical admissibility, equipresence, and locality). Multiscale modeling has been driven by the physical admissibility postulate even at the expense of the postulates of equipresence and locality. Physical admissibility essentially means identifying the physical mechanism or discrete microstructural feature at the particular length scale that is a root source of the phenomenological behavior.

Two different general multiscale methodologies exist starting from the solid mechanics continuum theory paradigm: hierarchical and concurrent. The key difference is the bridging methodology. In concurrent methods, the bridging methodology is numerical or computational in nature. In the hierarchical methods, numerical techniques are independently run at disparate length scales. Then a bridging methodology, such as statistical analysis methods, homogenization techniques, or optimization methods, can be used to distinguish the pertinent cause-effect relations at the lower scale to determine the relevant effects for the next higher scale.

One effective hierarchical method for multiscale bridging is the use of thermodynamically constrained internal state variables (ISVs) that can be physically based upon microstructure-property relations. It is a top-down approach, meaning the ISVs exist at the macroscale but reach down to various subscales to receive pertinent information. The ISV theory owes much of its development to the state variable thermodynamics constructed by Helmholtz [4] and Maxwell [5]. The notion of ISV was introduced into thermodynamics by Onsager [6, 7] and was applied to continuum mechanics by Eckart [8, 9].

The basic idea behind the theory of ISV is that, in order to uniquely define the Helmholtz free energy [4] of a system undergoing an irreversible process, one has to expand the dimensions of the state space of deformation and temperature (state variables commonly employed in classical thermodynamics to study elastic materials) by introducing sufficient number of additional state variables which are considered essential for the description of the internal structure with the associated length scales of the material in question. The number of these ISVs is related to material structure as well as to the degree of accuracy with which one wishes to represent the material response. The hierarchical methodology illustrates the different length scale analyses used and various bridges needed. (ISV = internal state variable, FEA = finite element analysis, EAM = Embedded Atom method, MEAM = modified Embedded Atom method, MD = molecular dynamics, MS = molecular statics, and DFT = Density Functional theory).

The ISV formulation is a means to capture the effects of a representative volume element and not all of the complex causes at the local level, and hence, an ISV will macroscopically average in some fashion the details of the microscopic arrangement. In essence, the complete microstructure arrangement is unnecessary as long

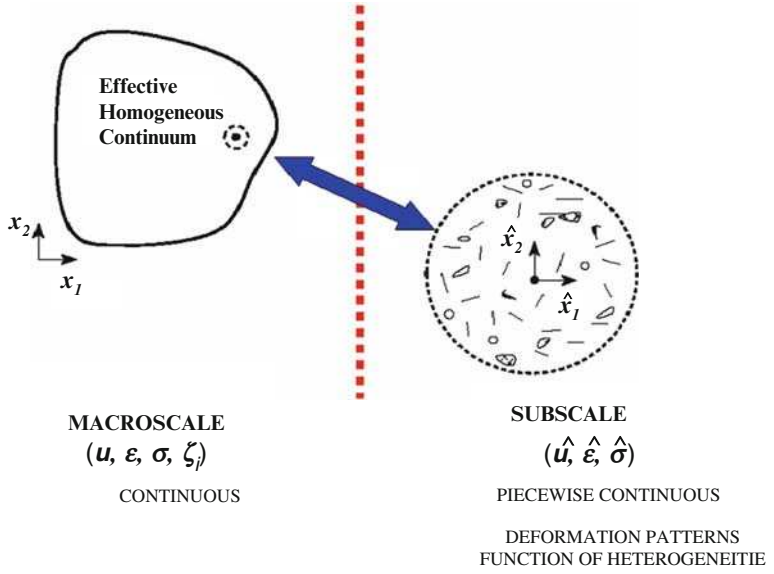

Fig. 4.2 Homogenization of discretized microstructural features into a continuum medium

as the macroscale ISV representation is complete [10]. Figure 4.2 illustrates that we can then "average" or "homogenize" the effect of the discrete feature into a continuum that includes a number of ISVs. As a result, the ISV must be based on physically observed behavior and constrained by the laws of thermodynamics [11]. Rice [12] and Kestin and Rice [13] added the notions of inelastic behavior into the context of ISV theory. The inelastic behavior of importance to design and analysis of metal structural components is typically plasticity, damage, and failure. For inelastic dissipative materials, the ISVs relate microstructural characteristics to mechanical behavior and are used in various materials, such as polymers, composites, and ceramics [14–19]. However, it may be argued that ISV theory probably had its greatest impact on metals. In the US, ISV theories have enjoyed success in solving practical engineering problems. The Mechanical Threshold Stress (MTS) Model [20–22] was developed at Los Alamos National Laboratory, and focused on the microstructural details in relation to mechanical properties. Freed [23] at NASA developed an ISV model under the paradigm of unified-creep-plasticity modeling. Bammann [24, 25] at Sandia National Laboratories developed an ISV modeling framework that was microstructurally based and fit into the unified-creep-plasticity paradigm. In Europe, Chaboche [26] focused on fatigue, large strain plasticity, and damage in his ISV formulations. Although many other ISV models could be discussed here, the above-mentioned theories have been successfully used in engineering practice on a routine basis for design and manufacturing for metal and polymer-based material systems.

ISV theory is important not only from a top-down approach, but the linking between scales as well as the different computational methods that can be employed

are also critical. Figure 4.3 shows a hierarchical multiscale modeling methodology illustrating the different bridges and analyses required to capture the pertinent plasticity, damage, and failure aspects of metal alloys for use in design of an automotive component. An example is given later which describes these different size scale analyses and their associated bridges are presented.

Before the term multiscale modeling was in vogue, methods of bridging lower length information into a continuum at a higher length scale were being addressed in the solid mechanics community. Eshelby [27, 28] created the modern "micro-mechanics" world of analysis, modeling, and simulation by asserting a "self-consistent" theme. Essentially, subscale hetereogeneities could be assigned an effect within the continuum. The continuum could be assigned as an element, a "Representative Volume Element" or RVE. As such, the composites, metallurgical and applied mechanics communities used this framework for different applications. Modern mixture theory, mean field theory [29], crystal plasticity, Method-of-Cells, Mura-Tanaka Method [30], Homogenization Theory, and the Generalized Method-of-Cells were developed from the self-consistent Eshelby formulation. Mura [31], Budiansky [32], and Nemat-Nasser and Lori [33] gave a thorough review of these micromechanical self-consistent methods.

A part of the self-consistent method is determining what the RVE should be and how the boundary conditions work down from higher scales to lower scales. Recently, Gokhale and Yang [34] performed a hierarchical multiscale modeling study examining different length scale microstructures with digital imaging

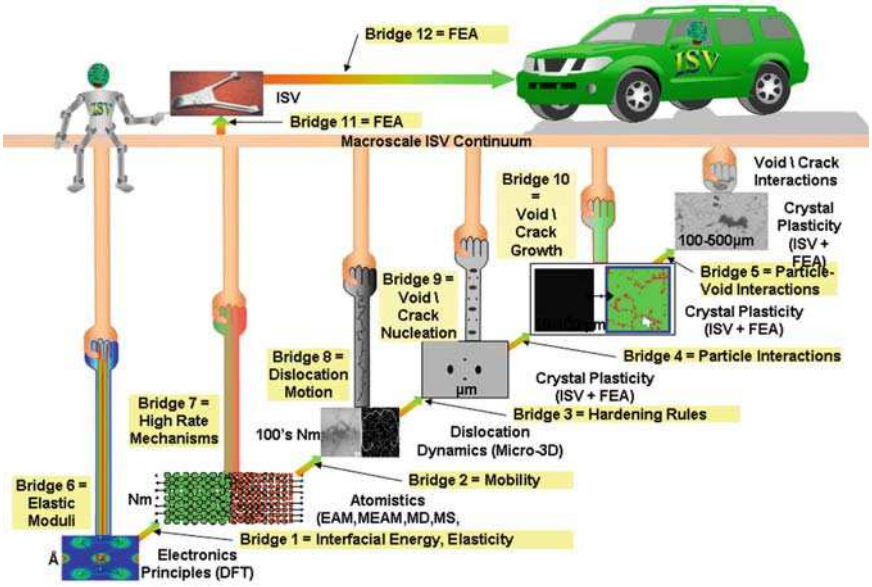

Fig. 4.3 Multiscale modeling example of a metal alloy used for design in an automotive component

methods and finite element analysis. The technique brought together effects of features at higher length damage evolution and local fracture processes occurring at lower length scales. Hao et al. [35] also employed hierarchical fracture methods at different scales.

In finalizing this section, it is worth noting that aside from the modern-day multiscale modeling using ISV theory and self-consistent theories, determining the length scale effects on mechanics properties has been around a long time and has been summarized by Bazant and Chen [36]. DaVinci in the 1500s made the statement that a longer rope with equal thickness compared to a smaller diameter rope was weaker than the latter. Galileo in the 1600s disagreed with DaVinci about the strengths and lengths of ropes as he studied the size effects of bones. Euler in the 1700s related buckling to a column length. In the 1800s, Cauchy related the stress state to radius of a cylinder. In the early 1900s, Bridgman [37] showed on many metal alloys that the notch radii change the stress state of the material. In all of these examples, the length scale parameter was related to the geometry of the component, not to anything internal to the component. Certainly, these types of size scale effects have been a part of modern finite element analysis. However, the multiscale modeling that we are discussing in this review addresses the issues of material micro structural effects on the mechanical properties in the absence and in the presence of these geometrical size scale effects.

4.3.2 Numerical Methods (Concurrent Methods)

Concurrent methods typically try to combine different scale algorithms together with matching procedures invoked in some overlapping domain in order to resolve the important multiscale physics. A good review of these concurrent methods and the associated challenges can be found in the books of Phillips [38] and Liu et al. [39] and the review articles of Fish [40] and de Pablo and Curtin [41]. Typical concurrent methods have two different length scales, or at most three different length scales, of interest in the formulations. Too many length scales are cost prohibitive.

The first and most active area of research for concurrent methods has been the coupling of atomistic-level simulations to continuum-level simulations at the same time with different information being shared between the two. The development of fine grid-coarse grid finite element methods [42] was the basis for these different concurrent multiscale methods. For multiscale modeling the fine grid method was traded for other lower length scale methods, such as atomistic methods. For example, Kohlhoff et al. [43, 44] were probably the first to join atomistic level simulations capabilities within a finite element code. Another example was the quasi-continuum approach of Tadmor et al. [45] that came about by joining the physics community Embedded Atom Method (EAM) molecular statics code developed by Baskes and colleagues [46, 47] at Sandia National Labs and the solid mechanics finite element formulations of Ortiz et al. [48]. The notion was to have

the atomistic method, local to a region where plasticity, fracture, or any activity causes dissipation, and where the finite element method would apply to the appropriate boundary conditions. Shenoy et al. [49] later applied the quasi-continuum method to interfaces, illustrating that an application of a concurrent multiscale modeling can be applied where otherwise single length scale analyses could not address. Miller et al. [50, 51] further extended the concurrent quasi-continuum application space to plasticity and fracture. Shenoy et al. [52] later added an adaptive finite element meshing capability to the quasi-continuum method in order to broaden the application space. At this time, Abraham et al. [53] with the help of Plimpton [54] from Sandia National Labs, used an atomistic-finite element code to examine fracture in brittle materials under dynamic loads. There was another group researching concurrent method at this time as well. Rudd and Broughton [55] and Broughton et al. [56] examined dynamic aspects of concurrent multiscale modeling with atomistics and finite elements and their inherent limitations on particular applications.

Others then went on to study various aspects of quasi-continuum concurrent multiscale methods. Lidirokas et al. [57] studied local stress states around Si nanopixels using this method. Bazant [58] argued that these atomistic-finite element multiscale methods cannot really capture inelastic behavior like fracture because the softening effect requires a regularization of the local region that is not resolved.

By the year 2000, the notion of concurrent multiscale modeling had diffused into the greater solid mechanics community at different length scales besides the atomic-continuum level. Shilkrot et al. [59, 60] introduced a method that essentially combines the quasi-continuum method with the discrete dislocation method. In this same spirit, Shiari et al. [61] and Dewald and Curtin [62] connected atomistics with dislocation dynamics simulations in a two-scale methodology to focus on grain boundary effects. At a higher length scale, Zbib and Diaz de la Rubia joined discrete dislocation methods with finite element methods [63]. Hence, the local geometric conditions and kinetics that controlled the dynamics of dislocations were placed into a continuum field theory code that could solve boundary value problems.

Although the crystal plasticity modeling community focused on several length scales in their simulations, the term concurrent multiscale modeling was not historically used. Because crystal plasticity formulations start at the scale of the grain and volume average up to yield polycrystalline results and the polycrystalline results can affect the results within the grain, they are in a sense a pseudo-concurrent method and really a self-consistent method. They can also bring in lower length scale effects in a hierarchical manner [64]. Crystal plasticity models became popular during the 1980s as a tool to study deformation and texture behavior of metals during material processing [65] and shear localization [66, 67]. The basic elements of the theory comprise kinetics related to slip system hardening laws to reflect intragranular work hardening, including self and latent hardening components [68], (2) kinematics in which the concept of the plastic spin plays an important role, and intergranular constraint laws to govern interactions

among crystals or grains. The theory is commonly acknowledged for providing realistic prediction/correlation of texture development and stress-strain behavior at large strains as it joins continuum theory with discretized crystal activity.

Similar to crystal plasticity modeling and simulation in which discrete entities, such as crystals, were placed in a larger continuum domain, Shephard et al. [69] discussed concurrent automatic interacting models at different scales considering geometric representations and discretizations required by microstructure. Still others have focused on the bridging algorithms: the bridging domain method of Xiao and Belytschko [70], the bridging scale method of Wagner and Liu [71], and Karpov et al. [72]. Non-reflecting boundary condition methods originating from the seminal work of Adelman and Doll [73] led to recent works of concurrent multiscale models of Cai et al. [74], Huang and Huang [75], Wagner et al. [76], Karpov et al. [72], and Park et al. [77]. Essentially, the non-reflecting boundary for the molecular dynamics (MD) allows for the simulation of a considerably smaller lattice around the local physics of interest, such as a crack tip, while keeping the effects of the eliminated degrees of freedom on the reduced MD system. Also in an effort to address the quasi-statics problem and the dynamics problems discussed by Horstemeyer et al. [78], Fish and Chen [79], and Fish and Yuan [80], who introduced time scale incongruencies along with size scale issues, Klein and Zimmerman [81] developed a concurrent method that could be used in one, two, and three dimensional analyses.

Concurrent multiscale methods have also been employed to address fatigue. Oskay and Fish [82] and Fish and Oskay [83] introduced a nonlocal temporal multiscale model for fatigue based upon homogenization theory. Although these formulations were focused on metals, Fish and Yu [84] and Gal et al. [85] used a similar concurrent multiscale method for analyzing fatigue of composite materials.

4.3.3 Materials Science Bridging

Perhaps the materials science community has had the greatest impact on modern multiscale modeling methods. When addressing the physical admissibility postulate for continuum theory, the materials science community has provided the data. It is inherent within the materials science community to study the various length scale effects, though they have not necessarily focused on multiscale modeling. The terminology typically used in the materials science community is "structure-property" relations. Essentially, it is the different structures within the material (grains, particles, defects, inclusions, etc.) that dictate the performance properties of the materials [86, 87].

Different scale features give different scale properties. At the smallest level, the lattice parameter is a key length scale parameter for atomistic simulations. Since atomic rearrangement is intimately related to various types of dislocations, Orowan [88], Taylor [89], Polyani [90], and Nabarro [91] developed a relationship for dislocations that related stress to the inverse of a length scale parameter, the

Burgers' vector [92], which laid the foundation for all plasticity theories. Nabarro [91] also showed that the diffusion rate is inversely proportional to the grain size, another length scale parameter. Hall [93] and Petch [94] related the work hardening rate to the grain size. Ashby [95] found that the dislocation density increased with decreasing second phase particle size. Frank and Read [96–98] showed that dislocation bowing is a function of spacing distance and size. And Hughes et al. [99, 100] discovered that geometrically necessary boundary spacing decreases with increasing strain.

Other experimental studies have revealed that material properties change as a function of size. For example, Fleck et al. [101] have shown in torsion of thin polycrystalline copper wires the normalized yield shear strength increases by a factor of three as the wire diameter is decreased from 100 to 12.5 μm. Stolken and Evans [102] observed a substantial increase in hardening during the bending of ultra thin beams. In micro-indentation and nano-indentation tests [103–108], the measured indentation hardness increased by a factor of two as the depth of indentation decreased from 10 to 1 μm. When Lloyd [109] investigated an aluminum-silicon matrix reinforced by silicon carbide particles, he observed a significant increase in strength when the particle diameter was reduced from 16 to 7.5 μm while holding the particle volume fraction fixed at 15%. Hughes et al. [99, 100] investigated deformation induced from frictional loading and found that the stresses near the surface were much greater than that predicted by the local macroscale continuum theory, that is, a length scale dependence was observed. Elssner et al. [110] measured both the macroscopic fracture toughness and the atomic work associated with the separation of an interface between two dissimilar single crystals. The interface (crack tip) between the two materials remained sharp, even though the materials were ductile and contained a large number of dislocations. The stress level necessary to produce atomic decohesion of a sharp interface is on the order of ten times the yield stress, while local theories predict that the maximum achievable stress at a crack tip is no larger than four to five times the yield stress.

In terms of damage/fracture, Griffith [111] found a relation between the crack length and the stress intensity factor. Before this time, Roberts-Austen [112] performed a set of experiments that showed the tensile strength of gold has a strong dependence on the impurity size. Recently, McClintock [113] determined the void growth rates as a function of the void size. Void/Crack nucleation was determined by various aspects of the second phase particle size distribution by Gangalee and Gurland [114]. Horstemeyer et al. [115, 116] and Potirniche et al. [117–120] determined the nearest neighbor distance as a length scale parameter for void coalescence modeling for different metals that was experimentally validated by Jones et al. [121]. It is clear that whether damage mechanics or fracture mechanics is employed, the length scale of interest is important to model this type of inelastic behavior.

In terms of fatigue, the materials science community has revealed different length scales of interest as well. Local inclusion/defects, such as pores, second phase particles, inclusions, and constituents, could induce local stress concentrations

which could be large enough based on the size of these defects, to induce fatigue cracks. Neuber [122] and Peterson [123] clearly showed the relation of notch root sizes on fatigue life. Harkegard [124] illustrated using elastic-plastic finite element simulation results that the local stress concentration at pores can induce fatigue cracks. Smith et al. [125, 126] performed studies on different notch root radii showing that fatigue life is directly related to the size of notches. Although these experimental studies included external notches, they are clearly significant to multiscale modeling as both internal and external notches could induce fatigue cracks. It was the works of Lankford et al. [127–129] that started addressing the difference of length scales related to fatigue crack initiation, small crack propagation, and long crack propagation. Couper et al. [130] and Major [131] experimentally determined that the total fatigue life was directly correlated to the length scale of the pore size in high cycle fatigue of cast aluminum alloys. Davidson et al. [132] and Laz and Hilberry [133] quantified fatigue crack mechanisms from different microstructural features and/or defects. These features confirmed Major's [131] analysis with pores, but also included other intermetallics and second phase particles. In an automotive aluminum alloy, Gall et al. [134–136] quantified the effect of particles, intermetallics, and particle clusters. Recently, Wang et al. [137] watched via in situ Scanning Electron Microscopy the growth of a small fatigue crack through a magnesium alloy that showed crack resistance arising from different size scale features: pores, dendrites, grains, and intermetallics. Kumar and Curtin [138] recently gave a review of various multiscale modeling issues and experiments related to fatigue cracks and the associated microstructure that affects crack growth.

In terms of cyclic plasticity, Shenoy et al. [139, 140], Wang et al. [137], and McDowell [141] performed hierarchical multiscale modeling of Ni-based superalloys employing internal state variable theory. Fan et al. [142] performed a hierarchical multiscale modeling strategy for three length scales.

In more recent years since the advent of parallel computing, computational materials science has revealed some various length scale dependencies on yield and plasticity as well. Horstemeyer et al. [64, 143–151] found that the yield stress is a function of the volume-per-surface-area length scale parameter that correlates well with dislocation nucleation. Figure 4.4 illustrates that for any kind of size scale experiment related to volume-per-surface-area or fundamental simulation capability where dislocation nucleation is critical, a clear relationship arises [152]. Potirniche et al. [118] showed at the atomic scale through molecular dynamics that void growth and coalescence showed length scale differences in the elastic region as the specimen size increased, but remained scale invariant in the plasticity regime.

Results from parallel computing have also helped understand local structure-property relations for fatigue. Fan et al. [153, 154], through finite element analysis, helped quantify the driving force-resistance of microstructurally small fatigue cracks at pores and defects. Potirniche et al. [119, 120] and Johnston et al. [155] employed computational methods to study fatigue crack growth at different length scales: atomic level and crystal level. Gall et al. [156] employed finite element simulations to understand the crack incubation processes that lead to a fatigue crack. After the crack has started but still in the microstructurally small regime,

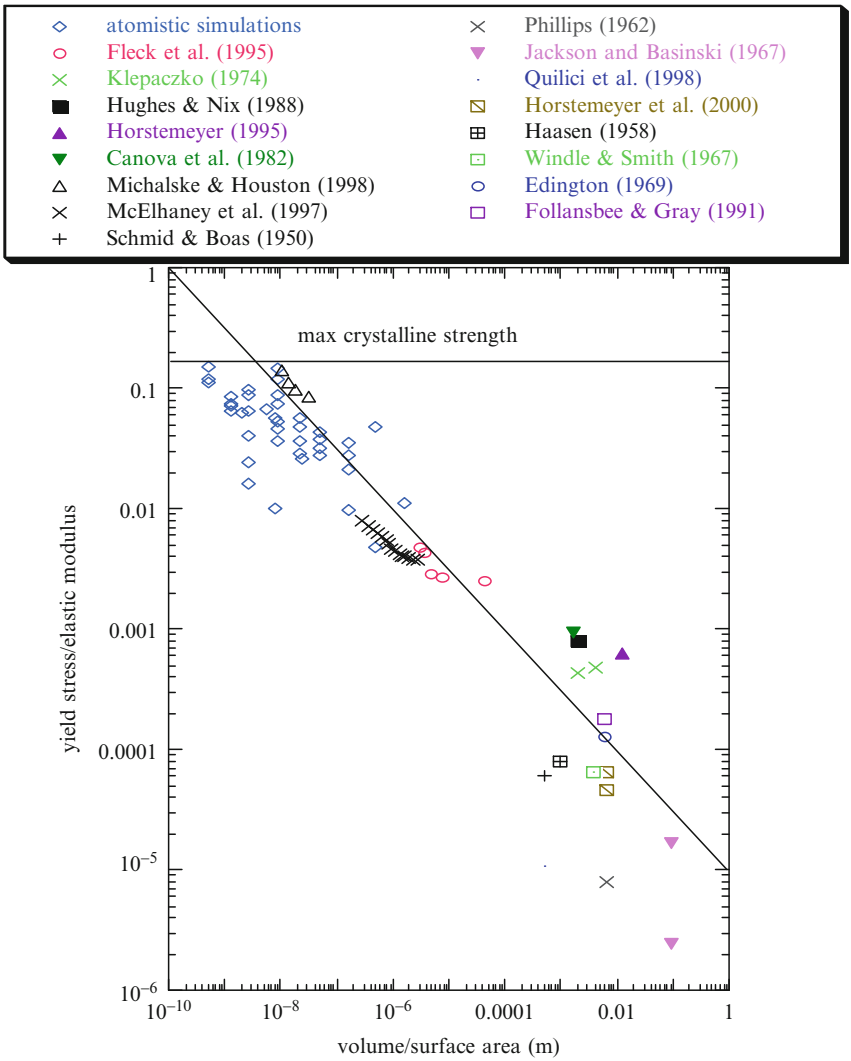

Fig. 4.4 Yield stress normalized by the elastic shear modulus plotted against a size scale parameter (volume per surface area) illustrating the six orders of magnitude of stress levels and ten orders of magnitude of size related to plastic behavior of single crystal metals [152]

Deshpande et al. [157, 158] examined the local plasticity arising from dislocations at a crack tip and the associated fracture growth using a dislocation dynamics theory. Morita and Tsuji [159], Mastorakos and Zbib [160], and Groh et al. [161] used dislocation dynamics theory in a computational setting to understand relationships of plasticity and crack sizes regarding fatigue crack growth.

One can summarize that the materials science multiscale frame of reference, whether it be from experiments or computations, has been a bottom-up approach in

trying to find the structure-property relationships. McDowell and Olson [162] gave a comprehensive summary of computational materials with respect to multiscale modeling and an associated educational program. The examples given here are certainly not all-inclusive but at least they are typical of most studies and substantiate the perspective.

4.3.4 Physics Perspective

At the lowest scales, computational physicists pursued both hierarchical and concurrent methods for joining the electronics principles scale simulations with the atomic scale simulations. Ramasubramaniam and Carter [163] summarized some of the current multiscale methods at the lower scales. In a concurrent manner, Lu and Kaxiras [164] and Choly et al. [165] coupled Density Functional Theory (DFT) with the EAM potentials at the atomic scale to analyze different dislocation behavior. Lu et al. [166] extended the original Tadmor et al. [45] quasi-continuum method to couple another length scale by implementing quantum mechanical DFT calculations so that three concurrent domains were represented. To accomplish this, Lu et al. [166] needed to include Ercolessi and Adams [167] and Li et al. [168] forced matching algorithms for the three disparate length scales. Still others have studied concurrent methods joining quantum models with DFT [169–172].

A different concurrent multiscale method developed within the physics community was termed by the authors as the "learn-on-the-fly" (LOTF) strategy [173]. In this scheme, simple forms of potentials are chosen to represent the interatomic forces. Unlike conventional empirical potentials whose parameters are global and constant, these parameterized potentials in the LOTF scheme are *local* and *variable* and can be changed at run time by means of accessory quantum calculations when deemed necessary. The original potential is assumed to be constructed to accurately describe bulk processes, such as the elastic deformation. Hence, most atoms in the system will experience elastic deformation most of the time, but when a defect or crack is introduced, the quantum calculations will be invoked. The classical potential "learns" and adapts to the local environment "on the fly." The missing information is computed using a "black box" engine based on a DFT or a tight-binding formalism. The dynamic force matching employed here includes the work of Li et al. [168].

Probably the most used hierarchical multiscale method that joined electronics principles simulation results to the atomic level came by means of the EAM or MEAM potentials for metals. The EAM and MEAM have been called "semi-empirical" interatomic potentials, because of their determination in a hierarchical manner. Daw and Baskes [46] were the first to propose a numerical method for calculating atomic energetics (EAM). The major component of EAM is an embedding energy of an atom determined by the lower scale local electron density into which that atom is placed. An embedding energy is associated with placing an atom in that electron environment to represent the many-body effect of the neighbors.

The formalism is nonlocal in nature, and hence, because of the many-body interactions, metal responses could be realized. Daw et al. [47] reviewed the basic method and several applications of EAM. The MEAM potential, later proposed by Baskes et al. [174–177], was the first semi-empirical atomic potential using a single formalism for fcc, bcc, hcp, diamond-structured materials and even gaseous elements, and produced good agreement with experiments or first principles calculations. The MEAM extended EAM to include angular forces similarly in the solid mechanics sense of bending of an Euler Beam to a Timoshenko Beam.

The EAM and MEAM potentials once determined from electronics principles calculations [178] have been used to reproduce physical properties of many metals, defects, and impurities. For example, EAM molecular statics, molecular dynamics, and Monte Carlo simulations were performed on hydrogen embrittlement effects on dislocation motion and plasticity [46, 179–181]. These potentials have been used to analyze plasticity [74, 144, 145, 148–150, 182, 183], cracks and fracture [117, 184], and fatigue [119, 120, 185, 186].

4.3.5 Mathematics Perspective

Although mathematics plays a major role in all of the previous perspectives (solid mechanics, numerical methods, materials science, and physics), there are aspects of the math perspective that purely start from mathematical concepts. Brandt [187] and Weinan and Engquist [188] have suggested various mathematical paradigms to address multiscale modeling. The previously discussed perspectives essentially use mathematics as a means to an end. It is worth mentioning that certain mathematical formulations have been developed for multiscale modeling, from a purely mathematical perspective. Some of the perspectives include dimensional analysis, fractal and self-similarity analysis, Percolation theory, and statistical design of experiments.

A good example of starting from a mathematical perspective is the work of Barenblatt [189], who using dimensional analysis and physical self-similarity arguments, described the art of scaling relationships. He demonstrated the concepts of intermediate asymptotes and the renormalization group as natural consequences of self-similarity, and showed how and when these tools could be used for different length scale analyses. While comparing dimensional analysis and renormalization group theory, Carpinteri et al. [190] examined the ductile to brittle transition in metals wherein by increasing the structural size, the tensile strength and fracture energy changed. In another dimensional analysis study, Cheng and Cheng [191] employed dimensional analysis with finite element simulations to quantify the size scale relationship with conical indentation of elastic-plastic work hardening behavior. Using asymptotic expansions, Ansini et al. [192] employed a nonlocal functional to capture behavior for a multiscale analysis and applied this analysis concept to a nonlinear elastic spherical shell.

Self-similarity is a mathematical concept in which fractals have been applied to predict or simulate some solid material behavior. A fractal is generally “a rough or

fragmented geometric shape that can be split into parts, each of which is (at least approximately) a reduced-size copy of the whole," [193]. A fractal typically has a coarse structure with a subscale fine structure that is approximately similar to the course structure. It is typically irregular having a Hausdorff dimension greater than its topological dimension. Long before Mandelbrot thought about fractals, the notion of self-similarity and the associated mathematics began in the seventeenth century when Leibniz considered recursive self-similarity. In Mandelbrot's work [194], the fracture surfaces of metals were argued to have fractal characteristics. In the same year, Mark and Aronson [195] suggested that fractals can be related to brittle fracture surfaces of rocks. Several years later, Chelidze and Guguen [196] found experimental evidences of fractal type fractures in different rock types. Mosolov et al. [197] then extended the application of fractal geometries to other brittle materials that fractured as a result of compressive loads.

In using differential self-similarity concepts, Dyskin [198] determined the effective characteristics and associated stress concentrations of pores, cracks, and rigid inclusions. He proposed a sequence of continua at increasing size scales with each representative volume element determined by an associated microstructure. Power laws with exponents represented the scaling of the microstructure and are not necessarily tied to the material fractal dimension. This formalism was based upon the earlier microstructurally-based representative volume element definition by Graham and Yang [199] and Lee and Rao [200], who discussed the pertinence of enlarging the size of an RVE because of the multitude of different microstructural features that require admission into an RVE. To numerically address these issues of length of the RVE with respect to the microstructures and their associated gradients and subsequent effects on the periodicity assumption, Fish and Wagiman [201], Fish and Yuan [202], and Nuggehally et al. [203] proposed enhancements to the homogenized solutions.

Contrary to self-similar concepts, He et al. [204] and Wang et al. [205] argued that once fracture occurs at a certain scale, the discontinuity invalidates any self-similar notion. In other words, the fracture introduces a singularity within the self-similar material at that scale. A scale lower would then not be self-similar.

Percolation theory has been another mathematical tool to address scaling issues. One of the earliest works on percolation theory related to size scale effects was that of Essam [206] who linked clusters of entities with different correlation functions. Greenspoon [207] employed an asymptotic analysis with a scaling parameter that quantified correlation lengths. Later, Kestin [208] presented an overview of percolation theory applications to different size scale issues. Percolation Theory has been used for different multiscale aspects of materials. Otsubo [209] used percolation theory to determine particle sizes in suspensions of polymer systems. Leclerc and Olson [210] proposed a percolation model for lignin degradation such that low values for the cluster size exponent obtained during wood degradation were in agreement with diffusion aggregation processes. In a different application, Fu et al. [211] employed a percolation model to describe porosity distributions in ceramic. Ostoja-Starzewski [212] combined a self-consistent method with a percolation model to describe size effects of an inelastic material with random

granular microstructure. In particular, the author found a decrease in scatter in strength with a decrease in specimen size.

In terms of different scale bridging, statistical methods can play a key role in determining which particular subscale features are most important. Bai et al. [213] gave a nice review of using statistical methods for multiscale modeling. Another example that summarizes statistical methods bridging many length scales was that discussed by Reichl [214]. However, the key is to determine the appropriate microstructural characteristic related to the pertinent statistics. For example, a dilemma might arise as the size of the representative volume element needs to be large enough to capture the statistics of the represented microstructures and defects, but must be small enough to represent a continuum element in finite element analysis. As discussed earlier, materials scientists may assert that dendrite cell size is a predominant feature on the fatigue life of a cast specimen as they performed structure-property experiments to quantify the effect. Even though there may be a direct correlation between the size scale feature called dendrite cell size and fatigue life, dendrite cell size may not be the cause of the fatigue failure. For example, as a casting solidifies, the dendrites push the porosity arising from hydrogen within the melt. As such, the dendrite cell size correlates with the porosity and scales with the pore size. Major [131], Zhang et al. [215], Horstemeyer et al. [147], and Horstemeyer and Wang [216] showed that it was the pore size and associated statistics related to pore nearest neighbor distance and pore volume fraction that were the critical cause-effect parameters related to fatigue life and not the dendrite cell size. However, it took experiments and statistical methods, coupled with finite element analysis, to help determine this relationship for a hierarchical multiscale method for fatigue.

In statistics, ANalysis Of VAriance (ANOVA) is a collection of statistical models and their associated procedures in which the observed variance is partitioned into components because of different explanatory variables. The initial techniques of the analysis of variance were developed by the statistician and geneticist R.A. Fisher in the 1920s and 1930s, and are sometimes known as Fisher's ANOVA or Fisher's analysis of variance due to the use of Fisher's F-distribution as part of the test of statistical significance.

These techniques by Fisher [217, 218] can help sort out the parametric effects efficiently and clear of a multiscale analysis. The Design of Experiments (DOE) approach, popularized by Taguchi [219, 220] in the field of quality engineering, has recently been utilized in various contexts of mechanics problems and design by Horstemeyer and Gokhale [221], and Horstemeyer and Ramaswamy [115], and Horstemeyer et al. [222]. The DOE methodology enables an investigator to select levels for each subscale parameter and then conduct numerical experiments in order to evaluate the effect of each parameter in an efficient manner. Any number of parameters and levels for each parameter can be placed in an orthogonal array, which lends itself to optimal determination of parametric effects. Here, orthogonality refers to the requirement that the parameters be statistically independent. The basic terminology of orthogonal arrays $L_a(b^c)$ is as follows: a denotes the number of calculations, b denotes the number of levels for each parameter and

c denotes the number of parameters. As such, many parameters can be evaluated with others at that particular scale and the most influential ones can be determined to be used for the next higher scale analysis.

4.4 Multiscale Modeling of Different Materials

The recent growth of multiscale modeling has permeated every material type known to mankind regarding structural members. Although most of the work has been focused on metal alloys as they have been used the most over time as reliable structural materials, multiscale modeling has also been employed for ceramics and polymer systems (both synthetic and biological).

4.4.1 Metals

Since most of the methods and examples in this review are focused on metals, this section will be shortened. Albeit, it is important to note that multiscale modeling has been applied to basic metal alloy structures such as face center cubic aluminum alloys, hexagonal close pack magnesium alloys, and body center cubic iron and steel based alloys.

4.4.2 Ceramics

The least of amount of multiscale modeling has probably been performed on ceramic materials, basically because they are the least used material system for structural applications, especially when large ductilities are required. Furthermore, since ceramics are essentially linear elastic, the need for multiscale modeling has not been warranted. However, some multiscale studies have certainly been performed on these materials. For example, Mauro and Varshneya [223, 224] performed multiscale modeling studies on various glass structures comprising different ceramics. Krishnamurthy et al. [225] developed a multiscale model for zirconia in which they studied oxygen diffusion. Hansen et al. [226], Schmittbuhl et al. [227] and Hansen and Schmittbuhl [228] employed multiscale modeling for brittle cracks focusing on surface roughness and related it to percolation theory.

4.4.3 Polymers

The use of multiscale modeling for polymers and polymer-based systems can be distinguished into synthetic (man-made) and biological (God-made) materials. Although synthetic polymers have been used as monolithic structural materials,

such as polyurethane, polypropylene, and rubber, probably the broadest usage of structural applications is in composites of some type in which short or long fibers that have high tensile strength are found. A further breakdown of biological materials can be done by dividing into human and animal materials and vegetation. A discussion of multiscale modeling opportunities with biological materials was presented by Chong and Ray [229].

4.4.3.1 Monolithic Synthetic Polymer Multiscale Modeling

Multiscale polymers, in the absence of strengthening or stiffening material, have multiscale structure depending on the volume fractions of crystalline and/or amorphous segments. For example, Theodurou [230] also performed a hierarchical multiscale analysis on amorphous polymers. Another multiscale study was that of Ismail et al. [231] who performed a hierarchical averaging scheme using wavelet transforms to study multiscale behavior of polymers. An example of the multiscale methodologies moving into the industrial sector is that of Bicerano et al. [232], who described their hierarchical multiscale modeling methodologies at The Dow Chemical Company. Yu and Fish [233] developed a multiscale, multiphysics concurrent method for analyzing viscoelastic behavior using asymptotic analysis to capture the spatially varying important length scales. Finally, Curgul et al. [234] performed MD simulations of amorphous polymer nanofibers (1.9–23.0 nm) to study their size-dependent properties. The fibers comprised chains that mimic polyethylene, with chain lengths ranging between 50 and 300 carbons. The result was that the glass transition temperature of these amorphous nanofibers decreased with a decreasing fiber diameter.

4.4.3.2 Composite Synthetic Polymer Multiscale Modeling

Next to metals, probably the synthetic polymer-based composites have been modeled most by hierarchical multiscale methods. Different multiscale formulations have been approached: top-down internal state variable approaches, self-consistent (or homogenization) theories, and nanoscale quantum-molecular scale methods.

The earliest works of trying to model different length scales of damage in composites were probably those of Halpin [235, 236] and Hahn and Tsai [237]. In these models, they tried to deal with polymer cracking, fiber breakage, and interface debonding between the fiber and polymer matrix, and delamination between ply layers. Each of these different failure modes was represented by a length scale failure criterion formulated within a continuum. As such, this was an early form of a hierarchical multiscale method. Later, Halpin and Kardos [238] described the relations of the Halpin-Tsai equations with that of self-consistent methods and the micromechanics of Hill [29].

The Halpin-Tsai equations were based upon purely mechanics arguments from micromechanics. It was not until Talreja [14–16], Chang and Allen [239],

Allen [240], Costanzo et al. [241], and Krajcinovic [242–244] that thermodynamics of appropriate internal state variables for damage in composites under mechanical loads were addressed. Similar to the metal plasticity theoreticians, these researchers employed Coleman and Gurtin's [11] thermodynamic framework to determine the kinetic equations. However, unlike the metal internal state variable community that could quantify the evolution equations for dislocations and damage, these polymer-based composites theoreticians did not propose evolutionary rate equations, but just damage state equations.

In terms of numerical procedures for multiscale modeling, Fish and Shek [245] laid out a numerical technique for global and local interactions for composites. Later, Fish and Yu [246] in a three-scale concurrent multiscale methodology for composites analysis introduced a nonlocal damage model.

Different studies using homogenization theory have been performed on composites structures. One such example was that of Belsky et al. [247] who presented a multiscale modeling method that included critical deformation modes, vibration and buckling modes, and failure modes (delamination, debonding, and microbuckling). Hassani and Hinton [248–250] published a set of papers focusing on the analytical and numerical methods for the theory of homogenization and optimization. They showed that the methods can be used for topological features, such as geometries and microstructures, to bridge two different length scales. Lourenco et al. [251] recently reviewed the multiscale aspects of masonry structures, which are really polymer based composites, using homogenization theory. Matous et al. [252] recently performed a multiscale analysis on heterogeneous thin layers using homogenization theory for cohesive failure.

Aboudi [253, 254] and Paley and Aboudi [255] developed various micromechanical finite element simulations at the mesoscale with the "Generalized Method of Cells." More recently, Williams and Tippetts [256] reviewed multiscale modeling approaches for polymer-based composites and proposed a model of their own. Their hierarchical multiscale model comprised three size scales. The macroscale was associated with the plate thickness and a mesoscale associated with the lamina thickness. The mesoscale focused on lamina and ply splitting processes using a cohesive zone model with adaptive meshing. The lowest length scale corresponded to a material point within each lamina, and was modeled by a new stochastic homogenization theory.

With the advent of nanomaterials, different types of polymer-based composites developed as multiple scale analysis down to the nanoscale became a trend for development of new materials with new properties. Multiscale materials modeling continue to play a role in these endeavors as well. For example, Qian et al. [257] developed multiscale, multiphysics numerical tools to address simulations of carbon nanotubes and their associated effects in composites, including the mechanical properties of Young's modulus, bending stiffness, buckling, and strength. Maiti [258] also used multiscale modeling of carbon nanotubes for microelectronics applications. Friesecke and James [259] developed a concurrent numerical scheme to evaluate nanotubes and nanorods in a continuum.

Wescott et al. [260] in a hierarchical sense used atomistic simulations, mesoscale simulations, and finite elements to examine the effect of nanotubes that were dispersed in polymers. This bottom-up multiscale method employed percolation notions in trying to bridge the effects of the subscale nanotubes.

4.4.3.3 Human and Animal Multiscale Modeling

The human body is a very complicated living machine differentiating itself from non-living matter and changing with higher frequency than the metal, ceramic, and synthetic polymers. All these make multiscale modeling with human difficult. Besides, the fact that the human has very different organ structures makes modeling the human (or any animal for that matter) even more complex. Even with these complexities, researchers have tried to distinguish the multiscale effects of the different organs.

For the vascular system, Lagana et al. [261] employed a hierarchical methodology for multiscale modeling of pulmonary and coronary perfusions in the cardiovascular system. Essentially, they studied different shunt size effect on the pressure of blood within the vessels.

For bone, several studies have been performed. Ho Ba Tho et al. [262] and Budyn and Hoc [263] studied human cortical bone with a multiscale modeling focus on aging and fracture. Fritsch and Hellmich [264] performed micromechanics simulations analyzing different microstructural patterns in bone, thereby, quantifying the anisotropic effects. For trabecular and cortical bone, Porter [265] employed a hierarchical multiscale modeling methodology by using a hybrid nanocomposite paradigm to analyze bone. Of course, bone is attached to other tissue, and so the various length scales related to these attachments can be an issue in modeling the human body. Katz et al. [266] performed a hierarchical multiscale characterization in order to quantify the structure-property relations for multiscale modeling of calcified tissues at the bone-tissue interface. For cartilage, the multiscale modeling has been limited to homogenization models [267]. Hellmich et al. [268] argued through multiscale modeling that trabecular bone and cortical bone have fundamentally the same materials although a different structural morphology. They argued that both types of bone comprise hydroxyapatite, collagen, ultrastructural water, non-collagenous organic materials, and marrow with water filling the Haversian canals. Homogenization theory was used to model the different scales of analysis. Taylor [269] reviewed the strength and fracture toughness of bone from a multiscale perspective. In this review, Taylor [269] not only discussed the morphology effects at each length scale, but the density variations and the ability to adapt its living structure as well. Kawagai et al. [270] in a multiple scale analysis that incorporated x-ray computed tomography quantified at different length scales the apatite crystallite orientation (texture) related to the stress state in that continuum point. A homogenization method was used to bridge the scales. Clearly anisotropic behavior was quantified arising from the crystallite orientation.

The brain has briefly been examined from a multiscale perspective. Imielinska et al. [271], in order to determine trauma injury to the brain under a ballistic impact or blast to the head, developed a multiscale high fidelity biomechanical and physiologically-based modeling tools. They employed their methodology on pigs, and hence, understanding of the human brain is still to be done.

To generalize the human body, Bassingthwaithte et al. [272] purported a multiscale modeling strategy for cell-to-organ systems. They employed self-consistent models at each scale to represent RVEs related to biophysical and biochemical rate of changes (protein, cells, tissues, and organs). For example, for a protein representation at a continuum level, the subscale information focused on gene signaling and regulation of transcription and translation.

4.4.3.4 Multiscale Modeling of Vegetation-Based Structural Materials

In terms of multiscale modeling for vegetation, there have been only a few studies. Silva [273] suggested a hierarchical method for analyzing naturally occurring bamboo for use in synthetic man-made structures. Since naturally occurring bamboo has complicated multiscale internal structures at different length scales, a homogenization model to represent the mechanical behavior was introduced. The homogenization included a functionally graded representation in a finite element analysis domain. Godin and Caraglio discussed and presented a model for the different topological length and time scale structures within trees. Their model supports multiscale, attributed and time-varying descriptions of trees intended to be used for plant analysis methodologies and plant growth simulations. Makela [274] presented a hierarchical multiscale model to address the dynamic growth of trees. In particular, the author included modeling for patterns as well as size growth. The motive was to try to quantify wood quality.

4.5 Multiscale Modeling for Design

A significant opportunity exists for multiscale modeling in the next wave of design paradigms for components, subsystems, or large scale systems by accounting for the structure-property relations which have a real impact on measured system response to design loads. As multiscale modeling is refined and enhanced, the degree of model accuracy and precision is directly related to the level of product design optimization which can be achieved. The method of combining multiscale modeling into simulation-based design concepts has several challenges, such as lack of validated techniques for bridging the various time and length scales, management of models with the associated uncertainties, management of a huge amount and variety of information, and development of simpler, user-friendly methods for efficient decision making.

Panchal et al. [275] discussed how multiscale modeling deals with efficient integration of information from multiscale models to gain a holistic understanding of the system, whereas multiscale design deals with efficient utilization of information to satisfy design objectives. In order to address the challenges associated with multiscale design, Panchal et al. [275] proposed a domain independent strategy based on generic interaction patterns between multiscale models.

In a different vein, Olson [86, 87, 276] has described the processing-structure-performance relationship as a function of multiscale, multilevel materials attributes that has lent itself to multiscale modeling and simulation. In the DARPA AIM project [277], a Ni-Base superalloy employing a hierarchical multiscale method was used to design a component in a gas turbine engine with the objective of increasing burst speed and decreasing the disk weight. The focus on materials design was exemplified in Olson [278] in which martensite was examined through a multiscale method.

While joining the Olson and Panchal et al. strategies, the Mistree [279] research group at Georgia Tech has focused on using hierarchical multiscale modeling to optimize materials design. The classical materials selection approach is being replaced by the *design* of material structure and processing paths based on a hierarchy of length scales for multifunctional performance requirements. In the work of Seepersad et al. [280, 281], they optimized the mechanical properties for cellular foam with voids.

4.6 Multiscale Modeling in Manufacturing

Besides design, another great opportunity for multiscale modeling is the venue of materials processing. Rapid prototyping and other materials processing techniques can facilitate tailoring microstructural topology with high levels of detail. This industrial framework makes it amenable for multiscale materials modeling to affect a paradigm shift with US manufacturing. Economists Grimes and Glazer of the Examination Bureau of Labor Statistics stated that the US has lost 18% of its manufacturing jobs from 1990 to 2003. Although higher labor costs in the US are a big factor, US industry has lacked improvements in innovative design. An upturn in the manufacturing industry clearly requires a competitive advantage through better design tools based on information technology and high-fidelity multiscale materials modeling and simulations and design optimization. Horstemeyer and Wang [216] argued that improved design/analysis capabilities based on recent scientific and engineering research advances will provide a substantial benefit to the US manufacturing industry, but to do so, multiscale modeling is needed in the mix. This applies to the general manufacturing industry, specific "made-to-order" manufacturing segments, and those involved with cutting edge technologies. Significant breakthroughs in the knowledge base, software integration, length/time scale bridging, and educational enterprise are required to reverse the negative manufacturing trend in the US. Currently, multiscale modeling can be used to

optimize the process-property-cost for processes such as forging, forming, casting, extrusion, rolling, stamping, and welding/joining.

4.7 Engineering Designs in Practice Using Multiscale Modeling

Two different metal alloy examples using multiscale modeling will next be shown to illustrate the integration of many disciplines described earlier. One example of optimizing an aluminum alloy based automotive control arm for a Cadillac automobile demonstrates multiscale modeling of plasticity and damage/failure in a hierarchical manner. Another example of employing multiscale modeling will be shown by optimizing a magnesium alloy with respect to fatigue that was used to redesign a Corvette cradle, which is the main structural undercarriage under the engine. These hierarchical multiscale modeling examples incorporate solid mechanics, mathematics, materials science, and physics with various bridging methodologies.

4.7.1 Plasticity-Damage Multiscale Modeling Example of Automotive Cadillac Control Arm Design

In designing a structural component, a failure analysis will typically include a finite element analysis and microstructural evaluation. Sometimes the microstructural evaluation will quantify the inclusion content (source of damage in a component) in a prioritized fashion differently than the finite element analysis. Let us consider the hypothetical situation exemplified in Fig. 4.5. Here we have an automotive control arm that has undergone certain boundary conditions in a finite element analysis. The finite element analysis with homogeneous microstructural considerations revealed that the highest Von Mises stress [282] occurred at point D. On the other hand, microstructural analysis using optical imaging revealed that the largest defect occurred at point B. Both the finite element analysis and microstructural analysis camps would argue about the location of final failure. However, in our example, both are wrong, because the final failure state is both a function of the initial inclusion state and the boundary conditions. As such, point A failed first. The key now is the development of a tool that captures point A failing first [146]. The effective solution to this structural dynamic analysis/design problem is the development of a hierarchical multiscale modeling methodology that admits the appropriate structure-property relations from each length scale so that proper heterogeneous microstructures can be included in a finite element analysis.

The fundamental difficulty in quantifying the structure-property relations arises because of the different length scales of microstructures and defects present within

Stress (from highest to lowest)	Inclusion (from most severe to less severe)	Damage (from most severe to less severe)
D	B	A
A	E	D
C	A	E
E	D	C
B	C	B

Fig. 4.5 Stress and inclusion analysis studies can be independently performed on this control arm, but both would give an erroneous location of failure, because damage accumulation is dependent upon both entities

a material. The challenge of developing a mathematical representation of these different length scale features and their associated evolution into various damage states is great. However, this lends itself to a hierarchical multiscale methodology in which multiple space scales and associated non-equilibrium evolution damage evolution need to be quantified.

In order to start the multiscale modeling, internal state variables were adopted to reflect void/crack nucleation, void growth, and void coalescence from the casting microstructural features (porosity and particles) under different temperatures, strain rates, and deformation paths [115, 116, 221, 283]. Furthermore, internal state variables were used to reflect the dislocation density evolution that affects the work hardening rate and, thus, stress state under different temperatures and strain rates [25, 283–285]. In order to determine the pertinent effects of the microstructural features to be admitted into the internal state variable theory, several different length scale analyses were performed. Once the pertinent microstructural features were determined and included in the macroscale internal state variable model, notch tests [216, 286] and control arm tests were performed to validate the model's precision. After the validation process, optimization studies were performed to reduce the weight of the control arm [287–289].

In order to quantify the structure-property relations at each scale, a multiscale hierarchy of numerical simulations was performed, coupled with experiments, to determine the internal state variable equations of macroscale plasticity and damage

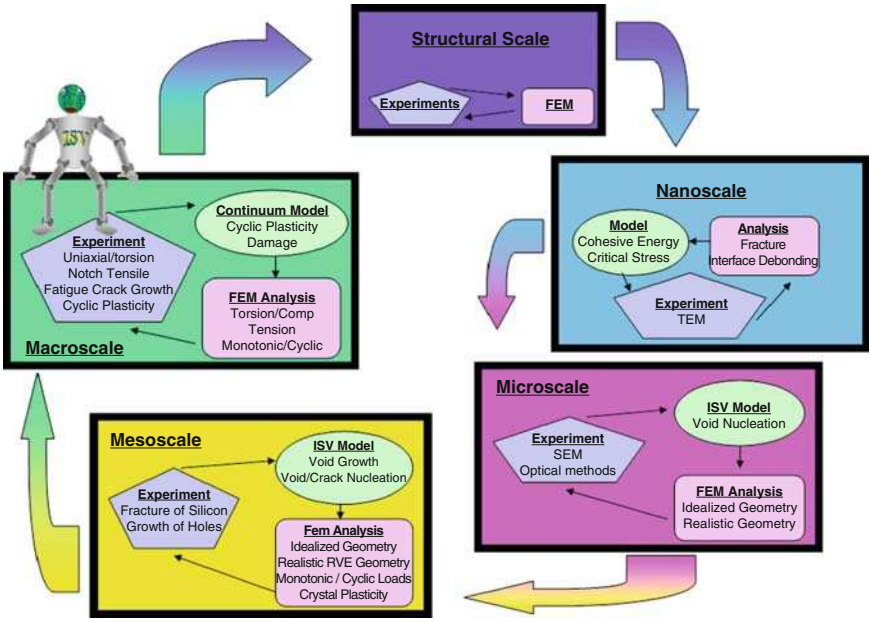

Fig. 4.6 Schematic illustrating the corroboration of multiscale modeling and multiscale experiments at each length scale and the pertinent effects being pushed up to the next higher length scale

progression as illustrated in Fig. 4.6. The microstructures/defects observed in the cast A356 aluminum alloy in descending order of deleterious effect were found to be large oxides/pores, smaller oxides/pores, silicon particles, dendrite cells size, and intermetallics. The attributes of these features that were included in the model were the size distributions, volume fractions, and nearest neighbor distances.

Now that the top-down internal state variable theory was established, the bottom-up simulations and experiments were required. At the atomic scale (nanometers), simulations were performed using Modified Embedded Atom Method, (MEAM) Baskes [176], potentials based upon interfacial atomistics of Baskes et al. [177] to determine the conditions when silicon fracture would occur versus silicon-interface debonding [156]. Atomistic simulations showed that a material with a pristine interface would incur interface debonding before silicon fracture. However, if a sufficient number of defects were present within the silicon, it would fracture before the interface would debond. Microstructural analysis of larger scale interrupted strain tests under tension revealed that both silicon fracture and debonding of the silicon-aluminum interface in the eutectic region would occur [290, 291].

Another important result from the atomistic simulations was that the stress-strain response of a region of material around an interface that debonded could be represented by an elastic fracture analysis at the next higher size scale if the interface was assumed to be larger than 40 Å. Hence, an elastic fracture criterion was used in the microscale finite element analysis, which focused on void-crack

nucleation and mesoscale (1–200 μm) finite element analyses, which focused on silicon-pore coalescence [216].

The micron size scale finite element analyses focused on the void-crack nucleation progression by examining the parameters that influenced silicon fracture and silicon-aluminum interface debonding [216]. In particular, we included temperature, shape, size, nearest neighbor distance, number density, prestrain history, and loading direction as parameters for the silicon in the finite element analyses. The parametric study employing an ANOVA design of experiments method clearly showed that the temperature dependence on void nucleation from silicon fracture and interface debonding was the most dominant influence parameter. To verify this result, we performed notch tensile tests at ambient temperature and the two extreme limits of temperatures that a control arm would experience were 222 K and 600 K [288]. By examining the fracture surfaces and cross-sections of deformed samples and counting the number of void nucleation sites, it was clear that at the coldest temperature, the largest voids nucleated and at the hottest temperature, the least amount of voids nucleated. Essentially, the colder temperatures induced a higher local stress state. The higher stresses fuse damage at an increased rate. These results corroborated the microscale finite element analyses and thus, a temperature dependence on the void nucleation rate was included in the macroscale ISV model. As a follow-on, strain rate tests were also performed in which the strain rate effect on void nucleation was quantified for the model [289].

An important set of experiments was performed to determine the void nucleation rate under different stress states and strain levels [287]. Interrupted equivalent strain test specimens that underwent tension, compression, and torsion were examined via optical imaging and the number densities of fractured/debonded particles were quantified. The experimental data showed that the void nucleation rate under torsion was the highest followed by tension and then by compression. Interestingly, the highest work hardening rate was exhibited in compression followed by tension and then by torsion. This inverse relationship of the work hardening rate to the void nucleation rate revealed a coupling between the stress state and damage progression. The void nucleation rate and work hardening rate differences were included in the macroscale void nucleation internal state variable model.

In the Mesoscale I analyses, the simulations focused on pores arising from silicon fracture and interface debonding that interacted with pores from the casting process. While performing these finite element analyses, the finite element meshes were constructed on real A356 micrographs. Hence, the sizes, distributions, and volume fractions of silicon, casting porosity, and dendrite cells were inherently imbedded in the simulations. Indenter tests were conducted on particular second phases to determine the elastic moduli of the silicon, intermetallics, and matrix aluminum. Compression tests were also conducted on the eutectic aluminum at different temperatures to obtain the stress-strain responses for the mesoscale analyses. These values were used for the finite element simulations. The progression of silicon fracture and interface debonding were matched with the interrupted strain experiments described earlier by a trial-and-error method for the local elastic fracture silicon stresses. The applied stress state was then compared with

temperature and strain rate. The results gave insight into the functional form of the equation needed for the macroscale coalescence equation [292]. Furthermore, temperature dependence was deemed as very important here. In fact, the influence of temperature on void coalescence was the opposite trend as that of void nucleation. For void nucleation, as the temperature decreased (increasing the stress level), the void nucleation rate increased. For void coalescence, as the temperature increased (increasing the plastic strain), the void coalescence rate increased. This temperature dependence was included in the macroscale coalescence equation.

The Mesoscale II finite element simulations (100–500 μm) focused on pore-pore interactions to give insight into coalescence from casting porosity. Similar to the void nucleation parametric study, an ANOVA design of experiments method was used by varying temperature, shape, size, nearest neighbor distance, number density, prestrain history, and loading direction and monitoring the total void growth and strain at localization [115]. The results showed that temperature again was a first order influence parameter on void coalescence because it increases the local plastic strains, but the size of pore and type of loading (triaxial state of stress) were first order influence parameters on strain localization. Furthermore, microporosity, prestrain history, and number density were first order influences, along with temperature, on the total void growth. Hence, these attributes were placed in the macroscale coalescence equation. The macroscale void growth and coalescence internal state variable equations were then tuned to other micromechanical simulations [116] that were performed to study the evolution rates under varying deformation and temperature.

Another important result from this study showed that if a pore was within eight diameters of another pore, the void growth rates would be enhanced. Alternatively, if a casting can have nearest neighbor distances of greater than eight pore diameters, the strain to failure would be increased.

Tension experiments on flat bars were performed to analyze void growth from surface pores under different temperatures. The surface pores were first measured in the virgin state and then the specimens were tested to a certain strain level. The identical voids were then measured again. This process occurred until the specimens fractured. The voids were more than eight diameters apart and hence, the results were used to determine the single void growth equation for the macroscale microstructure-mechanical property model. As it turned out, minimal void growth was measured from these surface pores until the final fracture occurred, indicating that void nucleation was probably more important than void growth and coalescence in this cast A356 aluminum alloy under uniaxial monotonic loads. Furthermore, little difference was observed from the temperature changes which indicated that macroscale void growth equation did not need to include the temperature dependence.

Given the subscale information, the macroscale total void volume fraction (cm) was a function of the void nucleation rate, void growth rate, and coalescence rate. The coalescence or void interaction rate arose from two sources: pores from silicon fracture and interface debonding interacting with casting pores and two or more casting pores interacting. Once the macroscale equations and the corresponding

material constants were determined from the aforementioned analyses, compression tests at different strain rates and temperatures were performed to determine the plasticity parameters [293].

Now that the multiscale modeling and experimentation methodology were completed, several types of macroscale tests (cm) were then performed to validate the methodology. First, cyclic uniaxial tests (Bauschinger effect tests) were performed in which tension was followed by compression and compression was followed by tension up to 2%, 3%, and 5% strain levels [64, 294]. Because the work hardening rate was different in compression than tension due to the preferred damage, the stress state at the end of the reverse test was different depending on the path history. Even with this complexity, the internal state variable plasticity-damage model was able to accurately capture this coupling of damage and plasticity. Typical power law plasticity formulations or other formulations that do not have the results of the structure-property relations determined from multiscale modeling would not capture this phenomenon. The second set of experiments included interrupted notch tests in which the specimens were analyzed nondestructively by x-ray tomography and analyzed via optical imaging analysis [286]. Void volume fractions, sizes, and distributions were quantified at failure, 90% of failure, 95% of failure, and 98% of failure, respectively. The finite element analyses, which included the macroscale microstructure-mechanical property model, gave very close results (to within 1%) to the x-ray tomography and optical imaging data.

Once the validation of the physics and verification of numerical implementation were completed, control arm simulations (m) were performed with two goals in mind: first, to finally judge the predictive capability of the model for a control arm, and second, use the model to optimize the control arm by adding mass to certain "weak" regions and taking away mass from "strong" regions. As it turned out, the simulations accurately predicted the final failure locations of the control arm as demonstrated by control arm experiments (Fig. 4.7).

The final step in the use of multiscale modeling methodology for this control arm redesign was employing an optimization algorithm to study the reduction of weight potential. A reliability-based optimization was used to integrate the multiscale modeling methodology with the redesign [78]. Although the methodology is generic for any multiscale modeling and redesign situation, the methodology was applied to redesigning a cast automotive control arm. This multiscale modeling example included quantifying uncertainties in the microstructure-property relationships, the influence of the uncertainties on the plasticity-damage constitutive relationship, and the integration of such models into engineering design of structural components subject to the internal state variable failure criteria. In doing so, a metamodeling approximation was found to be a necessary component of this efficient methodology when considering the noise and nonlinearities in the failure responses. The accuracy and performance of several parametric and non-parametric metamodels were compared to investigate the effect of microstructure-property relations and the associated uncertainties on the optimum design. The results showed that a Gaussian representation for the metamodel provided the best response for damage/failure. In the end, control arm weight was reduced approximately 25% of

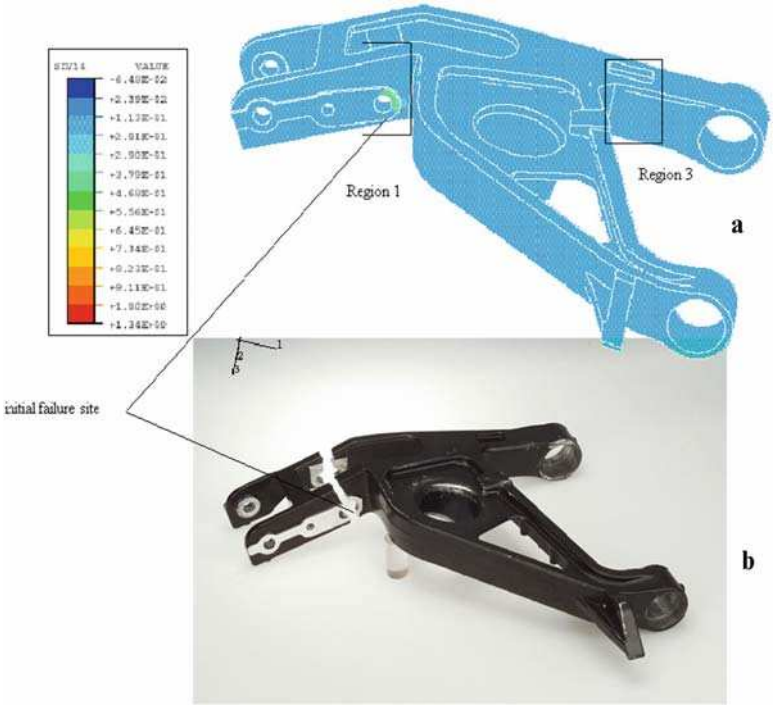

Fig. 4.7 (a) Control arm simulation result and (b) experimental result comparison showing the failure location. SDV14 is the total void volume fraction or damage level

the original weight with an increase in load-bearing capacity of 40%. Clearly, without the multiscale modeling that included the structure-property relations, the exact location and strain level of the failure would not have been realized and the optimization would have been fallible.

4.7.2 Multiscale Fatigue Modeling Example of Automotive Corvette Cradle

The corvette structural cradle that undergirds the engine and the associated components had been historically made of an aluminum alloy, but was being considered to be made of a magnesium alloy. To successfully use a cast magnesium alloy for such an important structural component, it is necessary to understand its resistance to fatigue. In trying to keep reliability with a new material, risk needs to be minimized. Similar to the control arm example, the standard method in determining failure locations is to perform a finite element analysis to obtain the highest stresses/strains in a particular region of the material. Some material from that region is then

typically extracted and small coupons are made for uniaxial, completely reversed tension-compression fatigue tests. These results are used to estimate the life of the component. Other material typically adjacent to the coupons is extracted for microstructure/inclusion analysis. Unfortunately, regions that may be important based on the stress analysis may not be important to the microstructural analysis. More importantly, it is the combination of the microstructure/inclusion content with the stress analysis that is needed to determine a precise location for fatigue failure. Therefore, a multiscale modeling effort with multiscale experiments was made to help redesign and evaluate various magnesium alloys for the cradle.

Figure 4.8 illustrates the same point as mentioned earlier for the aluminum control arm in which Region D clearly represents the highest stressed region for this Corvette cradle. The finite element analysis with homogeneous materials characteristics erroneously showed the failure location to be point D. Point C showed the most severe initial porosity. Point E actually is where the crack first occurred, so both locations were wrong and point E realized the combination of the defect state and the boundary value results. This demonstrates again that a clear connection between the microstructure/inclusion content and the mechanical properties is necessary for predicting the life of a structural component.

Cast magnesium alloys used for structural applications comprise a highly heterogeneous ductile matrix with several dominant types of inclusions that dictate fatigue resistance. We use the term inclusion as distinctly different from a crack, as the former occurs naturally as products of the casting process, while the latter is

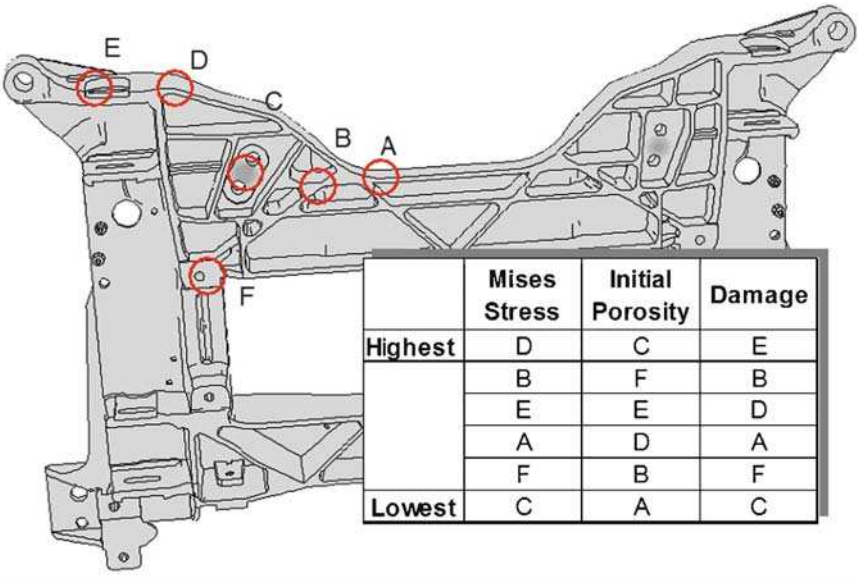

	Mises Stress	Initial Porosity	Damage
Highest	D	C	E
	B	F	B
	E	E	D
	A	D	A
	F	B	F
Lowest	C	A	C

Fig. 4.8 The highest stress from the finite element analysis was at point D and the worst inclusion (porosity) was located at point C. However, the greatest damage from fatigue occurred at point E, arising from the confluence of the stress state and the initial inclusion condition

usually a result of applied loading. The different types of inclusions comprise oxides, gas pores, shrinkage porosity, and distributed intermetallic particles. The matrix usually includes some percentage of aluminum (AM50 has 5% aluminum, AM60 has 6% aluminum, AZ91 has 9% aluminum, and AE44 has 4% aluminum) and is an elastic-plastic material with anisotropic work hardening arising from the hexagonal close pack structure. Large scale oxide films are prone to forming large fatigue cracks that propagate rapidly to premature failure and as such, are the most deleterious inclusion. These oxides can range from 200 to 600 μm. The second most deleterious inclusions are the gas pores. These gas pores, ranging from 30 to 500 μm, are especially potent in degrading the fatigue resistance as they serve as local stress concentration sites for formation of particularly large cracks that then propagate to premature failure. Another inclusion type operating at a different length scale is the shrinkage porosity that forms by entrapped hydrogen gas in the melt, which grows in concert with the dendrite cell size (secondary dendrite arm spacing) as microstructure coarsens with solidification. Both the gas pores and shrinkage porosity contribute significantly to the localization of cyclic plastic shear strain in the interdendritic regions under fatigue loading. Finally smaller distributed intermetallics on the order of several microns can affect the rate of crack propagation of small fatigue cracks and overall ductility. The most probable casting inclusion to cause fatigue failure was the gas pores as documented for different magnesium alloys [295–297].

The multistage fatigue model of McDowell et al. [298] was originally developed from multiscale modeling for aluminum alloys [299–301] and applied to these various magnesium alloys for redesign of the Corvette cradle [302]. For each type of inclusion, three different stages exist and each stage incurs a different number of cycles depending on the type of inclusion. The most significant aspect is that the different stages represent different length scales of crack lengths. The first stage is the incubation stage, designating pregnancy of the crack. Each type of inclusion incurs a different incubation life with the large oxide being the smallest. No length of crack is assumed here, only the size of the inclusion. The second stage is the Microstructurally Small Crack (MSC) growth regime in which the driving force is governed by the change in the crack tip displacement. In the MSC regime, the resistance from other inclusions in the crack path and the grain orientations and misorientations play a key role. This regime starts at approximately a micron and grows on the order of up to five grain lengths depending on what features are in the crack path. The final regime is the long crack regime, in which Paris Law [303] elastic type behavior takes over with the addition of crack closure coming from the plastic wake [304, 305]. We note that for automotive applications, 80–90% of the life is spent in the incubation and MSC regimes.

Figure 4.9 illustrates the multistage fatigue model's calibrated predictions for different types of inclusions illustrating the various length scales involved. It is to be noted that the final number of cycles decreases with increasing level of inclusion severity.

To understand the multistage fatigue crack mechanisms for the different inclusion types, multiscale modeling and experiments were performed to develop the

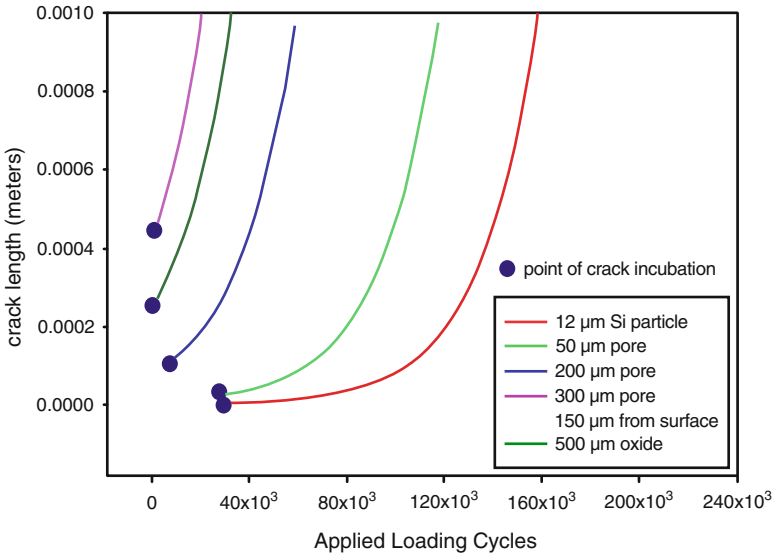

Fig. 4.9 Multistage fatigue model results illustrating the different length scale inclusions that affect the fatigue life

top-down model [298]. What the experiments could not provide (even with scanning electron microscopy imaging of the failure surfaces), was done by the micromechanical finite element simulations [135, 136, 152, 153, 306]. As quantification of the crack incubation and small crack formation stage experimentally was extremely difficult, micromechanical finite element simulations were used to help clarify our understanding of the microstructure-property relations and provide the needed information for the development of the multiscale fatigue model. Since quantification of the local cyclic plastic strain in the microstructure is essential in driving fatigue crack incubation, we focused on that aspect in the micromechanical finite element analyses using both idealized geometries and realistic geometries for the microstructure/inclusion morphology. In particular, we examined the effects of applied stress amplitude, microstructure-inclusion content on the maximum plastic shear strain for crack incubation and the cyclic crack tip opening displacement for MSC crack propagation. For the MSC crack propagation regimes, the effects of particle shape, particle size, particle nearest neighbor dimension, particle distribution, dendrite cell size, pore size, pore shape, pore nearest neighbor distance, and pore distribution were analyzed. In this context, such characteristics as crack driving force and crack closure behavior were quantified.

For the final magnesium alloy chosen for the Corvette cradle, the multistage fatigue model predicted the mean, upper bound, and lower bound strain-life response for the cast AE44 Mg alloy as shown in Fig. 4.10. To realize the upper bound prediction, an inclusion of five microns for a casting pore was assumed with no shrinkage porosity or oxides nearby. For the lower bound, a 1 mm diameter casting pore was used. A casting pore mean value of 400 μm was used to yield the

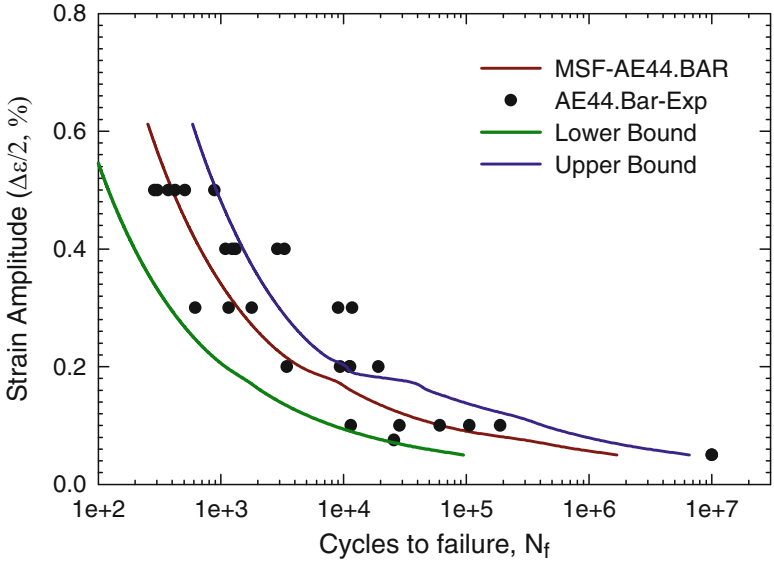

Fig. 4.10 Uniaxial strain-life experiments and multistage fatigue model predictions for AE44 specimens with predicted upper and lower bounds

mean strain-life curve. As such, the multistage fatigue model gave the designer a notion about not only the mean design for the AE44 mg alloy, but the upper and lower bounds as well. This model, coupled with the internal state variable model, was then applied to the Corvette cradle.

Figure 4.11 shows that the modeling and simulation results from using the internal state variable plasticity-damage model and the multistage fatigue model were excellent when compared to the experimental test results. Once this corroboration was finalized, the models were used to evaluate 35 boundary conditions that a Corvette would experience and verified that the AE44 Mg alloy was a good replacement for the previously cast aluminum alloy.

This example of using a hierarchical multiscale modeling methodology for redesign of the Corvette cradle shows that not only can the multiscale modeling be used for monotonic considerations like the control arm, but can be used for fatigue analysis as well.

4.8 Summary

Glimm and Sharp [307] proposed a challenge to the twenty-first century researcher to consider multiscale materials modeling as a new paradigm in order to realize more accurate predictive capabilities. The context is to predict the macroscale/structural scale behavior without disregarding the important smaller scale features.

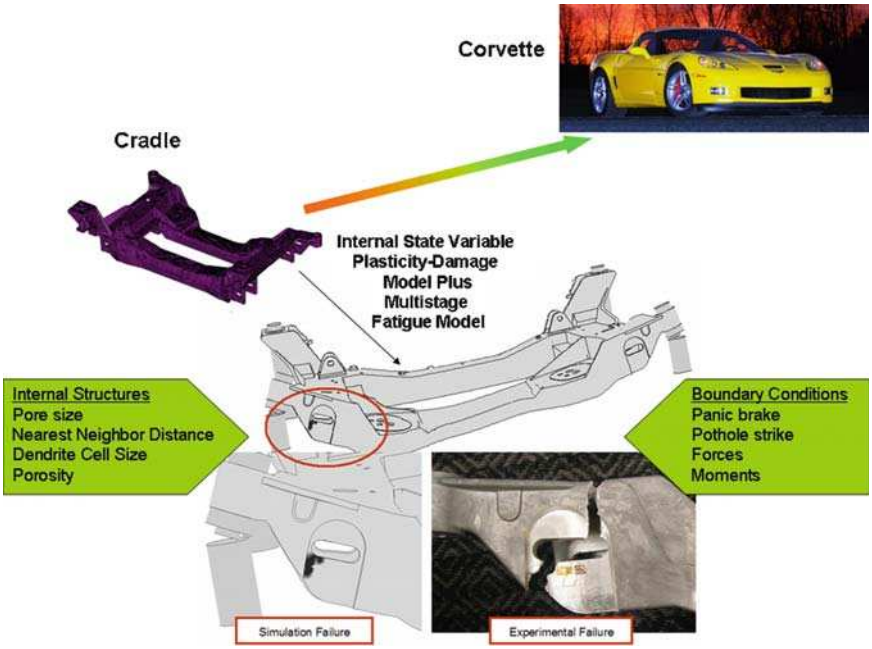

Fig. 4.11 Corvette cradle modeling and simulation results from the internal state variable plasticity-damage model coupled with the multistage fatigue model demonstrating the capability to predict the experimental result for redesigning the cradle from aluminum to magnesium

Multiscale modeling is a key for more accurate simulations for solid materials because of the heterogeneities arising from these subscale microstructures. As such, the notion of selecting or disregarding the subscale information requires interdisciplinary methods to make proper judgments. When selecting the appropriate subscale feature homogenization, self-consistent methods, percolation theory, etc. are needed to average out the effect within the continuum. As a consequence, the terminology and focus in recent years have helped to gain more accurate component and systems level answers. As demonstrated by several examples, multiscale modeling has the capability to ameliorate the better physics versus computational cost conundrum for simulation-based design and manufacturing. In the end, higher quality more optimized designs are admissible today because of the confluence of computing power, experimental validation techniques, and numerical algorithms available. For multiscale modeling to have even greater impact in manufacturing and design, efficiency even with greater accuracy requires that computational times of the concurrent multiscale methods should be on the order of the computation required for the more accurate treatment using the hierarchical methods. Nothing is really gained from concurrent multiscale methods if this is not true, since hierarchical multiscale methods could be run independently with lesser computational times. This, of course, limits the usage of concurrent methods usually to two or

three length scales, where hierarchical methods are not limited to just two length scales.

Although multiscale modeling has experienced some success with metals, the usage for polymer material systems has been lacking. In particular, the impact on biological tissue has yet to be realized. Furthermore, the common usage of multiscale modeling for design and manufacturing requires a paradigm shift for the industry. Kassner et al. [308] summarized the future needs of multiscale modeling for metallic and polymeric systems, essentially requesting for research related to multiscale modeling that deals with discontinuities/defect/microstructures.

Not mentioned in this review but certainly important to multiscale modeling related to solid mechanics are topics, such as self-assemblies, thin films, thermal barrier coatings, patterning, phase transformations, nanomaterials design, and semiconductors, all of which have an economic motivation for study. Studies related to these types of materials and structures require multiphysics formulations to understand the appropriate thermodynamics, kinetics, and kinematics.

Acknowledgments The author would like to thank the Center for Advanced Vehicular Systems at Mississippi State University for supporting this work, Jerzy Lesczczynski for his encouragement of documenting the current state of multiscale modeling, and Dean Norman for helping review this article.

References

1. V.E. Panin Foundations of physical mesomechanics. Phys. Mesomech. **1**, 5–20 (1998)
2. S. Yip Handbook of Materials Modeling. Springer-Verlag, The Netherlands (2005)
3. E.B. Tadmor et al Hierarchial modeling in the mechanics of materials. Int. J. Solids Struct. **37**, 379–389 (2000)
4. H. Helmholtz, *On the Conservation of Force* (Physical Society of Berlin, Berlin, 1847)
5. J.C. Maxwell On the dynamical evidence of molecular constitution of matter. J. Chem. Soc. London **28**, 493–508 (1875)
6. L. Onsager Reciprocal relations in irreversible processes. I. Phys. Rev. **37**, 405–426 (1931)
7. L. Onsager Reciprocal relations in irreversible processes. II. Phys. Rev. **38**, 2265–2279 (1931)
8. C. Eckart The thermodynamics of irreversible processes. I. The simple fluid. Phys. Rev. **58**, 267–269 (1940)
9. C. Eckart The thermodynamics of irreversible processes. IV. The theory of elasticity and anelasticity. Phys. Rev. **73**, 373–382 (1948)
10. E. Kroner, How the internal state of a physically deformed body is to be described in a continuum theory, *Proceedings of the 4th International Congress on Rheology*, (1960).
11. B.D. Coleman, M.E. Gurtin Thermodynamics with internal state variables. J. Chem. Phys. **47**, 597–613
12. J.R. Rice Constitutive equations in plasticity. J. Mech. Phys. Solids **9**, 433 (1971)
13. J. Kestin, J. R. Rice Paradoxes in the Application of Thermodynamics to Strained Solids. A Critical Review of Thermodynamics, ed by E.B. Stuart (Mono Book Corp., Baltimore, 1970), p. 275–280
14. R. Talreja Continuum modeling of damage in ceramic matrix composites. Mech. Matls. **12**, 165–180 (1991)

15. R. Talreja Further developments in continuum damage modeling of composites aided by micromechanics. ASME App. Mech. Div. **150**, 103 (1993)
16. R. Talreja, A damage mechanics based approach to durability assessment of composite materials, Composites and Finely Graded Materials, in ASME, *Materials Division*, vol. 80 ed. by T. Srinivasan et al. pp. 151–156 (1997)
17. O.A. Hasan, M.C. Boyce Constitutive model for the nonlinear viscoelastic viscoplastic behavior of glassy polymers. Polymer Eng. Sci. **35**, 331–334 (1995)
18. H.D. Espinosa et al A 3-D finite deformation anisotropic visco-plasticity model for fiber composites. J. Compos. Mater. 35(5):369–410 (2001)
19. B.A. Gailly, H.D. Espinosa Modeling of failure mode transition in ballistic penetration with a continuum model describing microcracking and flow of pulverized media. Int. J. Num. Meth. Eng. 54(3):365–398 (2002)
20. U.F. Kocks The relation between polycrystal deformation and single crystal deformation. Metal. Trans. 1(5):1121 (1970)
21. P.S. Follansbee Metallurgical applications of shock-wave and high-strain rate phenomena. DekkerL. E. Murr et al, NY, pp 451–479 (1986)
22. P.S. Follansbee, U.F. Kocks A constitutive description of the deformation of copper based on the use of the mechanical threshold stress as an internal state variable. Acta Mater. 36(1): 81–93 (1988)
23. A.D. Freed, Thermoviscoplastic model with application to copper, NASA Technical Paper, NASA Lewis Research Center, **2845**, 1–17 (1988)
24. D.J. Bammann An internal variable model of viscoplasticity. Intl. J. Eng. Sci. **22**, 1041–1053 (1984)
25. D.J. Bammann Modeling the temperature and strain rate dependent large deformation of metals. Appl. Mech. Rev. **43**, S312–319 (1990)
26. J.L. Chaboche Viscoplastic constitutive equations for the description of cyclic and anisotropic behavior of metals. Bull. de l' AcadSe'rie Sc. et Techn. 25(1):33 (1977)
27 J.D. Eshelby The determination of the elastic field of an ellipsoidal inclusion. Proc. R. Soc. Lond. A. Mat. Phys. Sci. **241**, 376–396 (1957)
28. J.D. Eshelby The elastic field outside an ellipsoidal inclusion. Proc. Royal Soc. Lond. A Mathl. Phys. Sci. 252(1271):561–569 (1959)
29. R. Hill Continuum micromechanics of elastoplastic polycrystals. J. Mech. Phys. Solids **13**, 89–101 (1965)
30. T. Mura, K. Tanaka Average stress in matrix and average elastic energy of materials with misfitting inclusions. Acta. Metal. **21**, 571–574 (1973)
31. T. Mura, *Micromechanics of Defects in Solids* (Martinus Nijhoff Publishers, Dordrecht 1982), ISBN 90-247-3343(HB)
32. B. Budiansky Micromechanics: Advances and Trends in Structural and Solid Mechanics. Pergamon Press, Oxford, pp 3–12 (1983)
33. S. Nemat-Nasser, M. Lori Micromechanics: Overall properties of heterogeneous materials. J. App. Mech **63**, 561 (1996)
34. A.M. Gokhale, S. Yang Application of image processing for simulation of mechanical response of multi-length scale microstructures of engineering alloys. Metal. Mat. Trans. A: Phys. Metall. Mat. Sci. **30**, 2369–2381 (1999)
35. S. Hao et al A hierarchical multi-physics model for design of high toughness steels. J. Comput.-Aided Mat. Des. **10**, 99–142 (2003)
36. Z.P. Bazant, E.P. Chen Scaling of structural failure. ASME Appl. Mech. Rev. **50**, 593–627 (1997)
37. P. W. Bridgman, The compressibility of thirty metals as a function of pressure and temperature, Proceedings of the American Academy of Arts and Science, vol. 58 (1923), pp. 164–242.
38. R. Phillips Crystals, Defects and Microstruct.: Model. Across Scales. University Cambridge Press, Cambridge (2001)

39. W.K. Liu et al Introduction to computational nanomechanics and materials. Nano Mechanics and Materials:-Theory, Multiscale Methods and Apllication. John Wiley and Sons, NewYork (2006)
40. J. Fish Bridging the scales in nanoengineering and science. J. Nanopart. Rsrch. **8**, 577–594 (2006)
41. J.J. De Pablo, W.A. Curtin Multiscale modeling in advanced materials research: Challenges, novel methods, and emerging applications. MRS Bulletin **32**, 905–909 (2007)
42. W. Hackbush Multi-Grid Methods and Applications. Springer, Berlin (1985)
43. S. Kohlhoff, S. Schmauder Atomistic Simulation of Materials: Eds. Vitek V, Srolovitz DJ Plenum Press, New York, pp 411–418 (1989)
44. S. Kohlhoff et al Crack propagation in bcc crystals studied with a combined finite-element and atomistic model. Phil. Mag. **64**, 851–878 (1991)
45. E.B. Tadmo et al Quasicontinuum analysis of defects in solids. Phil. Mag. A: Phys. Cond. Matt. Defects Mech. Prop. **73**, 1529 (1996)
46. M.S. Daw, M.I. Baskes Embedded-atom method: Derivation and application to impurities, surfaces, and other defects in metals. Phys. Rev. B **29**, 6443–6453 (1984)
47. M.S. Daw et al Embedded atom method–a review of theory and applications. Matls. Sci. Rep. A Rev. J. **9**, 251–310 (1993)
48. M. Ortiz et al A finite element method for localized failure analysis. Comp. Methods Appl. Mech. Eng. **61**, 189–214 (1987)
49. V.B. Shenoy et al Quasicontinuum models of interfacial structure and deformation. Phy. Rev. Lett. **80**, 742–745 (1998)
50. R. Miller et al Quasicontinuum simulation of fracture at the atomic scale. Model. Sim. Mat. Sci. Eng. **6**, 607–638 (1998)
51. R. Miller et al Quasicontinuum models of fracture and plasticity. Eng. Fract. Mech. **61**, 427–444 (1998)
52. V.B. Shenoy et al An adaptive finite element approach to atomic-scale mechanics–the quasicontinuum method. J. Mech. Phys. Solids **47**, 611–642 (1999)
53. F.F. Abraham et al Spanning the continuum to quantum length scales in a dynamic simulation of brittle fracture. Europhys. Lett. **44**, 783–787 (1998)
54. S.J. Plimpton Lammps code. J. Comp. Phys. **117**, 1–19 (1995)
55. R.E. Rudd, J.Q. Broughton Coarse-grained molecular dynamics and the atomic limit of finite elements. Phys. Rev. B **58**, R5893–R5896 (1998)
56. J.Q. Broughton et al Concurrent coupling of length scales: Methodology and application. Phys. Rev. B **60**, 2391–2403 (1999)
57. E. Lidorikis et al Coupling length scales for multiscale atomistics-continuum simulations: Atomistically induced stress distributions in Si/Si_3N_4 nanopixels. Phys. Rev. Lett. **87**, 086104 (2001)
58. Z.P. Bazant Can multiscale-multiphysics methods predict softening damage and structural failure? Mech. Am. Acad. Mech. **36**, 5–12 (2007)
59. L.E. Shilkrot et al Coupled atomistic and discrete dislocation plasticity. J. Mech. Phy. Solids **50**, 2085–2106 (2002)
60. L.E. Shilkrot et al Multiscale plasticity modeling: Coupled atomistics and discrete dislocation mechanics. J. Mech. Phy. Solids **52**, 755–787 (2004)
61. B. Shiari et al Coupled atomistic/discrete dislocation Simulations of Nanoindentation at Finite Temperature. J. Eng. Mat. Tech. Trans. ASME **127**, 358–368 (2005)
62. M.P. Dewald, W.A. Curtin Multiscale modelling of dislocation/grain boundary interactions. II. Screw dislocations impinging on tilt boundaries in Al. Phil. Mag. **87**, 4615–4641 (2007)
63. H.M. Zbib, D.D.L. Rubia A multiscale model of plasticity. Int. J. Plast. **18**, 1133–1163 (2002)
64. M.F. Horstemeyer et al Design of experiments for constitutive model selection: Application to polycrystals elastoviscoplasticity. Modelling Simul. Mater. Sci. Eng. **7**, 253–273 (1999)
65. P.R. Dawson On modeling of mechanical property changes during flat rolling of aluminum. Int. J. Solids Struct. **23**, 947–968 (1987)

66. D. Peirce, R.J. Asaro, Needleman A An analysis of nonuniform and localized deformation in ductile single crystals. Acta Metall. **30**, 1087–1119 (1982)
67. M.M. Rashid, S. Nemat-Nasser Modeling very large plastic flows at very large strain rates for large-scale computation. Comp. Meth. App. Mech. Eng. **94**, 201–228 (1990)
68. U.F. Kocks et al Texture and Anisotropy: Preferred Orientations in Polycrystals and Their Effect on Materials Properties. Cambridge University Press, NewYork (1998)
69. M.S. Shephard et al Automatic construction of 3-D models in multiple scale analysis. Comp. Mech. **17**, 196–207 (1995)
70. S.P. Xiao, T.A. Belytschko bridging domain method for coupling continua with molecular dynamics. Comp. Meth. Appl. Mech. Eng. **193**, 1645–1669 (2004)
71. G.J. Wagner, W.K. Liu Coupling of atomistic and continuum simulations using a bridging scale decomposition. J. Comp. Phy. **190**, 249–274 (2003)
72. E.G. Karpov et al A Green's function approach to deriving non-reflecting boundary conditions in molecular dynamics simulations. Int. J. Num. Meth. Eng **62**, 1250–1262 (2005)
73. S.A. Adelman, J.D. Doll Generalized Langevin equation approach for atom/solid-surface scattering: General formulation for classical scattering off harmonic solids. J. Chem. Phys. **64**, 2375–2388 (1976)
74. W. Cai et al Minimizing boundary reflections in coupled-domain simulations. Rev. Lett. **85**, 3213–3216 (2000)
75. W.E. Huang, Z.Y. Huang A dynamic atomistic-continuum method for the simulation of crystalline materials. J. Comp. Phys. **182**, 234–261 (2002)
76. G. J. Wagner et al., Comp. Meth. in Appl. Mech. Eng. **193**, 1579-1601 (2005)
77. H.S. Park et al The bridging scale for two-dimensional atomistic/continuum coupling. Phil. Mag. **85**, 79–113 (2005)
78. M.F. Horstemeyer et al A multiscale analysis of fixed-end simple shear using molecular dynamics, crystal plasticity, and a macroscopic internal state variable theory. Modell. Sim. Mat. Sci. Eng. **11**, 265–286 (2003)
79. J. Fish, W. Chen Discrete-to-continuum bridging based on multigrid principles. Comp. Meth. App. Mech. Eng. **193**, 1693–1711 (2004)
80. J. Fish, Z. Multiscale enrichment based on partition of unity. Int. J. Num. Meth. Eng. **62**, 1341–1359 (2005)
81. P.A. Klein, J.A. Zimmerman Coupled atomistic–continuum simulations using arbitrary overlapping domains. J. Comp. Phy. **213**, 86–116 (2006)
82. C. Oskay, J. Fatigue life prediction using 2-scale temporal asymptotic homogenization. Int. J. Num. Meth. Eng. **61**, 329–359 (2004)
83. J. Fish, C. A nonlocal multiscale fatigue model. Mech. Adv. Mat. Struct. 12 **6**, 485–500 (2005)
84. J. Fish, Q. Computational mechanics of fatigue and life predictions for composite materials and structures. Comp. Meth. App. Mech. Eng. **191**, 4827–4849 (2002)
85. E. Gal et al A multiscale design system for fatigue life prediction. Int. J. Multiscale Comp. Eng. **5**, 435–446 (2007)
86. G.B. Olson Systems design of hierarchically structured materials: Advanced steels. J. Comput.-Aided Mat. Des. **4**, 143–156 (1998)
87. G.B. Olson New age of design. J. Comput.-Aided Mat. Des. **7**, 143–144 (2000)
88. E. Orowan Zur kristallplastizität. I. Z. Phys. **89**, 605–659 (1934)
89. G. I. Taylor, The Mechanism of Plastic Deformation of Crystals. Part I. Theoretical, *Proceedings of the Royal Society of London Series A145* vol. 855 (1934), pp. 362–387 .
90. M.Z. Polyani Űber eine Art Gilterstorung die einen Kristall plastisch machen konnte. Z. Phys. **89**, 660–664 (1934)
91. F. Nabarro Mathematical theory of stationary dislocations. Adv. Phy. **1**, 269 (1952)
92. J.M. Burgers Some considerations on the fields of stress connected with dislocations in a regular crystal lattice. IProc. Kon. Ned. Akad. Wetenschap. **42**, 293 (1939)
93. E. O. Hall, The Deformation and Ageing of Mild Steel: III Discussion of Results, Proceedings of the Physical Society B, vol. 64 (1951), pp. 747–753.

94. N.J. Petch The cleavage strength of polycrystals. J. Iron Steel Ins. **174**, 25 (1953)
95. M. Ashby, in *Strengthening Methods in Crystals,* ed by A. Kelly, R.B. Nicholson (Applied Science Publishers, London 1971), p. 137
96. F.C. Frank The influence of dislocations on crystal growth. Discuss. Faraday Soc. **5**, 48 (1949)
97. F.C. Frank Crystal dislocations. Elementary concepts and definitions. Phil. Mag. **42**, 809 (1951)
98. W.T. Read Dislocations in Crystals. McGraw-Hill, New York, NY (1953)
99. D.A. Hughes et al Near surface microstructures developing under large sliding loads. J. Matls. Eng. Perf. **3**, 459–475 (1994)
100. D.A. Hughes, W.D. Nix The absence of steady-state flow during large strain plastic deformation of some Fcc metals at low and intermediate temperatures. Metall Matl. Trans. A **19**, 3013–3024 (1988)
101. N.A. Fleck et al Strain gradient plasticity: Theory and experiment. Acta Mater. **42**, 475–487 (1994)
102. J.S. Stolken, A.G. Evans A microbend test method for measuring the plasticity length scale. Acta Mater. **46**, 5109 (1998)
103. W.D. Nix Mechanical properties of thin films. Metall. Trans. 20A:2217–2245 (1989)
104. M.S. De Guzman et al The role of indentation depth on the measured hardness of materials. Matls. Rsrch. Sym. Pro. **308**, 613–618 (1993)
105. N.A. Stelmashenko et al Microindentations on W and Mo oriented single crystals: an STM study. Acta. Metall. Mate. **41**, 2855–5865 (1993)
106. Q. Ma, D.R. Clarke Size dependent hardness of silver single crystals. J. Mater. Res. **10**, 853–863 (1995)
107. W.J. Poole et al Micro-Hardness of annealed and work-hardened copper polycrystals. Scripta Metall. Mater **34**, 559–564 (1996)
108. K.W. McElhaney et al Determination of indenter tip geometry and indentation contact area for depth-sensing indentation experiments. J. Mater. Res. **13**, 1300–1306 (1998)
109. D.J. Lloyd Particle reinforced aluminium and magnesium matrix composites. Int. Mater. Rev. **39**, 1–23 (1994)
110. G. Elssner et al The influence of interface impurities on fracture energy of UHV diffusion bonded metal-ceramic bicrystals. Scripta Metall. Mater. **31**, 1037–1042 (1994)
111. A. Griffith The Phenomena of Rupture and Flow in Solids. Philos. Trans. Roy. Soc. of Lond. A **221**, 163-–198 (1921)
112. W.C. Roberts-Austen On certain mechanical properties of metals considered in relation to the periodic law. Philos. Trans. Roy. Soc. Lond. A **179**, 339–349 (1888)
113. F.A. McClintock A criterion for ductile fracture by the growth of holes. J. App. Mech. **35**, 363–371 (1968)
114. A. Gangalee, J. On the fracture of silicon particles inaluminum–silicon alloys. Trans. Metall. Soc. AIME **239**, 269–272 (1967)
115. M.F. Horstemeyer, S. Ramaswamy On factors affecting localization and void growth in ductile metals: a parametric study. Int. J. Damage Mech. **9**, 6–28 (2000)
116. M.F. Horstemeyer et al Micromechanical finite element calculations of temperature and void configuration effects on void growth and coalescence. Int J. Plasticity **16**, 979–1015 (2000)
117. G.P. Potirniche et al A molecular dynamics study of void growth and coalescence in single crystal nickel. Int. J. Plasticity **22**, 257–278 (2006)
118. G.P. Potirniche et al Lattice orientation effects on void growth and coalescence in fcc single crystals. Int. J. Plasticity **22**, 921–942 (2006)
119. G.P. Potirniche, M.F. Horstemeyer Lattice orientation effects on void growth and coalescence in fcc single crystals. Phil. Mag. Lett. **86**, 185–193 (2006)
120. G.P. Potirniche et al Atomistic modelling of fatigue crack growth and dislocation structuring in FCC crystals. Proc. Roy. Soc. London **462**, 3707–3731 (2006)
121. M.K. Jones et al A multiscale analysis of void coalescence in nickel. J. Eng. Matls. Tech. **129**, 94–104 (2007)

122. H. Neuber Theory of notch stresses. Berlin, Springer (1958)
123. R.E. Peterson In: Sines G, Waisman JL (eds) Metal Fatigue. McGraw-Hill, New York, NY, pp 293–306 (1959)
124. G. Harkegard Application of the finite element method to cyclic loading of elastic-plastic structures containing effects. Int. J. Fract. **9**, 322 (1973)
125. R.A. Smith, K.J. Miller Fatigue cracks at notches. Int. J. Mech. Sci. **19**, 11–22 (1977)
126. R.A. Smith et al Experimental and theoretical fatigue-crack propagation lives of variously notched plates. J. Strain Ana. Eng. Dsgn. **9**, 61–66 (1974)
127. J. Lankford, F.N. Kusenberger Initiation of fatigue cracks in 4,340 steel. Met. Trans. **4**, 553–559 (1973)
128. J. Lankford Inclusion-matrix debonding and fatigue crack intiation in low alloy steel. Met. Trans. **4**, 155–157 (1976)
129. J. Lankford et al The influence of crack tip plasticity in the growth of small fatigue cracks. Metall. Trans. A **4**, 1459–1588 (1984)
130. M.J. Couper et al Casting defects and the fatigue behaviour of an aluminium casting alloy. Fatigue Fract. Eng. Mat. Struct. **13**, 213–227 (1990)
131. J.F. Major Porosity control and the fatigue behavior in A356–T61 aluminum alloy. AFS Trans. **102**, 901–906 (1994)
132. D.L. Davidson et al The effects on fracture toughness of ductile-phase composition and morphology in Nb-Cr-Ti and Nb-Siin situ composites. Metall. Matls. Trans. A: Physl. Metall. Matls. Sci. **27**, 2540–2556 (1996)
133. P.J. Laz, B.M. Hillberry Fatigue life prediction from inclusion initiated cracks. Int. J. Fatigue **20**, 263–270 (1998)
134. K.A. Gall et al The debonding and fracture of Si particles during the fatigue of a cast Al-Si alloy. Met. Trans A **30**, 3079–3088 (1999)
135. K.A. Gall et al High cycle fatigue mechanisms in a cast AM60B magnesium alloy. Fatigue Frac. Eng. Mat. Struct. **23**, 159–172 (2000)
136. K.A. Gall et al Finite element analysis of the stress distributions near damaged Si particle clusters in cast Al–Si alloys. Mech. Mater. **32**, 277–301 (2000)
137. X.S. Wang et al Low-cycle fatigue small crack initiation and propagation behaviour of cast magnesium alloys based on in-situ SEM observations. Phil. Mag. **86**, 1581–1596 (2006)
138. S. Kumar, W.A. Curtin Crack interaction with microstructure. Mater. Today **10**, 34 (2007)
139. M.M. Shenoy et al Modeling effects of nonmetallic inclusions on LCF in DS nickel-base superalloys. Int. J. Fatigue **27**, 113–127 (2005)
140. M.M. Shenoy et al Estimating fatigue sensitivity to polycrystalline Ni-base superalloy microstructures using a computational approach. Fatigue Fract. Eng. Mat. Struct **30**, 889–904 (2007)
141. D.L. McDowell Simulation-assisted materials design for the concurrent design of materials and products. J. Mins. Metls. Matls. Soc. **59**, 21–25 (2007)
142. J. Fan et al Cyclic plasticity across micro/meso/macroscopic scales. Proc. R. Soc. London A **460**, 1477–1503 (2004)
143. M.F. Horstemeyer Damage influence on Bauschinger effect of a cast A 356 aluminum alloy. Scripta Mater. **39**, 1491–1495 (1998)
144. M.F. Horstemeyer, M.I. Baskes Atomistic finite deformation simulations: a discussion on length scale effects in relation to mechanical stresses. J. Eng. Matls. Techn. Trans. ASME **121**, 114–119 (1999)
145. M.F. Horstemeyer et al Length scale and time scale effects on the plastic flow of fcc metals. Acta Mateialia **49**, 4363–4374 (2001)
146. M. F. Horstemeyer, Mapping failure by microstructure-property modeling, in *Journal of Minerals, Metals and Materials Society*, ed. by J.J. Hoyt **53**, 9, 24–27 (2001b).
147. M. F. Horstemeyer et al., *From Atoms to Autos: Part 2 Fatigue Modeling*, Sandia National Laboratories Report, SAND2001-8,661 (2001).

148. M. F. Horstemeyer et al., J *Prospects in Mesomechanics*, edited by G. Sih, Theor. Appl. Fract. Mech. **37**, 49–98 (2001).
149. M.F. Horstemeyer et al A large deformation atomistic study examining crystal orientation effects on the stress–strain relationship. Int. J. Plasticity **18**, 203–209 (2002)
150. M.F. Horstemeyer et al Torsion/simple shear of single crystal copper. J. Eng. Matls. Tech. **124**, 322–328 (2002)
151. M. F. Horstemeyer, *Physically Motivated Modeling of Deformation-Induced Anisotropy*, PhD thesis, Georgia Institute of Technology (1995)
152. W.W. Gerberich et al Interpretations of indentation size effects. J. Appl. Mech. **69**, 443–452 (2002)
153. J. Fan et al Cyclic plasticity at pores and inclusions in cast Al–Si alloys. Eng. Fract. Mech. **68**, 1687–1706 (2001)
154. J. Fan et al Cyclic plasticity at pores and inclusions in cast Al–Si alloys. Eng. Fract. Mech. **70**, 1281–1302 (2003)
155. S. Johnston et al Three-dimensional finite element simulations of microstructurally small fatigue crack growth in 7,075 aluminium alloy. Fatigue Fract. Eng. Matl. Struct. **29**, 597–605 (2006)
156. K.A. Gall et al On the driving force for fatigue crack formation from inclusions and voids in a cast A356 aluminum alloy. Int.J. Fracture **198**, 207–233 (2001)
157. V.S. Deshpande et al Discrete dislocation plasticity modeling of short cracks in single crystals. Acta Mater. **51**, 1–15 (2003)
158. V.S. Deshpande et al Scaling of discrete dislocation predictions for near-threshold fatigue crack growth. Acta Mater. **51**, 4637–4651 (2003)
159. T. Morita and H. Tsuji, Zairyo*, J. of the Soc. of Matls. Sci*., *Japan,* **53** 647-653 (2004).
160. I.N. Mastorakos, H.M. Zbib DD simulations of dislocation-crack interaction during fatigue. J. ASTM Int. **4**, 1–9 (2007)
161. S. Groh et al Fatigue crack growth from a cracked elastic particle into a ductile matrix. Phil. Mag. **88**, 3565–3583 (2008)
162. D.L. McDowell, G.B. Olson Concurrent design of hierarchical materials and structures. Sci. Model. Sim. **15**, 207–240 (2008)
163. A. Ramasubramaniam, E.A. Carter Coupled quantum–atomistic and quantum–continuum mechanics methods in materials research. MRS Bulletin **32**, 913–918 (2007)
164. G. Lu, E. In: Rieth M et al (eds) Handbook of Theoretical and Computational Nanotechnology. Am. Sci. Publ, California (2004)
165. N. Choly et al Multiscale simulations in simple metals: A density-functional-based methodology. Phys. Rev. B **71**, 094101 (2005)
166. G. Lu et al From electrons to finite elements: a concurrent multiscale approach for metals. Physl. Rev. B Cond. Matt. Matls. Phys. **73**, 024108 (2006)
167. F. Ercolessi, J. Interatomic potentials from first-principles calculations: the force-matching method. Europhys. Lett. **26**, 583–588 (1994)
168. Y. Li et al Embedded-atom-method tantalum potential developed by the force-matching method. Phyl. Rev. B Cond. Mattr Matls. Phys **67**, 125101 (2003)
169. N. Govind et al Accurate ab initio energetics of extended systems via explicit correlation embedded in a density functional environment. Chem. Phys. Lett. **295**, 129 (1998)
170. Y.A. Wang et al Orbital-free kinetic-energy functionals for the nearly free electron gas. Phys. Rev. B **58**, 13465–13471 (1998)
171. Y.A. Wang et al Orbital-free kinetic-energy density functionals with a density-dependent kernel. Phys. Rev. B **60**, 16350–16358 (1999)
172. T. Kluner et al Prediction of electronic excited states of adsorbates on metal surfaces from first principles. Phys. Rev. Lett. **86**, 5954 (2001)
173. G. Csányi et al "Learn on the Fly": A hybrid classical and quantum-mechanical molecular dynamics simulation. Phys. Rev. Lett. **93**, 175503 (2004)

174. M.I. Baskes Application of the embedded-atom method to covalent materials: a semiempirical potential for silicon. Physl. Rev. Lett. **59**, 2666–2669 (1987)
175. M.I. Baskes et al Semiempirical modified embedded-atom potentials for silicon and germanium. Physl. Rev. B **40**, 6085–6100 (1989)
176. M.I. Baskes et al Atomistic calculations of composite interfaces. Modell. Simul. Mater. Sci. Eng. **2**, 505–518 (1994)
177. M.I. Baskes, R.A. Johnson Modified embedded atom potentials for HCP metals. Modell. Simul. Mater. Sci. Eng. **2**, 147–163 (1994)
178. B. Jelinek et al Modified embedded-atom method interatomic potentials for the Mg-Al alloy system. Physl. Rev. B **75**, 054106 (2007)
179. M.S. Daw, M.I. Baskes Semiempirical, quantum mechanical calculation of hydrogen embrittlement in metals. Physl. Rev. Lett. **50**, 1285–1288 (1983)
180. M.Q. Chandler Horstemeyer, MF, Baskes, MI, Gullett, PM, Wagner, GJ, Jelinek, B, Hydrogen effects on nanovoid nucleation in face-centered cubic single -crystals. Acta Mater. **56**, 95–104 (2008)
181. M.Q. Chandler et al Hydrogen effects on nanovoid nucleation at nickel grain boundaries. Acta Mater. **56**, 619–631 (2008)
182. H. Fang et al Atomistic simulations of Bauschinger effects of metals with high angle and low angle grain boundaries. Comp. Meth. App. Mech. Eng. **193**, 1789–1802 (2004)
183. K. Solanki et al Multiscale study of dynamic void collapse in single crystals. Mech. Matls. **37**, 317–330 (2005)
184. D. Farkas Atomistic studies of intrinsic crack-tip plasticity. MRS Bulletin **25**, 35–38 (2000)
185. D. Farkas Atomistic mechanisms of fatigue in nanocrystalline metals. Phys. Rev. Lett. **94**, 165502 (2005)
186. A. Luque et al Molecular dynamics simulation of crack tip blunting in opposing directions along a symmetrical tilt grain boundary of copper bicrystal. Fatigue Fract. Eng. Matls. Struct. **30**, 1008–1015 (2007)
187. A. Brandt Multiscale and Multiresolution Methods: Theory and Applications. Springer-Verlag, Heidelberg (2001)
188. E. Weinan, B. Heterogeneous multiscale methods. Comm. Math. Sci. **1**, 87–132 (2003)
189. G.I. Barenblatt *Scaling*, Cambridge Texts in Applied Mathematics. Cambridge University press, Cambridge (2003)
190. A. Carpinteri et al Cohesive crack model description of ductile to brittle size-scale transition: dimensional analysis vs. renormalization group theory. Eng. Fract. Mech. 70(14):1809–1839 (2003)
191. Y.T. Cheng, C.M. Cheng Fundamentals of nanoindentation and nanotribology. Matls. Rsrch. Soc. Sym. Proc. **522**, 139–144 (1998)
192. N. Ansini et al Multi-scale analysis by Gamma-convergence of a one-dimensional non-local functional related to a shell-membrane transition. SIAM J. Math. Ana. **38**, 944–976 (2006)
193. B.B. Mandelbrot et al Fractal character of fracture surfaces of metals. Nature **308**, 721–722 (1984)
194. B.B. Mandelbrot The Fractal Geometry of Nature. W. H. Freeman and Company, NewYork (1982)
195. D. M. Mark and P. B. Aronson, Scale-dependent fractal dimensions of topographic surfaces: An empirical investigation, with applications in geomorphology and computer mapping *Mathematical Geology* **16**, 7, 671–683 (Springer, 1984).
196. T. Chelidze, Y. Evidence of fractal fracture. Int. J. Rock Mech. Mining Sci. **27**, 223–225 (1990)
197. A.B. Mosolov et al Fractal Fracture of Brittle Bodies during Compression. Soviet Phys. **37**, 263–265 (1992)
198. A.V. Dyskin Micromechanics of materials. Int. J. Solids Struct. **42**, 477–502 (2005)
199. S. Graham, N. Representative volumes of materials based on microstructural statistics. Scripta Mater. **48**, 269–274 (2003)

200. S. Lee, R. Rao, Scale-based formulations of statistical self-similarity in images, *Proceedings of the International Conference on Image Processing*, ICIP, vol. 4 (2004), pp. 2323–2326
201. J. Fish, A. Wagiman, Adaptive, multilevel, and hierarchical computational strategies, *Winter Annual Meeting of the American Society of Mechanical Engineers*, vol. 157 (1992), pp. 95–117
202. J. Fish, Z. Multiscale enrichment based on partition of unity for nonperiodic fields and nonlinear problem. Comp. Mech. **40**, 249–259 (2007)
203. M.A. Nuggehally et al Adaptive model selection procedure for concurrent multiscale problems. Int. J. Multiscale Comp. Eng. **5**, 369–386 (2007)
204. G.W. He et al Multiscale coupling: Challenges and opportunities. Prog. Nat. Sci. **14**, 463–466 (2004)
205. H.Y. Wang et al Multiscale coupling in complex mechanical systems. Chem. Eng. Sci. **59**, 1677–1686 (2004)
206. J. W. Essam, Phase transitions and critical phenomena, *Conf. Proc. Cambridge Phil Soc.* 523–533 (1970)
207. S. Greenspoon Finite-size effects in one-dimensional percolation: a verification of scaling theory. Canadian J. Phys. **57**, 550–552 (1979)
208. H. Kestin Percolation theory for mathematicians. Bull. Amer. Math. Soc. **11**, 404–409 (1984)
209. Y. Otsubo Elastic percolation in suspensions flocculated by polymer bridging. Langmuir **6**, 114–118 (1992)
210. D.F. Leclerc, J.A. Olson A percolation-theory model of lignin degradation. Macromolecules **25**, 1667–1675 (1992)
211. R. Fu et al Interpretation of porosity effect on strength of highly porous ceramics. Scripta Metall. et Matl. **25**, 1583–1585 (1991)
212. M. Ostoja-Starzewski Mechanics of damage in a random granular microstructure: Percolation of inelastic phases. Int. J. Eng. Sci. **27**, 315–326 (1989)
213. Y.L. Bai et al Statistical mesomechanics of solid, linking coupled multiple space and time scales. App. Mech. Rev. **58**, 372–388 (2005)
214. L.E. Reichl A Modern Course in Statistical Physics. University of Texas Press, Austin (1980)
215. B. Zhang et al Microstructural effects on high-cycle fatigue-crack initiation in A356.2 casting alloy. Metall. Matls. Trans. A **30**, 2659—2666 (1999)
216. M.F. Horstemeyer, P. Wang Cradle-to-grave simulation-based design incorporating multiscale microstructure-property modeling: Reinvigorating design with science. J. Comput.-Aided Matls. Dsgn. **10**, 13–34 (2003)
217. R.A. Fisher Statistical Methods for Research Workers. Oliver and Boyd, Edinburg (1935)
218. R.A. Fisher The Design of Experiments. Oliver and Boyd, Edinburg (1935)
219. G. Taguchi System of Experimental Design: I and II. UNIPUB, New York (1987)
220. G. Taguchi Reports of statistical application research. JUSE **6**, 1–52 (1960)
221. M.F. Horstemeyer, A.M. Gokhale A void-crack nucleation model for ductile metals. Int. J. Solids Struct. **36**, 5029–5055 (1999)
222. M.F. Horstemeyer et al Using a micromechanical finite element parametric study to motivate a phenomenological macroscale model for void/crack nucleation in aluminum with a hard second phase. Mech. Matls. **35**, 675–687 (2003)
223. J.C. Mauro, A.K. Varshneya Multiscale modeling of $GeSe_2$ glass structure. J. Amer. Ceramic Soc. **89**, 2323–2326 (2006)
224. J.C. Mauro, A.K. Varshneya Ab initio modeling of volume–temperature curves for glass-forming systems. J. Non-Crystalline Solids **353**, 1226–1231 (2007)
225. R. Krishnamurthy et al Oxygen diffusion in yttria-stabilized zirconia: A new simulation model. J. Amer. Ceramic Soc. **87**, 1821–1830 (2004)
226. A. Hansen et al Roughness of crack interfaces. Phys. Rev. Lett. **66**, 2476–2479 (1991)
227. J. Schmittbuhl et al Roughness of interfacial crack fronts: Stress-weighted percolation in the damage zone. Phys. Rev. Lett. **90**, 045505 (2003)

228. A. Hansen, J. Origin of the universal roughness exponent of brittle fracture surfaces: stress-weighted percolation in the damage zone. Phys. Rev. Lett. **90**, 045504 (2003)
229. L. Chong, L.B. Ray Whole-istic biology. Science **295**, 1661 (2002)
230. D.N. Theodorou Hierarchical modeling of amorphous polymers. Comp. Phys. Comm. **169**, 82–88 (2005)
231. A.E. Ismail et al Using wavelet transforms for multiresolution materials modeling. Comp. Chem. Eng., Cont. Multiscale Distrib. Proc. Sys. **29**, 689–700 (2005)
232. J. Bicerano et al Polymer modeling at the dow chemical company. J. Macromolecular Sci. Poly. Rev. **44**, 53–85 (2004)
233. Q. Yu, J. Multiscale asymptotic homogenization for multiphysics problems with multiple spatial and temporal scales: a coupled thermo-viscoelastic example problem. Int. J. Solids Struct. **39**, 6429–6452 (2002)
234. S. Curgul et al Molecular dynamics simulation of size-dependent structural and thermal properties of polymer nanofiber. Macromolecules **40**, 8483–8489 (2007)
235. J.C. Halpin et al Time dependent static strength and reliability for composites. Compo. Mater. **4**, 462–474 (1970)
236. J.C. Halpin Structure-property relations and reliability concepts. J. Compo. Matls. **6**, 208–231 (1972)
237. H.T. Hahn, S.W. Tsai On the behavior of composite laminates after initial failures. J. Comp. Matls. **8**, 288–305 (1974)
238. J.C. Halpin, J.L. Kardos The halpin-tsai equations: A review. Poly. Eng. Sci. **16**, 344–352 (1976)
239. H.T. Chang, D.H. Allen Predicted dynamic response of a composite beam with history-dependent damage. Comp. Struct. **26**, 575–580 (1987)
240. D.H. Allen et al A cumulative damage model for continuous fiber composite laminates with matrix cracking and interply delaminations. ASTM Sp. Tech. Pub. **972**, 57–80 (1988)
241. F. Costanzo, D.H. Allen Micromechanics and homogenization of inelastic composite materials with growing cracks. J. Mech. Phys. Solids **44**, 333–370 (1996)
242. D. Krajcinovic Constitutive equations for damaging materials. J. App. Mech. **50**, 355–360 (1983)
243. D. Krajcinovic Continuum damage mechanics: When and how? Int. J. Damage Mech. **4**, 217 (1995)
244. D. Krajcinovic Damage Mechanics. Noth-Holland, New York, NY (1996)
245. J. Fish, K. Multiscale analysis of composite materials and structures. Comp. Sci. Tech. **60**, 2547–2556 (2000)
246. J. Fish, Q. Yu, Multiscale damage modeling for composite materials: Theory and computational framework, *Int. J. Num. Meth. Eng.*, **52**, 161–191 (2001), *5th US Nat. Cong. on Comp. Mech.*
247. V. Belsky et al Computer-aided multiscale modeling tools for composite materials and structures. Comp. Syst. Eng.: Int. J. **6**, 213–223 (1995)
248. B. Hassani, E. Hinton A review of homogenization and topology opimization II–analytical and numerical solution of homogenization equations. Comp. Struct **69**, 719–738 (1998)
249. B. Hassani, E. Hinton Comp. Struct. **69**, 707–717 (1998)
250. B. Hassani, E. Hinton A review of homogenization and topology optimization III–topology optimization using optimality criteria. Comp. Struct. **69**, 739–756 (1998)
251. P.B. Lourenco et al Analysis of masonry structures: review of and recent trends in homogenization techniques. Canadian J. Civil Eng. Special Issue on Masonry **34**, 1443–1457 (2007)
252. K. Matous et al Multiscale cohesive failure modeling of heterogeneous adhesives. J. Mech. Phys. Solids **56**, 1511 (2008)
253. J. Aboudi Micromechanical analysis of composites by the method of cells. App. Mech. Rev. **47**, 193–221 (1989)
254. J. Aboudi The generalized method of cells and high-fidelity generalized method of cells micromechanical models: A review. J Mech. Adv. Matls. Struct. **11**, 329–366 (2004)

255. M. Paley, J. Aboudi Micromechanical analysis of composites by the generalized cells model. Mech. Matls. **14**, 127–139 (1992)
256. T. O. Williams and T. B. Tippetts, Materials Damage Prognosis, *Proceedings of a Sym. of the Matls. Sci. and Tech. Conf.* 95–101 (2004)
257. D. Qian et al Mechanics of carbon nanotubes. App. Mech. Rev. **55**, 495–532 (2002)
258. A. Maiti Multiscale modeling with carbon nanotubes. Microelectron. J. **39**, 208–221 (2008)
259. G. Friesecke, R.D. James A scheme for the passage from atomic to continuum theory for thin films, nanotubes and nanorods. J. Mech. Phys. Solids **48**, 1519–1540 (2000)
260. J. Wescott et al Atomistic, mesoscale and finite element simulation of nanofube dispersion in polymers. VDI Berichte **1940**, 23–24 (2006)
261. K. Laganà et al Multiscale modeling of the cardiovascular system: application to the study of pulmonary and coronary perfusions in the univentricular circulation. J. Biomech. **38**, 1129–141 (2004)
262. H. B. Tho et al., Multi-scale characterization and modeling of human cortical bone, *Mat. Res. Soc. Symp. Proc.* p. 898 (2006).
263. E. Budyn, T. Multi-scale modeling of human cortical bone: Aging and failure studies. Mat. Rsrch. Soc. Sym. Pro.- Mech. of Bio. Bio-Inspired Matls **975**, 27–32 (2006)
264. A. Fritsch, C. Universal microstructural patterns in bone: Micromechanics-based prediction of anisotropic material behavior. Matls. Rsrch. Soc. Sym. Pro.-Mech. of Bio. Bio-Inspired Matls. **975**, 128–134 (2006)
265. D. Porter Pragmatic multiscale modeling of bone as a natural hybrid nanocomposite. Matls. Sci. Eng. A **365**, 38–45 (2004)
266. J.L. Katz et al Multiscale mechanics of hierarchical structure/property relationships in calcified tissues and tissue/material interfaces. Matls. Sci. Eng. C-Next Gen. Biomatls **27**, 450–468 (2007)
267. Z.A. Taylor, K. Miller Constitutive modeling of cartilaginous tissues: A review. J. App. Biomech. **22**, 212–229 (2006)
268. C. Hellmich et al Can the diverse elastic properties of trabecular and cortical bone be attributed to only a few tissue-independent phase properties and their interactions? Biomech. Model. Mechanobio. **2**, 219–238 (2004)
269. D. Taylor Fracture and repair of bone: a multiscale problem. J. Matls. Sci. **42**, 8911–8918 (2007)
270. M. Kawagai et al Multi-scale stress analysis of trabecular bone considering trabeculae morphology and biological apatite crystallite orientation. J. Soc. Matls. Sci. Japan **55**, 874–880 (2006)
271. C. Imielinska et al., *Multi-scale modeling of trauma injury*, Lecture Notes in Computer Science, LNCS - IV, Computational Science – ICCS, vol. 3(2006), p. 994 (2006), 822–830.
272. J.B. Bassingthwaighte et al., Strategies and tactics in multiscale modeling of cell-to-organ systems, Proceedings of the IEEE, vol. **94** pp. 819–830 (2006)
273. E.C.N. Silva et al Modeling bamboo as a functionally graded material: Lessons for the analysis of affordable materials. J. Matls. Sci. **41**, 6991–7004 (2006)
274. A. Makela Process-based modeling of tree and stand growth: Towards a hierarchical treatment of multiscale processes. Canadian J. Forest Res. **33**, 398–409 (2003)
275. J. H. Panchal et al., A strategy for simulation-based design of multiscale, multi-functional products and associated design processes, in *Proceedings of the ASME Int. Design Eng. Tech. Con. and Comp. and Info. in Eng. Con. - DETC2005*, **2B** pp. 845–857 (2005)
276. G.B. Olson Computational design of hierarchically structured materials. Science **277**, 1237–1242 (1997)
277. H. J. Jou et al., Computer simulations for the prediction of microstructure/property variation in aeroturbine disks, *Superalloys,* Warrendale, PA pp. 877–886 (2004)
278. G.B. Olson Advances in theory: Martensite by design. Matls. Sci. Eng. A **25**, 48–54 (2006)
279. F. Mistree et al., Robust concept exploration methods in materials design, *9th AIAA/ISSMO Sym. on Multidisci. Ana. and Opt.*, AIAA, 5,568 (2002)

280. C. C. Seepersad et al., Design of Multifunctional Honeycomb Materials, *9th AIAA/ISSMO Sym. on Multidisci. Ana. and Opt*., AAIA, 5,626 (2002)
281. C.C. Seepersad et al Robust design of cellular materials with topological and dimensional imperfections. J. Mech. Design **128**, 1285–1297 (2006)
282. R. Von Mises Mechanik der festen korper im plastisch deformablen zustand. Göttin. Nachr. Math. Phys. **1**, 582–592 (1913)
283. D.J. Bammann, E.C. Aifantis A model for finite-deformation plasticity. Acta Mech. **69**, 97–117 (1987)
284. D.J. Bammann, E.C. Aifantis A damage model for ductile metals. Nuc. Eng. Design **116**, 355–362 (1989)
285. D.J. Bammann et al Failure in ductile materialsusing finite element methods. In: Wierzbicki T et al (eds) Structure Crashworthiness and Failure. Elsevier Applied Science, The Universities Press (Belfast) Ltd, Belfast (1993)
286. M.F. Horstemeyer et al Numerical, experimental, nondestructive, and image analyses of damage progression in cast A356 aluminum notch tensile bars. Theor. App. Fracture Mech. **39**, 23–45 (2003)
287. K. Solanki et al., Integration of microstructure-property relationships in an internal state variable plasticity and damage constitutive model for reliability-based optimization in engineering design. (*submitted to Journal of Design Engineering*). (2008)
288. E. Acar et al Uncertainty Analysis of Damage Evolution Computed through Microstructure-Property Relations, *ASME 34th Design Automation Conference (DAC)*. NY, New York (2008)
289. X. Yin, S. Lee, W. Chen, W.K. Liu, M.F. Horstemeyer *A Multiscale Design Approach with Random Field Representation of Material Uncertainty*, ASME DETC08. NY, New York (2008)
290. M.D. Dighe et al Effect of loading condition and stress state on damage evolution of silicon particles in an Al-Si-Mg-Base cast alloy. Metall. Matls. Trans. A **33**, 555–565 (2002)
291. M.D. Dighe et al Effect of temperature on silicon particle damage in A356 alloy. Metall. Matls. Trans. A **29**, 905–908 (1997)
292. M.D. Dighe et al Effect of strain rate on damage evolution in a cast Al-Si-Mg base alloy. Metall. Matls. Trans. A **31**, 1725–1731 (2000)
293. M.F. Horstemeyer et al Modeling stress state dependent damage evolution in a cast Al-Si-Mg aluminum alloy. Theor. App. Fracture Mech. **33**, 31–47 (2000)
294. J.B. Jordon et al Damage and stress state influence on the Bauschinger effect in aluminum alloys. Mech. Matls **39**, 920–931 (2007)
295. H.E. Kadir et al Fatigue crack growth mechanisms in high-pressure die-cast magnesium alloy. Metall. Mat. Trans. A **39**, 190–205 (2008)
296. H.E. Kadiri et al Identification and modeling of fatigue crack growth mechanisms in a die-cast AM50 magnesium alloy. Acta Mater. **54**, 5061–5076 (2006)
297. M.F. Horstemeyer et al High cycle fatigue of a die cast AZ91E-T4 magnesium alloy. Acta Mater. **52**, 1327–1336 (2004)
298. D.L. McDowell et al Microstructure-based fatigue modeling of cast A356-T6 alloy. Eng. Fracture Mech. **70**, 49–80 (2003)
299. Y. Xue et al Micromechanisms of multistage fatigue crack growth in a high-strength aluminum alloy. Acta Mater. **55**, 1975–1984 (2007)
300. Y. Xue et al Multistage fatigue modeling of cast A356–T6 and A380-F aluminum alloys. Metall. Matls. Trans. **38**B:601–606 (2007)
301. Y. Xue et al Microstructure-based multistage fatigue modeling of aluminum alloy 7,075–T651. Eng. Fract. Mech. **74**, 2810–2823 (2007)
302. Y. Xue et al Microstructure-based multistage fatigue modeling of a cast AE44 magnesium alloy. Int. J. Fatigue **29**, 666–676 (2007)
303. P.C. Paris, F. Erdogan A critical analysis of crack propagation laws. Trans. ASME J. Basic Eng. D**85**, 528–534 (1963)

304. J. C. Newman, FASTRAN-2: A fatigue crack growth structural analysis program, *NASA-TM-104,159*, (NASA Langley Research Center, 1992)
305. J.C. Newman A review of modeling small-crack behavior and fatigue-life predictions for aluminum alloys. J. Fatigue Fract. Eng. Mat. Struct. **17**, 429–439 (1994)
306. K.A. Gall et al Atomistic simulations on the tensile debonding of an Aluminum–Silicon interface. J. Mech. Phys. Solids **48**, 2183–2212 (2000)
307. Glimm J, Sharp DH Multiscale science: A challenge for the twenty-first century. Siam News **30**, 1–7 (1997)
308. M.E. Kassner et al New directions in mechanics. Mech. Mater. **37**, 231–259 (2005)

Chapter 5
Challenging the Multiple Minima Problem: Example of Protein Folding

Lucjan Piela

Abstract There are plenty of possible structures (isomers) for a given number of atoms; their number quickly becoming astronomical for larger molecules. Usually only some of these structures (low-energy ones) play a role in experiments. However, in the theoretical description of the system in principle, all these structures have to be taken into account, a very costly adventure. Therefore, one of the challenges of chemistry (as well as of physics, biology, etc.) is the multiple minima problem, that is, how to identify the low-energy structures without calculating all possible configurations of atoms. The protein folding is given as an example of overcoming the multiple minima problem.

5.1 Introduction

If a sample of matter consisted of a few atoms, we in general, would have to do with only one or several possible stable configurations of them. In physical or chemical experiment, the sample consists usually of a huge number of atoms. This results in an astronomical number of potentially stable structures, and the only way to judge whether a particular structure has a chance to be observed is to compute the energies of all of them. After such a computing, the Boltzmann law says that (in the thermodynamic equilibrium) the lower the energy of a structure, the more probable the structure is. Usually there is no specific way to tell before calculation-whether the energy will be low or not. This confronts a theoretician with astronomical number of configurations to be checked.

Because of the fact that the electrons are light (and fast), while the nuclei are many thousands of times heavier (and slower), one may introduce averaging the

L. Piela (✉)
Department of Chemistry, University of Warsaw, Pasteura 1 02-093, Warsaw, Poland
e-mail: piela@tiger.chem.uw.edu.pl

J. Leszczynski and M.K. Shukla (eds.), *Practical Aspects of Computational Chemistry*, 137
DOI: 10.1007/978-90-481-2687-3_5,

positions of electrons at every fixed configuration of the immobile nuclei as if the nuclei had the infinite mass. This Born-Oppenheimer approximation makes the total (electronic) energy, E, a function of the configuration ($\mathbf{R}$) of the nuclei only, and $E(\mathbf{R})$ plays the role of the potential energy for the motion of the nuclei. The above mentioned stable configurations of atoms are associated with the minima of $E(\mathbf{R})$, each minimum giving rise to possible molecular vibrations around it (which prove the stability). It turns out that $E(\mathbf{R})$ is a complicated though smooth function of nuclear configurations $\mathbf{R}$. For rigid molecules, the values of some nuclear variables can be fixed, which greatly simplifies $E(\mathbf{R})$. Usually, even for nonrigid (flexible) molecules, a part of variables $\mathbf{R}$ is confined to a narrow range as to keep the assumed bond lengths in proper boundaries (virtually all calculations reported in the chemical literature use implicitly this arbitrary assumption, otherwise they would not be feasible). However, in polyatomic molecules, even as small as a dozen of atoms, $E(\mathbf{R})$ may still have a prohibitive number of minima, and for larger molecules, easily reach astronomical scale. It is understandable that such problems, which are practically unsolvable, are rarely considered in computational chemistry. The task of finding the global minimum among the multitude of other minima, whose complete exploration is not possible, is known as the multiple minima problem.

The multiple minima problem is ubiquitous in mathematical description of reality (physics, chemistry, biology, economy, etc.), and $E(\mathbf{R})$ is only an example of it. It is very unlikely that such kind of problems will find analytical solution, and thus, one has to rely on computers. The hope is that for certain class of approximations one can simplify $E(\mathbf{R})$ enough to overcome the multiple minima problem by extensive calculations.

An important part of proteins used by nature has a definite 3D shape (native state) attained at the end of a rather long process of folding after the protein is synthesized. The folding time sometimes reaches seconds, which is a very long time in the molecular time scale, and witnesses a complex kinetics of the folding. It is believed that the native state corresponds to the lowest-free energy conformation of the protein molecule, a property determined by the amino acid sequence of the protein ("thermodynamic hypothesis" [1]). In this article, we will concentrate on recent achievements in predicting a 3D structure of a protein from the known sequence of amino acids of which the protein molecule is composed. This particular multiple minima problem (called the protein folding) is notorious for an astronomical number of possible conformations. The 3D structure of the protein molecule in atomic resolution is necessary to determine its all important functions in biological systems. There are two experimental methods which in principle, can provide such information: the X-ray diffraction and the NMR measurements. The first method requires a good, quality crystal of the protein, and the second method is able to give some limits to a part of interatomic distances, which then may help guess the 3D structure. Both procedures require a large amount of high quality investigations. The problem is that only a tiny fraction of known proteins are expected to be crystallized. The fraction keeps decreasing despite the progress in crystallization as well as in X-ray and NMR techniques. This is because of spectacular progress in automatic sequencing of

DNA (like in the human genome project), which codes all the proteins of the species, each protein given as a sequence of amino acids. The estimated number of proteins in the terrestrial biological organisms is of the order of 10^7, while the number of the 3D structures (in the atomic resolution) deposited in the Protein Data Bank (as of 24 June 2008) is 47,526. Thus, theoretical prediction of the 3D shape of proteins, being potentially much faster than the X-ray and NMR techniques, seems to be a must for contemporary biology.

There are many numerical techniques to predict theoretically the 3D structure of a protein. Among most successful (although beyond the scope of the present paper) are those which compare the amino acid sequence of the protein under study with the sequences of the proteins for which the 3D structure is already known (alignment methods), and create an educated guess of the structure. In the present paper, we focus on the *ab novo* methods, which rely on considering physical interactions as the main factors determining the 3D structure.

5.2 Energy Landscape of Protein Molecule

Most important protein molecules found in nature have a very definite 3D form because this correct shape is a prerequisite for the biological functioning of the molecule. The shape has to be robust enough in order to preserve the biological function in various environments. Such robustness is assured by an ability of the protein molecule to fold to a unique (native) structure from many different starting geometries. This is possible because the conformational energy landscape for the protein exhibits usually a hierarchy of valleys, that is, there are supervalleys ("superbasins"), which contain smaller valleys, etc. It is assumed that the native 3D shape corresponds to the lowest-energy conformation. It turned out that, in addition, this lowest energy conformation (or a family of the native conformations) is separated from other ones by a considerable energy gap [2]. Thus, the energy landscape for natural proteins represents a kind of "funnel," a shape which greatly facilitates folding from many possible starting points (even through many folding paths) toward the unique native 3D conformation.

Contrary to the proteins found in nature, a synthetic protein with randomly generated amino acid sequence most likely would not fold to a unique native 3D shape, but many possible shapes of similar energy. To have a unique fold for a synthetic protein, one has to design its amino acid sequence in a special knowledge-based way, which will assure the funnel-like conformational energy landscape.

5.3 Coarse-Graining of the Landscape

A protein chain consists of quasi-rigid units, each unit being a peptide bond, –NH–CO–, in the form of nearly planar quadrangle (Fig. 5.1).

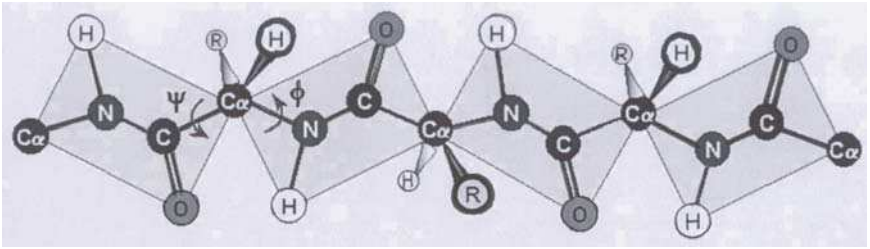

Fig. 5.1 The protein chain in atomic resolution. The chain consists of quasi-planar (nearly rigid) peptide bonds –NH–CO– connected by the C_α atoms. Each C_α atom has additionally the CH and CR bond, where R is the aminoacid side chain (one of the twenty used by nature). The figure shows also the ϕ, ψ angles (corresponding to a single amino acid). The conformation of the whole chain is determined by a set of ϕ_i, ψ_i angles, where i means the *i*th amino acid

A junction between the adjacent peptide bonds is formed by the carbon atoms C_α, each connecting a side chain R (there are twenty types of R corresponding to twenty amino acids used by nature). Figure 5.1 shows the two angles, ϕ and ψ, which determine the relative positions of the adjacent peptide bonds (assuming they are planar). In a protein composed of N peptide bonds, there are $N-1$ pairs of ϕ_i and ψ_i, one ϕ, ψ pair per one C_α atom. Their values determine the conformation of the protein backbone. Figure 5.2 shows the ϕ, ψ pairs found in the Protein Data Bank. As one can see, the observed ϕ, ψ pairs form clusters. The clusters are related to the minima in the conformational energy map (known as Ramachandran map [3]) of two adjacent peptide bonds connected by the $-C_\alpha HR-$ group as a function of ϕ and ψ (the map looks similar for all side chains R except glycine, for which R means tiny hydrogen atom, and proline, where R is not a side chain, but rather a ring involving the backbone). The Ramachandran map reveals the energy minima (about ten of them), having one to one correspondence with the clusters in Fig. 5.2. The main two minima, related to two largest clusters in Fig. 5.2, correspond to the α type structure (all $\phi \approx -80°$, all $\psi \approx -40°$, an α-helix) and the β type structure (all $\phi \approx -140°$, all $\psi \approx +140°$, close to an extended chain, like in Fig. 5.1). The α and β structures, the most important ones in proteins, form impressive patterns of the hydrogen bonds –N–H...O=C–: in the α-helix, the proton donor and proton acceptor come, respectively, from every *i*th and $(i-4)$-th amino acid, while in the β structures, the hydrogen bonds are formed by the lateral interaction between the extended chains (parallel or antiparallel). Since each peptide bond represents a large dipole moment, a low-energy conformation, such as an α-helix, usually corresponds to the alignment of these dipole moments along the intramolecular electric field [4].

Since the Ramachandran map contains about ten energy minima (i.e., stable conformations of two peptide bonds), a hundred amino acid protein (proteins may have several hundreds of amino acids) corresponds to an astronomic number of possible backbone conformations (of about 10^{100}). This number has to be additionally multiplied by a number of possible conformations of side chains (some of

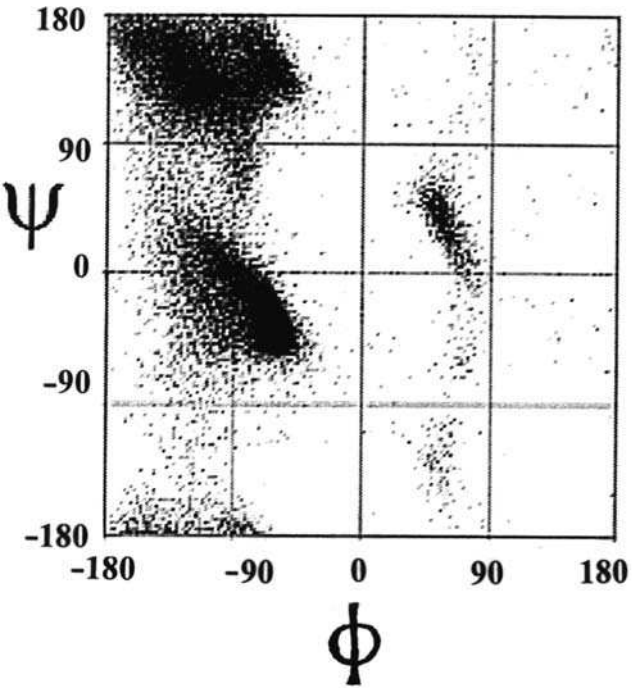

Fig. 5.2 The distribution of the experimentally observed ϕ, ψ angles (angles in degrees)

them may have several hundreds of conformations). This type of problems (with difficulties increasing exponentially) is notorious in mathematics as NP (non-polynomial) hard, and is currently considered as unsolvable.

Contemporary computers are not powerful enough to tackle such problems. One has to reduce radically the task of finding the global minimum of $E(\mathbf{R})$ by simplifying the representation of the protein molecule. A possible reduction could be achieved either by averaging the interatomic interactions [5] or (what is similar) the atoms themselves making them pseudoatoms, that is, fewer in number. The multiple minima problem can be overcome easily after the last averaging is made in a quite radical way (referred further as the REFINER model [6, 7]), by representing each amino acid (a dozen of atoms) by a single pseudoatom (a sphere of a certain radius) occupying the position of C_α, which is connected to a laterally protruding simplified side chain. The side chain is composed of 0, 1, 2 interconnected pseudoatoms ("united atoms") for short (only glycine), medium and long side chains, respectively. As a result, the whole protein molecule represents a chain of C_α pseudoatoms (each connected to a side chain in the united atom representation) bound by "virtual" C_α–C_α bonds with a constant distance of 3.8 Å. The protein chain is terminated on each side by two dummy atoms representing terminal groups.

5.4 Coarse-Grained Conformational Energy

It is possible to construct an expression $E(\mathbf{R})$ for energy of the protein molecule, which takes into account most important factors determining stability of any conformation (including its interaction with the solvent treated as effective medium) [8]. The local geometry of the chain, determined by the distances between ith and $i+3$, ith and $i+4$ and ith and $i+5$ C_α atoms as well as the torsional angles, is controlled by the short-range potentials, which depend also on the identity of the residues involved. The long-range interactions are taken into account by two contributions. The first is the contact-type potential for the side chain united atoms. Its strength is dependent on the nature of the side chains, as well as on the mutual orientation of the interacting chain fragments (parallel, antiparallel and intermediate) and contains the statistical information [9] based on the frequency of such interactions found in the Protein Data Bank. The second type of the long-range interaction gives an energy gain for the main-chain hydrogen bonds, which are considered as existing, if the C_α pseudoatoms have the geometry characteristic for the hydrogen bonded structures.

The REFINER model had been tested in the CASP5 (every second year community-wide Critical Assessment of Techniques for Protein Structure Prediction) experiment and in a benchmark of de novo prediction of protein fragments. Both tests have shown better performance than that achieved by standard molecular modeling tools. During the next round, CASP6 of the protein structure prediction, the REFINER model produced several very good predictions, especially in the new fold category.

5.5 Monte Carlo Procedure

$E(\mathbf{R})$ makes possible the study of the dynamics of the protein molecule. A typical Monte Carlo dynamics consists of aleatory drawing a ("current") conformation and comparing its energy (E_1) with the energy (E_2) of a next aleatory conformation. The side chain conformations are read from the database and stored in a rotamer library. The rotamers are divided into three groups, depending on three classes of the main chain local geometry. If $E_2 < E_1$, the second conformation becomes the current one, if not, the second conformation becomes the current one with the probability $\exp[-(E_2-E_1)/k_B T]$, where k_B is the Boltzmann constant and T is the absolute temperature (the procedure known as the Metropolis criterion). The drawing is repeated many times (this is called MC run), in our case 1,000,000 times. Ten replicas of the system under consideration have been used simultaneously, each replica at a different temperature (the temperatures distributed uniformly in a temperature range). Aleatory exchanges of the current conformations between neighboring replicas are allowed (with a generalized Metropolis criterion). Such a procedure (known as Replica Exchange Monte

Carlo method [10]) enhances the chance to escape from local energy minima traps and find the global minimum conformation.

5.5.1 *Example:* Ab novo *Prediction*

The current possibilities of prediction of 3D structure of a globular protein from its amino acid sequence are demonstrated in Fig. 5.3, which shows the theoretically predicted 3D structure by Koliński and Bujnicki [11] and the X-ray determined structure [12]. The Fig. pertains to the putative nitroreductase, one of the target proteins in the 2004 CASP6 competition. The molecule, a chain of 206 amino acids, altogether about 3,000 heavy atoms, is one of the 1,877 proteins of the bacterium *Thermotoga maritima* (a species that lives in geothermal marine sediments).

Both theory (CASP6 blind prediction, Fig. 5.3a) and experiment (carried out within CASP6 as well, Fig. 5.3b) give the target molecule containing five α-helices and two β-pleated sheets (wide arrows). These secondary structure elements interact and form the unique (native) tertiary structure, which is able to perform its biological function. Both structures in atomic resolution differ by the r.m.s. equal to 2.9 Å, which is a rather small deviation.

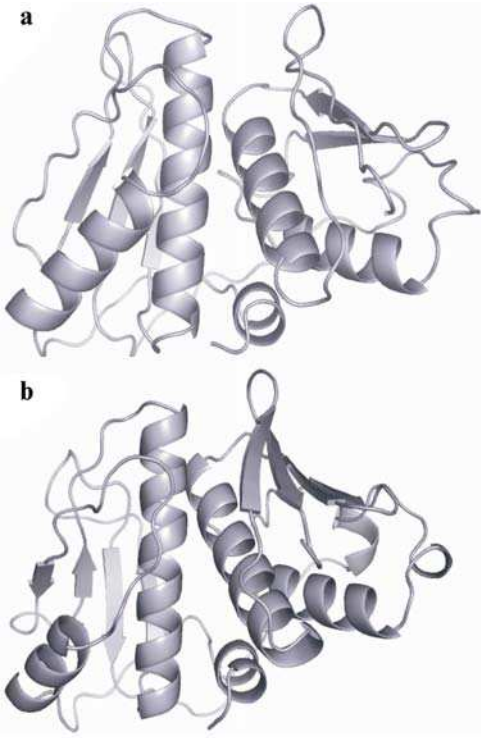

Fig. 5.3 Comparison of the theoretical and experimental 3D structure (ribbon representation) of the putative nitroreductase, one of the targets of CASP6 competition. The energy expression which was used in theoretical calculations takes into account the physical interactions (such as hydrogen bonds, hydrophobic interactions, etc.) as well as an empirical potential deduced from representative proteins' experimental structures deposited in the Brookhaven Protein Data Bank (no bias towards the target protein). (**a**) Predicted by Koliński and Bujnicki [11] by the Monte Carlo method, and (**b**) determined experimentally by X-ray diffraction [12]. Both structures in atomic resolution differ (r.m.s.) by 2.9 Å. Reproduced by courtesy of Professor Andrzej Koliński

5.5.2 *Example: Conformational Autocatalysis (A Model of Prion Propagation)*

Suppose we have a molecule with possible two conformations: A (of the lowest-energy one) and B (a metastable one, of higher energy). Let us consider two such molecules, one with the conformation A, and the other with the conformation B. Can the molecule with the conformation B induce the conformation B in the second molecule? If yes, this may be called the conformational autocatalysis. The idea is interesting because such a situation may happen in molecular crystal packing, and also in proteins (prion propagation). In the latter case, it would result in propagation of the metastable protein form (B) due to the protein–protein interaction, whereas the single protein molecule acquires the native A form.

Having such an efficient tool for predicting proteins' 3D structure as the REFINER model, could we design a protein exhibiting the conformational autocatalysis?

First, a sequence of 32 amino acids is designed in such a way as to ensure the existence of the global minimum basin of the α-helical character (in the form of a two-helix bundle), and a metastable basin of the β type (in the form of a four-member β barrel) [13]. The philosophy in this designing is the following. In the center are two glycines, which are notorious for their conformational flexibility (glycine's R is a hydrogen atom). This facilitates forming hairpin structures, a feature stabilizing both the expected α and β forms. Two other glycine residues are located, one in position 8 and one in 25 in order to make the chain more flexible over there, thereby, facilitating formation of the four member β barrel. The glutamic acids and lysines form a pattern known for stabilization of the α-helix (they also interact by strong electrostatic salt bridges $–NH_3^+ \ldots O^- OC–$). On the other hand, a pattern of valines and isoleucines was used, which is known for tendency to make β forms. By knowledge-based step-by-step tuning of the α and β tendencies (the starting α-helical patterns were gradually modified by introducing elements of the β type patterns), 14 oligopeptides of 32 amino acids have been selected.

All these 14 candidates turned out (this has been checked by performing long Monte Carlo runs) to have the α type global minimum ("native") in the form of a two α-helix bundle and a β type metastable basin (four-member β-barrel). Of these 14 sequences, only one, GVEIAVKGAEVAAKVGGVEIAVKAGEVAAKVG (*G* glycine, *V* valine, *E* glutamic acid, *I* isoleucine, *A* alanine, *K* lysine), exhibits the autocatalytic behavior of the following kind. A single molecule of the protein, when subject to an extensive Monte Carlo conformational search (Replica Monte Carlo method), practically always rapidly attains the global minimum of α-helical character (two-helical bundle with well pronounced hydrophobic interface), Fig. 5.4a, if the temperature exceeds a minimum temperature. Below this minimum temperature, besides the α-helical form, the β form (four-member β barrel) is also stable, Fig. 5.4b. If, however, two protein molecules interact, and one of them is frozen in the β metastable form (for a reason whatsoever, say, by a chemical or physical confinement), and the second molecule is allowed to fold, then it practically

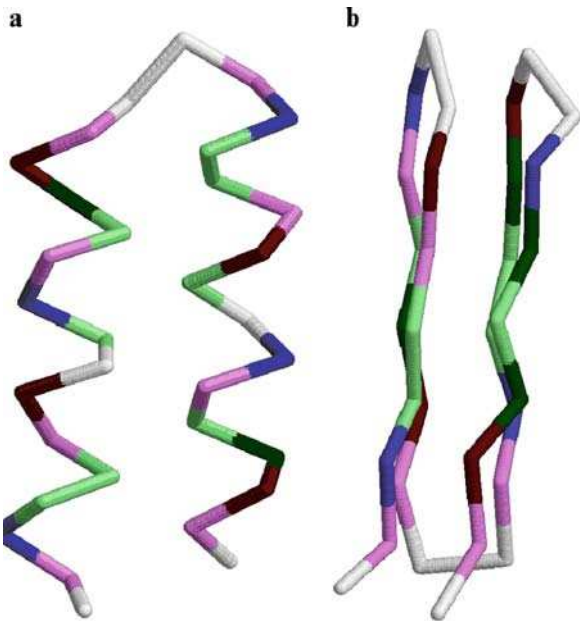

Fig. 5.4 The selected oligopeptide GVEIAVKGAEVAAKVGGVEIAVKAGEVAAKVG (only heavy atoms of the backbone are shown); *G* glycine, *V* valine, *E* glutamic acid, *I* isoleucine, *A* alanine, *K* lysine. (**a**) The lowest-energy α-helical conformation (two-helical bundle with well pronounced hydrophobic interface) and (**b**) the metastable β conformation (four-member β barrel) of the amino acid sequence. The sequence is a compromise between the α-helix making pattern and the β making pattern. The two glycines in the center of the sequence are expected to make a turn of the backbone, welcome for both α and β forms

always folds to the β (i.e., metastable form), Fig. 5.5. It was proved also that the third protein molecule continues to form a stack of molecules with such beta conformations (conformational autocatalysis). This model seems to mimic main features of spreading the prion diseases at molecular level.

5.6 Concluding Remarks

The protein folding, notorious for an astronomic number of possible conformations, is only an example of the multiple minima problem, inherently connected to all applications of theory to structural chemistry (isomers, supramolecular structures etc.). The multiple minima problem is also virtually ubiquitous in other sciences, and whenever a mathematical description is used, the situation is encountered more and more often. Despite the complexity of the protein folding, remarkable achievements in the prediction of the 3D structure of globular proteins are possible nowadays.

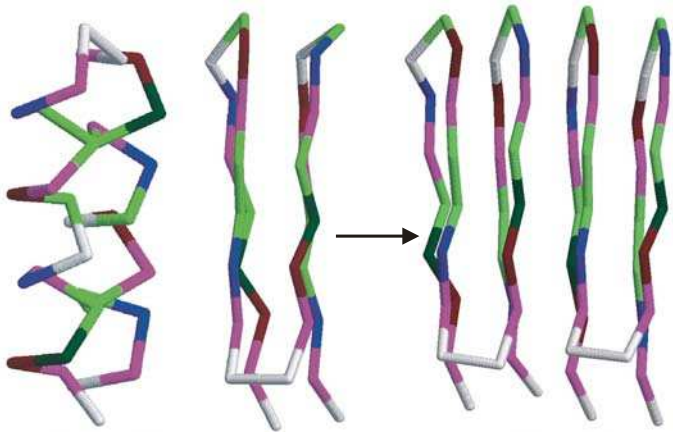

Fig. 5.5 A model of conformational autocatalysis for the oligopeptide of Fig.5.4. The lowest-energy α-helical form (two-helix bundle, *left-hand side*) interacts with the frozen metastable β form (four-member β barrel, *center*). After a long Monte Carlo run (symbolized by an *arrow*), which consists of a million of intermediate conformations of various type, both molecules form a strong complex of two β type metastable forms (*right*). During this run the α conformation unfolds and then refolds to the β conformation. Thus, the β metastable form plays a role of a catalyst in the transformation of the α native structure into the β form (autocatalysis)

It is instructive to see what kind of concepts have been used to overcome the multiple minima problem in this particular case, with a hope that a similar approach could help in other domains. Here is the list of decisive steps:

- In case of the protein folding, the most important was the Anfinsen paradigm [1] that the 3D native structure of an isolated protein molecule comes uniquely from its amino acid sequence (and not from its interaction with other molecules), and that the native structures of proteins correspond to the global minimum of the (free) energy of the molecule. The paradigm made possible to focus on low-energy structures as the most promising candidates for the native structure. Fortunately, such a paradigm is applicable generally in structural chemistry, where the lowest-energy structure is very important. In general applications (beyond chemistry), one has to define a function E to be optimized (target function).
- The next decisive step was radical simplifying the original system. First, water environment (water molecules) has been averaged out (taken into account only implicitly). Next, although for a chemist, it seemed indispensable to consider the protein molecule in its atomic resolution (and maybe even considering the quantum mechanical nature of its building blocks), the atomic interactions have been averaged by replacing the multi-atomic quasi-rigid subunits of the system, like peptide bonds and side chains, by pseudoatoms ("united atoms") treated as centers of interaction. Such an approach is possible in other branches of structural chemistry, provided that we limit ourselves to the energy range, which allows for treating some subunits as unchangeable.

- What helped next in case of proteins is that the quasi-rigid subunits (peptide bonds) are all the same, though perturbed by the presence of twenty possible side chains (which were treated almost case by case using also the pseudoatom concept). This approach may also help in other domains of chemistry.
- Fortunately enough, the energy landscape (target function) for natural proteins, simplified or not, has a funnel-like structure. This drives the search toward the global minimum. This might be the decisive factor in other domains: the global minimum of the target function should differ widely by its value from other (local) minima.
- In case of proteins, one of the most decisive facts was also the availability of the Protein Data Bank, a result of many-year extensive work of X-ray and NMR worldwide communities. Only thanks to the Protein Data Bank, it was possible to acquire gradually the necessary knowledge about what are and what decides the secondary structures, and to create the statistical potentials useful in such procedure as REFINER. The statistical potentials were able to compensate for our current lack of physical/chemical understanding of many-body interactions. Without a similar data base (in other domains of chemistry), it is difficult to imagine a proper calibration of theoretical tools.
- Only after these approximations were made, it was possible to construct the force field, simple enough to calculate the conformational energy very fast, yet taking into account all important contributions, including also the effective influence of the surrounding water (through assignment of side chain–side chain hydrophobic interactions). The force field coupled to the Monte Carlo procedure (a universal tool, available in other domains) made possible the search of the whole (simplified) conformational space and find the global minimum (native) structure of the protein.

Acknowledgments The author is very indebted to Professor Andrzej Koliński, Department of Chemistry, University of Warsaw, for kindly providing his results prior to publication.

References

1. C.B. Anfinsen, Principles that govern the folding of protein chains. Science **96**, 223–230 (1973)
2. E.I. Shakanovich, A.M. Gutin, Engineering of stable and fast-folding sequences of model proteins. Proc. Natl. Acad. Sci. USA **90**, 7195–7199 (1993)
3. G.N. Ramachandran et al., Stereochemistry of polypeptide chain configurations. J. Mol. Biol. **7**, 95–99 (1963)
4. L. Piela, H.A. Scheraga, On the multiple-minima problem in the conformational analysis of polypeptides. I. Backbone degrees of freedom for a perturbed α-helix. Biopolymers **26**, S33–S58 (1987)
5. L. Piela, Deformation Methods of Global Optimization in Chemistry and Physics, in *Handbook of Global Optimization*, vol. 2, ed. by P.M. Pardalos, H.E. Romeijn, H.E. Romeijn, H.E. Romeijn (Kluwer, Dordrecht, 2002), p. 461. ISBN 1-4020-0742-6
6. J. Skolnick et al., TOUCHSTONE: a unified approach to protein structure prediction. Proteins **53**(6), 469–479 (2003)

7. M. Boniecki et al., Protein fragment reconstruction using various modeling techniques. J. Comput. Aided Mol. Des **17**, 725–738 (2003)
8. A. Koliński, Protein modeling and structure prediction with a reduced representation. Acta Biochim. Polon. **51**, 349–371 (2004)
9. S. Miyazawa, R.L. Jernigan, Long- and short-range interactions in native protein structures are consistent/minimally frustrated in sequence space. Proteins **50**, 35–43 (2003)
10. R.H. Swendsen, J.-S. Wang, Replica Monte Carlo simulation of spin-glasses. Phys. Rev. Lett. **57**, 2607–2609 (1986)
11. A. Koliński, J.M. Bujnicki, Generalized protein structure prediction based on combination of fold-recognition with de novo folding and evaluation of models. Proteins **61**(S7), 84–97 (2005)
12. J. Moult et al., Critical assessment of methods of protein structure prediction. Proteins **61**(S7), 3–7 (2005)
13. E. Małolepsza et al., Theoretical model of prion propagation: A misfolded protein induces misfolding. Proc. Natl. Acad. Sci. USA **102**, 7835–7840 (2005)

Chapter 6
An Overview of σ-Hole Bonding, an Important and Widely-Occurring Noncovalent Interaction

Peter Politzer and Jane S. Murray

Abstract σ-Hole bonding is a highly directional noncovalent interaction between a positive region on a covalently-bonded Group IV–VII atom and a negative site on another molecule, e.g., a lone pair of a Lewis base. The positive region reflects the electron deficiency in the outer lobe of the *p*-type orbital involved in the covalent bond and is along the extension of this bond. There is now considerable experimental and computational evidence for σ-hole bonding. Within a given group, and for a particular Lewis base, the strength of the interaction increases with the polarizability of the atom and the electron-withdrawing power of the remainder of the molecule. For Groups IV–VI, there can be more than one σ-hole on the atom. For a series of Group IV–VII molecules, we give computed values of the positive surface electrostatic potentials associated with the σ-holes, and we also present some calculated interaction energies with different Lewis bases. σ-Hole bonding is competitive with hydrogen bonding, but the two can also accompany each other. The positive σ-holes usually exist in conjunction with negative regions on the remainders of the atoms' surfaces, so that interactions with electrophiles as well as nucleophiles are possible. It is, therefore, not valid to assign single global atomic charges in these instances. Examples of σ-hole bonding in molecular biology and crystal engineering are discussed.

6.1 The σ-Hole Concept: Origin

The term "σ-hole bonding" refers to an electrostatically-driven, highly-directional noncovalent interaction between a positive region on an atom in one molecule and a negative portion of a second molecule, often a lone pair of a Lewis base. Complexes

P. Politzer (✉) and J.S. Murray
Department of Chemistry, University of New Orleans, New Orleans, LA 70148, USA; Department of Chemistry, Cleveland State University, Cleveland, OH 44115, USA
e-mail: ppolitze@uno.edu,

J. Leszczynski and M.K. Shukla (eds.), *Practical Aspects of Computational Chemistry*, 149
DOI: 10.1007/978-90-481-2687-3_6,

formed in this manner have been known for well over a century, although it has been only gradually recognized how widespread their occurrence is.

Many of the early studies involved halogen or interhalogen molecules (e.g., Br_2, I_2, ICl, IBr) interacting with Lewis bases, such as amines and aromatic π-donors [1, 2]; however, it became evident that organic halides can also play the role of the electrophile [3, 4]. The intriguing feature in all of this is that it is in each instance a halogen atom that is interacting attractively with the Lewis base, and covalently-bonded halogens are typically viewed as being negative!

A decisive step in resolving this apparent paradox was the observation in 1992 by Brinck et al. [5] that the halogen atoms in several organic halides (CCl_4, CH_3Br, CBr_4) had regions of positive electrostatic potential on the outer portions of their otherwise negative surfaces, approximately on the extensions of the covalent bonds to these atoms (See, for example, Fig. 6.1.). The presence of such a positive potential, which was subsequently found in other halide molecules as well [6–10], readily explains the attraction for a nucleophile, such as a Lewis base.

What is the origin of this unexpected positive region on the outer side of a bonded electronegative atom? An answer to this was provided by Clark et al. [11]. When a half-filled *p*-type orbital of a halogen atom interacts to form a covalent bond, there results a deficiency of electronic charge in the outer noninvolved lobe of that orbital. This charge deficiency is the σ-hole, so named because it is centered along the extension of the bond. If the deficiency is sufficient, then the σ-hole acquires positive character and can interact attractively with a nucleophile. This is what came to be called "halogen bonding."

The σ-hole becomes more positive as the halogen atom is more polarizable and the remainder of the molecule more electron-withdrawing. Thus, the bromine in

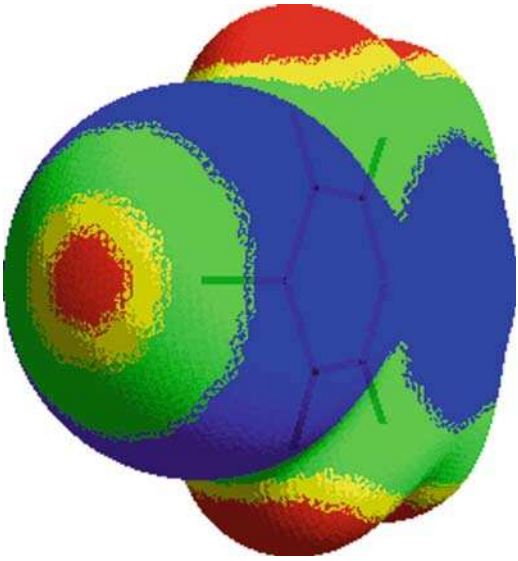

Fig. 6.1 Calculated electrostatic potential $V(\mathbf{r})$ on the molecular surface of 4-bromopyridine, BrC_5NH_4. Color ranges, in kcal/mol, are: *blue*, negative; *green*, from 0 to 10, *yellow*, from 10 to 14; *red*, more positive than 14. The bromine is to the *left* facing the viewer and has both positive and negative regions of electrostatic potential. Its most positive (*red*) region is along the extension of the C–Br bond, while its negative potential (*blue*) forms a ring around the bromine's lateral surface

CH_3Br has a positive σ-hole, but the less polarizable chlorine in CH_3Cl does not; however, it does have one in ClCN [10]. Covalently-bonded fluorine rarely has a positive σ-hole. These trends in the positive characters of σ-holes are reflected in the relative strengths of their interactions with a given Lewis base [8, 10, 12], as will be discussed in detail with reference to Tables 6.1 and 6.2.

In general, the strengths of halogen bonds are in the same approximate range as hydrogen bonds, usually less than about 12 kcal/mol, and they are in fact competitive with the latter [13–15]. Indeed, one explanation for the anesthetic action of some halogenated hydrocarbons, such as halothane ($CF_3CHBrCl$), is that the positive potentials associated with their hydrogens and halogens disrupt the hydrogen bonds in key brain proteins [9, 16–18].

A distinctive aspect of σ-hole bonding is its directionality. In the complex A-X···B formed between a halide A–X and a Lewis base B, the angle A–X–B is normally close to 180°. This follows from the σ-hole being concentrated along the extension of the A–X bond. In contrast, a hydrogen bond, A–H···B, is more likely to be nonlinear [1]; some examples will be given later.

As mentioned above, a positive σ-hole on a covalently-bonded halogen may exist in conjunction with negative potentials on the remainder of its surface, as is shown in Fig. 6.1. The halogen can then interact with negative regions on other molecules through its σ-hole and with positive regions through its sides. This was indeed observed in surveys of close contacts in crystals [19]. However, if the halogen is in a very strongly electron-withdrawing environment, e.g., the Br in BrCN [10] or in 3,5-dicyanobromobenzene [12], the electrostatic potential on its entire surface may be positive (the maximum value will still correspond to the σ-hole).

The existence of halogen bonding, while still rather unfamiliar to many researchers in chemistry and molecular biology, is now well established experimentally in these fields, and has been observed in the gaseous, liquid and crystalline phases [1–4, 7, 13, 14, 17, 19–29]. However, the term σ-hole bonding includes much more than just halogen bonding.

6.2 The σ-Hole Concept: Expansion

In the last few years, it has been recognized that the σ-hole concept is not limited to halogens, but is equally valid for covalently-bonded atoms of Groups IV–VI [30–32]. Thus, a sulfur atom, with two half-filled *p*-type orbitals involved in covalent bonds, will have a σ-hole on the extension of each bond [31]; one or both of these σ-holes may be positive, depending upon the partner in the bond. A pyramidal phosphorus has three σ-holes [30], any or all of which might be positive (Fig. 6.2), and a tetrahedral silicon, e.g., in $SiCl_4$, has four [32]. The fact that σ-holes are found on tetrahedral Group IV atoms shows that they can arise even from half-filled bonding orbitals that have a quite significant *s* contribution,

Table 6.1 Computed most positive ($V_{S,max}$) and most negative ($V_{S,min}$) electrostatic potentials on the indicated atoms, in kcal/mol (Calculations were at B3PW91/6-31G(d,p) level[a,b])

Molecule	Atom	$V_{S,max}$	$V_{S,min}$
Group IV			
CH_3Cl	C	–	–
CCl_4	C	8.5 (4)	–
CF_4	C	20.0 (4)	–
SiH_4	Si	13.0 (4)	–
SiH_3Cl	Si	31.0, 17.7 (3)[c]	–
SiF_4	Si	43.8 (4)	–
GeH_4	Ge	14.0 (4)	–
GeH_3Cl	Ge	36.1, 18.5 (3)[c]	–
GeF_4	Ge	46.4 (4)	–
Group V			
$(H_3C)_3N$	N	–	−34.3
NF_3	N	14.5 (3)	−5.3
$(H_3C)_3P$	P	–	−30.8
$(H_3C)_2P–OCH_3$	P	12.8	−24.8
PF_3	P	27.8 (3)	–
$(H_3C)_2P–CN$	P	28.2, 16.3 (2)[c]	−15.6
$(H_3C)_3As$	As	7.7 (3)	−25.1
$(H_3C)_2As–OCH_3$	As	17.3, 9.3[c]	−17.5
$(H_3C)_2As–CN$	As	30.2, 17.1 (2)[c]	−10.0
$As(CN)_3$	As	51.4 (3)	–
Group VI			
OF_2	O	13.8 (2)	−3.7 (2)
$(H_3C)_2S$	S	–	−25.7 (2)
$H_3C–S–OCH_3$	S	18.0	−20.4 (2)
$H_3C–S–F$	S	28.8, 4.9[c]	−15.7 (2)
SCl_2	S	25.1 (2)	−5.9 (2)
$(H_3C)_2Se$	Se	–	−24.0 (2)
$H_3C–Se–OCH_3$	Se	22.7, 8.1[c]	−19.6 (2)
$H_3C–Se–F$	Se	34.8, 9.6[c]	−15.0 (2)
$H_3C–Se–CN$	Se	35.1, 17.3[c]	−6.6 (2)
Group VII			
CF_4	F	–	−2.1
$F–C\equiv C–CN$	F	16.9	–
NF_3	F	3.0	−2.7, −2.0 (2)
OF_2	F	6.6	−4.3 (2)
$H_3C–Cl$	Cl	–	−16.6 (3)
CCl_4	Cl	18.3	−3.5
$F–CH_2–Cl$	Cl	3.5	−15.5
	F	–	−15.8
$F_3C–Cl$	Cl	16.3	−3.4 (3)
	F	–	−2.2 (3)
$Cl–OCH_3$	Cl	19.1	−14.4(2)
$Cl–CH_2–CH_2–NO_2$	Cl	7.8	−8.1
$Cl–C\equiv C–CN$	Cl	35.0	–
SCl_2	Cl	13.3	−5.9 (2)
$H_3C–Br$	Br	6.0	−15.2 (3)
$Br–C\equiv C–CH_3$	Br	22.6	−7.9
$Br–OCH_3$	Br	26.6	−12.7 (3)
$Br–CH_2–CH_2–NO_2$	Br	14.8	−6.8

(*continued*)

Table 6.1 (continued)

Molecule	Atom	$V_{S,max}$	$V_{S,min}$
Br–C≡C–CN	Br	41.6	–
Br–CN	Br	42.1	–
BrF	Br	47.5	−1.7 (4)
	F	–	−11.9 (4)
4-bromopyridine	Br	16.1	−7.6 (2)

[a]When there are more than one $V_{S,max}$ or $V_{S,min}$ of the same magnitude on a particular atom, this is indicated in parentheses

[b]The $V_{S,max}$ values, and some of the $V_{S,min}$, are from [10, 15, 30–32, 56]

[c]The lower $V_{S,max}$ is (are) on the extension(s) of the bond(s) to H or to CH_3

Table 6.2 Computed interaction energies ΔE (kcal/mol), angles (deg) and separations (A) for some σ-hole-bonded complexes

	Complex	Angle	Distance[a]	ΔE		Reference
				B3PW91	MP2-FC	
1	$H_3N\cdots BrCN$	N–Br–C:180	N···Br: 2.83	−6.9	−6.1	[15]
2	$H_3N\cdots BrC{\equiv}CCN$	N–Br–C: 180	N···Br: 2.88	−6.6	−5.8	[15]
3	$H_3N\cdots BrC{\equiv}CCH_3$	N–Br–C: 180	N···Br: 3.00	−4.0	−3.6	[15]
4	$HCN\cdots PF_3$	N–P–F: 173	N···P: 3.32	−1.4	−2.8	[30]
5	$HCN\cdots P(CN)_3$	N–P–C: 172	N···P: 3.01	−4.4	−7.6	[30]
6	$HCN\cdots As(CN)_3$	N–As–C: 167	N···As: 2.95	−5.4	−8.6	[30]
7	$HCN\cdots Se(CH_3)F$	N–Se–F: 180	N···Se: 2.89	−2.8	−5.2	[15]
8	$HCN\cdots SiF_4$	N–Si–F: 180	N···Si: 3.27	−1.6	−3.5	[32]
9	$H_3N\cdots Se(CH_3)OCH_3$	N–Se–O: 176	N···Se: 2.95	−8.2	−7.9	[15]
10	$H_3N\cdots As(CH_3)_2OCH_3$	N–As–O: 176	N···As: 3.40	−3.2	−3.7	[15]
11	$H_3N\cdots S(CN)_2$	N–S–C: 174	N···S: 2.82	−7.7	−8.0	[31]
12	$H_3N\cdots Se(CN)_2$	N–Se–C: 170	N···Se: 2.78	−9.5	−9.7	[31]
13	$H_3N\cdots SiH_3Cl$	N–Si–Cl: 180	N···Si: 2.49	−7.1	−6.4	[32]
14	$H_3N\cdots SiF_4$	N–Si–F: 180	N···Si: 2.10	−9.4	−11.4	[32]
15	$H_2O\cdots S(CH_3)_2O_2$	b	b	−8.3	−8.8	[36]
16	$Cl_2S\cdots SCl_2$	S–S–Cl: 169	S···S: 3.17	–	−5.5	[53]
17	$FH_2As\cdots AsH_2F$	As–As–F: 166	As···As: 2.90	–	−4.1	[53]
18	ClCN···ClCN	N–Cl–C: 180	N···Cl: 3.08	−2.4	−3.8	[10]
19	ClCN···ClCN···ClCN	N–Cl–C: 180	N···Cl: 3.01, 3.04	−5.4	−8.7	[10]
20	BrCN···BrCN	N–Br–C: 180	N···Br: 3.03	−3.2	−4.9	[10]
21	BrCN···BrCN···BrCN	N–Br–C: 180	N···Br: 2.98, 2.98	−7.3	−10.6	[10]
22	Pyrazine···BrC≡CBr	N–Br–C: 180	N···Br: 3.00	−2.9	−4.9	[10]

Geometry optimizations were B3PW91/6-311G(3df,2p); the ΔE are B3PW91/6-311G(3df,2p) and MP2-FC/6-311++G(3df,2p).

[a]For comparison, the sums of the van der Waals radii [59], are: N···Br: 3.40; N···P: 3.35; N···As: 3.40; N···Se: 3.42; N···S: 3.38; N···Si: 3.65; O···S: 3.35; S···S: 3.66; As···As: 3.70; N···Cl: 3.31; O···H: 2.69

[b]This complex involves four interactions: $H_2O\cdots S$, with O_a–S–O angle = 177°, S···O distance = 3.34 A; $O_b\cdots HOH$, with O_b–H–O angle = 147°, $O_b\cdots H$ distance = 1.99 A; and two $CH\cdots OH_2$, with C–H–O angles = 133, 130°, H···O distances = 2.44 A

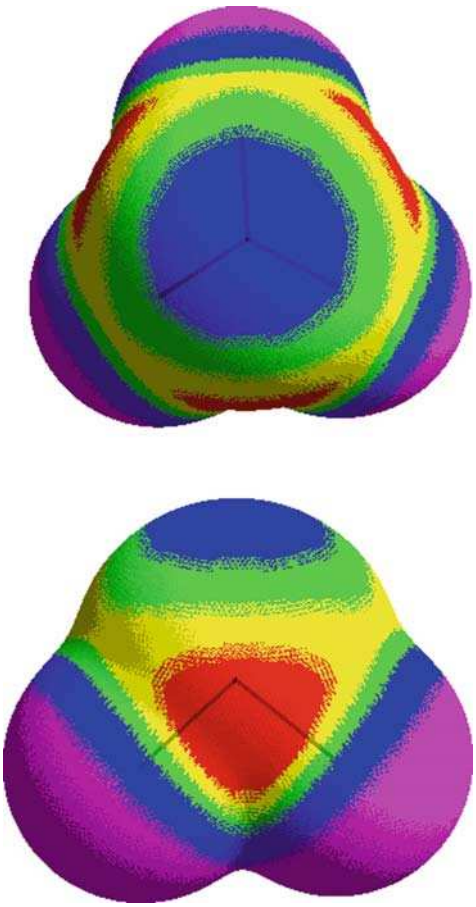

Fig. 6.2 Two views of the calculated electrostatic potential $V(\mathbf{r})$ on the molecular surface of PF_3. Color ranges, in kcal/mol, are: *purple*, negative; *blue*, 0 to 10; *green*, from 10 to 15, *yellow*, from 15 to 20; *red*, more positive than 20. In the *top view*, the phosphorus is facing the viewer. The three most positive regions of electrostatic potential (*red*) are along the extensions of the three F–P bonds. In the *bottom view*, we see the side of the phosphorus (*top*) and two of the fluorines (*bottom*). The most positive potential (*red*) is along the extension of one of the F–P bonds, the one for which the fluorine is facing into the plane of the page

although considerable *p* character is needed to give the well-established directionality of σ-hole interactions.

The preceding discussion relating to halogen σ-holes is fully applicable to Groups IV–VI. The positive character of the σ-hole increases with the polarizability of the Group IV, V or VI atom (i.e., C < Si < Ge < Sn, N < P < As < Sb and O < S < Se < Te) and with the electron-withdrawing power of the remainder of the molecule. The magnitudes of the interaction energies with a given Lewis base follow the same pattern. Carbon, nitrogen and oxygen (as also fluorine) will have a (weakly) positive σ-hole only when bonded to a very strongly electron-attracting group, such as CN or NO_2.

Computed data showing these trends will be discussed in conjunction with Tables 6.1 and 6.2. For Group VI [33–36] and for Group IV [37], there is also experimental evidence of interactions that are now identified as σ-hole bonding (although not so labeled in the past). For Group V, the evidence of σ-hole bonding

of which we are aware is so far only computational [30], probably because its occurrence in chemical and biological systems has simply not been recognized.

While σ-holes have generally been found to be associated with half-filled *p* or predominantly *p* bonding orbitals, these are not the only possibilities. In $(CH_3)_2SO$, $(CH_3)_2SO_2$ and Cl_3PO, natural bond orbital analyses show the O–S and O–P bonds to be single and coordinate covalent, *both* electrons coming from the sulfur and the phosphorus [32, 38]. Nevertheless, there are significantly positive σ-holes on the sulfurs and the phosphorus, on the extensions of these bonds; and their presence helps to account for $(CH_3)_2SO$ and $(CH_3)_2SO_2$ being such good solvents, as well as for their high boiling points.

6.3 Computational Results

There have been numerous computational studies of the noncovalent interactions to which we now refer (since 2007 [11]) as σ-hole bonding. Only a portion of these will be cited here. Most have dealt with Group VII (halogen bonding) [2, 8, 10, 12, 15, 20, 28, 39–44], some with Group VI [15, 31, 36, 38, 45–47] and a few with Groups V [15, 30, 32, 44] and IV [32, 48].

In this section, we present and discuss some of the computed results that we have obtained for Groups IV–VII. These include relevant features of molecular electrostatic potentials (Table 6.1) and key properties of σ-hole-bonded complexes (Table 6.2). All of the data in these tables are taken from our own work, some of it unpublished, so as to ensure consistency in procedure.

The electrostatic potential $V(\mathbf{r})$ that the nuclei and electrons of a molecule produce at any point $\mathbf{r}$ in the surrounding space is given by (6.1):

$$V(\mathbf{r}) = \sum_{\mathrm{A}} \frac{Z_{\mathrm{A}}}{|\mathbf{R}_{\mathrm{A}} - \mathbf{r}|} - \int \frac{\rho(r')\mathrm{d}\mathbf{r}'}{|\mathbf{r}' - \mathbf{r}|} \tag{6.1}$$

Z_{A} is the charge on nucleus A, located at $\mathbf{R}_{\mathrm{A}}$; and $\rho(\mathbf{r})$ is the molecule's electronic density function. The sign of $V(\mathbf{r})$ in any region depends upon whether the positive contribution of the nuclei or the negative one of the electrons is dominant there. It is important to note that $V(\mathbf{r})$ is a physical observable, which can be obtained experimentally, by diffraction techniques [49, 50], as well as computationally.

For analyzing noncovalent interactions, we typically evaluate $V(\mathbf{r})$ on a three-dimensional surface of the molecule. For this purpose, we use the 0.001 au (electrons/bohr^3) contour of its electronic density, as suggested by Bader et al. [51]. This surface encompasses at least 96% of the electronic charge of the molecule, and reflects its specific features, such as lone pairs, π electrons, strained bonds, etc., which is not true of surfaces created by overlapping atomic spheres.

We have shown that the features characterizing the electrostatic potential on a molecular surface, which we label $V_{\mathrm{S}}(\mathbf{r})$, can be used to develop quantitative

relationships for a variety of condensed phase physical properties that depend upon noncovalent interactions [52, 53]. Particularly relevant in the present context is that the most positive values associated with hydrogens ($V_{S,max}$) and the most negative values in negative regions ($V_{S,min}$) correlate well with empirical measures of hydrogen bond donating and accepting ability, respectively [54].

Table 6.1 lists a series of molecules containing Group IV, V, VI and VII atoms. In each instance, we have given the most positive and the most negative electrostatic potentials, the $V_{S,max}$ and the $V_{S,min}$, on the surfaces of these atoms, as defined by the 0.001 au contour of $\rho(\mathbf{r})$. The $V_{S,max}$ correspond to positive σ-holes, and are located approximately on the extensions of covalent bonds to the atoms. The $V_{S,min}$ are usually due to lone pairs. The calculations were carried out at the density functional B3PW91/6-31G(d,p) level, using the Gaussian 03 code [55].

The $V_{S,max}$ in Table 6.1 consistently show the interplay of the two factors mentioned earlier: the polarizability of the Group IV, V, VI or VII atom and the electron-withdrawing power of the atom(s) or group(s) to which it is covalently bonded. Consider, for example, $(H_3C)_3P$ and $(H_3C)_3As$. The methyl group is not electron-attracting enough to produce positive σ-holes on the phosphorus, but it does so on the more polarizable arsenic, which has a weak $V_{S,max}$ of 7.7 kcal/mole on the extension of each H_3C–As bond. However, replacing just one CH_3 by the highly inductive cyano group withdraws so much electronic charge that positive σ-holes appear not only on the extensions of the NC–P and NC–As bonds, but the H_3C–P and H_3C–As as well; the latter are of course not as strong as those associated with the CN group. In all instances, the arsenic $V_{S,max}$ are more positive than the phosphorus. Note that when the less inductive OCH_3 group, rather than the CN, replaces a CH_3 in $(H_3C)_3P$, a $V_{S,max}$ results only on the extension of the H_3CO–P bond. An analogous pattern is seen for sulfur and selenium in Group VI, when an electronegative fluorine replaces one of the methyl groups in $(H_3C)_2S$ and $(H_3C)_2Se$.

It is relatively rare to find significantly positive $V_{S,max}$ on the first-row atoms C, N, O and F, due to their low polarizabilities. However, the possibility does exist when they are bonded to significantly electron-withdrawing atoms or groups. Examples in Table 6.1 are CCl_4, CF_4, NF_3, OF_2 and F–C≡C–CN. In CCl_4, NF_3 and OF_2, all of the atoms have positive σ-holes, although those of the fluorines are weak.

As was just pointed out, it is quite possible for more than one atom in a given molecule to have a positive σ-hole. This is illustrated in Table 6.1 by CCl_4, OF_2, NF_3, and SCl_2, but, interestingly, not CF_4 or F_3C–Cl. Furthermore, a molecule having one or more positive σ-holes may also contain strongly positive hydrogens, and thus, be capable of both σ-hole and hydrogen bonding. The potent anesthetic halothane, $CF_3CHBrCl$, has $V_{S,max}$ on the hydrogen, bromine and chlorine [9]; and as mentioned earlier, its activity has been attributed to these positive sites interfering with hydrogen bonding in brain proteins [9, 16–18]. Dimethyl sulfoxide, $(H_3C)_2SO$, has a positive σ-hole on the sulfur and four positive hydrogen $V_{S,max}$ [38]; and dimethyl sulfone, $(H_3C)_2SO_2$, has two positive σ-holes on the sulfur and two quite positive hydrogen $V_{S,max}$. Thus as has been shown [38, 57], each of these molecules can simultaneously be involved in several noncovalent interactions, both

σ-hole and hydrogen bonding. This explains the high boiling points and remarkable effectiveness as solvents of dimethyl sulfoxide and dimethyl sulfone [38].

For examples of these and other σ-hole interactions, we proceed to Table 6.2. This shows some representative σ-hole-bonded complexes formed by molecules containing Group IV, V, VI and VII atoms. Geometries were optimized at the density functional B3PW91/6-311G(3df,2p) level. Interaction energies ΔE were obtained via (6.2),

$$\Delta E = E_{\text{complex}} - \sum E_{\text{reactant}} \tag{6.2}$$

in which E_{complex} and E_{reactant} refer to the respective energy minima at 0 K, as obtained by the B3PW91/6-311G(3df,2p) and single-point MP2-FC/6-311G++(3df,2p) calculations. The use of such large basis sets should minimize any basis set superposition error [58], which was accordingly not evaluated.

Table 6.2 confirms the highly directional, near-linear character of σ-hole bonds; the relevant angles are mostly between 170° and 180°. The separations between the interacting atoms are less than or about equal to the sums of the respective van der Waals radii (given in a footnote in the table).

The electrostatically-driven nature of σ-hole interactions can be seen in the approximate correlation between the magnitudes of $V_{S,max}$ and ΔE for a given Group and Lewis base. Thus, $|\Delta E|$ for **1**–**3** increases with the bromine $V_{S,max}$ (Table 6.1). In general, the magnitudes of ΔE for a particular Group and Lewis base follow the same patterns as do the $V_{S,max}$, increasing with the polarizability of the atom and the electron-withdrawing power of the remainder of the molecule. Compare HCN···$P(CN)_3$, **5**, with HCN···$As(CN)_3$, **6**, in Table 6.2, or H_3N···$Se(CH_3)OCH_3$, **9**, with H_3N···$Se(CN)_2$, **12**. Of course, the nature of the Lewis base also affects ΔE. For instance, H_3N···$Se(CH_3)OCH_3$, **9**, is more stable than HCN···$Se(CH_3)F$, **7**, even though the selenium $V_{S,max}$ is higher in the latter (Table 6.1). This is because the nitrogen in NH_3 has a stronger negative potential ($V_{S,min}$ = −46.3 kcal/mol) than that in HCN ($V_{S,min}$ = −32.9 kcal/mol).

Complex **15** illustrates in detail the possibility of simultaneous σ-hole and hydrogen bonding, which has already been discussed; in **15**, there is one O···S σ-hole bond and three O···H hydrogen bonds. Note the deviations of the hydrogen bonds from linearity. Another example in Table 6.2 is **14**, in which the very short N···Si separation can be attributed to the presence of several H···F hydrogen bonds, in addition to the N···Si σ-hole interaction [32]. We have encountered analogous situations elsewhere, for instance, with sulfur and selenium heterocycles [47].

A particularly important point can be brought out by returning briefly to Table 6.1. In the majority of the molecules, the Group IV, V, VI or VII atom has regions of negative potential, with $V_{S,min}$, in addition to the positive σ-hole(s) (see Fig. 6.1). The primary exceptions are the Group IV atoms, which are the least electronegative, and those that are linked to very strong electron-withdrawers [10, 12, 30, 31], such as the cyano group and sometimes fluorine (Fig. 6.2). Accordingly, most of these Group V–VII atoms are able to interact attractively

with not only nucleophiles, through their positive σ-holes, but also with electrophiles, through their negative regions. Considerable crystallographic evidence of this was already found quite some time ago, through extensive surveys of close contacts in the lattices of organic sulfides [33, 34] and organic halides [19], and it has also been observed computationally, e.g., by Bleiholder et al. [46].

As a consequence of this dual nature and interactive capability of these covalently-bonded atoms, it is clearly not valid to assign single global atomic charges to them, by any of the numerous procedures that have been proposed over the years. For example, the selenium in $H_3C–Se–OCH_3$ has two $V_{S,max}$ of 22.7 and 8.1 kcal/mol and two $V_{S,min}$ of −19.6 kcal/mol (Table 6.1). It would certainly be misleading to assign any global charge to this selenium; even an overall net charge would not allow for the possibility of interactions with both nucleophiles and electrophiles in different directions.

A striking demonstration of this is an atom in one molecule interacting attractively with its counterpart in a second identical molecule, as in complexes **16** and **17** in Table 6.2 [56]. In these, the attraction is between a positive σ-hole on one sulfur or arsenic and a negative region on the sulfur or arsenic in the other (identical) molecule. In terms of global atomic charges, this would appear to be "like attracting like."

It has been pointed out that the possibility of an atom in a molecule having both positive and negative regions on its surface should be taken into account in designing force fields, e.g., for molecular dynamics [7, 56]. These often describe electrostatic interactions in terms of a single point charge associated with each atom.

Table 6.2 also includes several complexes that are intended to illustrate the very important role that σ-hole bonding can play in formulating new compounds, usually solids. For instance, **18** and **19**, and again **20** and **21** show how molecules having both a σ-hole and a basic site can assemble into chain-like structures of many units [10]. Note that in these systems, the magnitudes of ΔE for **19** and **21** are more than twice those of **18** and **20**, perhaps reflecting the "cooperativity effect" mentioned by Grabowski and Bilewicz [41]. Another option is chains of alternating molecules, one of which has two positive σ-holes and the other having two basic sites. Complex **22** could be the repeating unit in such a chain, the *para* nitrogens in each pyrazine interacting with the bromines in each BrC≡CBr. One can readily imagine two- and three-dimensional structures as well and involving Group IV, V and VI atoms. Anions having more than one Lewis base site, such as $Au(CN)_4^-$, are often useful building blocks for these purposes [17]. Such "crystal engineering" will be discussed further in a later section.

6.4 On the Nature of σ-Hole Bonding

The formation, the characteristic directionality and the relative strengths of the noncovalent bonds that have been discussed can be explained in a very direct and straightforward manner in terms of electrostatic attractions between positive σ-holes and negative sites. The σ-hole concept is, moreover, fully compatible with

the anisotropy ("polar flattening") that has been attributed to the charge distributions of covalently-bonded halogens in particular [20, 60, 61], but can be expected for Groups IV–VI as well. Polar flattening, which was observed crystallographically by Stevens in solid Cl_2 [62, 63], refers to the electron density being diminished along the extension of the covalent bond to the halogen as compared to its lateral sides. This simply reflects the electronic charge deficiency in the outer lobe of the half-filled *p*-type bonding orbital of the halogen, i.e., the σ-hole (The effects of σ-holes can also be seen in atomic quadrupoles [64].). However, it should be kept in mind that this charge anisotropy is not necessarily sufficient in itself to lead to a noncovalent interaction. It is present, for example, in the chlorine in H_3C–Cl, which does have a σ-hole, but a negative one. The same is true of most organic fluorides. The anisotropy, or charge deficiency, must be significant enough to result in a *positive* σ-hole, such as those recorded in Table 6.1. (The chlorines in Cl_2 also have positive σ-holes [8]; in the crystal lattice, these can be seen to be interacting with negative portions of neighboring Cl_2 molecules [62, 63].)

The interactions to which we refer as σ-hole bonding have sometimes been interpreted in terms of charge transfer from the Lewis base into an antibonding orbital associated with the covalent bond to the Group V–VII atom [2, 36, 65]. However, this would imply a weakening of that covalent bond, which is inconsistent with the fact that some of these interactions result in an *increase* (blue shift) in its stretching frequency [40, 43, 44]. (Whether a blue shift or a red shift occurs depends upon the natures of both participants in the interaction.)

Finally, it is appropriate to mention the charge-transfer treatments of donor–acceptor complexes that were developed by Mulliken [66] and Flurry [67], which have occasionally been invoked in connection with halogen bonding [1, 2, 68]. These methodologies, which are within valence bond and molecular orbital frameworks, respectively, encompass a broad range of donor–acceptor interactions. For example, Flurry's approach was used to interpret the interactions of CO and O_2 with hemoglobin [69]; Mulliken described the ground state of a complex as a resonance hybrid of primarily a "no-bond" form with a small contribution from a dative structure corresponding to electron transfer from donor to acceptor [66]. The natures of the no-bond form and of the electron transfer are not specified in detail. There is also an excited state of the complex in which the roles of the no-bond and dative structures are reversed, the latter now being dominant. A major emphasis of Mulliken's analysis is on the absorption band associated with the transition from the ground to the excited state.

The Mulliken and the Flurry formalisms cover a much greater variety of complexes than the σ-hole concept, which has so far been applied only to covalently-bonded atoms of Groups IV–VII interacting with negative sites. However, there is considerable overlap, for example, Mulliken's approach has been used extensively in connection with the interactions of halogen and interhalogen molecules with different Lewis bases [1, 2, 66, 68], which we would call σ-hole bonding (Halogen and interhalogen molecules do have positive σ-holes; note, for instance, BrF in Table 6.1 and Cl_2 and Br_2 in Politzer et al. [8].).

An important distinction, however, is that the σ-hole concept focuses upon the ground state of the complex, rather than its transition to the excited state. The electrostatic attraction between a positive σ-hole and a negative site on the other molecule is what holds together Mulliken's "no-bond" form of the complex. This electrostatic attraction naturally induces some minor polarization of both participants, which is represented in Mulliken's treatment by the small contribution from the dative structure. Thus, the σ-hole concept should be viewed as complementing the Mulliken and the Flurry methodologies for a certain class of noncovalent complexes, explaining the nature of the bonding in the ground state and its directionality.

6.5 Significance of σ-Hole Interactions

The importance, widespread occurrence and potential applications of σ-hole bonding are increasingly being recognized. Until now, the emphasis has been on Group VII (halogen bonding) and to a lesser extent, upon Group VI, but it can be expected that interest in Groups IV and V will soon develop.

Molecular biology is replete with examples of halogen bonding. For instance, a recent survey of crystal structures of halogenated nucleic acids and proteins showed numerous short, near-linear C–X···O contacts (X=Cl, Br or I) [7]. Receptor recognition of thyroid hormones appears to involve I···O interactions [2, 23]. Known cases of inhibitors acting through halogen bonding demonstrate its potential in drug design [7]. Conformational equilibria are sometimes governed by σ-hole bonding, and is well established for halogenated systems [7, 70]. It has also been found in thiazole and selenazole nucleosides [35, 71].

Halogen bonding has been successfully exploited in crystal engineering, i.e., the design and preparation of new crystalline solids [10, 17, 25, 28, 29, 61, 72, 73]. This has produced a variety of systems, frequently co-crystals, composed of one-, two- and three-dimensional networks of molecules (closed-shell or radicals) or ions, linked through halogen bonds. These can have important applications as conducting and superconducting or magnetic materials in nonlinear optics as coatings, etc. It is now recognized that Group VI molecules can also offer significant possibilities for crystal engineering (through σ-hole bonding) [31, 45, 46], and we anticipate that this will similarly be true of Groups IV and V.

References

1. A.C. Legon, Prereactive complexes of dihalogens XY with Lewis bases B in the gas phase: A systematic case for the halogen analogue B···XY of the hydrogen bond B···HX. Angew. Chem. Int. Ed. Engl. **38**, 2686–2714 (1999)

2. W.T. Pennington et al., Halogen bonding with dihalogens and interhalogens, in *Halogen Bonding: Fundamentals and Applications*, Structure and Bonding, vol. 126, ed. by P. Metrangolo, G. Resnat (Springer, Berlin, 2008), pp. 65–104
3. H.A. Bent, Structural chemistry of donor–acceptor interactions. Chem. Rev. **68**, 587–648 (1968)
4. O. Hassel, Structural aspects of interatomic charge-transfer bonding. Science **170**, 497–502 (1970)
5. T. Brinck et al., Surface electrostatic potentials of halogenated methanes as indicators of directional intermolecular interactions. Int. J. Quantum Chem. **44**, 57–64 (1992)
6. J.S. Murray et al., Molecular surface electrostatic potentials in the analysis of non-hydrogen-bonding noncovalent interactions. Proc. Indian Acad. Sci. **106**, 267–275 (1994)
7. P. Auffinger et al., Halogen bonds in biological molecules. Proc. Natl. Acad. Sci. **101**, 16789–16794 (2004)
8. P. Politzer et al., An overview of halogen bonding. J. Mol. Model. **13**, 305–311 (2007)
9. G. Trogdon et al., Molecular surface electrostatic potentials and anesthetic activity. J. Mol. Model. **13**, 313–318 (2007)
10. P. Politzer et al., Halogen bonding and the design of new materials: Organic bromides, chlorides and perhaps even fluorides as donors. J. Mol. Model. **13**, 643–650 (2007)
11. T. Clark et al., Halogen bonding: The σ-hole. J. Mol. Model. **13**, 291–296 (2007)
12. K. Riley et al., Br···O complexes as probes of factors affecting halogen bonding: Interactions of bromobenzenes and bromopyrimidines with acetone. J. Chem. Theor. Comput. **5**, 155–163 (2009)
13. T. Di Paolo, C. Sandorfy, On the hydrogen bond breaking ability of fluorocarbons containing higher halogens. Can. J. Chem. **52**, 3612–3622 (1974)
14. E. Corradi et al., Halogen bonding versus hydrogen bonding in driving self-assembly processes. Angew. Chem. Int. Ed. Engl. **39**, 1782–1786 (2000)
15. P. Politzer et al., σ-Hole bonding and hydrogen bonding: competitive interactions. Int. J. Quantum Chem. **107**, 3046–3052 (2007)
16. J.R. Trudell, E. Bertaccini, Molecular modeling of specific and non-specific anaesthetic interactions. Br. J. Anaesth. **89**, 32–40 (2002)
17. P. Metrangolo et al., Halogen bonding based recognition processes: A world parallel to hydrogen bonding. Acc. Chem. Res. **38**, 386–395 (2005)
18. C. Sandorfy, The site of action of general anesthetics: A chemical approach. Collect. Czech. Chem. Commun. **70**, 539–549 (2005)
19. N. Ramasubbu et al., Angular preferences of intermolecular forces around halogen centers: Preferred directions of approach of electrophiles and nucleophiles around carbon-halogen bond. J. Am. Chem. Soc. **108**, 4308–4314 (1986)
20. J.P.M. Lommerse et al., The nature and geometry of intermolecular interactions between halogens and oxygen or nitrogen. J. Am. Chem. Soc. **118**, 3108–3116 (1996)
21. P.L. Wash et al., Nitrogen-halogen intermolecular forces in solution. J. Am. Chem. Soc. **121**, 7973–7974 (1999)
22. Q. Chu et al., Fluorine-containing donor–acceptor complex: Infinite chain formed by oxygen–iodine interaction. J. Am. Chem. Soc. **123**, 11069–11070 (2001)
23. A. Wojtczak et al., Structure of rat transthyretin (rTTR) complex with thyroxine at 2.5 A resolution: First non-biased insight into thyroxine binding reveals different hormone orientation in two binding sites. Acta. Cryst. D **57**, 1061–1070 (2001)
24. E. De Moliner et al., Alternative binding modes of an inhibitor of two different kinases. Eur. J. Biochem. **270**, 3174–3181 (2003)
25. C. Guardigli et al., Design and synthesis of new tectons for halogen bonding-driven crystal engineering. Supramol. Chem. **15**, 177–188 (2003)
26. H. Loc Nguyen et al., Halogen bonding: A new interaction for liquid crystal formation. J. Am. Chem. Soc. **126**, 16–17 (2004)

27. R. Glaser et al., ^{13}C NMR study of halogen bonding of haloarenes: Measurements of solvent effects and theoretical analysis. J. Am. Chem. Soc. **126**, 4412–4419 (2004)
28. S. Berski et al., Dominant role of C–Br···N Halogen bond in molecular self-organization. Crystallographic and quantum-chemical study of Schiff-base-containing triazoles. J. Phys. Chem. B **108**, 12327–12332 (2004)
29. P. Metrangolo et al., Engineering functional materials by halogen bonding. J. Polym. Sci. A **45**, 1–15 (2007)
30. J.S. Murray et al., A predicted new type of directional noncovalent interaction. Int. J. Quantum Chem. **107**, 3046–3052 (2007)
31. J.S. Murray et al., σ-Hole bonding: Molecules containing group VI atoms. J. Mol. Model. **13**, 1033–1038 (2007)
32. J.S. Murray et al., Expansion of the σ-hole concept. J. Mol. Model. **15**, 723–729 (2009)
33. R.E. Rosenfeld Jr. et al., Directional preferences of nonbonded atomic contacts with divalent sulfur. 1. Electrophiles and nucleophiles. J. Am. Chem. Soc. **99**, 4860–4862 (1977)
34. T.N. Guru Row, R. Parthasarathy, Directional preferences of nonbonded atomic contacts with divalent sulfur in terms of its orbital orientations. 2. S–S Interactions and nonspherical shape of sulfur in crystals. Am. Chem. Soc. **103**, 477–479 (1981)
35. B.M. Goldstein et al., ^{77}Se NMR and crystallographic studies of selenazofurin and its 5-amino derivative. J. Am. Chem. Soc. **112**, 8265–8268 (1990)
36. M. Iwaoka et al., Quantitative evaluation of weak nonbonded Se–F interactions and their remarkable nature as orbital interactions. J. Am. Chem. Soc. **124**, 1902–1909 (2002). and references therein
37. J.R. Witt et al., The crystal structures of $BrC(CN)_3$, $ClC(CN)_3$ and $CH_3C(CN)_3$. Acta Cryst. **B28**, 950–955 (1972)
38. T. Clark et al., Why are dimethyl sulfoxide and dimethyl sulfone such good solvents? J. Mol. Model. **14**, 689–697 (2008)
39. G. Valerio et al., Halogen bonding in fluoroalkylhalides: A quantum chemical study of increasing fluorine substitution. J. Phys. Chem. A **104**, 1617–1620 (2000)
40. W. Wang et al., Theoretical study on the blueshifting halogen bond. J. Phys. Chem. A **108**, 1799–1805 (2004)
41. S.J. Grabowski, E. Bilewicz, Cooperativity halogen bonding effect–ab initio calculations on H_2CO···(ClF) n Complexes. Chem. Phys. Lett. **427**, 51–55 (2006)
42. K.E. Riley, K.M. Merz Jr., Insights into the strengths and origins of halogen bonding: The halobenzene-formaldehyde dimer. J. Phys. Chem. A **111**, 1688–1694 (2007)
43. K.E. Riley, P. Hobza, Investigations into the nature of halogen bonding including symmetry adapted perturbation theory analyses. J. Chem. Theor. Comput. **4**, 232–242 (2008)
44. J.S. Murray et al., Blue shifts vs. red shifts in σ-hole bonding. J. Mol. Model. **14**, 699–704 (2008)
45. A.F. Cozzolino et al., The nature of the supramolecular association of 1,2,5-chalcogenadiazoles. J. Am. Chem. Soc. **127**, 3184–3190 (2005)
46. C. Bleiholder et al., Theoretical investigations on chalcogen–chalcogen interactions: What makes these nonbonded interactions bonding? J. Am. Chem. Soc. **128**, 2666–2674 (2006)
47. J.S. Murray et al., Simultaneous σ-hole and hydrogen bonding by sulfur- and selenium-containing heterocycles. Int. J. Quantum Chem. **108**, 2770–2781 (2008)
48. I.S. Ignatyev, H.F. Schaefer III, Stable hexacoordinated neutral complexes between silyl halides and two water or two ammonia molecules: SiX_4Y_2 (X=H, F, Cl; Y=H_2O, NH_3). J. Phys. Chem. A **105**, 7665–7671 (2001)
49. R.F. Stewart, On the mapping of electrostatic properties from Bragg diffraction data. Chem. Phys. Lett. **65**, 335–342 (1979)
50. P. Politzer, D.G. Truhlar (eds), *Chemical Applications of Atomic and Molecular Electrostatic Potentials* (Plenum, New York, 1981)
51. R.F.W. Bader et al., Properties of atoms in molecules: Atomic volumes. J. Am. Chem. Soc. **109**, 7968–7979 (1987)

52. J.S. Murray, P. Politzer, Statistical analysis of the molecular surface electrostatic potential: An approach to describing noncovalent interactions in condensed phases. J. Mol. Struct. (Theochem) **425**, 107–114 (1998)
53. P. Politzer, J.S. Murray, Computational prediction of condensed phase properties from statistical characterization of molecular surface electrostatic potentials. Fluid Phase Equil. **185**, 129–137 (2001)
54. H. Hagelin et al., Family-independent relationships between computed molecular surface quantities and solute hydrogen bond acidity/basicity and solute-induced methanol O–H infrared frequency shifts. Can. J. Chem. **73**, 483–488 (1995)
55. M.J. Frisch et al., Gaussian 03, Revision C.02. (Gaussian, Wallingford, 2004)
56. P. Politzer et al., σ-Hole bonding between like atoms; a fallacy of atomic charges. J. Mol. Model. **14**, 659–665 (2008)
57. U. Onthong et al., X-ray and neutron diffraction studies and molecular dynamics simulations of liquid DMSO. Phys. Chem. Chem. Phys. **6**, 2136–2144 (2004)
58. S. Grimme, Semiempirical GGA-type density functional constructed with a long-range dispersion correction. J. Comput. Chem. **27**, 1787–1799 (2006)
59. A. Bondi, van der Waals volumes and radii. J. Phys. Chem. **68**, 441–451 (1964)
60. S.L. Price et al., The nature of –Cl···Cl– intermolecular interactions. J. Am. Chem. Soc. **116**, 4910–4918 (1994)
61. M. Fourmigué, P. Batail, Activation of hydrogen- and halogen-bonding interactions in tetrathiafulvalene-based crystalline molecular conductors. Chem. Rev. **104**, 5379–5418 (2004)
62. E.D. Stevens, Experimental electron density distribution of molecular chlorine. Mol. Phys. **37**, 27–45 (1979)
63. V.G. Tsirelson et al., Topological definition of crystal structure: Determination of the bonded interactions in solid molecular chlorine. Acta Cryst. A **51**, 143–153 (1995)
64. H. Toril, The role of atomic quadrupoles in intermolecular electrostatic interactions of polar and nonpolar molecules. J. Chem. Phys. **119**, 2192–2198 (2003)
65. C. Cohen-Addad et al., Nature of S···O interaction in short X-S···O contacts: Charge density experimental studies and theoretical interpretation. J. Chem. Soc. Perkin Trans. **2**, 191–196 (1984)
66. R.S. Mulliken, Molecular compounds and their spectra. III. The interaction of electron donors and acceptors. J. Phys. Chem. **56**, 801–822 (1952)
67. R.L. Flurry Jr., Molecular orbital theory of electron donor-acceptor complexes. I. A simple semiempirical treatment. J. Phys. Chem. **69**, 1927–1933 (1965)
68. S.V. Rosokha, J.K. Kochi, X-ray structures and electronic spectra of the π-halogen complexes between halogen donors and acceptors with π-receptors, in *Halogen Bonding: Fundamentals and Applications*, Structure and Bonding, vol. 126, ed. by P. Metrangolo, G. Resnat (Springer, Berlin, 2008), pp. 137–160
69. P. Politzer, A charge-transfer interpretation of the interactions of hemoglobin with oxygen and carbon monoxide. Biochim. Biophys. Acta **153**, 799–803 (1968)
70. A.R. Voth et al., Directing macromoelcular conformation by halogen bonds. Proc. Nat. Acad. Sci. U S A **104**, 6188–6193 (2007)
71. F.T. Burling, B.M. Goldstein, Computational studies of nonbonded sulfur–oxygen and selenium–oxygen interactions in the thiazole and selenazole nucleosides. J. Am. Chem. Soc. **114**, 2313–2320 (1992)
72. P. Metrangolo et al., Halogen bonding in crystal engineering, in *Halogen bonding: Fundamentals and Applications*, Structure and Bonding, vol. 126, ed. by P. Metrangolo, G. Resnati (Springer, Berlin, 2008), pp. 105–136
73. M. Fourmigué, Halogen bonding in conducting or magnetic molecular materials, in *Halogen Bonding: Fundamentals and Applications*, Structure and Bonding, vol. 126, ed. by P. Metrangolo, G. Resnati (Springer, Berlin, 2008), pp. 181–207

Chapter 7
σ-Bond Prevents Short π-Bonds: A Detailed Theoretical Study on the Compounds of Main Group and Transition Metal Complexes

Biswarup Pathak, Muthaiah Umayal, and Eluvathingal D. Jemmis

Abstract The unusual shortness of the bond length in several main group and transition metal compounds is explained on the basis of their π-alone bonding. The detailed electronic structure calculation on C_2, HBBH, and $Fe_2(CO)_6$ shows that each of them has two π-alone bonds (unsupported by an underlying σ-bond), whereas B_2 has two-half π-bonds. The C–C bond length in C_2 is 1.240 Å, shorter than any C–C double (σ + π, in C_2H_4, C–C = 1.338 Å) bonded species. The B–B bond distance in B_2 (1.590 Å, two half-π bonds) is shorter than any B–B single σ-bonded (~1.706 Å) species. The calculated Fe–Fe bond distance of 2.002 Å in $Fe_2(CO)_6$ is shorter than those of some experimentally known M–M single bonded compounds in the range of 2.904–3.228 Å. Here, our detailed studies on the second and third row diatomics (five, six, seven and eight valence electrons species) and transition metal complexes show that π-alone bonds left to themselves are shorter than σ-bonds; in many ways, σ-bonds prevent π-bonds from adopting their optimal shorter distances.

7.1 Introduction

The concept of σ-, π- and δ-bonds is ingrained into the thought process of chemists. The cylindrically symmetrical σ-bond is traditionally estimated to be stronger than the π-bond, which in turn, is stronger than the δ-bond. The linear overlap of orbitals in the σ-bond is supposed to be more effective than the sideways overlap available in the π- and δ-bonds (Scheme 7.1a). Closely related to the discussion of σ-, π- and δ-bonds and their bond strengths is the issue of bond

B. Pathak, M. Umayal and E.D. Jemmis (✉)
Department of Inorganic and Physical Chemistry, Indian Institute of Science Education and Research Thiruvananthapuram, Transit Campus, CET, TVM 695016, Kerala, India
e-mail: jemmis@ipc.iisc.ernet.in

J. Leszczynski and M.K. Shukla (eds.), *Practical Aspects of Computational Chemistry*, 165
DOI: 10.1007/978-90-481-2687-3_7,

Scheme 7.1 Overlapping Orbitals

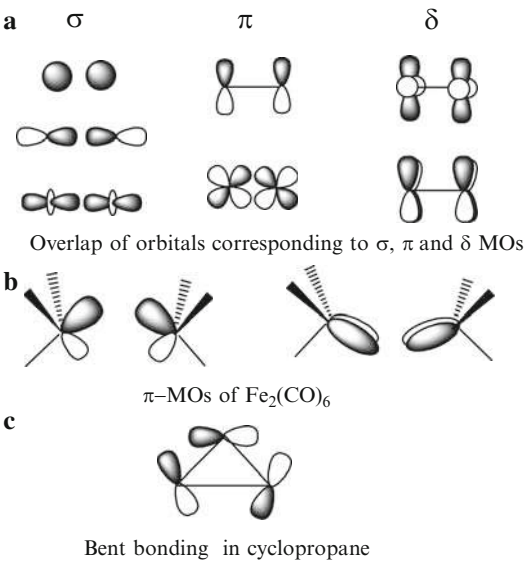

length. The decrease of bond length in going from a single σ-bond to multiple bonds involving σ and π components is exemplified by $H_3C–CH_3$, $H_2C=CH_2$, and HC≡CH with C–C bond length of 1.538, 1.338, and 1.203 Å, respectively [1–3]. In transition metal chemistry, there are familiar examples of short M–M quadruple bonds constituted from one σ-, two π-, and one δ-bonds as in $Re_2Cl_8^{-2}$ of 2.240 Å [4]. Very recently, Roos et al. [5] concluded that the maximum number of covalent chemical bonds between two shared atoms will be six. To find the molecules with the highest bond order, they theoretically studied the transition metal dimers of chromium (Cr_2), molybdenum (Mo_2) and tungsten (W_2), respectively. They predict that the maximum number of chemical bonds will be six because the atoms of these transition metals have six outer, or "valence" orbitals, all of which are available for bonding. In this perspective, Frenking et al. have reported [6] that six is the maximum limit for the covalent bonds between equal atoms, but a measure of bond order between unequal atoms requires more developed model that includes electrostatic interaction. The calculated short M–M bond distances are 1.66, 1.95, and 2.01 Å for Cr_2, Mo_2 and W_2, respectively. Power [7] has demonstrated that the multiple bonding between transition metals can be achieved by reducing the number of ligands, so that the number of valence orbitals and electrons available to form metal–metal bonds is optimized. It is always seen that the bond length decreases as the bond order increases. In these discussions, the σ-bond is considered to be the strongest and the bond strength is thought to be inversely proportional to the bond length. However, the variation of orbital overlap as a function of internuclear distance (Fig. 7.1) shows that maximum overlap occurs at shorter distances for π- and δ-bonds.

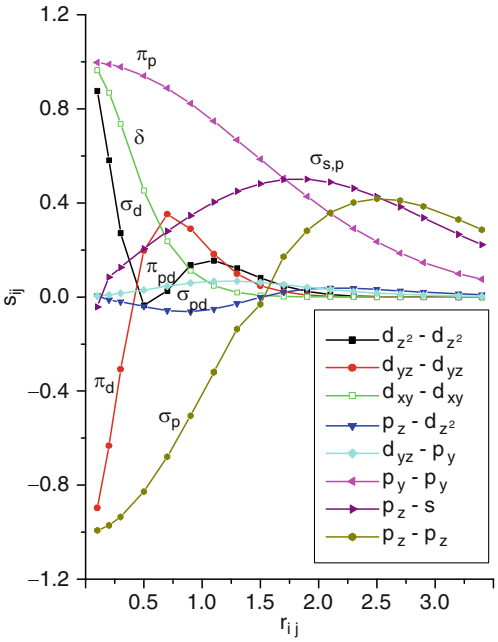

Fig. 7.1 Variation of orbital overlap (s_{ij}) as a function of internuclear distance (r_{ij}) using contracted Gaussian orbitals corresponding to a minimal basis of Fe

The shortness of bond length due to π-alone bonding has been in the literature for some time. In 1980, Bruna et al. [8] theoretically reported the possible lowest lying states of the isovalent series of diatomics CN^+, Si_2, SiC, CP^+, and SiN^+. Comparisons with corresponding experimental data for C_2 led to the conclusion that π^4 ($^1\Sigma^+$) configuration has uniformly shorter R_e than their $\pi^3\sigma^1$ ($^3\prod$) counterparts by 0.07–0.10 Å. Corresponding bond lengths for the $\pi^2\sigma^2$ ($^1\Sigma^+$) species are seen to increase by an additional 0.1 Å. The trend in relative bond lengths was explained on the basis of stronger bonding character of the π-bonding MO than their corresponding σ species. In 2000, Sason Shaik et al. investigated [9] whether Pauling's statement [10] "the energy of an actual bond between unlike atoms is greater than (or equal to) the energy of a normal covalent bond between these atoms" is valid for π-bonds or not. They have calculated the π-bond energies in the inter- and intra-row double bonded species $H_mA{=}BH_n$ (where A, B = C, N, O Si, P and S) using VB theory. Their test reveals that Pauling's statement extends to π-bonds made from constituents belonging to the same row of the Periodic Table, but breaks down for comparisons involving inter-row π-bonds. This breakdown originates in the constraint applied by the σ frame which results in overstretched heteronuclear π bonds relative to homonuclear π bonds, thus disabling a comparison in the light of Pauling's statement. In a recent article, Pyykkö et al. reported the triple-bond covalent radii for nearly all elements from Be to E112 (eka-mercury) [11]. Comparisons are made to fit with experimental data. There are many π-alone double bonded species which have comparable bond distances as those of triple

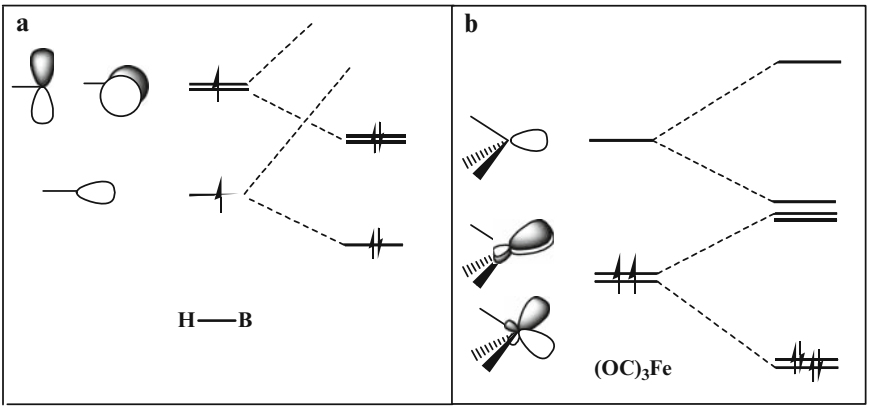

Scheme 7.2 Interaction diagram for the formation of (**a**) H_2B_2 and (**b**) $Fe_2(CO)_6$

bonded species. It is, therefore, logical to anticipate that π-bonds (unsupported by an underlying σ-bond) could be shorter than σ-bonds, but the difficulty in designing structures with π-alone-bonds has given below. The σ-levels (sp^x hybrid orbitals) of common main group fragments, such as –BH, –CH and $–CH_2$, are lower in energy than the p orbitals that form the π-bonds. As a result, π-bonds always come with the underlying σ-bond (Scheme 7.2a) which largely dictates a "base line" distance. Transition metal fragments provide an opportunity to reverse this situation. For example, the degenerate π-type frontier orbitals of the $Fe(CO)_3$ fragment are lower in energy than the symmetric σ-orbital (Scheme 7.2b). It is, therefore, logical to anticipate shorter than usual M–M bond lengths in dimers of such fragments.

In this chapter, we have studied a list of inter- and intra-row main group (five, six, seven and eight valence electrons species) as well as few transition metal compounds. We attempted to explain their unusual shortness on the basis of their detailed electronic structures.

7.2 Computational Details

The main group diatomic compounds are optimized at the CCSD(T) level [12–14] using the GAUSSIAN 03 program [15]. Frequency calculations confirmed the nature of the stationary points. The standard 6-311++G (p, d) basis set was employed for all atoms. In addition, for comparisons and calibration, we have done optimization as well as frequency calculation at the QCISD(T) level [16] using same basis set. The transition metal complexes are studied using B3LYP/LANL2DZ [17, 18] level of theory. Natural Bond Orbital (NBO) [19] analysis is also done at the same level.

7.3 Results and Discussion

7.3.1 Short Bonds in Main Group Compounds

The influence of π-bonds in reducing bond lengths can be seen in many familiar examples. The C–C bond in cyclopropane is anticipated to be weak owing to strain. However, the C–C distance is shown to be shorter (1.510 Å) [20] than is the case for regular C–C bonds (1.538 Å). Optimum overlap for the orbitals, oriented in a sideways manner in the bent bonds (Scheme 7.1c), occurs at shorter distances than for a conventional σ-bond, explaining the short distance of a strained bond. The shorter distances necessary to obtain optimum overlap for these π-type MOs result in shorter than expected bond lengths. The fact that cyclopropane has several characteristics that are similar to olefins, is in tune with this. If the shorter distances are a requirement for optimum overlap for π-MOs, these requirements must also exist in multiple bonds involving σ- and π-bonds. The π-bonds, however, are forced by the overwhelming σ-bonds to be at non-optimal overlapping distances.

First, row diatomics provide examples where π-orbitals are filled before σ. The diatomic C_2 has a ground state $^1\Sigma_g^+$ with a double bond [21–23], both components of which are π-bonds (Scheme 7.3a). Relative to the standard triple bond in N_2, the $3\sigma_g$ molecular orbital in C_2 is unoccupied. The bond distance in C_2 of 1.240 Å is shorter than any σ + π carbon–carbon double bond by a large margin. Another example is B_2 [24, 25] with two electrons less than C_2; B_2 has two half π-bonds (Scheme 7.3d). The distance of 1.590 Å in B_2 is shorter than any B–B single σ-bond. Among the heavier main group elements with weak σ-bonds, there are examples of distorted structures with short π distances [26], arising from dative interactions.

The preference of π-bonds for short distances is further supported by the study of the excited states of C_2 [22]. A triplet state obtained by shifting (Scheme 7.3b) one

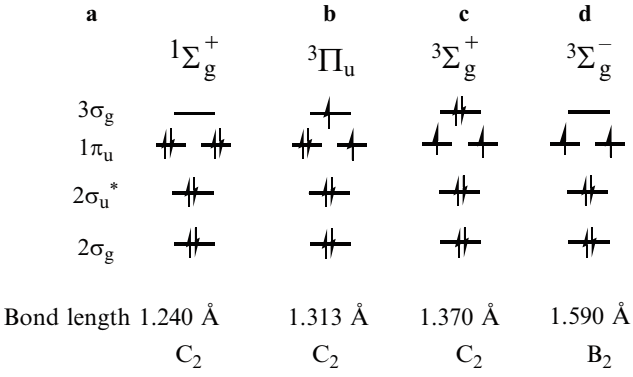

Scheme 7.3 Experimental bond lengths of C_2 (**a**) $^1\Sigma_g^+$, (**b**) $^3\prod_u$, (**c**) $^3\Sigma_g^+$ and of B_2 (**d**) $^3\Sigma_g^-$. Bond length of C_2 (**c**) $^3\Sigma_g^+$ is obtained from calculations at B3LYP/6-311+G* method

of the electrons from the π-bonding MO of C_2 to the vacant σ-bonding MO should increase the C–C distance. This is indeed found to be the case. Thus, $^3\Pi_u$ state of C_2 has a bond length of 1.313 Å. Another triplet state ($^3\Sigma_g^+$) obtained by shifting another electron from π to σ-level is calculated to have a bond length of 1.370 Å (Scheme 7.3c).

7.3.2 *Five Valence Electron Diatomic Species*

Five valence electrons diatomic species can have a half π-alone bond. The ground electronic state of five valence electron species, AlBe, BeB, MgB and CaB, is $^2\prod (1\sigma_g^2 1\sigma_u^2 1\pi^1)$, calculated theoretically [27, 28]. To the best of our knowledge, no experimentally characterized ground state structure has been reported for these species. But the theoretical study predicts that these species may contain half π-alone bonds. The electronic ground state of the five valence cationic species, B_2^+, Al_2^+, Ga_2^+, BAl^+, and $AlGa^+$, has been reported [29] as $^2\Sigma_g^+$ ($1\sigma_g^2 1\sigma_u^2 2\sigma_g^1$) where the valence electrons are occupied in the σ-level. The anionic five valence electrons species Be_2^- has been studied theoretically [30, 31] where the calculated ground electronic state changes with the method of calculation. The metastable state of Be_2^- has been characterized experimentally [32] with a life time >180 μs.

Our calculation on these five valence electron species shows that the bond length decreases considerably when the valence electron shifted from σ to the π-level (Table 7.1). The $^2\prod$ ($1\sigma_g^2 1\sigma_u^2 1\pi^1$) electronic state is more stable state for the AlBe, AlMg, BeB and Al_2^+ species, whereas $^2\Sigma_g^+$ ($1\sigma_g^2 1\sigma_u^2 2\sigma_g^1$) is more stable for the rest.

Table 7.1 The (E1–E2) bond lengths (Å) of the $^2\Sigma_g^+$ ($1\sigma_g^2 1\sigma_u^2 2\sigma_g^1$) and $^2\prod$ ($1\sigma_g^2 1\sigma_u^2 1\pi^1$) electronic state and their relative energies (R.E. in kcal mol^{-1}) calculated at CCSD(T)/6-311++G** level of theory

		E1–E2				E1–E2	
E1E2	State	Cal.	R.E.	E1E2	State	Cal.	R.E.
AlBe	$1\sigma_g^2 1\sigma_u^2 2\sigma_g^1$	2.626	2.09	BAl^+	$1\sigma_g^2 1\sigma_u^2 2\sigma_g^1$	2.724	0.00
	$1\sigma_g^2 1\sigma_u^2 1\pi^1$	2.430	0.00		$1\sigma_g^2 1\sigma_u^2 1\pi^1$	2.424	11.25
AlMg	$1\sigma_g^2 1\sigma_u^2 2\sigma_g^1$	3.302	3.33	BC^{2+}	$1\sigma_g^2 1\sigma_u^2 2\sigma_g^1$	NC	
	$1\sigma_g^2 1\sigma_u^2 1\pi^1$	2.900	0.00		$1\sigma_g^2 1\sigma_u^2 1\pi^1$	NC	
BeB	$1\sigma_g^2 1\sigma_u^2 2\sigma_g^1$	2.132	8.21	SiB^{2+}	$1\sigma_g^2 1\sigma_u^2 2\sigma_g^1$	NC	
	$1\sigma_g^2 1\sigma_u^2 1\pi^1$	1.946	0.00		$1\sigma_g^2 1\sigma_u^2 1\pi^1$	NC	
MgB	$1\sigma_g^2 1\sigma_u^2 2\sigma_g^1$	2.412	27.75	AlC^{2+}	$1\sigma_g^2 1\sigma_u^2 2\sigma_g^1$	NC	
	$1\sigma_g^2 1\sigma_u^2 1\pi^1$	2.152	0.00		$1\sigma_g^2 1\sigma_u^2 1\pi^1$	NC	
B_2^+	$1\sigma_g^2 1\sigma_u^2 2\sigma_g^1$	2.174	0.00	$AlSi^{2+}$	$1\sigma_g^2 1\sigma_u^2 2\sigma_g^1$	NC	
	$1\sigma_g^2 1\sigma_u^2 1\pi^1$	1.787	8.48		$1\sigma_g^2 1\sigma_u^2 1\pi^1$	NC	
Al_2^+	$1\sigma_g^2 1\sigma_u^2 2\sigma_g^1$	3.188	0.00	$MgBe^-$	$1\sigma_g^2 1\sigma_u^2 2\sigma_g^1$	2.805	0.75
	$1\sigma_g^2 1\sigma_u^2 1\pi^1$	2.796	14.58		$1\sigma_g^2 1\sigma_u^2 1\pi^1$	2.758	0.00

NC not converged

7.3.3 Six Valence Electron Diatomic Species

B_2 and its isovalent systems have been studied theoretically, as well as experimentally. The diatomic B_2 has a ground state $^3\Sigma_g^-(\sigma_g^2\sigma_u^2\pi_u^2)$ with two half π-bonds [24]. The distance of 1.590 Å in B_2 is shorter than any B–B single (~1.706 Å) [33] σ-bond. The calculated B–B bond lengths in B_2^+ (π^1), B_2 ($\pi^1\pi^1$), B_2^- ($\pi^2\pi^1$), and B_2^{2-} ($\pi^2\pi^2$) are 1.790, 1.614, 1.586, and 1.587 Å (Scheme 7.2), respectively. So, the bond length decreases as their π-alone bond order increases. The B–B bond length in B_2 differs considerably while comparing with its other different electronic states. It has been found that the extra occupancy in π-levels leads to a much shorter bond

Table 7.2 The (E1–E2) bond lengths (Å) of the various electronic state and their relative energies (R.E. in kcal mol^{-1}) calculated at CCSD(T)/6-311++G** level of theory along with the experimental bond lengths wherever available

E1E2	State	E1–E2			E1E2	State	E1–E2	
		Exp.	Cal.	R.E.			Cal	R.E.
B_2	$(\pi_u^1\pi_u^1)$	1.590[16]	1.611	00.00	C_2^{2+}	$(\pi_u^1\pi_u^1)$	1.465	10.56
	$(\sigma_g^1\pi_u^1)$		1.770	08.33		$(\sigma_g^1\pi_u^1)$	1.473	00.00
	(σ_g^2)		1.917	25.70		(σ_g^2)	NC	NC
Al_2	$(\pi^1\pi^1)$		2.480	01.48	Si_2^{2+}	$(\pi_u^1\pi_u^1)$	2.417	23.05
	$(\sigma_g^1\pi_u^1)$	2.701[20]	2.705	00.00		$(\sigma_g^1\pi_u^1)$	2.751	00.00
	(σ_g^2)		2.956	08.52		(σ_g^2)	3.059	−11.45
AlB	$(\pi^1\pi^1)$		2.044	00.00	CSi^{2+}	$(\pi_u^1\pi_u^1)$	1.954	20.75
	$(\pi_u^1\sigma_g^1)$		2.220	00.53		$(\pi_u^1\sigma_g^1)$	2.276	00.00
	(σ_g^2)		2.425	14.17		(σ_g^2)	2.535	07.42
BeC	$(\pi_u^1\pi_u^1)$		1.520	38.5800	BBe^-	$(\pi_u^1\pi_u^1)$	1.839	00.00
	$(\pi_u^1\sigma_g^1)$		1.678	0.00		$(\pi_u^1\sigma_g^1)$	1.984	07.92
	(σ_g^2)		NC	–		(σ_g^2)	2.070	23.67
SiBe	$(\pi_u^1\pi_u^1)$		2.135	05.29	MgB^-	$(\pi_u^1\pi_u^1)$	2.277	00.00
	$(\sigma_g^1\pi_u^1)$		2.287	00.00		$(\pi_u^1\sigma_g^1)$	2.484	01.73
	(σ_g^2)		NC	–		(σ_g^2)	NC	–
MgC	$(\pi_u^1\pi_u^1)$		2.102	00.00	$AlBe^-$	$(\pi_u^1\pi_u^1)$	2.308,	00.00
	$(\pi_u^1\sigma_g^1)$		2.392	27.39		$(\sigma_g^1\pi_u^1)$	2.470	04.89
	(σ_g^2)		2.117	33.88		(σ_g^2)	2.569	20.36
MgSi	$(\pi_u^1\pi_u^1)$		2.560	15.79	$AlMg^-$	$(\pi_u^1\pi_u^1)$	2.741	00.00
	$(\pi_u^1\sigma_g^1)$		2.863	00.00		$(\pi_u^1\sigma_g^1)$	2.988	02.90
						(σ_g^2)	3.095	15.84
BC^+	$(\pi_u^1\pi_u^1)$		1.503	00.00	Be_2^{2-}	$(\pi_u^1\pi_u^1)$	2.014	27.73
	$(\sigma_g^1\pi_u^1)$		1.733	13.08		$(\sigma_g^1\pi_u^1)$	2.291	00.00
	(σ_g^2)		2.093	42.86		(σ_g^2)	2.328	03.00
BSi^+	$(\pi_u^1\pi_u^1)$		1.935	07.19	Mg_2^{2-}	$(\pi_u^1\pi_u^1)$	3.380	02.61
	$(\sigma_g^1\pi_u^1)$		2.123	00.00		$(\sigma_g^1\pi_u^1)$	3.424	00.00
	(σ_g^2)		2.462	13.50		(σ_g^2)	NC	
AlC^+	$(\pi_u^1\pi_u^1)$		1.964	00.00	$MgBe^{2-}$	$(\pi_u^1\pi_u^1)$	2.794	03.13
	$(\sigma_g^1\pi_u^1)$		2.614	02.84		$(\sigma_g\pi_u^1)$	2.799	00.00
	(σ_g^2)		2.727	32.14		(σ_g^2)	2.765	01.13
$AlSi^+$	$(\pi_u^1\pi_u^1)$		2.434	03.98				
	$(\sigma_g^1\pi_u^1)$		2.826	00.00				
	(σ_g^2)		3.026	15.29				

than if it would have occupied a σ-level (Table 7.2). The neutral isovalent systems are Al_2, AlB, MgSi, MgC, BeSi, and BeC (Table 7.2). The ground state of Al_2 is $^3\prod_u$, characterized theoretically as well as experimentally. AlB, MgSi, BeSi, and MgC have $^3\Sigma^-$ ground state which has been calculated theoretically [34]. The isovalent diatomic cations are BC^+, $AlSi^+$, AlC^+, BSi^+, SiC^{2+}, C_2^{2+}, and Si_2^{2+}. The theoretically calculated BC^+ has $^3\Sigma^-$ ground state [35]. We have studied three different electronic states by shifting the electrons from a π- to σ-level. The $^3\Sigma_g^-$ ($\pi_u^1\pi_u^1$) state is the relatively most stable state for B_2, AlB, MgB, MgC, BC^+, AlC^+, BBe^-, MgB^-, and $AlMg^-$, whereas $^3\prod_u$ ($\sigma_g^1\pi_u^1$) is for the other diatomic molecules (Table 7.2). So, it is the early intra or inter-row diatomic molecules which have more tendencies to form π-bonds rather than σ [36]. Here, we need a molecule where $^3\Sigma_g^-$ and $^3\prod_u$ states lie very close in energy because this can be a borderline molecule between the σ- and π-alone bonded species. The $^3\Sigma_g^-$ state of AlB is more stable by 0.53 kcal mol^{-1} than its $^3\prod_u$ state, whereas the most stable $^3\prod_u$ ($\sigma_g^1\pi_u^1$) electronic state of Al_2 is stable by1.48 kcal mol^{-1}. These are the two examples where the energy difference between those two states is very less. In AlB, π-level comes just below σ, whereas in Al_2, σ-level comes below π-level. These are the two examples where the σ- and π-levels just crosses each other.

7.3.4 Seven Valence Electron Diatomic Species

Here, we have studied four different electronic states, [$^2\prod$ ($\pi_u^2\pi_u^1$), $^4\Sigma^-$($\sigma_g^1\pi_u^1\pi_u^1$), $^2\prod$ ($\sigma_g^2\pi_u^1$), and $^2\Sigma^-$ ($\sigma_g^1\pi_u^2$)], for each of the seven valence electrons species (Table 7.3). The ground electronic state of SiB, BC, SiAl, AlC is $^4\Sigma^-$ ($\sigma^1\pi^1\pi^1$), which has been characterized experimentally as well as theoretically [37, 38]. The theoretical ground state of BN^+ is $^4\Sigma^-$ [39]. The $^4\Sigma^-$ electronic state is more stable state for all the seven valence electron species as some of these are characterized experimentally. The calculated bond lengths of $^4\Sigma^-$ electronic state of BC (1.518 Å) and AlC (1.974 Å) are very close to the experimental data available for BC (1.491 Å) and AlC (1.955 Å). For these diatomic species, the bond length increases considerably when the electrons are shifted from a π- to σ-level as seen in the previously discussed diatomic species, even though energy decreases.

7.3.5 Eight Valence Electron Diatomic Species

The ground state of C_2 is $^1\Sigma_g^+$ where all the four valence electrons are in π-levels. The isovalent neutral diatomic species are Si_2, BN, BP, AlN, and AlP. The experimentally [24, 36] characterized ground state and an excited state of Si_2 is $^3\Sigma_g^-$ ($\sigma_g^2\pi_u^1\pi_u^1$, Si–Si = 2.246 Å) and $^3\prod_u$ ($\pi_u^3\sigma_g^1$, Si–Si = 2.155 Å), respectively. So, in the $^3\prod_u$ electronic state, the Si–Si bond length is shortened by 0.091 Å which is the result of an extra occupancy in the π-levels. Our calculations show that $^3\prod_u$ is

Table 7.3 The (E1–E2) bond lengths (Å) of the various electronic state and their relative energies (R.E. in kcal mol^{-1}) calculated at CCSD(T)/6-311++G** level of theory along with the experimental bond lengths wherever available

E1E2	State	E1–E2			E1E2	State	E1–E2	
		Exp.	Cal.	R.E.			Cal.	R.E.
BC	$(\pi_u^2\pi_u^1)$		1.427	0.00	CN^{2+}	$(\pi_u^2\pi_u^1)$	1.320	0.00
	$(\sigma_g^1\pi_u^2)$		1.517	19.26		$(\sigma_g^1\pi_u^2)$	1.442	19.87
	$(\sigma_g^1\pi_u^1\pi_u^1)$	1.491	1.518	−11.95		$(\pi_u^1\pi_u^1\sigma_g^1)$	1.495	−23.28
	$(\sigma_g^2\pi_u^1)$		1.639	29.45		$(\sigma_g^2\pi_u^1)$	2.125	1.37
BSi	$(\pi_u^2\pi_u^1)$		1.846	04.37	CP^{2+}	$(\pi_u^2\pi_u^1)$	1.690	28.50
	$(\sigma_g^1\pi_u^2)$		1.927	0.00		$(\sigma_g^1\pi_u^2)$	1.765	0.00
	$(\sigma_g^1\pi_u^1\pi_u^1)^{22}$		1.926	−16.08		$(\sigma_g^1\pi_u^1\pi_u^1)$	1.772	−14.63
	$(\sigma_g^2\pi_u^1)$		2.129	08.56		$(\sigma_g^2\pi_u^1)$	2.114	13.47
AlC	$(\pi_u^2\pi_u^1)$		1.873	06.29	SiN^{2+}	$(\pi_u^2\pi_u^1)$	1.718	20.84
	$(\sigma_g^1\pi_u^2)$		1.861	0.00		$(\sigma_g^1\pi_u^2)$	1.716	17.06
	$(\pi_u^1\pi_u^1\sigma_g^1)$	1.955	1.974	−27.46		$(\pi_u^1\pi_u^1\sigma_g^1)$	2.152	−43.06
	$(\sigma_g^2\pi_u^1)$		2.116	15.82		$(\sigma_g^2\pi_u^1)$	2.324	0.00
AlSi	$(\pi_u^2\pi_u^1)$		2.287	02.41	SiP^{2+}	$(\pi_u^2\pi_u^1)$	2.493	28.50
	$(\sigma_g^1\pi_u^2)$		2.429	01.33		$(\sigma_g^1\pi_u^2)$	2.414	5.37
	$(\sigma_g^1\pi_u^1\pi_u^1)^{22}$		2.419	−22.01		$(\sigma_g^1\pi_u^1\pi_u^1)$	2.398	−7.22
	$(\sigma_g^2\pi_u^1)$		2.620	0.00		$(\sigma_g^2\pi_u^1)$	2.674	0.00
BN^+	$(\pi_u^2\pi_u^1)$		1.363	0.00	B_2^-	$(\pi_u^2\pi_u^1)$	1.582	0.00
	$(\sigma_g^1\pi_u^2)$		1.444	22.35		$(\sigma_g^1\pi_u^2)$	1.683	09.95
	$(\pi_u^1\pi_u^1\sigma_g^1)$		1.472	−19.30		$(\sigma_g^1\pi_u^1\pi_u^1)$	1.644	−13.95
	$(\sigma_g^2\pi_u^1)$		2.046	51.96		$(\sigma_g^2\pi_u^1)$	1.731	13.22
BP^+	$(\pi_u^2\pi_u^1)$		1.762	00.00	Al_2^-	$(\pi_u^2\pi_u^1)$	2.454	07.37
	$(\sigma_g^1\pi_u^2)$		1.869	07.18		$(\sigma_g^1\pi_u^2)$	2.570	0.00
	$(\sigma_g^1\pi_u^1\pi_u^1)$		1.884	−21.70		$(\sigma_g^1\pi_u^1\pi_u^1)$	2.549	10.51
	$(\sigma_g^2\pi_u^1)$		2.304	20.68		$(\sigma_g^2\pi_u^1)$	2.708	−07.59
AlN^+	$(\pi_u^2\pi_u^1)$		1.767	0.00	AlB^-	$(\pi_u^2\pi_u^1)$	2.017	0.00
	$(\sigma_g^1\pi_u^2)$		NC	–		$(\sigma_g^1\pi_u^2)$	2.138	08.98
	$(\pi_u^1\pi_u^1\sigma_g^1)$		3.162	−36.45		$(\sigma_g^1\pi_u^1\pi_u^1)$	2.083	−15.96
	$(\sigma_g^2\pi_u^1)$		1.952	24.62		$(\sigma_g^2\pi_u^1)$	2.218	07.64
AlP^+	$(\pi_u^2\pi_u^1)$		2.191	0.00	BBe^{2-}	$(\pi_u^2\pi_u^1)$	1.839	06.91
	$(\sigma_g^1\pi_u^2)$		2.430	19.56		$(\sigma_g^1\pi_u^2)$	1.851	13.29
	$(\pi_u^1\pi_u^1\sigma_g^1)$		2.636	−32.35		$(\pi_u^1\pi_u^1\sigma_g^1)$	1.905	−08.12
	$(\sigma_g^2\pi_u^1)$		2.899	26.67		$(\sigma_g^2\pi_u^1)$	1.933	0.00
SiC^+	$(\pi_u^2\pi_u^1)$		1.739	04.44	MgB^{2-}	$(\pi_u^2\pi_u^1)$	2.320	02.14
	$(\sigma_g^1\pi_u^2)$		1.867	02.46		$(\sigma_g^1\pi_u^2)$	2.318	0.00
	$(\sigma_g^1\pi_u^1\pi_u^1)$		1.819	−32.97		$(\pi_u^1\pi_u^1\sigma_g^1)$	2.330	−6.51
	$(\sigma_g^2\pi_u^1)$		1.999	0.00		$(\sigma_g^2\pi_u^1)$	2.418	01.81
C_2^+	$(\pi_u^2\pi_u^1)$		1.319	0.00	$AlBe^{2-}$	$(\pi_u^2\pi_u^1)$	2.328	00.95
	$(\sigma_g^1\pi_u^2)$		1.461	19.56		$(\sigma_g^1\pi_u^2)$	2.407	02.65
	$(\sigma_g^1\pi_u^1\pi_u^1)$		1.419	−15.22		$(\sigma_g^1\pi_u^1\pi_u^1)$	2.379	−10.91
	$(\sigma_g^2\pi_u^1)$		1.556	26.67		$(\sigma_g^2\pi_u^1)$	2.428	0.00
Si_2^+	$(\pi_u^2\pi_u^1)$		2.191	13.17	$AlMg^{2-}$	$(\pi_u^2\pi_u^1)$	2.794	0.49
	$(\sigma_g^1\pi_u^2)$		2.360	06.58		$(\sigma_g^1\pi_u^2)$	2.895	10.00
	$(\sigma_g^1\pi_u^1\pi_u^1)$		2.277	−14.74		$(\sigma_g^1\pi_u^1\pi_u^1)$	2.827	−9.45
	$(\sigma_g^2\pi_u^1)$		2.474	0.00		$(\sigma_g^2\pi_u^1)$	2.886	00.00

more stable by only 0.66 kcal mol^{-1} than the $^3\Sigma_g^-$ state. The previous theoretical studies show that these are the two lowest lying electronic states for Si_2, and $^3\Sigma_g^-$ is the ground state. Though the energy difference between these two states is very less (0.66 kcal mol^{-1}), the bond lengths differ considerably because of an electron's occupancy in the σ- or π-level. The experimentally characterized ground state of BN and AlN is $^3\prod_u$. The hetero-diatomics, BP and AlP, to-date, has not been characterized experimentally. The theoretically calculated ground state of BP and AlP is $^3\prod_u$ [40]. In all the eight valence electron diatomic species, the bond length decreases as the σ-bond order increases or π-bond order decreases. The available experimental data support these results. The calculated bond lengths (Table 7.4) of C_2, Si_2, BN, and CN^+ are very close to the experimental data available for them. The C–C experimental bond length in C_2 decreases by 0.069 Å (Table 7.4), close to the calculated value of 0.070 Å, when one of the π-electrons shifts to the σ-level. Similarly, the experimental bond length in Si_2, BN, CN^+ supports our results that the element-element bond lengths increase considerably (Table 7.4) when one of the π-electrons shifts to the σ-level.

7.3.6 Short Bonds in Transition Metal Complexes

In the ML_3 (d^8) transition metal fragments, the degenerate π-type frontier orbitals are lower in energy than the symmetric σ-orbital (Scheme 7.2b). It is, therefore, logical to expect π-alone bonds in the transition metal complexes. The $Fe_2(CO)_6$ is calculated to be a minimum in its potential energy surface [41], with relatively short predicted metal–metal distance of 2.002 Å (Fig. 7.2). Compared with experimentally known compounds, such as $Mn_2(CO)_{10}$ (Mn−Mn = 2.904 Å) or $M_2(Cp)_2(CO)_6$ (M=Cr, Mo and W), which have only M−M single bonds in the range of 3.221–3.228 Å, the metal–metal bond length in $Fe_2(CO)_6$ is very short indeed [42–44]. The short bond length and a simple-minded application of the 18-electron rule would suggest a Fe–Fe quadruple bond. A detailed interaction diagram (Fig. 7.2) provides an occupancy of $1a_1'$, $1e'$, $1e''$, $1a_2''$ and $2e'$ levels (counting from HOMO-7, as $1a_1'$) for the 16 valence electrons, corresponding to σ, π/δ, π*/δ*, σ*, and two π levels. Thus, the formal net M–M bonding is provided by two π-type molecular orbitals, (Scheme 7.1b). At the long distances, direct CO···CO interactions in $(OC)_3Fe\text{-}Fe(CO)_3$ are minimal, so that the eclipsed conformation with better overlap is favored. This is to be contrasted with the rotational preferences of ethane [45–47].

Independent of the conformation, the bond multiplicity must be only two. If the shorter distances are a requirement for optimum overlap for π-MOs, these requirements must also exist in multiple bonds involving σ- and π-bonds. The π-bonds, however, are forced by the overwhelming σ-bonds to be at non-optimal overlapping distances. While there are many factors that contribute to the observed bond lengths in a binuclear transition metal complex, shorter distances would be mandated by π- and δ-MOs for optimum overlap. The π-alone-bonding proposed for $Fe_2(CO)_6$ allows π-bonds to attain their natural shorter distances. The overlap of

Table 7.4 The (E1–E2) bond lengths (Å) of the various electronic state and their relative energies (R.E. in kcal mol^{-1}) calculated at CCSD(T)/6-311++G** level of theory along with the experimental bond lengths wherever available

Species	State	E1–E2		R.E	Species	State	E1–E2	
		Exp.	Cal.				Cal.	R.E.
C_2	$(\pi_u^2\pi_u^2)$	1.243	1.259	00.00	CS^{2+}	$(\pi_u^2\pi_u^2)$	1.540	20.41
	$(\pi_u^2\sigma_g^1\pi_u^1)$	1.312	1.329	01.84		$(\pi_u^2\sigma_g^1\pi_u^1)$	1.617	00.00
	$(\sigma_g^2\pi_u^1\pi_u^1)$		1.383	17.47		$(\sigma_g^2\pi_u^1\pi_u^1)$	1.980	3.97
	$(\pi_u^2\sigma_g^2)$		1.397	36.95		$(\pi_u^2\sigma_g^2)$	1.916	35.86
Si_2	$(\pi_u^2\pi_u^2)$		2.088	14.61	SiO^{2+}	$(\pi_u^2\pi_u^2)$	1.548	20.75
	$(\pi_u^2\sigma_g^1\pi_u^1)$	2.155	2.173	00.00		$(\pi_u^2\sigma_g^1\pi_u^1)$	1.872	00.00
	$(\sigma_g^2\pi_u^1\pi_u^1)$	2.246	2.264	0.66		$(\sigma_g^2\pi_u^1\pi_u^1)$	2.264	−21.85
	$(\pi_u^2\sigma_g^2)$		2.305	13.92		$(\pi_u^2\sigma_g^2)$	2.234	36.59
BN	$(\pi_u^2\pi_u^2)$	1.283	1.276	00.00	SiS^{2+}	$(\pi_u^2\pi_u^2)$	1.962	28.57
	$(\pi_u^2\sigma_g^1\pi_u^1)$	1.329	1.338	00.20		$(\pi_u^2\sigma_g^1\pi_u^1)$	2.166	00.00
	$(\sigma_g^2\pi_u^1\pi_u^1)$		1.489	24.99		$(\sigma_g^2\pi_u^1\pi_u^1)$	2.520	−26.23
	$(\pi_u^2\sigma_g^2)$		1.446	61.48			2.465	11.16
BP	$(\pi_u^2\pi_u^2)$		1.689	07.81	B_2^{2-}	$(\pi_u^2\pi_u^2)$	1.582	07.34
	$(\pi_u^2\sigma_g^1\pi_u^1)$		1.757	00.00		$(\pi_u^2\sigma_g^1\pi_u^1)$	1.634	00.00
	$(\sigma_g^2\pi_u^1\pi_u^1)$		1.964	18.04		$(\sigma_g^2\pi_u^1\pi_u^1)$	1.651	−2.62
	$(\pi_u^2\sigma_g^2)$		1.938	43.43		$(\pi_u^2\sigma_g^2)$	1.680	11.24
AlN	$(\pi_u^2\pi_u^2)$		NC	–	Al_2^{2-}	$(\pi_u^2\pi_u^2)$	2.468	09.18
	$(\pi_u^2\sigma_g^1\pi_u^1)$		1.662	7.23		$(\pi_u^2\sigma_g^1\pi_u^1)$	2.557	00.00
	$(\sigma_g^2\pi_u^1\pi_u^1)$		1.941	−38.98		$(\sigma_g^2\pi_u^1\pi_u^1)$	2.610	0.34
	$(\pi_u^2\sigma_g^2)$		1.922	0.00		$(\pi_u^2\sigma_g^2)$	2.659	09.95
AlP	$(\pi_u^2\pi_u^2)$		2.097	12.55	AlB^{2-}	$(\pi_u^2\pi_u^2)$	2.025	21.45
	$(\pi_u^2\sigma_g^1\pi_u^1)$		2.225	0.00		$(\pi_u^2\sigma_g^1\pi_u^1)$	2.090	00.00
	$(\sigma_g^2\pi_u^1\pi_u^1)$		2.421	−2.22		$(\sigma_g^2\pi_u^1\pi_u^1)$	2.139	1.68
	$(\pi_u^2\sigma_g^2)$		2.403	29.20		$(\pi_u^2\sigma_g^2)$	2.175	11.77
CN^+	$(\pi_u^2\pi_u^2)$	1.173	1.172	00.00	BC^-	$(\pi_u^2\pi_u^2)$	1.396	02.13
	$(\pi_u^2\sigma_g^1\pi_u^1)$	1.247	1.251	05.87		$(\pi_u^2\sigma_g^1\pi_u^1)$	1.448	00.00
	$(\sigma_g^2\pi_u^1\pi_u^1)$		1.369	26.32		$(\sigma_g^2\pi_u^1\pi_u^1)$	1.504	6.23
	$(\pi_u^2\sigma_g^2)$		1.367	62.97		$(\pi_u^2\sigma_g^2)$	1.518	26.90
SiP^+	$(\pi_u^2\pi_u^2)$		2.000	19.55	BSi^-	$(\pi_u^2\pi_u^2)$	1.818	08.14
	$(\pi_u^2\sigma_g^1\pi_u^1)$		2.094	00.00		$(\pi_u^2\sigma_g^1\pi_u^1)$	1.878	00.30
	$(\sigma_g^2\pi_u^1\pi_u^1)$		2.231	−7.84		$(\sigma_g^2\pi_u^1\pi_u^1)$	1.982	8.54
	$(\pi_u^2\sigma_g^2)$		2.242	13.40		$(\pi_u^2\sigma_g^2)$	1.995	0.00
CP^+	$(\pi_u^2\pi_u^2)$		1.578	17.37	AlC^-	$(\pi_u^2\pi_u^2)$	1.816	11.94
	$(\pi_u^2\sigma_g^1\pi_u^1)$		1.634	00.00		$(\pi_u^2\sigma_g^1\pi_u^1)$	1.897	00.00
	$(\sigma_g^2\pi_u^1\pi_u^1)$		1.769	15.15		$(\sigma_g^2\pi_u^1\pi_u^1)$	1.954	4.98
	$(\pi_u^2\sigma_g^2)$		1.792	32.61		$(\pi_u^2\sigma_g^2)$	1.980	23.67
SiN^+	$(\pi_u^2\pi_u^2)$		1.578	18.81	$AlSi^-$	$(\pi_u^2\pi_u^2)$	2.242	10.42
	$(\pi_u^2\sigma_g^1\pi_u^1)$		1.683	00.00		$(\pi_u^2\sigma_g^1\pi_u^1)$	2.338	00.00
	$(\sigma_g^2\pi_u^1\pi_u^1)$		1.797	−3.37		$(\sigma_g^2\pi_u^1\pi_u^1)$	2.432	0.82
	$(\pi_u^2\sigma_g^2)$		1.788	32.33		$(\pi_u^2\sigma_g^2)$	2.456	15.99
N_2^{2+}	$(\pi_u^2\pi_u^2)$		1.139	00.00	CO^{2+}	$(\pi_u^2\pi_u^2)$	1.166	25.26
	$(\pi_u^2\sigma_g^1\pi_u^1)$		1.248	04.57		$(\pi_u^2\sigma_g^1\pi_u^1)$	1.254	00.00
	$(\sigma_g^2\pi_u^1\pi_u^1)$		1.367	20.75		$(\sigma_g^2\pi_u^1\pi_u^1)$	1.254	0.00
	$(\pi_u^2\sigma_g^2)$		1.421	38.12		$(\pi_u^2\sigma_g^2)$	1.735	60.55
P_2^{2+}	$(\pi_u^2\pi_u^2)$		2.457	15.28				
	$(\pi_u^2\sigma_g^1\pi_u^1)$		2.055	00.30				
	$(\sigma_g^2\pi_u^1\pi_u^1)$		2.168	−12.70				
	$(\pi_u^2\sigma_g^2)$		2.244	0.00				

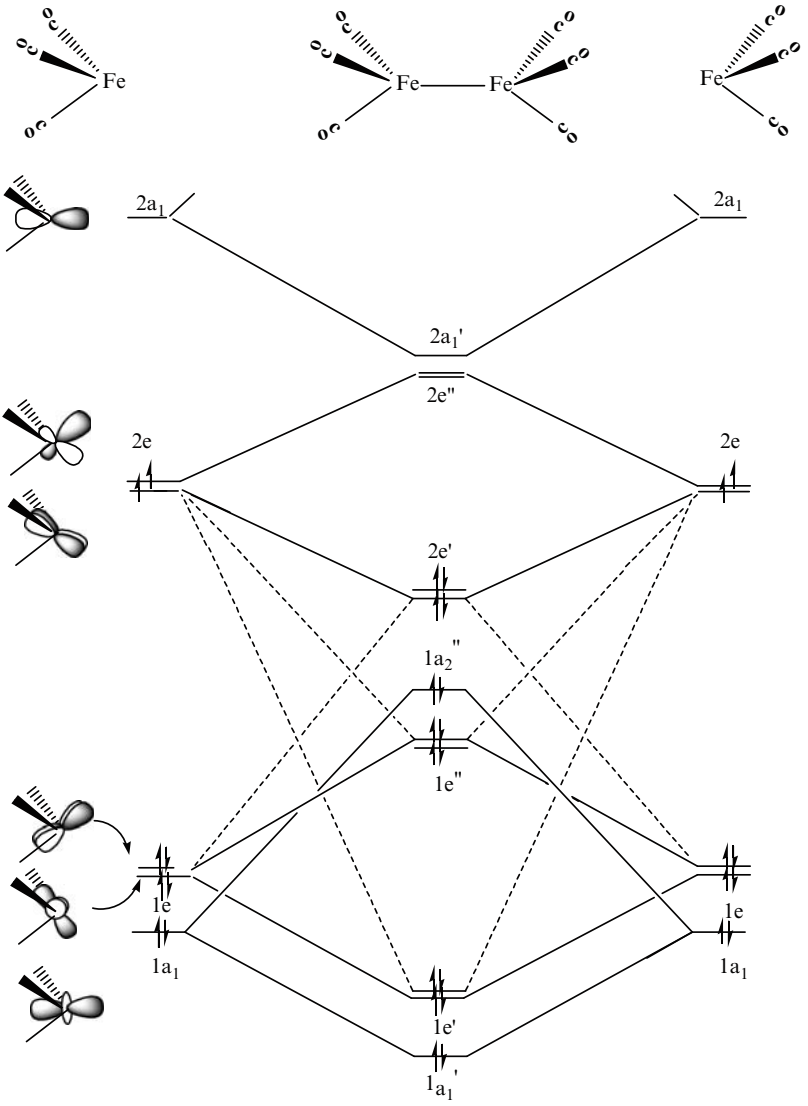

Fig. 7.2 Interaction diagram between two $Fe(CO)_3$ fragments to give $(OC)_3Fe\text{-}Fe(CO)_3$

orbitals in π-bonds in $Fe_2(CO)_6$ (Scheme 7.1b) is similar to the bent bonds of cyclopropane (Scheme 7.1c). The influence of σ-bonds in bond lengthening is seen in $L_3M\text{-}ML_3$ complexes with six valence electrons. According to the ordering of MO energy levels (Fig. 7.2), such compounds should be triply bonded with one σ-bond and two π-bonds ($1a_1'$, $1e'$). The bond is expected to be longer due to its σ-component. There are four examples from literature, namely $Mo_2(CH_2Ph)_2(NMe_2)_4$ 2.20 Å, $Mo_2(O^iPr)_2(SC_6H_2Me_3)_4$ 2.23 Å, $Mo_2(OC(CF_3)_2CH_3)_6$ 2.23 Å, and $W_2Br_2(NEt_2)_4$

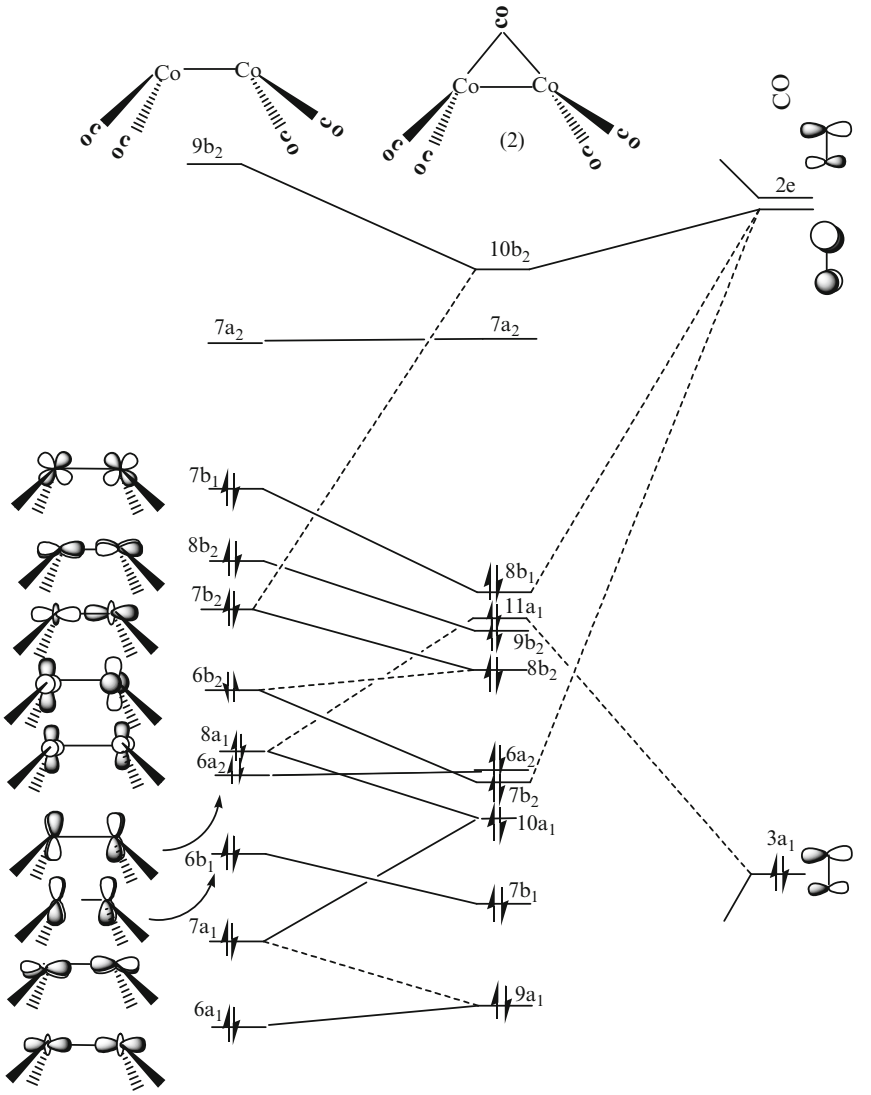

Fig. 7.3 Interaction diagram between $(OC)_2Co\text{-}Co(CO)_2$ and CO fragments to give $Co_2(CO)_5$

2.30 Å [48–51]. While these distances are not directly comparable, the M–M bond distances are much longer than that calculated for $Fe_2(CO)_6$.

The bonding in $Co_2(CO)_5$ presents a similar situation [52]. Its structure is best analyzed by bringing a $Co_2(CO)_4$ and a CO in a bridging arrangement. The C_{2v} geometry of $Co_2(CO)_5$ provides (Fig. 7.3) an occupancy of $5a_1$, $7b_1$, $10a_1$, $7b_2$, $6a_2$, $8b_2$, $9b_2$, $11a_1$ and $8b_1$ levels for the 18d electrons, corresponding to σ, σ*, π, π*, δ, δ*, and π levels. Thus, the net M–M bonding is provided by one π- type

molecular orbital. So the electronic structure of the d^9–d^9 $Co_2(CO)_4$ is predicted to have a π-bond. The interaction with the bridging carbonyl decreases the antibonding character of the σ* to some extent. The Mullikan population, an indication of bond strength, remains the same before and after the interaction. Thus, despite the short distance, only a formal single bond (π-bond) may be assigned to the Co–Co interaction in $Co_2(CO)_5$. While it is tempting to assume exact cancellation of a bond when both the bonding and the corresponding antibonding orbitals are occupied, this is never the case. We have analyzed the nature and the extent of bonding in some of these molecules by overlap populations and electron density analysis. Any method of estimating the bond strength based on overlap population has limitations.

Similarly, quantitative comparisons of bond order indices of different pairs of atom are also difficult. Despite these limitations, we have found it profitable to compare the Mulliken overlap populations and NBO atom–atom overlap weighted NAO bond order calculated at B3LYP/LANL2DZ for all molecules. The overlap population and the bond orders calculated for C_2 (0.728, 2.104) are between those of C_2H_4 (0.596, 1.288) and C_2H_2, (1.007, 2.640). Comparisons of overlap populations are even more difficult in the transition metal complexes. We have calculated the NBO bond order for the binuclear complexes $[M_2(Cp)_2(CO)_6]$ which are known to have single σ bonds. The values are 0.044 (M=Cr), 0.141 (M=Mo) and 0.170 (M=W). This is to be compared with the bond order of 0.951 calculated for $Re_2Cl_8^{-2}$ which is known to have a Re–Re quadruple bond. The bond order for $Fe_2(CO)_6$ (0.353) and $Co_2(CO)_5$ (0.218) is much lower than those for the quadruple bonded $Re_2Cl_8^{-2}$, justifying the bond order analysis. Similar conclusions can be obtained by taking any other method of estimating bond orders and overlap populations. The variation of the electron density [53] at the center of the C−C bond in C_2, C_2H_2, C_2H_4 and C_2H_6 (0.2690, 0.3741, 0.3064 and 0.2198 a.u., respectively) indicates that in the absence of a full fledged sigma bond, the electron density in the middle of C_2 is as lower as anticipated.

7.4 Conclusions

The detailed electronic structures of (five, six, seven and eight valence electrons) inter- and intra-row main-group diatomic species shows that the element-element bond length decreases considerably when their π-levels are filled up, instead of σ. The unusual shortness in the main group diatomic species is explained on the basis of their π-alone bonding. This is found in the transition metal complexes [$Fe_2(CO)_6$, $Co_2(CO)_5$] as the frontier orbitals are reversed (Scheme 7.2b) in comparison to the main-group fragments (Scheme 7.2a) where the σ-levels (sp^x hybrid orbitals of common main group fragments, such as –BH, –CH and –CH_2) are lower in energy than the p orbitals that form the π-bonds. Our work suggests that it may be profitable to leave out σ-bonds while designing molecules with unusually short bond length!

References

1. G.J.H. Vannes, A. Vos, Single-crystal structures and electron density distributions of ethane, ethylene and acetylene. I. Single-crystal X-ray structure determinations of two modifications of ethane. Acta Cryst. B **34**, 1947–1956 (1978)
2. G.J.H. Vannes, A. Vos, Single-crystal structures and electron density distributions of ethane, ethylene and acetylene. III. Single-crystal X-ray structure determination of ethylene at 85 K. Acta Cryst. B **35**, 2593–2601 (1979)
3. R.K. Mcmullan et al., Structures of cubic and orthorhombic phases of acetylene by single-crystal neutron diffraction. Acta Cryst. B **48**, 726–731 (1992)
4. F.A. Cotton et al., The crystal and molecular structure of dipotassium octachlorodirhenate(III) dihydrate, $K_2[Re_2Cl_8]2H_2O$. Inorg. Chem. **4**, 330–333 (1965)
5. B.O. Roos et al., Reaching the maximum multiplicity of the covalent chemical bond. Angew. Chem. Int. Ed. **46**, 1469–1472 (2007)
6. G. Frenking, R. Tonner, Theoretical chemistry: The six-bond bound. Nature **446**, 276–277 (2007)
7. T. Nguyen et al., Synthesis of a stable compound with fivefold bonding between two chromium(I) centers. Science **310**, 844–847 (2005)
8. P.J. Bruna, Theoretical prediction of the potential curves for the lowest-lying states of the isovalent diatomics CN^+, Si_2, SiC, CP^+, and SiN^+ using the *ab initio* MRD-CI method. J. Chem. Phys. **72**, 5437–5445 (1980)
9. J.M. Galbraith et al., π-Bonding in second and third row molecules: Testing the strength of linus's blanket. Chem. Eur. J. **6**, 2425–2434 (2000)
10. L. Pauling, *The Nature of the Chemical Bond*, 2nd edn. (Cornell University Press, Ithaca, NY, 1945)
11. P. Pyykkö et al., Triple-bond bovalent radii. Chem. Eur. J. **11**, 3511–3520 (2005)
12. K. Raghavachari et al., A fifth-order perturbation comparison of electron correlation theories. Chem. Phys. Lett. **157**, 479–483 (1989)
13. R.J. Bartlett et al., Non-iterative fifth-order triple and quadruple excitation energy corrections in correlated methods. Chem. Phys. Lett. **165**, 513–522 (1990)
14. G.E. Scuseria, The open-shell restricted Hartree-Fock singles and doubles coupled-cluster method including triple excitations CCSD (T): Application to C_3^+. Chem. Phys. Lett. **176**, 27–35 (1991)
15. M. J. Frisch et al., Gaussian 03, Revision C.02, Gaussian, Inc. (Wallingford CT, 2004)
16. J.A. Pople et al., Quadratic configuration interaction. A general technique for determining electron correlation energies. J. Chem. Phys. **87**, 5968–5975 (1987)
17. A.D. Becke, Density-functional thermochemistry. III. The role of exact exchange. J. Chem. Phys. **98**, 5648–5652 (1993)
18. C. Lee, Development of the Colle-Salvetti correlation-energy formula into a functional of the electron density. Phys. Rev. B **37**, 785–789 (1988)
19. A.E. Reed et al., Intermolecular interactions from a natural bond orbital, donor-acceptor viewpoint. Chem. Rev. **88**, 899–926 (1988)
20. P. Rademacher, Photoelectron spectra of cyclopropane and cyclopropene compounds. Chem. Rev. **103**, 933–976 (2003)
21. J.G. Fox, G. Hertzberg, Analysis of a new band system of the C_2 molecule. Phys. Rev. **52**, 638–643 (1937)
22. R.S. Mulliken, Note on electronic states of diatomic carbon, and the carbon–carbon bond. Phys. Rev. **56**, 778–781 (1939)
23. E.A. Ballik, D.A. Ramsay, Ground state of the C_2 molecule. J. Chem. Phys. **31**, 1128–1128 (1959)
24. K.P. Huber, G. Herzberg, *Molecular Spectra and Molecular Structure·IV. Constants of Diatomic Molecules* (Van Nostrand-Reinhold Co, New York, 1979)

25. L.B. Knight et al., Laser sputtering generation of B2 for ESR matrix isolation studies: Comparison with ab initio CI theoretical calculations. J. Am. Chem. Soc. **109**, 3521–3525 (1987)
26. P.P. Power, π-Bonding and the lone pair effect in multiple bonds between heavier main group elements. Chem. Rev. **99**, 3463–3504 (1999)
27. G.L. Gutsev et al., Structure and stability of the AlX and AlX^- species. J. Chem. Phys. **110**, 2928–2935 (1999)
28. M. Pelegrini et al., MRSDCI study of the two lower-lying doublet electronic states of the BeB, MgB, and CaB molecules. Int. J. Quantum Chem. **95**, 205–212 (2003)
29. P.J. Bruna, F. Grein, Hyperfine coupling constants and electron-spin *g*-factors of B_2^+, Al_2^+, Ga_2^+, BAl^+, BGa^+, and $AlGa^+$: An *ab initio* study. J. Chem. Phys. **117**, 2103–2111 (2002)
30. P.J. Bruna et al., Beryllium-beryllium bonding. 1. Energetics of protonation and hydrogenation of beryllium dimer and its ions. J. Phys. Chem. **96**, 6269–6278 (1992)
31. L.G. Kaplan et al., Nondipole bound anions: Be_2^- and Be_3^-. J. Chem. Phys. **117**, 3687–3693 (2002)
32. R. Middleton, J. Klein, Production of metastable negative ions in a cesium sputter source: Verification of the existence of N_2^- and CO^-. Phys. Rev. A **60**, 3786–3799 (1999)
33. A. Moezzi et al., Enhanced thermal stability in organodiborane(4) compounds: Synthesis and structural characterization of MeO(Mes)BB(Mes)OMe, Mes_2BB(Mes)OMe, Mes_2BB (Mes)Ph, and Mes_2BB(Mes)CH_2SiMe_3 (Mes = 2,4,6-$Me_3C_6H_2$). Organometallics **11**, 2383 (1992)
34. J. Kalcher, A.F. Sax, Ab initio investigation on the negative ion states of the X–Y (X = C, Si; Y = Be, Mg) diatomics. J. Mol. Struct.: THEOCHEM **498**, 77–85 (2000)
35. S. Midda, A.K. Das, Spectroscopic constants and molecular properties of diatomic carbides. J. Mol. Spectroscopy **224**, 1–6 (2004)
36. T.L. Windus, M.S. Gordon, π-Bond strengths of H_2X:YH_2: X = Ge, Sn; Y = C, Si, Ge, Sn. J. Am. Chem. Soc. **114**, 9559–9568 (1992)
37. L.B. Knight et al., Laser vaporization generation of the SiB and SiAl radicals for matrix isolation electron spin resonance studies; comparison with theoretical calculations and assignment of their electronic ground states as $X\ ^4\Sigma$. J. Chem. Phys. **98**, 6749–6757 (1993)
38. D. Tzeli, A. Mavridis, First-principles investigation of the boron and aluminum carbides BC and ALC and their anions BC- and AlC-1. J. Phys. Chem. A **105**, 1175–1184 (2001)
39. S.P. Karna, F. Grein, High-multiplicity states of BN and BN+ obtained by configuration-interaction studies. Chem. Phys. Lett. **144**, 149–152 (1988)
40. B. Miguel et al., Theoretical study of low-lying electronic states of BP molecule. Chem. Phys. Lett. **381**, 720–724 (2003)
41. Y. Xie et al., Binuclear homoleptic iron carbonyls: Incorporation of formal iron-iron single, double, triple, and quadruple bonds, $Fe_2(CO)_x$ ($x = 9, 8, 7, 6$). J. Am. Chem. Soc. **122**, 8746–8761 (2000)
42. R. Binachi et al., Experimental electron density analysis of $MN_2(CO)_{10}$: Metal–metal and metal-ligand bond characterization. Inorg. Chem. **39**, 2360–2366 (2000)
43. R.D. Adams et al., Unusual structural and magnetic resonance properties of dicyclopentadienylhexacarbonyldichromium. J. Am. Chem. Soc. **96**, 749–754 (1974)
44. R.D. Adams et al., Molecular structures and barriers to internal rotation in bis (eta. 5-cyclopentadienyl)hexacarbonylditungsten and its molybdenum analog. Inorg. Chem. **13**, 1086–1090 (1974)
45. V. Pophristic, L. Goodman, Hyperconjugation not steric repulsion leads to the staggered structure of ethane. Nature **411**, 565–568 (2001)
46. F.M. Bickelhaupt, E.J. Baerends, The case for steric repulsion causing the staggered conformation of ethane. Angew. Chem. Int. Edn. Engl. **42**, 4183–4188 (2003)
47. F. Weinhold, Rebuttal to the Bickelhaupt-Baerends case for steric repulsion causing the staggered conformation of ethane. Angew. Chem. Int. Edn. Engl. **42**, 4188–4194 (2003)

48. M.J. Chetcuti et al., Bis[benzylbis(dimethylamido)molybdenum] and -tungsten (M.tplbond.M) compounds and their reactions with carbon dioxide and 1,3-diaryltriazenes. A radical difference. J. Am. Chem. Soc. **104**, 4684–4686 (1982)
49. M.H. Chisholm, J.F. Corning, J.C. Huffman, The molybdenum-molybdenum triple bond. 14. Preparation and characterization of mixed alkoxy-thiolate compounds of formula $Mo_2(OR)_2(SAr)_4$. Inorg. Chem. **23**, 754–757 (1984)
50. T.M. Gilbert et al., Synthesis and electronic properties of triply bonded hexakis(fluoroalkoxy) dimolybdenum complexes. Structure of $Mo_2[OCMe(CF_3)_2]_6$ and investigation of the nature of the frontier orbitals in triply bonded M_2X_6 compounds. Inorg. Chem. **31**, 3438–3444 (1992)
51. M.H. Chisholm et al., The tungsten-tungsten triple bond. 5. Chlorine atom substitution reactions involving dichlorotetrakis(diethylamido)ditungsten. Preparation, properties, structures, and dynamical solution behavior of bis(trimethylsilylmethyl)-, dibromo- and diiodotetrakis(diethylamido)ditungsten. Inorg. Chem. **16**, 320–328 (1977)
52. J.P. Kenny et al., Cobalt–cobalt multiple bonds in homoleptic carbonyls? $Co_2(CO)_x$ ($x=5$–8) structures, energetics, and vibrational spectra. Inorg. Chem. **40**, 900–911 (2001)
53. R.F.W. Bader, *Atoms in Molecules: A quantum Theory* (Clarendon Press, Oxford, 1994)

Chapter 8
QSAR Models for Regulatory Purposes: Experiences and Perspectives

Emilio Benfenati

Abstract Quantitative structure–activity relationships (QSARs) are more and more discussed and used in several situations. Their application to legislative purposes stimulated a large debate in Europe on the recent legislation on industrial chemicals. To correctly assess the suitability of QSAR, the discussion has to be done depending on the target. Different targets modify the model evaluation and use. The application of QSAR for legislative purposes requires keeping into account the use of the values obtained through the QSAR models. False negatives should be minimized. The model should be robust, verified, and validated. Reproducibility and transparency are other important characteristics.

8.1 The Modeling Context for QSAR

The quantitative structure–activity relationship (QSAR) model is by definition a model. Any model, such as animal model (also called in vivo) or in vitro model, is a system that applies to a specific situation, and thus, it is useful to study, evaluate, or assess a more complex system, which cannot be used experimentally for investigation. Thus, any model is a simplification of the target object of the study, and the model is useful for this or not depending on its purpose. It is also possible to imagine a series of models, each addressing one or more features of the more complex system.

Quite often the model is adopted empirically, on the basis of the available resources or tools. QSAR models that aim to address a certain legislative scope should refer to the legislation itself, both for the development of the model, and for the evaluation of the suitability of the purpose.

E. Benfenati (✉)
Istituto di Ricerche Farmacologiche "Mario Negri", Via Giuseppe La Masa, 19 20156, Milano, Italy
e-mail: benfenati@marionegri.it

J. Leszczynski and M.K. Shukla (eds.), *Practical Aspects of Computational Chemistry*, 183
DOI: 10.1007/978-90-481-2687-3_8,

Different legislations exist, addressing different aspects in different countries. We will refer mainly to the new European legislation called REACH: registration, evaluation, assessment, and restriction of chemicals, which deals with all industrial chemicals on the European market [1]. Such a legislation is a complex one, the most complex dealing with chemicals in Europe, and thus, it offers a good range of topics to be discussed.

REACH aims to protect both the environment and human health from the industrial chemicals used in Europe, which refer to tens of thousands of substances. In this case, the ideal systems to be evaluated are human health and environment. However, the legislation defines a series of models, which can be used to assess the effects on these two major systems. Animal models are quite often mentioned, in case of toxicity studies and bioaccumulation. Examples of such models are models using rat and fish. Rat and mouse, typically, are used as models for human health, and fish is useful for environmental endpoints. However, it is well recognized that humans are different from rodents for a series of biochemical processes. To study carcinogenicity, for instance, a battery of tests is common, using rat and mouse, both male and female animals. Differences are often found in the different rodent experiments, and this highlights the problems in extrapolating results to humans. Still, in vivo experiments are a fundamental way to study toxicity.

Similar considerations can be done in the case of environmental endpoints. In this case, the target system to be protected is the ecosystem, which includes several fish species, other animals, and other organisms. It is well known that there are different species sensitivities in fish, birds, etc. Some organisms are typically used, but it is not certain that these organisms are always the most sensitive.

8.2 The QSAR Model Theory

The basic assumption of the QSAR model is that the activity under evaluation can be studied, and/or predicted using the chemical information of a certain compound. For the relationship between the activity and the chemical information, a mathematical function can be used.

In the specific case of the evaluation of a qualitative relationship, for instance, between the presence of a certain chemical fragment and the occurrence of a certain toxicity effect, the typical name is structure–activity relationship (SAR). Here, we will discuss QSAR and SAR together.

Thousands of QSAR models have been published and reported. A quite large series of activities have been used for QSAR, including physico-chemical, toxicological, ecotoxicological, and environmental properties. Examples of common QSAR models are models for water solubility, fish toxicity, mutagenicity, and for environmental degradation.

The chemical information can be expressed in a large number of ways. Classical QSAR models used physico-chemical experimental values measured in

the laboratory [2, 3]. However, the current procedure is to use calculated chemical parameters [4–6]. In this way, the QSAR models are exploited to their full capability as they do not depend on any a priori condition, such as availability of experimental values of certain physico-chemical properties.

Chemical information can be expressed in a number of ways. Chemical descriptors are commonly used in QSAR. There are thousands of chemical descriptors possibly used in QSAR. Indeed, programs such as DRAGON and CODESSA, just to name a couple, can calculate thousands of parameters [7, 8]. Chemical descriptors have different complexities. Some of them do not require any information on the structure, such as molecular weight. Others refer to the bidimensional structure, such as the number of double bonds. While some others require tridimensional information, such as molecular volume. Chemical descriptors can be geometrical, topological, quantum-mechanical, electrostatical, etc. There are a few books describing chemical descriptors [7, 8].

Another way to describe the chemical information is using fragments. Also, in this case, thousands of fragments can be used. This kind of chemical information allows fast QSAR models.

Chemical descriptors can be easily obtained from the SMILES structure, which is another simple way to get chemical information useful for QSAR modeling purposes [9].

More complex ways exist, which offer powerful capabilities, and are useful in certain situations. CoMFA methods, for instance, overlap a series of structures on the basis of a common molecular moiety. The differences in the electrostatic and sterical behavior are then assessed in relationship to the property to be modeled [10].

An even more complex approach is to evaluate the interaction between the chemical substance and the biological receptor at the basis of the biochemical process. Docking methods are used, which need a tridimensional description of both the receptors and the chemical ligand. Docking methods and CoMFA are very useful for certain endpoints of interest for regulation, such as endocrine disruptor studies. However, these methods do not represent the typical QSAR models for regulatory purposes [10].

The third fundamental component in the QSAR model is the mathematical algorithms. Many methods have been used, and in the last years, there has been an increase of the methods, and hence, quite probably this trend will continue, introducing many other methods [4–6]. Classical QSAR methods, used decades ago, were simple linear relationships. Corwin Hansch has been a pioneer of these methods [2]. An example can be the linear relationship between the fish toxicity and the partition coefficient between octanol and water, called Kow [3]. Kow, and its logarithm, called log P, is still the most popular chemical descriptor used in QSAR models for fish toxicity, and it is the base of software programs used by the US Environmental Protection Agency for fish toxicity [11]. The theoretical assumptions for the use of log P are that (1) octanol mimics the lipophylic component of the fish cell, and (2) the toxic effect is due to the adsorption of the chemical substance into the cell.

Other chemical descriptors have been used to model other properties, or to improve the QSAR models with log *P*. The attempt has been to avoid the errors of the QSAR models. Indeed, some chemicals were not correctly modeled, and other descriptors have been introduced, producing multilinear relationships. The theoretical assumptions were modeled keeping into account other physico-chemical parameters, such as chemical reactivity, through chemical descriptors, such as the energy of the highest occupied molecular orbital (HOMO) and the lowest unoccupied molecular orbital (LUMO).

Thus, multilinear models were introduced, and then a wide series of tools, such as nonlinear models, including artificial neural networks, fuzzy logic, Bayesian models, and expert systems. A number of reviews deal with the different techniques [4–6]. Mathematical techniques have also been used to keep into account the high number (up to several thousands) of chemical descriptors and fragments that can be used for modeling purposes, with the problem of increase in noise and lack of statistical robustness. Also in this case, linear and nonlinear methods have been used, such as principal component analysis (PCA) and genetic algorithms (GA) [6].

8.3 The QSAR Model Practice

A QSAR model is typically developed starting with a number of compounds, which are used as training set. The QSAR model is a chemometric method that extracts the knowledge relative to the population of chemical compounds with certain associated property values, such as toxicity.

Classical QSAR models were focused on a rather small number of compounds. The basic assumption was that a certain model is specific for a certain chemical class, sharing a common skeleton. Modifications of some simple chemical features were reflected in the property. Thus, for instance, a series of linear alcohols present aquatic toxicity, which varies in a rather linear way with the chain length [3].

At the end of the last century, many studies attempted to model heterogeneous series of chemical compounds, using a series of chemical descriptors [4–6, 12]. This was a result both of the challenge to address a more complex target, and of the availability of more complex modeling tools, such as a series of chemical descriptors and more powerful mathematical techniques.

The theoretical challenge was to better model chemical compounds presenting a series of functional groups, and more complex structures. However, with time, there has also been a shift in the use of the QSAR models. Indeed, society sectors have shown interest on the possibility to use QSAR models as predictive tools. Prediction can be useful for the development of new chemicals, with certain properties, and the drug companies have been very active in this, developing and adopting tools that are in many cases different from those used for ecotoxicological and environmental purposes. Prediction can be used for evaluation of toxicity and environmental properties, and in that case, the regulators are of interest in the QSAR models.

This shift of the use forced a different evaluation of the model, toward a more statistical evaluation. The first QSAR models were evaluated in their capability to fit the property data with one or more chemical descriptors, but no proof was given about the predictivity of the model. Today, a number of criteria are requested to check if a model is predictive or not [13–15].

Thus, there is also a shift in the purpose on the modeling studies. Initially, the chemical descriptors were in most of the cases discussed in their physico-chemical meaning, and the relationship between a certain property and a chemical descriptor was discussed for a possible mechanism.

In the more recent years, also due to (1) a much larger number of chemical descriptors, (2) the introduction of data mining tools (software), (3) the availability of more powerful computer (hardware), and (4) (in a minor extent) the increased number of property data, research addressed not the individual one-by-one manual investigation on the relationship between a single property and a single descriptor, but thousands of possible relationships simultaneously and automatically. Indeed, what human experts did manually, for instance, in the case of the identification of a certain chemical fragment as responsible for a certain carcinogenic effect has been to identify a pattern of effects more frequent in the case of nitrosoamines. But, a computer program can efficiently replicate such a manual screening, and indeed, the performances of human and computer predictions for carcinogenicity are similar [16].

This modified scenario has several consequences in the perspectives of the QSAR modeling and its applications. It is now clear that there are several applications, and several techniques. It is beneficial that several approaches are tested, new methods developed, new techniques introduced, and more application scenarios evaluated. What should be avoided is a confusion on the fact that there are different purposes, and that each application may have different needs, and that the different schools of thinking and methodologies put a priori requirements, which may be good in a certain context, but not in a second one.

Currently, there are two main uses of QSAR and in silico modeling techniques, including the COMFA and docking studies. One is for drug applications, and another one is for ecotoxicological, toxicological, and environmental ones. Many techniques are the same, but there are two quite different communities and conferences for the different applications. In fact, drug companies are interested in the applications for the development of new drugs. This process basically needs tools for rapid screening of a very large number of possible chemicals, up to millions of virtual structures. For this purpose, fragments or structural keys are generated. The software starts from simple bidimensional structures. In several cases, these structures are large collections of quite related compounds, sharing a common skeleton. In a second phase, more detailed studies are done on a more limited number of chemicals, and for this, tridimensional structures are used, and even chiral information. Docking studies are quite common to better investigate the candidate drugs.

Typically, the studies want to avoid false positives. A false positive is a compound that is predicted with certain properties, but then it results to be false. The drug companies do not want to invest money for the final development of a new

drug, and at a certain level, they find that for some reasons the candidate compound is not suitable. The drug companies prefer to loose some candidate drugs, but proceed with the good ones only because the experimental work is very expensive.

8.4 The Regulatory Perspective

The approach of the studies for environmental and health protection is quite different.

There is the need of a better knowledge on chemical toxicological properties, in general, for a safer environment and to protect human health, and in particular, to face the challenges of legislations. In Europe, legislation, such as the REACH, requires that all industrial chemicals on the European market (in an amount exceeding one ton per year) will be evaluated on the basis of the impact on humans and environment. REACH also wants to avoid excessive use of resources and animals for experiments, and promotes the use of alternative methods, including QSAR.

The European legislation for cosmetics is even more in favor of alternative methods, since the use of animals will be banned in the next few years.

This need requires unprecedented efforts for QSAR, which can be used for the specific purposes of chemical assessment and evaluation.

There are some unique features that characterize the desirable properties of QSAR models for regulatory purposes, and may not apply for QSAR models for other applications, such as models to be used by the industry for the development of a new product or drug.

Thus, the legislative basis and the law purposes have to be understood.

8.4.1 Identifying the Legislative Target

Let us consider the case of the REACH legislation, which is one of the most complex European legislations. As we said, the target is the protection of humans and environment. The evaluation of this target is complex, and thus, the law requires keeping into account all possible sources of information. The law defines preferred procedures to get the data, and a number of protocols are listed. If official protocols are not used, experiments performed according to good laboratory practice (GLP) are preferable. However, all pieces of information should be evaluated, even experiments not done in GLP, considering their reliability and relevance.

Thus, the law acknowledges that the task is a difficult one, and solicits an integrated approach, using and combining different elements for the evaluation. Indeed, we have to remember that the human target can be studied through animal models, but in any case, the animal (typically rat and mouse) models are, indeed, models. Similarly, a model done on selected species is only partial for the

evaluation of the effects on the ecosystem, in which multiple species and factor are present.

Typically, the philosophy of the QSAR method has been to mimic the animal model (or anyhow the experimental mode, such as mutagenicity and degradation). Actually, a broader view, considering the target of the legislation, is to directly address the final target (humans and ecosystem), and thus, evaluate for this purpose the validity of the QSAR model.

This changes the perspective of the evaluation. Theoretically, we can imagine two situations: (1) a suitable experimental model exists, or (2) it does not. In the first case, the QSAR models can be evaluated considering what we loose, comparing the results of the experimental model and of the QSAR model, which will not be 100% efficient. In case that an experimental model does not exist, we can evaluate how much we "gain," in terms of better knowledge, using the QSAR model. In practice, there are several situations in which the experimental models are not perfect, or even do not exist. For instance, the REACH legislation claims as important the endocrine disruptor activity of the chemical substances, but for this and other activities, there is a lack of suitable experimental procedures, where QSAR may help [10].

8.4.2 Satisfying the Legislative Context

In the earlier section, we have discussed the importance of the legislative target to be addressed. Since a model is dedicated for a specific purpose and we are speaking about models for legislative purposes, it is fundamental to understand the legislative target. The legislation and the regulations also specify the operative procedure(s), which should be followed in most of the cases. These procedures and the target should be carefully evaluated. Indeed, these characterize both the input and output of the QSAR model. Not all inputs are the same, and not all outputs are appropriate, even if on a general basis they may look so. For instance, not all fish toxicity data are the same. Depending on the legislative context, some fish data are preferable as they are specified by the regulation. For instance, we notice that in Europe and USA, different fish species are used. Fathead minnow is a typical fish present in the American lakes, and this specific organism has been selected in the USA.

Thus, it should be preferable to develop QSAR using data only on the basis of data obtained according to the specific guideline or protocol defined by the law. And this depends on the law.

But the output of the model has to be carefully evaluated according to the law. For instance, some regulations address chemicals according to property categories, such as carcinogenic or not, toxic for aquatic organism, etc. The purpose can be classification and labeling. In other cases, a continuous dose is necessary , e.g., the aquatic toxicity (toward fish, for instance) has to be compared with an exposure value to assess if there will be a toxic effect in fish for the environmental concentration that may occur. This is the case of risk assessment. Thus, we can have

models for fish toxicity, for instance, as classifier or regression models, depending on the law. Furthermore, within the same law, we may have different requests, depending on the tonnage of the chemical on the market, for instance, within the REACH legislation. And different toxicity thresholds may be defined within different regulations.

In summary, it is clear that the output of the model is also affected by the legislation, and different models may be suitable for different legislative purposes.

While in general, we can summarize the typical QSAR scheme as follows:

Data → Information → Knowledge

Where, *data* are the raw data (toxicity and chemical); *information* is the elaborated data as processed during the modeling phase; and *knowledge* is the final model output.

The scheme must be modified as follows in case of the specific application, and the legislative one in particular:

Experimental Method → Data → Information → Knowledge → Use

Where, *experimental method* is the procedure used to obtain the experimental data as defined by the law; and *use* is that defined by the law for the toxicity value or class [17].

This modification places demands on each phase of the modeling process.

8.4.3 Specific Requirements

QSAR models for legislative purposes have to show that the predicted value has a certain quality. However, its assessment is not easy. In the last year, the debate on the real validity of the QSAR models has seen both supporters and critics. Thousands of models have been produced, and this complicates the evaluation. Indeed, the prediction of some easy physico-chemical properties is surely simpler, while some complex toxicity endpoints, such as carcinogenicity, is much more problematic. But, how to measure the performances and reliability of the QSAR models?

This point is a general one, independent of the specific application. The Organisation for Economic and Co-operational Development (OECD) proposed five principles within the guidelines for the validation of regulatory QSAR models (18). OECD says that a model should be associated with the following informations:

1. A defined endpoint
2. An unambiguous algorithm
3. A defined domain of applicability
4. Appropriate measures of goodness-of-fit, robustness, and predictivity
5. A mechanistic interpretation, if possible

Basically, the meaning of these principles is to ensure clarity on a series of fundamental issues. The endpoint has to be defined according to the first principle, in order to understand, for instance, if different models give different results because they are based on different data. However, if this is the case, it is also

quite important to link the kind of data to the specificity of the law. This aspect is obviously more relative to the relevance of the model than to its reliability, but the appropriateness of one model or another is also related to the relevance.

The second principle stresses on the transparency of the model. Regulators cannot rely on something that cannot be verified. This refers to all model components, such as data, descriptors, equations, rules, etc.

Thus, full transparency is at the basis of the credibility of any model to be used for official purposes, but this issue generated a debate on the possible use of confidential components in the model, such as data or algorithms. On one hand, confidential data may increase the basis of the model, but on the other hand, they limit the model transparency. Similarly, commercial software will not release full details of the algorithm.

A point that is often not fully realized is that the chemical descriptors, as typically obtained with commercial software, are quite ambiguous because the exact mathematic equation used to get the descriptor value is not available, and different software or even different versions of the same software may produce different values for, apparently, the same descriptor.

The applicability domain study should define in which conditions it is likely that the model does not work well.

We have already discussed about the different targets for a model to be good in fitting or in prediction. For regulatory purposes, there has to be a proof that the QSAR model also applies for the prediction of the property of *new* chemicals, and so this has to be specifically addressed. This fact introduced the accent on the statistical validation of the model. The fourth principle wants to ensure that a suitable check is done, on a statistical point of view, to verify that the model is not simply working for the limited number of chemicals used for the training set. A number of techniques are available, and they should be used.

The fifth principle, i.e., the mechanistic interpretation, is an added value. The OECD principle means that "The absence of a mechanistic interpretation for a model does not mean that a model is not potentially useful in the regulatory context. The intent of Principle 5 is not to reject models that have no apparent mechanistic basis" [18]. We notice, as previously discussed, that there are two different perspectives: to build up a model, which predicts a value, or to develop a model that is useful to study a phenomenon. These two targets are independent. Different techniques can be applied, and we can imagine a model that is only predictive, but without studying the reasons why certain descriptors are used, or vice versa, we can imagine a model that is only dedicated to understand why certain phenomena occur, for instance, if we want to study why the chlorinated methanes have a given toxicity. In this case, all toxicity data are available, but we may want to investigate the role of the chlorine atom in the phenomenon.

We agree that an explanation on the possible role of a certain chemical fragment or descriptor increases the model acceptability. However, care should be given not to confound a possible explanation with a proved mechanism. Furthermore, as we have said, calculated descriptors are nowadays much more common than experimental ones. Log *P*, a very popular descriptor, used also because it is

conceptually linked to a plausible mechanism of action in fish toxicity models, is actually calculated using tens of fragments and parameters, whose role on the fish toxicity is obscure. This indicates that the issue of mechanism is complex.

Within the five principles, there are some interesting consequences, for instance, about the quality of the data. There should be a check of the input values. In case of toxicity values, some databases are good, but others not. We compared different official databases on pesticides and found differences. Worst is the case of data taken from the literature. But this aspect is not limited to the property values. We found many mistakes even in the chemical structures, which have been reported in journals. All these checks require time and efforts, and are not typically done when a QSAR model is studied for academic research. Vice versa, in case of a model to be proposed as a model for regulatory purposes, efforts should be dedicated to the quality check of the data.

Besides the five OECD principles, there are other issues, more specific for the legislative context. We have already discussed the issue of false positives for drug companies as a critical aspect in the development of new pharmaceuticals. In case of models for legislative purposes, i.e., to protect environment and human health, the philosophy is the opposite. Indeed, regulators pay much more attention to false negatives. In case of classifiers, the accent is typically given on false positives and negatives. However, recently, we underlined the importance to pay attention to false negatives also for regression models [13].

Furthermore, the models have to be reproducible. The model should give the same result when used by different users in different locations. This fact may lead to a preference toward easier models. Depending on the method for QSAR, some steps may be critical for reproducibility. Indeed, some approaches require manual optimization of the tridimensional structure of the chemical, e.g., in the case of tridimensional descriptors. In other cases, stochastic processes are used. Some more complex models done by skilled operators, such as docking, can be critical. Another source of variability is the software version or brand, even for simple bidimensional descriptors.

The uncertainty of a given endpoint should be characterized because it affects the uncertainty of the QSAR model [19]. The uncertainty of the final model cannot be superior to the uncertainty of the input data, and it is assumed to have values predicted with a precision superior to that of the experimental laboratory model.

It is important to notice that uncertainty is a fundamental parameter not only for QSAR, but also for any method used for chemical assessment.

8.5 The Practical Issues and Feasibility

Regulation solicits QSAR scientists on a wider series of endpoints. The QSAR models for regulatory properties are numerous, and several targets are complex.

For instance, REACH may ideally stimulate QSAR research on all the many endpoints listed. For some of these endpoints, the number of data is definitely

insufficient, and for many others, there are problems, but in theory, REACH considers the possibility to have QSAR models for all endpoints.

Another aspect is that multiple QSAR models can exist, and indeed this is likely. The consequences of such a complex picture, with many endpoints and models based on different approaches, are that it is not realistic to have a single approach, but the models have to be modulated considering these issues. Different approaches can be used for the same target and they improve the reliability of the prediction. In some cases, they have been combined into a unified system to improve overall results. This is the case of the models for regulatory purposes developed within the project DEMETRA (see below).

Thus, for certain endpoints, several QSAR models exist, but not for all endpoints of interest.

It is also unlikely that in the near future, QSAR models will cover all requested endpoints, because QSAR models are based on the experimental data. For a certain number of endpoints, the availability of experimental data is limited, and this poses a formidable obstacle to the development of suitable models.

The available models can be academic studies, publicly available or commercial ones. Academic studies require to strictly follow the written procedure that has been described by the authors. In many cases, literature studies took data from the literature, without paying much attention to the check of the data.

The user has to calculate the chemical descriptors and use the equation of the model, when given in an explicit way.

Publicly available models may be open source or not. Another difference is that some models require calculation of the chemical descriptors as a separate task, while others simply need the chemical structure. Examples are the EPA [11] and DEMETRA models [20].

There is a number of commercial software programs, such as TOPKAT [21], MULTICASE [22], HazardExpert [23], and DEREK [24]. They address a number of endpoints. In some cases, they only give SAR models, most typically they predict a continuous value.

The REACH legislation stimulated the discussion about QSAR models. Some models are specific for a very focused chemical class. This is quite typical of the academic models of the classical QSAR studies. Commercial and public models are more typically suitable for a large variety of chemical compounds, even if in some cases, they are composed by a certain number of sub-models, each specific for a certain chemical class.

It may be advisable to use more than one QSAR model to achieve a more robust reliability. Indeed, each model has pros and cons.

If a consensus is reached, the user is more confident. A critical situation may appear in case of conflicting results. A simple approach is to adopt a conservative strategy and get the worst case. A different strategy may be to associate a higher uncertainty to the predictions in case of disagreement. A third strategy is to develop a suitable system capable to deal with multiple inputs. This is the case of the above-mentioned hybrid models, which needs a specific study for the optimization of the final results.

Another difference in the models is that some are fixed, focused for a certain target, and optimized for that. It is the case of many of the commercial programs and of the public models from EPA and DEMETRA.

Another approach is to offer flexible tools for QSAR modeling, such as the OECD toolbox [25].

In the case of the fixed models, the optimization and check of the quality criteria are done. Flexible models have to provide a solid support of the appropriateness for the procedure adopted for the model development.

8.6 European Projects on QSAR and Regulations

8.6.1 The DEMETRA Project

The DEMETRA project [20, 26] represents the first important case of a European project to develop QSAR models for regulatory purposes. DEMETRA developed five free models to determine the ecotoxicity of pesticides using endpoints that include trout, daphnia, bees, and quails (oral and dietary exposure). Since the target was to develop models for the user, these five endpoints were decided by them, not by the developers.

The following were the criteria for the selection: the frequency at which each endpoint is requested; number of animals used in the study; the severity/cruelty of the study; the proportion of the toxicity/exposure ration that does not trigger further testing; the availability of data, etc.

We notice that in practically all cases, a QSAR model was developed having only considered the data availability, without the other assessment evaluation carried out for the DEMETRA project.

DEMETRA clearly stated the requirements for the data to be used because the models were based on the Pesticide Directive, and only the data produced according to the protocols defined in the directive were used.

Regulators and stakeholders within DEMETRA project defined that an accepted uncertainty of the toxicity experimental data was a factor of 4. If the data uncertainty for the same chemical was higher, the chemical was not used for the model in the training set. Here, we notice that QSAR studies do not involve looking at the uncertainty of the property/toxicity value, thereby highlighting the difference between typical and regulatory models.

DEMETRA compared data from three reputable databases. Again, DEMETRA did not merge chemicals, but in this way increased the data quality using the uncertainty requirements defined earlier. Indeed, the presence of data with uncertainties higher than a factor of 4 resulted, for the purposes of model development, in the deletion of the chemical in question. This approach is unusual in QSAR modeling, and again shows the higher attention paid to the quality of the toxicity data employed.

Different partners within DEMETRA checked all chemical structures independently, at least twice, to be sure that they were correct, and limited numbers of errors were found. Such quality control processes are typically not carried out in depth, owing to the time and other resources required.

The full details of the DEMETRA project are available, with full description and explanation [26] and the models and structures are also available [20].

The model's validity was confirmed by checking the model performances against two large set of compounds not used in the development of the model [26, 27].

The DEMETRA models have been optimized to minimize the number of false negatives in order to achieve a safer regulatory application. Conversely, evaluation using only squared statistical parameters (such as R^2), which deal with false positives and negatives in the same manner, is typical in QSAR modeling.

DEMETRA optimized the algorithms' coefficients fixing them in the freely-available software to produce the same result in all European countries.

8.6.2 The CAESAR Project

The EC funded project CAESAR is developing models for five endpoints specifically related to the REACH legislation [28]. The five endpoints are bioconcentration factor, skin sensitization, carcinogenicity, reproductive toxicity, and mutagenicity (in vivo studies). These five endpoints have been chosen because they are among those that will require more animal tests. Actually, other studies are also supposed to use many animals, but they were excluded because of lack of sufficient experimental values.

The approach of CAESAR is quite similar to that of DEMETRA. So far good results have been obtained for the bioconcentration factor (BCF) in fish, superior to those of other models. Models have been tested with an external validation set. The model gives as prediction the BCF as continuous value, but it has been optimized to reduce false negatives. In the specific case of the REACH legislation, which is the target of the project, bioaccumulative chemicals are defined if the BCF value is above 3.3 in logarithmic unit. This shows another example of the specificity of the models, because different threshold may apply in other countries.

Several BCF models have been developed, but they have been integrated into a single hybrid model, which optimizes the performances.

The QSAR models are freely available.

8.6.3 The CHEMOMENTUM Project

The EC funded project CHEMOMENTUM will also implement QSAR models for pesticides and industrial chemicals, taken from the DEMETRA and CAESAR projects, and presented in a more user-friendly form [29].

However, the main target of CHEMOMENTUM will be to develop a flexible system, capable to develop automatic QSAR models for many purposes. The user will be capable to take data from one source, chemical structures from a second one, use software from the calculation of chemical descriptors, and QSAR models within another software. All these steps are typically done manually in the development of the QSAR models. CHEMOMENTUM will offer a unique system based on the Grid technology, so that the different data and software packages may be physically distant, but this will not be a problem for the user. The system will take care for the management of these complex parts. CHEMOMENTUM will also integrate docking in the same environment. The user has the option to plan different workflows. The automated workflows are based on various tools, present in the Grid structure. UNICORE is at the basis of the Grid technology, which allows a safe exchange of data.

The advantages of CHEMOMENTUM are numerous. For regulatory purposes, there will be models already optimized for REACH. For instance, a model is under development for the BCF, based on the high-quality data provided by the project CAESAR. Independent models will be obtained using the automatic modeling procedure.

CHEMOMENTUM will allow the use of tridimensional descriptors within the automatic workflow, and in this way, the limitations we mentioned above are solved. Indeed, no manual optimization step is necessary, and this means a high reproducibility.

Furthermore, CHEMOMENTUM will generate a QMRF automatically, relative to the developed models, and this will facilitate the comparison and acceptance of the models.

The fact that the workflow is codified means that the complete QSAR model procedure is fully traceable. This is a unique feature offered by CHEMOMENTUM, thanks to its approach. The complete traceability of the individual steps is the optimal condition for the reproducibility and verifiability of the QSAR models. These characteristics are very valuable for REACH.

CHEMOMENTUM is working with the XML standard. XML has been identified as the preferable standard within the information technology community for QSAR (see for instance the US EPA DSSTox database and the EC projects CHEMOMENTUM, DEMETRA, and OpenMolGRID).

8.6.4 The OSIRIS Project

OSIRIS is another EC project fully dedicated to the REACH legislation [30]. The purposes of OSIRIS are broader than the simple QSAR models. OSIRIS wants to develop an intelligent testing strategy capable to assess whether the data for a certain chemical compound is sufficient or not. We have mentioned that the REACH legislation requires that sufficient data should be provided for a safe use of chemical compounds on the European market. On the basis of the different

tonnage, use and toxicity, different data are requested. The purpose of OSIRIS is to integrate all these elements into a tool. Specific software will be developed to assist users.

Here, the important aspect is that the QSAR models, from different sources, and also those developed within CAESAR, for instance, will be integrated, evaluating their possible use. Indeed, the final target of the registration is the overall information about the acceptability or otherwise of the chemical substance. It may happen that for a certain compound, the toxicity is not so critical because the exposure scenario reduces the concern, for instance. Thus, QSAR is only one component of a more complex strategy for the evaluation of the chemical substances. Multiple factors have to be considered, and also data from different sources. OSIRIS will be important because it will organize these multiple sources into a combined scheme, and thus provide practical examples of the use of QSAR. It is also important to notice that this means that the QSAR methods are tools that are suitable for integration with other approaches, not necessarily alternative, but supplementary tools.

8.7 Open Issues

As we said, QSAR is a possible tool to explore toxicity. Other tools have clear advantages because they refer to an experimental check of the result. New in vivo tools will be developed, useful to investigate toxicity phenomena, and many in vitro methods are under development.

The challenge will be on the integration of more and more complex data. Thousands of new data will be produced with the "omics" technologies, and this will provide further inputs to the research. Not only in silico methods, such as QSAR models, but also more complex tools will offer new perspectives if they will be capable to integrate the more complex information.

Regulations, such as REACH, anticipate that new tools will be available, and amendments to the regulation are foreseen in a few years.

Today QSAR are not suitable for many endpoints. For instance, for endocrine disruptors, models using docking software are often used. These models have some advantages because they clearly relate to the knowledge on the binding of a ligand to the receptor, such as estrogen receptor. In this case, there is good knowledge on the structure of the receptor, and the mechanism is known, and so the predictions can be based on this. Of course, in many other cases, such a detailed knowledge on the receptor basis of the effect is not available, and hence, this approach cannot be used.

A fundamental problem is the lack of experimental data. In this direction, the above-mentioned new omics techniques can provide useful resources.

There is the need of comparison and integration of different QSAR methodologies. The regulatory needs forced the debate on the comparison of the models. New efforts have to be put in this direction because there are many open problems. The components of the QSAR models are still in many cases not fully clarified.

The data are in many cases confidential, and the uncertainty unknown. Such a lack of knowledge is a problem, not only for QSAR, but first of all for the clear evaluation of the toxicity data.

Of course, this applies to QSAR for regulatory purposes more than in other cases. Industry can of course use its own confidential data for internal purposes, something that will not adversely affect the model.

There are still many errors in the chemical structure, and this aspect deserves more attention. We found very high percents of errors of chemical structures in scientific papers of QSAR. In case of models for regulatory purposes this kind of error should be minimized.

Chemical descriptors are in most of the cases obtained with equations that are not known. Even if the references to certain general equations are given, in practice, it is difficult to replicate the results obtained with chemical descriptors. As we have discussed, chemical descriptors based on tridimensional structures are subject to manual optimization, and this may change the descriptor values. But even in the case of other simpler descriptors, we found that using software from two different commercial sources, the results may be different. Even the use of two different versions of the same software may provide different results for the same descriptor. Even descriptors, which seem simple, such as number of double bonds, or of aromatic rings, are critical because they depend on how tautomers and aromaticity are considered in the different software, or are sensitive to the structure format that is used.

It is understandable that software producers are continuously improving their equations, and may find errors, which are corrected. But the lack of transparency in the used equations reduces the overall transparency and reproducibility of the results.

Again, these considerations are more typical for models for regulatory purposes. Expert modelers can explore complex situations using their experience, even if the possibility of applying the procedure in external situations or by other users is limited.

Of course, similar considerations about transparency can be done for the software used for the QSAR modeling. If the software is not explained, for commercial or other reasons, there are problems for the reproducibility and transparency of the tool.

There will not be a unique model for a certain endpoint. New experimental data will be produced, increasing the number of chemicals with available experimental data, and thus, the theoretical knowledge basis; there will be new chemical descriptors and new mathematical tools available. It is likely that there will be a continuous improvement with time.

This is a positive situation. It is also positive that for the same endpoint, there are, even now, different models. This offers a more robust series of tools to the user, mainly if these tools are based on different assumptions and adopt different techniques, such as fragments of chemical descriptors, linear or nonlinear systems, etc. It is not ideal to search for the best model. It is preferable to have a battery of tools, which, together, are in general more robust toward errors.

This complexity, however, needs better studies on how to integrate the different tools. This approach is also complicated by the lack of transparency of the individual QSAR models.

Acknowledgements We gratefully acknowledge the financial contribution of the European Commission's CAESAR (Contract SSPI 022674), OSIRIS (Contract GOCE-CT-2007-037017), and CHEMOMENTUM projects (Contract MIF1-CT-2006-039036).

References

1. Regulation (EC) No 1907/2006 of the European Parliament and of the Council of 18 December 2006 concerning the Registration, Evaluation Authorisation and Restriction of Chemicals (REACH). http://eur-lex.europa.eu/LexUriServ/site/en/oj/2006/l_396/l_39620061230en00010 849.pdf
2. C. Hansch et al., The correlation of biological activity of plant growth-regulators and chloromycetin derivatives with hammett constants and partition coefficients. J. Am. Chem. Soc. **85**, 2817–2824 (1963)
3. J. Hermens, Quantitative Structure–Activity Relationships for Predicting Fish Toxicity, in *Practical Applications of Quantitative Structure–Activity Relationships in Environmental Chemistry and Toxicology*, ed. by W. Karcher, J. Devillers (Kluwer, Dordrecht, 1990), pp. 263–280
4. G.C. Gini, A.R. Katritzky (Eds), *Predictive Toxicology of Chemicals: Experiences and Impact of AI Tools*. AAAI 1999 Spring Symposium Series. (AAAI Press, Menlo Park, 1999).
5. J. Devillers (ed), *Neural Networks in QSAR and Drug Design* (Academic Press, London, 1996)
6. J. Devillers (ed), *Genetic Algorithms in Molecular Modeling* (Academic Press, London, 1996)
7. R. Todeschini, V. Consonni, *Handbook of Molecular Descriptors* (Wiley-VCH, Weinheim, 2000)
8. M. Karelson, *Molecular Descriptors in QSAR/QSPR* (Wiley, New York, 2000)
9. A.A. Toropov, E. Benfenati, SMILES in QSPR/QSAR modeling: Results and perspectives. Curr. Drug Dis. Technol. **4**, 77–116 (2007)
10. E. Benfenati, A. Roncaglioni, In silico-aided prediction of biological properties of chemicals: Oestrogen receptor-mediated effects. Chem. Soc. Rev. **37**, 441 (2008)
11. Estimation Programme Interface (EPI) Suite. US EPA. http://www.epa.gov/opptintr/exposure/pubs/episuite.htm
12. J. Devillers, Application of QSARs in Aquatic Toxicology, in *Computational Toxicology: Risk Assessment for Pharmaceutical and Environmental Chemicals*, ed. by S. Ekins (Wiley, Hoboken, 2007), pp. 651–675
13. E. Benfenati et al., Validation of the Models, in *Quantitative Structure–Activity Relationships (QSAR) for Pesticide Regulatory Purposes*, ed. by E. Benfenati (Elsevier, Amsterdam, 2007), pp. 185–199
14. L. Eriksson et al., Methods for reliability, uncertainty assessment, and applicability evaluations of regression based and classification QSARs. Environ. Health Perspect. **111**, 1361–1375 (2003)
15. A. Golbraikh, A. Tropsha, Beware of q2!. J. Mol. Graph Model. **20**, 269–276 (2002)
16. R. Benigni et al., The expanding role of predictive toxicology: An update on the (Q)SAR models for mutagens and carcinogens. J. Environ. Sci. Health C **25**, 53–97 (2007)
17. E. Benfenati, Predicting toxicity through computers: a changing world. Chem. Cent. J. **1**, 32 (2007)

18. OECD. OECD Principles for the Validation, for Regulatory Purposes, of (Quantitative) Structure–Activity Relationship Models. Paris, France. http://www.oecd.org/document/23/0,3343,en_2649_34379_33957015_1_1_1_1,00.html
19. E. Benfenati, The specificity of the QSAR models for regulatory purposes: the example of the DEMETRA project. SAR QSAR Environ. Res. **18**, 209–220 (2007)
20. DEMETRA EC project. http://www.demetra-tox.net
21. TOPKAT software. http://www.accelrys.com/products/topkat/
22. MULTICASE software. http://multicase.com/products/prod09.htm
23. HazardExpert software. http://www.compudrug.com/
24. DEREK software. http://www.lhasalimited.org/index.php?cat = 2&sub_cat = 64
25. OECD QSAR Toolbox. http://www.oecd.org/document/23 /0,3343,en_2649_37465_33957015_1_1_1_37465,00.html
26. E. Benfenati (ed), *Quantitative Structure–Activity Relationships (QSAR) for Pesticide Regulatory Purposes* (Elsevier, Amsterdam, 2007)
27. C. Porcelli et al., Regulatory perspectives in the use and validation of QSAR. A case study: DEMETRA model for daphnia toxicity. Environ. Sci. Technol. **42**, 491–496 (2008)
28. CAESAR EC project. http://www.caesar-project.eu
29. CHEMOMENTUM EC project. http://www.chemomentum.org
30. OSIRIS project. http://www.osiris-reach.eu

Chapter 9
Quantitative Structure–Activity Relationships (QSARs) in the European REACH System: Could These Approaches be Applied to Nanomaterials?

Tomasz Puzyn, Danuta Leszczynska, and Jerzy Leszczynski

Abstract The European Union REACH system governs inventory of chemicals that are produced in large quantities (more than 1 ton per year). Since nanomaterials are becoming a distinct group of chemicals, differing from bulk substances by physicochemical properties and toxicity, the registration requirements for them should be reviewed and adapted according to their specificity. One of the promising computational techniques that can assist in obtaining required characteristics of the nanomaterials is (quantitative) structure–activity ((Q)SAR) methodology. This chapter reviews the current status of the nanomaterials under the REACH regulation and discusses the advances and challenges of (Q)SAR development for nanomaterials. Though this approach has been mainly applied to obtain information on physicochemical properties of selected nanospecies, its application to predict their toxicity will require genuine collaboration between modelers and experimentalists.

9.1 Role of Computational Chemistry in REACH

According to the novel European regulations named REACH System (Registration, Evaluation, Authorization of Chemicals), every chemical substance introduced into the market at the total amount of more than 1 ton per year has to be registered in the European Chemicals Agency (ECHA). Moreover, if the yearly production or import of the substance exceeds 10 tons, a comprehensive Chemical Safety Report (CSR) is required for the registration [1, 2].

T. Puzyn[1,2], D. Leszczynska[1,3], and J. Leszczynski[1] (✉)
[1]NSF CREST Interdisciplinary Nanotoxicity Center, Department of Chemistry and Biochemistry, Jackson State University, 1325 Lynch, St Jackson MS 39217-0510, USA; [2]Laboratory of Environmental Chemometrics, Faculty of Chemistry, University of Gdańsk Sobieskiego 18, 80-952 Gdańsk, Poland; [3]Department of Civil and Environmental Engineering, Jackson State University, 172 1325 Lynch St, Jackson, MS 39217-0510, USA
e-mail: jerzy@icnanotox.org, danuta@icnanotox.org

J. Leszczynski and M.K. Shukla (eds.), *Practical Aspects of Computational Chemistry*, 201
DOI: 10.1007/978-90-481-2687-3_9,

The REACH system was initiated to improve the protection of human health and the environment from the risk that can be posed by chemicals, to enhance the competitiveness of the EU chemicals industry (a key sector for European economy), to promote alternative methods for the assessment of hazards of substances, and to ensure the free circulation of substances on the international market of the European Union. The regulation was formally enforced on 1 June 2007. However, according to the REACH schedule, the registration procedures started from 1 June 2008 [1, 2].

It is also worth noting that substances already placed in the market are under the purview of REACH. These substances are the so-called "phase-in chemicals," because they may be only preregistered recently (deadline: the end of 2008), whereas the registration should be completed in different phases over the time until 31 May 2018. Priorities and deadlines for registration of the phase-in substances are based on the quantity of the substance manufactured or imported per year [1, 2].

Among a variety of information needed to prepare a registration dossier and the CSR, there are physicochemical, toxicological, and ecotoxicological data. Examples of the required endpoints are: vapor pressure, water solubility, *n*-octanol/water partition coefficient, skin sensitization, mutagenicity, reproductive toxicity, aquatic toxicity, bioaccumulation in aquatic species, persistence in the environment, ability to environmental long-range transport, etc. The data can either reflect direct experimental results or, under some circumstances, can be obtained from computational studies. Moreover, REACH not only allows employing computational chemistry methods for predicting the endpoints instead of the experiment, but even strongly promotes such solutions. The Article 13 says [1]:

> In particular for human toxicity, information shall be generated whenever possible by means other than vertebrate animal tests, through the use of alternative methods, for example, in vitro methods or qualitative or quantitative structure-activity relationship models or from information from structurally related substances (grouping or read-across).

Therefore, qualitative and quantitative structure–activity [(Q)SAR] methods are even more strongly recommended than the experimental testing. This strategy results in decreasing costs of registration and reducing number of animal experiments. From the opposite point of view, a great number and structural diversity of manufactured chemicals make a big challenge for computational chemists.

9.2 (Q)SAR Methodology

(Q)SAR methods are based on the assumption that the variance in the endpoint for a group of similar chemicals is determined by the variance in their molecular structures. Consequently, when the values of the endpoint are available only for a part of the group, it is possible to interpolate the lacking data from an appropriate mathematical model. Such a model should correlate the endpoint (dependent

variable) with a set of independent variables, which are a numerical representation of molecular structures, the so-called "molecular descriptors." Note, the endpoint can be related either to toxicity (activity) or physicochemical properties. In the latter case, to highlight the character of the endpoint, the name "Quantitative Structure – Property Relationship (QSPR)" is used [3, 4].

Until now, more than 3,000 different molecular descriptors have been developed [5]. In recent studies, the descriptors are computationally generated either from a formula or molecular model of the chemical. However, in some cases, experimentally measured properties might also be utilized for that purpose. The molecular descriptors can be classified according to their "dimensionality." The simplest, zero-dimensional (0D) ones are the constitutional descriptors, directly derived from the formula (e.g., the number of atoms in the molecule, the number of halogen atoms, etc.). One-dimensional (1D) descriptors reflect bulk properties (e.g., *n*-octanol/water partition coefficient). Two-dimensional (2D) descriptors refer to the way the atoms are connected in the molecule. A variety of 2D descriptors (called "topological descriptors") is calculated by applying the molecular graph theory, whereby particular atoms are treated as edges, while bonds – as vertices of a graph representing the molecule. Other important types of 2D descriptors are linear notation systems, e.g., the SMILES notation. Three-dimensional (3D) descriptors are obtained from 3D molecular geometry [5].

The molecular geometry should be optimized first at the appropriate level of quantum-mechanical theory. Geometry optimization might significantly increase the cost of computations; thus, the level of the theory should be chosen with care [6]. For typical molecules, relatively fast semi-empirical methods (e.g., RM1, PM6) can be employed [7, 8]. By applying either RM1 or PM6 method, it is possible to obtain a model of almost similar predictive ability to that of models based on Density Functional Theory (DFT) [9]. However, since quality of the semi-empirical results depends on how much the target compound is similar to the compounds originally used for parameterization of the method, one should not choose the semi-empirical methods for unusual chemical structures. In such a case, DFT methods (e.g., B3LYP functional) seem to be a better choice. It is worth highlighting that even slower (comparing to the semiempirics) DFT methods are currently much more efficient than the basic quantum-mechanical tool – ab initio ("from the beginning") scheme based on the Hartree–Fock (HF) method. On one hand, calculations performed at DFT level are much faster than the ab initio calculations. On the other hand, accuracy of the results is, in most cases, similar to the accuracy of ab initio post-HF methods taking into account electron correlation (i.e., second order of Møller-Plesset perturbation method, MP2). The examples of 3D descriptors derived from quantum-mechanical calculations include: dipole moment, polarizability, hyperpolarizability, partial charges on atoms, etc. Some authors distinguish an additional group of the descriptors: four-dimensional (4D) ones. However, there is no consensus about the fourth dimension. Four-dimensional descriptors can be defined as molecular properties arising from interactions of the molecule with probes characterizing the surrounding space. This representation is typical for the grid-based QSAR techniques (e.g., CoMFA, SOMFA, CoMSIA) [5, 10]. But the

term "4D" might be also used for expressing stereodynamic representation of a molecule, including flexibility of bonds, conformational behavior, etc. According to this point of view, the activity of particular conformers can be substantially different. Therefore, the 3D descriptors calculated for only one optimized geometry might be insufficient in such a case [5, 11, 12]. In any case, selection of the appropriate type of descriptors is a serious challenge for the modeler. Usually, the attempts should be made in the order of increasing dimensionality, taking into account any suggestions from toxic mechanism of action (if the endpoint is related to toxicity) or physical–chemical phenomena (if the physicochemical endpoint is modeled) [13].

QSARs, like every model, should be developed based on experimental data of high quality. "Quality" in the context of QSAR modeling means that uncertainty of the experimental results must be always lower than the variance within a group of studied compounds. Also, the probability of existing serious errors in the data has to be minimized by employing only sufficiently trained staff and equipped laboratory. But, even if the personnel are well-trained and the laboratory is well-equipped, measures will be always associated with a systematic error resulting from, for example, specific conditions, reagents, etc. Therefore, the data should be carefully examined before application for further modeling. In the ideal situation, all the measurements provided should be a single, standardized protocol. Moreover, the information on the intra-laboratory and inter-laboratory variability should be given as well [14].

By developing the molecular descriptors and linking them to experimental data for the endpoint, it is possible to begin modeling. It is worth mentioning that many procedures in QSAR nowadays have been standardized. Therefore, a modeler has to keep in mind that if the results are expected to be used for regulatory purpose, both the models and the way of presenting the results from modeling should fulfill many conditions.

The most important one is that the model should be appropriately validated to confirm the reliability of its predictions. First rules of the validation were worked out in March 2002 at an international workshop held in Setubal, Portugal ("Setubal Rules"). In November 2004, the rules were discussed and modified by the OECD Work Program on QSAR; they are now known as the "OECD Principles." According to these principles, each QSAR model should be associated with: (a) a well-defined endpoint; (b) an unambiguous algorithm; (c) a defined domain of applicability; (d) appropriate measures of goodness-of-fit, robustness and predictivity; and (v) a mechanistic interpretation, if possible [15, 16].

"Well-defined endpoint" means that the experimental data should refer to a single mechanism and, ideally, should be measured according to the same protocol. Moreover, the specific endpoint being predicted by the model has to be described so that the user can judge whether the intended use is appropriate [15, 16].

In general, the rules pay a close attention to transparency when the model and the results are presented. Not only well described data, but also "an unambiguous algorithm" must allow everybody to be able to repeat the modeling. Therefore, the model cannot be reported as a "black box," but all necessary details on the mathematical method, descriptors, etc. should be given in the report [15, 16]. Currently, the universal

format of such reports, namely QSAR Model Reporting Formats (QMRFs) and QSAR Model Reporting Formats (QPRFs) has been proposed [17].

The mathematical methods that are usually applied for defining the structure–activity relationships should be mentioned here. Basically, the choice of a method depends on the character of the endpoint and linearity of the relationship between the endpoint and the descriptors. If the endpoint is expressed quantitatively, a wide range of linear and nonlinear regression techniques can be employed. Otherwise, if the data have only qualitative character, the choice is limited to classification methods. Among the regression techniques, for example, there are commonly known methods such as : multiple linear regression (MLR), ordinary least squares (OLS), partial least squares (PLS), artificial neural networks (ANN) and many more. The most commonly used classifiers are: SIMCA, k-nearest neighbor (kNN) technique and supporting vector machines (SVM). The methods are often combined with a genetic algorithm (e.g., GA-PLS, GA-ANN, GA-kNN), which is applied to find the most optimal combination of the molecular descriptors (inputs for the model) [15, 16].

The next important term mentioned by the OECD principles is "domain of applicability" (AD). The AD refers to that region of the molecular feature space (the space defined by the molecular descriptors) and the model response, wherein the model produces reliable predictions. Since every model is calibrated based on the finite number of training compounds, quality of prediction for the new (target) compounds depends on how much the target compounds are structurally similar to the training set. It is also possible that some compounds initially selected for training the model, for some reasons (i.e., different mechanism of action), do not meet the basic QSAR assumption. In such cases, the predicted results (model response) would be substantially different from the experimental data and the compound should be probably removed from the training set. There are some techniques recommended for validation of the AD, for instance the range-based methods, the convex-hull method, the Williams plot (a plot of standardized residuals vs. leverage values), and the kernel density approach. But it is quite normal that the results of AD validation with particular methods can slightly differ from each other. In fact, it is always better to use more than one technique and discuss the results in terms of confidence limits (reliability) rather than strict borders of the domain. Also note that when a compound is found outside of the domain, it does not mean that the prediction is totally wrong. It simply means that the result is less reliable because the value was extrapolated (not interpolated) by the model [15, 16, 18, 19].

The fourth recommendation of the OECD experts is related to appropriate measuring and reporting goodness-of-fit, robustness, and predictivity of the model. The main intention was to clearly distinguish, whether a measure was derived only from the training set, from the internal validation (i.e., cross-validation, where the same chemicals are used for training and validation, but not at the same time) or from validation with use of an external set of compounds, not previously engaged in model optimization and/or calibration (external validation). A widely applied measure of fit is the squared correlation coefficient $R^2 = 1 - (\mathrm{RSS}/\mathrm{TSS})$, where RSS is the residual sum of squares and TSS is the total sum of squares

in the training set. However, one should remember that even if the R^2 is high for the particular model, nothing is known about robustness and predictive ability of the model. A corresponding measure for cross-validation is $Q^2 = 1\text{-(PRESS/TSS)}$, where PRESS is the predictive sum of squares, calculated for the compounds temporarily excluded from the training set and used for validation. Relatively high value of Q^2 (i.e., $Q^2 > 0.7$) also does not say anything about the predictivity of the model. It only informs that the model is robust, which means that the parameters of the model do not change significantly, whenever few training compounds are temporarily excluded from the training process. Only the validation coefficient, $Q^2_{\text{Ext}} = 1\text{-(PRESS}_{\text{Ext}}/\text{TSS})$, calculated based on the predictive sum of squares in the external validation set ($\text{PRESS}_{\text{Ext}}$) might be treated as a real measure of the model's predictivity [15, 16]. Models characterized by high values of Q^2_{Ext} usually have Q^2 high also. But, as Golbraikh and Tropsha [20] have demonstrated, the opposite relationship is not always true. Therefore, the external validation, after the initial verification of robustness, is the only way to prove the predictive ability of the QSAR model [16].

Finally, every QSAR model should be consistent with the knowledge from chemistry and toxicology on fundamental physical–chemical processes and mechanisms of toxic action. Mechanistic interpretations of QSARs are based on the selected molecular descriptors. Thus, the interpretation and selection of the descriptors during development of a model might be considered as one iterative process. The final mechanistic rationale can be established *a priori*, when the mechanism is known, or *a posteriori*, when the descriptors are selected on the basis of statistical fit alone. In the latter case, the model can shed new light on the problem, if mechanistic information of the process had not been available before [15, 16]. Moreover, the interpretation of some descriptors might not be direct and can depend on the context. For example, the energy of the highest occupied molecular orbital (HOMO) can be interpreted, according to the Koopman's theorem, as the negative value of ionization potential. However, in one of our contributions, we already used HOMO as an indicator of the substitution pattern for a group of halogenated congeneric compounds knowing that the ionization potential strictly depends on the substitution pattern in this group [21].

There are, of course, opponents of replacing the experiments by QSAR-like computational methods. Their main argument, especially against toxicity testing with QSAR, is a possibility of making the false positive prediction error (i.e., active, but predicted as nonactive). However, we do believe that if the model is properly validated and the results treated with extreme criticism, probability of such error is very low, even negligible.

9.3 Problematic Nanomaterials

In the past few decades, the standard elementary school definition of the difference between atoms and molecules was: the molecule is the tiniest part of a substance,

which keeps its properties unchanged. In the context of our current knowledge on nanoparticles and nanomaterials, this is clearly incorrect.

Definition of the "nanoscale" covers all species having at least one diameter of 100 nm or less. When nanoparticles are intentionally synthesized to be used in a range of consumer goods, they are called "nanomaterials." Without doubt, one can say that we are now at the beginning of "nanoindustrial revolution." Different types of nanomaterials are frequently applied in electronics, space technology, cosmetics and sunscreens production, medicine and pharmacy, solar energetics, textile industry, sport equipment, and many other areas [22, 23].

The increasing popularity of nanomaterials is due to their uniqueness when compared to the physical and chemical properties of bulk substances [22]. For instance, nano-sized metals, when they are compressed into solid objects, exhibit up to five times higher hardness than corresponding microcrystals. Band gap of semiconductor nanoparticles significantly decreases with decreasing size [24]. Finally, although atomic weight of carbon nanotubes is about one-sixth of the weight of steel, their Young's modulus and tensile strength are, respectively, 5 and 100 times higher than those of steel [25].

However, the exceptional size-specific behavior of nanomaterials in combination with their relatively large surface-to-volume ratio might result in potential risk for human health and the environment [26–28]. For example, fullerene (C_{60}) particles suspended in water are characterized by antibacterial activity against *Escherichia coli* and *Bacillus subtilis* [29] and by cytotoxicity to human cell lines [30]. Single- and multiwalled carbon nanotubes (CWCNTs and MWCNTs) are toxic to human cells as well [31, 32]. Nano-sized silicon oxide (SiO_2), anatase (TiO_2), and zinc oxide (ZnO) can induce pulmonary inflammation in rodents and humans [33–35].

Therefore, the "nano-enthusiasm" should be accompanied by extreme care to avoid repeating the stories of other "miracle substances" such as PCBs, DDT, and asbestos. Although it is impossible (and perhaps unnecessary) to stop expanding nanotechnology, a comprehensive risk assessment of nanomaterials must simultaneously be performed. This idea has become an official standpoint of the European Commission, expressed in two communications: *Towards a European strategy for nanotechnology* [36] and *Nanosciences and nanotechnologies: an action plan for Europe 2005–2009* [37].

A chance for more responsible manufacturing and better controlling of synthesized nanomaterials would be application of the REACH system. In 2006, an amendment to REACH proposing authorization of nanomaterials, according to their specific properties, has been announced. Unfortunately, the proposal was voted down; thus, the final version of REACH does not contain any specific requirements for registration and authorization of nanomaterials. In 2008, the Commission reviewed the current legislation and pointed out that nanomaterials have been covered by the European definition of "substance." Therefore, when an existing chemical substance, already placed on the market as bulk material, is introduced in a nanomaterial form, the registration dossier will have to be updated by including specific properties of the nanoform. In consequence, if hazard and risk

associated with the nanomaterial is identified, additional testing or information may be required [38]. Also, this document [38] highlighted existing lack of knowledge and standardized testing protocols for nanomaterials. Continuously, generated information from a wide range of research activities should lead to appropriate changes of legislation, if necessary. Moreover, the Commission intends to report on progress in this field within next 3 years.

According to the *ETUC Resolution on nanotechnologies and nanomaterials* submitted by European Trade Union Confederation, ETUC [39] a necessary change in the REACH system is to decrease the one-ton-threshold for registration of nanomaterials. In addition, the obligation to prepare the CSR for production volume above 10 ton per year may generate a loophole allowing many manufacturers or importers to avoid assessing the risk before bringing nanomaterials to the market. Thus, preparing the CSR should be obligatory for each nanomaterial substance to protect the workers and the environment. This example illustrates how the society worries about nanotechnology development and how urgently comprehensive scientific information on hazard and risk of nanomaterials is required.

9.4 Nano-QSAR Challenges

In 2007, the Scientific Committee on Emerging and Newly-Identified Health Risks (SCENIHR) published a document entitled: *Opinion on the appropriateness of the risk assessment methodology in accordance with the technical guidance documents for new and existing substances for assessing the risk of nanomaterials* [40]. The document discusses recent research needs in the field of nanoscience. Among the others, the authors highlight that QSAR methodology applied to certain bulk chemicals has serious limitations with respect to nanoparticles and development of new protocols for nano-QSAR represents a significant and challenging task.

A group of nanomaterials, as the only criterion of membership becomes particle size, is very diversified. Particular members of the group differ from each other by molecular geometry (i.e., nanotubes, fullerenes, crystal structures, clusters, etc.) and physicochemical characteristics (i.e., organic, inorganic, semiconductors, isolators, metals, nonmetals, etc.). Thus, it may and should be assumed that they also differ by the mechanism of action and – in consequence – defining one common applicability domain and QSAR model for all of them is impossible.

Until now, at least two systems of nanomaterials classification have been proposed. According to the first one [41, 42], nanoparticles can be divided, based on their dimensionality, into three groups: (a) 1D: nanowires, nanotubes, very thin fibers, capillaries, and pores; (b) 2D: carbon nanotubes formed by rolling graphene layers, cylinders, and fullerenes; and (c) 3D: clusters, crystals, and larger structures. The second one [43] introduces nine categories, namely: (a) spherical or compact particles; (b) high aspect ratio particles; (c) complex nonspherical particles; (d) compositionally heterogeneous particles – core surface variation; (e) compositionally heterogeneous particles – distributed variation; (f) homogeneous agglomerates;

(g) heterogeneous agglomerates; (h) active particles; and (i) multifunctional particles. The second classification is actually recommended by the European Joint Research Center [44].

As mentioned in the Sect. 9.2, both molecular descriptors and experimental data of high quality are required to construct a plausible model. According to suggestion by Oberdörster [45], particle size is not the only possible factor influencing toxicity of nanomaterials. The following features should be also considered: size distribution, agglomeration state, shape, porosity, surface area, chemical composition, structure-dependent electronic configuration, surface chemistry, surface charge, and crystal structure. Novel "nano-descriptors" should reflect these characteristics.

Descriptors of size, agglomeration state, shape, porosity, and surface could be obtained from images taken by scanning electron microscopy (SEM), transmission electron microscopy (TEM), and atomic force microscopy (AFM) [46].

Descriptors representing structure-dependent electronic configuration, surface chemistry, and surface charge can be generated by performing quantum-mechanical calculations. But nanomaterials are relatively large systems from the viewpoint of computational chemistry. Thus, since calculations of quantum-mechanical descriptors at the proper level of the theory for whole system can be impossible, some simplifications have to be introduced (e.g., calculations for only fragments, clusters) or additional approaches (e.g., periodic calculations) have to be applied. For instance, Shukla and Leszczynski [47] calculated the first ionization potential, electron affinity, HOMO-LUMO band gaps, isolated atom energies, cohesive energies, and cohesive energies per atom for small (containing between 40 and 144 atoms) carbon fullerenes, nano-disks, nano-capsules, and nano-bowls (whole structures) utilizing B3LYP functional (Density Functional Theory), and the Pople's type basis set 6-31G(d) concluding that the properties significantly changed with size. On the contrary, ab initio and DFT study concluded that only twelve-atoms-fragments yield important characteristics for substituted fullerene molecules [48]. In the case of nano-sized metal oxides, electron-dependent properties change rapidly, usually between 1 and 10 nm. For larger systems, the properties are the same as those of the bulk. For example, for $(TiO_2)_n^-$ clusters, the adiabatic detachment energy and HOMO-LUMO gap converges when $n \leq 7$ [49, 50]. Similarly, the band gap of ZnO nanoparticles decreases with increasing particle radius reaching the bulk value at about 4 nm [51]. This indicates that it is unnecessary to construct larger molecular models for the study of metal oxides nanoparticles of size between 10 and 100 nm.

Chemical composition and connectivity can be represented by a wide range of indexes derived from the already mentioned molecular graph theory (MGT) or graphs of atomic orbitals (GAO). The former theory has been used by Faulon and his group [52–55] to develop the signature molecular descriptor approach applicable for fullerene-type particles and nanotubes. The developed algorithm calculates the signature within five steps: (a) constructing of a subgraph containing all atoms and bonds that are at a distance no greater than the given signature height; (b) labeling the vertices in a canonical order; (c) constructing a tree spanning all the edges; (d) removing of all canonical labels that appear only one time, and

(e) writing the signature by reading the tree in a depth-first order [55]. The signature can be then used directly as a descriptor or the common topological parameters can be calculated based on them [52]. According to the latter (GAO) method [56–58], a molecule is represented by a graph consisting of vertexes representing particular orbitals (i.e., 1s, 2s, 2p, 3s, etc.) and edges connecting the orbitals between atoms. An example of a molecular descriptor derived from GAO is represented by the DCW_{AO} descriptor calculated according to this equation:

$$DCW_{AO} = \prod_k \{CW(AO_k)CW(\delta_k)\},$$

where AO_k is the atomic orbital, which is the image of the kth vertex in the GAO; δ_k is the vertex degree in GAO; $CW(AO_k)$ and $CW(\delta_k)$ are correlation weights determined by the Monte Carlo optimization method [59].

A detailed discussion of experimental in vitro and in vivo testing methodologies and results is not the purpose of this chapter. There are some comprehensive reviews covering this topic. For instance, the contribution by Oberdörster et al. [45] who have summarized recent data and highlighted gaps in this field; two works [60, 61] review data on environmental and human effects of carbon nanotubes in relation to their properties; a paper [62] that discusses toxicological endpoints of combustion-derived nanoparticles; a review [63] of quantum dots toxicity; an excellent review devoted to toxicity of particular nanomaterials classes by Borm et al. [26]; and many others.

However, the available data in most cases are insufficient to develop a QSAR model along with the previously discussed five OECD recommendations. Generally, the number of compounds tested with the same protocol is usually too small to split the data into a training set and a validation set. For example, Brunner et al. [64] investigated an influence of chemical composition and catalytic activity of four nano-sized metal oxides (TiO_2, Fe_2O_3, Mn_3O_4, Co_3O_4) on inducing oxidative stress in human lung epithelial cells. In an earlier contribution [65] , some of the authors studied in vitro cytotoxicity of seven nanoparticles (Fe_2O_3, asbestos, ZnO, CeO_2, ZrO_2, TiO_2, and $Ca_3(PO_4)_2$) based on another type of human and rodent cells. Unfortunately, neither the first nor the second set of data are applicable for QSAR development, because of very limited number of observations. Moreover, both the data sets cannot be combined, since the protocol of testing and perhaps also mechanism of action is different for each case.

Taking into account the difficulties in the calculation of molecular descriptors and a limited number of systematic experimental data for nanomaterials, one cannot expect a great progress in the field of the nano-QSAR yet. But, there are examples of preliminary models giving some hope for further perspectives.

Toropov et al. [66] constructed two models predicting water solubilities and *n*-octanol/water partition coefficients for carbon nanotubes utilizing the chiral vector components as descriptors. They obtained very high values of correlation coefficients ($R^2 = 0.999$) for both the training and the validation sets. But, since both

the sets contained only eight compounds (16 in total), the ratio of the compounds to the number of descriptors (8:2) was very low, which might suggest overparametrization of the model.

Toropov and Leszczynski [67] also predicted the Young's modulus for metal oxides, nitrides, mullite, and silicon carbide by using a DCW descriptor defined as follows:

$$\mathrm{DCW} = \prod_k \mathrm{CW}(I_k)$$

The descriptor was a product of the correlation weights, $CW(I_k)$, calculated by the Monte Carlo method for each k^{th} element of a special SMILES-like notation introduced by the authors. The notation codes the following characteristics: the atom composition, the type of substance (bulk or not, ceramic or not), and the temperature of synthesis. The QSAR model constructed in this way was validated with the use of many different splits into training ($n=21$) and validation ($n=8$) sets. Individual sub-models are characterized by high goodness-of-fit ($0.972<R^2<0.982$) and satisfactory external predictivity ($0.862<Q^2_{\mathrm{Ext}}<0.918$). The descriptors-to-compounds ratio (21:1) was also satisfactory. However, since the authors have not investigated the applicability domain of the model, it is not known if all the compounds (metal oxides, nitrides, mullite, and silicon carbide) can be truly modeled together.

Martin et al. [68] have modeled together solubility of 14 polycyclic aromatic hydrocarbons (PAHs) and fullerene in octanol and heptane utilizing descriptors calculated with the CODESSA package [69]. Also in this case, the applicability domain has not been validated. The structural difference between planar PAHs and spherical fullerene is probably too large for making reliable predictions. Moreover, the experimental solubilities of fullerene in both solvents ($\log S=-4.09$ in heptane and $\log S>4.18$ in octanol) are significantly lower than the solubilities of PAHs ($-3.80<\log S<0.22$ in heptane; $-3.03<\log S<-0.02$ in octanol).

Other interesting QSAR models were developed to describe the influence of different solvents on solubility of fullerene C_{60} [70, 71]. This is, in fact, a kind of reverse modeling, where the endpoint is defined for the same molecule in different conditions (i.e., solvents). Sivaraman [71] investigated solubility of C_{60} in alkanes, alkyl halides, alcohols, cycloalkanes, alkylbenzens, and aryl halides by using connectivity indexes, numbers of atoms, polarizability, and the variables indicating the substitution pattern as the molecular descriptors for the solvents. Similarly, Liu et al. [70] employed the CODESSA descriptors for the same purpose. Unfortunately, both the models have not been externally validated, so their ability to predict solubility of C_{60} in new solvents could be questionable.

The same modeling scheme has been employed by Toropov et al. [72], who once again used the DCW descriptor. But, in this case, the descriptor denoted the variance in a set of 26 organic solvents coded with the SMILES notation. The model was externally validated, which confirmed its predictivity. The values of

R^2 and Q^2_{Ext} were 0.81 and 0.79, respectively. Recently, the four-variable MLR model was applied to 122 various organic solvents and provide even more reliable predictions than the investigation performed on much smaller pool of solvents [73].

As one can notice, most of the published models predict physicochemical endpoints only. As far as we know, there is only one contribution presenting application of the QSAR approach for estimation of toxicity [74]. Toropov et al. [74] have successfully predicted toxicity of seven nano-sized inorganic oxides (SnO_2, CuO, La_2O_3, Al_2O_3, Bi_2O_3, SiO_2, and V_2O_3) against bacteria *E. coli* based on a model calibrated with other seven oxides (ZnO, TiO_2, Fe_2O_3, Y_2O_3, ZrO_2, In_2O_3, and Sb_2O_3). The authors applied the SMILES-like descriptors encoding symbols of atoms as well as the number and type (single or double) of bonds. The values of R^2 for the training set and the external test set were satisfactory: 0.991 and 0.823, respectively.

Although we do believe in appropriateness of QSAR methodology for nanomaterials, it is evident that development of QSARs is very limited because it lacks systematic experimental data. Without that, even designing of new, specific "nano-descriptors" is impossible, since their applicability cannot be verified.

9.5 Conclusions

It is obvious that in near future, some specific restrictions for nano-sized species would be introduced. This can, for example, force industry to prepare the chemical safety report for nanomaterials even if the total quantity of produced nanomaterial does not exceed the threshold of 1 ton per year. The REACH system promotes alternative ways of testing, that is represented by the QSAR methodology. Therefore, in next few years, QSAR modeling can become a very good (an inexpensive) solution for increasing nano-market in Europe. However, a QSAR model is plausible only if it fulfills comprehensive criteria of validation. Unfortunately, a lack of appropriate experimental data restrains development of nano-QSARs. The only way to solve the problem is to establish a strict collaboration between experimentalists and QSAR modelers. The role of the QSAR modelers might be especially important at the stage of planning the experiments. Only if the experiments are designed correctly, further application of statistic methods would provide reliable and useful data.

Acknowledgement The authors thank the NSF CREST Interdisciplinary Nanotoxicity Center (grant number HRD-0833178) and High Performance Computational Design of Novel Materials (HPCDNM) – Contract no. W912HZ-07-C-0071 funded by the Department of Defense through the U.S. Army Engineer Research and Development Center, Vicksburg, Mississippi for their support. This project was also partially financed by the European MF EOG funds. Tomasz Puzyn thanks the Foundation for Polish Science for support through the HOMING Program. The project was co-financed by the Polish Ministry of Science and Higher Education (grant no. DS/8430-4-0171-9).

References

1. Regulation (EC) No 1907/2006 of the European Parliament and of the Council of 18 December 2006 concerning the Registration, Evaluation, Authorisation and Restriction of Chemicals (REACH), establishing a European Chemicals Agency, and amemding Directive 1999/45/EC and repealing Council Regulation (EEC) No 793/93 and Commission Regulation (EC) No 1488/94 as well as Council Directive 76/769/EEC and Commission Directives 91/155/EEC, 93/67/EEC, 93/105/EC and 2000/21/EC, Official Journal of the European Union, L 396/1; The European Parliament and the Council of the European Union, Brussels, 2006
2. Guidance on registration, Guidance for the implementation of REACH; European Chemicals Agency, Helskinki, 2008
3. T.W. Schultz et al., Quantitative structure-activity relationships (QSARS) in toxicology: A historical perspective. THEOCHEM **622**, 1–22 (2003)
4. T.W. Schultz et al., The present status of QSAR in toxicology. THEOCHEM **622**, 23–38 (2003)
5. R. Todeschini et al., *Handbook of Molecular Descriptors* (Wiley-VCH, Weinheim, 2000)
6. F. Jensen, *Introduction to Computational Chemistry* (Wiley, Chichester, 1999)
7. G.B. Rocha et al., RM1: A reparameterization of AM1 for H, C, N, O, P, S, F, Cl, Br, and I, J. Comput. Chem. **27**, 1101–1111 (2006)
8. J.J.P. Stewart, Optimization of parameters for semiempirical methods V: Modification of NDDO approximations and application to 70 elements. J. Mol. Model. **13**, 1173–1213 (2007)
9. T. Puzyn et al., Calculation of quantum-mechanical descriptors for QSPR at the DFT level: Is it necessary? J. Chem. Inf. Model. **48**, 1174–1180 (2008)
10. T.I. Opera et al., 3D-QSAR of human immunodeficiency virus (I) protease inhibitors. III. Interpretation of CoMFA results. Drug Des. Discov. **12**, 29–51 (1994)
11. M. Ravi et al., 4D-QSAR analysis of a set of ecdysteroids and a comparison to CoMFA modeling. J. Chem. Inf. Comput. Sci. **41**, 1587–1604 (2001)
12. O. Mekenyan et al., In silico modelling of hazard endpoints: Current problems and perspectives. SAR QSAR Environ. Res. **14**, 361–371 (2003)
13. V.E. Kuz'min et al., Hierarchic system of QSAR models (1D-4D) on the base of simplex representation of molecular structure. J. Mol. Model. **11**, 457–467 (2005)
14. M.T.D. Cronin et al., Pitfalls in QSAR. THEOCHEM **622**, 39–51 (2003)
15. Guidance Document on the Validation of (Quantitative) Structure Activity Relationship [(Q)SAR] Models, No. 69; OECD Series on Testing and Assessment; Organisation of Economic Cooperation and Development: Paris, France, 2007. http://www.oecd.org. Accessed May 2008
16. P. Gramatica, Principles of QSAR models validation: Internal and external. QSAR Comb. Sci. **26**, 694–670 (2007)
17. JRC, European Chemicals Bureau, Computational Toxicology Group. http://ecb.jrc.it/qsar/. Accessed May 2008
18. L. Eriksson et al., Methods for reliability and uncertainty assessment and applicability evaluations of classification- and regression-based QSARs. Environ. Health Perspect. **111**, 1361–1375 (2003)
19. T.I. Netzeva et al., Current status of methods for defining the applicability domain of (quantitative) structure-activity relationships – The report and recommendations of ECVAM Workshop 52. Altern. Lab. Anim. **33**, 155–173 (2005)
20. A. Golbraikh et al., Beware of q2!. J. Mol. Graph. Model. **20**, 269–276 (2002)
21. T. Puzyn et al., How do the partitioning properties of polyhalogenated POPs change when chlorine is replaced with bromine? Environ. Sci. Technol. **42**, 5189–5195 (2008)
22. K. Thomas et al., Research strategies for safety evaluation of nanomaterials, Part VIII: International efforts to develop risk-based safety evaluations for nanomaterials. Toxicol. Sci. **92**, 23–32 (2006)

23. Market outlook for nanomaterials for electronics applications: Semiconductors, solar displays, sensors, RFID, Lighting The Information Network: New Tripoli, PA, 2008. http://www.theinformationnet.com
24. K.J. Klabunde, Introduction to Nanotechnology, in *Nanoscale Materials in Chemistry*, ed. by K.J. Klabunde (Wiley Interscience, New York, 2001)
25. A.G. Mamalis, Recent advances in nanotechnology. J. Mater. Process. Technol. **181**, 52–58 (2007)
26. P.J. Borm et al., The potential risks of nanomaterials: A review carried out for ECETOC. Part. Fibre Toxicol. **3**, 11 (2006)
27. M.R. Wiesner et al., Assessing the risks of manufactured nanomaterials. Environ. Sci. Technol. **40**, 4336–4345 (2006)
28. S. Zuin et al., Effect-Oriented Physicochemical Characterization of Nanomaterials, in *Nanonotoxicology: Characterization, Dosing and Health Effects*, ed. by N.A. Monteiro-Riviere, C.L. Tran (Informa Healthcare USA, New York, 2007)
29. D.Y. Lyon et al., Bacterial cell association and antimicrobial activity of a C-60 water suspension. Environ. Toxicol. Chem. **24**, 2757–2762 (2005)
30. C.M. Sayes et al., The differential cytotoxicity of water-soluble fullerenes. Nano Lett. **4**, 1881–1887 (2004)
31. A. Magrez et al., Cellular toxicity of carbon-based nanomaterials. Nano Lett. **6**, 1121–1125 (2006)
32. F.R. Tian et al., Cytotoxicity of single-wall carbon nanotubes on human fibroblasts. Toxicol. In Vitro **20**, 1202–1212 (2006)
33. T. Gordon et al., Pulmonary effects of inhaled zinc-oxide in human-subjects, guinea-pigs, rats, and rabbits. Am. Ind. Hyg. Assoc. J. **53**, 503–509 (1992)
34. B. Rehn et al., Investigations on the inflammatory and genotoxic lung effects of two types of titanium dioxide: Untreated and surface treated. Toxicol. Appl. Pharmacol. **189**, 84–95 (2003)
35. Y. Chen et al., Comparing study of the effect of nanosized silicon dioxide and microsized silicon dioxide on fibrogenesis in rats. Toxicol. Ind. Health **20**, 21–27 (2004)
36. Towards a European strategy for nanomaterials, COM(2004) 338; European Commission: Brussels, 2004
37. Nanosciences and nanotechnologies: An action plan for Europe 2005 – 2009, COM(2005) 243; European Commission, Brussels, 2005
38. Communication from the Commission to the European Parliament, The Council and the European Economic and Social Committee: Regulatory aspects of nanomaterials, SEC (2008) 2036; Commision of the European Communities, Brussel, 2008
39. ETUC Resolution on nanotechnologies and nanomaterials, European Trade Union Confederation, Brussels, 2008
40. The appropriateness of the risk assessment methodology in accordance with the Technical Guidance Documents for new and existing substances for assessing the risks of nanomaterials, European Commision, Scientific Committee on Emerging and Newly-Identified Health Risks, Brussels, 2007
41. I.P. Suzdalev, Size effects and intercluster interactions in nanosystems. Zh. Obshch. Khim **72**, 611–616 (2002)
42. V.Y. Shevchenko et al., The structural diversity of the nanoworld. Glass Phys. Chem. **29**, 577–582 (2003)
43. A.D. Maynard et al., Assessing exposure to airborne nanomaterials: Current abilities and future requirements. Nanotoxicology **1**, 26–41 (2007)
44. A. Worth, Computational nanotoxicology – towards a structure-activity based paradigm for investigationg the activity of nanoparticles. In Icon Workshop. Towards Predicting Nano-Bio Interactions, Zurich, Switzerland, 2007
45. G. Oberdörster et al., for ILSI Research Foundation/Risk Science Institute Nanomaterial Toxicity Screening Working Group. Principles for characterizing the potential human health

effects from exposure to nanomaterials: Elements of a screening strategy. Part. Fibre Toxicol. **2**, 8, (2005)
46. M.A. Poggi et al., Scanning probe microscopy. Anal. Chem. **76**, 3429–3443 (2004)
47. M.K. Shukla et al., A density functional theory study on the effect of shape and size on the ionization potential and electron affinity of different carbon nanostructures. Chem. Phys. Lett. **428**, 317–320 (2006)
48. T.M. Simeon et al., Ab initio quantum chemical studies of fullerene molecules with substituents $C_{59}X$ [X=Si, Ge, Sn], $C_{59}X^-$ [X=B, Al, Ga, In], and $C_{59}X^+$[N, P, As, Sb]. Int. J. Quantum Chem. **105**, 429–436 (2005)
49. Z.W. Qu et al., Theoretical study of the electronic structure and stability of titanium dioxide clusters $(TiO_2)_n$ with n = 1–9. J. Phys. Chem. B **110**, 8998–9007 (2006)
50. H.J. Zhai et al., Probing the electronic structure and band gap evolution of titanium oxide clusters $(TiO_2)_n^-$ (n = 1–10) using photoelectron spectroscopy. J. Am. Chem. Soc. **129**, 3022–3026 (2007)
51. L.M. Kukreja et al., Variable band gap ZnO nanostructures grown by pulsed laser deposition. J. Cryst. Growth **268**, 531–535 (2004)
52. J.L. Faulon et al., The signature molecular descriptor. 1. Using extended valence sequences in QSAR and QSPR studies. J. Chem. Inf. Comput. Sci. **43**, 707–720 (2003)
53. J.L. Faulon et al., The signature molecular descriptor. 2. Enumerating molecules from their extended valence sequences. J. Chem. Inf. Comput. Sci. **43**, 721–734 (2003)
54. C.J. Churchwell et al., The signature molecular descriptor. 3. Inverse-quantitative structure-activity relationship of ICAM-1 inhibitory peptides. J. Mol. Graph. Model. **22**, 263–273 (2004)
55. J.L. Faulon et al., The signature molecular descriptor. 4. Canonizing molecules using extended valence sequences. J. Chem. Inf. Comput. Sci. **44**, 427–436 (2004)
56. I. Gutman et al., The graph of atomic orbitals and its basic properties. 1. Wiener index. MATCH Commun. Math. Comput. Chem. **53**, 215–224 (2005)
57. I. Gutman et al., The graph of atomic orbitals and its basic properties. 2. Zagreb indices. MATCH Commun. Math. Comput. Chem. **53**, 225–230 (2005)
58. A.P. Toropova et al., QSPR modeling mineral crystal lattice energy by optimal descriptors of the graph of atomic orbitals. Chem. Phys. Lett. **428**, 183–186 (2006)
59. A.A. Toropov et al., An application of graphs of atomic orbitals for QSAR modeling the toxicity of metal oxides. Chemosphere, 2009 (submitted)
60. A. Helland et al., Reviewing the environmental and human health knowledge base of carbon nanotubes. Environ. Health Perspect. **115**, 1125–1131 (2007)
61. K. Donaldson et al., Carbon nanotubes: A review of their properties in relation to pulmonary toxicology and workplace safety. Toxicol. Sci. **92**, 5–22 (2006)
62. K. Donaldson et al., Combustion-derived nanoparticles: A review of their toxicology following inhalation exposure. Part. Fibre Toxicol. **2**, 10 (2005)
63. R. Hardman, A toxicologic review of quantum dots: Toxicity depends on physicochemical and environmental factors. Environ. Health Perspect. **114**, 165–172 (2006)
64. T.J. Brunner et al., In vitro cytotoxicity of oxide nanoparticles: Comparison to asbestos, silica, and the effect of particle solubility. Environ. Sci. Technol. **40**, 4374–4381 (2006)
65. L.K. Limbach et al., Oxide nanoparticle uptake in human lung fibroblasts: Effects of particle size, agglomeration, and diffusion at low concentrations. Environ. Sci. Technol. **39**, 9370–9376 (2005)
66. A.A. Toropov et al., Predicting water solubility and octanol water partition coefficient for carbon nanotubes based on the chiral vector. Comput. Biol. Chem. **31**, 127–128 (2007)
67. A.A. Toropov et al., A new approach to the characterization of nanomaterials: Predicting Young's modulus by correlation weighting of nanomaterials codes. Chem. Phys. Lett. **433**, 125–129 (2007)
68. D. Martin et al., QSPR modeling of solubility of polyaromatic hydrocarbons and fullerene in 1-octanol and *n*-heptane. J. Phys. Chem. B **111**, 9853–9857 (2007)

69. A.R. Katritzky et al., CODESSA PRO. COmprehensive DEscriptors for Structural and Statistical Analysis, University of Florida, USA, 2001–2005. http://www.codessa-pro.com. Accessed June 2007
70. H. Liu et al., Accurate quantitative structure-property relationship model to predict the solubility of C60 in various solvents based on a novel approach using a least-squares support vector machine. J. Phys. Chem. B **109**, 20565–20571 (2005)
71. N. Sivaraman et al., QSPR modeling for solubility of fullerene (C_{60}) in organic solvents. J. Chem. Inf. Comput. Sci. **41**, 1067–1074 (2001)
72. A.A. Toropov et al., QSPR study on solubility of fullerene C_{60} in organic solvents using optimal descriptors calculated with SMILES. Chem. Phys. Lett. **441**, 119–122 (2007)
73. T. Petrova et al., Modeling of fullerene C_{60} solubility in organic solvents: The use of quantum-chemical and topological descriptors in QSPR study. J. Nanopart. Res., 2009 (submitted)
74. A.A. Toropov et al., QSAR modeling toxicity of nanosized oxides towards *E. coli* bacteria using the SMILES-based optimal descriptors. Chem. Biol. Drug Des., 2009 (submitted)

Chapter 10
Structure–Activity Relationships in Nitro-Aromatic Compounds

R.A. Vogt, S. Rahman, and C.E. Crespo-Hernández

Abstract Many nitro-aromatic compounds show mutagenic and carcinogenic properties, posing a potential human health risk. Despite this potential health hazard, nitro-aromatic compounds continue to be emitted into ambient air from municipal incinerators, motor vehicles, and industrial power plants. As a result, understanding the structural and electronic factors that influence mutagenicity in nitro-aromatic compounds has been a long standing objective. Progress toward this goal has accelerated over the years, in large part due to the synergistic efforts among toxicology, computational chemistry, and statistical modeling of toxicological data. The concerted influence of several structural and electronic factors in nitro-aromatic compounds makes the development of structure–activity relationships (SARs) a paramount challenge. Mathematical models that include a regression analysis show promise in predicting the mutagenic activity of nitro-aromatic compounds as well as in prioritizing compounds for which experimental data should be pursued. A major challenge of the structure–activity models developed thus far is their failure to apply beyond a subset of nitro-aromatic compounds. Most quantitative structure–activity relationship papers point to statistics as the most important confirmation of the validity of a model. However, the experimental evidence shows the importance of the chemical knowledge in the process of generating models with reasonable applicability. This chapter will concisely summarize the structural and electronic factors that influence the mutagenicity in nitro-aromatic compounds and the recent efforts to use quantitative structure–activity relationships to predict those physicochemical properties.

R.A. Vogt, S. Rahman and C.E. Crespo-Hernández (✉)
Department of Chemistry, Case Western Reserve University, 10900 Euclid Avenue, Cleveland, OH 44106, USA
e-mail: carlos.crespo@case.edu

J. Leszczynski and M.K. Shukla (eds.), *Practical Aspects of Computational Chemistry*, 217
DOI: 10.1007/978-90-481-2687-3_10,

10.1 Introduction

Nitro-polycyclic aromatic hydrocarbons, referred to as nitro-aromatic compounds hereafter, constitute one of the most troubling classes of environmental pollutants. They are derivatives of polycyclic aromatic hydrocarbons (PAHs) that contain two or more fused aromatic rings made of carbon and hydrogen atoms and at least one nitro group (Fig. 10.1). Concern about these compounds arises partly from their ubiquity: nitro-aromatic compounds are released to the environment directly from a variety of incomplete combustion processes [1] and are also formed in situ by atmospheric reactions of PAHs [2]. Nitro-aromatic compounds have been found in grilled food; in diesel, gasoline, and wood-smoke emissions; and are commonly found in atmospheric particulate matter, natural waters, and sediment [3–8].

The larger concern about nitro-aromatic compounds is that environmental exposure to these molecules can cause cancer in humans and in other living organisms. Nitro-aromatic compounds are acutely toxic, mutagenic, and carcinogenic in laboratory mammals and in vitro test systems [6, 8]. Despite the potential negative impact of nitro-aromatic compounds on human health, they continue to be emitted into ambient air from municipal incinerators [9], motor vehicles (particularly from diesel exhausts) [10, 11], industrial power plants [12], and other sources. Evidence

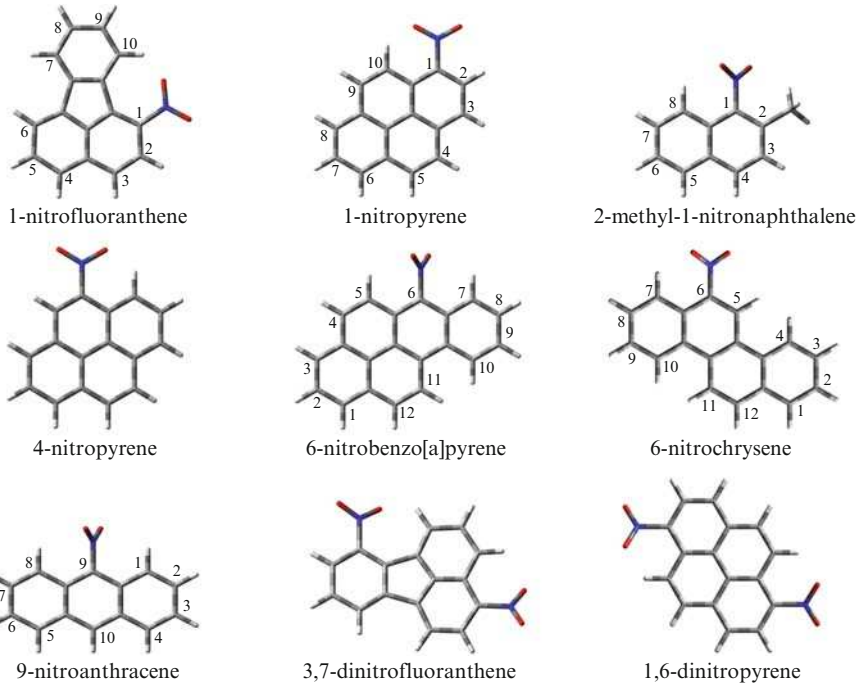

Fig. 10.1 Structures, names and numbering of representative nitro-aromatic compounds

suggests that nitro-aromatic compounds contribute as much as 10% of the total mutagenicity of inhalable, suspended particles in polluted areas [2, 13]. Epidemiological studies show that exposure to diesel exhaust and urban air pollution is associated with an increased risk of lung cancer [7]. Tobacco smoking remains the leading cause of lung cancer in humans. However, interest in assessing the potential risk of nitro-aromatic compounds to humans and in studying their structure–activity relationships (SARs) have increased over the years. This is largely due to the observation of increased lung cancer risk from exposure to particulate air pollution and the detection of nitro-aromatic compounds in lungs of nonsmokers with lung cancer [14].

The current state of knowledge about how structural and electronic factors influence biological activity in nitro-aromatic compounds is succinctly surveyed in this contribution. Knowledge of the likely roles played by physicochemical factors in mediating the biological activity of nitro-aromatic compounds should provide fundamental information to predict their mutagenic potential, and to assist in the process of screening and prioritizing compounds for further experimental analysis. The emphasis of the present work is twofold: (1) to highlight the structural and functional changes that influence the ability of a nitro-aromatic compound to induce toxicity; and (2) to summarize current efforts by many groups to develop SARs that can assist in predicting the mutagenic properties of nitro-aromatic compounds.

This chapter is organized as follows: Sect. 10.2 presents the assay that is broadly used to assess the mutagenicity of nitro-aromatic compounds and general information about the different tester strains commonly used. Sect. 10.3 summarizes the metabolic pathways leading to the biological activity of nitro-aromatic compounds. This section is followed by a discussion of the most common structural and electronic factors known, thus far, to affect the mutagenic activity in these compounds. Finally, efforts to quantitatively model the SARs in nitro-aromatic compounds using molecular descriptors and statistical approaches are presented, followed by a brief suggestion of how computational chemists can further advance this topical and exciting area of research.

The authors would like to emphasize that excellent reviews about the biological activity of nitro-aromatic compounds in bacterial and mammalian cells have been presented, several of which have discussed SARs in nitro-aromatic compounds to some extent [3, 6, 8, 15–20]. The present survey is meant to complement those previous works.

10.2 The Ames *Salmonella Typhimurium* Assay

The Ames *Salmonella typhimurium* assay [3, 21–26] is the most widely used test to evaluate the mutagenic activity of xenobiotic compounds. The assay serves as a quick and relatively inexpensive test to estimate the carcinogenic potential of a compound. It makes use of a variety of bacterial strains to screen compounds for

their mutagenic activity and to determine the metabolic pathways responsible for their mutagenic potency. The Ames assay uses modified *S. typhimurium* strains that are specifically altered at the hisG gene to obstruct histidine production. The bacterial strains are grown in an environment limited of histidine. As the histidine is consumed, only the revertants that are mutated by the xenobiotic compound are able to adapt to become histidine self-sufficient. Hence, the number of revertant colonies is directly proportional to the mutagenicity of the xenobiotic compound [27].

Different Salmonella strains have been engineered to test for different types of mutations and metabolic pathways. Initially, the strains, TA1535 and TA1538, were developed to test for base-pair substitution mutations and for frame-shift mutations at the site of the histidine gene, respectively [27]. Strains TA100 and TA98 were produced by adding a resistance factor to TA1535 and TA1538, respectively. The TA100 and TA98 strains are widely used as they are more sensitive to mutagenic activity, making them a more effective means of testing for mutagens [27].

Through additional modifications to the tester strains, the Ames assay can also be used to elucidate the metabolic pathways that lead to mutagenesis. Strains deficient or abundant in the enzymes necessary for nitroreduction pathways have been developed. TA98NR is deficient in nitroreductase, while TA98/1,6-DNP_6 is deficient in *O*-acetyltransferase; two major enzymes in metabolic pathways leading to mutation [28]. The strains YG1021 and YG1024 are derivatives of TA98 that overproduce nitroreductase enzymes and *O*-acetyltransferase enzymes, respectively, while YG1041 is a TA98 derivative that overproduces both enzymes [29]. Strains YG1026 and YG1029 are derivatives of TA100 that also overproduce nitroreductase and acetyltransferase, respectively [28]. Other tester strains are available that differ slightly, testing for different types of mutations or mutations with a different sequence of nucleic acids at the target gene. However, the tester strains mentioned above are the ones most commonly used to investigate the mutagenicity in nitro-aromatic compounds. A rat liver homogenate fraction, termed S9, is often added to the tester strains in order to include an additional mono-oxygenase enzymatic system for further metabolic activation of the mutagenic compounds [17, 28].

Despite the wide use and general success of the Ames assay in studying the mutagenic properties in nitro-aromatic compounds, it has been shown that the mutagenic potency and metabolic pathways leading to biological activity in nitro-aromatic compound can be different in bacterial versus mammalian cells [8, 17]. For example, nitro-aromatic compounds can be metabolized by reductive and oxidative pathways in mammalian cells, while bacterial enzymes in *S. typhimurium* only metabolize nitro-aromatic compounds via nitro group reduction [3, 15, 24, 26, 30, 31]. Likewise, 1-nitropyrene is a potent mutagen in bacteria, but it is only weakly mutagenic in mammalian cells [17]. 6-nitrobenzo[a]pyrene is not a direct-acting mutagen in *S. typhimurium* assay [21] but can become potent direct-acting mutagen in human intestinal microflora [32]. Thus, confirmatory tests using laboratory animals are essential for a proper assessment of the mutagenic potency of a given compound.

In what follows, no explicit attention is given to the specific type of assays or tester strains used to determine the mutagenic activity in nitro-aromatic compounds. This particular choice is made consciously, as the emphasis of this work is on the structural and electronic factors that modulate the mutagenic activity of the nitro-aromatic compounds in general. The interested readers are recommended to refer to the original works for more detailed discussions.

10.3 Metabolic Activation

When nitro-aromatic compounds are incorporated in tester strains or laboratory animals, referred to as biological system hereafter, they often undergo a series of biochemical transformations that are collectively known as metabolism. It is, thus, instructive to briefly introduce the metabolic pathways that nitro-aromatic compounds might undergo before establishing connections between structural/electronic factors and mutagenic activity. At least five metabolic activation pathways have been identified in the formation of mutations and/or DNA binding to *S. typhimurium* in *in vitro* or *in vivo* studies (Fig. 10.2) [15, 30, 33–36]. The activation pathways include: (1) nitro-reduction; (2) nitro-reduction followed by esterification; (3) ring-oxidation; (4) ring-oxidation followed by nitro-reduction; and (5) ring-oxidation followed by nitro-reduction and esterification [17]. Aerobic metabolism generally forms oxidized metabolites, such as dihydrodiols, diol epoxides, hydroquinones,

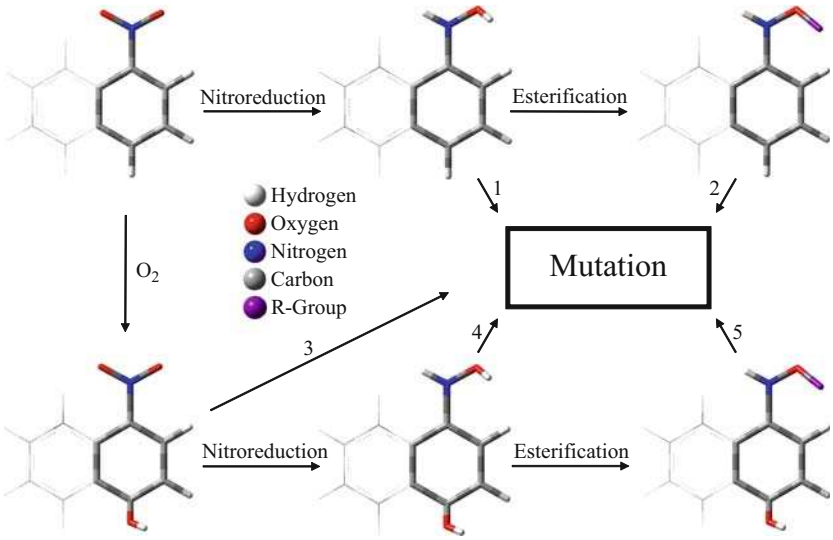

Fig. 10.2 Metabolic activation pathways leading to mutation in nitro-aromatic compounds. Ring-oxidation might occur in the ortho, meta, or para position. Shown in the figure is the para metabolic ring-oxidation. Figure adapted from [15]

quinones, benzylic alcohols, and ketones [15, 37]. Depending on the particular nitro-aromatic compound, one or more of these pathways may be relevant for its metabolic activation.

Nitroreduction is thought to be the most important pathway linked to the mutagenesis of nitro-aromatic compounds [8, 17]. Metabolic reduction of nitro-aromatic compounds involves at least three sequential steps: (1) reduction of the nitro group to the corresponding nitroso-aromatic compound; (2) further reduction to the *N*-hydroxyamino aromatic compound; and (3) final reduction to the amino-aromatic compound (see Fig. 10.2) [17]. The *N*-hydroxyamino metabolite has been shown to bind to DNA [38]. However, some *N*-hydroxyamino metabolites require extra activation through *O*-esterification to exert the maximum biological activity [33, 39, 40]. The covalent binding of a metabolite to cellular DNA forms DNA adducts that can then initiate mutation or tumor formation in biological systems. In fact, covalent binding of reactive metabolites to cellular DNA is considered a critical step in the multistage process leading to tumor formation [17]. It should be noted that the ultimate biological impact that a nitro-aromatic compound might have will depend on whether or not it undergoes bio-activation in the first place, its inherent toxicity, and if the biological system is capable of detoxifying and/or repairing the biochemical transformation(s). A detailed discussion of many of the DNA-nitro-aromatic adducts formed and the possible repair processes taking place in biological systems is outside the scope of the present work and interested readers are referred to some of the excellent reviews that have been published in recent years [5, 8, 17].

10.4 Structural and Electronic Factors Modulating Biological Activity

The following section illustrates the key structural and electronic factors that play a role in the direct-acting mutagenicity of nitro-aromatic compounds.

10.4.1 Orientation and Position of the Nitro Group

The orientation of the nitro group is an important structural factor that influences the mutagenic activity of nitro-aromatic compounds. In general, nitro groups *peri* to two hydrogen atoms are expected to be in a perpendicular or near perpendicular orientation relative to the aromatic rings (Fig. 10.3a), while nitro groups *peri* only to one hydrogen atom are expected to stay in a parallel orientation (Fig. 10.3b) [15, 17, 31, 41]. The preferred perpendicular orientation of the nitro group *peri* to two hydrogen atoms is due to the steric hindrance that restricts the torsion angle of the nitro group. It has been suggested that nitro-aromatic compounds with their nitro

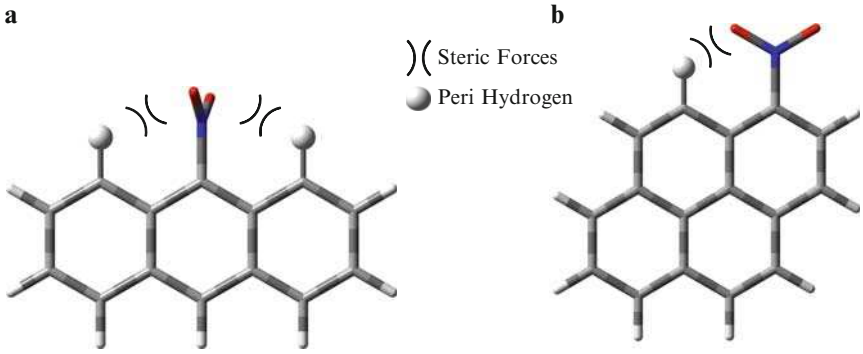

Fig. 10.3 The nitro group in (**a**) 9-nitroanthracene is *peri* to two hydrogen atoms while in (**b**) 1-nitropyrene is *peri* to one hydrogen atom. Steric forces resulting from the *peri* hydrogen atoms force the nitro group to be out-of-plane relative to the aromatic moiety

group oriented perpendicular or nearly perpendicular to the plane of the aromatic rings generally exhibit weak or no mutagenicity [31, 41–44]. Sera et al. [28] studied 22 different mono-, di-, and trinitrophenanthrene derivatives, and observed that nitrophenanthrene derivatives with nitro groups having torsion angles below 10° were more mutagenic than those with torsion angles above 50°. The torsion angles of the studied nitrophenanthrene derivatives were calculated previously by Fukuhara et al. using the AM1 semi-empirical method [45]. For example, 1,5-, 1,10- and 4,9-dinitrophenanthrene (with calculated torsion angles of 30.2 and 89.8°, 63.0 and 64.5°, and 80.1 and 24.6°, respectively) showed weaker mutagenic potency than other dinitrophenanthrene derivatives. Conversely, dinitrophenanthrene derivatives with parallel or near parallel torsion angles exhibited high mutagenic activity.

The lower mutagenic potency in nitro-aromatic compounds having perpendicular or near perpendicular nitro groups is thought to be due to steric constraints, which can decrease the ability of the nitro-aromatic compound to fit into the active site of the enzyme [42]. Other researchers have suggested that the reduced derivatives of these compounds may undergo redox cycling to regenerate the parent nitro compound after enzymatic nitro-reduction [5] or that the perpendicular orientation of the nitro-aromatic compound may not allow the formation of stable *N*-hydroxyamine metabolites, an important intermediate in the direct-acting mutagenicity of nitro-aromatic compounds [17].

The position of the nitro group is also an important structural factor in determining the biological activity in nitro-aromatic compounds. This is evident from studies that show markedly different mutagenic potency in structural isomers of nitro-aromatic compounds [3, 15, 24, 26, 30, 31, 44, 46]. Structural isomers like 1-, 2-, 3-, and 6-nitrobenzo[a]pyrene have dramatically different mutagenic potency [47–49]: 6-nitrobenzo[a]pyrene is a weak mutagen, while 1-, 2-, and 3-nitrobenzo [a]pyrene are potent mutagenes [47–49].

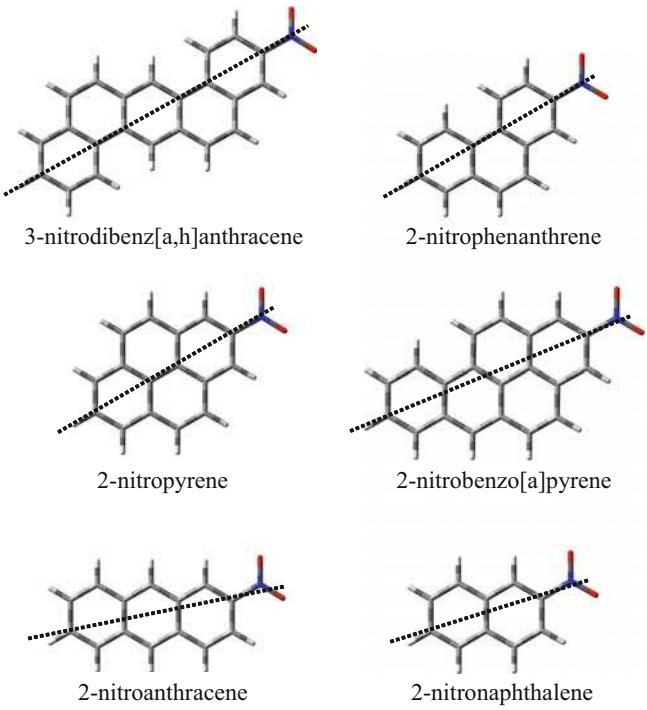

Fig. 10.4 Representative nitro-aromatic compounds having the nitro group located on the longest axis. The longest axis for each compound is denoted with a *dashed line*

Yu et al. [50] showed that isomers of nitro-aromatic compounds with their nitro substituent situated along the longest axis of the molecule, exhibited the highest direct-acting mutagenicity (Fig. 10.4). The authors found that 2-nitrophenanthrene, 2-nitropyrene, 2-nitrochrysene, 2-nitrobenz[a]anthracene, 2-nitrobenzo[a]pyrene, and 3-nitrobenz[a,h]anthracene, all of which have nitro groups along the longest axis of the molecule, exhibit higher mutagenicity than their corresponding isomers. The longest-axis hypothesis is in agreement with the nitro-group orientation relationship described above, since nitro-aromatic compounds with nitro substituents oriented perpendicular to the plane of aromatic rings have, in general, their nitro group situated either at or near the shortest axis of the molecule and exhibit weak mutagenic activity [50].

As described in the previous section, enzymatic nitro-reduction is an important metabolic pathway that forms N-hydroxyamine metabolites and determines the direct-acting mutagenicity of nitro-aromatic compounds. Thus, it has been suggested that the higher mutagenic potency in nitro-aromatic compounds having the nitro group along the longest axis of the molecule is due to their ability to stabilize the *N*-hydroxyamine metabolites by induction and resonance effects more efficiently than their corresponding isomers [17].

10.4.2 *Effect of the Reduction Potential of the Nitro-Aromatic Compound*

Since nitro-reduction is an important metabolic pathway in the direct-acting mutagenicity of many nitro-aromatic compounds (see Sect. 10.3 above), the energy required to reduce the nitro group has been studied by various researchers. The half-wave reduction potential is a measure of the tendency of a chemical species to acquire electrons and to be reduced. The less negative the reduction potential, the easier it is to reduce the chemical species. As might be expected, correlations have been found between the reduction potential and the direct-acting mutagenicity of nitro-aromatic compounds [8, 17, 28, 44, 51, 52]. Klopman et al. [52] were the first to show that there is a relationship between the direct-acting mutagenicity of nitro-aromatic compounds and their first half-wave reduction potential. The authors found linear relationships between the first half-wave reduction potentials of nitro-aromatic compounds and the logarithm of their mutagenic potency. It was shown that LUMO energies, obtained using Hückel calculations, correlate linearly with the first half-wave reduction potentials. Thus, the authors suggested that calculations of LUMO energies can be used successfully to predict the mutagenicity of nitro-aromatic compounds.

Lopes and co-workers recently observed that as the electrochemical half-wave reduction potentials of the nitro-aromatic compounds become more negative, the compound's direct-acting mutagenicity decreases [53]. This is in agreement with earlier studies showing that the extent of direct-acting mutagenicity correlates with the reduction potential and LUMO energies in compounds having nitro groups parallel or near parallel to their aromatic plane (Ex. 1-nitronaphthalene, 1-nitropyrene and 1-nitrobenzo[a]-pyrene) [28, 44, 52]. The direct-acting mutagenicity of the nitro-aromatic compounds investigated by Lopes et al. decreases as follow: 3-nitrofluoranthene (-0.51 V) $\gg$ 1-nitropyrene (-0.61 V) $>$ 6-nitrochrysene (-0.64 V) $\gg$ 9-nitroanthracene (-0.84 V), which correlates with the decreases in their half-wave reduction potentials.

The half-wave reduction potential of 3-nitrofluoranthene, 1-nitropyrene, 6-nitrochrysene, and 9-nitroanthracene is also in reasonable agreement with the estimated orientation of their nitro group. For example, 9-nitroanthracene has the nitro group perpendicular or near perpendicular to the aromatic plane and shows the most negative half-wave reduction potential. This is thought to be due to steric hindrance of the nitro group with the two hydrogen atoms in *peri* positions (see Fig. 10.3). On the other hand, 1-nitrofluoranthene, 1-nitropyrene, and 6-nitrochrysene have only one hydrogen atom *peri* to the nitro group, and thus, are expected to attain near parallel nitro group orientations. The parallel or near parallel nitro group orientation should increase the conjugation of the nitro group π-electrons with those of the aromatic rings, explaining their less negative reduction potentials and the ease of activation of these compounds by enzymatic nitro-reduction.

Importantly, Fu and co-workers have shown that correlations of the first half-wave reduction potentials with direct-acting mutagenicity are valid only when the

compounds have similar molecular size [17, 41, 44]. It was shown that nitro-aromatic compounds having similar first half-wave reduction potentials and parallel or near parallel nitro group orientation exhibit markedly different mutagenic activity [44]. Thus, the first half-wave reduction potential does not always correlate with the direct-acting mutagenicity in nitro-aromatic compounds having parallel or nearly parallel nitro group orientation. The authors presented evidence suggesting that although nitro-aromatic compounds with perpendicular nitro groups generally have very weak or no direct-acting mutagenicity, nitro-aromatic compounds with perpendicular nitro groups that have a relatively low first half-wave reduction potential could exhibit direct-acting mutagenicity. It was proposed that a combination of the nitro group orientation and the first half wave potential might be used to predict the direct-acting mutagenicity in nitro-aromatic compounds that are structurally similar [41].

10.4.3 Molecular Size, Number of Nitro Groups, and Structural Arrangement

The mutagenicity of nitro-aromatic compounds is influenced by the number of aromatic fused rings. Nitro-aromatic compounds with three and four rings are, in general, more mutagenic than those with two rings. In a literature review of 32 nitro-aromatic compounds having three fused rings, it was found that 31% of those nitro-aromatic compounds have low mutagenic potency, while 69% have medium mutagenic potency [8]. Likewise, 30% of the nitro-aromatic compounds examined that have four rings exhibit a high mutagenic potency, 63% a medium mutagenic potency and only 7% show a low mutagenic potency. This tendency toward a higher mutagenic potency with a greater number of rings is not followed in nitro-aromatic compounds with five rings [8], suggesting that the dimension of the nitro-aromatic compound also plays a role in the biological activity of these compounds (see below).

The increase in mutagenic potency with molecular size depends sensitively on the number of nitro groups that the compound has [8]. Evidence shows that the mutagenicity of a nitro-aromatic compound increases if an additional nitro group is present. For example, a second nitro group increases the mutagenic potency in nitrofluorenes, nitrophenanthrenes, nitrofluoranthenes, nitropyrenes and nitrobenzo[*a*]pyrenes. Compounds like 3,7- and 3,9-dinitrofluoranthene, 1,6- and 1,8-dinitropyrene and 3,6-dinitrobenzo[*a*]pyrene have the highest mutagenic potency measured to date. However, the mutagenic potency of a given nitro-aromatic compound did not continue to increase with the addition of a third or a fourth nitro group.

The structural arrangement and dimension can also influence the mutagenic potency of nitro-aromatic compounds. Vance and Levin studied the mutagenic potency of nitro-aromatic compounds in the naphthalenic and benzylic series

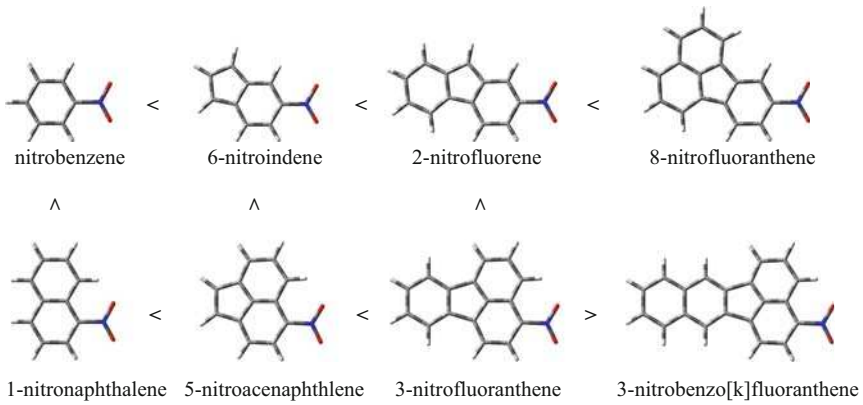

Fig. 10.5 Comparison of the mutagenic potency of nitro-aromatic compounds in the naphthalenic and benzylic series as the molecular dimensionality increases. Inequality symbols indicate the relative mutagenic potency of each compound. Figure adapted from [54]

shown in Fig. 10.5 [54]. It was observed that the mutagenic potency increases in going from 1-nitronaphthalene to 3-nitrofluoranthene, but decreases in 3-nitrobenzo [k]fluoranthene. The decrease in mutagenicity in 3-nitrobenzo[k]fluoranthene suggests that the length of the nitro-aromatic compound in the naphthalenic series affects its biological activity. A comparison of 2-nitrofluorene with 8-nitrofluoranthene and 3-nitrofluoranthene suggests that the degree of aromaticity also plays a role in the bioactivity of these compounds. 8-nitrofluoranthene and 3-nitrofluoranthene are more mutagenic than 2-nitrofluorene, even though the latter is of similar length to the former compounds. The additional benzene rings in 8-nitrofluoranthene and 3-nitrofluoranthene increase their aromaticity compared to 2-nitrofluorene. The additional benzene ring has been suggested to stabilize the insertion of the aromatic compound in DNA by increasing the base-stacking forces through π–π electronic interactions [55].

10.4.4 Substituents Other than Nitro Group

Substituents other than the nitro group affect the mutagenicity in nitro-aromatic compounds. El-Bayoumy et al. showed that methyl substitution of nitronaphthalenes and nitrobiphenyls decreases their mutagenic potency to some extent [56]. In a related study, the authors showed that 11-methyl-6-nitrochrysene is more mutagenic than 6-nitrochrysene, while 5-methyl-6-nitrochrysene is less mutagenic than 6-nitrochrysene [57]. Vance and co-workers examined several 2,7-disubstituted fluorene derivatives of amino-, nitroso-, and nitrofluorenes to determine the physicochemical basis for their mutagenic activity [58]. A reasonable correlation was

found between the inductive and resonance effects of electron-withdrawing substituents at C7 in 2-nitrofluorenes derivatives and their increases in their mutagenicity. Electron-donating substituents at C7 were found to decrease the mutagenic potency of 2-aminofluorenes, 2-nitrosofluorene, and 2-nitrofluorene. Acetylation of hydroxy or amino groups at C7 increases the mutagenic potency of 2-nitrofluorene, which was proposed to be due to a decrease in the electron-donating ability of the hydroxy or amino functionality. Vance et al. argued that the physical properties of a second functional group may exert their effect(s) at three different points in the metabolic activation of 2,7-disubstituted fluorene derivatives: initial reduction of the nitro group (redox effect), stabilization of the hydroxylamine (inductive effect), and stabilization/destabilization by resonance and inductive effects of the nitrenium ion, which is the ultimate electrophilic metabolite that binds covalently to DNA.

Klopman and Rosenkranz analyzed the structures of 53 nitroaromatic compounds using the Computer Assisted Structure Evaluation (CASE) program for their ability to induce mutation [59]. Four key chemical fragments were identified, two associated with mutagenic activity, and two related with deactivating properties. For example, the structural analysis showed that substitution at the carbon para to the nitro group is required for mutagenicity, while the presence of a hydrogen atom in that position prevents it. It was also shown that the coexistence of activating and deactivating fragments on the same molecule results in a nitro-aromatic compound with weak or no mutagenic activity. The authors hypothesized that deactivating fragments may represent part of the molecular structure where detoxification takes place, while activating fragments may be regions where the enzymes binds to the nitro-aromatic compounds for metabolic activation during nitro-reduction.

Klein et al. found that the mutagenic potency of ortho substituted 4-nitrobiphenyl derivatives decreases with growing steric demand of the alkyl substituents [60]. The reduction in mutagenicity was correlated with the deviation of the nitro group from parallel orientation relative to the aromatic rings. Alkyl groups in the 2′-position of 4-nitrobiphenyl also reduce the mutagenic activity with an increase in substituent size, and eliminate the mutagenic activity completely for the most sterically hindered alkyl substituents like 2′-*iso*propyl-,2′,4′,6′-trimethyl-4-nitrobiphenyl. In this group of 4-nitrobiphenyl derivatives, the parallel orientation of the nitro group was not affected, but the two aromatic rings of 4-nitrobiphenyl were twisted. The authors suggested that the twist of the aromatic rings is associated with a less effective charge delocalization of the metabolite nitrenium ion, which may explain the reduction or complete elimination in mutagenicity observed in 4-nitrobiphenyl derivatives that were substituted in the 2′-position with alkyl groups.

In a subsequent study, Boche and co-workers synthesized various derivatives of 4-nitrobiphenyl, 4-nitrosobiphenyl, 2-aza-4-nitrobiphenyl and 2-nitrofluorene having alkyl substituents away from the nitro group. Specifically, the substitutions were in the 4′-position for nitrobiphenyls and in the 7′-position for 2-nitrofluorenes. It was found that the mutagenicity of all compounds decreases with an increase in steric forces of the attached alkyl groups [61]. The authors suggest that the changes in molecular shape caused by the bulky substituents may be responsible for the

reduced mutagenic potency by interfering with intercalation into DNA because the addition of alkyl substituents should not influence the orientation of the nitro group or the orientation of the phenyl rings in the biphenyl compounds.

Juneja et al. [62] studied various nitro-substituted phenyl alkyl/aryl thioethers and nitroso-substituted phenyl alkyl/aryl thioethers and found different mutagenic potency between saturated and unsaturated substituents. The relative mutagenic potency among p-nitrophenyl thioethers having saturated or unsaturated substituents decreases in the following order: allyl > phenyl > benzyl > butyl > propyl > ethyl > methyl. Compounds having alkyl chain substituents with six to twelve carbon atoms were found to be nonmutagenic. In the case of various ortho, meta and para isomers of nitrodiphenyl thioethers, compounds having the nitro group at the para position were mutagenic, whereas those having the nitro group ortho and meta were not. In addition, the reduction of the nitro to a nitroso group altered the biological activity of the ortho and meta isomers in such a way that *ortho*-nitroso-diphenyl thioether exhibited mutagenicity, whereas the meta-isomer remained nonmutagenic.

10.4.5 Summary of the Structural and Electronic Factors Influencing the Mutagenic Activity

The discussion above makes clear that a combination of many structural and electronic factors influences the mutagenic activity of nitro-aromatic compounds. In particular, the mutagenic activity of a nitro-aromatic compound can be affected by the orientation of the nitro group and its position, the reduction potential, the molecular size (degree of aromaticity, number of fused aromatic rings, dimension, inductive and resonance effects), and steric effects. The complex interplay of these factors makes the development of SARs a considerable paramount challenge. However, as discussed in the next section, mathematical models that include a statistical analysis of the "weight" that each of these factors have in modulating the biological activity of nitro-aromatic compounds seem to be a promising and efficient method for predicting mutagenic activity and guiding the prioritization of compounds for which experimental data are yet to be obtained.

10.5 Quantitative Structure–Activity Relationships (QSARs)

It has long been recognized that knowledge of the physicochemical (topological, structural, and electronic) factors that dictate biological activity in a set of related compounds (congeners) for which toxicological data are available can greatly help in evaluating the mutagenic potential of unstudied compounds. The application of SARs in theoretical models is of great importance because it makes use of the

wealth of existing chemical knowledge to the understanding of the interactions between compounds and biological systems. In particular, quantitative structure–activity relationships (QSARs) permit an efficient and inexpensive assessment of the physicochemical properties that affect the toxicity of a class of compounds. Over the years, QSARs have been one of the basic tools of modern medicinal chemistry and pesticide design, and are playing an increasingly important role in the environmental sciences [63–68].

Typically, QSARs are derived from the statistical analysis of a training set of compounds, and thus, most models have an inherent empirical character. This empirical character makes of paramount importance a clear definition of the class of compounds to which a particular QSAR applies. It is also imperative that the predictive power that a QSAR model has for congener compounds outside the training set be evaluated. Perhaps two of the most attractive attributes that QSAR have in toxicology are: (1) their contribution to the identification of the key topological, structural, and electronic factors that mediate the biological activity of a given class of compounds; and (2) the ability to provide mathematical models to predict the activity of related compounds for which no experimental results are available. Ultimately, the knowledge gathered from QSAR should facilitate the preliminary screening assessment of environmentally-concerning classes of compounds and the sorting of compounds according to their likely toxicity for the purpose of further experimentation. A brief overview of some of the most important molecular descriptors predicted from QSAR modeling to influence the biological activity in nitro-aromatic compounds is presented in this section. A compilation of some of the QSAR models that have been developed for nitro-aromatic compounds is shown in Table 10.1. The readers are referred to several excellent reviews that have appeared in recent years for an in-depth discussion of QSAR models and their extent of applications for a wide variety of chemicals [55, 63, 69].

One of the first QSAR models of nitro-aromatic compounds was developed by Walsh and Claxton [70]. The authors evaluated the mutagenic activity of 114 nitro-aromatic compounds using pattern-recognition techniques. The aim of the analysis was to predict if a compound was mutagenic or not mutagenic. The set of compounds used included 64 mutagenic and 50 nonmutagenic compounds. From a total of more than 100 topological, structural, and electronic descriptors, 19 were found to be significant after statistical analysis. The statistically relevant descriptors were related to the molecular size and branching of the compounds. The developed QSAR model classified 96% of the compounds correctly. In a subsequent analysis, 109 compounds were used as training set, while five compounds were used as test set. The QSAR model classified 89% of the molecules correctly. As an additional validation test, the authors selected ten related compounds from the literature, and the QSAR model was able to correctly predict the mutagenic activity of all of them.

The relationship between mutagenicity and the LUMO energies of 20 nitro-aromatic compounds was studied by Maynard et al. [71] using the STO-3G method. The authors concluded that reduction of the nitro group was the dominant metabolic pathway affecting the biological activity of the investigated compounds. Lopez de Compadre et al. [72] re-examined the data of Maynard et al. [71], including the

Table 10.1 Compilation of representative Quantitative Structure–Activity Relationships (QSAR) models for nitro-aromatic compounds

QSAR Model[a]	References
$\mathrm{TA100} = -46.342\mathrm{LUMO} + 8.583$ $n = 20$, $r = -0.75$, $F = 20.5$	[71]
$\mathrm{TA98} = -64.892\mathrm{LUMO} + 11.559$ $n = 20$, $r = -0.82$, $F = 35.9$	[71]
$\log \mathrm{TA100} = -1.91\mathrm{LUMO} + 1.30 \log P - 6.59$ $n = 18$, $r = 0.874$, $s = 0.783$	[72]
$\log \mathrm{TA98} = -2.82\mathrm{LUMO} + 1.48 \log P - 8.59$ $n = 20$, $r = 0.926$, $s = 0.737$	[72]
$\log \mathrm{TA98} = 0.65(\pm 0.16) \log P - 2.90(\pm 0.59) \log(\beta 10^{\log P} + 1) - 1.38(\pm 0.25)$ LUMO $+ 1.88(\pm 0.39) I_1 - 2.89(\pm 0.81) I_a - 4.15(\pm 0.58)$ $n = 188$, $r = 0.900$, $s = 0.886$, $\log P = 4.93$, $\log \beta = 5.48 = F_{1,181} = 48.6$	[77]
$\log \mathrm{TA100} = 1.20(\pm 0.15) \log P - 3.40(\pm 0.74) \log(\beta 10^{\log P} + 1) - 2.50(\pm 0.32)$ LUMO $- 3.50(\pm 0.82) I_a + 1.86(\pm 0.74) I_{ind} - 6.39(\pm 0.73)$ $n = 117$, $r = 0.886$, $s = 0.835$, $\log P = 5.44(\pm 0.24)$, $\log \beta = -5.7$, $F_{1,110} = 24.7$	[74]
$\log \mathrm{SOSIP} = 1.07(\pm 0.36) \log P - 1.57(\pm 0.57)\mathrm{LUMO} - 6.41(\pm 1.8)$ $n = 15$, $r = 0.922$, $2 = 0.534$, $F_{1,12} = 36.21$	[75]
$\log \mathrm{SOSIP} = -33.1(\pm 11.9) q_{c2} + 1.00(\pm 0.26) \log P - 1.50(\pm 0.49) I_{sat} - 1.19$ $(\pm 0.49) MR - 0.76(\pm 0.49) I_{5,6} - 3.76(\pm 1.56)$ $n = 40$, $r = 0.900$, $s = 0.475$, $F_{1,34} = 9.76$	[75]
$\log \mathrm{TD}_{50} = 1.01 + 0.29\Omega^1 \mu_9^H - 0.23\Omega^2 \mu_6^H - 0.38\Omega^3 \mu_{15}^H - 0.22\Omega^4 \mu_0 \mu_{15}^{GM} + 0.32\Omega^5 \mu_1 \mu_4^{Dip} + 0.16\Omega^6 \mu_0 \mu_{11}^{MR} - 0.33\Omega^4 \mu_{11}^{MR}$ $n = 48$, $r = 0.889$, $R^2 = 0.791$, $S = 0.424$, $F = 21.627$, $p < 10^{-5}$, $\rho = 6$, $q^2 = 0.666$, $S_{CV} = 0.536$	[83]
$\log \mathrm{TA100} = -59.07(\pm 6.72) + 2.61(\pm 0.21)\mathrm{CIC1} + 92.75(\pm 11.50) PW\ 2$ $n = 48$	[55]
$\log \mathrm{TA100} = -3.6518 + 1.8371(\pm 0.1459)^3\chi^v + 0.4719(\pm 0.3219)^3\chi^{shape}$ $n = 48$, $SE = 0.8135$, $R^2 = 0.7789$, $R^2A = 0.7691$, $F = 79.284$	[84]

[a]See glossary for parameter definitions

lipophilicity (log P) descriptor in their analysis. The authors showed that inclusion of the lipophilicity parameter substantially improved the ability of the QSAR equations to model the mutagenicity of the nitro-aromatic compounds. In a subsequent work, Lopez de Compadre et al. [73] studied the mutagenicity of a wider set of nitrofluorene derivatives in addition to other nitro-aromatic compounds. The hydrophobicity descriptor was found to be the major factor predicting the mutagenic activity of the nitro-aromatic compounds. It was also predicted that electron-attracting elements in the aromatic rings could enhance the mutagenicity in nitro-aromatic compounds.

A QSAR model was developed to test the mutagenicity of 117 nitro-aromatic compounds in bacterial strain cells without metabolic activation [74]. It was shown that hydrophobicity plays a crucial role in determining the relative mutagenicity of most of the compounds studied. The mutagenicity of the nitro-aromatic compounds increases slowly at low log$P$ and then decreases rapidly at high log P. It was suggested that a combination of adverse hydrophobic and steric effects could explain these observations. In a subsequent analysis, Debnath and Hansch [75]

expanded the QSAR modeling of the mutagenic activity in nitro-aromatic compounds. The authors concluded that the relative mutagenicity is bi-linearly dependent on hydrophobicity, and linearly dependent on the LUMO energy of the nitro-aromatic compounds.

Benigni et al. [76] used the QSAR models developed by Debnath et al. [75] to predict nonmutagenic activity in nitro-aromatic compounds. Only a few nonmutagenic nitro-aromatic compounds were predicted to have very low potency, whereas all other compounds were predicted to have high or very high mutagenic potency. According to Benigni and co-workers, the reason for the unsatisfactory predictions was that the lipophilicity parameter, which was the major determinant of the mutagenic potency in the QSAR models of Debnath et al., cannot discriminate between mutagenic or nonmutagenic compounds. Thus, Benigni et al. [76] argued that the rate-limiting steps that determine if a set of compounds is mutagenic, can be different, and thus, require different descriptors than those used to model mutagenic potency.

The QSAR models developed by Debnath [74, 75, 77] were also not able to predict correctly the mutagenicity of nitrofuran derivatives. Thus, Debnath et al. [78] combined the QSAR models with a comparative molecular field analysis in an effort to predict the mutagenicity of the nitrofuran derivatives. The comparative molecular field analysis is a procedure used to evaluate the role that steric factors play in determining the mutagenicity of compounds [79]. The authors proposed that the partial atomic charge of the carbon atom attached to the nitro group is the most important parameter explaining the mutagenic behavior in nitrofuran derivatives, while lipophilicity and steric factors play a secondary role.

Other groups have also used the comparative molecular field analysis procedure to elucidate how steric factors affect the mutagenicity in nitro-aromatic compounds [80, 81]. It was found that the molecular regions associated with the mutagenicity in nitro-aromatic compounds were those with high electronic density or with electron deficiency [81]. Fan et al. suggested that the electron-deficient regions may be associated with the metabolic pathways leading to nitro-reduction in nitro-aromatic compounds while the electron-rich regions may be involved in oxidative activation pathways [81]. Mersch-Sundermann et al. [82] also investigated the structural basis of mutagenicity of nitrofuran derivatives. Out of nine major structural fragments that were found to influence the mutagenicity of the nitrofuran derivatives, the most important parameter was the nitro group substituent in the position 2 of the furan ring. The lipophilicity parameter and the addition of one or more aromatic rings to the 2-nitrofuran moiety were also correlated with an increase in the mutagenic activity of the nitrofuran derivatives.

Helguera-Morales et al. [83] used a topological sub-structural molecular design (TOPS-MODE) approach to predict the carcinogenicity of 48 nitro-aromatic compounds in female rodents. Topological descriptors are derived mainly from knowledge of the connectivity between atoms within a molecule, and are based to some extent on information on atom types and their electronic environment. The model was able to describe 79.1% of the experimental data. It was found that the carcinogenic activity of the compounds analyzed increases in the presence of a primary

amine group bonded to the aromatic ring. This increase was proportional to ring aromaticity. It was also shown that a nitro group bound to an aromatic carbon exhibits a much greater contribution to carcinogenic activity than one bound to an aliphatic carbon atom. In addition, it was observed that the presence of hydrazine fragments in compounds with nitro groups decreases the carcinogenic potency.

Gramatica and co-workers [55] have recently studied a set of 48 nitro-aromatic compounds to model their mutagenic properties using QSAR regression methods. It was shown that best descriptors to model the mutagenic activity of those nitro-aromatic compounds can be selected independently of the composition of the external prediction set of compounds used to validate the QSAR model. This allowed the authors to propose a multiple linear regression model based on just two topological molecular descriptors to predict the mutagenicity in nitro-aromatic compounds. The more relevant molecular descriptor provides information on molecular size and suggests that biological activity increases with an increase in the number of rings and nitro groups in a series of congeners. It was shown that information related to the molecular shape also correlates with activity: nitro-aromatic compounds with a rounder rather than a more linear molecular shape are more bioactive. Singh et al. [84] studied the same set of 48 nitro-aromatic compounds and arrived at similar conclusions using in the initial model a different set of molecular descriptors. Gramatica and co-workers recently extended their QSAR models to include 70 oxo-, nitro- and unsubstituted aromatic compounds [85]. The best QSAR models show good predictive performance (sensitivity of 69.2–87.1% and specificity of 62.5–87.5%) to mutagenic activity. The authors emphasize that external validation of an otherwise internally robust QSAR model is necessary to achieve maximum predictability. Benigni and Bossa recently arrived at a similar conclusion regarding the successful predictability of QSAR models in general [69].

10.5.1 Summary on the QSAR Models

Inspection of Table 10.1 shows that most QSAR models highlight the significance of hydrophobicity, steric effects (molecular size and shape) and LUMO energies in modeling the physicochemical factors that influence the mutagenic activity in nitro-aromatic compounds. These molecular descriptors are in reasonably good agreement with the SARs described in Sect. 10.4. However, in many instances, there are marked discrepancies between the actual mutagenic potency of nitro-aromatic compounds and the mutagenic potency predicted by a given QSAR model. A major limitation of the QSAR models developed thus far is their applicability to a subset of related compounds (congeners), but not to nitro-aromatic compounds in general. This limitation makes the use of QSAR models for preliminary screening assessment of nitro-aromatic compounds and for sorting them according to their likelihood of toxicity of questionable value. As noted recently by Benigni [63, 69] and Gramatica [55], most QSARs papers point to statistics as the most important

confirmation of the validity of a model; however, the experimental evidence shows the importance of chemical knowledge in the process of generating models with reasonable applicability.

10.6 Outlook

Significant advancements in understanding the physicochemical factors that influence the mutagenic activity in nitro-aromatic compounds have occurred in recent years. Successful SARs using toxicological data have been published and their correlations with the metabolic pathways have been elucidated. Promising quantitative-structure–activity-relationships have been recently developed using multiple linear regression algorithms to predict the mutagenic potency and the mutagenicity of nitro-aromatic compounds. Ultimately, the synergistic work between toxicology, SAR and QSAR areas of research will bring us closer to a complete molecular understanding of the physicochemical factors that influence the mutagenicity in nitro-aromatic compounds.

Despite many exciting developments in toxicology, SARs and QSARs research, much work is still needed. Most nitro-aromatic compounds of environmental concern have not been studied experimentally or computationally. The ability of QSAR models to predict the mutagenic potency in nitro-aromatic compounds is still under scrutiny. Further work is needed to validate the accuracy of the semi-empirical methods that are routinely used to obtain the structural and electronic properties of nitro-aromatic compounds in SAR and QSAR applications. Unpublished results [86] show that optimizations using AM1 and PM3 semi-empirical methods, as given in Gaussian 03 suite of programs [87], result in the prediction of multiple local minima in the ground state potential energy surface of many nitro-aromatic compounds. The optimized geometry depends greatly on the nitro group torsion angle of the initial guess geometry. Furthermore, different global minima in nitro-aromatic compounds are generally predicted using AM1 and PM3 computational methods. The calculated global minimum of a nitro-aromatic compound can have a nitro group torsion angle with a difference in excess of 30° between AM1 and PM3 methods. Inconsistency has also been observed in predicting the LUMO energies of nitro-aromatic compounds using AM1 versus PM3 force fields; with some families of nitro-aromatics compounds showing opposite trends in LUMO energy [86]. High-level *ab initio* or density functional calculations are urgently needed. Some efforts at obtaining accurate molecular descriptors for nitro-aromatic compounds are currently underway in several research groups [88–91]. Certainly, the small computational demand of semi-empirical methods makes them an ideal tool for analysis of numerous compounds with sizable molecular size. Thus, high-level *ab initio* or density functional calculations of nitro-aromatic compounds might find their way as a basis for a more accurate parameterization of semi-empirical methods.

Acknowledgments This research was supported by a grant from the ACS Petroleum Research Fund, Type DNI. The authors also thank the Department of Chemistry, Case Western Reserve University and the National Science Foundation, Academic Careers in Engineering and Science Program (NSF ACES) for financial support.

Glossary of Molecular Descriptors of Table 10.1

LUMO	Energy of the lowest unoccupied molecular orbital
log P	Logarithm of the octanol/water partition coefficient (descriptor pertaining to the hydrophobic character of the molecule)
log TA100	Mutagenic activity in TA100 strain cells
log TA98	Mutagenic activity in TA98 strain cells
LUMO	Energy of the lowest unoccupied molecular orbital
I_a	Indicator variable for which the value is 1 if an acenthrylene ring is present; otherwise the value is zero
I_1	Indicator variable for which the value is 1 for compounds with three or more fused rings; otherwise the value is zero
I_{and}	Indicator variable for which the value is 1 for 1- and 2-methylindazole derivatives; otherwise the value is zero
$\log\beta$	5.48 for the log TA98, and −5.7 for the log TA100
SOSIP	SOS induction potential in E.coli PQ37, measure the genotoxicity of the compound
q_{c2}	Partial atomic charge on the carbon attached to the nitrogen of the nitro group
I_{sat}	Indicator variable for which the value is 1 for saturated ring compounds; otherwise the value is zero
$I_{5,6}$	Indicator variable for which the value is 1 for compounds with substituents at the 5- or 6- position of 2-nitronaphtofurans and pyrenofurans; otherwise the value is zero
MR	Molecular refractivity, which is a measure of the substituent bulk for any substituents that are next to the nitro group, negative coefficient indicates its detrimental effect toward log SOSIP
TD_{50}	Carcinogenic potency
$\Omega^1\mu_9^H, \Omega^2\mu_6^H, \Omega^3\mu_{15}^H$	Descriptors related to hydrophobicity
$\Omega^5\mu_1\mu_4^{Dip}$	Descriptor related to dipole moment
$\Omega^4\mu_0\mu_{15}^{GM}$	Descriptor related to the Gasteiger-Marsili charge
$\Omega^6\mu_0\mu_{11}^{MR}, \Omega^7\mu_{11}^{MR}$	Descriptors related to molar refractivity (similar to MR above)
CIC1	Descriptor that gives information regarding molecular size; the more rings and nitro groups the more active the compound is

PW2	Descriptor related to the shape of the molecule; the less linear and more circular the molecule the more active the compound is
$^3\chi^v$ and $^2\chi^{shape}$	Descriptors that weights the contributions of compound's size and shape to mutagenicity

References

1. Diesel and gasoline engine exhausts and some nitroarenes. In *IARC Monographs on the Evaluation of Carcinogenic Risks to Humans*, vol **46** (World Health Organization, International Agency for Research on Cancer, Lyon, 1989).
2. R. Atkinson, J. Arey, Mechanisms of the gas-phase reactions of aromatic hydrocarbons and PAHS with OH and NO_3 radicals. Polycyclic Aromat. Compd. **27**, 15–40 (2007)
3. H. Tokiwa, Y. Ohnishi, Mutagenicity and carcinogenicity of nitroarenes and their sources in the environment. Crit. Rev. Toxicol. **17**, 23–60 (1986)
4. L. Möller et al., Nitrated polycyclic aromatic hydrocarbons: A risk assessment for the urban citizen. Environ. Health Perspect. **101**, 309–315 (1993)
5. V. Purohit, A.K. Basu, Mutagenicity of nitroaromatic compounds. Chem. Res. Toxicol. **13**, 673–692 (2000)
6. H. Yu, Environmental carcinogenic polycyclic aromatic hydrocarbons: Photochemistry and phototoxicity. J. Environ. Sci. Health C. Environ. Carcinog. Ecotoxicol. Rev. **C20**, 149–183 (2002)
7. V.M. Arlt, 3-Nitrobenzanthrone, a potential human cancer hazard in diesel exhaust and urban air pollution: A review of the evidence. Mutagenesis **20**, 399–410 (2005)
8. In *IPCS INCHEM, Selected Nitro- and Nitro-Oxy-Polycyclic Aromatic Hydrocarbons. Environmental Health Criteria (EHC) Monographs*, vol **229** (WHO, Geneva, 2003).
9. A. Kamiya, Y. Ose, Isolation of dinitropyrene in emission gas from a municipal incinerator and its formation by a photochemical reaction. Sci. Total Environ. **72**, 1–9 (1988)
10. T. Handa et al., In situ emission levels of carcinogenic and mutagenic compounds from diesel and gasoline engine vehicles on an expressway. Environ. Sci. Technol. **18**, 895–902 (1984)
11. T. Henderson et al., Triple-quadrupole mass spectrometry studies of nitroaromatic emissions from different diesel engines. Environ. Sci. Technol. **17**, 443–449 (1983)
12. A. Hönor et al., Monitoring polycyclic aromatic hydrocarbons in waste gases. J. Chromatogr. A **710**, 129–137 (1995)
13. A. Albinet et al., Sampling precautions for the measurement of nitrated polycyclic aromatic hydrocarbons in ambient air. Atmos. Environ. **41**, 4988–4994 (2007)
14. H. Tokiwa et al., The presence of mutagens/carcinogens in the excised lung and analysis of lung cancer induction. Carcinogenesis **14**, 1933–1938 (1993)
15. P.P. Fu, Metabolism of nitro-polycyclic aromatic hydrocarbons. Drug Metab. Rev. **22**, 209–268 (1990)
16. P.P. Fu et al., DNA adducts and carcinogenicity of nitro-polycyclic aromatic hydrocarbons. Environ. Health Perspect. **102**(6), 177–183 (1994)
17. P.P. Fu, D. Herreno-Saenz, Nitro-polycyclic aromatic hydrocarbons: A class of genotoxic environmental pollutants. J. Environ. Sci. Health C. Environ. Carcinog. Ecotoxicol. Rev. **C17**, 1–43 (1999)
18. F.A. Beland, F.F. Kadlubar, Metabolic activation and DNA adducts of aromatic amines and nitroaromatic hydrocarbons, in *Handbook on Experimental Pharmacology,* **94**, ed. by C.S. Cooper, P.L. Grover (Springer, Heidelberg, 1990), pp. 267–325

19. F.A. Beland, M.M. Marques, DNA adducts of nitropolycyclic aromatic hydrocarbons. IARC Sci. Publ. **125**, 229–244 (1994)
20. T. Sugimura, S. Takayama, Biological actions of nitroarenes in short-term tests on Salmonella, cultured mammalian cells and cultured human tracheal tissues: Possible basis for regulatory control. Environ. Health Perspect. **47**, 171–176 (1983)
21. M.W. Chou et al., Synthesis, spectral analysis, and mutagenicity of 1-, 3-, and 6-nitrobenzo[a] pyrene. J. Med. Chem. **27**, 1156–1161 (1984)
22. B.S. Hass et al., Mutagenicity of the mononitrobenzo[a]pyrenes in Chinese hamster ovary cells mediated by rat hepatocytes or liver S9. Carcinogenesis **7**, 681–684 (1986)
23. R.H. Heflich et al., Mutagenicity of 1-, 3- and 6-nitrosobenzo[a]pyrene in *Salmonella typhimurium* and Chinese hamster ovary cells. Mutat. Res. Lett. **225**, 157–163 (1989)
24. H.S. Rosenkranz, R. Mermelstein, Mutagenicity and genotoxicity of nitroarenes. All nitro-containing chemicals were not created equal. Mutat. Res. Rev Genet. **114**, 217–267 (1983)
25. J.R. Thornton-Manning et al., Microsomal activation of 1- and 3-nitrobenzo[a]pyrene to mutagens in Chinese hamster ovary cells. Mutagenesis **3**, 233–237 (1988)
26. C.M. White, *Nitrated Polycyclic Aromatic Hydrocarbons* (Heidelberg, New York, 1985)
27. B.N. Ames et al., Methods for detecting carcinogens and mutagens with the salmonella/ mammalian-microsome mutagenicity test. Mutat. Res. **31**, 347–363 (1975)
28. N. Sera et al., Mutagenicity of nitrophenanthrene derivatives for *Salmonella typhimurium*: Effects of nitroreductase and acetyltransferase. Mutat. Res. **349**, 137–144 (1996)
29. Y. Hagiwara et al., Specificity and sensitivity of *Salmonella typhimurium* YG1041 and YG1042 strains possessing elevated levels of both nitroreductase and acetyltransferase activity. Mutat. Res. **291**, 171–180 (1993)
30. F.A. Beland et al., The in vitro metabolic activation of nitro polycyclic aromatic hydrocarbons. ACS Sym. Ser. **283**, 371–396 (1985)
31. P.P. Fu et al., Effects of nitro substitution on the in vitro metabolic activation of polycyclic aromatic hydrocarbons, in *Polycyclic Aromatic Hydrocarbon Carcinogenesis: Structure–Activity Relationships*, ed. by S.K. Yang, B.D. Silverman (CRC Press, Florida, 1988), pp. 37–65
32. P.P. Fu et al., Nitroreduction of 6-nitrobenzo[a]pyrene: A potential activation pathway in humans. Mutat. Res. Lett. **209**, 1213–1219 (1988)
33. P.J. Andrews et al., Identification of the DNA adduct formed by metabolism of 1, 8-dinitropyrene in *Salmonella typhimurium*. Carcinogenesis **7**, 105–110 (1986)
34. K.K. Colvert, P.P. Fu, Xanthine oxidase-catalyzed DNA binding of dihydrodiol derivatives of nitro-polycyclic aromatic hydrocarbons. Biochem. Bioph. Res. Co. **141**, 245–250 (1986)
35. J.A. DiPaolo et al., Nitration of carcinogenic and noncarcinogenic polycyclic aromatic hydrocarbons results in products able to induce transformation of Syrian hamster cells. Carcinogenesis **4**, 357–359 (1983)
36. M.Y. Wang et al., Microsomal metabolism of 3-nitrobenzo[a]pyrene: Effect of the nitro substituent on the regioselective metabolism of benzo[a]pyrene. J. Chinese Biochem. Soc. **17**, 1–11 (1988)
37. P.P. Fu, L.S. Von Tungelin, Metabolic formation of stable 9-nitroanthracene 1, 2- and 3, 4-epoxides. Polycyclic Aromat. Compd. **2**, 29–37 (1991)
38. R.H. Heflich et al., 1-Nitrosopyrene: An intermediate in the metabolic activation of 1-nitropyrene to a mutagen in *Salmonella typhimurium* TA1538. Mutat. Res. **149**, 25–32 (1985)
39. E.K. Fifer et al., Synthesis and mutagenicity of 1-nitro-6-nitrosopyrene and 1-nitro-8-nitrosopyrene, potential intermediates in the metabolic activation of 1, 6- and 1, 8-dinitropyrene. Carcinogenesis **7**, 65–70 (1986)
40. R.H. Heflich et al., DNA adduct formation and mutation induction by nitropyrenes in Salmonella and Chinese hamster ovary cells: Relationships with nitroreduction and acetylation. Environ. Health Perspect. **62**, 135–143 (1985)
41. P.P. Fu et al., Metabolism of isomeric nitrobenzo[a]pyrenes leading to DNA adducts and mutagenesis. Mutat. Res. **376**, 43–51 (1997)

42. P.P. Fu et al., The orientation of the nitro substituent predicts the direct-acting bacterial mutagenicity of nitrated polycyclic aromatic hydrocarbons. Mutat. Res. **143**, 173–181 (1985)
43. P.P. Fu et al., Effect of the orientation of nitro substituent on the bacterial mutagenicity of dinitrobenzo[e]pyrenes. Mutat. Res. Lett. **225**, 121–125 (1989)
44. H. Jung et al., Nitro group orientation, reduction potential, and direct-acting mutagenicity of nitro-polycyclic aromatic hydrocarbons. Environ. Mol. Mutagen. **17**, 169–180 (1991)
45. K. Fukuhara et al., Di- and Trinitrophenanthrenes: Synthesis, Separation, and Reduction Property. Chem. Res. Toxicol. **8**, 47–54 (1995)
46. IARC monographs on the evaluation of carcinogenic risks to humans. Diesel and gasoline engine exhausts and some nitroarenes. International Agency for Research on Cancer, *IARC monographs on the evaluation of carcinogenic risks to humans / World Health Organization*, vol **46** (International Agency for Research on Cancer, Lyon 1989), 1–458.
47. M.W. Chou et al., Multiple metabolic pathways for the mutagenic activation of 3-nitrobenzo [a]pyrene. Carcinogenesis **6**, 1235–1238 (1985)
48. M.W. Chou et al., Metabolism of 1-nitrobenzo[a]pyrene by rat liver microsomes to potent mutagenic metabolites. Carcinogenesis **7**, 1837–1844 (1986)
49. J.N. Pitts Jr. et al., Isomeric mononitrobenzo[a]pyrenes: Synthesis, identification and mutagenic activities. Mutat. Res. **140**, 81–85 (1984)
50. S. Yu et al., Mutagenicity of nitro-polycyclic aromatic hydrocarbons with the nitro substituent situated at the longest molecular axis. Mutat. Res. **283**, 45–52 (1992)
51. M. Arlt Volker et al., Mutagenicity and DNA adduct formation by the urban air pollutant 2-nitrobenzanthrone. Toxicol. Sci. **98**, 445–457 (2007)
52. G. Klopman et al., Relationship between polarographic reduction potential and mutagenicity of nitroarenes. Mutat. Res. **126**, 139–144 (1984)
53. W.A. Lopes et al., Electrochemical reduction potentials of 1-nitropyrene, 9-nitroanthracene, 6-nitrochrysene and 3-nitrofluoranthene and their correlation with direct-acting mutagenicities. J. Braz. Chem. Soc. **16**, 1099–1103 (2005)
54. W.A. Vance, D.E. Levin, Structural features of nitroaromatics that determine mutagenic activity in *Salmonella typhimurium*. Environ. Mutagen. **6**, 797–811 (1984)
55. P. Gramatica et al., Approaches for externally validated QSAR modelling of Nitrated Polycyclic Aromatic Hydrocarbon mutagenicity. SAR QSAR Environ. Res. **18**, 169–178 (2007)
56. K. El-Bayoumy et al., The influence of methyl substitution on the mutagenicity of nitronaphthalenes and nitrobiphenyls. Mutat. Res. **81**, 143–153 (1981)
57. K. El-Bayoumy et al., The effects of bay-region methyl substitution on 6-nitrochrysene mutagenicity in *Salmonella typhimurium* and tumorigenicity in newborn mice. Carcinogenesis **10**, 1685–1689 (1989)
58. W.A. Vance et al., Disubstituted amino-, nitroso-, and nitrofluorenes: A physicochemical basis for structure–activity relationships in *Salmonella typhimurium*. Environ. Mutagen. **9**, 123–141 (1987)
59. G. Klopman, H.S. Rosenkranz, Structural requirements for the mutagenicity of environmental nitroarenes. Mutat. Res. **126**, 227–238 (1984)
60. M. Klein et al., From mutagenic to non-mutagenic nitroarenes: Effect of bulky alkyl substituents on the mutagenic activity of 4-nitrobiphenyl in *Salmonella typhimurium*. Part I. Substituents ortho to the nitro group and in 2′-position. Mutat. Res. **467**, 55–68 (2000)
61. M. Klein et al., From mutagenic to non-mutagenic nitroarenes: Effect of bulky alkyl substituents on the mutagenic activity of nitroaromatics in *Salmonella typhimurium*. Part II. Substituents far away from the nitro group. Mutat. Res. **467**, 69–82 (2000)
62. T.R. Juneja et al., Effect of various alkyl and unsaturated substituents on the mutagenicity of some nitrophenyl thioethers. Mutat. Res. **495**, 97–102 (2001)
63. R. Benigni, Structure–activity relationship studies of chemical mutagens and carcinogens: Mechanistic investigations and prediction approaches. Chem. Rev. **105**, 1767–1800 (2005)
64. R. Franke, *Theoretical Drug Design Methods* (Elsevier, New York, 1984)
65 R. Franke, A. Gruska, *General Introduction to QSAR* (CRC Press, Boca Raton, 2003)

66. C. Hansch, A. Leo, *Exploring QSAR. 1. Fundamentals and applications in chemistry and biology* (American Chemical Society, Washington, DC, 1995)
67. H. Kubinyi (ed), *3D QSAR in Drug Design: Theory Methods and Applications* (ESCOM Science Publishers, The Netherlands, 1993)
68. M.S. Tute, *Comprehensive Medicinal Chemistry* (Pergamon Press, New York, 1990)
69. R. Benigni, C. Bossa, Predictivity of QSAR. J. Chem. Inf. Model. **48**, 971–980 (2008)
70. D.B. Walsh, L.D. Claxton, Computer-assisted structure–activity relationships of nitrogenous cyclic compounds tested in Salmonella assays for mutagenicity. Mutat. Res. **182**, 55–64 (1987)
71. A.T. Maynard et al., An Ab initio study of the relationship between nitroarene mutagenicity and electron affinity. Mol. Pharmacol. **29**, 629–636 (1986)
72. R.L. Lopez de Compadre et al., The role of hydrophobicity in the Ames test. The correlation of the mutagenicity of nitropolycyclic hydrocarbons with partition coefficients and molecular orbital indexes. *Int. J. Quantum Chem.* **34**, 91–101 (1988).
73. R.L. Lopez de Compadre et al., LUMO energies and hydrophobicity as determinants of mutagenicity by nitroaromatic compounds in *Salmonella typhimurium. Environ. Mol. Mutagen.* **15**, 44–55 (1990).
74. A.K. Debnath et al., Quantitative structure–activity relationship investigation of the role of hydrophobicity in regulating mutagenicity in the Ames test: 2: Mutagenicity of aromatic and heteroaromatic nitro compounds in *Salmonella typhimurium* TA100. Environ. Mol. Mutagen. **19**, 53–70 (1992)
75. A.K. Debnath, C. Hansch, Structure–activity relationship of genotoxic polycyclic aromatic nitro compounds: Further evidence for the importance of hydrophobicity and molecular orbital energies in genetic toxicity. Environ. Mol. Mutagen. **20**, 140–144 (1992)
76. R. Benigni et al., QSAR models for both mutagenic potency and activity: Application to nitroarenes and aromatic amines. Environ. Mol. Mutagen. **24**, 208–219 (1994)
77. A.K. Debnath et al., Structure–activity relationship of mutagenic aromatic and heteroaromatic nitro compounds. Correlation with molecular orbital energies and hydrophobicity. J. Med. Chem. **34**, 786–797 (1991)
78. A.K. Debnath et al., Mechanistic interpretation of the genotoxicity of nitrofurans (antibacterial agents) using quantitative structure–activity relationships and comparative molecular field analysis. J. Med. Chem. **36**, 1007–1016 (1993)
79. R.D. Cramer III et al., Comparative molecular field analysis (CoMFA). 1. Effect of shape on binding of steroids to carrier proteins. J. Am. Chem. Soc. **110**, 5959–5967 (1988)
80. G. Caliendo et al., Shape-dependent effects in a series of aromatic nitro compounds acting as mutagenic agents on *S. typhimurium* TA98. SAR QSAR Environ. Res. **4**, 21–27 (1995)
81. M. Fan et al., Comparison of CoMFA models for *Salmonella typhimurium* TA98, TA100, TA98+S9 and TA100+S9 mutagenicity of nitroaromatics. SAR QSAR Environ. Res. **9**, 187–215 (1998)
82. V. Mersch-Sundermann et al., The structural basis of the genotoxicity of nitroarenofurans and related compounds. Mutat. Res. **304**, 271–84 (1994)
83. A.H. Morales et al., Quantitative structure activity relationship for the computational prediction of nitrocompounds carcinogenicity. Toxicology **220**, 51–62 (2006)
84. J. Singh et al., Mutagenicity of nitrated polycyclic aromatic hydrocarbons: A QSAR investigation. Chem. Biol. Drug Design **71**, 230–243 (2008)
85. E. Papa et al., Prediction of PAH mutagenicity in human cells by QSAR classification. SAR QSAR Environ. Res. **19**, 115–127 (2008)
86. R.A. Vogt et al., unpublished results
87. M.J. Frisch et al., *Gaussian 03* (Gaussian, Wallingford, 2004)
88. V. Librando et al., Computational study on dipole moment, polarizability and second hyperpolarizability of nitronaphthalenes. THEOCHEM **856**, 105–111 (2008)

89. V. Librando et al., Electronic properties of some nitrobenzo[a]pyrene isomers: A possible relationship to mutagenic activity. J. Mol. Model. **14**, 489–497 (2008)
90. K.K. Onchoke et al., Density functional theoretical study of nitrated polycyclic aromatic hydrocarbons. Polycyclic Aromat. Compd. **24**, 37–64 (2004)
91. K.K. Onchoke et al., Structure and vibrational spectra of mononitrated benzo[a]pyrenes. J. Phys. Chem. A **110**, 76–84 (2006)

Chapter 11
Molecular Modeling as an Auxiliary Method in Solving Crystal Structures Based on Diffraction Techniques

Janusz Lipkowski and Kinga Suwińska

Abstract On the basis of a series of practical examples, the importance of molecular modeling in structure analysis is illustrated. The situations presented prove usefulness of modeling procedures in (1) solving difficult crystal structures, with orientational, partial disordering in particular; (2) explaining erroneously determined molecular structures and deriving the correct solutions; (3) determining long range order–disorder phenomena, for example, polytypism of intercalated layered structures; and (4) dealing with multicomponent guest species absorbed in porous crystal structures. It is believed that molecular modeling will soon become an intrinsic part of structure determination procedures using diffraction data.

11.1 Introduction

X-ray structural analysis or, more generally, structure determination based on the analysis of diffraction pictures, is very a reliable method delivering us enormous amount of chemical information. These techniques are commonly considered objective, that is, independent of preliminary assumptions. In this chapter, some criticism of this common belief is given, though it is not the intention of the authors to question the importance and validity of the diffraction techniques. On the contrary, our aim is to stress the importance and value of structural data derived from diffraction, but we would also emphasize the important role of creating and developing structural models by other approaches and subsequent use of the models in structure analysis. Molecular modeling is one, if not the most important, possibility to do this.

J. Lipkowski and K. Suwińska (✉)
Institute of Physical Chemistry, Polish Academy of Sciences, Kasprzaka, 44/52, 01 224 Warszawa, Poland
e-mail: janusz.lipkowski@wp.pl

J. Leszczynski and M.K. Shukla (eds.), *Practical Aspects of Computational Chemistry*, 241
DOI: 10.1007/978-90-481-2687-3_11,

There are two main purposes of involving molecular modeling in structure analysis:

- To assist structure analysis by improving the model used for refinement and/or the analysis of partial disordering of molecular moieties in the crystal
- To derive structural information which is not attainable from structure analysis

Both the above mentioned situations will be illustrated below by examples taken from real structure analysis, that is, these are practically important cases, not just imaginary ones.

11.2 Analysis of Partially Disordered Structures

11.2.1 Solving the Structural Problem

In structure determination from X-ray diffraction data, it sometimes happens that, on the Fourier maps, parts of the coming out structure are unclear. Fuzzy electron density maps may present problems in determining even the approximate positions of the respective fragments of the structure being analyzed. For example, the layered structure of the inclusion (intercalation) compound formed by $Ni(NCS)_2$ $(4\text{-methylpyridine})_4$ (host) and methylcellosolve (guest) [1]. The guest molecules are (Fig. 11.1) located on twofold crystal axes of unit cell symmetry and are orientationally disordered as shown in the picture.

The correct orientations were found by molecular mechanics, and thus, the found positions corresponding to the energy minima have been subsequently refined by least squares procedure, as usual in X-ray structure refinement. The most important aspects here are the following:

- Correct positions and orientations of the guest molecules cannot be derived directly from diffraction data, and some sort of "guess" is necessary before proceeding to further steps of structure solution and refinement. Molecular modeling is a perfect tool to do the "guess" step and gives it physical meaning as well.
- Molecular geometry of the guest molecules cannot be reliably determined in partially disordered crystal structures as in the example given above. Refinement of the structure based on diffraction data is unstable, that is, the resulted geometry of the guest molecules which comes out from simple, not constrained refinement, is unrealistic. Molecular modeling is the way to improve the situation. Geometry of the guest is optimized by, for instance, empirical force field calculations, and kept unchanged during subsequent steps of structure refinement.

A nice illustration of the latter conclusion is taken from the crystal structure of azulene (guest) inclusion compound. The host is the same as in the previous example, also the host crystal structure is very similar here.

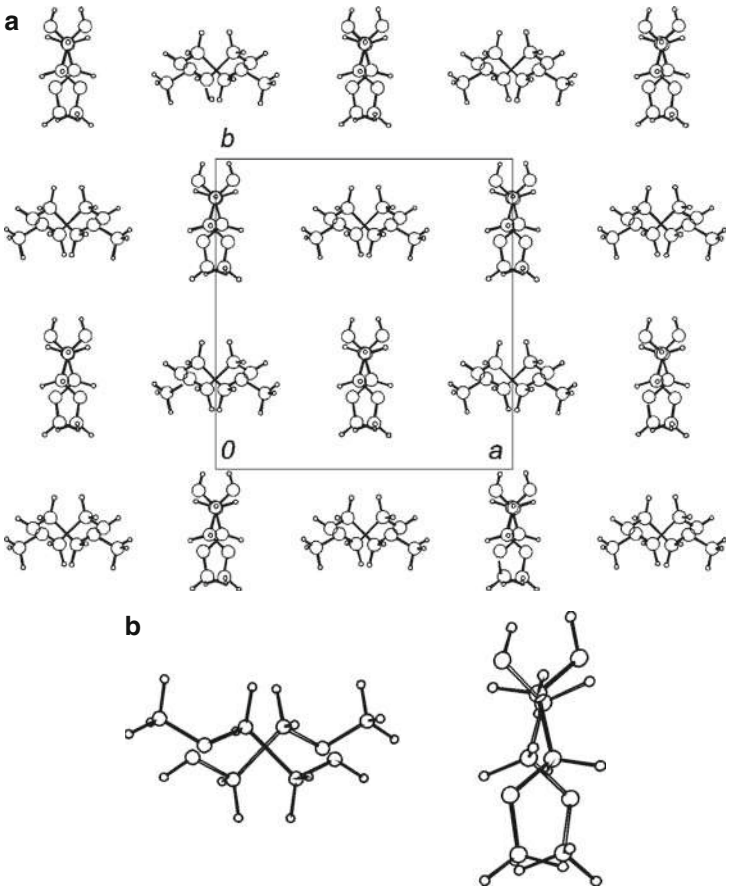

Fig. 11.1 (**a**) Arrangement of guest methylcellosolve molecules in layered clathrate of the host $Ni(NCS)_2(4\text{-methylpyridine})_4$. (**b**) Mutual orientation of the guest molecules in the layered structure displayed in (**a**)

There are two, not related by crystal symmetry, layers of guest azulene molecules in the solid (Fig. 11.2). Electron density maps do not provide any clear suggestion concerning the orientation and geometry of azulene moieties in the layers, but their approximate locations may be determined. Again, molecular modeling was used as the rescue technique to find the possible orientations of the guest molecules. The resulted situation is more complex compare to the previous example. Azulene molecules assume more than just two orientations (Fig. 11.3). By using modeling techniques, one may find the possible positions and their respective occupation factors. It is very nice to see that the site occupation factors coming from molecular modeling comply well with the final values obtained by subsequent structure refinement.

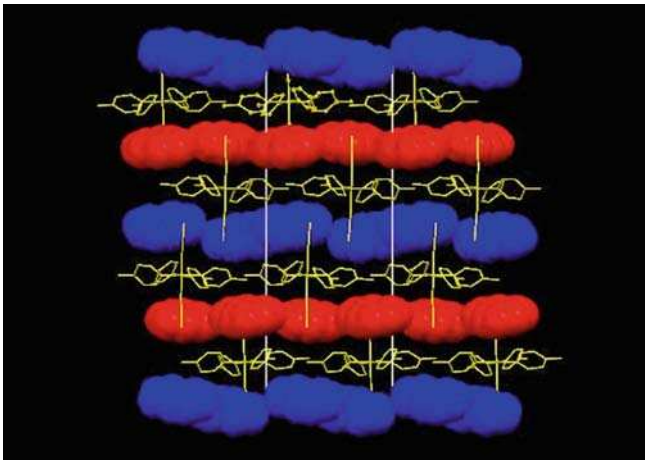

Fig. 11.2 A view of molecular packing in the $Ni(NCS)_2(4\text{-methylpyridine})_4$ layered structure [2] (host molecules shown in the capped sticks mode, hydrogen atoms are omitted for the sake of clarity). Guest azulene molecules are shown in the space filling mode, the two layers of the guest non-related by crystal symmetry are distinguished by different colors

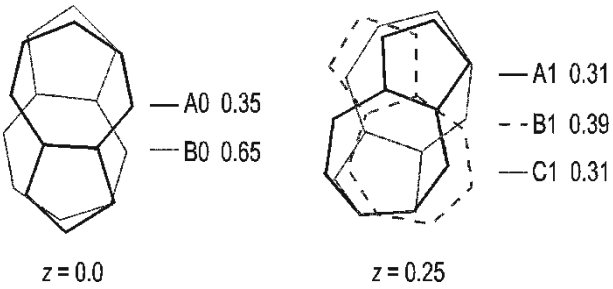

Fig. 11.3 Mutual orientations of azulene molecules in the layered structure shown on Fig. 11.2, at two levels of z coordinate: $z=0$ corresponds to the layer with *blue color*, $z=0.25$ to the *red one*. A, B, and C stand for different orientations at respective levels, numbers indicate site occupation factors for each of the particular orientations

11.2.2 Correcting Erroneously Determined Geometry of Molecules

In contrast to the examples described above, there are partially disordered structures which may mimic ordered ones but with false or deformed geometry of molecular moieties. As a convenient example, the semi-clathrate hydrate[1] of *tetra*(iso-amyl)

[1]The term *semi-clathrate* refers to solid inclusion compounds where, in addition to non-bonded, clathrate interactions, there is a contribution of chemical bonding. In the example used above, this "chemical" contribution is of ionic nature: fluoride anion from the ammonium salt is incorporated into the water host framework linked *via* hydrogen bonds. Thus, the host has anionic character and guest-host interactions have ionic component.

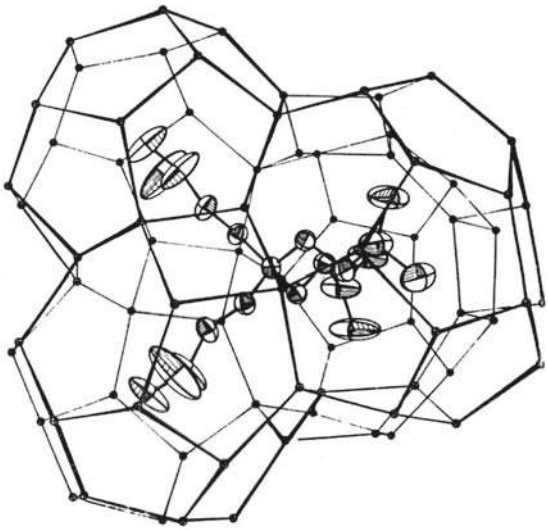

Fig. 11.4 Cavity in the *tetra* (iso-amyl)ammonium fluoride hydrate. Host water molecules are represented as *black dots* linked by hydrogen bonds. Fluoride anion is incorporated into this framework (exact position remains unknown). *Tetra*(iso-amyl)ammonium cation is included in the cavity, its atoms are given by thermal ellipsoids (ORTEP plot)

ammonium fluoride may be taken. The crystal structure of the compound, as originally determined, is shown in Fig. 11.4 [3]. It may be seen on the thermal ellipsoids that the end parts of the iso-amyl cations display pronounced thermal displacements. Also, when the geometry of the iso-amyl chains was carefully examined, it was clear that something is wrong with it since the end part was closer to the geometry of the (CH_2)–C=(CH) type rather than that of (CH_2)–CH–(CH_2) as expected. It is rather typical for inclusion compounds that the cavity may be occupied by a mixture rather than monocomponent guest species. It was, thus, essential to analyze possible reasons of this unexpected result of structure analysis. The question was: is it likely that the guest species used was contaminated with amylidene compound? It took us almost 4 years to answer this question and to eliminate all possible chemical mistakes and ambiguities in the above respect. At the end, we may have been confident that there was no chemical mistake made, and to put in other words, we had pure *tetra*(iso-amyl)ammonium in the cavity, but its geometry was false. To solve the problem and to answer the question why the apparent geometry was wrong, molecular modeling (EFF) was used and the result is shown in Fig. 11.5. The end part of the alkyl chain is orientationally disordered, and there are two orientations differing in site occupancy. The less populated orientation is twisted from the main one by about 30°. Superposition of the two orientations "produces" erroneous geometry of the resulting species which is a kind of intermediate between the two orientations. Using the results from molecular modeling to refine the crystallographic structure gave very good results. Again, geometry of the disordered moiety comes from modeling and cannot, as a rule, be derived directly from the diffraction data; it is simply confirmed in the structure refinement procedure.

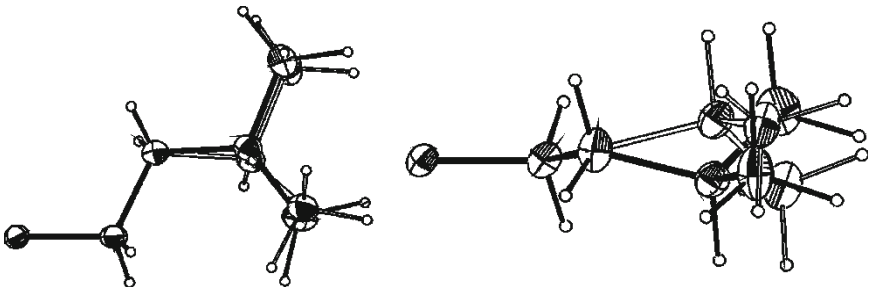

Fig. 11.5 Two orientations of the iso-amyl group in the clathrate structure shown in Fig. 11.4. *Dark bonds* correspond to the more populated orientation (70%), the other part has 30% of site occupancy. Two projections are given: perpendicular to the N–C–C fragment and parallel to it [4].

11.2.3 Correcting Disordered Structures

Perhaps the most dramatic example of this sort is the structure of layered inclusion compound of 1-methylnaphthalene (the host complex same as in the first example above). As in the case of azulene compound,[2] guest species are contained in two, not related by crystal symmetry, layers. The structure was solved based on good diffraction data set and the result seemed complete and satisfactory.[3] There was, however, one problem which could not be explained on the basis of X-ray data. The two, not related by crystal symmetry, guest 1-methylnaphthalene molecules differ slightly in geometry (Fig. 11.6) [5]. The differences, although small, seem significant as in some parts are greater than 4σ.[4] There is no clear explanation of the differences, even careful analysis of molecular librational motion in the crystal did not reveal any good reason for that.

As an appropriate illustration of possible errors in situations like in the example discussed here, the apparent dependence of molecular geometry upon temperature is given in Fig. 11.7a and b. Although there is not, seemingly, any systematic trend in the observed values as a function of temperature, in some fragments of the molecule, geometry variation with temperature is very impressive. However, all these are apparent [6].

In order to find a possible disordering of the guest, the isomorphous replacement method was used. 1-methylnaphthalene was replaced with 1-bromonaphthalene, and the resulted inclusion compound was isostructural with the methylnaphthalene one.

---

[2] The host structures are similar.

[3] The paper was accepted for publication in *Acta Crystallographica* which is known for high criticism toward the methodological part of experimental and computational content. Differences in molecular geometry between the two guests have been discussed in the paper, though no clear reason could be found.

[4] Standard deviation calculated from experimental data.

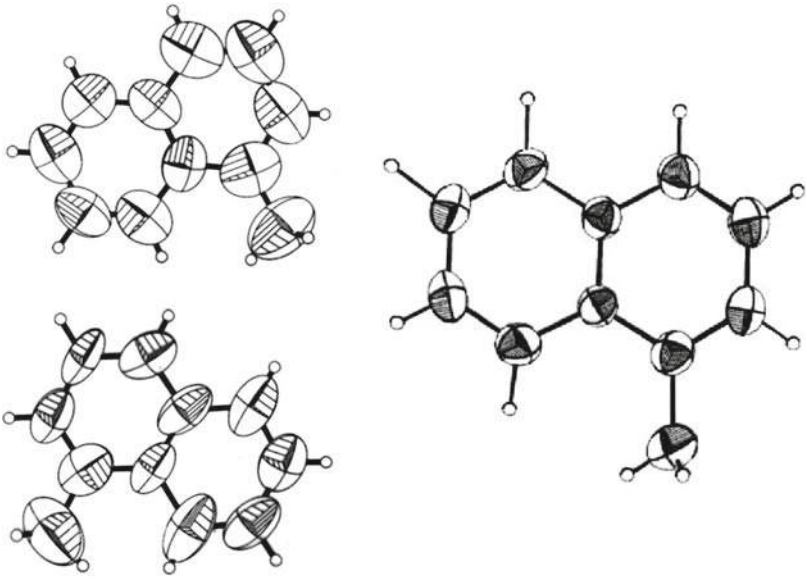

Fig. 11.6 Two, non-related by crystal symmetry, 1-methylnaphthalene (*guest*) molecules as obtained by X-ray structure determination (*left*) and the molecule after modeling and refinement procedure (cf. text below)

The geometrical differences between the two molecules of guest 1-bromonaphthalene are dramatic indeed (Fig. 11.8). Such differences cannot, of course, be attributed to any intermolecular interactions, and it is clear that molecular disordering is the reason for all these geometrical differences. Only bromine atom could be found for the second guest orientation, but this was a good starting point for molecular modeling. The result is depicted in Fig. 11.8. The two, not related by crystal symmetry, positions for the guest molecule differ in disordering possibilities [7]. The second (less populated) orientation is different in both layers, and thus, the apparent deformation of the guest is also different. Again, the site occupation factors calculated by molecular mechanics and originating from subsequent structure refinement are very close to each other; what nicely confirms the validity of modeling procedures, however simple.

11.3 Long Range Ordering Problems

11.3.1 Polytypism in Layered Structures

As may clearly be seen from the examples described above, structure analysis cannot be an *autonomous* technique in solving structure from X-ray diffraction data when the structure is partially disordered. There is some more information

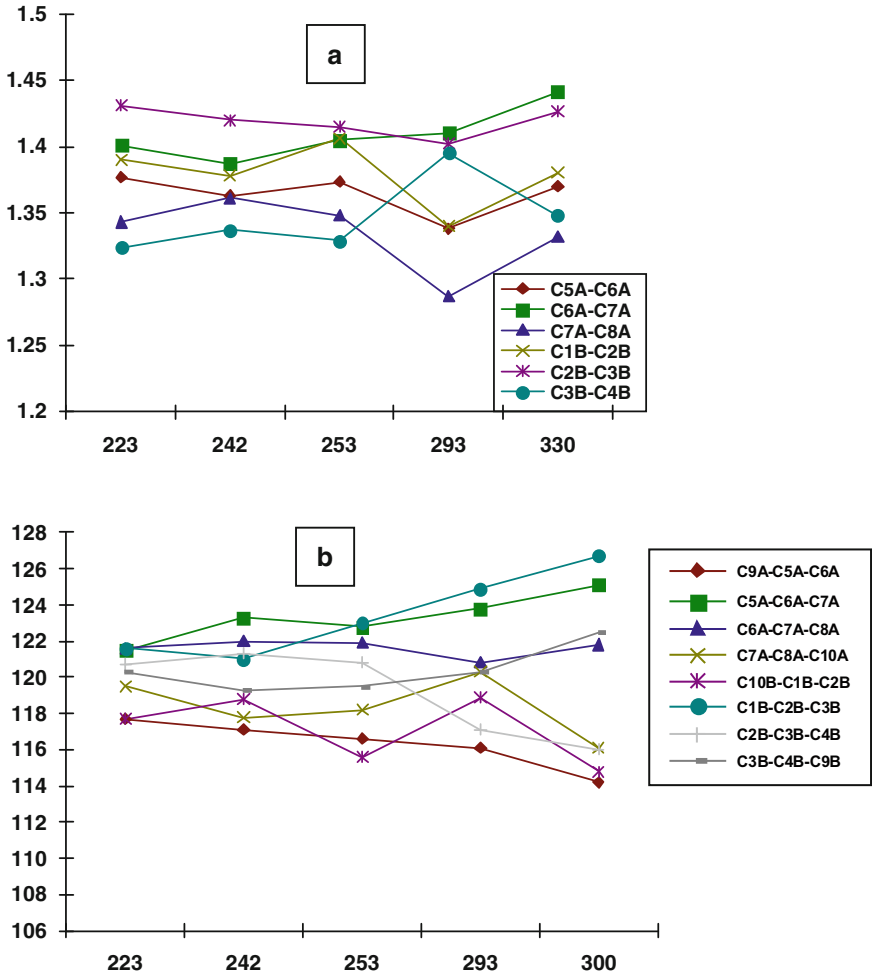

Fig. 11.7 Apparent temperature dependence of selected bond distances (**a**) in Angstrom units and angles (**b**) (in degrees) in the naphthalene rings in the 1-methylnaphthalene clathrate

which commonly is not attainable from direct diffraction studies but may be important for understanding the structure. The example discussed above, the layered inclusion compound of 1-methylnaphthalene, will be discussed in this context.

Let us consider the following questions

- If the guest molecules can adopt two orientations each with the less populated one having s.o.f.[5] equal, approximately, to 20%, what is the real situation in the crystal?

[5] Site occupation factor.

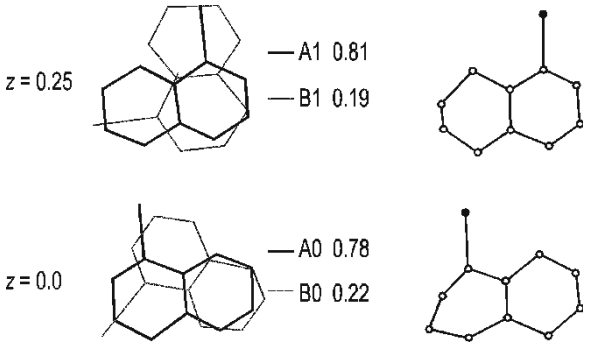

Fig. 11.8 Two 1-bromonaphthalene molecules in the layered clathrate isostructural with the one depicted in Fig. 11.2. The two non-related by crystal symmetry molecules as obtained by structure refinement and the respective orientational disordering modes which produce apparent molecular deformations (Notations as in Fig. 11.3)

- Are the molecules statistically distributed over the two possible orientations in the crystal?
- Is there a long range order, for example, ordered layers of the guest in orientation A and B, with respective probabilities?[6]

If we analyze the results of molecular modeling (Table 1), it seems there is an interesting situation in the structure with, again, difference between the layers of the guest. In one of the layers ($z=0$), the calculated energy of the guest B0-B0 intermolecular interactions with neighboring guest species does not depend, in practical terms, on their mutual orientations, while in the other ($z=0.25$), the situation is different. Molecules in orientation B1 prefer to be surrounded by guest molecules in the same orientation.[7] It may suggest ordering within the layers and disordering in long range, i.e., alteration of the layers in the solid. This kind of structural information is an *added value* coming from molecular modeling.

Table 11.1 Calculated energy of intermolecular interactions (kcal/mol) between guest molecules in layered clathrate, in orientations as in Fig. 11.8

z = 0			z = 0.25		
Central guest / Neighbouring guest	A0	B0	Central guest / Neighbouring guest	A1	B1
A0	–27.6	–26.1	A1	–29.0	–24.7
B0		–26.0	B1		–27.6

[6]For instance, every fifth layer might contain guest molecules in orientation B.

[7]The option B surrounded by A is ignored in view of their relative occupancies in the structure.

Although the result might, in principle, be analyzed by advanced X-ray diffraction techniques, it is certainly beyond the possibilities of standard, routine approaches.

The examples shown above clearly demonstrate the potential of molecular modeling for structure analysis. Modeling helps to solve difficult structural problems and adds new information concerning long range intermolecular interactions.

Molecular modeling is of routine use in protein crystallography. The authors believe it will also happen in the, so-called, small molecule crystallography in which molecular modeling will be incorporated as an intrinsic part of routine procedures. Small molecule crystallography now contains quite sizeable structural problems, with atomic aggregates of more than 200[8] in the asymmetric unit, more and more often present problems with partial molecular disordering, inclusion of foreign species (solvents), and generally, become quite complex structural objects.

11.3.2 Long Range Structural Correlations

Supramolecular crystallography can, by principle, present problems like the ones discussed above since the components are held together by rather weak intermolecular forces. Orientational disordering, guest substitution, non-stocichiometry are typical phenomena in this class of solids. Therefore, one may predict large usefulness of modeling techniques. Diffraction methods will certainly benefit from molecular modeling and more generally, our knowledge on structural features and behavior of supramolecular compounds will depend on reasonable and clever use of modeling. As an example, not discussed here in any detail, one may imagine dynamic properties of molecular solids. Let us consider the channel type supramolecular compound formed by $Ni(NCS)_2(4\text{-methylpyridine})_4$ (host) with a variety of guests (Fig. 11.9).

In this structure, the guest species are *meta*-bromonitrobenzene molecules.[9] In the picture (b), host molecules are omitted for the sake of clarity. Guest molecules display very interesting behavior. At "high temperatures",[10] they are orientationally disordered around the threefold axes and centers of symmetry. On cooling, ordering takes place in two steps. At first, just two-thirds of the guest molecules get ordered positions (as shown in the drawing of Fig. 11.8), and at lower temperatures, the ordering extends to the remaining one-third.[11] It may easily be seen in the picture that there must be some sort of "communication" between the channels of guest

[8] Hydrogen atoms are not included in such calculations as contributing very little to the overall diffraction.

[9] *Ortho*-bromonitrobenzene as well as *ortho*- and *meta*-dinitrobenzenes form isostructural compounds of this type, $Zn(NCS)_2(4\text{-methylpyridine})_4$ and $Cu(NCS)_2(4\text{-methylpyridine})_4$ (host) complexes with a variety of guest molecules are known as well.

[10] "Low" and "high" are relative to the guest species. *meta*-bromonitrobenzene shows the transition at about 60°C, while *meta*-dinitrobenzene shows transition of this sort at about 95°C.

[11] Description is somewhat simplified here. The "ordered" guest molecules shown on the picture still have some 10–15 % of disordering over two different orientations. This, however, is qualitatively different from the symmetric disordering around the threefold axis.

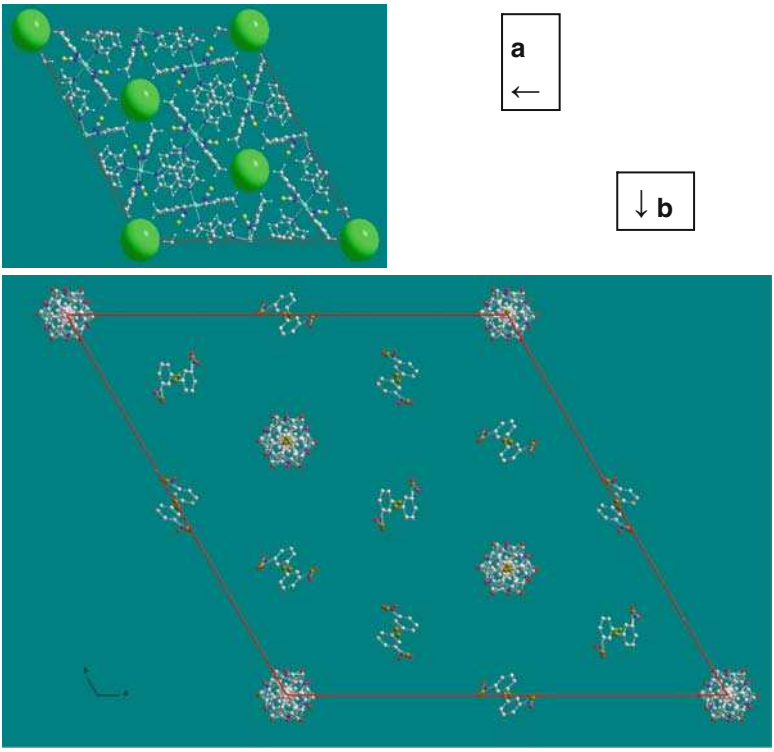

Fig. 11.9 $Ni(NCS)_2(4\text{-methylpyridine})_4$ (*host*) channel clathrate with *meta*-bromonitrobenzene (*guest*) at temperature above 65°C (**a**) and between 200 and 65°C. On (**a**) *green spheres* represent disordered guest species, on (**b**) host molecules are omitted for clarity [8]

molecules; the channels "know" in a way what is their surroundings, ordered or not. Distances between the channels are rather significant and it is not clear yet how this "information" is transferred throughout the crystal lattice. This sort of questions awaits explanation. Advanced modeling might greatly contribute to answer the question, though simple options, limited to interactions between nearest neighbors, are unsatisfactory.

11.3.3 Multicomponent Inclusion – Structural Models

The very last example here refers to the, so-called, organic zeolites. There are several structures which belong to this class of inclusion compounds and their physicochemical properties are remarkable, being of particular interest to separation science. An example of crystal structure of the compounds is given in Fig. 11.10 [9].

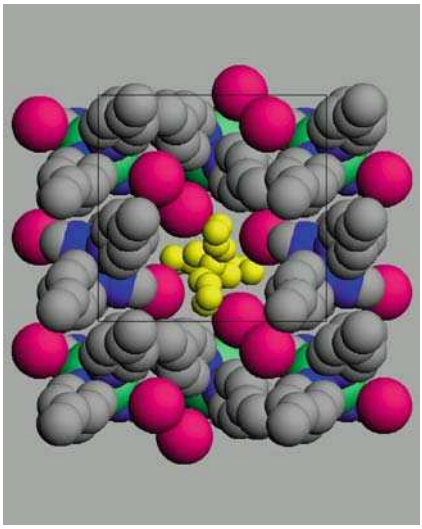

Fig. 11.10 Crystal structure of organic zeolite formed by $Ni(NCS)_2(4\text{-methylpyridine})_4$. *Yellow spheres* represent symbolically the empty space available for guest species

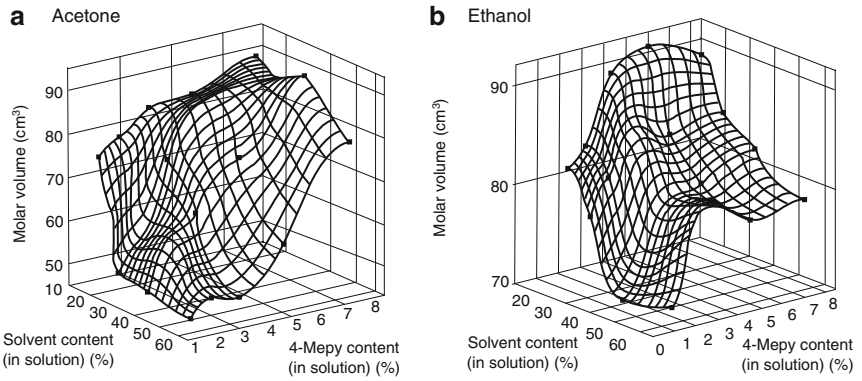

Fig. 11.11 Flexibility of the organic zeolite structure (cf. Fig. 11.10 above) expressed in terms of molar volume of the empty space (calculated as the difference between the molar volume of the solid and the volume of the host) at equilibrium with mixed solvents acetone/4-methylpyridine and ethanol/4-methylpyridine

What seems particularly interesting, from physicochemical point of view and in view of possible applications, is the flexibility of the structure. Depending on the composition of the mother solution, with which the solid is at equilibrium, the structure may expand or shrink preserving its main structural features (Fig. 11.11) [10].

A variety of guests may be absorbed in organic zeolite and just very simple examples of the resulted structures are solved by X-ray diffraction. This is due to fuzzy electron density maps in the guest region when it is a chemical mixture or it is orientationally disordered. A rare example of the two-component guest zeolite structure is given below [11] (Fig. 11.12).

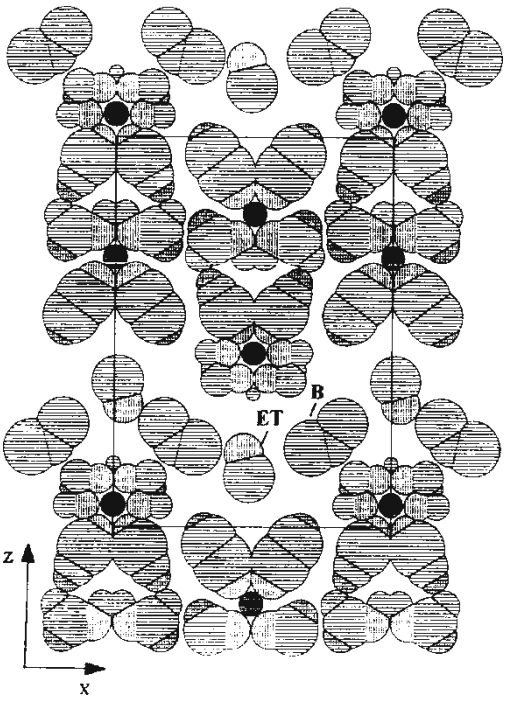

Fig. 11.12 A section drawing displaying the mutual positions of the host and guest species in organic zeolite (cf. Fig. 11.10). The guest is a two-component mixture of ethanol (ET) and benzene (B)

11.4 Concluding Remarks

There are many situations where direct structure determination is impossible or not reliable due to a variety of reasons as discussed above. Thus, molecular modeling is more than welcome to intervene in solving the problems.

In order to solve all the questions briefly listed above and to better understand physicochemical behavior of molecular (or supramolecular) solids, we need more imagination. This grows on experience, both experimental and mental, both on diffraction methods of structure solution and modeling techniques of what might happen in the structure.

The disordering problems are discussed here based on the authors' own experience and selected results. The problem is very common, however, and if it does not appear in the literature as often as it comes out in the laboratory work, it is simply because the authors have the tendency to skip over this kind of difficulty and chose another solvent, other conditions, etc. Let us opine that in such a way, we miss some important information on the chemical compounds we have in our hands. Structural analysis produces snapshots of molecular (supramolecular) structures, and if we are able to take snapshots of molecules in different supramolecular environment, it gives us much broader experimental experience. It is hoped that greater availability of X-ray diffraction techniques and structure solution software will not only bring a

great number of straightforward structures, but also encourage the researchers to undertake difficult problems, and to make molecular modeling to better understand the structural features of matter.

References

1. K. Suwińska, unpublished results
2. J. Lipkowski, Clathrate inclusion compounds of bis(isothiocyanato) tetrakis(4-methylpyridine) nickel (II). Part V: naphthalene clathrate. Acta. Cryst. **B38**, 1745–1749 (1982)
3. J. Lipkowski et al., A novel clathrate hydrate structure of tetra-iso-amyl ammonium fluoride. J. Incl. Phenom. Mol. Recogn. Chem. **9**, 275–276 (1990)
4. J. Lipkowski et al., Phase and X-ray study of clathrate formation in the tetraisoamylammonium fluoride water system. J. Incl. Phenom. Mol. Recogn. Chem. **17**, 137–148 (1994)
5. J. Lipkowski et al., Clathrate inclusion compounds of bis(isothiocyanato) tetrakis (4-methylpyridine) nickel (II). Part III: 1-methylnaphthalene clathrate. Acta. Cryst. **B38**, 416–421 (1982)
6. J. Lipkowski, K. Suwińska – unpublished results
7. J. Lipkowski et al., Some symmetry aspects of layered-clathrate structures formed by $Ni(NCS)_2(4\text{-methylpyridine})_4$. J. Incl. Phenom. **2**, 327–332 (1984)
8. J. Lipkowski – in preparation
9. A. Yu Manakov et al., Zeolite like sorption of volatile organics in β-$[CuL_2]$ (L=$\{CF_3COCH\text{-}COC(CH_3)_2OCH_3\}^-$). J. Phys. Chem. B **104**, 12111–12118 (2000)
10. J. Lipkowski, Werner Clathrates, in "*Comprehensive Supramolecular Chemistry*", ed. by J.L. Atwood, J.E.D. Davies, D.D. MacNicol, F. Vögtle, J.-M. Lehn, "*Solid-State Supramolecular Chemistry: Crystal Engineering*", Vol. 6, ed. by D.D. MacNicol, F. Toda and R. Bishop (Pergamon, New York, 1996), pp. 691–714
11. A.Yu Manakov et al., New crystal structures of -$[Ni(NCS)_2(4\text{-methylpyridine})_4]$ clathrates with furan, tetrahydrofuran, methylene chloride, benzene + ethanol and methylcellosolve as guest molecules. J. Incl. Phenom. Mol. Recogn. Chem. **26**, 1–20 (1996)

Chapter 12
Dihydrogen Bonds: Novel Feature of Hydrogen Bond Interactions

Sławomir J. Grabowski and Jerzy Leszczynski

Abstract The term dihydrogen bond (DHB) describes two hydrogen atoms being usually in contact closer than the corresponding sum of van der Waals radii. One of the hydrogen atoms is negatively charged while the second has a positive charge. This type of interaction was found in the crystal structures of metal-organic compounds in the middle of 1990s. There has been a vast number of theoretical and experimental studies on DHBs. Generally, it is the interaction between the Lewis acid and the Lewis base, similarly as a hydrogen bond (HB). Numerous investigations show that the DHB can be considered as a special type of HB since the analyses of energetic, geometrical, and topological parameters show similarities between both types of interactions.

12.1 Hydrogen Bond and Dihydrogen Bond Interactions

Hydrogen bond (HB) is an interaction of vast importance in various physical, chemical, bio-chemical, and life processes [1, 2]. Hence there has been a great number of studies on this type of interactions, both theoretical and experimental [3]. It is worth mentioning that the structure of species that are involved in HBs is often investigated, the nature of this kind of interaction is analyzed, and occasionally, it is a subject of disputes and debates. There are many definitions and statements concerning the HB. The most common seems to be the early one of Pauling [4] who suggested that "under certain conditions an atom of hydrogen is attracted by rather strong forces to two atoms, instead of only one, so that it may be considered to be acting as a bond between them. This is called the hydrogen bond." Pauling

S.J. Grabowski[1,2] and J. Leszczynski[1] (✉)
[1]NSF CREST Interdisciplinary Nanotoxicity Center, Department of Chemistry and Biochemistry, Jackson State University, Jackson, MS 39217, USA; [2]Department of Chemistry, University of Łódź, 90-236 Łódź, ul.Pomorska 149/153, Poland
e-mail: jerzy@icnanotox.org

J. Leszczynski and M.K. Shukla (eds.), *Practical Aspects of Computational Chemistry*, 255
DOI: 10.1007/978-90-481-2687-3_12,

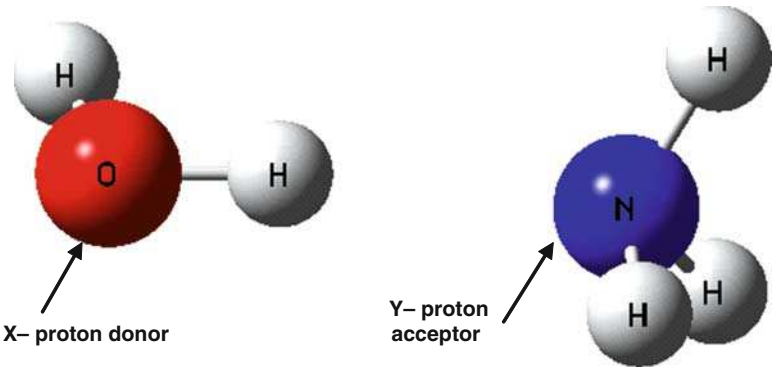

Fig. 12.1 The water–ammonia complex connected through O–H···N hydrogen bonding

also stated that the HB "is formed only between the most electronegative atoms" and that the weaker connection of H-atom is mostly electrostatic in nature. The HB is often designated as X–H···Y, where X is the proton donor (X–H is the proton donating bond) while Y is the proton acceptor; X and Y possess the excess of negative charge while H-atom is positively charged ($X^{-\delta}$-$H^{+\delta}$···$^{-\delta}Y$). Hence, such systems as O–H···O, N–H···O, N–H···N, and O–H···S are most often analyzed and presented as the HB interactions. Pauling also claimed that the Y center forming the proton acceptor should contain at least one free electron pair [4]. Figure 12.1 presents the scheme of the water–ammonia complex, where water is the proton donating molecule (O is the proton donor) while ammonia is the proton acceptor since it possesses the nitrogen acceptor center. This is the classical example of the interaction possessing characteristics being in line with the Pauling's definition.

This meaning and definition of HB was revised and modified in the last century, and additionally, criteria for its existence were introduced. For example, it was stated that the proton–acceptor distance (H···Y) should be shorter than the corresponding sum of van der Waals radii, the proton donating bond (X–H) is elongated as a result of complexation, and there is the concomitant red shift of the respective stretch frequency [1]. The hydrogen bonding energy should be meaningfully greater than the energy of weak van der Waals interaction (~0.01–0.1 kcal/mol). However, the value of the HB energy should also be much lesser than the energy of the typical covalent bond (~100 kcal/mol) [5]. Different ranges of hydrogen bonding energy are proposed in monographs and review articles but the range of 2–40 kcal/mol is most often cited [2].[1] It is often pointed out that the electron charge transfer from the proton acceptor to the proton donating part of the complex is a characteristic for HB [6]. However, it should be mentioned that

[1] The hydrogen bond energy possesses a negative value and more negative value indicates stronger interaction. However, very often, for the convenience of explanations the absolute values are given in the texts. The same concerns the ranges of the energies given here, the positive values will be given hereafter through the whole text. The true negative values are included in tables and figures.

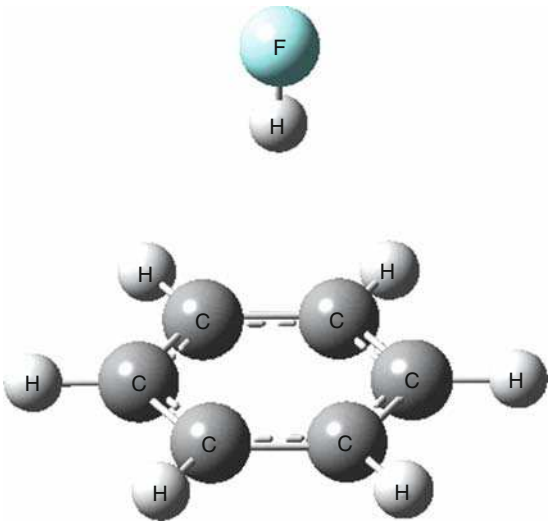

Fig. 12.2 The benzene–hydrogen fluoride complex connected through F–H···π hydrogen bonding

almost all the characteristics briefly mentioned here were contested in numerous studies. It was stated that not only electronegative atoms may act as the proton donor but also as the proton acceptor [2]. It has been proven that carbon atom may act as the proton donor [7], but also it may act sometimes as the proton acceptor, even the C–H···C interactions were analyzed as the HBs [2]. Interestingly, not only the one-center proton acceptors have been considered to form HBs; also, π-electrons play such a role and thus in addition to the classic complexes, the O–H···π, N–H···π, and C–H···π HBs were analyzed [2]. Thus, the next characteristic of HB calling for acceptors to possess at least one lone electron pair is not a valid rule. Figure 12.2 presents the scheme of benzene–hydrogen fluoride complex, which was often analyzed from experimental [8] as well as theoretical point of view [9]. This is F–H···π hydrogen-bonded complex since hydrogen fluoride is the proton donating moiety while π-electrons of benzene act as the proton acceptor.

It is worth mentioning that the other characteristics that seemed to be attributed to HB are not fulfilled. It is not required that H···Y distance is shorter than the van der Waals sum radii since HB is mostly an electrostatic interaction and it acts far beyond the van der Waals cut-off.[2] Besides, the X–H···Y interactions with X or/and Y centers of not high electronegativity (C or Si atoms) are rather weak with the interaction energies lower than the lower range limit of 2 kcal/mol. These energies are often close to energies of the van der Waals interactions. The other strong evidence of the existence of HB, the elongation of the proton donating bond, and the corresponding red-shift of the stretching X–H mode may also be contested.

[2]The attractive electrostatic interactions are proportional to $\sim R^{-2}$ and the van der Waals ones to $\sim R^{-6}$ (R is the distance between the interacting species). Hence, the electrostatic interactions "converge to zero" much slower than the van der Waals interactions.

The interactions were found and analyzed where the X–H shortens as a result of the HB formation and there is the concomitant blue shift of the respective stretch frequency [10].

It seems that problems of the unequivocal classification, if any specific interaction is HB, are not related to the definition. The Pauling definition of hydrogen bonding and the other definitions of hydrogen bonding contain at least a few statements or characteristics. Since there are numerous interactions, more or less, fulfilling such statements, these classifications are vague. Moreover, there exist different fixed values characterizing the HB. Among them are the interaction energy range or the van der Waals proton–acceptor distance cut-off. For example, one can get confused if any interaction of the strength being slightly below 2 kcal/mol should be classified as the HB. There are also debates and disputes if the HB is electrostatic or rather a covalent interaction [2, 5].[3]

One can conclude that the variety of different interactions that are often classified as the HBs may be the reason why the problems with unequivocal classification of interactions appear. This is also the case for so-called dihydrogen bonds (DHBs), often designated as X–H···H–Y [11]. Such systems have been found and analyzed in the crystal structures of metal-organic compounds in the middle of 1990s [12, 13]. It was found that there are the H···H contacts in crystals slightly shorter than the corresponding sum of the van der Waals radii where one of H-atoms is positively charged and covalently connected with the typical proton donor (N, O, F, etc.), while the second H-atom possesses the excess of negative charge and is connected with transition metal atom or with boron. It may be treated as a special type of HB since the negatively charged H-atom plays a role of the proton acceptor. It was found that such interactions are rather strong, usually even stronger than the typical HBs. The further studies have shown that not only transition metal or boron may be connected with negative H-atom to form the DHBs [14, 15]. Figure 12.3 presents three neighboring molecules in the crystal structure of boraneamine [16]. These species are connected through N–H···H–B DHBs. One can observe that there are two N–H proton donating bonds oriented toward the H-atom, which is connected with boron and which plays the role of the proton acceptor. Since there are two proton donors and one proton acceptor, such an interaction is named the acceptor bifurcated HB [2]. There are the other numerous crystal structures where the DHBs exist. It seems to be a very important interaction that often stabilizes the crystal structures and also influences the arrangement of molecules in crystals. It is worth mentioning that the dihydrogen-bonded systems were analyzed from both the experimental and theoretical point of view and the number of studies on this type of interactions increased rapidly in the recent years.

[3] This is discussed in the next sections.

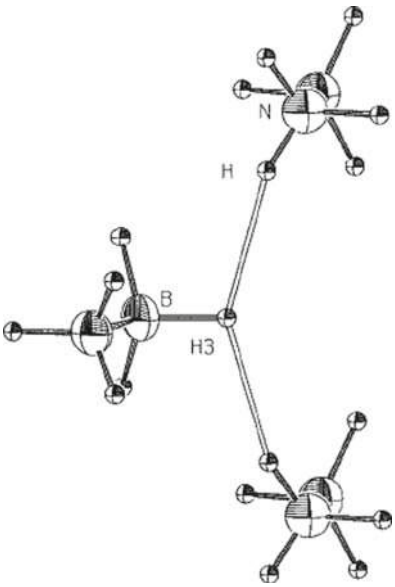

Fig. 12.3 The closest N–H···H–B contacts for the neutron diffraction crystal structure of boraneamine. Reprinted with permission from Klooster et al. [16], copyright 1999, American Chemical Society, Washington, DC

12.2 The Theoretical Methods Applied to Analyze and Characterize the Hydrogen and Dihydrogen Bonds

12.2.1 The Hydrogen Bond Energy

Since DHB may be treated as a special kind of HB, the methods and approaches presented in this section are generally related to the HBs. It was mentioned in Sect. 12.1 that the energy of HBs are positioned between those of covalent bonds and van der Waals interactions. Such energy is calculated in the following way. If two species R_1–X–H and Y–R_2 are connected through the X–H···Y HB, the energy ΔE expressed by (12.1) is often named as the HB energy.

$$\Delta E = E(R_1 - X - H \cdots Y - R_2) - E(R_1 - X - H) - E(Y - R_2) \qquad (12.1)$$

Generally, this is the binding energy since it relates to the stabilization of two interacting species. However, the HB is often the most important intermolecular interaction. Hence, the energy expressed by (12.1) may be treated as the one that measures the strength of HB. The stabilization of the R_1–X–H···Y–R_2 complex is connected with the H-bond formation; thus, ΔE value is negative (see Footnote 1). The binding energy is often calculated within the supermolecular approach. This means that for R_1–X–H···Y–R_2 complex the geometries of R_1–X–H and Y–R_2 subsystems are considered with their corresponding energies. Such an approach does not take into account the deformation of interacting species, which is the result

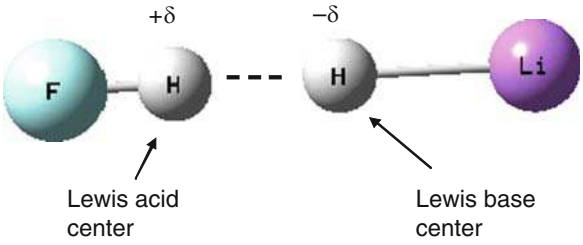

Fig. 12.4 The F–H···H–Li complex connected through dihydrogen bond

of complexation. Hence, the deformation energy is often included in (12.1) to calculate the HB energy. The other correction includes the so-called basis set superposition error (BSSE) [17]. The zero-point vibrational energy (ZPVE) correction should also be included in the calculations to generate accurate results.

It is worth mentioning that the binding energies for dihydrogen-bonded systems often exceed 10 kcal/mol. For example, different methods and levels of approximation applied for the linear complex of hydrogen fluoride (Lewis acid) and the lithium hydride (Lewis base) – (Fig. 12.4.) estimating this energy within 10–12 kcal/mol [18]. Similarly, for the other related linear complexes[4] where DHBs exist, the binding energies are relatively high. For example, the HB energy for the translinear dimer of water amounts to ~5 kcal/mol.

To better describe the nature of the considered hydrogen or DHB, it is useful to decompose the interaction energy into various components. According to the approach of Kitaura and Morokuma, the SCF interaction energy (ΔE_{SCF}) may be decomposed into the following energy terms [19].

$$\Delta E_{SCF} = ES + PL + EX + CT + MIX \tag{12.2}$$

Briefly speaking, ES is the electrostatic interaction energy between the undistorted charge distributions of two interacting monomers. PL is the polarization interaction energy, which may be defined as the energy of the distortion of charge distributions of monomers as an effect of complexation. CT is the energy of charge transfer from one molecule to the other as the effect of the complex formation. EX is the exchange energy that results from the electron clouds repulsion. MIX is the energy difference between SCF interaction energy and the sum of these four components and is named as "the coupling energy term." EX is the repulsive energy term; thus, it is positive while ES, PL, and CT are usually negative attractive energy terms. It is worth mentioning that ΔE_{SCF} neglects the electron correlation energy (*CORR*). The methods that take into account the correlation of

[4]These linear systems are often not in local minima. However, the recent studies (Grabowski et al., in preparation) show that the complexes being in minima are very close, in geometry and energy, to the linear structures.

electrons allow estimate *CORR*. The latter one may be further decomposed and its most important attractive term is the *dispersion interaction energy (DIS)*.

The decomposition scheme proposed by Kitaura and Morokuma is one of the first introduced. Hence, this scheme is very well known, often applied and included into different theoretical codes, for example, it is implemented in Gamess program. However, the various decomposition schemes of the interaction energy were later proposed. Among them is, for example, the intermolecular Møller-Plesset perturbation theory (IMPPT) [20] or SAPT (Symmetry Adapted Perturbation theory) approach [21, 22]. There is also the variation–perturbation approach [23], which was applied in studies presented in the following sections. For the latter scheme, the total interaction energy as well as all of its components is free of BSSE due to the full counterpoise correction. Moreover, there is not the MIX component since all energy terms are well decomposed. The delocalization term (DEL) within this scheme roughly corresponds to the sum of CT and POL components of the Kitaura and Morokuma approach.

There have been various attempts to evaluate molecular interactions using the energy decomposition approaches. For example, the decomposition scheme of the interaction energy was applied to analyze the following complexes: $LiH\cdots H_2$, $LiH\cdots CH_4$, $LiH\cdots C_2H_6$, and $LiH\cdots C_2H_2$, and these systems were compared with the water dimer [24]. Owing to such an analysis, it was possible to classify the linear $LiH\cdots C_2H_2$ complex as connected through –C–H···H–Li DHB where acetylene molecule is the proton donor and negatively charged hydrogen of lithium hydride is the proton acceptor center. Besides, it was revealed for the $LiH\cdots C_2H_2$ complex that the electrostatic term is the most important among the other attractive interaction energy terms. The binding energy of this system is equal to 4.3 kcal/mol.[5] The H···H intermolecular distance for this complex amounts to 1.98 Å, less than the corresponding sum of van der Waals radii (2.2–2.4 Å). The latter results are similar to those obtained for the water dimer where the O–H···O HB exists and where the electrostatic interaction also represents the most important attractive energy. The binding energy amounts to about 4.5 kcal/mol for water dimer. The other lithium hydride systems [24] are mainly bound by dispersion interaction; thus, they should be classified as van der Waals complexes.[6]

One can conclude that the DHB possesses all main characteristics usually attributed to HB: the appropriate strength since the binding energy is well positioned within the expected range (2–40 kcal/mol); the proton acceptor distance less than the sum of van der Waals radii; and the electrostatic nature of interaction. It will be validated in the following sections that the other characteristics attributed to HB are also relevant for the DHB.

[5] MP4/aug-cc-pVTZ level of approximation.

[6] It was mentioned earlier that the dispersion interaction energy (DIS) is the most important attractive term of the correlation energy (CORR); it is usually attributed to the van der Waals interactions, physical meaning of the latter is usually the sum of attraction (DIS) and the repulsive exchange energy (EX).

12.2.2 The Quantum Theory of "Atoms in Molecules" (QTAIM)

The quantum theory of "atoms in molecules" (QTAIM) [25, 26] is based on analyses of the electron density distribution. The electron density of such systems such as simple molecules or ions, and also complexes, complex molecular and ionic aggregates, as well as crystals may be analyzed using this approach. QTAIM is a powerful tool that allows characterizing of various interactions: covalent bonds, ionic bonds, van der Waals interactions and, what is the most important for this review, also HBs. The analysis of critical points of the electron density is very useful. For the critical points (CPs), the gradient of electron density, ρ(r), vanishes:

$$\nabla \rho_C = 0. \tag{12.3}$$

There are four categories of stable critical points: maxima in ρ(r) correspond to attractors that are attributed to nuclei, minima are connected with the cage points (CCPs), two kinds of saddle points, the bond critical points (BCPs), and the ring critical points (RCPs). It is possible to find the line of the lowest energy density, which connects attractors attributed to the interacting atoms. This is the bond path (BP). Such a line is usually not curved in the case of covalent bonds or any other nonbonding interactions (HBs also). However, the cases are known where BP is not accurately the straight line. The point characterized by the lowest electron density on BP is named the BCP. The set of all BPs and critical points of the considered system is called a molecular graph. Figure 12.5 presents the molecular graph of the F–H···H–Li complex, which was mentioned earlier. This is very important that the BPs represent not only typical covalent bonds but also the nonbonding interactions, as for example, H···H intermolecular interaction (Fig. 12.5). The characteristics of BCP are very useful in analyzing the considered interaction. The electron density at BCP (ρ_C) and its Laplacian ($\nabla^2\rho_C$) are the most often presented in QTAIM. It was found in the numerous studies that the electron density at BCP often well correlates with the strength of an interaction [27]. There exist linear correlations between ρ_C and the other measures of the strength of interaction (often even for heterogeneous samples of complexes) [28]. The value of $\nabla^2\rho_C$ is also informative. The negative $\nabla^2\rho_C$ value means that there is the concentration of the electron density within the atom–atom interaction region. Negative value of $\nabla^2\rho_C$ shows that there is shared interaction – covalent bond. Such a value is detected for H–F BCP (Fig. 12.5). The positive value of $\nabla^2\rho_C$ is typical for closed-shell interaction, ionic bond

Fig. 12.5 Molecular graph of the F–H···H–Li complex, *big circles* correspond to attractors, *small red circles* to BCPs, the BPs are also given (*pink lines*)

(LiH – Fig. 12.5), van der Waals interaction, and not very strong HBs (H···H interaction, Fig. 12.5.).

The Virial theorem leads to the relation between the Laplacian of the electron density at BCP and its other characteristics.

$$(1/4)\nabla^2\rho_C = 2G_C + V_C \tag{12.4}$$

The values of (12.4) are expressed in atomic units. G_C designates the local kinetic energy density at BCP and V_C is the local potential energy density at BCP. H_C is the total electronic energy density at BCP and it is the sum of G_C and V_C. V_C is always negative and G_C is positive, hence if V_C outweighs 2 times, the value of G_C then the Laplacian is negative, and one may assume covalent interaction. In case of very strong HBs, $\nabla^2\rho_C$ is negative at the BCP corresponding to the proton–acceptor interaction. This occurs for both H···F interactions of $[FHF]^-$ ion. This was also found for the experimental electron density of the crystal structure of benzylacetone where intramolecular O···H···O HB exists and where for both H···O contacts Laplacian values of the electron density at corresponding BCPs are negative. Very often, such a situation is attributed to the covalent character of HB interaction. However, sometimes $\nabla^2\rho_C$ is positive but V_C outweighs only one-time G_C value. In such a case, the total electron energy density, H_C, is negative and the interaction is partially covalent in nature. Such a case occurs for the F–H···H–Li dihydrogen-bonded system where for H···H BCP $\nabla^2\rho_C$ is positive but H_C is negative. Rozas, Alkorta, and Elguero proposed the following classification of HBs: for weak ones both $\nabla^2\rho_C$ and $H_C>0$; for medium and strong, H-bonds; $\nabla^2\rho_C>0$ and $H_C<0$, while for very strong ones both $\nabla^2\rho_C$ and $H_C<0$ [29].

The QTAIM parameters may also be useful to analyze the other interactions, for example, the intramolecular DHBs. Similarly, as it is in the case of HBs where the proton donor and the proton acceptor may belong to the same species, malonaldehyde is an example for the existence of intramolecular HB. Figure 12.6 presents the relief map of the species where intramolecular O–H···H–B interaction exists [30].[7] This relief map is displayed in the plane of the molecule. Interestingly, the intramolecular DHBs often occur in the crystal structures. The first studies on DHBs in crystals of metal-organic compounds have also examined this type of interactions [11].

There are the other methods – experimental as well as theoretical – to analyze hydrogen and DHBs. However, because of the scope of this review, only a few directly connected with studies discussed here are presented.

[7]The calculations of (1Z)-2-borylethen-1-ol were performed at the MP2/6-311++G(d,p) level of approximation

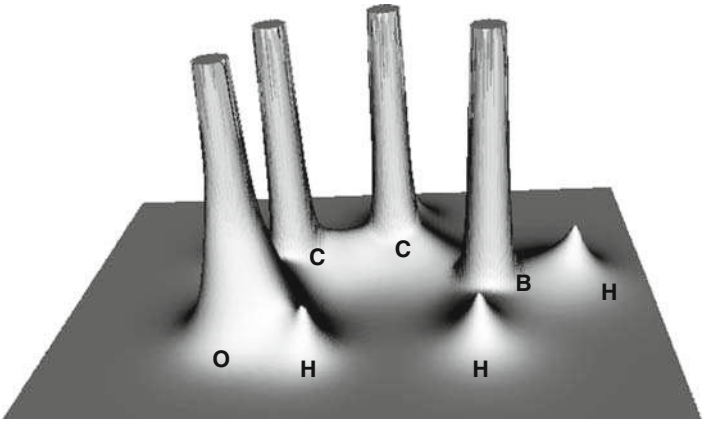

Fig. 12.6 Relief map of the electron density of (1Z)-2-borylethen-1-ol

12.3 Variety of Dihydrogen Bonds Interactions

It was pointed out that the hydrogen bonding, as it is positioned between weak van der Waals interactions and much stronger covalent bonds, is an interaction without borders [31]. It means that there are not "sharp" borders between these classes of interactions. Very weak C–H···Y interactions are often analyzed. Sometimes, it is very difficult to classify them as HBs since they are rather van der Waals type of interactions. Similarly, very strong HBs often exist, which possess numerous characteristics of covalent bonds. However, in such a case, one should consider the belief that the H-atom situated between two heavier, usually electronegative atoms, cannot be divalent. The electrostatic-covalent hydrogen bond model (ECHBM) was proposed [32], where the authors claim that there are three classes of very strong HBs: negatively charge assisted hydrogen bond – CAHB(−), positively charge assisted hydrogen bond – CAHB(+), and resonance assisted hydrogen bond – RAHB. Numerous examples of such compounds have been found where the Laplacian of the electron density at the proton–acceptor BCP is negative. This indicates the concentration of the electron density in this interatomic region attributed to the covalent character of interaction. For such interactions, the proton–acceptor distance is very short, sometimes close to the lengths of typical covalent bonds. The other characteristics may include covalent nature: the strength of HB (the binding energy of about 20 kcal/mol or even more) and the decomposition of the interaction energy. It was found that for covalent in nature and very strong HBs, the delocalization interaction energy term (DEL) is the most important attractive term (more important than the electrostatic term) [33]. This shows that very strong HBs are covalent in nature and not electrostatic, if one assumes that the DEL term is attributed to covalency.

The similar situation occurs for the DHBs, which can be very weak (even for C–H···H–C DHBs only a slight charge difference was revealed between the

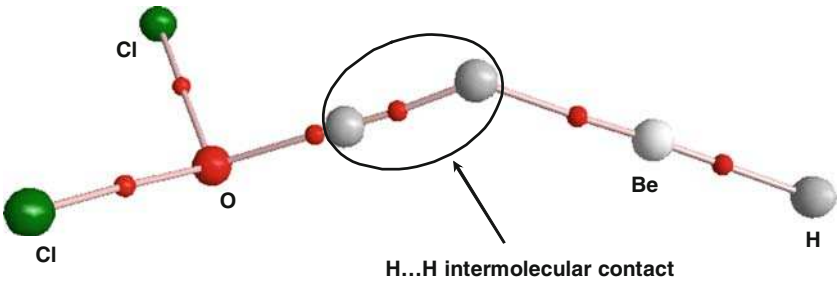

Fig. 12.7 Molecular graph of $Cl_2OH\cdots HBeH$ complex

H-atoms [34]).[8] On the other side, there are very strong DHBs possessing all characteristics of the very strong and covalent in nature HBs mentioned above.

Figure 12.7 presents the molecular graph of $Cl_2OH\cdots HBeH$ complex where the intermolecular O–H···H–Be DHB exists. It was found that this structure corresponds to the stable energetic minimum [35]. This is the shortest ever found theoretically intermolecular contact (H···H) since it amounts to only 1.049 Å. On the other hand, such a short contact represents the proton–acceptor distance.[9] It is worth mentioning that the other shortest contact was revealed for bifluoride $(FHF)^-$ ion. For this system, the H···F equivalent distances amount to 1.1–1.2 Å. The exact value depends on the type of experimental measurements or the applied method of calculations [36].

For the $Cl_2OH\cdots HBeH$ complex, other characteristics indicating the covalent character of H···H interaction exist. The binding energy is equal to 22.7 kcal/mol and the transfer of electron charge from the proton acceptor (BeH_2) to the proton donor (Cl_2OH^+) is equal to 353 millielectrons.[10] For comparison, such an acceptor–donor transfer for O–H···O HB in water dimer amounts to ~20 millielectrons. Such a large electron transfer for the dihydrogen-bonded system has to be associated with the large electron density redistribution as a result of the complexation. Table 12.1 presents the components of decomposition of the interaction energies for $H_2OH^+\cdots HBeH$ complex and its derivatives. For all complexes, the binding energy (ΔE) is close to 20 kcal/mol or even exceeds this value. The only exception ($H_2OH^+\cdots HBeF$ complex) is characterized by an energy of ~14 kcal/mol. This is because of weaker Lewis base properties of H-atom of HBeF (F is the electron withdrawing substituent). Generally, for all these species, the delocalization energy is the most important attractive term exceeding the electrostatic term. One can also observe that in all cases presented in Table 12.1 (except of water dimer given for

[8] There are also H–H stabilizing interactions [26] not classified as the Lewis acid–Lewis base ones and being different in nature than DHBs, H–H interactions often concern C–H···H–C systems (like for example in diphenyl molecule).

[9] There is the O–H proton donating bond (of Cl_2OH^+ ion) and $^{-\delta}H$ acceptor (the BeH_2 molecule).

[10] These values, as well as H···H distance, for the $Cl_2OH\cdots HBeH$ complex were obtained at the MP2/aug-cc-pVTZ//MP2/aug-cc-pVDZ level of approximation (BSSE correction included).

Table 12.1 Interaction energy terms (in kcal/mol), calculated at MP2/6-311++G(d,p) level of approximation

Complex	EL	EX	DEL	CORR	ΔE
$H_2OH^+\cdots HBeH$	−12.16	19.94	−23.95	−3.37	−19.54
$H_2OH^+\cdots HBeBeH$	−17.27	27.72	−35.64	−4.01	−29.19
$H_2OH^+\cdots HBeF$	−6.10	15.86	−19.69	−4.03	−13.96
$HClOH^+\cdots HBeH$	−12.57	24.70	−29.87	−4.72	−22.45
$Cl_2OH^+\cdots HBeH$	−13.25	33.81	−43.12	−6.42	−28.99
$Cl_2OH^+\cdots HBeF$	−6.01	24.10	−30.00	−7.08	−18.99
$(H_2O)_2$[a]	−8.75	6.78	−2.19	−0.29	−4.46

For the convention of signs see Footnote 1

[a]Water dimer for comparison

comparison), the exchange repulsive term is greater than the corresponding modulus of the electrostatic term. This means that the electrostatic attractive interaction cannot compensate the repulsive forces. This also indicates that the systems are stable due to the electron charge redistribution as an effect of the complexation. Different situation is found for the water dimer characterized by the O–H...O hydrogen bonding. For this system, the electrostatic energy exceeds the exchange repulsion and it is the most important attractive energy. The importance of DEL term for the complexes presented in Table 12.1 indicates that their DHBs are probably covalent in nature. This may be confirmed by the QTAIM results.

Table 12.2 presents the intermolecular H···H distances that are very close to 1 Å or they are slightly longer. The proton–acceptor H...O distance for H-bonded water dimer is much greater, but it is still significantly shorter than the corresponding sum of oxygen and hydrogen van der Waals radii (~2.6 Å). Also, the corresponding characteristics of BCPs of H···H interactions are presented in Table 12.2. One can observe high ρ_C-values (for example, for the $Cl_2OH^+\cdots HBeH$ complex it amounts to ~0.1 a.u.). Such ρ_C-values are usually observed for the covalent bonds (order of 0.1 a.u.), while for the closed-shell interactions, the values are of the order of 0.01 a.u. For two of the complexes, the $\nabla^2\rho_C$ values are positive, and for the remaining four cases, they are negative. However, for all complexes presented in Table 12.2, H_Cs are negative. This means that the H···H interactions presented here are covalent ones ($\nabla^2\rho_C<0$) or at least partly covalent ($H_C<0$) in nature. Similar results as for the complexes of hydronium ion were also obtained for $NH_4^+\cdots HBeH$ and its derivatives [37]. Alkorta and coworkers have analyzed very strong DHBs. For example, they have predicted for the $LiNCH^+\cdots HLi$ complex the binding energy of 27.1 kcal/mol and the H···H distance equal to 1.309 Å [38].[11] These are the examples of very strong DHBs overlapping (as measured by the values of various energetic, geometrical, and QTAIM parameters), with the typical covalent bonds or even possessing the characteristics of the covalent interactions.

[11]The calculations were performed at the MP2/aug'-cc-pVTZ level of approximation.

Table 12.2 The H···H distances (in Å) and the QTAIM characteristics of the corresponding BCP (in a.u.) for the complexes of H_2OH^+···HBeH and its simple derivatives

Complex	$R_{H\cdots H}$	ρ_C	$\nabla^2\rho_C$	H_C
H_2OH^+···HBeH	1.229	0.0617	0.0239	−0.0238
H_2OH^+···HBeBeH	1.127	0.0830	−0.0351	−0.0429
H_2OH^+···HBeF	1.280	0.0525	0.0402	−0.0168
$HClOH^+$···HBeH	1.157	0.0757	−0.0097	−0.0356
Cl_2OH^+···HBeH	1.057[b]	0.1019	−0.0992	−0.0610
Cl_2OH^+···HBeF	1.133	0.0789	−0.0191	−0.0386
$(H_2O)_2$[a]	1.959	0.0231	0.0912	0.0023

[a]Water dimer for comparison, the results concern H···O contact and the corresponding BCP
[b]This value is slightly different from the one presented earlier (1.049 Å), since the value from table represents the MP2/6-311++G(d,p) results while the previous values were obtained at the MP2/aug-cc-pVDZ level

Very recently, various DHB complexes were analyzed [39].[12] The complexes of ammonia and hydronium ions were included in this analysis, in addition to the complexes with acetylene and methane, and their derivatives. Generally, in such complexes, lithium hydride and berylium hydride (and its fluorine derivative) act as the Lewis bases (proton acceptors) while hydronium ion, ammonia ion, methane, acetylene, and their simple derivatives act as the proton donors. Therefore, it was possible to investigate the wide spectrum of DHB interactions, starting from those that possess the covalent character and extending to the systems that are difficult to classify as DHBs (since they rather possess the characteristics of the van der Waals interactions). Figure 12.8 displays the relationship between H···H distance and the electron density at H···H BCP.[13] One can observe the H···H distances close to 1 Å, (as for the covalent bond lengths) and also the distances of about 2.2–2.5 Å, typical for the van der Waals contacts. This also holds for the ρ_C-values – of the order of 0.1 a.u. as for the covalent bonds and much smaller values as for the HBs and weaker interactions.

Interestingly, the results and observations presented here indicate that the DHBs, similarly as HBs, cover the wide spectrum of interactions. It was claimed earlier that the HBs possess covalent character for very strong interactions, while for strong and medium strength interactions, they are electrostatic in nature [2, 32]. The similar findings are presented below for DHBs.

[12]MP2/6-311++G(d,p) level calculations were carried out.

[13]This is the exponential relationship which only roughly expresses the dependence. Since electron density at BCP (ρ_C) and the proton – acceptor distance may be treated as rough measures of the strength of interaction thus such correlation was found. To analyze the sample of complexes in detail, one should take into account $\ln(\rho_C)$ to observe the possible sub-samples of all species taken into account.

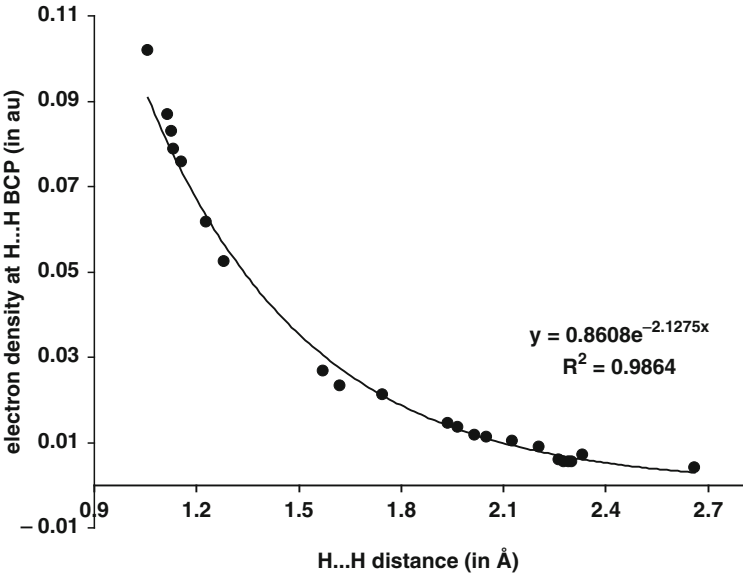

Fig. 12.8 The relationship between H···H intermolecular distance (in Å) and the electron density at the corresponding BCP – ρ_C (in a.u.)

12.4 Dihydrogen Bonds and the Other Nonbonding Interactions

There are various studies indicating a vital role of the HBs in architecture of the crystal structures [1, 2]. HBs are often responsible for the arrangement of molecules and/or ions in crystals. The same applies to the DHBs [11] that exist particularly in the metal-organic crystal structures. There very often the H-atoms connected with transition metals possess the excess of the negative charge and hence may act as the proton acceptor centers. Amusingly, both the HBs and DHBs are classified as the nonbonding interactions despite the "bond" term in their names.

Are the other nonbonding interactions responsible for the arrangement of the molecules in crystals? If one excludes the strong, long-range electrostatic interactions and restricts consideration to the typical crystals of organic and metal-organic compounds, the halogen bond seems to be counterpoint to the HB [40]. It was concluded that the halogen bond formation is sometimes preferable if compared with the possibility of the formation of the HB. Halogen bond is the Lewis acid–Lewis base R_1–C–Hal···Y–R_2 interaction where R_1–C–Hal is the Lewis acid with halogen atom (Hal) center and Y–R_2 is the Lewis base, Y designates typical electronegative atom such as O, N, etc. Halogen atom (except of fluorine) is usually connected with carbon atom and the halogen bond is stronger for heavier Hal atoms.

Figure 12.9 illustrates the neighboring molecules in the crystal structure of trichloroacetic acid. One can observe the centrosymmetric dimers of acid connected

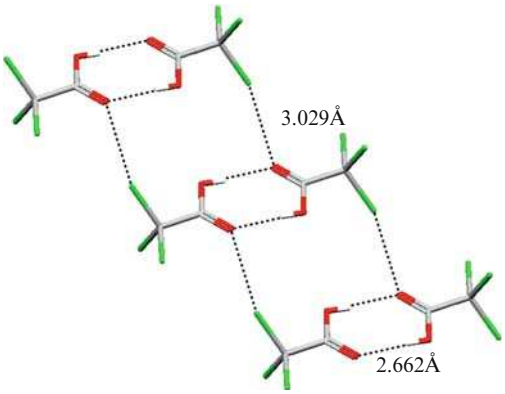

Fig. 12.9 Network of intermolecular contacts in crystal structures of trichloroacetic acid (TCACAD01 – taken from Cambridge Structural Database [41])

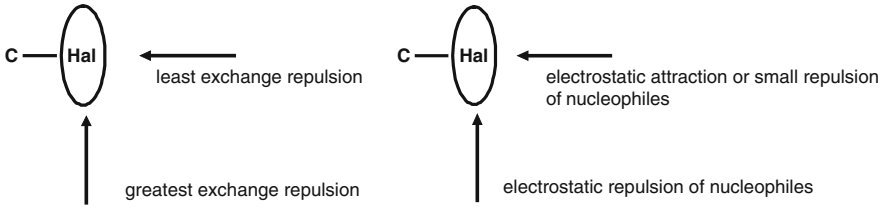

Fig. 12.10 The anisotropy of van der Waals radius of halogen (based on the scheme from [42])

through equivalent O–H···O HBs (O···O distance is equal to 2.662 Å). However, there are also halogen bonds, C–Cl···O=C interactions, where Cl···O distance is equal to 3.029 Å and is shorter than the corresponding sum of van der Waals radii. C–Hal···Y halogen bonds are usually linear or nearly linear.

What is the reason that two electronegative atoms (halogen and Y) may be in contact creating the stable energetically complexes? This is explained very often by the anisotropy of van der Waals radius of halogen atom [42]. Figure 12.10 displays the example of explanation of the anisotropy of halogen atom van der Waals radius given by Zordan and coworkers [42]. It seems that there is the greater exchange and electrostatic repulsion in the direction perpendicular to the C–Hal bond. Therefore, the Hal···Y connections are possible in line of the C–Hal bond.

There is also another type of the nonbonding interaction, not investigated extensively, with the hydrogen atom possessing the excess of negative charge and situated among two electropositive centers [43]. Since the charge distribution is inversed when compared with HB, such a type of the interaction was named *inverse hydrogen bonding*. However, such a term is sometimes proposed for the blue-shifting HBs [10]. Therefore, the *hydride bond* term was proposed recently for the former bonding [44]. If one designates such an interaction as $X–H^{-\delta}···Y$, then X–H acts as the Lewis base and Y is the Lewis acid center. Alkorta and coworkers have pointed out that the DHB may be treated as hydride as well as HB. It is

possible since it possesses the characteristics of both these interactions, the proton donating bond and the proton acceptor (the negatively charged hydrogen atom acting as the Lewis base [45]).

It was found that the selected hydride bonds are characterized by relatively high values of the binding energies [44].[14] The Li^+···HBeH, Na^+···HBeH, and Mg^{2+}···HBeH complexes were analyzed. It was revealed that for the latter complex, the binding energy amounts to ~60 kcal/mol. One could expect covalent character for such type of interaction. The decomposition of the interaction energy shows that the delocalization is the most important attractive term. However, the QTAIM parameters do not indicate the negative Laplacian of the electron density values for the H···Y interactions (only for the complex with magnesium H_C is negative, but very close to zero). This shows very unique and different from the HB characteristics of the hydride bond interaction. Hydride bond, B–H···Na^+ interaction, was found by Cotton et al. in the crystal structure of diniobium tetragonal lantern compound [46] as the one that influences the arrangement of species in the crystal structure (Fig. 12.11).

Among other types of bonding one should refer to the agostic bond [47] analyzed in numerous crystal structures that seems to be a special type of the hydride bond [44]. The agostic bond represents weak interaction between C–H bond (or Si–H)

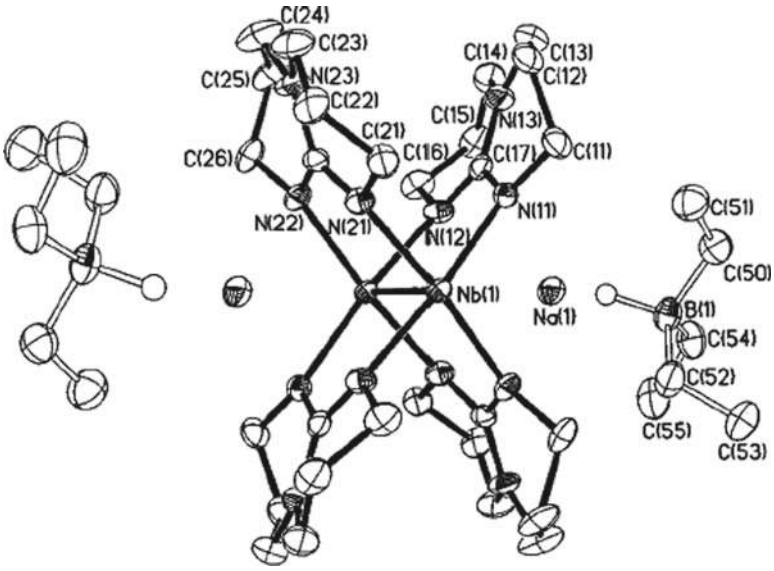

Fig. 12.11 Thermal ellipsoid plot of the crystal structure fragment containing B–H···Na^+ hydride bond (B(1)-H···Na(1) – *right side* of the picture), atoms are shown at the 50% probability level; except of H-atoms that are only designated by *small white circles*. Reprinted with permission from Cotton et al. [46], copyright 1998, American Chemical Society, Washington, DC

[14] The calculations were carried out up to MP2/aug-cc-pVQZ level of approximation.

and the transition metal or bond. However, sometimes the other, nontransition metals, are also mentioned as involved in such a type of interaction. It was indicated for few model agostic interactions that H-atom of C–H bond acts as the Lewis base since H-atom possess the negative charge. Additionally, the decomposition of the interaction energy has revealed that for the agostic bonds, similarly as for hydride bonds [44], delocalization outweighs the electrostatic interaction energy term.

Another not common, so-called halogen–hydride interaction exists that possesses the characteristics of both the halogen and hydride bonding [48]. It is designated as C–Hal$^{+\delta}\cdots{}^{-\delta}$H–Y where C–Hal acts as the Lewis acid (as for the halogen bonds), and H–Y acts as the Lewis base (as for the hydride bonds). Different model complexes were analyzed. For example, for the $F_3CCl\cdots HLi$ complex, the binding energy was found to be 3.54 kcal/mol[15] and for the other systems this value was even lower. The Cambridge Structural Database (CSD) [41] was searched for all the C–Cl$\cdots{}^{-\delta}$H–Me (Me = metal) interactions. Only four interactions were found with the Cl···H distances in the range of 2.7–3.0 Å, slightly less than the corresponding sum of the van der Waals radii. Since these results are based on the X-ray diffraction measurements, they do not represent a strong evidence for the existence of halogen–hydride interactions in the crystal structures. The reason is that the X-ray measurement is the diffraction of X-rays on electrons. Therefore, the results are the positions of maxima of electron densities attributed to the positions of atoms. The neutron diffraction results are appropriate to study the structures that contain the H-atoms since there is the diffraction of neutrons on nuclei. So one obtains directly their positions. In the X-ray measurements for heavy non-hydrogen atoms, the electron density maxima are practically at the same positions as the corresponding nuclei. However, for the hydrogen atom, the electron density maximum is significantly shifted, usually toward the heavy atom connected by a covalent or polar bond with hydrogen. Another limit of the X-ray measurement is that there is the lower accuracy of the determination of the positions of the electron density maxima for H-atoms in comparison with such positions for the non-hydrogen atoms. The differences between X-ray and neutron diffraction results are summarized by Jeffrey [36].

Figure 12.12 illustrates all types of interactions analyzed briefly in this section. For all considered cases, there is the electron charge transfer from the Lewis base to the Lewis acid. As it was explained in this review, the dihydrogen bonding is the special type of hydrogen bonding since it possesses the characteristics of the former interaction. Hydrogen bonding is the unique Lewis acid–Lewis base interaction, which may also be treated as the Brønsted acid–Brønsted base interaction [49]. DHB is positioned (Fig. 12.12) between the hydrogen and hydride bonding and links the features of both the interactions. Similarly, halogen–hydride bonding is placed between the hydride and halogen bonds.

There are three main nonbonding interactions presented within this classification (Fig. 12.12): hydrogen, hydride, and halogen bonds. DHB and halogen–hydride are

[15] The calculations were performed at MP2/aug-cc-pVTZ level of approximation.

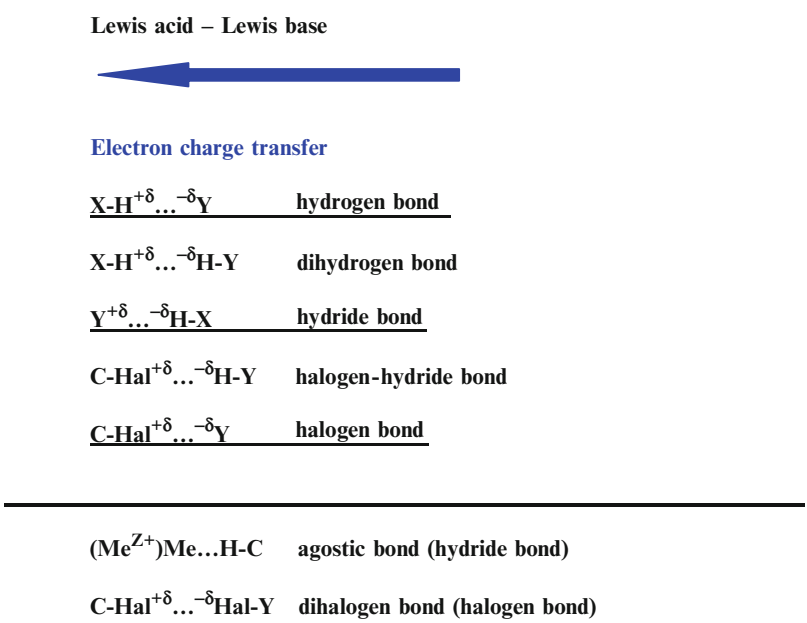

Fig. 12.12 Different types of nonbonding Lewis acid–Lewis base interactions

"mixed" ones. The agostic and dihalogen bonds are also included as a special case of the hydride and halogen bonds, respectively. The additional explanation is needed in the case of dihalogen bond. Figure 12.10 shows that halogen atom connected with carbon may act as the Lewis acid in line of the C–Hal bond and as the Lewis base in perpendicular direction to the C–Hal bond (for example, as the proton acceptor). Hence, the dihalogen bond is possible if the interacting species are properly oriented [50]. It is not so rare and it was found in numerous crystal structures as well as it has been analyzed theoretically [51]. There are the other unique nonbonding interactions, also existing in crystal structures, which may or may not be classified as one of the types presented in Fig. 12.12. However, only several examples are presented in this review to show how the DHB may be positioned among the other numerous and different in nature interactions.

12.5 Summary

DHB is a special type of the HB where the negatively charged hydrogen plays a role of the proton acceptor (Lewis base). Additionally, DHB may be treated as the class of hydride bond. In the other words, DHB possesses characteristics of both the hydrogen and hydride bonds.

It is possible to find numerous characteristics of DHB, and all of them are very similar to those for the HBs. They include decomposition of the interaction energy, the range of binding energies and H···H distances, and the QTAIM parameters. Numerous studies show that the DHB is, similarly as HB, "an interaction without borders" [31]. It means that there are very weak DHBs, close to van der Waals interactions, weak and medium in strength, strong, and very strong ones overlapping with covalent bonds.

Acknowledgments The authors thank for support from the NSF CREST Interdisciplinary Nanotoxicity Center (grant number HRD-0833178).

References

1. G.A. Jeffrey, W. Saenger, *Hydrogen Bonding in Biological Structures* (Springer, Berlin, 1991)
2. G.R. Desiraju, T. Steiner, *The Weak Hydrogen Bond in Structural Chemistry and Biology* (Oxford University Press, New York, 1999)
3. S.J. Grabowski (ed), *Hydrogen Bonding – New Insights*, Vol. 3 of the series: Challenges and Advances in Computational Chemistry and Physics, J. Leszczynski, editor of the series, (Springer, Dordrecht, 2006)
4. L. Pauling, *The Nature of the Chemical Bond*, 3rd edn. (Cornell University Press, Ithaca, 1960)
5. S.J. Grabowski, Theoretical studies of strong hydrogen bonds. Annu. Rep. Prog. Chem. Sec. C **102**, 131–165 (2006)
6. S. Scheiner, *Hydrogen Bonding: A Theoretical Perspective* (Oxford University Press, New York, 1997)
7. R. Taylor, O. Kennard, Crystallographic evidence for the existence of C–H···O, C–H···N, and C–H···Cl hydrogen bonds. J. Am. Chem. Soc **104**, 5063–5070 (1982)
8. F.A. Baiocchi et al., Molecular beam studies of hexafluorobenzene, trifluorobenzene, and benzene complexes of hydrogen fluoride. The rotational spectrum of benzene-hydrogen fluoride. J. Phys. Chem. **87**, 2079–2084 (1983)
9. H. Tachikawa, Ionization dynamics of the benzene-HF complex: A direct ab initio dynamics study. J. Phys. Chem. A **103**, 6873–6879 (1999)
10. P. Hobza, Z. Havlas, *Blue-shifting hydrogen bonds*. Chem. Rev. **100**, 4253–4264 (2000)
11. V.I. Bakhmutov, *Dihydrogen bonds, principles, experiments, and applications* (John Wiley & Sons, Hoboken, 2008)
12. J. Wessel et al., An unconventional intermolecular three-center N–H···H_2Re hydrogen bond in crystalline $[ReH_5(PPh_3)_3]$·indole·C_6H_6. Angew. Chem. Int. Ed. Engl. **34**, 2507–2509 (1995)
13. R.H. Crabtree et al., A new intermolecular interaction: Unconventional hydrogen bonds with element-hydride bonds as proton acceptor. Acc. Chem. Res. **29**, 348–354 (1996)
14. R. Custelcean, J.E. Jackson, Dihydrogen bonding: Structures, energetics, and dynamics. Chem. Rev. **101**, 1963–1980 (2001)
15. L.M. Epstein, E.S. Shubina, New types of hydrogen bonding in organometallic chemistry. Coord. Chem. Rev. **231**, 165–181 (2002)
16. W.T. Klooster et al., Study of the N–H···H–B dihydrogen bond including the crystal structure of BH_3NH_3 by neutron diffraction. J. Am. Chem. Soc **121**, 6337–6343 (1999)
17. S.F. Boys, F. Bernardi, The calculations of small molecular interaction by the difference of separate total energies. Some procedures with reduced errors. Mol. Phys. **19**, 553–566 (1970)

18. S.J. Grabowski, High-level ab initio calculations of dihydrogen-bonded complexes. J. Phys. Chem. A **104**, 5551–5557 (2000)
19. K. Kitaura, K.A. Morokuma, A new energy decomposition scheme for molecular interactions within the Hartree-Fock approximation. Int. J. Quantum Chem. **10**, 325–331 (1976)
20. K. Szalewicz, B. Jeziorski, Symmetry-adapted double-perturbation analysis of intramolecular correlation effects in weak intermolecular interactions. Mol. Phys. **38**, 191–208 (1979)
21. K. Szalewicz, B. Jeziorski, in *Molecular Interactions, from van der Waals to Strongly Bound Complexes*, ed. by S. Scheiner (Wiley, Chichester, 1997), p. 3
22. B. Jeziorski, K. Szalewicz, Intermolecular Interactions by Perturbation Theory, in *Encyclopedia of Computational Chemistry*, ed. by P. von Rague Schleyer, N.L. Allinger (Wiley, Chichester, 1998)
23. W.A. Sokalski et al., An efficient procedure for decomposition of the SCF interaction energy into components with reduced basis set dependence. Chem. Phys. Lett. **153**, 153–159 (1988)
24. H. Cybulski et al., Characterization of dihydrogen-bonded D-H···H-A complexes on the basis of infrared and magnetic resonance spectroscopic parameters. J. Chem. Phys. **119**, 5094–5104 (2003)
25. R.F.W. Bader, *Atoms in Molecules. A Quantum Theory* (Oxford University Press, New York, 1990)
26. C. Matta, R.J. Boyd (eds), *Quantum Theory of Atoms in Molecules: Recent Progress in Theory and Application* (Wiley, New York, 2007)
27. L.F. Pacios, Change with the intermolecular distance of electron properties of hydrogen bond dimers at equilibrium and non-equilibrium geometries. Struct. Chem. **16**, 223–241 (2005)
28. S.J. Grabowski, Hydrogen bonding strength – measures based on geometric and topological parameters. J. Phys. Org. Chem **17**, 18–31 (2004)
29. I. Rozas et al., Behavior of ylides containing N, O, and C atoms as hydrogen bond acceptors. J. Am. Chem. Soc. **122**, 11154–11161 (2000)
30. I. Alkorta et al., How to determine whether intramolecular H···H interactions can be classified as dihydrogen bonds. J. Phys. Chem. A **112**, 2721–2727 (2008)
31. G.R. Desiraju, Hydrogen bridges in crystal engineering: Interactions without borders. Acc. Chem. Res **35**, 565–573 (2002)
32. G. Gilli, P. Gilli, Towards an unified hydrogen-bond theory. J. Mol. Struct. **552**, 1–15 (2000)
33. S.J. Grabowski et al., Quantitative classification of covalent and noncovalent H-bonds. J. Phys. Chem. B **110**, 6444–6446 (2006)
34. K.N. Robertson et al., C–H···H–C interactions in organoammonium tetraphenylborates: another look at dihydrogen bonds. Can. J. Chem. **82**, 727–743 (2003)
35. S.J. Grabowski et al., How short can the H···H intermolecular contact be? New findings that reveal the covalent nature of extremely strong interactions. J. Phys. Chem. A **109**, 4331–4341 (2005)
36. G.A. Jeffrey, *An Introduction to Hydrogen Bonding* (Oxford University Press, New York, 1997)
37. S.J. Grabowski et al., Strong dihydrogen bonds – ab initio and "atoms in molecules" study. Chem. Phys. Lett. **386**, 44–48 (2004)
38. I. Alkorta et al., Ab initio study of the structural, energetic, bonding, and IR spectroscopic properties of complexes with dihydrogen bonds. J. Phys. Chem. A **106**, 9325–9330 (2002)
39. S.J. Grabowski et al., Wide spectrum of H···H interactions: van der Waals contacts, dihydrogen bonds and covalency. Chem. Phys. **337**, 68–76 (2007)
40. P. Metrangolo, G. Resnati, Halogen bonding: a paradigm in supramolecular chemistry. Chem. Eur. J. **7**, 2511–2519 (2001)
41. F.H. Allen, O. Kennard, 3D search and research using the Cambridge Structural Database. Chem. Des. Autom. News **8**, 31–37 (1993)
42. F. Zordan et al., Supramolecular chemistry of halogens: Complementary features of inorganic (M-X) and organic (C-X′) halogens applied to M-X···X′-C halogen bond formation. J. Am. Chem. Soc. **127**, 5979–5989 (2005)
43. I. Rozas et al., Inverse hydrogen-bonded complexes. J. Phys. Chem. A **101**, 4236–4244 (1997)

44. S.J. Grabowski et al., Hydride bonding – ab initio studies of BeH_2···Li+, BeH_2···Na+ and BeH_2···Mg^{2+} model systems. Chem. Phys. Lett. **422**, 334–339 (2006)
45. I. Alkorta et al., Non-conventional hydrogen bonds. Chem. Soc. Rev. **27**, 163–170 (1998)
46. F.A. Cotton et al., Triply bonded Nb_2^{4+} tetragonal lantern compounds: Some accompanied by novel B–H···Na^+ interactions. J. Am. Chem. Soc. **120**, 6047–6052 (1998)
47. W. Scherer, G.S. McGrady, Agostic interactions in d0 metal alkyl complexes. Angew. Chem. Int. Ed. **43**, 1782–1806 (2004)
48. P. Lipkowski et al., Properties of the halogen–hydride interaction: An ab initio and "atoms in molecules" analysis. J. Phys. Chem. A **110**, 10296–10302 (2006)
49. L. Sobczyk et al., Interrelation between H-Bond and Pi-electron delocalization. Chem. Rev. **105**, 3513–3560 (2005)
50. M. Formigué, P. Batail, Activation of hydrogen- and halogen-bonding interactions in tetrathiafulvalene-based crystalline molecular conductors. Chem. Rev. **104**, 5379–5418 (2004)
51. S.J. Grabowski et al., Attractive halogen–halogen interactions: CF_3Cl···FH and CF_3Cl···FCH_3 dimers. Chem. Phys. **327**, 151–158 (2006)

Chapter 13
Catalytic Decomposition of Organophosphorus Compounds

A. Michalkova and J. Leszczynski

Abstract Organophosphorus compounds have several applications (agricultural, industrial, and military). Nevertheless, assessments of the hazards from these applications quite often do not take into account chemical processes during their interactions with environment. The management of contaminants requires considerable knowledge and understanding of contaminant behavior. Unique properties of clay minerals and metal oxides, such as high adsorption and catalytic ability, have resulted in their applications as natural adsorbents and catalysts in the development of cleanup technologies. Knowledge of molecular structure, transformation mechanisms, and the spectrum of potential intermediates/products of the contaminant decomposition is helpful for developing remediation processes. An understanding of the physical characteristics of the adsorption sites of selected soil ingredients, the physical and chemical characteristics of the contaminant, details of sorption of contaminants on soil and in water solution, and also their distribution within the environment is of particular interest. Application of computational chemistry (CC) can provide deeper insight into the aforementioned characteristics of organophosphorus compounds.

This review summarizes experimental and theoretical studies which are used to develop theoretical models that explain and predict how clay minerals and metal oxides can affect the adsorption and decomposition of selected organophosphorus compounds. The results can contribute to a better knowledge of the impact of such processes on existing remedial technologies and in the development of new removal and decomposition techniques.

A. Michalkova and J. Leszczynski (✉)
NSF CREST Interdisciplinary Nanotoxicity Center, Department of Chemistry and Biochemistry, Jackson State University, Jackson MS, USA
e-mail: jerzy@icnanotox.org

J. Leszczynski and M.K. Shukla (eds.), *Practical Aspects of Computational Chemistry*, 277
DOI: 10.1007/978-90-481-2687-3_13,

13.1 Introduction

13.1.1 Organophosphorus Compounds, Clay Minerals, and Metal Oxides

13.1.1.1 Organophosphorus Compounds

There are almost 900 different bug killers (pesticides) that can be used in the United States. A small number (37) of these compounds belong to a class of insect killers (insecticides) known as organophosphates [1]. In health, agriculture, and government, the word "organophosphates" refers to a group of insecticides or nerve agents. Nerve agents are clear and colorless and may possess no odor or faint, sweetish smell. They are extremely dangerous and can enter the body through the air or on contact with the skin. They can be released using bombs, missiles, spray tanks, rockets, and land mines.

Dr. Gehard Schrader, a German pesticide specialist, created the first nerve agent called Tabun on 23 December 1936 [2]. American classification of Tabun is GA; all nerve agents of this origin are called the G-series nerve agents. Dr. Schrader also developed the second nerve agent in 1938 called Sarin [3, 4]. Both agents can be deadly if people are exposed to them. There is no known use of Sarin in wartime; it is speculated that Sarin was used by Iraqis in a town during the Iran-Iraqi war in the late 1980s. Terrorists did use Sarin for the first time on 20 March 1995. The terrorist group named Aum Shinrkyo released Sarin in an attack on a Tokyo subway, which resulted in the death of seven and injured 5,500 passengers. It is possible that many countries have access to these dangerous weapons, and future human exposure to nerve agents is possible [5, 6]. The American classification of Sarin, as the second G agent, is GB. The third nerve agent is Soman IV, the deadliest of them. Soman was created in 1944, toward the end of World War II. The discoverer of Soman IV was Richard Kuhn. The American classification of Soman IV is GD. A dosage of 350 mg of GD per seventy kilograms of tissue will kill a human in less than 15 mins. This occurs because of the blockage of an enzyme called acetylcolinesterase (AChE). If the body does not get AChE, the involuntary muscular movements stop, the heart stops, lungs stop passing oxygen to the blood, and one dies of suffocation. Acetylcholine is a common neurotransmitter found in the central and peripheral nervous system. In normal action, acetylcholine is released from an axon terminal; it moves across the synaptic cleft to bind to a receptor on the other side of the synapse (on the postsynaptic membrane) (Fig. 13.1). In the peripheral nervous system, acetylcholine is located at the "neuromuscular junction" where it acts to control muscular contraction. Acetylcholine is also used in the autonomic nervous system. The action of acetylcholine is terminated by an enzyme called AChE. When nerve agents are present, they bind to a fragment of the AChE molecule. This inactivates AChE and blocks its action, which prevents the breakdown of acetylcholine. Therefore, acetylcholine builds up, continues to work, and causes a "jam" in the nervous system.

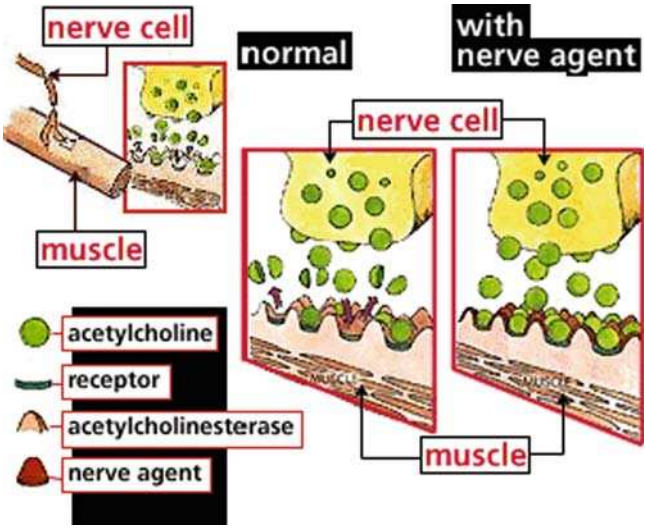

Fig. 13.1 Schema showing how the nerve agents work during blocking acethylcholinesterase

Table 13.1 Toxicity of selected nerve agents which have lethal effects on man

	LCt_{50} Inhalation (mg min/m^3)	LD_{50} Skin (mg/individual)
Tabun	200	4,000
Sarin	100	1,700
Soman	100	300
VX	50	10

By the mid-1950s, a group of more stable nerve agents had been developed, known as the V-agents in the American nomenclature [7]. They are approximately tenfold more poisonous than Sarin, and are thus among the most toxic substances ever synthesized. VX (O-ethyl-*S*-[2(diisopropylamino)ethyl] methylphosphonothiolate) is an extremely toxic substance whose sole application is as a nerve agent [8]. VX is currently considered to be the most toxic substance yet discovered. As a chemical weapon, it is classified as a weapon of mass destruction by the United Nations in UN Resolution 687. Production and stockpiling of VX was outlawed by the Chemical Weapons Convention of 1993.The VX nerve agent is the most well-known of the V-series of nerve agents, and is considered an area denial weapon due to its physical properties.

In Table 13.1, the estimated values of the doses, which have lethal effects on man, are presented. LD_{50} expresses the dose at which 50% of the exposed population will die as a result of their injuries. A different measure is used for inhalation, the product of the concentration (C) and the length of exposure (t). Again, L stands for lethal, and 50 for 50% effect. The toxicity sequence is the same for the two

routes of exposure, but the differences are much greater in skin exposure. This is mainly caused by the more volatile nerve agents evaporating from naked skin. If the evaporation is prevented, e.g., by tightly fitting clothing, the difference will be smaller [9].

13.1.1.2 Clay Minerals and Metal Oxides

Clays belong to the phyllosilicates group composed of two-dimensional structures. Phyllosilicates are aluminum silicates that form tetrahedral (fourfold coordination) and octahedral (sixfold coordination) sheets according to a cation and anion ratio [10, 11]. The cations in tetrahedral coordination include mostly Si^{4+}. Substitution of Si^{4+} by Al^{3+} often occurs in the tetrahedral sheets, and substitution of Al^{3+} by Mg^{2+} can occur in the octahedral sheets. Clays primarily exist as very small particles (~2 μm in diameter) with a high specific surface area and a high chemical surface activity [12]. They are found in soil, lending to their importance in agriculture and the environment. Their structural diversities provide the functionality that is expected to give rise to important properties such as adsorption of ions and molecules. Minerals of the kaolinite group have 1:1 dioctahedral structure with a $Al_2Si_2O_5(OH)_4$ common chemical formula [13]. Dickite (a member of this group) differs from kaolinite in the layer stacking. The unit cell of dickite consists of two kaolinite layers, and is twice as large as the unit cell of kaolinite. The layers are kept together by hydrogen bridges between surface hydroxyl groups of the octahedral side and the basal oxygen atoms of the tetrahedral side [14] (Figs. 13.2 and 13.3).

Metal oxides are widely used reagents which can be applied for many industrial needs, such as air pollution monitoring systems, food industry, medical diagnosis equipment, etc. [15].

Metal oxide nanoparticles have been considered as solid reagents that adsorb and simultaneously destroy toxic substances. Due to their high surface area, metal oxide nanoparticles are very good as adsorbents, catalyst and catalyst support [16] (Fig. 13.4). An efficient application of metal oxides for nerve agent detection has been demonstrated (see for example references 15, 17–20). Metal oxide sensors are commonly used to monitor a variety of toxic and inflammable gases. The sensing mechanism is based on electrical conductance change upon surface reduction–oxidation (redox) reactions with gas species. In recent years, several metal oxides, for example, magnesium oxide (MgO) and calcium oxide (CaO), have received increased attention as potential adsorbents for the decomposition of chemical warfare agents. It was found that nanocrystalline MgO can destroy organophosphorus compounds. MgO, in a nanoparticle form, has been successfully used as a destructive adsorbent for nerve agents [21]. The term “destructive adsorbent” is intended to describe its ability to efficiently adsorb and at the same time to chemically decompose incoming adsorbate. Calcium oxide also possesses unique nanoparticle surface properties. CaO is highly ionic with a high melting point and large surface area and high surface reactivity. Calcium oxide has some advantages.

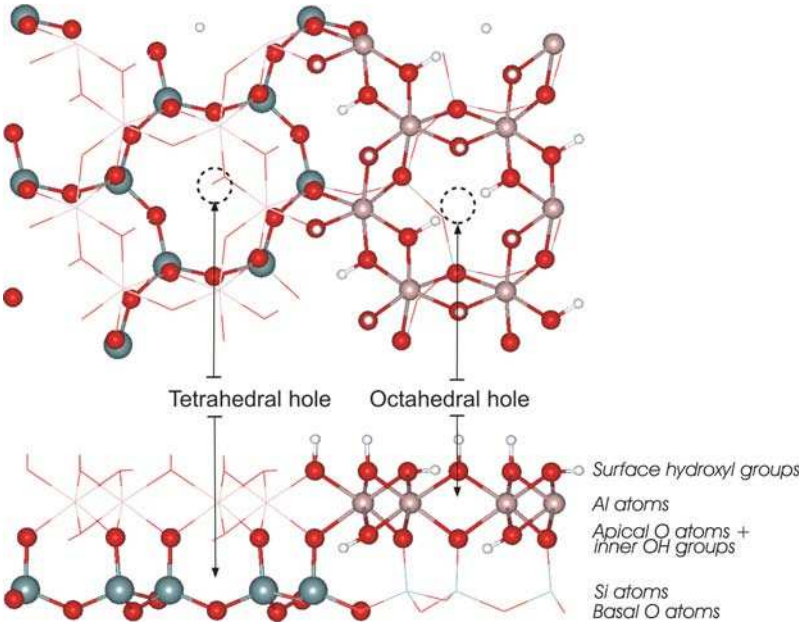

Fig. 13.2 Structure of clay mineral dickite

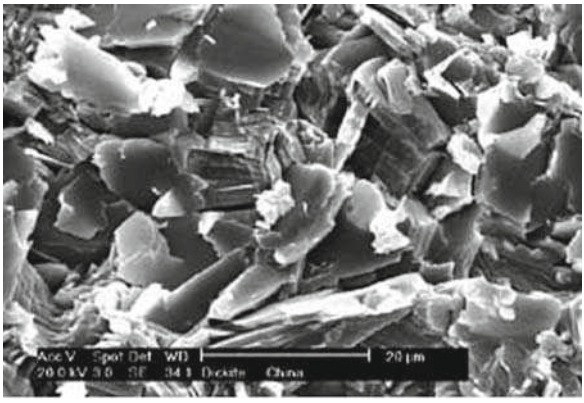

Fig. 13.3 Dickite rock, Songyang County, China Field of view approximately 70 µm wide

It is a nontoxic compound, is easy to handle and store, stable, cheap, and exhibits very high capacities for adsorption [16].

The search for a noncorrosive decontamination of sensitive material and skin after exposure by toxic chemicals like pesticides and nerve agents, is an important but challenging task. Therefore, the development of cost-effective cleanup

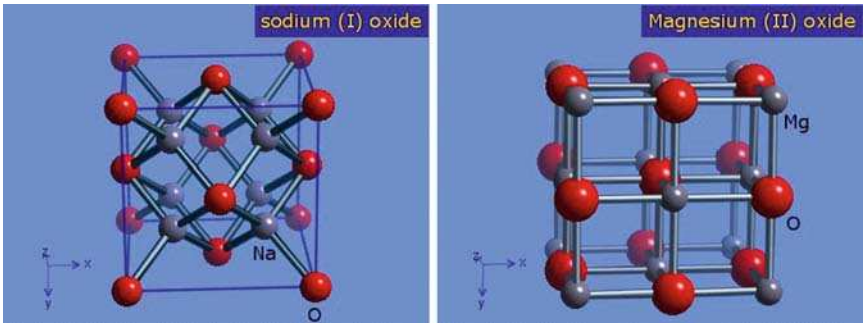

Fig. 13.4 Crystal structure of sodium and magnesium oxide

technologies for organophosphorus compounds is a high priority for environmental restoration research. Understanding the catalytic decomposition of organophosphorus compounds represents a crucial step for devising new methods for the protection of personnel exposed to chemical warfare agents and other chemically similar industrial compounds [1]. It is vital to have a fundamental knowledge of the chemical–physical behaviors of these organic molecules in soil, groundwater and industrially important materials. One potentially valuable aspect of understanding this fundamental behavior and we believe, a valuable contribution into characterizing the fate of organophosphorus compounds is a detail study of their interactions with specific surfaces. Therefore, the fundamental chemistry controlling these interactions should be understood in order to develop the best strategy in the management of contaminated soils. Also, in the case of title compound, it can lead to better technologies for their catalytic decomposition since the degradation of organophosphorus compounds is of great importance for health and environmental safety [1].

This review provides information related to the methods which are currently most suitable for the remediation of contaminated soils and water. The development of a deeper understanding of the physical and chemical processes involved in the degradation of contaminants will facilitate the establishment of more cost-effective and efficient remedial action plans that are protective of human health and the environment.

13.2 Computational Methods and Models

Understanding and comparing degradation pathways of nerve agents on catalyst (clays and metal oxides) enable theoretical predictions as to the most likely intermediate and final products, thereby shortening the period of expense and experimentation. This review is devoted to explore fundamental capabilities of CC techniques including the ab initio methods as tools to characterize properties of

nerve agents interacting with such species. Moreover, the nature of the interactions between an adsorbate and adsorbent can be well described by means of quantum-chemical calculations [22].

13.2.1 Quantum-Chemical Approximations for the Modeling of Surface Reactivity

Quantum-chemical analysis provides a wide array of powerful tools that have been underutilized in deciphering the complex reactions affecting organophosphorus compounds. Molecular modeling has become an inseparable part of research activities devoted to gaining an understanding of the molecular basis of chemical processes. Cluster approximation has been widely used for studying interactions of molecules with all types of solids and their surfaces [23]. This approach is powerful in calculating the systems with deviations from the ideal periodic structure like doping and defects.

A physical approach to the electronic structure problems of solids contrasts sharply with the notion that local interactions dominate the structure and properties of molecular systems. Hence, it is very appealing to replace the infinite solid, which is difficult to treat quantum-chemically, by finite sites that can model considered species. Intuitively, cutouts from the bulk or the surface are made and treated like molecules. This type of method is called the cluster approach, and the models made as cutouts of the periodic structure are called cluster models [22].

According to the cluster approach, one can consider a limited number of atoms around the active sites and then apply the quantum-chemical description to a fragment of the solid, referred to as a cluster. This is the easiest and chemically the best procedure when a local description of the adsorption or catalytic site governs the considered process. To make the cluster neutral, the broken bonds, resulting from a homolitic cut off of the chemical bonds in the crystal, are electrically balanced by monovalent atoms. In the framework of the cluster approach, an enormous number of investigations have been published, which include the description of the different properties of the oxide surfaces. The utility of the cluster approach in describing zeolites [23], an extremely functional class of aluminosilicate minerals exploited for their high capacity for cation exchange, has also been demonstrated.

The most important disadvantage of the cluster model is the relatively small size of the considered system. Embedded and dipped cluster models are usually used to overcome this problem. They are considered not only because the cluster models need corrections for neglected interactions with their surrounding, but also because they are a promising alternative to the calculation of large cells (“supercells”) [23]. The extension of the model and the inclusion of the interaction of the cluster with the surroundings into the calculation are implemented in different ways, depending on the type of the investigated phase (ionic, covalent solids, or metals) [22].

13.3 Adsorption and Decomposition of Organophosphorus Compounds on Clay Minerals and Metal Oxides

Quantum-chemical analysis provides a wide array of powerful tools that have been underutilized in deciphering the complex reactions affecting warfare agents. The computational approach secures development of extensive knowledge of such processes without exposing researchers to their deadly outcome. Therefore, this review is mainly devoted to summarize the results of the theoretical studies of organophosphates interacting with catalytic surfaces (clay minerals and metal oxides).

13.3.1 Interactions of Nerve Agents with Clay Minerals

To the best of our knowledge, there are no experimental investigations of the interaction of nerve agents with clay minerals. However, several experimental studies of adsorption of phosphate molecules on the surface of clay minerals were published [24–33]. We only review some of these studies since their subject does not directly concern the goal of this review. The adsorption of tricresyl phosphate isomers on kaolin, alumina, and montmorillonite was studied [24]. The amount of TCP isomers adsorbed on different minerals follows the given order: alumina<kaolin<montmorillonite. DMMP interacts with the interlamellar exchangeable cation in montmorillonite, and displaces water from the interlamellar space [25]. Sample preparation methods for FTIR analysis of dimethyl-methylphosphonate – montmorillonite sorption mechanism was also studied [26]. Adsorption decreases with the presence of Cu and in solution. The interactions of GPS adsorbed on montmorillonite were found to differ in many cases from interactions of glycine with montmorillonite [29]. The authors concluded that none of the methods affects the interpretation of the sorption mechanism. Adsorption–desorption of glyphosate (GPS) on montmorillonite in the presence of cupper was investigated [31]. Several experimental works were devoted to the study of interactions of Sarin and Soman with aqueous soils [34–37].

Theoretical studies provide an alternative way of study processes involving nerve agents. An ONIOM study of the adsorption of Sarin on dickite (a 1:1 dioctahedral clay mineral of the kaolinite group) [38] was performed. The two layer ONIOM method using combinations of quantum-mechanical methods was applied for the studied species [39]. The investigated systems of organophosphate with catalytic fragments were divided into two layers which were treated with different computational methods (the B3LYP/6-31G(d) level of theory for the High layer). The layers are conventionally known as the Low (lower layer the mineral fragment) and the High layers (the target molecule with the upper layer of the mineral fragment). The ONIOM energy of the system is then obtained from three independent calculations.

$$E(\text{ONIOM2}) = E_{\text{model high}} - E_{\text{model low}} + E_{\text{real low}}. \tag{13.1}$$

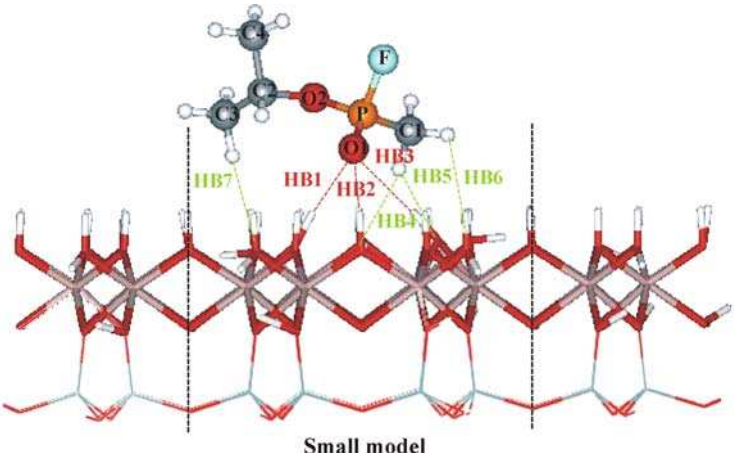

Fig. 13.5 The optimized structure of Sarin adsorbed on the octahedral surface of dickite obtained using the ONIOM(B3LYP/6-31G(d,p):PM3) method

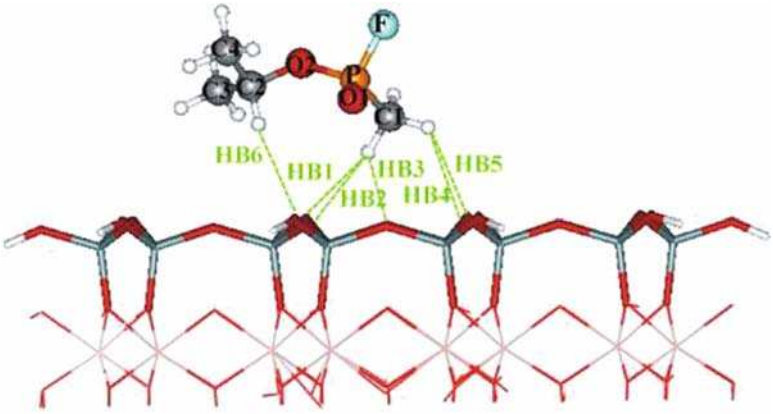

Fig. 13.6 The optimized structure of Sarin adsorbed on the tetrahedral surface of dickite obtained using the ONIOM(B3LYP/6-31G(d,p):PM3) method

Real denotes the full system, which only needs to be calculated at the lowest computational level. The additional system is defined as the *model* system. This type of adsorption results in the polarization and the electron density redistribution of GB and GD on the surface of the mineral. This corresponds to the formation of attractive contacts between GB and GD agents and the surface of dickite.

The polarization of the organic molecule is more significant in the case of adsorption on the octahedral side (see Figs. 13.5 and 13.6). The adsorption energies obtained at the ONIOM(B3LYP/6-31G(d,p):PM3) level of theory and using large models of the mineral for the adsorption systems of GB and GD on the octahedral surface of dickite, are about −16 and −15 kcal/mol, respectively. In the case of

adsorption on the tetrahedral surface, the interaction energies of the adsorption systems with GB and GD are approximately −7.0 and −9.0 kcal/mol, respectively. GB is adsorbed more preferably on the octahedral aluminum-hydroxide surface than on the tetrahedral silica surface [38]. In the case of adsorption on the octahedral surface, an analysis of the interaction energy components indicates the importance of electrostatic and delocalization binding contributions. The additional local minima of adsorbed Sarin on the tetrahedral and octahedral surfaces of dickite were found. They are characterized by different involvement of the fluorine atom in intermolecular interactions. H-bonds are weaker in comparison with H-bonds in which the P=O oxygen atom participates.

The structures and interactions of Sarin and Soman with edge tetrahedral fragments of clay minerals have been studied [40]. In addition, the adsorption mechanism of Sarin and Soman on these mineral fragments containing the Si^{4+} and Al^{3+} central cations was investigated. The calculations were performed using the B3LYP and MP2 levels of theory in conjunction with the 6-31G(d) basis set. The charge of the systems and the termination of the mineral fragment are the main contributing factors to the formation of intermolecular interactions in the studied species. In neutral complexes, Sarin and Soman are physisorbed on these mineral fragments due to the formation of C–H. . .O and O–H. . .O hydrogen bonds. The chemical bond is formed between a phosphorus atom of Sarin and Soman and an oxygen atom of the −2 charged clusters containing an Al^{3+} central cation (Fig. 13.7) and −1 charged complexes containing a Si^{4+} central cation (chemisorption). Sarin and Soman interact mostly in the similar way with the same terminated edge mineral fragments containing different central cations. Interestingly, the interaction energies of the complexes with an Al^{3+} central cation are larger than corresponding values for the Si^{4+} complexes. The interaction enthalpies of all studied systems corrected for the basis set superposition error were found to be negative. However, based on the Gibbs free energy values, only strongly interacting complexes containing a charged edge mineral fragment with an Al^{3+} central cation are stable at room temperature. It was concluded that Sarin and Soman will be adsorbed

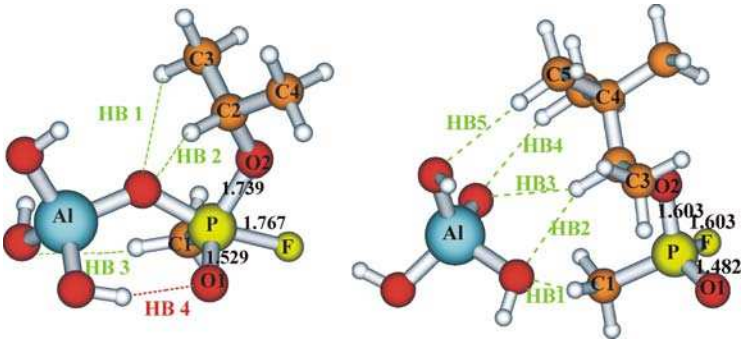

Fig. 13.7 The optimized structure of Sarin- and Soman-$[AlO(OH)_3]^{2-}$ systems obtained at the B3LYP/6-31G(d) level of theory

preferably on this type of edge mineral surfaces. Moreover, based on the character of these edge surfaces, the tetrahedral edge mineral fragment can provide effective centers for dissociation.

Theoretical studies of the interactions of phosphate with silica and hectorite were published by Murashov and Leszczynski [41], and by Hartzell et al. [42]. The ab initio calculations of hydrogen-bonded complexes of dihydrogen and dimethylphosphate anions with ortosilicic acid have shown that the phosphate groups can form strong hydrogen-bonded complexes with the silanols of the silica surface with stabilization energies of ca. −14 kcal/mol per hydrogen bond [41]. A molecular dynamics study of the large tributylphosphate complex of europium provides a test of the sensitivity of force field calculations to predict the behavior of molecules within the interlayer of a trioctahedral smectite clay, hectorite [42]. A cluster quantum-chemical study [43] of DMMP adsorption on magnesium oxide nanoparticles has also been published. On the basis of the calculation results, the possible mechanism of destructive adsorption of DMMP on MgO is discussed. Moreover, theoretical studies of the structures and properties of Sarin and Soman [44] and different conformers of Tabun [45] were also published. The most stable conformers of Sarin and Soman were determined in high-level-correlated calculations [44]. Both molecules are found to have three low-energy conformers each. For both Sarin and Soman, two of the lowest energy conformers have almost the same energies with a very small barrier separating the corresponding minima. The third conformer of Sarin is found to lie about 1 kcal/mol above the lowest energy form. For Soman, the corresponding value is equal to about 4 kcal/mol. Conformational studies have been carried out on two different enantiomers of Tabun at the DFT and MP2 levels of theory to generate potential low energy surfaces in the gas phase as well as in an aqueous environment [45]. The structures of the low energy conformers, together with their molecular electrostatical potential surfaces, have been compared with those of the nonaged acetylcholinesterase-tabun complex in order to locate the active conformer of the molecule.

13.3.2 Interactions of Nerve Agents and Their Simulants with Metal Oxides

The basic experimental studies of the interactions between organophosphorus compounds and metal oxide surfaces have been carried out intensively during the last several years. Metal oxides, such as MgO, Al_2O_3, FeO, CaO, TiO_2 α-Fe_2O_3, ZnO, and WO_3, are currently under consideration as destructive adsorbents for the decontamination of chemical warfare agents [46, 47]. For example, several studies have addressed adsorption of dimethyl methylphosphonate (DMMP) (a widely used model compound for the simulation of interactions of phosphate esters with a surface) on the surface of these metal oxides [48–60]. In most of these works, the authors have observed that, at first, DMMP is adsorbed molecularly via hydrogen

bonding of the phosphoryl oxygen to a surface at an acid site, followed by stepwise elimination of the methoxy groups which combine with surface hydrogen atoms to yield methanol that evolves from the surface. The final product recorded for the reactions with these oxides is a surface-bound methylphosphonate, with the P–CH_3 bond intact. On the basis of observations, it was concluded that not only surface defect sites are responsible for the decomposition of DMMP, but that Mg^{2+} and O^{2-} ions in the regular oxide surface also take part in the process. For organophosphorus compounds, the heats of adsorption were found high and have shown an insignificant dependence on the substituent effects [52]. Study of Kanan and Trip [59] has shown that the adsorption of DMMP on SiO_2 is remarkably different from the adsorption of DMMP on WO_3, TiO_2, and Al_2O_3 (DMMP adsorbs through formation of two H-bonds with the methoxy groups). The decomposition of DMMP occurs with the loss of methoxy groups on WO_3, TiO_2, and Al_2O_3, whereas molecular desorption occurs on the high surface area SiO_2 powders. In previous works [61–63], the authors, using solid-state MAS NMR technique, found that Sarin (GB, isopropyl methylphosphonofluoridate ($C_4H_{10}FO_2P$)), Soman (GD – 3, 3-dimethyl-2-butyl methylphosphonoflouridate ($C_7H_{16}FO_2P$)), VX and mustard (HD – bis(2-chloroethyl)sulfide) hydrolyze on the surface of the very reactive MgO, CaO and Al_2O_3 nanoparticles. GD forms both GD-acid and methylphosphonic acid (MPA). VX and GD hydrolyze to yield surface-bound complexes of nontoxic ethyl methylphosphonate and pinacolyl methylphosphonate, respectively. Sarin undergoes initial molecular adsorption on aluminum oxide at unsaturated Al sites, followed by slow hydrolysis at room temperature [64].

Theoretical works that address the interactions of organophosphate compounds with silica and aluminum oxide were also published [65, 66]. It was found that energetics and geometry of adsorption for DMMP and Sarin on *a*-SiO_2 depend on the local Si–OH environment [65]. The most stable adsorption geometry of DMMP on silica involves hydrogen bonding between two Si–OH groups and the O atom of the P=O group. H-bonding to more than one functional group is seen in this work for adsorption of DMMP in a metastable configuration with one H-bond to the O atom of a CH_3–O–P group and a second to the P=O. It is also seen for Sarin adsorption (again in a metastable configuration) *via* the O atom of the *iPr*–O–P group, where a second H-bond to the F atom also forms.

The characteristics of DMMP and Sarin, with respect to adsorption on the *a*-SiO_2 surface, are very much similar. In the case of the DMMP adsorption on alumina, the energetically favorable mode of adsorption was found to be the Al···O=P dative-bond formation [66]. "Side-by-side" comparison of the *ab initio* results for DMMP and Sarin indicates that DMMP is a reasonably good simulant. In both considered cases, the energetically favorable geometry for adsorption on γ-Al_2O_3 is the same. The adsorption energies are comparable ($\Delta E_{ads} = -57.5$ Kcal/mol for DMMP and −49.2 Kcal/mol for Sarin, both for $Al_{20}O_{30}$ at the B3LYP/6-311G(df) level) after BSSE correction. However, for reasons which are unclear at present, ΔE_{ads} is about 8.3 kcal/mol greater for DMMP than for Sarin.

The adsorption and decomposition of Sarin on the magnesium oxide surface were studied at the B3LYP/6-31G(d) and MP2/6-31G(d) levels of theory [38].

Sarin was found to be physisorbed (the nanosurface and hydroxylated small fragment; this is undestructive adsorption) or chemisorbed (destructive adsorption) on MgO. The physisorption of GB on the surface of MgO occurs due to the formation of hydrogen bonds and ion–dipole and dipole–dipole interactions between adsorbed GB and the surface. The chemisorption occurs due to the formation of covalent bonds between the target molecule and the surface (Fig. 13.8). The adsorption results in the polarization and the electron density redistribution of GB. The adsorption energy obtained at the MP2/6-31G(d) level of theory for the most stable chemisorbed system is about −50 kcal/mol. Sarin adsorbed on the nanosurface of hydroxylated small fragment of MgO is much less stable than Sarin adsorbed on the nonhydroxylated small fragment of MgO. The adsorption energy of Sarin adsorption systems on MgO is proportional to the number and strength of formed covalent bonds between Sarin and the surface.

Also the reaction pathways of Sarin decomposition catalyzed by selected forms of MgO were investigated [38]. In the case of the decomposition on the nonhydroxylated MgO surface, the removal of fluorine from Sarin was modeled. Fluorine was transferred from Sarin into binding distance with the Mg atom of the MgO surface (Fig. 13.9). It was revealed that such a structure provides a reliable model for the reaction mechanism. A two-step reaction mechanism was assumed. In the first step, Sarin creates a stable adsorbed complex with MgO through three chemical bonds with the MgO surface (the A1-GB model). It is expected that the transfer of the fluorine atom to the surface of MgO is accompanied by a change in the conformation of Sarin. In the second step, the bond between P and F is broken (the A1(t)-GB model); the fluorine atom is transferred to the Mg atom of the surface; and the remaining part of Sarin adopts the most energetically favorable conformation (the A1(f)-GB model).

The interactions of diisopropylfluorophosphate (DFP) with model MgO and CaO surfaces have been investigated using density functional (DFT) and Møller–Plesset second order perturbation techniques [67]. Geometries of considered complexes were fully optimized at the DFT level. The calculated interaction energies and the corresponding thermodynamic properties show that DFP is physisorbed on these two model oxide surfaces and the adsorption on the MgO surface is stronger.

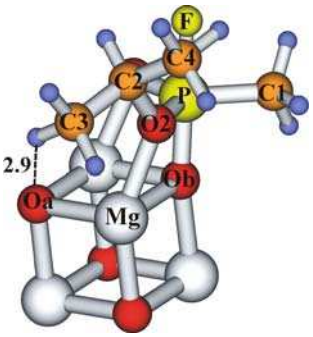

Fig. 13.8 The optimized structure of Sarin (GB) adsorbed on the nonhydroxylated Mg_4O_4 fragment obtained at the B3LYP/6-31G(d) level of theory (the A1-GB model)

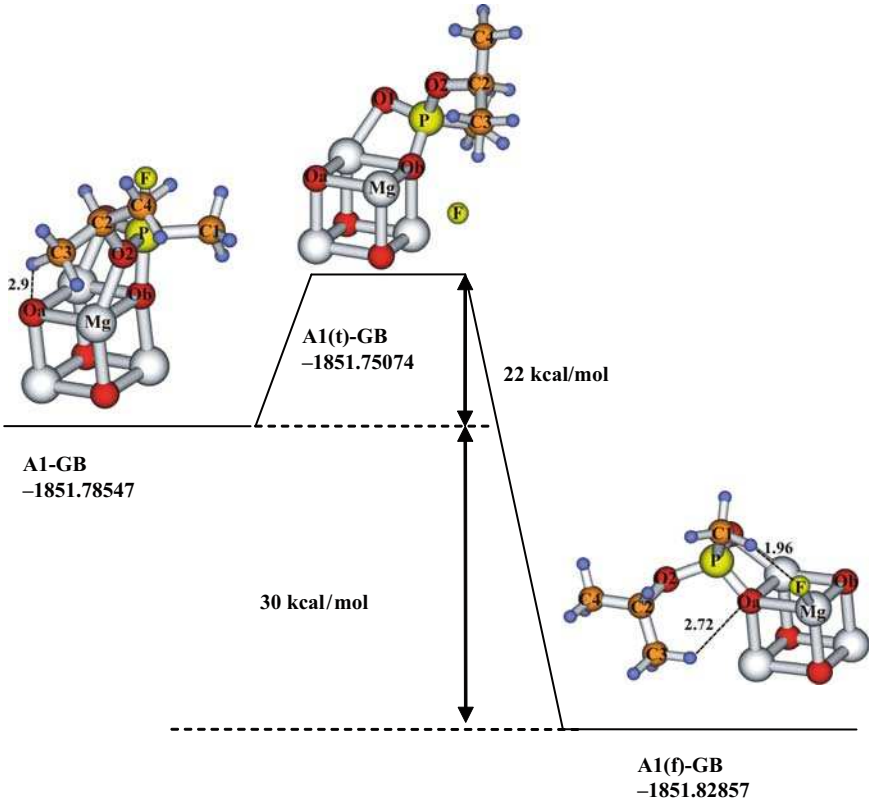

Fig. 13.9 The reaction pathway of the decomposition of Sarin (GB) on nonhydroxylated MgO surface from the reactant (the A1-GB model) through transition state (the A1(t)-GB model) to the product (A1(f)-GB model) obtained at the B3LYP/6-31G(d) level of theory

Analyzes of the calculated IR and Raman spectra point out to the enhancement of the P=O stretching mode with respect to the isolated DFP, and this property could be used to detect nerve-agents using surface-enhanced Raman spectroscopy.

The DFT/B3LYP and MP2 calculations of the adsorption of Tabun (GA) on the model nonhydroxylated and hydroxylated CaO indicate that GA is strongly bonded (chemisorbed) to the nonhydroxylated CaO (A1-GA) through the P=O bond [68]. Although the interactions in the second model of this complex (A2-GA) are competitive with A1-GA, the second model is not energetically feasible from the energy difference of these two complexes. In the hydroxylated complexes (B-GA and C-GA), the interactions are competitive and weak in nature (physisorption). The AIM studies and MEP surface analyzes of these complexes also support this fact (Fig. 13.10). The strong interaction of the P=O bond with the surface indicates that the A1-GA type of complex could be useful for GA detection (surface-enhanced Raman spectroscopy), while our previous investigation of the

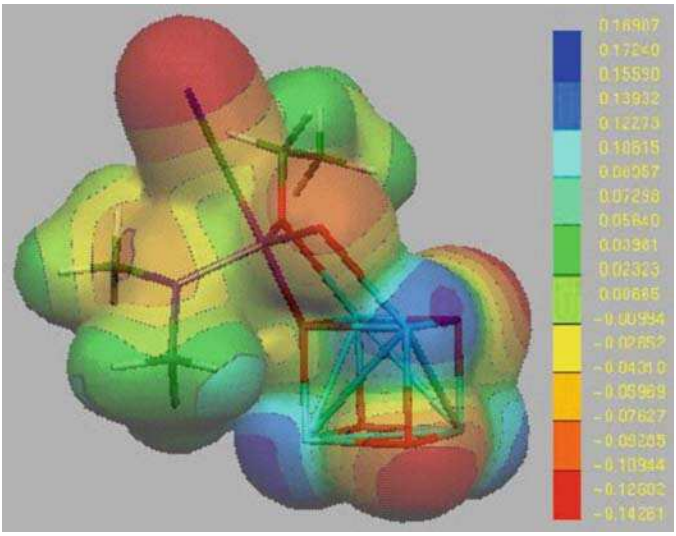

Fig. 13.10 MEP on the isodensity surfaces of the A1-GA complex (DFT/B3LYP level)

sarin. . .MgO systems [38] indicates that weakly bound B-GA and C-GA are useful for the hydrolysis of GA

Ab initio study of the adsorption of dimethyl methylphosphonate (DMMP) and trimethyl phosphate (TMP) on three types of models simulating the calcium oxide surface (nonhydroxylated Ca_4O_4, completely hydroxylated $Ca_4O_4(OH)_2H_2$ and partially hydroxylated $Ca_4O_4(OH)H$) was performed [69]. The target molecule and the surface hydroxyl groups were optimized, while the CaO fragment was kept frozen. The intermolecular interactions were investigated applying the Bader's Atoms in Molecules theory. The maps of electrostatic potential of the studied adsorption systems were also produced. The interaction energies of studied adsorption systems corrected by the basis set superposition error were obtained. The most energetically favorable adsorption of DMMP and TMP was found at the configuration where the oxygen atoms of the P=O and methoxy groups point toward the Ca cation of the surface (Fig. 13.11). The P atom points toward the O atom of the surface, and forms a P–O chemical bond. This configuration was revealed for the nonhydroxylated and partially hydroxylated CaO-DMMP and CaO-TMP systems. The presence and number of surface hydroxyl groups on the CaO models play a key role in the adsorption of studied compounds. DMMP and TMP were found to be much less stable on the completely hydroxylated CaO surface where they are adsorbed only via weak electrostatic interactions and H-bonding to the surface oxygen atoms and hydroxyl groups. TMP was found to be slightly more stable on this type of surface than DMMP. The difference in stability is even larger if one compares this TMP system with the complex of Tabun adsorbed on completely hydroxylated CaO surface model [68].

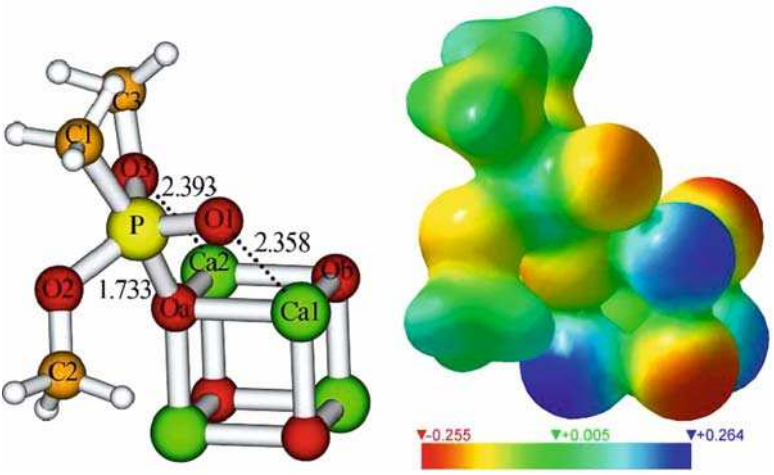

Fig. 13.11 The optimized geometry of DMMP adsorbed on the nonhydroxylated CaO surface A1-DMMP obtained at the B3LYP/6-31G(d) level of theory

13.4 Summary

The development of cost-effective, cleanup technologies for organophosphorus contaminants continues to be a high priority for environmental restoration research. Such development involves the coordination of experimental and theoretical investigations to integrate both technological and fundamental aspects of key processes. Although the major processes affecting the natural and engineered treatment of organophosphates have been appreciated qualitatively, many questions remain regarding reaction mechanisms. Computational simulation methods allow successful investigation of the properties of large molecular complexes in order to answer remaining questions that are essential for the development of cleanup technologies for contaminants of soils and ground water. Novel information can be provided about possible path of degradation of nerve agents to be used for design efficient adsorbents and catalysts for their degradation.

The interactions of organophosphates nerve agents and their simulants with clay minerals [39, 41–43] and metal oxides [38, 65–69] have been studied in several theoretical works. In the case of adsorption, the initial step involves the binding of the phosphoryl oxygen to an acidic site of metal oxide. A number of studies revealed that the initial chemisorption leads to the decomposition of the target molecule where different products are formed, depending on the type of organophosphorus compound and metal oxide. For example, decomposition of DMMP on MgO proceeds via a simple path [56] where, in the second step, the loss of two methoxy groups is observed with the presumed evolution of methanol from the surface. Theoretical works of adsorption and decomposition of selected organophosphates were devoted to the study of the dependence of these reactions on several

factors and the influence of the nature of the metal oxide and the clay surface. Several different initial positions and orientations of organophosphate molecules on models of metal oxides and clays were found.

The main conclusion of this review is about the factors that significantly influence the surface reactivity of clays and metal oxides as catalysts. Among such factors are the type of the acidic site, the adsorption site, the central cation, the size of the fragment and the presence of water. The organophosphorus compounds can be chemisorbed (though the formation of chemical bonds) [38, 41, 66] or physisorbed (due to the formation of mainly hydrogen bonds) [38, 39, 41, 65, 67] on selected types of catalytic surfaces. In the case of Sarin, it was found that chemisorption on the MgO surface can lead to its decomposition. An energetic diagram that predicts possible intermediates and final products of Sarin decomposition by different adsorption sites of magnesium oxide fragments was theoretically predicted [38]. Comparison of the adsorption of nerve agent and their simulants reveals that the most known simulant DMMP is less stable on metal oxide surface than real nerve agent Tabun [69]. Moreover, it was concluded that such studies could be used to guide detection of nerve-agents using surface-enhanced Raman spectroscopy [67].

Acknowledgments This work was facilitated by the support of the Chemical Materials Computational Modeling (CMCM) funded by the Department of Defense through the U. S. Army Engineer Research and Development Center (Vicksburg, MS) grant no. W912HZ-04-2-0002, the Army High Performance Computing Research Center and the Army Research Laboratory (ARL) grant no. DAAD19-01-02-0014, the Office of Naval Research grant no. N00034-03-1-0116. We would like to thank the Mississippi Center for Supercomputing Research for a generous allotment of computer time.

References

1. J.G. Ekerdt et al., Surface chemistry of organophosphorus compounds. J. Phys. Chem. **92**, 6182–6188 (1988)
2. http://en.wikipedia.org/wiki/Tabun_%28nerve_gas%29
3. B. Simpson, Sarin nerve gas – or how i learned to stop worrying and love pon-1. Biotech. J. **2**, 100–105 (2004)
4. http://www.dupont.com/safety/en/downloads/NerveAgentChemicalDataSheets.PDF
5. K.J. Ewing, B. Lerner, Infrared detection of the nerve agent sarin (isopropyl methylphosphonofluoridate) in water using magnesium oxide for preconcentration. Appl. Spectrosc. **55**, 407–411 (2001)
6. V. Haensel, R. Burwell, Catalysis. Sci. Am. **225**, 46–58 (1971)
7. Y-Ch Yang et al., Autocatalytic hydrolysis of v-type nerve agents. J. Org. Chem. **61**, 8407–8413 (1996)
8. http://www.dsf.health.state.pa.us/health/cwp/view.asp?a=171&q=233733
9. FOA. *A FOA Briefing Book on Chemical Weapons* (FOA, Stockholm, Sweden, 1992)
10. R.L. Bates, *Stone, Clay, Glasses: How Building Materials Are Found and Used* (Erslow, New York, 1987)

11. S.W. Baile, Structures of Layered Silicates, in *Crystal Structures of Clay Minerals and Their X-ray Identification*, ed. by G.W. Brindley, G. Brown (Mineralogical Society, London, 1980), pp. 6–28
12. A. Chagas, J. Simoni, *Encyclopedia of Surface and Colloid Science: Thermodynamics of Clay Surfaces* (Taylor and Francis, New York, 2002), pp. 5355–5364
13. A.C.D. Newman (ed), *The Chemistry of Clays and Clay Minerals (Mineralogical Society Monograph No. 6)* (Longman Scientific and Technical, London, 1987)
14. E. Nemecz, *Clay Minerals* (Akademiai Kiado, Budapest, Hungary, 1981)
15. Q. Yu et al., Integration of metal oxide nanobelts with microsystems for nerve agent detection. Appl. Phys. Lett. **86**, 063101–063103 (2005)
16. G.M. Medine et al., Synthesis and adsorption properties of intimately intermingled mixed metal oxide nanoparticles. J. Mater. Chem. **14**, 757–763 (2004)
17. A. Khaleel et al., Nanocrystalline metal oxides as new adsorbents for air purification. Nanostruct. Mater. **11**, 459–468 (1999)
18. J. Ahdjoudj et al., Hartree–Fock periodic study of the chemisorption of small molecules on TiO_2 and MgO surfaces. Catal. Today **50**, 541–551 (1999)
19. A.A. Tomchenko et al., Detection of chemical warfare agents using nanostructured metal oxide sensors. Sens. Actuators B Chem. **108**, 41–55 (2005)
20. W.S. Lee et al., The sensing behavior of SnO_2-based thick-film gas sensors at a low concentration of chemical agent simulants. Sens. Actuators B Chem. **108**, 148–153 (2005)
21. O. Koper et al., Destructive adsorption of chlorinated hydrocarbons on ultrafine (nanoscale) particles of calcium oxide. Chem. Mater. **5**, 500–505 (1993)
22. J. Sauer, Molecular models in ab initio studies of solids and surfaces: From ionic crystals and semiconductors to catalysts. Chem. Rev. **89**, 199–255 (1989)
23. J. Sauer, Theoretical study of van der Waals complexes at surface sites in comparison with the experiment. Chem. Rev. **94**, 2095–2160 (1994)
24. K. Takimoto et al., Effect of linear-dodecylbenzenesulfonate and humic acid on the adsorption of tricresyl phosphate isomers onto clay minerals. Environ. Sci. Technol. **32**, 3907–3912 (1998)
25. J.M. Bowen et al., Fourier transform infrared and Raman spectra of dimethyl methylphosphonate adsorbed on montmorillonite. Environ. Sci. Technol. **22**, 1178–1181 (1988)
26. J.M. Bowen et al., Comparison of sample preparation methods for the Fourier transform infrared analysis of an organo-clay mineral sorption mechanism. Anal. Chem. **61**, 2047–2050 (1989)
27. M. Levesque, M. Schnitzer, Organo-metallic interactions in soils: 6. Preparation and properties of fulvic acid-metal phosphates. Soil Sci. **103**, 183–190 (1967)
28. R.J. Hance, Adsorption of glyphosate by soils. Pest. Sci. **23**, 363–366 (1976)
29. S. Shoval, S. Yariv, The interaction between roundup (glyphosate) and montmorillonite; Part 1, Infrared study of the sorption of glyphosate by montmorillonite. Clays Clay Miner. **27**, 19–28 (1979)
30. P. Sprankle et al., Adsorption, mobility and microbial degradation of glyphosate in the soil. Weed Sci. **23**, 229–234 (1975)
31. E. Morillo et al., Adsorption of glyphosate on the clay mineral montmorillonite: Effect of cu(II) in solution and adsorbed on the mineral. Environ. Sci. Technol. **31**, 3588–3592 (1997)
32. J.S. McConnell, L.R. Hossner, pH-dependent adsorption isotherms of glyphosate. J. Agric. Food Chem. **33**, 1075–1078 (1985)
33. R.L. Glass, Adsorption of glyphosate by soils and clay minerals. J. Agric. Food Chem. **35**, 497–500 (1987)
34. M. Kataoka et al., Effect of cation-exchange pretreatment of aqueous soil extracts on the gas chromatographic–mass spectrometric determination of nerve agent hydrolysis products after *tert*.-butyldimethylsilylation. J. Chromatogr. A **824**, 211–221 (1998)
35. W.D. Vermilion, M.D. Crenshaw, In-line respeciation: an ion-exchange ion chromatographic method applied to the separation of degradation products of chemical warfare nerve agents in soil. J. Chromatogr. A **770**, 253–260 (1997)

36. M. Kataoka et al., Effect of pedological characteristics on aqueous soil extraction recovery and tert-butyldimethylsilylation yield for gas chromatography-mass spectrometry of nerve gas hydrolysis products from soils. Environ. Sci. Technol. **35**, 1823–1829 (2001)
37. P. D'Agostino et al., Determination of Sarin, Soman and their hydrolysis products in soil by packed capillary liquid chromatography–electrospray mass spectrometry. J. Chromatogr. A **912**, 291–299 (2001)
38. A. Michalkova et al., Theoretical study of the adsorption and decomposition of sarin on magnesium oxide. J. Phys. Chem. B **108**, 5294–5303 (2004)
39. M. Svensson et al., ONIOM: A multi-layered integrated MO+MM method for geometry optimizations and single point energy predictions. A test for Diels–Alder reactions and $Pt(P(t\text{-}Bu)_3)_2+H_2$ oxidative addition. J. Phys. Chem. **100**, 19357–19363 (1996)
40. A. Michalkova et al., Theoretical study of adsorption of Sarin and Soman on tetrahedral edge clay mineral fragments. J. Phys. Chem. B **110**, 21175–21183 (2006)
41. V.V. Murashov, J. Leszczynski, Adsorption of the phosphate groups on silica hydroxyls: An ab initio study. J. Phys. Chem. A **103**, 1228–1238 (1999)
42. C.J. Hartzell et al., Molecular modeling of the tributyl phosphate complex of europium nitrate in the clay hectorite. J. Phys. Chem. A **102**, 6722–6729 (1998)
43. N.U. Zhanpeisov et al., Cluster quantum chemical study of the interaction of dimethyl methylphosphonate with magnesium oxide. J. Phys. Chem. **98**, 10032–10035 (1994)
44. A. Kaczmarek et al., Sarin and Soman: Structure and properties. Struct. Chem. **15**, 517–525 (2004)
45. Y. Paukku et al., Investigation on the low energy conformational surface of tabun to probe the role of its different conformers on biological activity. Chem. Phys. Lett. **422**, 317–322 (2006)
46. Y-Ch Yang et al., Decontamination of chemical warfare agents. Chem. Rev. **92**, 1729–1743 (1992)
47. Y.-C. Yang, Chemical reactions for neutralizing chemical warfare agents. Chem. Ind. **9**, 334–337 (1995)
48. M.K. Templeton, W.H. Weinberg, Adsorption and decomposition of dimethyl methylphosphonate on an aluminum oxide surface. J. Am. Chem. Soc. **107**, 97–108 (1985)
49. M.K. Templeton, W.H. Weinberg, Decomposition of phosphonate esters adsorbed on aluminum oxide. J. Am. Chem. Soc. **107**, 774–779 (1985)
50. Y.-X. Li, K.J. Klabunde, Nano-scale metal oxide particles as chemical reagents. Destructive adsorption of a chemical agent simulant, dimethyl methylphosphonate, on heat-treated magnesium oxide. Langmuir **7**, 1388–1393 (1991)
51. Y.-X. Li et al., Fourier transform infrared photoacoustic spectroscopy study of the adsorption of organophosphorus compounds on heat-treated magnesium oxide. Langmuir **7**, 1394–1399 (1991)
52. M. Atteya, K.J. Klabunde, Nanoscale metal oxide particles as chemical reagents. Heats of adsorption of heteroatom containing organics on heat-treated magnesium oxide samples of varying surface areas. Chem. Mater. **3**, 182–187 (1991)
53. Y.-X. Li et al., Adsorption and decomposition of organophosphorus compounds on nanoscale metal oxide particles. In situ GC-MS studies of pulsed microreactions over magnesium oxide. Chem. Mater. **4**, 323–330 (1992)
54. M.A. Henderson et al., A TPD/AES study of the interaction of dimethyl methylphosphonate with iron oxide (α-Fe_2O_3) and silicon dioxide. J. Phys. Chem. **90**, 4607–4611 (1986)
55. B. Aurian-Blajeni, M.M. Boucher, Interaction of dimethyl methylphosphonate with metal oxides. Langmuir **5**, 170–174 (1989)
56. M.B. Mitchell et al., Adsorption and decomposition of dimethyl methanephosphonate on metal oxides. J. Phys. Chem. B **101**, 11192–11203 (1997)
57. V.N. Sheinker, M.B. Mitchell, Quantitative study of the decomposition of dimethyl methylphosphonate (DMMP) on metal oxides at room temperature and above. Chem. Matter. **14**, 1257–1268 (2002)

58. M.B. Mitchell et al., Decomposition of dimethyl methylphosphonate (DMMP) on supported cerium and iron co-impregnated oxides at room temperature. J. Phys. Chem. B **107**, 580–586 (2003)
59. S.M. Kanan, C.P. Tripp, An infrared study of adsorbed organophosphonates on silica: a prefiltering strategy for the detection of nerve agents on metal oxide sensors. Langmuir **17**, 2213–2218 (2001)
60. S.M. Kanan et al., A comparative study of the adsorption of chloro- and non-chloro-containing organophosphorus compounds on WO_3. J. Phys. Chem. B **106**, 9576–9580 (2002)
61. G.W. Wagner et al., Reactions of VX, GD, and HD with nanosize MgO. J. Phys. Chem. B **103**, 3225–3228 (1999)
62. G.W. Wagner et al., Reactions of VX, GD, and HD with nanosize CaO: Autocatalytic dehydrohalogenation of HD. J. Phys. Chem. B **104**, 5118–5123 (2000)
63. G.W. Wagner et al., Reactions of VX, GB, GD, and HD with nanosize Al_2O_3. Formation of aluminophosphonates. J. Am. Chem. Soc. **123**, 1636–1644 (2001)
64. A.E.T. Kuiper et al., The role of heterogeneity in the kinetics of a surface reaction. I. Infrared characterization of the adsorption structures of organophosphonates and their decomposition. J. Catal. **43**, 154–167 (1976)
65. V.C. Bermudez, Computational study of the adsorption of trichlorophosphate, dimethyl methylphosphonate, and Sarin on amorphous SiO_2. J. Phys. Chem. C **111**, 9314–9323 (2007)
66. V.C. Bermudez, Quantum-chemical study of the adsorption of DMMP and Sarin on λ-Al_2O_3. J. Phys. Chem. C **111**, 3719–3728 (2007)
67. W. Kolodziejczyk et al., Probing the role of P=O stretching mode enhancement in nerve-agent sensors: Simulation of the adsorption of diisopropylfluorophosphate on the model MgO and CaO surfaces. Chem. Phys. Lett. **450**, 138–143 (2007)
68. A. Michalkova et al., Theoretical study of adsorption of tabun on calcium oxide clusters. Chem. Phys. Lett. **438**, 72–77 (2007)
69. Y. Paukku et al., Adsorption of dimethyl methylphosphonate and trimethyl phosphate on calcium oxide: An ab initio study. Struct. Chem. **19**, 307–320 (2008)

Chapter 14
Toward Understanding of Hydrogen Storage in Single-Walled Carbon Nanotubes by Investigations of Chemisorption Mechanism

T.C. Dinadayalane and Jerzy Leszczynski

Abstract We provide an overview of experimental and theoretical studies on hydrogen storage in single-walled carbon nanotubes (SWNTs) via chemisorption mechanism. The atomic hydrogens that are generated by dissociation of H_2 molecules bind with carbon atoms of nanotubes, leading to strong C–H bonds in the chemisorption process. Recent experimental study indicates that 5.1 ± 1.2 wt% hydrogen storage could be achieved by hydrogenation (chemisorption process) of SWNTs. Our computational study shows that chemisorptions of one and two hydrogen atoms on the external surface of (3, 3), (4, 4), (5, 5), and (6, 6) armchair SWNTs are highly exothermic processes. Furthermore, two hydrogen atoms favor to bind at adjacent positions rather than at alternate carbon sites. This is different from the results reported on zigzag nanotubes. The chemisorptions of one and two hydrogen atoms significantly alter the C–C bond lengths of SWNTs in the vicinity of hydrogen addition due to the change of hybridization of carbon atom(s) from sp^2 to sp^3 at the chemisorption site(s). The effect of increasing the length of SWNTs on the geometries and the reaction energies of hydrogen chemisorption has also been explored. The high exothermicity of the chemisorption of hydrogen atoms on the surface of SWNTs explains the reason for the requirement of high temperature to remove hydrogen from hydrogenated SWNTs.

14.1 Introduction

In recent years, the society encounters two major challenges: (a) remarkable increase of fuel prices due to lot of demand and shrinking availability of fossil fuels; and (b) the global warming, which is otherwise known as the potential

T.C. Dinadayalane and J. Leszczynski (✉)
NSF CREST Interdisciplinary Nanotoxicity Center, Department of Chemistry and Biochemistry, Jackson State University, Jackson, MS 39217, USA
e-mail: jerzy@icnanotox.org

J. Leszczynski and M.K. Shukla (eds.), *Practical Aspects of Computational Chemistry*, 297
DOI: 10.1007/978-90-481-2687-3_14,

climate change due to ever-increasing use of fossil fuels. One of the important solutions that can be applied to solve these problems is to utilize different energy carriers. Scientists all around the world have been working hard to find out viable alternatives for the fossil fuels for more than a decade. Hydrogen is believed to be one of the best substitutes for fossil fuels in the future. There are five different stages in the hydrogen-economy infrastructure: production, storage, delivery, conversion, and application. The most challenging and critical issue of a viable hydrogen economy is the hydrogen storage. Material scientists and chemists focus on possible ways to produce and store hydrogen in electric power plants and vehicles. To facilitate hydrogen-powered transport, it is crucial to discover ways to store hydrogen efficiently and safely. Many researchers have reported the storage of hydrogen in lightweight materials (nanomaterials) [1–3].

Carbon nanotubes (CNTs) are renowned for hydrogen storage after the pioneering work by Dillon et al. who proposed that CNTs can be an efficient, cheap, and rechargeable storage media for small-scale fuel cells. The storage capacity of 5–10 wt% was estimated by temperature programmed desorption (TPD) spectroscopy [1]. This report has generated vast interest to utilize nanostructured carbon materials, such as CNTs and graphite nanofibers for hydrogen storage [2, 3], to deliver a viable material to meet the US Department of Energy (DOE) target of 6.5 wt% at ambient temperature and pressure. In comparison to the traditional metal hydrides, CNTs have the advantages of lightweight, large exposed surface, and remarkable electronic and mechanical properties. Therefore, they are considered as potential materials for hydrogen storage.

CNTs were accidentally discovered in 1991 by Iijima [4]. CNTs are extended tubes of rolled graphene sheets and are classified into two types: multi-walled (two or more concentric tubes) and single-walled (one tube) CNTs (Fig. 14.1). They are generally a few nanometers in diameter and several micrometers (10^{-6}m) to centimeters long. Apart from Iijima et al. [5], Bethune et al. [6] reported the syntheses of single-walled carbon nanotubes (SWNTs). A single-walled CNT can be viewed as a graphene rolled up into a seamless cylinder with diameter on the order of a nanometer and it looks like rolled up chicken wire with hexagonal cells. A pair of indices (n,m) called the chiral vector is used to describe how the graphene sheet is rolled into a nanotube. The integers n and m denote the number of unit vectors along two directions in the honeycomb crystal lattice of the graphene. If $m=0$, the nanotubes are called "zigzag." If $n=m$, the nanotubes are called

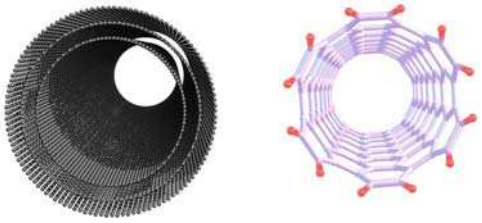

Fig. 14.1 Structures of multi- and single-walled carbon nanotubes

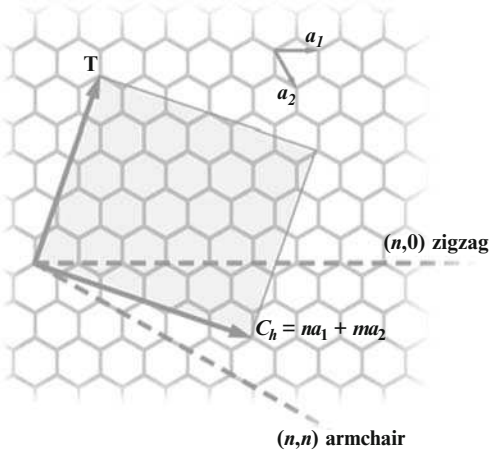

Fig. 14.2 Schematic of how to "roll up" honeycomb structure of a graphene sheet into the nanotube. A pair of indices (n,m) is called the chiral vector; T denotes the tube axis; a_1 and a_2 are the unit vectors of graphene sheet in real space

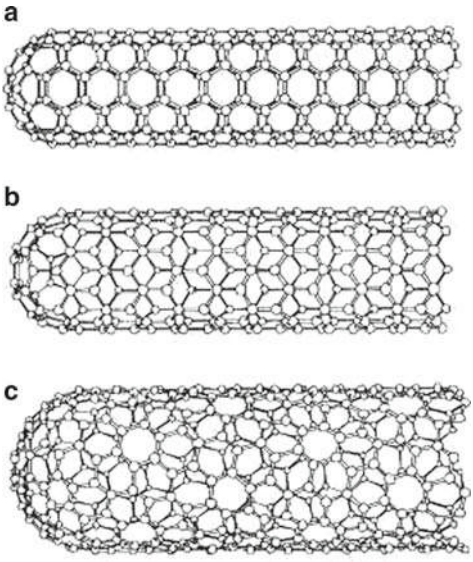

Fig. 14.3 Representative structures of (**a**) armchair, (**b**) zigzag, and (**c**) chiral type single-walled carbon nanotubes

"armchair." Otherwise, they are called "chiral." Figure 14.2 depicts the way of rolling up of a graphene sheet into SWNT, and Fig. 14.3 shows the representative structures of three different types of SWNTs.

For the application of SWNTs in hydrogen storage, several questions can arise: (a) What is the mechanism of interaction between the hydrogen molecule and SWNT?, (b) Can a H_2 molecule be adsorbed both inside and outside SWNT or only one side?, (c) What is the nature and strength of the binding?, and (d) Can the strength of the binding be modified by changing the curvature of the surface or by coadsorption of the metal atom(s)/ion(s) or by the presence of defects in the

SWNT? The answers to these questions will provide an understanding of the interaction between atomic or molecular hydrogen and SWNT. Such an understanding will be helpful to design and render SWNT based material that will be safe, efficient, economical, and rechargeable medium for hydrogen storage.

Physisorption and chemisorption are the two different mechanisms that have been proposed for the hydrogen storage in SWNTs [7–9]. In the physisorption process, molecular hydrogen does not dissociate and it binds with the SWNT through weak van der Waals interactions. The binding of hydrogen can occur at three different sites in SWNTs in the physisorption process: (a) on top of a carbon atom, (b) at the middle of a C–C bond, and (c) at the center of a hexagon. Han and Lee showed that physisorption of H_2 outside the SWNT with a vertical orientation to the tube axis above the center of the hexagon is the most stable state of physisorption and its binding energy is very weak (−0.79 kcal/mol) for (10, 0) zigzag tube [9]. Hydrogen atoms can form covalent bonds with carbon atoms of the SWNT due to the presence of a large number of unsaturated C=C bonds. The atomic hydrogens, generated by dissociation of H_2 molecules, bind with carbon atoms of SWNTs, leading to strong C–H bonds in the chemisorption process. Covalent binding of atomic hydrogen on the sidewalls of SWNTs results in the disruption of bonding network due to changing of carbon atom hybridization from sp^2 to sp^3. On the other hand, the aromatic bonding framework of SWNT is not altered in the physisorption of hydrogen molecule. Many of the theoretical studies examined the physisorption of hydrogen molecules inside or outside SWNTs, while the studies on the chemisorption of hydrogen atoms on the surface of SWNTs are limited [7–12]. The reaction pathway from physisorption to chemisorption of hydrogen on the surface of (10, 0) zigzag tube was reported by Han and Lee [9].

The aim of this review is to provide an overview of experimental and theoretical studies on the hydrogen storage using single-walled CNTs via chemisorption mechanism. In the following sections, first, the available experimental investigations on the hydrogen chemisorption in SWNTs have been briefly outlined; second, the theoretical studies concerning the chemisorption of hydrogen atoms on the surface of SWNTs are given; and third, selected properties of hydrogenated SWNTs are discussed. We provide an elegant summary and outlook in the final section.

14.2 Experimental Studies on the Hydrogenation of SWNTs

For more than a decade, SWNTs have been considered as potential candidates for hydrogen storage. In order to evaluate such applications of the CNTs, it is necessary to prove the hydrogen adsorption in SWNTs by means of spectroscopic techniques as well as microscopic images. Spectroscopic characterization of hydrogenated SWNTs would enhance research interest on their hydrogen storage applications. Experimental studies indicated that hydrogenation on the external surface of SWNTs is more practical and the hydrogen coverage varies with the experimental

conditions [13, 14]. There are two important questions arising for hydrogen storage in SWNTs via chemisorption mechanism. One is how much hydrogen can be stored in SWNTs, and the other is related to the reversibility of chemisorbed hydrogens. Khare et al. reported covalent bonding of atomic hydrogen with carbon atoms of nanotubes and confirmed the C–H bond formations by infrared (IR) spectroscopy [14]. Ultraviolet photoelectron spectroscopy study showed that atomic hydrogen can create a C–H bond with carbon atoms of SWNTs [15]. These experimental studies demonstrated that a sufficient amount of hydrogen can be stored in SWNTs by chemisorption mechanism. However, the exact amount of hydrogen storage capacity was not reported [14, 15]. In the past few years, there has been a breadth of investigations on hydrogen storage in SWNTs by chemisorption mechanism [7–17]. Chiarello et al. revealed that dissociation of H_2 molecule took place and it is followed by C–H bond formation with SWNT at room temperature and at the pressure of 2.6×10^{-2}Pa [18]. They provided first vibrational spectroscopic evidence of the dissociation of H_2 molecules interacting with the surface of SWNTs. The C–H stretching vibration was noted as a fingerprint for the chemisorbed hydrogen.

In 2001, Pekker et al. prepared hydrogenated single-walled and multi-walled CNTs, as well as graphite via a dissolved metal reduction method with Li and methanol in liquid ammonia, which can be considered as a modified Birch reduction method [19]. High-resolution transmission electron microscopy (TEM) showed corrugated and disordered structures of SWNTs due to the influence of hydrogenation on SWNTs and this observation supports the formation of covalent C–H bonds. Hydrogenated carbonaceous materials are stable up to 400°C and decomposed with the simultaneous formations of hydrogen and a small amount of methane beyond 400°C. The molar ratio of the evolved H_2 and CH_4 is 90:10 for hydrogenated SWNTs.

Experimental investigation based on X-ray photoelectron spectroscopy (XPS) and X-ray absorption spectroscopy (XAS) has recently shown that SWNTs can be hydrogenated with atomic hydrogen in a reversible way [13]. The diameters of CNTs in this study range from 1 to 1.8 nm. The changes in the XPS spectrum of SWNT before and after hydrogen adsorption evidenced the hydrogenation process (Fig. 14.4). The changes in the XA spectra due to hydrogenation clearly indicate the potential of SWNT as a hydrogen storage material. Nikitin et al. showed that 5.1 ± 1.2 wt% hydrogen storage could be achieved by hydrogenation of SWNTs [13]. They added that hydrogen storage through chemisorption in SWNTs is possible with technologically sufficient hydrogen weight capacity. This experimental spectroscopic study attracted research interest on single layers of graphite for hydrogen storage and theoretical modeling of X-ray absorption spectra to validate the experimental results [16].

Zhang et al. have recently reported the hydrogenation of SWNTs by H-plasma treatment [17]. The hydrogenation on the surface of SWNTs was confirmed by atomic force microscopy (AFM). Further, the hydrogenation of SWNTs was elucidated by infrared (IR) and Raman spectroscopy measurements. IR spectra showed vibration bands in the range of 2,750–3,000 cm^{-1} for the hydrogenated SWNTs.

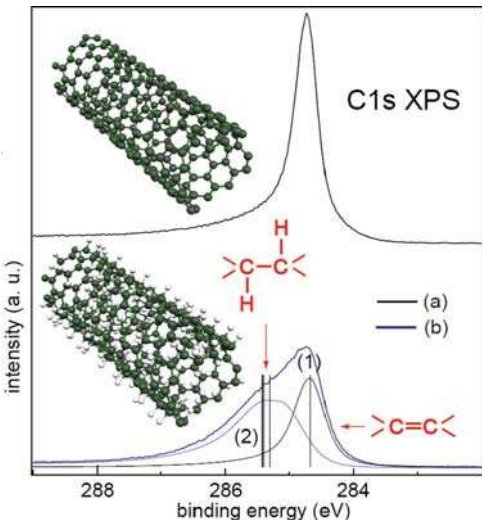

Fig. 14.4 Carbon 1s XPS spectra of a clean SWNT film (*black*) and SWNT film after hydrogenation (*blue*). Peak 1 at higher energy (lower binding energy) corresponds to the signal from carbon atoms unaffected by hydrogenation; whereas peak 2 at lower energy is due to hydrogen-coordinated carbon atoms. The theoretical values of the carbon 1 score-level chemical shifts due to C–H bond formation for different types of SWNTs are shown as vertical lines

The peak at ~2,920 cm^{-1} was tentatively assigned to sp^3 C–H stretching or asymmetric stretching of sp^3 CH_2 group. The IR frequencies clearly suggest the formation of C–H bond on the external surface of SWNT. Upon thermal annealing, the dehydrogenation occurred from 200 to 500°C. Such a wide range of temperature is due to inhomogeneities in the SWNTs that indicate the existence of C–H bonds with different bond strengths. It was reported that hydrogenation of SWNTs by H-plasma treatment cuts smaller diameter nanotubes more easily than larger tubes. Also, the semi-conducting nature of SWNTs is enhanced by sidewall hydrogenation and this is reversible upon thermal annealing at 500°C [17].

Meletov et al. have investigated the characterization of physisorbed molecular hydrogen and the covalently bonded hydrogen in the hydrogenated SWNTs using Raman spectroscopy [20]. They revealed that Raman spectroscopy could be useful to distinguish adsorbed molecular hydrogen from that of the covalently bonded one and also useful for the study of hydrogen distribution in the hydrogenated single-walled CNTs. Their study involved SWNTs of diameter 1.4–1.6 nm for hydrogenation at high pressure and at elevated temperature. Raman frequencies of the C–H stretching vibrations of the covalently bonded hydrogen and the H–H stretching vibration of physisorbed molecular hydrogen appear at 2,800–3,000 and 4,130–4,160 cm^{-1}, respectively. It was reported that the hydrogen atoms, which are randomly chemisorbed on SWNTs, were removed by annealing of the hydrogenated SWNTs in vacuum or in air [20]. This observation is similar to the recent study of Zhang et al. [17].

Very recently, Yang et al. proposed a spillover mechanism for a material consisting of a hydrogen dissociation source and SWNT receptor for hydrogen binding as shown in Fig. 14.5 [10]. They demonstrated that multiple binding sites are available for the spillover hydrogen on the surface of SWNTs. Their experimental investigations were performed with a carbon bridged composite material

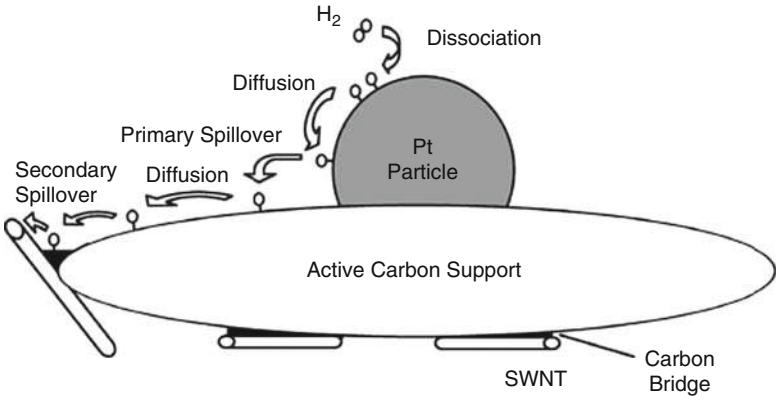

Fig. 14.5 Proposed mechanism for primary and secondary spillover hydrogen binding with carbon nanotube. Reproduced with permission from [10], copyright 2006 American Chemical Society

containing SWNTs at 298 K and at the pressures up to 10 MPa. Yang et al. revealed that significant hydrogen storage capacity can be achieved using CNTs at ambient conditions. In the spillover process, a flux of atomic hydrogen generated by dissociation of molecular hydrogen upon interacting with platinum flows onto the carbon based materials in the vicinity of catalytic particles through a bridge built with carbonized sugar molecules.

Experimental studies revealed that temperature of nearly 500–600°C is required to release the hydrogen atoms chemisorbed on the surface of SWNTs [16, 17, 19]. This temperature is very high to fully accomplish the hydrogen storage in SWNTs. Computational chemistry is useful to understand why such high temperature is required to release hydrogen from hydrogenated SWNTs.

14.3 Theoretical Studies on the Chemisorption of Hydrogen Atoms on SWNTs

The research on the chemisorption of hydrogen atoms on the surface of SWNTs is growing rapidly over the last 3 years. Some of the recent experimental studies [10, 13, 17] stimulated computational investigations toward hydrogen chemisorptions on the sidewalls of SWNTs [10, 21, 22]. Tailoring of CNT structures needs to be thoroughly explored, since the CNTs promise superior hydrogen storage. Research attention should be focused on the understanding of the mechanism of hydrogen storage in SWNTs and how to modify the SWNTs that could release stored hydrogen at ambient temperature and pressure. Modeling studies enable an understanding of physics and chemistry of hydrogen interactions with the SWNTs. Computational studies play an important role in guiding experimentalists in the past [23, 24]. Theoretical studies predicted that hydrogen storage in SWNTs will be

very effective by hydrogen chemisorption mechanism at the high pressure/high temperature [10, 25–27].

Density functional theory (DFT) calculations showed that hydrogen storage capacity of up to 7.5 wt% could be achieved through chemisorption of hydrogen atoms on the sidewalls of SWNTs [26, 27]. Fully exohydrogenated SWNTs are stable up to the radius of the (8, 8) armchair SWNT, and the binding energy is inversely proportional to the diameter [28]. Using DFT calculations, Yang and Ni reported that the storage capacity of hydrogen depends significantly on the diameters of SWNTs [29]. They also found that nanotubes with diameters of 1 nm can achieve coverage of 80% at ambient temperature and low pressure, which is in agreement with the experimental results. They showed that hydrogen storage is more efficient for the smaller size SWNTs. They examined the variation of the hydrogen coverage with the change of temperature and pressure. The temperature for hydrogen coverage should be lower than 500 K for the (6, 0) tube and 400 K for the (8, 0) SWNT in order to obtain the SWNT-based hydrogen storage medium for practical applications. It was shown that two hydrogen atoms prefer to form a dimer on two neighboring carbon atoms. As the coverage increases, the repulsions between hydrogen atoms become stronger because the distances between hydrogen atoms become shorter [29].

Computational investigations provide interesting insights into the details of H-chemisorption on SWNTs. Theoretical studies showed that the carbon atom, which forms the C–H bond by hydrogen chemisorption on SWNT, is pulled out of the plane of the nanotube sidewall. The effect of pulling out of carbon atom depends on the nanotube curvature [23]. Chen et al. recently reported that chemisorption energies of hydrogen on the external surface of (5, 5) SWNT are considerably stronger than (9, 9) SWNT. Furthermore, the coadsorption of two hydrogen atoms on opposite sides is not energetically favorable [23]. Yang et al. [10] and Chen et al. [23] independently reported that both for the armchair and zigzag SWNTs, the chemisorption of hydrogen atom on the internal surface of SWNTs is much weaker than external surface due to the curvature effect.

Bauschlicher investigated different percentage of hydrogen coverage on (10, 0) zigzag SWNT using the ONIOM (our own N-layered integrated molecular orbital and molecular mechanics [30]) approach. The ONIOM approach is a mixed, two-level approach that treats a small section of the system accurately and the rest at a lower level. Bauschlicher calculated the binding energies for the tube with one and two hydrogen atoms, and also 24, 50 and 100% coverage. He reported that half-coverage is more favorable than full-coverage and it corresponds to ~4% by weight storage of hydrogen [31, 32]. Han and Lee demonstrated that the most stable state for the chemisorption of two hydrogen atoms is above two adjacent carbon atoms of a hexagon of (10, 0) zigzag tube. The energy barrier of the reaction from physisorption to chemisorption is ~79 kcal/mol, and thus, the reaction is not spontaneous at room temperature [9].

Experimental data suggested the dissociation of hydrogen molecule into hydrogen atoms followed by atomic hydrogen spillover [10] or hydrogenation reactions [13, 17, 19] for significant amount of hydrogen storage. Theoreticians continue

their efforts to provide a rationale for the mechanism of hydrogen storage. Computational studies toward molecular level understanding of chemisorption of hydrogen on SWNTs, i.e., adsorption of hydrogen at low occupancies, will be useful for experimentalists to design and achieve SWNT-based materials that will have efficient hydrogen storage and desorption at ambient temperature and pressure. Very recently, Yang et al. have investigated the chemisorption of hydrogen at low occupancies (i.e., binding of one and two hydrogen atoms) on SWNTs using ab initio molecular orbital calculations to understand the dissociation and spillover phenomenon of hydrogen [10]. They pointed out that binding energy of H atom depends on H occupancy, tube diameter and chirality. Moreover, exohedral binding of H is more favorable than endohedral binding due to easier conversion of sp^2 to sp^3 hybridization of carbon of exterior walls upon H binding (see Figs. 14.6 and 14.7) [10]. The ab initio HF/3-21G(d) geometry optimizations revealed that the length of three adjacent C–C bonds in the region of hydrogen chemisorption increased from 1.42 to 1.52 Å. It was reported that the two hydrogen atoms prefer to bind at the adjacent positions than at the alternate carbon atoms on the external surface of zigzag SWNTs. This was attributed to the crowding effect [10].

Previous computational studies reported that the bond lengths of newly formed C–H bonds are ~1.1 Å for hydrogen chemisorbed SWNTs [9, 10]. Arellano et al. estimated the energy barriers of more than 2.5 eV for the dissociation of H_2 on the surface of (5, 5) and (6, 6) SWNTs [33]. Chen et al. found that the dissociation of H_2 on very small diameter armchair (3, 3) SWNT was not possible at room temperature because of high energy barrier of 2.7 eV [34]. Froudakis studied

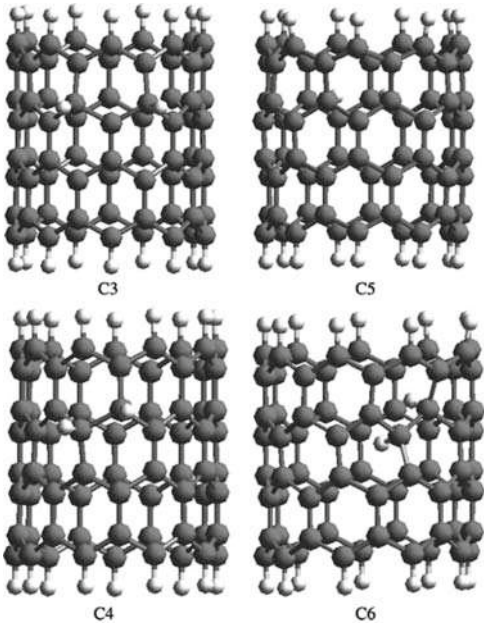

Fig. 14.6 Two H-atoms chemisorbed in (9, 0) zigzag SWNT. Two alternate H's on the exterior wall (**C3**) and interior wall (**C5**); two adjacent H's on the exterior wall (**C4**) and interior wall (**C6**). Small *white balls* are hydrogen atoms. Reproduced with permission from [10], copyright 2006 American Chemical Society

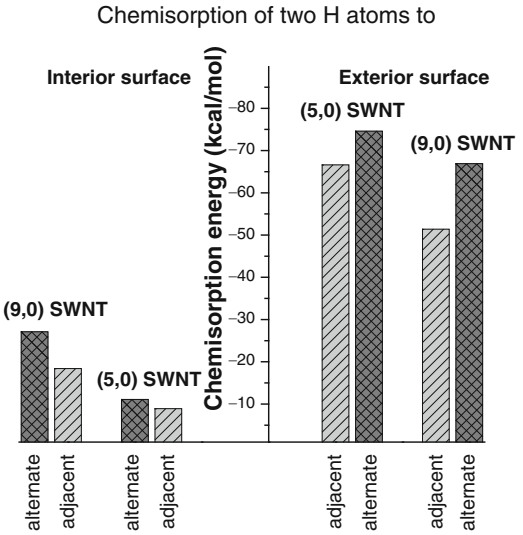

Fig. 14.7 Plot showing the chemisorption energy for the binding of two hydrogen atoms at alternate and adjacent positions of the interior and exterior walls of (5, 0) and (9, 0) zigzag SWNTs. The data were taken from [10]

hydrogen chemisorption on the surface of (4, 4) armchair SWNT using a mixed quantum mechanics/molecular mechanics (QM/MM) model. He revealed that changing of tube shape occurred during the hydrogen chemisorption, which caused an enlargement of the tube volume by 15% [35]. Hydrogenation of a chiral single-walled (6, 4) CNT has been investigated using DFT (B3LYP) by Jia et al. [36]. This study indicated an interesting point that the hydrogenation of the (6, 4) SWNT can be well predicted using the topology of the highest occupied molecular orbital (HOMO). In the chemisorption of hydrogen on (6, 4) SWNT, the C–C bonds around the binding site become single bonds and the bond lengths elongate from 1.38–1.44 to 1.50–1.57 Å. It was also noted that the lengths of the C–C bonds far away from the binding sites were also perturbed [36].

Recently, we have investigated chemisorption of one hydrogen atom and two hydrogen atoms at different positions (i.e., 1-2, 1-2′, 1-3 or 1-4 positions) on the external surface of (3, 3), (4, 4), (5, 5), and (6, 6) armchair SWNTs of 9 and 15 carbon atom layers (Fig. 14.8) [21]. We have considered the chemisorption of hydrogen atoms only on the outer wall of SWNT (exohedral addition) since Yang et al. clearly demonstrated that the addition of hydrogen to the outer wall is considerably more favored than those to the inner wall of SWNT (endohedral addition) [10]. Our study was intended to examine whether the positional preference for the attachment of two hydrogen atoms is same or different for the armchair and zigzag SWNTs. Also, we explored the effect of tube length and diameter on the hydrogen atom chemisorption energies.

The calculations were performed at the DFT, B3LYP/6-31G(d) level using Gaussian 03 software [37]. All the pristine and hydrogenated nanotubes were fully optimized within the symmetry constrains. Frequency calculations were carried out for the optimized geometries of (3, 3) and (4, 4) SWNTs of nine carbon

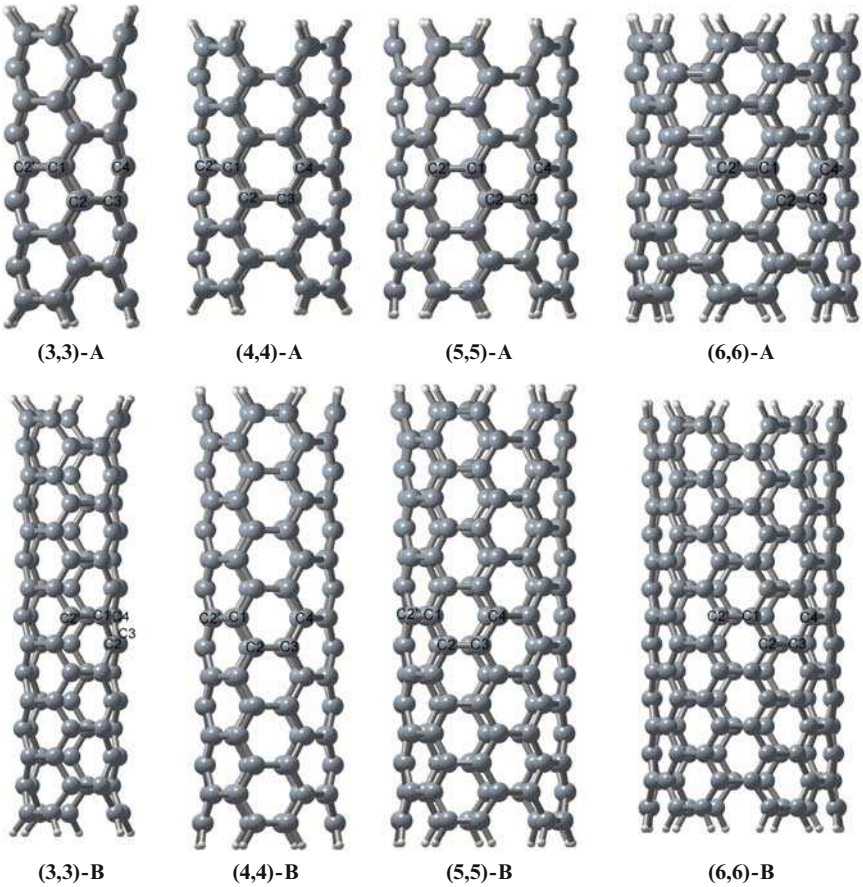

Fig. 14.8 B3LYP/6-31G(d) optimized structures of (3, 3), (4, 4), (5, 5) and (6, 6) armchair SWNTs of 9 and 15 carbon layers. The carbon atom sites for H-atom chemisorption are labeled. The structures are reproduced with permission from [21], copyright 2007 American Chemical Society

layers and their hydrogen chemisorbed structures to determine the nature of the stationary points. The frequency calculations for other CNT structures were not performed since they are computationally prohibitive. The reaction energies for hydrogen chemisorption (E_r) on the external surface of SWNTs have been calculated using the formula given below:

$$E_r = E_{SWNT+nH} - E_{SWNT} - nE_H, \tag{14.1}$$

where $E_{SWNT+nH}$ denotes the total energy of hydrogen chemisorbed nanotube; n represents the number of hydrogen atoms chemisorbed; and E_{SWNT} and E_H correspond to the energies of pristine nanotube and the hydrogen atom, respectively.

The reaction energy E_r can also be considered as hydrogen chemisorption energy. The chemisorption of hydrogen is an exothermic process if the value of E_r is negative.

Analysis of the optimized geometries indicates that chemisorptions of one and two hydrogen atoms significantly alter the C–C bond lengths of armchair SWNTs in the vicinity of hydrogen addition. This is due to the change of hybridization of carbon atom(s) from sp^2 to sp^3 at the chemisorption site(s) as addressed in earlier studies [10, 13, 19]. The bond lengths of bare SWNTs range from 1.41 to 1.46 Å. In the region of H-chemisorption, many of the bond distances are longer than 1.5 Å that represents a typical bond length of sp^2–sp^3 C–C single bond. This indicates weakening of C–C bond in the region of hydrogen chemisorption. The bond lengths of newly formed C–H bonds in the H-chemisorbed nanotubes are ~1.1 Å. The C1–C2′ bond length in **(3, 3)-B_H(1, 2′)** is 2.697 Å, whereas it is 1.67 Å in **(3, 3)-A_H(1, 2′)**; (where **H(1, 2′)** indicates two hydrogen atoms bonded to C1 and C2′). This is surprising because the C1–C2′ bond has ruptured in the longer tube, i.e., 15 carbon layered tube of (3, 3) SWNT, upon two hydrogen addition at C1 and C2′ positions but it is elongated to a large extent in nine carbon layered tube of (3, 3) SWNT. The bond breaking of a particular circumferential C–C bond in (3, 3) SWNT upon the chemisorption of two hydrogen atoms can be attributed to the local strain existing at that region of SWNT. In structural aspects, the small diameter (3, 3) nanotube behaves differently from larger diameter nanotubes considered in our study.

Figure 14.9 shows that the chemisorption reactions of one and two hydrogen atoms on the surface of the armchair nanotubes are highly exothermic. The

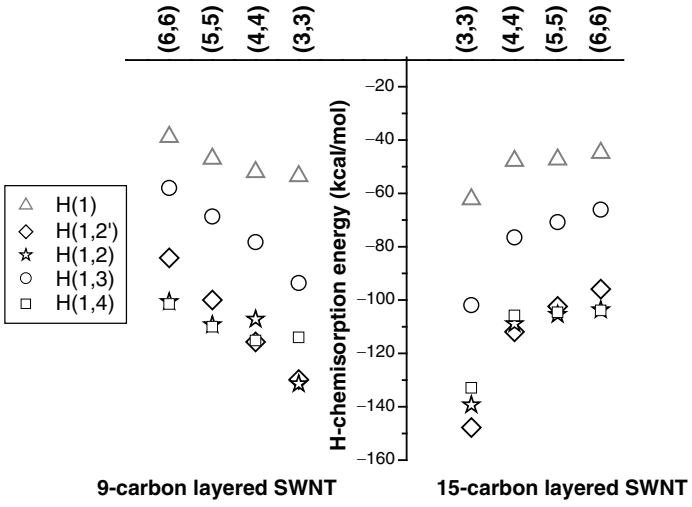

Fig. 14.9 The variation of H-chemisorption energies at the B3LYP/6-31G(d) level for the chemisorption of one and two hydrogen atoms on the external surface of (3, 3), (4, 4), (5, 5) and (6, 6) armchair single-walled carbon nanotubes (SWNTs) of 9 and 15 carbon layers

exothermicity for the addition of two H atoms is greater than two times that of one H chemisorption, except for H(1, 3) addition. We have noticed a competition between H(1, 2) and H(1, 4) addition for (5, 5) and (6, 6) SWNTs, while such a competition is not observed in the case of smaller diameter (3, 3) and (4, 4) SWNTs. It is important to mention that increasing the length of the tube has pronounced effect on the exothermicity of hydrogen chemisorption. Tube diameter has significant influence on the H-chemisorption energy. The exothermicity of hydrogen chemisorption decreases while going from (3, 3) to (6, 6) armchair SWNTs, but the opposite trend was observed for zigzag type SWNTs [10]. Figure 14.9 shows that irrespective of the length and diameter of the SWNTs considered, the addition of H(1, 3) is thermodynamically less favored compared to H(1, 2) and H(1, 2′) additions. This observation is different from the results reported recently for zigzag type nanotubes by Yang et al. [10]. The chemisorption of two hydrogen atoms is highly exothermic process when the bond rupture occurs upon hydrogenation of circumferential C–C bond of SWNT.

14.3.1 Computed Vibrational Frequencies of Hydrogen Chemisorbed SWNTs

The B3LYP/6-31G(d) level vibrational frequencies of newly formed C–H bonds of hydrogen chemisorbed nanotubes of (3, 3) and (4, 4) are listed in Table 14.1. The vibrational frequencies were scaled with a scaling factor of 0.9614 [38]. Table 14.1 shows that the computed C–H stretching frequencies are in the range of 2800–3,000 cm^{-1}, which is in good agreement with the recent experimental reports [14, 17]. This type of theoretical support will enhance the research interest of experimentalists working in the field of CNT based hydrogen storage medium. Our computational study reveals that C–H stretching frequencies can be used to characterize the H-chemisorption on nanotubes of different diameters and the positions of different number of hydrogen atoms chemisorbed on the surface of armchair SWNTs. It should be noted that thermodynamically less stable H(1, 3)

Table 14.1 Vibrational frequencies (ν, cm^{-1}) corresponding to the newly formed C–H bonds of the hydrogen chemisorbed (3, 3) and (4, 4) SWNTs of nine carbon layers.

(3,3) SWNT		**(4,4) SWNT**	
Positions of H-attachment	ν (cm^{-1})	Positions of H-attachment	ν (cm^{-1})
H(1)	2893.3 (17.8)	**H(1)**	2854.1 (25.4)
H(1, 2′)	2949.1 (2.4); 2967.6 (17.9)	**H(1, 2′)**	2894.8 (3.2); 2913.4 (32.5)
H(1, 2)	2901.1 (5.6); 2915.8 (52.1)	**H(1, 2)**	2875.8 (10.0); 2897.4 (42.5)
H(1, 3)	2837.0 (36.1); 2854.6 (47.6)	**H(1, 3)**	2782.8 (94.8); 2806.9 (48.4)
H(1, 4)	2880.3 (25.2); 2880.6 (35.9)	**H(1, 4)**	2852.7 (44.5); 2852.8 (14.9)

Vibrational frequencies were scaled with a scaling factor of 0.9614 [38]. IR intensities (in km/mol) are given in parentheses

chemisorbed SWNTs exhibit lower values of C–H stretching frequencies compared to other hydrogen chemisorbed nanotubes [H(1), H(1, 2), H(1, 2′), and H(1, 4)] considered in this study (Table 14.1).

From the literature on CNT based hydrogen storage, one learns that relying on physisorption alone will lead to a bond that is too weak, and chemisorption will result in a formation of a bond that is too strong. Controlling the type and size of tubes and dopants is expected to tune the SWNTs for hydrogen sorption to occur at desired temperature and pressure. Therefore, a thorough research on modifying CNT systems (by introducing defects such as Stone-Wales defects [39] and vacancy defects [40]) is required to tune and enhance the hydrogen storage capabilities of the nanotubes. Such studies are underway in our group. The dependence on local defect structure and the mechanism of hydrogen storage in SWNTs require extensive theoretical studies to establish the basic principles and design strategies for improved hydrogen storage. It should be noted that the importance of single transition metal or metal cluster adsorption with SWNT for efficient hydrogen storage has been highlighted [41, 42]. Chen et al. demonstrated that intercalation of alkali atom would considerably enhance the hydrogen storage [2]. Strong interactions between experiment and theory will provide unprecedented capability to design more efficient and safe SWNT-based hydrogen storage materials.

14.3.2 Hydrogenation of SWNT Beyond Hydrogen Storage

The chemisorption of hydrogen atoms on the external surface of SWNTs can be used to tailor both the physical and chemical properties of CNTs. Computational studies showed that attachment of hydrogen atoms induces change in the electronic and molecular structures of SWNTs [30, 36, 43]. For instance, hydrogenation of zigzag SWNT with half coverage on the external surface makes them metallic with very high density of states at the Fermi level.

Hydrogenation on the surface of SWNTs has a significant effect on the magnetic properties. Using first-principles calculations, Pei et al. recently demonstrated that different distributions of hydrogen atoms on the surface of SWNTs by chemisorption have substantial effect on the magnetic properties of SWNTs [43]. Recent experimental study of Zheng et al. has reported that hydrogenation of SWNT using H-plasma treatment converts the metallic SWNT to semi-conducting SWNT. They also stated that different band gaps were obtained due to different percentage of hydrogen coverage and hydrogen position. SWNTs were reported to have different electrical properties due to diverse structures based on the diameter and chirality. Similar to other experimental studies [16, 17, 19], Zheng et al. revealed that 600°C (or higher temperature) is required to break C–H bonds of hydrogenated SWNTs [44]. In agreement with the experimental results, the computed band gap values vary based on the number and position of hydrogen atoms chemisorbed on the surface of SWNTs (Fig. 14.10). We observed that the length of the tube has

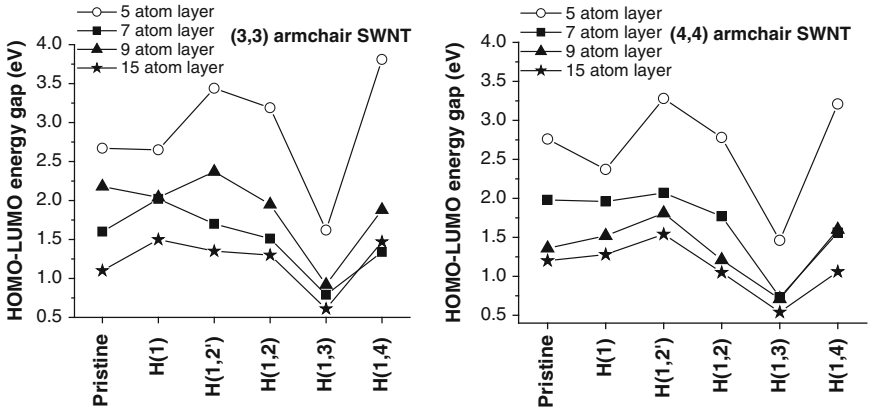

Fig. 14.10 Variation of band gap values by the chemisorption of hydrogen atoms on the external surface of (3, 3) and (4, 4) armchair SWNTs of different length (carbon atom layer). The band gap values were taken from [22]

significant effect on the band gap values. Further information on the structures, energetics, and physico-chemical properties of SWNTs and some of their potential applications can be obtained from the book chapter published recently [45].

14.4 Summary and Outlook

We have outlined the experimental results of hydrogen chemisorption on the surface of single-walled CNTs. Some of the theoretical results relevant to this field are also provided here. We feel that the basic research is essential for identifying novel materials and the processes that can provide potential breakthroughs to achieve the hydrogen fuel initiative (HFI) goals. Although many experimental and theoretical studies have been performed in order to understand the hydrogen storage mechanism in SWNTs, the real storage capacity of these species is still not clear. Thus, the nanotube based hydrogen storage materials that are efficient, safe and practical have not yet been found. Still much more theoretical and experimental investigations are required in the field of hydrogen storage in SWNTs to develop future SWNT-based hydrogen storage materials.

Acknowledgments This work was supported by the High Performance Computational Design of Novel Materials (HPCDNM) Project funded by the Department of Defense through the U.S. Army Engineer Research and Development Center (Vicksburg, MS), Contract W912HZ-06-C-0057, and the Office of Naval Research (ONR), Grant 08PRO2615-00/N00014-08-1-0324. We thank Dr. A. Nikitin for providing us Fig. 14.4 and his encouragement.

References

1. A.C. Dillon et al., Storage of hydrogen in single-walled carbon nanotubes. Nature **386**, 377 (1997)
2. P. Chen et al., High H_2 uptake by alkali-doped carbon nanotubes under ambient pressure and moderate temperatures. Science **285**, 91 (1999)
3. D.J. Browning et al., Studies into the storage of hydrogen in carbon nanofibers: Proposal of a possible reaction mechanism. Nano Lett. **2**, 201 (2002)
4. S. Iijima, Helical microtubules of graphitic carbon. Nature **354**, 56 (1991)
5. S. Iijima, T. Ichihashi, Single-shell carbon nanotubes of 1-nm diameter. Nature **363**, 603 (1993)
6. D.S. Bethune et al., Cobalt-catalysed growth of carbon nanotubes with single-atomic-layer walls. Nature **363**, 605 (1993)
7. V. Barone et al., Interaction of atomic hydrogen with single-walled carbon nanotubes: A density functional theory study. J. Chem. Phys. **120**, 7169 (2004)
8. J. Li et al., Theoretical evaluation of hydrogen storage capacity in pure carbon nanostructures. J. Chem. Phys. **119**, 2376 (2003)
9. S.S. Han, H.M. Lee, Adsorption properties of hydrogen on (10, 0) single-walled carbon nanotube through density functional theory. Carbon **42**, 2169 (2004)
10. F.H. Yang et al., Adsorption of spillover hydrogen atoms on single-wall carbon nanotubes. J. Phys. Chem. B **110**, 6236 (2006)
11. H.-S. Kim et al., Hydrogen storage in Ni nanoparticle-dispersed multiwalled carbon nanotubes. J. Phys. Chem. B **109**, 8983 (2005)
12. A. Ansón et al., Hydrogen capacity of palladium-loaded carbon materials. J. Phys. Chem. B **110**, 6643 (2006)
13. A. Nikitin et al., Hydrogenation of single-walled carbon nanotubes. Phys. Rev. Lett. **95**, 225507 (2005)
14. B.N. Khare et al., Functionalization of carbon nanotubes using atomic hydrogen from a glow discharge. Nano Lett. **2**, 73 (2002)
15. P. Ruffieux et al., Hydrogen adsorption on sp^2-bonded carbon: Influence of the local curvature. Phys. Rev. B **66**, 245416 (2002)
16. O. Wessely et al., Dynamical core-hole screening in the x-ray absorption spectra of hydrogenated carbon nanotubes and graphene. Phys. Rev. B **76**, 161402 (2007)
17. G. Zhang et al., Hydrogenation and hydrocarbonation and etching of single-walled carbon nanotubes. J. Am. Chem. Soc. **128**, 6026 (2006)
18. G. Chiarello et al., Vibrational and electronic properties of hydrogen adsorbed on single-wall carbon nanotubes. Phys. Rev. B **69**, 153409 (2004)
19. S. Pekker et al., Hydrogenation of carbon nanotubes and graphite in liquid ammonia. J. Phys. Chem. B **105**, 7938 (2001)
20. K.P. Meletov et al., Raman study of the high-pressure hydrogenated single-wall carbon nanotubes: In search of chemically bonded and adsorbed molecular hydrogen. Chem. Phys. Lett. **433**, 335 (2007)
21. T.C. Dinadayalane et al., Chemisorption of hydrogen atoms on the sidewalls of armchair single-walled carbon nanotubes. J. Phys. Chem. C **111**, 7376 (2007)
22. A. Kaczmarek et al., Effect of tube length on the chemisorptions of one and two hydrogen atoms on the sidewalls of (3, 3) and (4, 4) single-walled carbon nanotubes: A theoretical study. Int. J. Quantum Chem. **107**, 2211 (2007)
23. L. Chen et al., Mechanistic study on hydrogen spillover onto graphitic carbon materials. J. Phys. Chem. C **111**, 18995 (2007)
24. T. Yildirim et al., First-principles investigation of structural and electronic properties of solid cubane and its doped derivatives. Phys. Rev. B **62**, 7625 (2000)

25. T. Yildirim et al., Pressure-induced interlinking of carbon nanotubes. Phys. Rev. B **62**, 12648 (2000)
26. S.P. Chen et al., Chemisorption of hydrogen molecules on carbon nanotubes under high pressure. Phys. Rev. Lett. **87**, 205502 (2001)
27. K.A. Park et al., Adsorption of atomic hydrogen on single-walled carbon nanotubes. J. Phys. Chem. B **109**, 8967 (2005)
28. T. Yildirim et al., Exohydrogenated single-wall carbon nanotubes. Phys. Rev. B **64**, 075404 (2001)
29. X. Yang, J. Ni, Calculations of hydrogen coverage on single-walled carbon nanotubes: Dependence on nanotube size, temperature, and pressure. Phys. Rev. B **74**, 195437 (2006)
30. M. Svensson, ONIOM: A multilayered integrated MO + MM method for geometry optimizations and single point energy predictions. A test for Diels–Alder reactions and $Pt(P(t\text{-}Bu)_3)_2 + H_2$ oxidative addition. J. Phys. Chem. **100**, 19357 (1996)
31. C.W. Bauschlicher Jr., High coverage of hydrogen on a (10, 0) carbon nanotube. Nano Lett. **1**, 223 (2001)
32. C.W. Bauschlicher Jr., Hydrogen and fluoride binding to the sidewalls of a (10, 0) carbon nanotube. Chem. Phys. Lett. **322**, 237 (2000)
33. J.S. Arellano et al., Interaction of molecular and atomic hydrogen with (5, 5) and (6, 6) single-wall carbon nanotubes. J. Chem. Phys. **117**, 2281 (2002)
34. G. Chen et al., Theoretical study of the adsorption of H_2 on (3, 3) carbon nanotubes. Phys. Rev. B **72**, 045444 (2005)
35. G.E. Froudakis, Hydrogen interaction with single-walled carbon nanotubes: A combined quantum-mechanics/molecular-mechanics study. Nano Lett. **1**, 179 (2001)
36. G. Jia et al., Electronic structures and hydrogenation of a chiral single-wall (6, 4) carbon nanotube: A density functional theory study. Chem. Phys. Lett. **418**, 40 (2006)
37. M.J. Frisch et al., Gaussian 03, Revision C.02 (Gaussian, Wallingford, 2004)
38. A.P. Scott, L. Radom, Harmonic vibrational frequencies: An evaluation of Hartree-Fock, Møller-Plesset, quadratic configuration interaction, density functional theory, and semiempirical scale factors. J. Phys. Chem. **110**, 16502 (1996)
39. T.C. Dinadayalane, J. Leszczynski, Stone-Wales defects with two different orientations in (5, 5) single-walled carbon nanotubes: A theoretical study. Chem. Phys. Lett. **434**, 86 (2007)
40. A.J. Lu, B.C. Pan, Interaction of hydrogen with vacancies in a (12, 0) carbon nanotube. Phys. Rev. B **71**, 165416 (2005)
41. S. Dag et al., Adsorption and dissociation of hydrogen molecules on bare and functionalized carbon nanotubes. Phys. Rev. B **72**, 155404 (2005)
42. P.O. Krasnov, Clustering of Sc on SWNT and reduction of hydrogen uptake: Ab-initio all-electron calculations. J. Phys. Chem. C **111**, 17977 (2007)
43. X. Pei et al., Effects of different hydrogen distributions on the magnetic properties of hydrogenated single-walled carbon nanotubes. Phys. Rev. B **73**, 195417 (2006)
44. G. Zheng et al., Transition of single-walled carbon nanotubes from metallic to semiconducting in field-effect transistors by hydrogen plasma treatment. Nano Lett. **7**, 1622 (2007)
45. T.C. Dinadayalane, J. Leszczynski, Toward Nanomaterials: Structural, Energetic and Reactivity Aspects of Single-Walled Carbon Nanotubes, in *Nanomaterials: Design and Simulation*, ed. by P.B. Balbuena, J.M. Seminario (Elsevier, Amsterdam, 2007), p. 167

Chapter 15
Quantum Monte Carlo for Electronic Structure

William A. Lester Jr.

Abstract It is anticipated that quantum Monte Carlo methods will experience a tremendous growth in usage with the need for high accuracy in the determination of the electronic structure of atoms, molecules, and solids in increasingly more complicated systems. Complexity arising in biological systems, nanosystems in a variety of geometries, and a range of chemical composition will dictate the use of these methods because they provide the capability of rapid adaptation to large multiprocessor computing environments.

15.1 Introduction

Monte Carlo methods employ random numbers to solve problems. The range of problems that may be treated by Monte Carlo is large. These include simulation of physical (and other) processes, integration of multi-dimensional integrals, and applications in statistical mechanics; see, for example [1, 2]. The treatment of problems arising in the field of quantum mechanics using Monte Carlo is generally referred to as quantum Monte Carlo (QMC); see, for example [3–5].

The equation that, in principle, describes the behavior of electrons in atoms and molecules is the Schrödinger equation (SE). This equation can only be solved exactly for the simplest atom, namely, hydrogen. This circumstance has led to major intellectual efforts to obtain increasingly more accurate solutions to this equation for systems of a wide variety of interest. The SE is a partial differential equation in $3n+3N$ variables. Here n refers to the number of electrons, and N gives the number of nuclei of the system. For atoms, the number of nuclei is trivial, but

W.A. Lester Jr. (✉)
Department of Chemistry, Kenneth S. Pitzer Center for Theoretical Chemistry, University of California, Berkeley, CA 94720-1460 and Chemical Sciences Division, Lawrence Berkeley National Laboratory, Berkeley, California 94720, USA
e-mail: walester@lbl.gov

J. Leszczynski and M.K. Shukla (eds.), *Practical Aspects of Computational Chemistry*,
DOI: 10.1007/978-90-481-2687-3_15,

for molecules, this number can become quite large even reaching hundreds. In the latter case, the number of electrons can be many times larger as one sees immediately in thinking of molecules in terms of constituent atoms. In many instances, a major simplification can be introduced owing to the fast motion of electrons compared to the much slower movement of heavier nuclei. This is the essence of the Born–Oppenheimer (BO) approximation [6] that treats nuclei as fixed in positions about which the electrons of the system move. The BO approximation makes possible the separation of the total SE for a molecular system into an SE for electronic motion that describes the motion of the electrons moving about the nuclei, and a nuclear SE that describes the motion of the nuclei.

The present discussion is focused on approaches for solving the electronic SE for molecular systems using QMC methods. Note that QMC methods, differing in some details, are used to solve the nuclear SE [7, 8]. Attempts to solve the electronic SE have a long history dating back to the advent of quantum mechanics [9]. A major stumbling block to the advancement of the field was the evaluation of integrals of the electron repulsion operator r_{ij}^{-1} of the Hamiltonian that arise in the computation of the expectation value of the energy. The mathematical structure of these integrals is of a form that no efficient procedure could be identified to carry out the evaluation for polyatomic molecules unless the wave function was written as a product of one-electron functions or orbitals. This meant that no wave function could be expressed explicitly in terms of functions dependent on the relative positions of the electrons, if the system had more than two electrons. During the period of these developments, orbitals were expressed as exponential functions (Slater type orbitals, STOs) [6, 9], which have the property of being solutions to the central field problem for atoms, i.e., a potential that depends only on the distance of an electron from the nucleus. For molecular applications, it is more convenient to use Gaussian type orbitals (GTOs) that lead to integrals that can be readily evaluated unlike those encountered using STOs for many-center molecules [6, 9].

In years past, considerable effort went into the construction of wave functions. A form that was of high interest and remains so because of its mathematical structure is a single determinant. The method that yields the best single determinant wave function is the Hartree–Fock (HF) approximation. The latter approach retains interest because the problem is well defined as that of a system in which each of the n electrons of the system moves in the field of the $n-1$ other electrons of the system. The difference between the energy resulting from the solution of the HF equations, i.e., the HF energy, and the exact nonrelativistic energy defines another important energy of the molecular system, called the correlation energy. The amount of correlation energy recovered in a calculation provides a measure of the quality of a post-HF approach, i.e., a method that goes beyond the HF method by taking into account dependence of electron motion on other electrons of the system [6, 9].

The post-HF approaches that have been pursued have typically taken two forms. One is based on the variational principle in which the lowest energy of the system can be obtained by varying parameters of an assumed functional form [6, 9]. The other approach is perturbation theory, which in its early development, was based on using the solutions of a known system to obtain the energy of a system that did not differ much from the known system.

Recent perturbation theory developments are given in the form of either Moeller–Plesset expansions [6, 9] or coupled cluster expansions [6, 9]. The latter approaches now generate some of the most accurate energies for many-electron systems. However, the accuracy of variational and CC methods is determined by the one-particle (basis set) and the many-particle (determinants or configuration state functions) expansions employed. Because the latter are slowly convergent in an orbital representation, computational cost and storage demands can grow quickly with expansion length and limit the size of systems that can be treated to high accuracy. Despite these problems, much success has been achieved with these methods because the errors arising with them are reasonably well understood, leading often to consistent cancelations and reliable calibration of errors.

In light of the success of the CC approaches, why then is there interest in QMC methods? The main reason is that QMC methods have been found to be as accurate as CC methods, but scale better with system size than CC methods. The scale factor for the latter is 7 or higher which is to be compared with cubic dependence for QMC. Recent advances have reduced the dependence for QMC to less than cubic [10–14].

Another aspect that makes QMC appealing is that at present, the fastest computers available for the largest calculations derive their speed from the concurrent use of many processors. The CC methods are currently unable to take efficient advantage of these systems owing to required communication between processors. Although QMC has a smaller scale factor with system size, the linear coefficient of the scale factor is large leading to relatively high computational requirements.

15.2 The QMC Method

The application of QMC to the electronic structure of atoms and molecules began with the work of Anderson in the mid-1970s [15]. The major difference between QMC and expansion methods is the QMC determination of the energy as an average over points representing solutions to the SE. In some cases, such as the ground states of H_2 and He, the exact solution is directly obtained unlike expansion approaches that require many-parameter wave functions of high complexity to achieve the exact solution. The precision of QMC is determined by how accurately the exact wave function can be approximated. With QMC systems beyond two-electron ground states, the quality of the calculation as measured by the energy is directly connected with the nodes of the many-electron wave function, as will be discussed. Much has been achieved with the QMC method in the computation of energies and selected other properties for atoms and molecules [16, 17].

There are a number of QMC approaches being pursued that are variously labeled as variational MC (VMC), diffusion MC (DMC), auxiliary field QMC [18], and reptation QMC [19]. The methods that have found the most application to molecules are the leading two listed; and these will be the focus of further comments.

15.2.1 Variational Monte Carlo

The variational method of quantum chemistry for the determination of the energy has a direct analog in QMC. This is a consequence of the capability of the MC method to perform integration, and should not be confused with MC integration of the integrals that arise in basis set expansion methods. An important branch of QMC is the development of compact and accurate wave functions characterized by explicit dependence on interparticle distances: electron–electron and electron–nucleus that are typically written as a product of an independent particle function and a correlation function. Such wave functions lead one immediately to the VMC method for evaluation [3–5]. Wave functions constructed following VMC can also serve as importance functions for the more accurate DMC variant of QMC.

To evaluate an expectation value with the VMC method, a Metropolis walk is generally employed [20, 21]. The procedure begins with an initial distribution of points generated using a wave function obtained from an independent electronic structure method, followed by selection of subsequent sets of points until the collection of points is distributed as mod squared of the trial wave function, i.e., $|\Psi_T^2|$. This convergence step is rapid and generally poses little problem. Additional points are sampled to compute expectation values. The chief difficulty lies typically in high serial correlation in a statistical sense among sampled points. To the extent correlation exists, efficiency in computing expectation values is reduced. Despite such correlation, VMC computations employing this approach are relatively inexpensive. A simple algorithm given by Reynolds et al. [22] is quite suitable. More recently, Umrigar et al. have developed an improved Metropolis walk [23].

15.2.2 Diffusion Monte Carlo

We now turn to approaches that begin with an arbitrary initial function and can, in principle, be iterated to an exact or accurate solution of the SE. The earliest approach is Green's function Monte Carlo (GFMC) in which the time-independent Schrödinger equation is employed [24]; DMC was developed later and follows from the time-dependent SE (TDSE) in imaginary time.

The DMC method achieves the lowest-energy eigenfunction by employing the quantum mechanical evolution operator in imaginary time [25]. For an initial function expanded in eigenstates, one finds that contributions of the excited states decay exponentially fast with respect to the ground state.

It was recognized early that using information about a distribution function improves the efficiency of a Monte Carlo calculation [1]. This is importance sampling, which carries over to QMC where the trial wave function serves as an importance function that produces improved sampling. Into the late 1980s, the most common form of QMC trial wave function was a product of an approximate HF function and a correlation function, i.e., a function explicitly dependent on

interparticle distance. With increased experience, it became clear that improved results and better precision required more complex trial functions typically given by compact multi-determinant functions constructed following configuration interaction, multi-configuration HF and complete active space approaches.

15.2.2.1 Importance Sampling

The GFMC and DMC methods benefit in the same way from importance sampling. The idea is to choose a trial function Ψ_T resembling the desired state, form a new function that is a product of the known trial function and the unknown exact wave function of the system. This new distribution f is governed by the differential equation obtained from the TDSE in imaginary time by multiplying the TDSE by the known function, and then expressing the resultant equation in terms of the distribution f.

Three terms result from this procedure: one arising from the kinetic energy operator that can be associated with diffusion if f is positive definite, another term that involves a gradient of a function that has the effect of moving the system from regions of high potential to low potential, and a third term that describes a first-order rate process. A benefit that results from importance sampling is that the first-order rate process is governed by the difference of a reference energy and the local energy where the local energy has replaced the Coulomb potential of the TDSE.

15.2.2.2 Trial Functions

The trial function plays a crucial role in DMC. The most significant properties of the trial function are the average of the local energy, given by $H\Psi_T(R)/\Psi_T(R)$, i.e., the VMC energy, and its smoothness, which is reflected in the statistical variance. As the VMC energy approaches the exact energy, the trial function approaches the eigenfunction for the given state of the system. As the variance approaches zero, the local energy becomes constant and an eigenfunction is obtained. The VMC energy and the variance are important measures of trial function quality.

As improved trial functions were developed, simple optimization methods for obtaining parameter values were no longer adequate. The most common application is minimization of local energy fluctuations about a reference energy chosen as, or close to, an estimate of the nonrelativistic BO energy. The motivation is that the local energy approaches the exact energy as the trial function approaches the exact function.

It may seem that minimization of the energy should be a valid approach to trial function optimization. As it turns out, minimization of the energy using a fixed sample is problematic because it is easy for a few very low energies to dominate the sample. In this case, the optimization is not reliable and a good trial function is not obtained. This is not a concern in variance minimization because the variance is bounded from below by zero. However, even for variance minimization, care

must be taken in varying linear coefficients of the determinants and linear and nonlinear orbital parameters because they affect the nodes that are of particular importance for reasons that will be discussed next.

15.2.2.3 The Fixed-Node Approximation

A way to sample the fermion ground state without approximation is to choose a nodal structure and to attach a sign to each walker that changes when a node is crossed. After sufficient simulation, the lowest-energy state with nodes due to antisymmetry will be obtained. Unfortunately, the distribution describing the ground state is the difference between a positive distribution and a negative distribution. This gives rise to instability because the time dependence of the fermionic distribution and therefore, that of the fermion ground state are obtained as the difference between two bosonic populations. As a consequence, the fermion ground state possesses statistical error that increases exponentially fast with imaginary time. Although methods have been proposed and implemented that seek to reduce this instability, the node problem has prevented exact treatments with small statistical error for systems containing atoms beyond Li in the periodic table.

The other option for finding an antisymmetric ground state is stable, but approximate. It was pioneered by Anderson and requires the solution to vanish at predetermined nodes by not allowing the walk to cross a node [25]. This approach is termed fixed-node DMC and is a procedure in which the random walk is not allowed if, as a consequence, f changes sign. The ground state is not represented as the difference between two unconfined bosonic distributions; instead, it is given as a set of bosonic distributions, each confined within a nodal volume. These confined distributions are independent of each other and are found by solving the SE within each volume. In most applications, the nodal structure is chosen to be that of the trial function. In this case, the trial function determines accuracy as well as precision.

The important point is that the accuracy of the nodal structure determines the accuracy of the sampled solution. Since symmetry requirements only partially specify nodal structure, nodes cannot be fully specified except for the simplest cases. The inability to specify exactly the nodes of the wave function leads to error in solutions to the SE and the computed energy, referred to as the fixed-node error. It has been shown that the fixed-node energy is an upper bound to the exact ground-state energy [22].

15.2.2.4 Excited States

Although the previous discussion has focused on ground states, the DMC method can also be applied to the calculation of electronically excited states. This is most simply achieved using the fixed-node approximation. Note that the ground state of a fermion system is itself an excited state. It is the lowest antisymmetric state of the system.

When using a trial function in the fixed-node approximation, the DMC solution will have nonzero overlap with the trial function. To obtain excited state antisymmetric wave functions require an antisymmetric trial function that has no overlap with the electronic ground state. If the excited state is of a different symmetry than the ground state, all that is required of the trial function is that it has the symmetry of the excited state. In this case, the computed energy will be an upper bound to the exact energy. When the desired state is not the lowest state of a given symmetry, good results have been computed using a trial function that is a good approximation to the state of interest obtained using available ab initio expansion methods [26]. The energy from this procedure is not an upper bound to the excited state of interest and care must be exercised in its implementation. A trial function approximating this state is useful, but the variational principle no longer holds.

15.2.2.5 Pseudopotentials in QMC

Atoms beyond the first row of the periodic table and molecules containing such atoms are commonly treated in QMC by an approach that avoids explicit consideration of core electrons; see, for example [3, 27]. The reason is the very considerable increase in computer time imposed by core electrons. For many properties of chemical interest, core electrons play a relatively minor role. The origin of the increase of computer time has been analyzed in various ways, but a major factor is differing time scales for valence and core electrons [28–30]. Just as pseudopotentials can serve to reduce the computational effort in basis set methods, they play an equivalent, if not more after important, role in QMC because of the heavy computational demands of sampling core electrons relative to valence electrons.

15.3 Applications of DMC

The most widely computed quantity by DMC approaches is the total energy. Following are a couple of findings that provide insight on the capability of the DMC method.

15.3.1 O_4

The O_4 species has relevance for atmospheric processes. A recent DMC study has addressed the difficulties in describing the passage from a singlet O_4 reactant to two ground state O_2 triplet products [31]. The authors carefully addressed the issue of accurate differences of total energies for barriers and other properties. In this study, the exceptional step was taken of varying the multi-reference character of the nodes that made possible very high accuracy for energy differences.

15.3.2 Free Base Porphyrin

Accurate DMC calculations of allowed and nonallowed transitions in porphyrin have been reported [32]. The vertical transition between the ground state singlet and the second excited state singlet as well as the adiabatic transition between the ground state and the lowest triplet state were computed for this 162-electron system. The DMC results were found to be in excellent agreement with experiment.

15.3.3 EPLF for Spheroidene

To understand chemical processes, it is useful to have information besides total energies. Electron localization methods provide insight on the behavior of electrons in molecules. Properties, such as electron density, spin density, and the electron pair localization function (EPLF) [33], can routinely be computed by post-processing. The EPLF provides a quantitative description of electron pairing in molecular systems and has similarities to the electron localization function (ELF) of Becke and Edgecombe [34]. The QMC method is a particularly well-suited approach for obtaining such information because the simple and general definition of EPLF is easily evaluated in QMC.

Figure 15.1 represents slices of the EPLF function for the carotenoid spheroidene in the ground state singlet and the first-excited triplet state in the $z=0$ plane. The different values represent the different levels of electron pair localization for that particular region, larger values indicate higher degree of localization. Most of the EPLF values obtained for this system are less than 0.1, which indicates a high level of delocalization due to its conjugated polyene structure. Important differences can be seen between the singlet and the triplet state. While the singlet appears to have no spin-polarized (gray) regions, the triplet state does possess such regions near the outer boundary of the molecule. Gray regions show where excess alpha electron density is paired.

15.4 Closing Statement

In this chapter, I have provided a brief overview of the QMC method for electronic structure with emphasis on the more accurate diffusion Monte Carlo (DMC) variant of the method. The high accuracy of the approach for the computation of energies is emphasized, as well as the adaptability to large multiprocessor computers. Recent developments are presented that shed light on the capability of the method for the computation of systems larger than those accessible by other first principles quantum chemical methods.

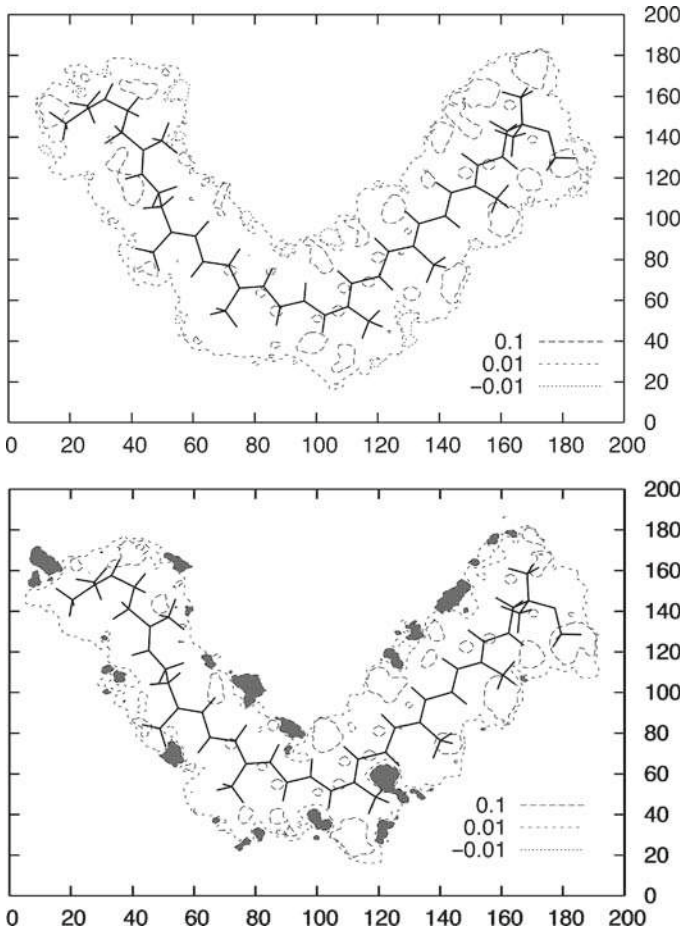

Fig. 15.1 Plot of the $z=0$ plane of the electron pair localization function (EPLF) function values for Spo in the ground state singlet (*top*), and the triplet state (*bottom*). The triplet state shows spin-polarized regions (*dark gray*) that are absent in the singlet state. The EPLF domain for both plots is $[-0.1{:}0.1]$.

Acknowledgments This research was supported by the Director, Office of Science, Office of Basic Energy Sciences, Chemical Sciences Division of the U.S. Department of Energy under Contract No. DE-AC03-76SF00098, and by the U.S. National Science Foundation under grant 0809969. Sect. 15.3.3 was taken from the author's publication: Austin et al. [35].

References

1. J.M. Hammersley, D.C. Handscomb, *Monte Carlo Methods* (Methuen, London, 1964)
2. M.H. Kalos, P.A. Whitlock, *Monte Carlo Methods* (Wiley, New York, 1986)

3. B.L. Hammond, W.A. Lester Jr., P.J. Reynolds, *Monte Carlo Methods in Ab Initio Quantum Chemistry* (World Scientific, Singapore, 1994)
4. A. Aspuru-Guzik et al., in Quantum Monte Carlo: Theory and Applications to Atomic, Molecular and Nano Systems, ed. by M. Rieth, W. Schommers. *Handbook of Theoretical and Computational Nanotechnology*, vol. 3 (American Scientific Publishers, Stevenson Ranch, CA, 2005), pp. 644–702
5. J.B. Anderson, *Quantum Monte Carlo* (Oxford, New York, 2007)
6. A. Szabo, N.S. Ostlund, *Modem Quantum Chemistry* (MacMillan, New York, 1982)
7. M.J.T. Jordan et al., in *Quantum Effects in Loosely Bound Complexes*. Proceedings of the Pacifichem Symposium on Advances in Quantum Monte Carlo. ACS Symposium Series, ed. by J.B. Anderson, S.M. Rothstein, vol. 953 (American Chemical Society, Washington, DC, 2007), pp. 101–140
8. A.B. McCoy, in *Vibrational Excited States by Diffusion Monte Carlo*. Proceedings of the Pacifichem Symposium on Advances in Quantum Monte Carlo. ACS Symposium Series, ed. by J.B. Anderson, S.M. Rothstein, vol. 953 (American Chemical Society, Washington, DC, 2007), pp. 147–164
9. L. Piela, *Ideas of Quantum Chemistry* (Elsevier, New York, 2007)
10. A.J. Williamson et al., Linear-scaling quantum Monte Carlo calculations. Phys. Rev. Lett. **87**, 246406 (2001)
11. S. Manten, A. Lüchow, Improved Scaling in Diffusion Quantum Monte Carlo with Localized Molecular Orbitals, in *Quantum Monte Carlo Methods, Part II*, ed. by S.M. Rothstein, W.A. Lester Jr., S. Tanaka (World Scientific, Singapore, 2002), pp. 30–40
12. S. Manten, A. Lüchow, Linear scaling for the local energy in quantum Monte Carlo. *J. Chem. Phys.* **119**, 1307–1312 (2003)
13. A. Aspuru-Guzik et al., A sparse algorithm for the evaluation of the local energy in quantum Monte Carlo. J. Comp. Chem. **26**, 708–715 (2005)
14. A. Aspuru-Guzik et al., Zori 1.0: A parallel quantum Monte Carlo electronic package. J. Comp. Chem. **26**, 856–862 (2005)
15. J.B. Anderson, A random-walk simulation of the Schrödinger equation: H_3^+. *J. Chem. Phys.* **63**, 1499–1503 (1975)
16. A. Lüchow, J.B. Anderson, Monte Carlo methods in electronic structures for large systems. Ann. Rev. Phys. Chem. **51**, 501–526 (2000)
17. W.M.C. Foulkes et al., Quantum Monte Carlo simulations of solids. Rev. Mod. Phys. **73**, 33–83 (2001)
18. W.A. Saidi, S. Zhang, H. Krankauer, Bond breaking with auxiliary field quantum Monte Carlo. J. Chem. Phys. **127**, 144101 (2007) (and references contained therein)
19. W.K. Yuen, T.F. Farrar, S.M. Rothstein, No-compromise reptation quantum Monte Carlo. J. Phys. A: Math. Theor. **40**, F639–F646 (2007) (and references contained therein)
20. N. Metropolis et al., Equation of state calculations by fast computing machines. *J. Chem. Phys.* **21**, 1087–1092 (1953)
21. D. Bressanini, P.J. Reynolds, Between classical and quantum Monte Carlo methods: "Variational" QMC. Adv. Chem. Phys. **105**, 37 (1998)
22. P.J. Reynolds et al., Fixed-node quantum Monte Carlo for molecules. J. Chem. Phys. **77**, 5593–5603 (1982)
23. C.J. Umrigar, M.P. Nightingale, K. Runge, A diffusion Monte Carlo algorithm with very small time-step errors. J. Chem. Phys. **99**, 2865–2890 (1993)
24. J.W. Moskowitz, K.E. Schmidt, *Can Monte Carlo Methods Achieve Chemical Accuracy? Monte Carlo Methods in Quantum Problems* (Reidel, Dordrecht, 1982), pp. 59–70
25. J.B. Anderson, Quantum chemistry by random walk. H ^{2}P, H_3^+ D_{3h} ^{1}A'$_1$, H_2 $^3\Sigma_u^+$, H_4 $^1\Sigma_g^+$, Be ^{1}S. J. Chem. Phys. **65**, 4121–4127 (1976)
26. R.M. Grimes et al., Quantum Monte Carlo approach to electronically excited molecules. J. Chem. Phys. **85**, 4749–4750 (1986)

27. M. Burkatzki, C. Filippi, M. Dolg, Energy-consistent pseudopotentials for quantum Monte Carlo calculations. J. Chem. Phys. **126**, 234105 (2007) (and references contained therein)
28. D.M. Ceperley, The statistical error of green's function Monte Carlo. J. Stat. Phys. **43**, 815–826 (1996)
29. M.M. Hurley, P.A. Christiansen, Relativistic effective potentials in quantum Monte Carlo calculations. J. Chem. Phys. **86**, 1069–1070 (1987)
30. B.L. Hammond, P.J. Reynolds, W.A. Lester Jr., Valence quantum Monte Carlo with ab initio effective core potentials. J. Chem. Phys. **87**, 1130–1136 (1987)
31. M. Caffarel et al., Multireference quantum Monte Carlo study of the O_4 molecule. Phys. Rev. Lett. **99**, 153001 (2007)
32. A. Aspuru-Guzik et al., Quantum Monte Carlo for electronic excitations of free-base porphyrin. J. Chem. Phys. **120**, 3049–3050 (2004)
33. A. Scemama, P. Chaquin, M. Caffarel, Electron pair localization function: A practical tool to visualize electron localization in molecules from quantum Monte Carlo data. *J. Chem. Phys.* **121**, 1725–1735 (2004)
34. A.D. Becke, K.E. Edgecombe, A simple measure of electron localization in atomic and molecular systems. J. Chem. Phys. **92**, 5397–5403 (1990)
35. B. Austin et al., in *Linear-Scaling Evaluation of the Local Energy in Quantum Monte Carlo*. Proceedings of the Pacifichem Symposium on Advances in Quantum Monte Carlo. ACS Symposium Series, ed. by J.B. Anderson, S.M. Rothstein, vol. 953 (American Chemical Society, Washington, DC, 2007), pp. 55–68

Chapter 16
Sequential Monte Carlo and Quantum Mechanics Calculation of the Static Dielectric Constant of Liquid Argon

Kaline Coutinho and Sylvio Canuto

Abstract A combined and sequential use of Monte Carlo simulation and quantum mechanics calculations is made to obtain the static dipole polarizability, and the related dielectric constant of atomic argon, in the liquid phase. Using Metropolis Monte Carlo simulation, within the NPT ensemble, the structure of liquid argon is obtained at $T = 91.8$ K and $P = 1.8$ atm. Seventy statistically relevant configurations are sampled for quantum mechanical calculations of the static dipole polarizability. Each configuration is composed of 14 Ar atoms, corresponding to the first solvation shell. Using these structures' density-functional theory, calculations are performed within the B3P86 hybrid functional and the aug-cc-pVDZ basis set to obtain statistically converged values for the dipole polarizability. Three different models are used to extract the polarizability per atom. From the calculated density and dipole polarizability, the static dielectric constant is obtained using the simple Clausius-Mossotti relation. Our best result indicates a dipole polarizability of 11.6 a_0^3 and a dielectric constant of 1.52 in agreement with an experimentally available result of 1.53.

16.1 Introduction

In recent years, there has been an increased need for a proper treatment of the effects of a surrounding medium on the electronic properties of a probe atomic, molecular or biomolecular system. Great progress has been obtained with continuum models [1–5], wherein the solvent is described in some average way and represented by its macroscopic constants. Although successful in some cases, the statistical nature of the liquid environment is not considered in such models.

K. Coutinho and S. Canuto (✉)
Instituto de Física, Universidade de São Paulo, CP 66318, São Paulo, SP 05315-970, Brazil
e-mail: canuto@if.usp.br

J. Leszczynski and M.K. Shukla (eds.), *Practical Aspects of Computational Chemistry*, 327
DOI: 10.1007/978-90-481-2687-3_16,

Furthermore, applications in the case of neutral atoms are more difficult because of the lack of electrostatic moments in the atom for describing the interaction with the environment. A proper treatment of liquid systems should consider its statistical nature [6, 7] as there are many possible geometrical arrangements accessible to the system at nonzero temperature. Thus, liquid properties are best described by a statistical distribution [8–11], and all properties are obtained from statistical averaging over ensembles. Thus, in this direction, it is important to use statistical mechanics, with some sort of computer simulation of liquids [6, 7], combined with quantum mechanics to obtain the electronic property of interest.

In this chapter, we use the sequential Monte Carlo quantum mechanics (S-MC/QM) methodology [12–15] to calculate the static dielectric constant of liquid argon. We first generate the structure of the liquid using Metropolis Monte Carlo. Next, statistically relevant configurations are separated and submitted to quantum mechanical calculations. Several QM calculations are necessary to obtain the ensemble average that is necessary to characterize the statistical nature of the liquid. Statistically converged results are obtained. The mean dipole polarizability of liquid argon is studied using density-functional theory (DFT) in the hybrid B3P86 exchange-correlation functional [16, 17]. Recent study at the Hartree-Fock level using extended basis set for the "solute" Ar atom and a modest basis set for the rest, the "solvent" Ar atoms[18], suggested a minor decrease of ~2% compared to the gas phase situation. Later [19] we have also dedicated to the calculation of the dipole polarizability of liquid argon using the B3P86/aug-cc-pVDZ model and obtained that the polarizability in the liquid situation got slightly increased by 5%. In this work, we extend our studies using different and complementary models to the calculation of the dipole polarizability of liquid argon and use these to obtain a theoretical value of the static dielectric constant.

16.2 Methods

16.2.1 Monte Carlo Simulation

The Monte Carlo (MC) simulation is performed using standard procedures [7] for the Metropolis sampling technique in the NPT ensemble. We use the image method combined with the periodic boundary conditions of a cubic box. We use 500 Ar atoms at $T = 91.8$ K and $P = 1.8$ atm. The atoms interact by the Lennard-Jones potential with parameters, ε=0.2378 kcal mol^{-1} and, $\sigma = 3.41$ Å, developed and tested by Maitland and Smith [20]. In the calculation of the pair-wise energy, each atom interacts with all others within a separation that is smaller than the half size of the box. For separations larger than this, we evaluate the long range correction using the pair radial distribution function [7], G(r)$\approx$1. One MC step is concluded after selecting one atom randomly and trying to translate it in all the Cartesian

directions. The maximum allowed displacement of the atoms is auto-adjusted to give an acceptance rate of new configurations around 50%. The simulation was performed with the DICE program [21].

The simulation involves first, a thermalization stage, which is then followed by an averaging stage of 10.5×10^6 MC steps. Radial distribution functions and liquid configurations are also generated during the averaging stage of the simulation. After completing the cycle over all 500 atoms, a configuration of the liquid is generated and separated. Thus, the total number of configurations generated by the MC simulation is 21×10^3.

Quantum mechanical calculations are performed on these configurations generated by the MC simulation. As successive configurations are statistically correlated, they will not give important additional information to the average. Therefore, to sample efficiently the configurations for the subsequent QM calculations, we calculate the auto-correlation function of the energy [22, 23] to obtain the interval of statistical correlation. This interval represents the number of successive MC steps necessary to generate statistically uncorrelated configurations, i.e., configurations that have less than 13% of statistical correlation [12–15, 22, 23]. Then, from the 21×10^3 successive configurations generated by the MC simulation, we selected 70 statistically uncorrelated ones, separated by an interval of 300, that represent the entire simulation [22, 23]. This is a very efficient procedure to sample configurations and as we shall see, the statistically converged result for the dipole polarizability of liquid Ar is obtained already after the use of only 50 of these statistical uncorrelated configurations.

16.2.2 Quantum Mechanical Calculations

This chapter mostly deals with the calculation of the dipole polarizability, α, of Ar in the liquid phase, and therefrom, the dielectric constant, ε. To perform that, we made first-principle calculations over 70 selected configurations that composed of one Ar atom surrounded by the first solvation shell (n Ar atoms). As the appropriate Boltzmann weights are included in the Metropolis Monte Carlo sampling technique, the average value of the dipole polarizability, or any other property calculated from the MC configurations, is given as a simple average over all the values calculated for each configuration.

An important aspect in the study of the dipole polarizability of a reference molecule in solution is related to the separability problem, i.e., the distinction between the reference and the environment. Of course, the application of an external static homogeneous electrical field affects both the reference and the solvent molecules (in the present case, atoms). The use of response function, thus avoiding the external field, minimizes this problem, but still has the conceptual problem of distinguishing the solute and the solvent. It is normally assumed that a simple separability is a reasonable first approximation, particularly for weakly interacting systems. The *interaction* polarizability of weakly interactive systems

was analyzed before [24]. For a homogeneous liquid, this problem is perhaps less critical because one can define a dipole polarizability per molecule, provided a sufficiently large number of molecules is included. This, however, is seldom the case.

16.2.2.1 The Separability of the Dipole Polarizability

To calculate the average dipole polarizability, $\langle\alpha\rangle$, of the liquid Ar, we used three different theoretical models for partitioning the solute and solvent contributions. One should not be confused by the statistical average and the mean value of the dipole polazizability. The *mean* dipole polarizability comes from using the diagonal components of the polarizability tensor. The *average* dipole polarizability refers to the statistical distribution. Note that in the liquid case, the (statistical) average dipole polarizability is obtained from the distribution of individually calculated mean dipole polarizability of the different configurations sampled from the MC simulation.

Model 1: This model assumes the separability as an approximation, which has been successfully used before [18, 24–26]. In this model, the polarizability of a system X in the solution, $\alpha_{\mathrm{sln}}(X)$, is obtained from the polarizability of the solute + n solvent, $\alpha(X + n_{\mathrm{solv}})$, minus the polarizability of the solvent without the solute, $\alpha(0 + n_{\mathrm{solv}})$, i.e.:

$$\alpha_{\mathrm{sln}}(X) = \alpha(X + n_{\mathrm{solv}}) - \alpha(0 + n_{\mathrm{solv}}). \tag{16.1}$$

Note the two terms, $\alpha(X + n_{\mathrm{solv}})$ and $\alpha(0 + n_{\mathrm{solv}})$, are calculated for the same MC configurations and same theoretical models, but with and without the solute, respectively. Therefore, in the configuration without the solute, there is a vacancy in the center of the configuration, and the difference of these two terms gives the polarizability of the solute under the environment of the solvent. The separation is expected to work well for the cases where the interaction polarizability is small. This is expected to be the case of liquid argon.

Model 2: This model admits the use of a limited basis set and corrects for the superposition error according to the counterpoise method [27], as it is usually done in the calculation of binding energies. In this model, the polarizability of a system X in the solution, $\alpha_{\mathrm{sln}}{}^{\mathrm{CP}}(X)$, is obtained from the polarizability of the solute + n solvent, $\alpha(X + n_{\mathrm{solv}})$, minus the polarizability of the solvent without the solute, but leaving the basis set of the solute, $\alpha(\mathrm{BS\_}X + n_{\mathrm{solv}})$, i.e.:

$$\alpha_{s\,\mathrm{ln}}{}^{\mathrm{CP}}(X) = \alpha(X + n_{\mathrm{solv}}) - \alpha(\mathrm{BS\_}X + n_{\mathrm{solv}}). \tag{16.2}$$

This method was also used by Morita and Kato [18].

Model 3: This model can be used only in the case of homogeneous liquids, as it is the case here. Therefore, as the solute and the solvent are the same entity X, the

polarizability of a system X in the liquid phase, $\alpha_{liq}(X)$, is obtained dividing the polarizability of the $(1 + n)$ X, $\alpha(X + n_{solv})$, by $n + 1$, i.e.:

$$\alpha_{liq}(X) = \alpha(X + n_{solv})/(n + 1). \tag{16.3}$$

This is the method used in our earlier investigation [19].

A comparison between these three theoretical models will be made here. One aspect that should be emphasized is that the results reported are statistically converged, and therefore, statistical discrepancies are not included. All the QM calculations were made with the Gaussian98 program [28].

16.3 Results

16.3.1 The Structure of Liquid Argon

The structure of liquids can be analyzed by the calculated radial distribution function (RDF), which defines the solvation shells. In Fig. 16.1, the calculated RDF of the liquid Ar is shown, and in Table 16.1, the structure is compared with the experimental results. Four solvation shells are well defined. The spherical integration of these peaks defines the coordination number, or the number of atoms in each solvation shell. The first shell that starts at 3.20 Å has a maximum at 3.75 Å, and ends at 5.35 Å, has an average of 13 Ar atoms. Therefore, in the first solvation shell, there is a reference Ar atom surrounded by other neighboring 13 Ar atoms. All the maxima of the RDF, shown in Table 16.1, are in good agreement with the experimental results obtained by Eisenstein and Gingrich [29], using X-ray diffraction in the liquid Ar in the same condition of temperature and pressure. The calculated

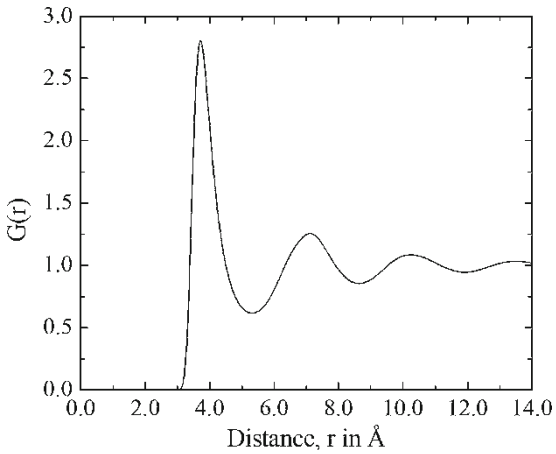

Fig. 16.1 The radial distribution function of liquid Ar

Table 16.1 Comparison of the calculated structure of liquid Argon with the experimental data obtained by X-ray diffraction in the same thermodynamic condition ($T = 91.8$ K and $P = 1.8$ atm)

	Solvation shell			
	First	Second	Third	Fourth
Experiment [29]	3.79 ± 0.05 Å	6.91 ± 0.05 Å	10.31 ± 0.05 Å	13.67 ± 0.05 Å
This work	3.75 ± 0.10 Å	7.05 ± 0.10 Å	10.25 ± 0.10 Å	13.55 ± 0.10 Å
Coordination (up to distance)	13 atoms (5.35 Å)	56 atoms (8.70 Å)	148 atoms (11.95 Å)	

The density obtained from the simulation is 1.362 ± 0.015 $g cm^{-3}$. The experimental density [29] is 1.365 $g cm^{-3}$

density is 1.362 ± 0.015 $g cm^{-3}$, in very good agreement with the experimental data of 1.365 $g cm^{-3}$ [29] obtained for the same thermodynamic condition. The results of Table 16.1, together with the calculated density, give a clear indication that the structure of liquid argon and the calculated density are very well described in our MC simulation. These structures are now used to obtain the average dipole polarizability and the dielectric constant of liquid argon. These results will give a clear indication of the importance of the polarization effects of argon in changing from the gas to the liquid phase.

16.3.2 Polarizability and Dielectric Constant of Liquid Argon

Before presenting the calculated results for the mean dipole polarizability in the liquid case, we first discuss the QM results for the isolated Ar atom. There has been a great interest in the dipole polarizability of Ar and it has been subjected to numerous theoretical investigations. As the largest system considered here is composed of 14 argon atoms, some compromising is necessary in the extension of the basis set. The present theoretical result for the dipole polarizability of the free Ar atom, $\alpha_{gas}(Ar)$, obtained with B3P86/aug-cc-pVDZ, is 9.98 a_0^3, and with B3P86/aug-cc-pVTZ, it is 11.08 a_0^3. The study by Lupinetti and Thakkar [30] gives a good account of previous studies and puts forward the recommended non-relativistic value for isolated Ar as 11.065 ± 0.05 a_0^3, which is indeed close to the experimentally suggested values of 11.070 ± 0.007 a_0^3[31] and 11.078 ± 0.010 a_0^3[32]. The recent study of Wheatley [33] using TD-CCSD, obtained the value of 11.1 a_0^3. The result using the aug-cc-pVDZ basis set is in acceptable agreement with experiment, involving an important saving in computational demands. For the largest case of explicit 14 Ar atoms, each QM calculation involves a total of 378 gaussian basis functions. Note that distributing basis functions over the explicit outer solvent atoms gives a diffuse representation for the reference argon atom.

Using the configurations extracted from the MC simulation, composed of 1 + 13 Ar atoms, corresponding to the first solvation shell, we calculated the dipole polarizability. A summary of the calculated results obtained for the polarizability of liquid Ar is presented in Table 16.2 for the three theoretical models used here. As it can be seen, all results for the liquid case are larger than the calculated value in the

Table 16.2 The calculated values of the dipole polarizability (in a_0^3) of Ar using the first solvation shell

Model 1	α(Ar + 13_Ar)	α(0 + 13_Ar)	α_{sln}(Ar)	ε^a
Solute (aug-cc-pVDZ)Solvent (aug-cc-pVDZ)	147.14 ± 0.06	135.55 ± 0.06	11.59 ± 0.04	1.519
Model 2	α(Ar + 13_Ar)	α(BS + 13Ar)	α_{sln}^{CP}(Ar)	
Solute (aug-cc-pVTZ)Solvent (6-31 + G(d))	94.39 ± 0.21	83.04 ± 0.21	11.35 ± 0.01	1.507
Model 3	α(Ar + 13_Ar)		α_{liq}(Ar)	
Solute (aug-cc-pVDZ)Solvent (aug-cc-pVDZ)	147.14 ± 0.06		10.51 ± 0.01	1.464

[a]Experimental result is $\varepsilon = 1.53$. Three different models of calculation are shown (see text). All calculations are performed with the B3P86 functional. Uncertainties are statistical errors. The corresponding result for the isolated atom is 9.98 a_0^3[32, 35]

gas phase. These results indicate that the dipole polarizability increases in the condensed phase. In Model 1, the calculated average value of the mean dipole polarizability in the liquid condition used here, gives the result of 11.59 a_0^3. This represents an increase of 16% compared to the result for isolated argon. Using Model 2 gives a value that is only slightly smaller, 11.35 a_0^3. Considering Model 3, one obtains the smaller value for the polarizability, suggesting that 14 argon atoms are not enough to represent the homogeneous liquid case as it involves a large number of peripheral atoms. It can be seen that all results are larger than the result of 10.33 a_0^3 obtained by Morita and Kato [18]. Model 1 with the value of $\langle\alpha\rangle = 11.59\ a_0^3$ is considered here our best result.

Before considering the dielectric constant, it is important to discuss the statistical reliability of the polarizability results. Statistical convergence of the dipole polarizability represents statistical convergence also for the dielectric constant derived from it. To demonstrate the statistical convergence, Fig. 16.2 shows the calculated average of the polarizability in Model 1, with increasing number of configurations used. As it can be seen, the results are converged after *ca*. 50 QM calculations. This is a consequence of the efficient sampling based on the use of statistically relevant configurations. In addition, Fig. 16.3 shows the histogram and the normal distribution of calculated values for the dipole polarizability. Also shown (below in Fig. 16.3) are all the 70 individually calculated values.

Having obtained statistically converged results for the dipole polarizability of liquid argon, we now consider the resulting values for the dielectric constant. Again, we use the three theoretical models and simply obtain the dielectric constant ε, from the dipole polarizability, using the Clausius-Mossotti equation [34]:

$$\frac{\varepsilon - 1}{\varepsilon + 1} = \frac{4\pi\alpha}{3}\rho\frac{N_A}{M}, \tag{16.4}$$

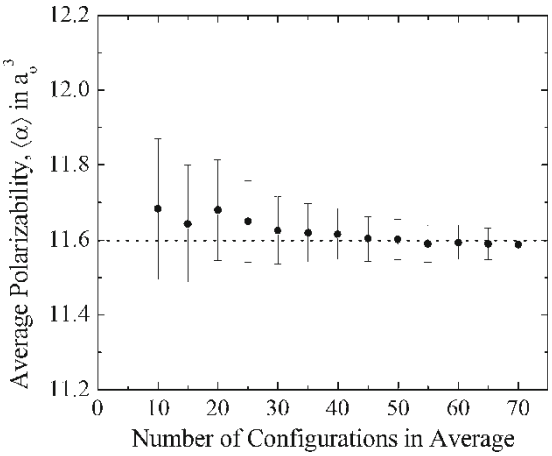

Fig. 16.2 Convergence of the average value of the mean dipole polarizability of liquid Ar using Model 1, with respect to the number of MC structures included in the quantum calculation. The error bars are the statistical error of the average

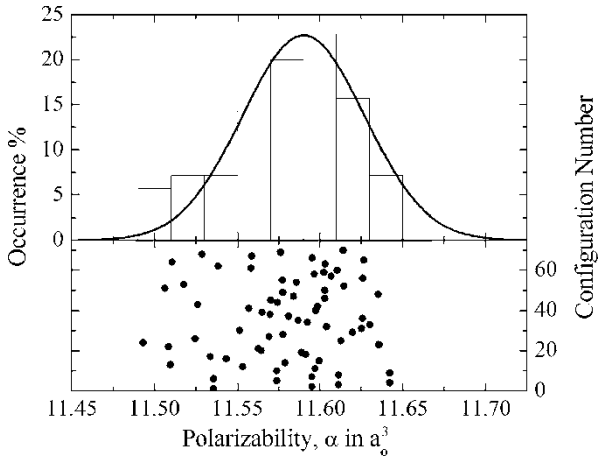

Fig. 16.3 Histogram and normal distribution of calculated values for the dipole polarizability of liquid Ar, using Model 1. Average polarizability is $\langle\alpha\rangle$=11.59 a_0^3 and statistical error s=0.03 a_0^3. Also shown (below) are the individually calculated mean dipole polarizabilities of the different configurations used

where α is the calculated dipole polarizability, ρ is the calculated density, M is the molar mass and N_A is Avogadro number. The results for the calculated dielectric constants are also shown in Table 16.2, along with the corresponding polarizability values. The result of 11.59 a_0^3 leads to a dielectric constant of 1.52. There is apparently no experimental result at the same thermodynamic condition ($P = 1.8$ atm, $T = 91.8$ K). However, this value of ε is in excellent agreement with the available experimental result [35] of 1.53, obtained in close condition ($P = 1.0$ atm, $T = 87.4$ K).

16.4 Concluding Remarks

The sequential QM/MM methodology has been employed to analyze the dipole polarizability of liquid argon. Using Monte Carlo simulation and the autocorrelation function of the energy, statistically relevant configurations are sampled for quantum mechanics calculations. Using the radial distribution function, we separated the first solvation shell, composed of 14 Ar atoms. Density-functional theory calculations within the hybrid B3P86/aug-cc-pVDZ model were used. Three different models were adopted to extract the mean dipole polarizability per atom. All these models suggest that the dipole polarizability in the liquid case, in the thermodynamic condition adopted here, is increased compared to gas phase. These results are then used in the simple Clausius-Mossotti equation to obtain theoretically the dielectric constant of liquid argon. Our best result indicates a dipole polarizability of 11.6 a_0^3 and a dielectric constant of 1.52 (for $P = 1.8$ atm, $T = 91.8$ K) in very good agreement with an experimentally available result of 1.53 (for $P = 1.0$ atm, $T = 87.4$ p;K). These results lend credence to the combined use of classical simulation statistical mechanics and quantum mechanics for the description of the dielectric properties of simple liquids.

Acknowledgments This work has been partially supported by CNPq, CAPES, and FAPESP (Brazil).

References

1. O. Tapia, O. Goscinski, Self-consistent reaction field theory of solvent effects. Mol. Phys. **29**, 1653–1661 (1975)
2. J.L. Rivail, D. Rinaldi, A quantum chemical approach to dielectric solvent effects on molecular liquids. Chem. Phys. **18**, 233–242 (1976)
3. J. Tomasi, M. Persico, Molecular interactions in solutions: An overview of methods on continuous distribution of the solvents. Chem. Rev. **94**, 2027–2094 (1994)
4. M.M. Karelson, M.C. Zerner, Theoretical treatment of solvent effects on electronic spectroscopy. J. Phys. Chem. **96**, 6949–6957 (1992)
5. J. Tomasi, Thirty years of continuum solvation chemistry: A review, and prospect for the near future. Theor. Chem. Acc. **112**, 184–203 (2004)
6. D.M. Heyes, The Liquid State. Applications of Molecular Simulations (Wiley, New York, 1998)
7. M.P. Allen, D.J. Tildesley, Computer Simulation of Liquids (Clarendon Press, Oxford 1987)
8. J.T. Blair, K. Krogh-Jespersen, R.M. Levy, Solvent effects on optical absorption spectra. The $^1A_1 \rightarrow {}^1A_2$ transition of formaldehyde in water. J. Am. Chem. Soc. **111**, 6948–6956 (1989)
9. J. Gao, Monte Carlo quantum mechanical-configuration interaction and molecular mechanics simulation of solvent effects on the n – π* blue shift of acetone. J. Am. Chem. Soc. **116**, 9324–9328 (1994)
10. J. Zeng et al., Solvent effects on molecular spectra. I. Normal pressure and temperature Monte Carlo simulations of the structure of dilute pyrimidine in water. J. Chem. Phys. **99**, 1482–1495 (1993)

11. K. Coutinho, S. Canuto, Solvent effects in emission spectroscopy: A Monte Carlo quantum mechanics study of the n – π* shift of formaldehyde in water. J. Chem. Phys. **113**, 9132–9139 (2000)
12. K. Coutinho, S. Canuto, Solvent effects from a sequential Monte Carlo-quantum mechanics approach. Adv. Quantum Chem. **28**, 89–105 (1997)
13. K. Coutinho et al., A Monte Carlo-quantum mechanics study of the solvatochromic shifts of the lowest transition of benzene. J. Chem. Phys. **112**, 9874–9880 (2000)
14. H.C. Georg et al., Solvent effects on UV-visible absorption spectrum of benzophenone in water: A combined Monte Carlo quantum mechanics study including solute polarization. J. Chem. Phys. **126**, 034507-1–034507-8 (2007)
15. T.S. Almeida et al., Electronic properties of liquid ammonia: A sequential molecular dynamicso/quantum mechanics approach. J. Chem. Phys. **128**, 014506-1–014506-9 (2008)
16. A.D. Becke, Density-functional thermochemistry.III. The role of exact exchange. J. Chem. Phys. **98**, 5648–5852 (1993)
17. J.P. Perdew, Density functional approximation for the correlation energy of the inhomogeneous electron gas. Phys. Rev. B **33**, 8822–8824 (1986)
18. A. Morita, S. Kato, An ab initio analysis of medium perturbation on molecular polarizabilities. J. Chem. Phys. **110**, 11987–11998 (1999)
19. K. Coutinho, S. Canuto, Sequential Monte Carlo/quantum mechanics study of the dipole polarizability of atomic liquids: The argon case, in Atoms, Molecules and Clusters in Electric Fields. Theoretical Approaches to the Calculation of Electric Polarizabilities, ed. by G. Maroulis (Imperial College Press, London, 2006), pp. 405–420
20. G.C. Maitland, E.B. Smith, The intermolecular pair potential of argon. Mol. Phys. **22**, 861–868 (1971)
21. K. Coutinho, S. Canuto, DICE: A general Monte Carlo program for liquid simulation (University of São Paulo, Brazil (, 2000)
22. T. Malaspina et al., Ab initio calculation of hydrogen bonds in liquids: A sequential Monte Carlo quantum mechanics study of pyridine in water. J. Chem. Phys. **117**, 1692–1699 (2002)
23. S. Canuto et al., New developments in Monte Carlo/quantum mechanics methodology. The solvatochromism of β-carotene in different solvents. Adv. Quantum Chem. **41**, 161–183 (2002)
24. G. Maroulis, Static hyperpolarizability of the water dimer and the interaction hyperpolarizability of two water molecules. J. Chem. Phys. **113**, 1813–1820 (2000)
25. K.V. Mikkelsen et al., Sign change of hyperpolarizabilities of solvated water. J. Chem. Phys. **102**, 9362–9367 (1995)
26. S. Canuto et al., The dipole polarizability of F^- in aqueous solution. A sequential Monte Carlo/quantum mechanics study. Adv. Quantum Chem. **48**, 141–150 (2005)
27. F.B. van Duijneveldt et al., State of the art in counterpoise theory. Chem. Rev. **94**, 1873–1885 (1994)
28. M.J. Frisch et al., Gaussian 98, Revision A.6, Gaussian, Inc. (Pittsburgh, PA, 1998)
29. A. Eisenstein, N.S. Gingrich, The diffraction of X-ray by argon in the liquid, vapor, and critical region. Phys. Rev. **62**, 261–270 (1942)
30. C. Lupinetti, A.J. Thakkar, Polarizabilities and hyperpolarizabilities for the atoms, Al, Si, P, Cl and Ar:Coupled cluster calculations. J. Chem. Phys. **122**, 44301-1–44301-7 (2005)
31. U. Hohm, K. Kerl, Interferometric measurement of the dipole polarizability of molecules between 300 K and 1100 K. Monochromatic measurements at $\lambda = 632.99$ nm for the noble gases and H_2, N_2, O_2, and CH_4. Mol. Phys. **69**, 819–831 (1990)
32. D.R. Johnston et al., Dielectric constants of imperfect gases.I. Helium, argon, nitrogen, and methane. J. Chem. Phys. **33**, 1310–1317 (1960)
33. R.J. Wheatley, Time-dependent coupled-cluster calculations of polarizabilities and dispersion energy coefficients. J. Comput. Chem. **29**, 445–450 (2008)
34. H. Frölich, Theory of Dielectrics (Clarendon Press, Oxford, 1958)
35. D.R. Lide (ed), Handbook of Chemistry and Physics, 73rd edn. (CRC Press, Boca Raton, 1993), p. 9.51

Chapter 17
CO_2(aq) Parameterization Through Free Energy Perturbation/Monte Carlo Simulations for Use in CO_2 Sequestration

Thomas J. Dick, Andrzej Wierzbicki, and Jeffry D. Madura

Abstract The gaseous and solution phase structures of CO_2(aq) are investigated to aid in the development of CO_2(aq) MM parameters for use in the CO_2 sequestration modeling studies. Previous experimental and computational studies indicate two energetic minima for the interaction of a single CO_2 and single water molecule, termed the T-structure and H-structure. For the determination of the energetic minima, ab initio calculations were performed, and the minima were found to have the respective values of -3.0 and -2.1 kcal/mol. From these ab initio calculations, a set of MM parameters were developed to reproduce the gas phase geometry and energetics. The gas-phase parameters were used as starting points in the aqueous phase parameter development, which used free energy perturbation Monte Carlo (FEP/MC) simulations to calculate the solubility of CO_2 in aqueous solution as a function of temperature. Parameters were developed for CO_2 to be used in the aqueous solution using the TIP3P, TIP4P, and TIP4P-Ew water models. The CO_2(TIP4P-Ew) model was found to reproduce the solubility as a function of temperature to within 1% of the experimental solubility. Further testing of the CO_2(TIP4P-Ew) model is done in the second part of this work, in which the solubility is calculated in several salt and brine solutions.

17.1 Introduction

Molecular simulations have been used for more than the past 50 years to observe properties of bio-molecules, organic, and inorganic compounds in their natural

T.J. Dick[1], A. Wierzbicki[2], and J.D. Madura[3] (✉)
[1]Department of Chemistry and Physics, Carlow University, 3333 Fifth Ave. Pittsburgh, PA 15213, USA; [2]Department of Chemistry, University of South Alabama, Mobile, AL 36688, USA; [3]Center for Computational Sciences, Department of Chemistry and Biochemistry, Duquesne University, 600 Forbes Ave., Pittsburgh, PA 15282, USA
e-mail: jdmadura@me.com

J. Leszczynski and M.K. Shukla (eds.), *Practical Aspects of Computational Chemistry*, 337
DOI: 10.1007/978-90-481-2687-3_17,

environment on a time scale that is not feasible with current experimental techniques [1, 2]. Data from molecular simulations have been used to save huge amount of resources in the scientific community, but still are only as reliable as the work that was put into the simulation and its preparation. Considerable work is still needed in the area of understanding phase transition phenomenon on the molecular level. This work investigates energetic, thermodynamic, and structural properties of several aqueous solutions dealing with various types of phase transitions, either with the solution itself, or with the particles being introduced into the solutions. For the CO_2 to be sequestered in a brine aquifer, the CO_2 must undergo a phase transition from the gaseous phase to the aqueous phase. There are many factors that influence this process, and the different salt solutions are investigated as to which concentrations or types of ions have the most significant effect on the thermodynamic properties of the solution.

Experimental investigations of carbon dioxide mineral trapping have been started, but there is little understanding of the processes involved on the molecular level, due to the complex nature of the brine and the physical conditions present in the brine aquifers. One such complexity issue is the dissolution of CO_2 from the gaseous phase into aqueous solution. This process is thermodynamically unfavorable with a $\Delta_r G^o$ value of 2.00 kcal/mol, in pure water at STP [3]. This becomes even more thermodynamically unfavorable as salts are introduced into the solution. Figure 17.1 shows how the solubility of CO_2 in aqueous solution is also dependent upon the salt concentration and salt composition, even from simple salt solutions. According to Fig. 17.1, there is no correlation with size and the ability for the solution to uptake the CO_2.

From the literature, it is known that two energetic minima for the CO_2:H_2O complex exist, described by Sadlej et al. and called the H-structure and the

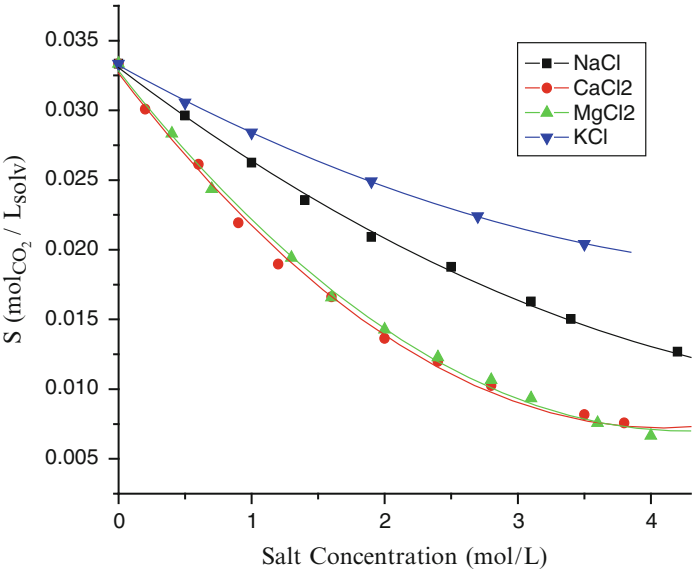

Fig. 17.1 CO_2 solubility as a function of aqueous salt concentration for four simple salt solutions [25]

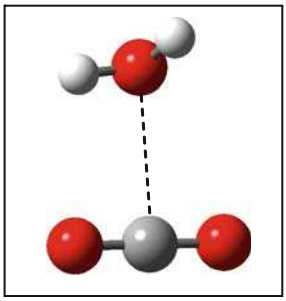

Fig. 17.2 The configuration of the T-structure by Sadlej et al. [5]

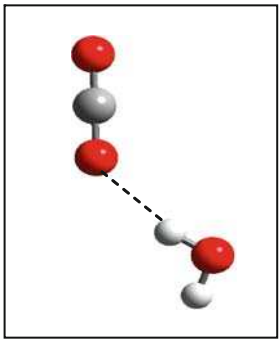

Fig. 17.3 The configuration of the H-structures by Sadlej et al. [5]

T-structure, based on the position and orientation between the molecules in the complex [4, 5]. One noted exception in the configurations shown was that Sadlej et al. constrained the T-structure to C_{2V} symmetry, based on assumptions from experimental microwave data by Petersen and Klemperer [6]. Shown in Figs. 17.2 and 17.3 are the T-structure and the H-structure, respectively.

17.2 Computational Methods

17.2.1 Gas Phase Calculations

The ab initio calculations were completed for a CO_2 molecule, a single water molecule, and the CO_2:H_2O complex for multiple levels of theory and basis sets in order to calculate the interaction energy of the complex. Interaction energies were calculated as follows:

$$\Delta E = E(\mathrm{AB}) - E(\mathrm{A}) - E(\mathrm{B}), \tag{17.1}$$

where ΔE is the interaction energy, E(AB) is the energy of the complex, and E(A) and E(B) are the energies of the isolated CO_2 and water molecules [7].

Optimizations of the T and H complexes were carried out using quantum computational methods. A thorough evaluation of the CO_2:H_2O complex was achieved by varying the level of theory. Hartree–Fock (HF), density functional theory (DFT), Möller–Plesset perturbation theory (MPPT), and coupled clusters with single and double excitations (CCSD) approximation methods were used with the 3-21G, 6-31G, 6-31G(d), aug-cc-pvdz, and aug-cc-pvtz basis sets. The density functional theory used in the calculations was the Becke3 exchange 1993 functional with the Lee, Yang, and Parr nonlocal functional corrections (B3LYP) [8, 9]. For the most complete QM study of the complex, the use of polarized split-valence basis sets were employed to allow the molecular orbitals to change shape [7, 10]. The investigation with the increasing levels of theory was an attempt to converge the binding energies. All electronic structure calculations were done using Gaussian 98 [11] and Gaussian03 [12].

The minima were obtained, and frequency calculations were computed for most of the complexes with the previously mentioned methods and basis sets. The energetic minima were calculated for the T-structure in both the C_{2v} constrained form, and with an unconstrained geometry for the ab initio calculations [4, 5]. All of the ab initio calculations were performed as optimizations using analytical first derivatives and then followed by frequency calculations to validate the minima. Except for a few selected cases for which the minima were not able to be obtained, the energetic minima were found to have no negative frequencies, concluding that a minimum was found for the complex. For the previous computational studies by Sadlej et al. [5], the MP2 through MP4STDQ methods were used in conjunction with the medium-polarized basis sets of Sadlej et al. These basis sets consist of (10s6p4d/6s4p) primitives contracted to [5s3p2d/3s2p] orbitals for the S(spd) basis set, while the addition of extra larger polarizable f functions led to the larger S(spfd) and the D(spfd) basis sets.

17.2.2 Classical Simulations

For the classical simulations, including both the MM minimizations and MC simulations, a classical force field was used to model the CO_2:H_2O interactions. Water molecules in the bulk phase simulations were modeled in the same fashion. DYNAMO v.2 [13] was used to perform the MM minimizations and BOSS v.4.5 was used in the MC simulations, including the free energy perturbation calculations [14]. The MM minimizations were done using several steps of steepest decent gradient followed by conjugate gradient, to find the lowest energy structures; the complexes binding energies were calculated using the same method described in the previous section. To ensure that the true minima were found, the step size and the number of steps in the minimization schemes were varied, along with the gradient convergence criteria. The NPT MC simulations used the standard acceptance/rejection ratio of 0.40/0.60, which has been shown to give reasonable sampling in simulations [10].

17.2.3 Solubility Calculations

The calculation of the CO_2 solubility in aqueous solution was based upon the equations of Swope and Andersen [15]. When a chemical system is in equilibrium, the chemical potential of a gas phase particle and the particle in solution must be equal [16]. From this, we can show that the solubility of a gas particle in solution is given by:

$$\mathrm{S} = \left(\rho^{\mathrm{o}}_{\mathrm{Ag}}/\rho^{\mathrm{o}}_{\mathrm{w}}\right) \exp\left[-\beta \int_0^1 \mathrm{d}\xi \mathrm{U}(\xi)\right], \tag{17.2}$$

where $\rho^{\mathrm{o}}_{\mathrm{Ag}}$ is the number density of the solute particle in the gas phase with a partial pressure of 1 atm, $\rho^{\mathrm{o}}_{\mathrm{w}}$ is the number density of the pure solvent, and $U(\xi)$ is the potential energy (PE) function, which describes the interactions between the solute and solvent. The PE function shown above is a function of a particular coupling parameter ξ, which is integrated from zero to unity [15]. This coupling parameter ξ, represents the parameters that are used to describe the atomistic interactions between the solute particle, which in this case is the CO_2, and the rest of the system. The integration from zero to one over the entire molecular parameters, gives the outcome of inserting a solute particle into solution, as the coupling goes from zero to unity. This calculation of solubility is dependent upon the number density of the solvent, which must be calculated from the solution in which the coupling constant is set to zero. To determine the potential energy, $U(\xi)$, one must examine the thermodynamic principles that are presented by the physical condition of the sequestration process.

From thermodynamics, the chemical potential of a system is defined as follows:

$$\mu = \left(\frac{\partial G}{\partial \mathrm{n}_i}\right)_{T,P}, \tag{17.3}$$

where ∂G is the differential of the Gibbs energy and ∂n_i is the differential of the number of particles [17]. Since the solubility is proportional to the chemical potential, it can be deduced that the unknown function, which is dependent upon the coupling parameter, is the change in Gibbs energy as the solute particle's parameters are adjusted from zero to the full force field values through a gradual increase. This relationship can be shown as follows:

$$\int_0^1 U(\xi)\mathrm{d}\xi \rightarrow \int_{i=0}^{i=1} G(n_i)\mathrm{d}n_i \tag{17.4}$$

By introducing a single solute particle into solution, (17.4) can be integrated to show that the free energy of solvation for that solute is obtained by calculating the energy during the perturbation process. Thus, the calculation of the Gibbs energy of

the solute particle leads to potential of mean force calculations, using the free energy perturbation theory (FEP). The change in Gibbs energy at the standard state between two systems can be calculated by

$$\Delta G = -k_{\mathrm{B}} T \ln \left\langle \exp\left(-(E_j - E_i)/k_B T\right) \right\rangle_i, \tag{17.5}$$

where k_{B} is the Boltzmann constant, T is the temperature of the system, and E_i and E_j are the energies of two systems, i and j, where the difference between i and j is the nonbonded terms of the solute particle, while the solvent parameters [14, 18]. To perform this type of simulation, the system i is perturbed to system j throughout the simulation and the difference between the respective potential energies of systems i and j is related to the system's change in Gibbs energy by averaging the total number of instantaneous perturbations. If the magnitude of the potential energy change is kept small, the FEP method is able to accurately follow the potential energy surface for the insertion of the solute. The total free energy is calculated by summing the contributions from all of the small perturbations.

Potential problems for the calculation of the free energies include deviation from the true Gibbs energy which can be avoided as follows. As the coupling parameter approaches zero, the free energy could approach infinity if the solute particle's nonbonded terms are scaled down rapidly; however, if the integral is broken down into small enough steps, ΔG can be calculated accurately as the solute particle's nonbonded terms go to zero. Another potential problem for the free energy perturbation calculation is that the volume of the solute particle will scale down much faster than the charge (q) of the system. By remembering the Lennard–Jones's nonbonded parameters, mixing rules are defined as:

$$\sigma_{ij} = \left[\frac{\left(\sigma_{ii} + \sigma_{jj}\right)}{2}\right] \tag{17.6}$$

$$\varepsilon_{ij} = \left[\left(\varepsilon_{ii}\varepsilon_{jj}\right)^{\frac{1}{2}}\right] \tag{17.7}$$

One can see that the volume is an addition of the individual terms and the energy well-depth is a product of the individual terms. If the nonbonded parameters are scaled down at the same rate, the system could get stuck in a local minimum, not allowing for proper sampling of the system, and therefore, overestimating the ΔG, or the system may not follow the appropriate free energy path and deviate accordingly. This will be more prevalent with the water models being used, TIP3P, TIP4P, and TIP4P-Ew, since there is no σ value for the hydrogen atoms of the molecule, and thus, the only volumetric constraint comes from the CO_2 model's σ [18, 19]. This problem can be avoided by splitting up the integral of the coupling parameter into two sections, the scaling down of the charge followed by the electrostatic terms. To split up the coupling parameter integral, two sets of simulations sets can be performed sequentially. The first set of simulations scale the full particle's

nonbonded terms to a second set of nonbonded terms that are the same Lennard–Jones (LJ) terms, with the charge on the atoms of the molecule now being zero. The second set of simulations start with the potentials obtained from the first simulation and then scaled down the LJ terms to zero to make a dummy atom in the solution. The addition of all of the perturbations in the simulations yields the total Gibbs free energy for the insertion of a general solute particle into solution.

It should be noted that either the insertion or annihilation of the particle can be used to calculate the Gibbs energy of solvation, and both are related by a change of sign. With an appropriate method for solving the solubility calculations in aqueous solution, such as the one presented here, one can parameterize a model of CO_2 for a particular water model to reproduce these values over an extended thermodynamic window, such as over a desired temperature range that would encompass any type of brine aquifer.

The solubility calculations and the analysis simulations were both carried out using free energy perturbation (FEP) and standard MC protocols, respectively; for the aqueous carbon dioxide simulations, the CO_2 molecule was solvated in 512 water molecules and periodic boundary conditions were used. The pressure was set at 1.0 atm in the isothermal-isobaric ensemble; for the FEP calculations, the temperature was varied from 288 to 313 K. All of the simulation systems were allowed to equilibrate for $>4 \times 10^6$ single particle configurations and data gathering was carried out for 8 blocks of 5×10^5 configurations for each of the 42 perturbations in the FEP calculations and for 24 blocks of 5×10^5 configurations in the solvent structure analysis. This allowed for proper solvent equilibration around the solute particle as the particles' parameters are perturbed from zero to unity. The energies were computed using the appropriate Lennard–Jones and electrostatic interaction parameters for each of the water models. The potential energy of the system was calculated by the following equations, where the total nonbonded energy is defined as follows:

$$U(r)_{\text{nonbonded}} = \sum U(r)_{\text{LJ}} + \sum U(r)_{\text{Electrostatic}}. \tag{17.8}$$

Equation (8) can be shown in terms of the explicit molecule parameters by showing:

$$U(r) = \left\{4\varepsilon\left[\left(\frac{\sigma}{r}\right)^{12} - \left(\frac{\sigma}{r}\right)^{6}\right]\right\} + \left\{\frac{q_i q_j}{4\pi\varepsilon_o r_{ij}}\right\}, \tag{17.9}$$

where the $U(r)$ is the potential energy of the system that is summed over all of the Lennard–Jones and all the electrostatic interactions. For the potential energy of the system to be calculated, the Lennard–Jones (LJ) and the electrostatic interactions are calculated separately. The LJ interactions are calculated between a pair of atoms and are based on a cut-off distance that has been determined from experiment. All of the parameters for the carbon dioxide were modified to obtain accurate aqueous solvated structures. The TIP3P, TIP4P, and TIP4P-Ew models were used for the solubility calculations for their robust nature, common use in the literature, and

ability to reproduce certain properties of water, as has been discussed in the literature [2, 20, 21].

17.3 Results and Discussion

17.3.1 Gas Phase Calculations

Using ab initio quantum chemical calculations, the 1:1 CO_2:H_2O complex was investigated to find the energetic minima. First, principle quantum mechanical calculations were performed with and without symmetry constraints on the complex to investigate the validity of this assumption. The global minimum was found to be a planar structure with C_{2V} symmetry with the C atom of the CO_2 measured to the O atom of the H_2O, at a distance of 2.906 Å, with the H atoms pointing away from the CO_2. The well-depth of this configuration was found to be 4033.8 cm^{-1} (2.53 kcal/mol). This structure was referred to as the T-structure; for comparison to the experiment, the C–O distance of 2.906 Å was compared to the experimental distance of 2.836 Å. Results were explained as the incompleteness of the basis sets to describe the system. The second minimum was found with the O–H bond of the H_2O being almost linear with the CO_2 with an angle between the two of 10° and a distance of 4.434 Å. The H_2O was also tilted slightly from the CO_2 axis at an angle of 118°. The well-depth of this structure was 2388.1 cm^{-1} (1.50 kcal/mol). This was referred to as the H-structure, and although the distance cannot be confirmed by experiment, the spectrum indicates the occurrence of a second minimum.

For this study, the T-structure is the global minimum for the CO_2:H_2O complex in all the levels of theory and basis sets. It exhibits two electrostatic interactions between the carbon dioxide and the water at the lower levels of theory, one between the oxygen of the water with the carbon of the CO_2 and the second between a hydrogen of the water and an oxygen of the CO_2. Shown in Tables 17.1 and 17.2 are the interaction energies and geometric distances between the CO_2 and water for the T-structure. This is in disagreement with the reported T-structure by Sadlej, where he held the CO_2:H_2O T-structure complex in C_{2V} symmetry, which would prevent the second electrostatic interaction between the molecules from forming at lower levels of theory, but as the level of theory increases, the structure adopts more of the

Table 17.1 Interaction energies of the T-structure (energies given in kcal/mol)

b.s. /method	B3LYP	HF	MP2	MP3	MP4	CCSD
3-21G	−8.30	−7.79	−6.64	−7.45	−6.91	−7.16
6-31G	−5.18	−5.81	−4.46	−5.48	−4.96	−5.45
6-31G(d)	−3.41	−3.10	−3.69	−3.82	−3.68	−3.72
aug-cc-pCDZ	−1.95	−2.67	−2.99	−2.95	−3.00	−3.02
aug-cc-pVTZ	−1.79	−2.56	−2.81	−2.92	−3.00	−2.99[a]

[a]Values indicate single point calculations on the structure using the next lower level of theory

Table 17.2 Geometry of T-structure: The distance between the C(CO_2) and the O(H_2O) (in Å)

b.s. /method	B3LYP	HF	MP2	MP3	MP4	CCSD
3-21G	2.514	2.592	2.616	2.525	2.583	2.562
6-31G	2.576	2.586	2.696	2.619	2.659	2.647
6-31G(d)	2.772	2.774	2.749	2.723	2.721	2.730
aug-cc-pvdz	2.847	2.841	2.783	2.816	2.785	2.778
aug-cc-pvtz	2.869	2.858	2.777	2.768	2.779	2.778[a]

[a]Values indicate single point calculations on the structure using the next lower level of theory

Table 17.3 Interaction energies of the H-structure (energies given in kcal/mol)

b.s. /method	B3LYP	HF	MP2	MP3	MP4	CCSD
3-21G	−4.38	−4.16	−4.34	−4.29	−4.34	−4.32
6-31G	−3.03	−2.91	−2.74	−2.92	−2.89	−3.19
6-31G(d)	−2.07	−1.77	−2.25	−2.21	−2.21	−2.19
aug-cc-pvdz	−1.36	−1.33	−2.11	−2.10	−2.08	−2.07[a]
aug-cc-pvtz	−1.35	−1.24	−2.05	−2.08	−2.12[a]	−2.11[a]

[a]Values indicate single point calculations on the structure using the next lower level of theory

C_{2V} symmetry, although total symmetry is never quite achieved, even for the best model used in this study, CCSD/ aug-cc-pvtz. From the T-structure ab initio data, it is observable that the energies of interaction and the distances between the molecules converge going across and down the tables, converging in both the levels of theory and in number of basis sets, respectively. The convergence of the methods and basis sets reaches a limiting value of −3.0 kcal/mol for the interaction energy and 2.78 Å for the distance between the molecules. These are the values that will be used in the comparison with the molecular mechanics values for the single CO_2 water interactions. This distance is only slightly closer in value to the reported value of 2.836 Å than that of the previously reported literature value, even though a significantly larger and more diffuse basis set was used.

The second minimum found was for the H-structure, which was similar to that found by Sadlej. The H-structure exhibits hydrogen bonding between a hydrogen of the water molecule and an oxygen of the CO_2 molecule. Shown in Tables 17.3 and 17.4 are the respective interaction energies and geometric distances between the CO_2 and the water molecule. As seen in the T-structure ab initio data, the H-structure ab initio data also converge going across and down the tables, converging in both the levels of theory and in number of basis sets, respectively. The convergence of these values reaches a limiting value of −2.1 kcal/mol for the interaction energy and 2.20 Å for the distance between the molecules. As before, these are the values that will be used in the comparison with the molecular mechanics values, which was the ultimate goal at the start of this study.

The literature force field models were used with the TIP3P water model to calculate the interaction of the CO_2 with a single water molecule, as was done in the ab initio calculations presented above [22–24]. When the literature CO_2 complexes were compared to the ab initio complexes, the Steele model provided the best match with the ab initio data, with an interaction energy and distance of

Table 17.4 Geometry of H-structure: The distance between the $O(CO_2)$ and the $H(H_2O)$ (in Å)

b.s. /method	B3LYP	HF	MP2	MP3	MP4	CCSD
3-21G	1.997	2.061	2.055	2.059	2.056	2.060
6-31G	2.082	2.136	2.161	2.147	2.161	2.160
6-31G(d)	2.195	2.301	2.216	2.228	2.233	2.261
aug-cc-pvdz	2.234	2.355	2.182	2.196	2.203	2.261[a]
aug-cc-pvtz	2.266	2.382	2.187	2.198	2.203[a]	2.261[a]

[a]Values indicate single point calculations on the structure using the next lower level of theory

Table 17.5 Comparison of interaction energies of the literature CO_2 models, using the TIP4P water model, to the ab initio calculations (interaction energies given in kcal/mol)

	T-structure		H-structure	
	MM	Δ(QM–MM)	MM	Δ(QM–MM)
EPM [23]	−2.26	−0.74	−1.93	−0.17
Murthy [22]	−2.08	−0.92	−1.73	−0.37
Steele [24]	−2.27	−0.73	−1.98	−0.12
EPM2 [23]	−2.26	−0.74	−1.94	−0.16
TJDM1	−2.65	−0.35	−2.08	−0.02

Table 17.6 Comparison of geometric distances of the literature CO_2 models to the ab initio calculations (distances given in Å)

	T-structure		H-structure	
	MM	Δ(QM–MM)	MM	Δ(QM–MM)
EPM [23]	2.934	−0.134	2.010	−0.190
Murthy [22]	2.935	−0.135	2.038	−0.162
Steele [24]	2.838	−0.038	1.880	−0.320
EPM2 [23]	2.914	−0.114	1.993	−0.207
TJDM1	2.808	+0.008	2.008	−0.192

−2.27 kcal/mol and 2.84 Å, respectively, for the T-structure, and −1.98 kcal/mol and 1.88 Å, respectively, for the H-structure. This yielded a difference, when compared to the ab initio, of −0.7 kcal/mol and −0.04 Å for the T-structure, and −0.12 kcal/mol and −0.32 Å for the H-structure. The deviations of the literature CO_2 models from the ab initio data are noted to be not within reasonable agreement, and therefore, would not be accurate in gas phase simulations. A comparison of the molecular force field model's interaction energies and interaction distances can be seen in Tables 17.3 and 17.4. The failure of the literature CO_2 force field models to reproduce the interactions with water in the gas phase reveals a weak point in these models for use in simulations with water. A comparison of the interaction energies and distance can be seen in Tables 17.5 and 17.6, respectively. Further simulations done using FEP/MC simulations will reveal their ability to reproduce bulk properties of CO_2 in aqueous solution.

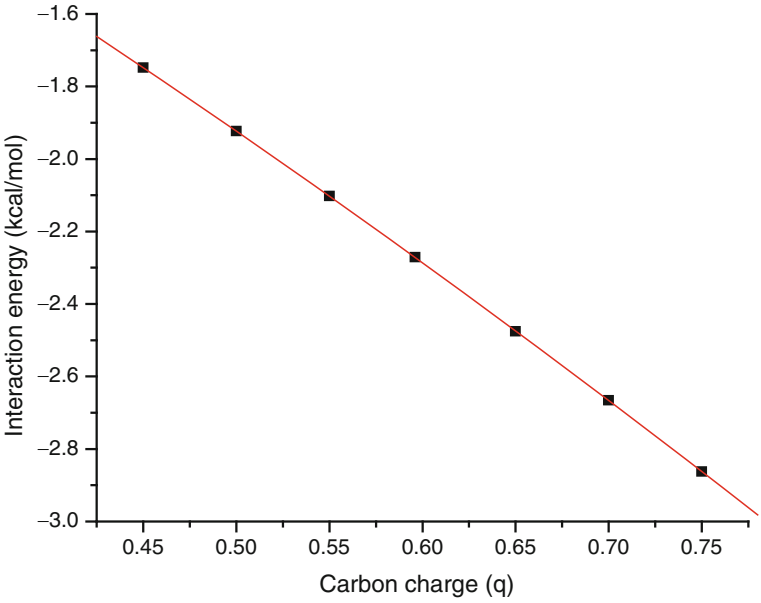

Fig. 17.4 The change in interaction energy as the charge is varied on the carbon atom for the T-structure

The development of force field parameters that are suitable for gas phase CO_2: H_2O interactions was achieved by minimizing the error of both the MM calculated H-structure and the T-structure against the QM convergence structures. To start the development of the TJDM1 model, the intramolecular description terms were all adjusted $\pm 10\%$ of the original values, which were started from the Steele structure, and the difference in the energetics and structure was noted. From this, it was found that the charge was contributing the most in the energetics and structure deviation, followed by σ, and then the well depth, ε. Figure 17.4 shows the variation in the interaction energy as the charge on the carbon atom is changed. To minimize the change in the original parameters, the charge was optimized first, followed by σ, and finally ε, although all of the possibilities were investigated. Several other trials were attempted using other error minimization processes, but it was found that the previously mentioned one was the closest to the original parameters. These parameters were used in the initial solubility calculations, but were modified to achieve the correct solubility; the difference between the original development described here and the final was found to be $<1\%$, and thus, the original parameters are omitted, but noted to give slightly better structural properties by $<2\%$. The MM minimizations were performed using a variety of minimization steps in order to insure the finding of the lowest energy structure with some degree of accuracy. It was found that no improvement was gained by going over 100 steps of steepest decent, followed by 200 steps of conjugate gradient minimization steps in the minimization process, when starting from a reasonable starting structure. It is also

Table 17.7 Force field parameters for the developed CO_2(TIP3P), CO_2(TIP4P), and CO_2(TIP4P-Ew) carbon dioxide models

Model		ε [kcal/mol]	σ [Å]	q [e]
CO_2(TIP3P)	C	0.08763	2.452	0.720
	O	0.13714	3.080	−0.360
CO_2(TIP4P)	C	0.06762	2.620	0.700
	O	0.18814	2.930	−0.350
CO_2(TIP4P-Ew)	C	0.067929	2.620	0.680
	O	0.198140	2.924	−0.340

noted that the tolerance for the minimization method was kept low, in order that the barrier from the T-structure to the H-structure was not crossed in the process. The final set of parameters for the TJDM1 model, seen in Table 17.7, yielded the best result and had a larger charge and smaller LJ radius than the literature models. A comparison of the interaction energies and distance for both the ab initio values and the literature models can be seen in Tables 17.5 and 17.6. Notice that there is significant improvement over the literature values.

17.3.2 CO_2 Solubility and Local Solvent Structure

To finalize the development of the aqueous CO_2 force field parameters, the CO_2 model was used in free energy perturbation Monte Carlo (FEP/MC) simulations to determine the solubility of CO_2 in water. The solubility of CO_2 in water is calculated as a function of temperature in the development process to maintain transferability of the CO_2 model to different simulation techniques and to quantify the robustness of the technique used in the solubility calculations. It is also noted that the calculated solubility is based upon the change in the Gibbs energy of the system and that parameter development must account for the entropy/enthalpy balance that contributes to the overall structure of the solute and solvent over the temperature range being modeled [17].

Shown in Fig. 17.5 is the comparison between the calculated solubility as a function of temperature for the TJDM1, Steele, and EPM2 CO_2 models using the TIP3P water model, against the experimental solubility curve [25, 26]. The solubility of CO_2 in aqueous solution is found to show significant error, when calculated with the literature CO_2 models; the best literature model was found to be the Steele model, as the calculated solubility was found to be ~45% of the experimental solubility. This study is in agreement with previous computational studies by Vorholz et al. of CO_2 solubility in aqueous solution, but reproduction of the experimental solubility as a function of temperature with better precision is needed over the selected temperature range [27]. The precision of the previous study was not enough to detect differences in the solubility from small external influences, such as small changes in salt concentration, as is needed in application dealing with CO_2 sequestration. The reproduction of the solubility curve as a function of temperature prompted the development of aqueous phase CO_2 models for use

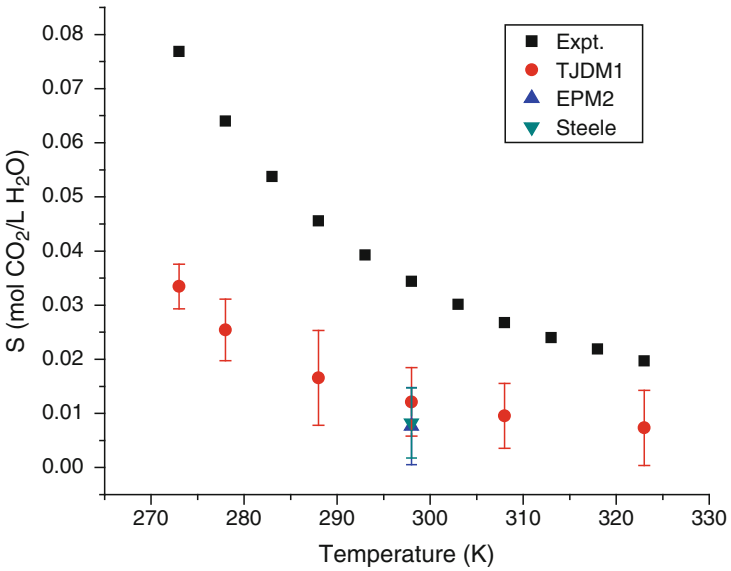

Fig. 17.5 The calculated solubility as a function of temperature of CO_2 in water at 1 atm using literature and developed CO_2 models. The literature models' solubility is only given at 298 K for clarity [23–26]

with the popular TIP3P, TIP4P, and TIP4P-Ew water models that can predict the minute changes in solubility from external influences. The TIP4P, and even more so the TIP4P-Ew water models have also been shown to more accurately describe more generalized properties of water than its predecessor, TIP3P, with only small increases in computational costs, and offer a more stable density curve to start the solubility curve as a function of temperature [1, 28, 29]

Development of the force field parameters using the solubility calculation techniques is similar to the previously described MM error minimization process. First, the solubility was calculated as the force field parameters were incrementally varied $\pm 2\%$ of the values determined in the previous MM minimization process to determine the sensitivity of the calculated solubility to each of the force field parameters. The "mapping" of the complex solubility surface as a function of temperature, with respect to the changing parameters, was useful in determining the quantitative amount to change the parameters, when tuning each of the individual parameters. Similarly, as found in the previous error minimization process, it was found that the charge q had the most profound effect on the change in the desired property, followed by σ, and then ε. However, during the fine tuning of the force field parameters, the latter two parameters were adjusted more frequently, as it was found that the charge was considered too drastic a change and influenced the overall temperature dependence by shifting and inflecting the curve in the solubility graph. Both the sigma and epsilon force field parameters changed the overall shape of the solubility curve with much more control, as their overall sensitivity was less than that of the charge; however, all possibilities were investigated with respect to

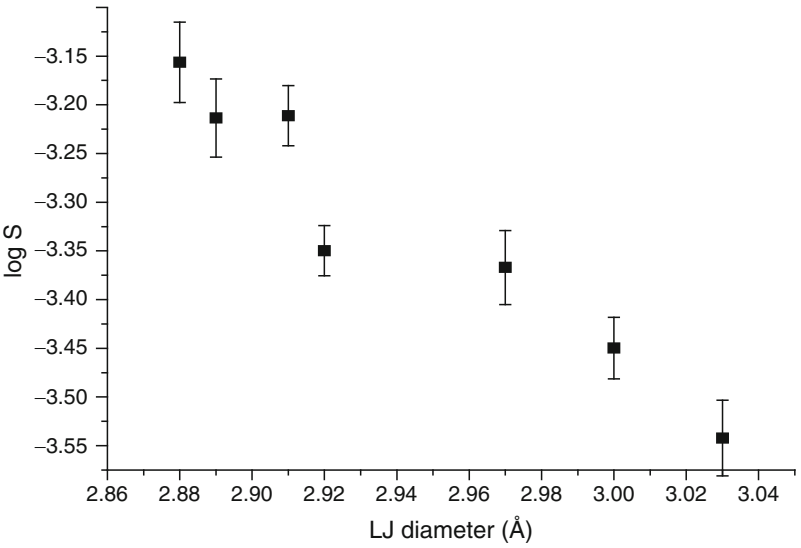

Fig. 17.6 A free energy curve generated from varying the O-σ values, while holding the well depth constant, in the bulk solution parameterization process using the TIP4P water model

the starting parameter in the minimization process. A small section of the solubility mapping, which is resulting from a free energy surface, can be seen in Fig. 17.6. This was taken from the mapping of the solubility as the LJ diameter for the oxygen was varied and all other parameters were kept constant; the oxygen parameters were set at $q=-0.3375$ and $\varepsilon=0.198140$, and the carbon parameters were set at $q=0.6750$, $\varepsilon=0.067629$, and $\sigma=2.620$.

Careful consideration was taken in the parameterization process to insure that the parameters were deemed reasonable for the atom types, using the OPLS-AA force field atom types as a comparison. As one of the goals of this project was to ensure that robustness was achieved in many different calculated properties of the newly developed model, several sets of simulations were also performed to ensure that the parameters could achieve a reasonable agreement with experiment. Some of the properties calculated included the gas phase density, the partial molar volume in aqueous solution, and the bulk solvent structure as well. The calculation of the solubility was discussed in the previous section; for the parameterization process and the viewing of these results, the solubility will be reported in log S values, as many of the literature values are reported as log S values, and therefore, the comparison would not lose any sensitivity due to rounding error from the log value.

As shown in Fig. 17.7, the CO_2 models developed for aqueous simulations, show drastic improvement over the previous model(s). The CO_2(TIP3P) model shows improvement in the quantitative agreement with the experimental data, although the overall shape of the solubility curve is not obtained. This can most likely be explained by the ability of the TIP3P water model to accurately reproduce the experimental density curve over the temperature range in question; for most

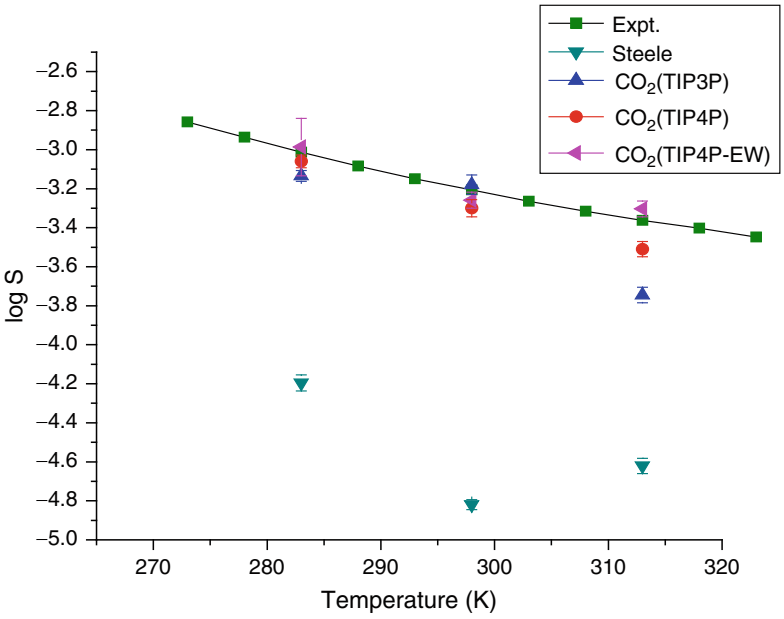

Fig. 17.7 The calculated solubility of CO_2 in water at 1 atm using the Steele [24] CO_2 [*down triangle, green*] model with TIP3P water, the developed CO_2(TIP3P) [*up triangle, blue*], CO_2(TIP4P) [*circle, red*], CO_2(TIP4P-Ew)[*left pointing triangle, pink*] models with their respective water models, compared against the experimental values [*square, black*] [25, 26]

of the density curve, the TIP3P model underestimates the density considerably [28–34]. Significant improvement in the shape of the curve is obtained with the CO_2(TIP4P) model. The solubility curve is reasonably modeled over the temperature range presented, but the solubility curve is shifted below the experimental curve, showing the ability of the model to underestimate the solubility of CO_2 in aqueous solution. Again, an explanation for this systematic error could be the density curve of TIP4P over the temperature range in question. The third CO_2 model developed in this work, is the CO_2(TIP4P-Ew) for use with the TIP4P-Ew water model. The overall success of this model shows both quantitative and qualitative agreement with the experimental density curve. This phenomenon of solubility, and in general, hydrophobic hydration vs. the density curve of the pure solvent has been discussed in the literature and is further validated in this work [35]. As discussed in the literature, the properties of water are highly sought after, but reproduced only to the degree of which they were parameterized under certain conditions [28, 29]. Thus, it would seem that with increasing computational intensity for the water model, although it may be insignificant to the degree of exactness in these simulations, the solubility curve in aqueous solution over the temperature range of 283–323 K is reproduced reasonably well. Table 17.7 shows the developed parameters for the CO_2(TIP3P), CO_2(TIP4P), and CO_2(TIP4P-Ew) models.

For a more generalized approach to this solubility problem, the question of reproducibility of experimentally known properties of water seems to be in order. Previous computational studies have suggested that the insertion of compounds in aqueous solution is vastly dependent upon the ability of the water model to reproduce structural properties at the desired conditions. Even so, this comparative type of analysis would only be effective in ideal solutes or apolar solutes in the solution. If the solute was to deviate from this spherical shape, the method would need to be modified accordingly. One may even suggest that the CO_2 may be treated as more of a single LJ sphere with a series of charges that would reproduce the quadrapole moment, and therefore, coordinate the water in an appropriate solvation, although further study of the aqueous CO_2 system would be needed to confirm this.

When changing force field parameters of a compound, overall exactness of the model is determined by the parameterization criteria. As this work was parameterized to reproduce the solubility, which is related to the thermodynamic quantity of free energy, this raises the question of solvent structure, as the structure–energy relationship is evident even in the gas phase interactions. One way to test the solvent structure is to check the density of the aqueous solution as a rough estimate of the ability of the model to reproduce the correct intermolecular interaction between the solute and the solvent. For this purpose, additional MC simulations were carried out on the developed models to test their ability to reproduce the experimental density of solution, at the specified concentration. The density was calculated using the experimentally derived density equations for carbon dioxide in aqueous solution from Teng et al., which is calculated from the V_ϕ of the CO_2(aq) and the density of the pure solvent [36, 37].

All of the developed models reproduce the calculated density for a 0.11 M solution of CO_2 to within 2% of the calculated value of 1.260 g/cm^3. The CO_2(TIP3P) model was found to underestimate the density by $<$1.8%, the CO_2(TIP4P) model underestimating it by 1.3%, and the CO_2(TIP4P-Ew) model overestimating it by 1.1%. This validation of the model is open to interpretation, as this may be a canceling of error by overestimating and underestimating the different enthalpic and entropic contributions to the solvent structure. Solvent structure analysis has been done to further justify the models and give insight into the immediate structure of the solvent around the CO_2.

The structure of the water around the CO_2 molecule was analyzed to determine if the main contributing gas phase structures, the T-structure and the H-structure, are contributing structure in the aqueous phase. Shown in Fig. 17.8a–d are the radial distribution functions (RDFs) for the carbon (C) and oxygen (O) of the CO_2 with the OW and HW of the water molecules in the system. The C–OW RDFs, shown in Fig. 17.8a, shows some of the similarities in the structure of the water surrounding the developed CO_2 models. From this figure, it is seen that the first peak for the CO_2(TIP3P) and CO_2(TIP4P-Ew) models occurs at 3.9 Å and is shifted to by −0.1 Å for the CO_2(TIP4P) model. The first minima for the models occur at 5.2 Å, except for the CO_2(TIP4P-Ew) model, where these are shifted by 0.2 Å. A similar trend is seen in Fig. 17.8b, for the C–HW RDF, where the CO_2(TIP3P) and CO_2(TIP4P) models are similar in structure, but the CO_2(TIP4P-Ew) model exhibits

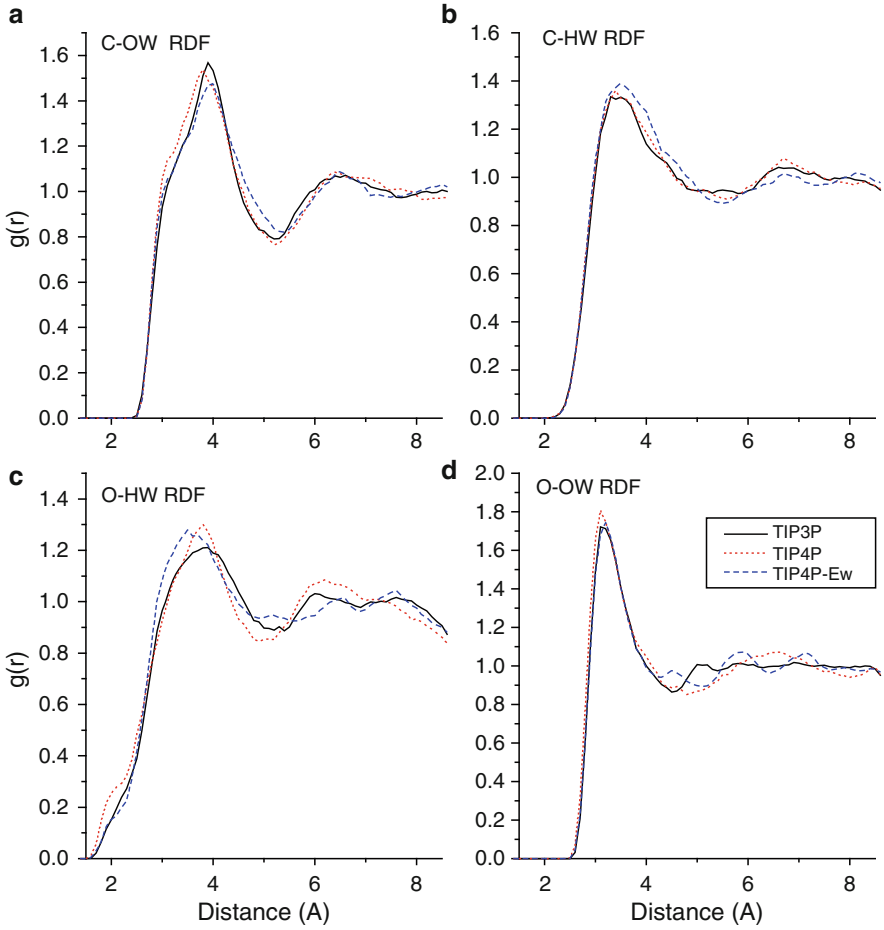

Fig. 17.8 (**a–d**) Radial distribution functions (RDFs) of the C–OW (**a**), C–HW (**b**), O–HW (**c**), and O–OW (**d**) for the CO_2(TIP3P), CO_2(TIP4P), and CO_2(TIP4P-Ew) carbon dioxide models with their respective water models; simulations run at 298 K and 1 atm

slight differences from the first two models mentioned. The first peak for the CO_2(TIP4P-Ew) model is at 3.2 Å and the peak is much broader across the tailing end than the non-Ewald CO_2 models. Figure 17.8c shows the signs on difference between the 3-point water parameterized model and the 4-point water parameterized models. The latter two models show much more definition in the first peak, which occurs at 3.7 Å for the CO_2(TIP4P-Ew) model. In Fig. 17.8d, the RDFs for the O–OW interactions show a very defined peak for all of the CO_2 models developed at 3.5 Å. This peak is much more defined than any of the other RDFs, and since all models show lower than bulk probability in the <3.0 Å region for the O–HW RDFs in Fig. 17.8c, we can conclude that there is a wide variety of hydrogen bonding structures with the ends of the CO_2 molecule. This is expected as the

temperature is high enough for a significant amount of hydrogen bond breakage in the temperature selected for the simulation.

From the RDFs in Fig. 17.8, it is seen that there are no true H-structure or T-structures orientations associated with the bulk solvation of the CO_2 molecule. Although there exist no true H or T-structures with the solvated CO_2 molecule, the bulk structure may be associated with one more than the other. Examining the C–OW RDFs in Fig. 17.8a, it appears as if the first peak is constructed of two peaks coming in close contact with each other. This would suggest that there are two competing structure types for the solvation of the molecule, although the probability for the first of the two is less , with respect to distance. There is also significantly less solvent accessible surface area for the water to interact with the carbon than the oxygen of the CO_2. If there exists any external influence to the solvent structure, such as a salt ion, it would depend on the strength of the hydrogen bond network that the molecule has around it, in order for the influence to have any effect. Even if this influence would have any effect, there still is no evidence that it would promote or hinder either of the gas phase structures without further analysis of the solvent structure with these factors included in the simulation, and even more ideal, with different simulations with increasing concentration of these influences. Thus, it can only be said that there are both types of structure, referring to the H and T-structure, but there can be no definition of which is more probable, although it appears as if both are equally probable.

As the developed models were parameterized to reproduce solution phase interaction, the developed models were tested for the reproduction of the gas phase geometries and energetics, as was done for the literature CO_2 models. For each of the developed models, when considering all four criteria of T and H-structure interaction energies and distances, the comparison to the quantum mechanical values is significantly better than those of the literature models, as seen in Tables 17.8 and 17.9, and compared to the previously shown values for the literature models in Tables 17.5 and 17.6. Although some of the values are reasonably reproduced, such as the CO_2(TIP3P) distance values for the H and T-structures, the energetics are enough to show that these models are not adequate for reproduction of gas phase properties. Thus, the authors acknowledge that these are not suitable parameters for gas phase CO_2/H_2O interactions, and are considered purely as solution phase parameters for carbon dioxide. Since the scope of this work is primarily for investigation of solution phase CO_2 properties, development of the gas phase parameters was not pursued further.

Table 17.8 Comparison of interaction energies between water and CO_2 for developed CO_2 models with the ab initio limiting values (interaction energies given in kcal/mol)

	T-structure		H-structure	
	MM	Δ(QM–MM)	MM	Δ(QM–MM)
CO_2 (TIP3P)	−2.64	−0.36	−1.89	−0.21
CO_2 (TIP4P)	−2.75	−0.04	−2.54	0.44
CO_2 (TIP4P-Ew)	−2.48	−0.52	−2.36	0.26

Table 17.9 Comparison of distances between water and CO_2 for developed CO_2 models to the ab initio limiting values (distances given in Å)

	T-structure		H-structure	
	MM	Δ(QM–MM)	MM	Δ(QM–MM)
CO_2 (TIP3P)	2.80	0.02	2.20	0.00
CO_2 (TIP4P)	2.87	0.09	1.94	−0.26
CO_2 (TIP4P-Ew)	2.84	0.06	1.96	−0.24

17.4 Conclusions

Interactions of CO_2 with water were analyzed using molecular simulations. Both the gas phase and bulk solution were analyzed and different properties for the CO_2 were calculated and analyzed. Force field parameters were developed for both the gas phase interaction of CO_2 with water and also for CO_2 in aqueous solution. These parameters were tested for various energetic, thermodynamic, and structural properties.

For the gas phase interaction of water with CO_2, two minima were found for the interaction of a CO_2 molecule with a water molecule referred to as the T-structure and the H-structure by Sadlej et al. [5]. These structures are confirmed in this work from the ab initio calculations, where the T-structure was found to have an interaction energy of −3.0 kcal/mol with a distance between the molecules of 2.78 Å and was found to be the global minimum. The H-structure, a local minimum, was found to have an interaction energy of −2.1 kcal/mol and a distance of 2.20 Å between the molecules. It was found that none of the literature CO_2 models reproduced the gas phase structures or energetics to any degree of certainty. The literature force field CO_2 models were used to calculate the interaction energies with water to investigate if they are appropriate for such a calculation. It was found that the literature models used in this study are not appropriate for gas phase interactions of CO_2 with water. An initial CO_2 model, termed the TJDM1 model, was parameterized to reproduce the gas phase geometry and energetics to a higher degree of success than the literature models. This model's parameters were used as the starting point in the bulk phase solubility parameterization process.

Bulk phase aqueous CO_2 parameters were developed in order to reproduce the solubility curve as a function of temperature from 283 to 323 K in aqueous solution. Three models were developed, the CO_2(TIP3P), the CO_2(TIP4P), and the CO_2(TIP4P-Ew) models, for use with the respective TIP3P, TIP4P, and TIP4P-Ew water models. All the three models reasonably reproduce the solubility over the temperature range specified, with the higher the cost of the water model, the better the match with the experimental results. The newly developed models show a structural similarity, with a loosely related solvation shell of water. It was found that there exists no real correlation to the gas phase structures, but a reasonable amount of similarity to the structures is seen. Analysis of additional solutes in the solution, such as simple salt solutions and brine solutions, will reveal additional information about the strengths of the solvation shells and their ability to hinder

electrostatic interactions between the CO_2 and ions. Gas phase calculations of the developed models were performed with water molecules to test the phase properties of the parameters; it was found that although the developed parameters did better than the literature models, they were still not suitable for use in gas phase CO_2/water simulations.

Acknowledgments This work was funded in part by the NSF (CHE-0723109, CHE-0321147, AAB/PSC CHE-030008P); Department of Education (P116Z040100, P116Z050331, and P116Z080180), NETL, Pittsburgh, PA; the Silicon Graphics Inc.; James River Technical, Inc.; Gaussian Corporations; the National Science Foundation under Grant No. CHE-0616674; co-funded by the Division of Chemistry; the Office of Polar Programs; and the EPSCoR Office.

References

1. G.W. Robinson et al., *Water in Biology Chemistry and Physics* (World Scientific, Singapore, 1996)
2. K.B. Lipkowitz, D.B. Boyd, *Reviews in Computational Chemistry, vol. 13* (Wiley, New York, 1999)
3. W. Stumm, J. Morgan, *Aquatic Chemistry* (Wiley, New York, 1996)
4. J. Sadlej et al., Ab initio study of energy, structure and dynamics of the water–carbon dioxide complex. J. Chem. Phys. **109**, 3919 (1998)
5. J. Sadlej, P. Mazurek, Ab initio calculations on the water-carbon dioxide system. Theochem **337**, 129 (1995)
6. K.I. Peterson, W. Klemperer, Structure and internal rotation of H_2O–CO_2, HDO–CO_2, and D_2O–CO_2 van der Waals complexes. J. Chem. Phys. **80**, 2439 (1984)
7. J. Foresman, A. Frisch, *Exploring Chemistry with Electronic Structure Methods*, 2nd edn. (Gaussian, Pittsburgh, 1993)
8. A.D. Becke, Density-functional thermochemistry. III. The role of exact exchange. J. Chem. Phys. **98**, 5648 (1993)
9. C. Lee et al., Development of the Colle-Salvetti correlation-energy formula into a functional of the electron density. Phys. Rev. B Condens. Matter Mater. Phys. **37**, 785 (1988)
10. A. Leech, *Molecular Modeling Principles and Applications*, 2nd edn. (Prentice Hall, Harlow, 2001)
11. M.J. Frisch et al., *Gaussian 98, Revision A.9* (Gaussian, Pittsburgh, 1998)
12. M.J. Frisch et al., *Gaussian 03, Revision B.03* (Gaussian, Pittsburgh, 2003)
13. M.A. Field, *Practical Intoduction to the Simulation of Molecular Systems* (Cambridge University Press, Cambridge, 1999)
14. W. Jorgensen, *BOSS; Version 4.3 ed* (Yale University, New Haven, 2002)
15. W. Swope, H. Andersen, A molecular dynamics method for calculating the solubility of gases in liquids and the hydrophobic hydration of inert-gas atoms in aqueous solution. J. Phys. Chem. **88**, 6548 (1984)
16. T. Hill, *Statistical Mechanics* (McGraw-Hill, New York, 1956)
17. K. Dill, S. Bromberg, *Molecular Driving Forces* (Garland Science, New York, 2003)
18. W.L. Jorgensen, C. Ravimohan, Monte Carlo simulation of differences in free energies of hydration. J. Chem. Phys. **83**, 3050 (1985)
19. W.L. Jorgensen et al., Comparison of simple potential functions for simulating liquid water. J. Chem. Phys. **79**, 926 (1983)
20. P. Mark, L. Nilsson, Structure and dynamics of the TIP3P, SPC, and SPC/E water models at 298 K. J. Phys. Chem. A **105**, 9954 (2001)

21. D.E. Smith, A.D.J. Haymet, Free energy, entropy, and internal energy of hydrophobic interactions: Computer simulations. J. Chem. Phys. **98**, 6445 (1993)
22. C.S. Murthy et al., Interaction site models for carbon dioxide. Mol. Phys. **44**, 135 (1981)
23. J. Harris, K. Yung, Carbon dioxide's liquid–vapor coexistence curve and critical properties as predicted by a simple molecular model. J. Phys. Chem. **99**, 12021 (1995)
24. W.A. Steele, G. Birnbaum, Molecular calculations of moments of the induced spectra for N_2, O_2, and CO_2. J. Chem. Phys. **72**, 2250 (1980)
25. A. Yasunishi, F. Yoshida, Solubility of carbon dioxide in aqueous electrolyte solutions. J. Chem. Eng. Data **24**, 11 (1979)
26. R. Wiebe, V.L. Gaddy, The solubility of carbon dioxide in water at various temperatures from 12 to 40° and at pressures to 500 atmospheres. Critical phenomena. J. Am. Chem. Soc. **62**, 815 (1940)
27. J. Vorholz et al., Vapor + liquid equilibrium of water, carbon dioxide, and the binary system, water + carbon dioxide, from molecular simulation. Fluid Phase Equilib. **170**, 203 (2000)
28. T.J. Dick, J.D. Madura, Chapter 5: A Review of the TIP4P, TIP4P-EW, TIP5P, and TIP5P-E Water Models, in *Annual Reports in Computational Chemistry, vol 1*, ed. by D.C. Spellmeyer (Elsevier, Amsterdam, 2005)
29. H.W. Horn et al., Development of an improved four-site water model for biomolecular simulations: TIP4P-Ew. J. Chem. Phys. **120**, 9665 (2004)
30. B. Guillot, A reappraisal of what we have learnt during three decades of computer simulations on water. J. Mol. Liquids **101**, 219 (2002)
31. W.L. Jorgensen, C. Jenson, Temperature dependence of TIP3P, SPC, and TIP4P water from NPT Monte Carlo simulations: Seeking temperatures of maximum density. J. Comput. Chem. **19**, 1179 (1998)
32. W.L. Jorgensen et al., *Book of Abstracts, 218th ACS National Meeting*, New Orleans, 22–26 Aug 1999, HYS-149
33. W.L. Jorgensen, J.D. Madura, Temperature and size dependence for Monte Carlo simulations of TIP4P water. Mol. Phys. **56**, 1381 (1985)
34. W.L. Jorgensen et al., *Book of Abstracts, 219th ACS National Meeting*, San Francisco, CA, 26–30 March 2000
35. D. Paschek, Temperature dependence of the hydrophobic hydration and interaction of simple solutes: An examination of five popular water models. J. Chem. Phys. **120**, 6674 (2004)
36. L. Hnedkovsky et al., Volumes of aqueous solutions of CH_4, CO_2, H_2S and NH_3 at temperatures from 298.15 K to 705 K and pressures to 35 MPa. J. Chem. Thermodyn. **28**, 125 (1996)
37. H. Teng et al., Solubility of liquid CO_2 in water at temperatures from 278 K to 293 K and pressures from 6.44 MPa to 29.49 MPa and densities of the corresponding aqueous solutions. J. Chem. Thermodyn. **29**, 1301 (1997)

Chapter 18
Free Energy Perturbation Monte Carlo Simulations of Salt Influences on Aqueous Freezing Point Depression

Thomas J. Dick, Andrzej Wierzbicki, and Jeffry D. Madura

Abstract Free energy perturbation Monte Carlo (FEP/MC) simulations are performed for both the liquid and solid phases of water to determine the melting temperature of several popular three and four-site water models. Gibbs free energy vs. temperature plots are constructed from the simulations to determine the melting temperature. For the liquid phase, standard FEP/MC simulations are used to calculate the free energy relative to the gas phase at multiple temperatures. The free energy of the solid phase relative to the gas phase is calculated at multiple temperatures using the lattice-coupling method. The intersection of the free energy regression lines determines the estimate of the melting temperature. Additionally, simulations were carried out for simple salt solutions to determine the freezing point depressions (FPD). The simulations reproduce the FPD as a function of salt concentration for solutions of NaCl, KCl, $CaCl_2$, and $MgCl_2$.

18.1 Introduction

Computational studies have advanced the study of the solid phase of water and of the interfacial region where the phase transition occurs [1–5]. As water exhibits very unusual properties in the liquid phase, it also exhibits peculiar properties in the solid phase as well. Much about the structure of ice is known from x-ray diffraction experiments or computational studies. Some experiments have been performed on the interfacial region between the liquid and solid phase of water to understand the freezing process, but additional studies are still needed to characterize the

T.J. Dick[1], A. Wierzbicki[2], and D. Madura[3] (✉)
[1]Department of Chemistry and Physics, Carlow University, 3333 Fifth Ave., Pittsburgh, PA 15213, USA; [2]Department of Chemistry, University of South Alabama, Mobile, AL 36688, USA; [3]Center for Computational Sciences, Department of Chemistry and Biochemistry, Duquesne University, 600 Forbes Ave., Pittsburgh, PA 15282, USA
e-mail: jdmadura@me.com

J. Leszczynski and M.K. Shukla (eds.), *Practical Aspects of Computational Chemistry*, 359
DOI: 10.1007/978-90-481-2687-3_18,

interfacial region with respect to contributions to the free energy from solutes. With an understanding of free energy contributions from different sizes and types of solutes, advancements can be made in the area of antifreeze solutions.

In this study, the calculation of the free energy change for the transition from the liquid to gas phase is performed by doing standard free energy calculations [6–10]. For the calculation of the free energy for the transition from the gas to the solid phase, a more robust simulation method is employed. The lattice-coupling-expansion method is used to determine the free energy of an ice crystal going from a thermodynamically stable ice crystal to an ideal gas through a systematic pathway [11–18]. First, the stable crystal is simulated in an isothermal-isobaric ensemble for an extended data gathering period. This system is gradually perturbed from the crystal to an ideal Einstein crystal lattice through a series of simulations that place a simple harmonic spring potential between the atom sites and the ideal crystal lattice sites [16]. As the harmonic potential is increased from zero to unity, the difference in the free energy is measured by taking the difference between the potential energies of the two individual systems and using the standard method of free energy perturbation to calculate the Gibbs energy difference. By using sufficient number of perturbation steps and enough Monte Carlo sampling steps, statistical confidence is gained in the calculation of the free energy change from the ice lattice state to the Einstein crystal state.

18.2 Methodology

One way to quantitatively determine the freezing temperature of a substance is by using the free energy change over a temperature range for both the different phases. If the number of molecules is kept constant in the isothermal-isobaric simulation, the chemical potential is equivalent to the Gibbs energy of the system. The Gibbs free energy as a function of temperature was first calculated for the water phase. For this calculation, a standard free energy perturbation simulation was performed for the insertion of a gas-phase water molecule into the solution. The perturbation calculation originates in the ideal gas phase, as there is no interaction of the water molecule with itself for a rigid water molecule with no internal degrees of freedom, to the bulk phase with a full interaction potential. Due to the step size that is allowed in the simulation, the water has the ability to relax around the solute as it is introduced into the system, thereby allowing for a smooth thermodynamic surface to be followed during the course of the simulation.

In the case of determining the freezing temperature, a more robust calculation for the solid phase must be completed, as the solid lattice free energy calculation must consider factors, such as the Pauling entropy. For this reason, the lattice-coupling-expansion method, which incorporates such factors, is employed for these types of simulations. For the Einstein lattice used in the simulations, a $6 \times 4 \times 4$ unit cell was used, which consists of 768 water molecules. This simulations size was

chosen to provide a 12.5 Å cushion that is required for accurate energy calculations when using Ewald summations [19–21]. (18.1) shows the relationship of the potential energy function as it is related to the position, orientation, and coupling parameter; it is noted that if the coupling parameter remains zero, or if there is no spring constant, the potential energy remains that of the pure ice lattice [16].

$$U\ \lambda = \int_0^1 \mathrm{d}\lambda \left\langle \sum_{i=1}^{N} \alpha (r_i - r_{0,i})^2 \right\rangle_{\lambda} \tag{18.1}$$

$$U_I\ r^N, \Omega^N; \lambda = U\ r^N, \Omega^N + \lambda \sum_{i=1}^{N} \alpha (r_i - r_{0,i})^2 \tag{18.2}$$

As the spring constant is increased by multiplying it by a coupling parameter going from zero to unity, it is turned on to its full potential. If the spring constant is large enough to hold the ice crystal into an Einstein crystal orientation in the conditions of the simulation, then the spring constant is large enough for that particular set of conditions. On the other extreme, if the spring constant is too large, the system would be perturbed to its final state too quickly, thereby not allowing the free energy path to be followed. Results from these types of simulation pitfalls could lead to random thermodynamic states, and therefore, erroneous free energy values. A balance between the spring constant must be observed, and if, and only if, this can be maintained, (18.1) can be justified in calculating the contribution to the potential energy and then added to the unperturbed system potential to obtain (18.2), which is the potential energy of the system due to the spring constant [16].

Once the Einstein crystal lattice thermodynamic state has been reached, it must then be perturbed to another known state or a state that is comparable to the liquid simulation or to one that can be thermodynamically obtained from perturbation from the liquid state. In this case, the Einstein lattice was perturbed to an ideal gas state by performing a volume expansion in three dimensions and calculating the free energy as it is perturbed from on volume size to the next larger volume size. Again, care was taken in making sure that the free energy path was closely followed. In this manner, the volume step size perturbation was based upon the natural volume fluctuation in the system; the standard deviation of the volume in the unperturbed system was allowed to be the standard deviation of the gaussian curve that generated the appropriate volume step size. This volume expansion perturbation selection allows for the system to follow the thermodynamic pathway from the Einstein lattice to the ideal gas state in a smooth and gradual manner. To test the methodology of the lattice-coupling-expansion method, other water models were selected, for which the melting temperature had been determined previously by similar methods [17, 22].

Simulations can be performed at various temperatures to find the free energies of the two phases as a function of temperature. The weighted points, which are based

on the individual simulations at each temperature, are used to derive a weighted linear regression by using a standard sum of squares:

$$\mathrm{SS}_w = \sum_i w_i \; y_i - b_0 - b_1 x_i \,^2 \tag{18.3}$$

By minimizing the error between b_0 and the b_1 simultaneously, which are respectively the intercept and the slope of the graph, one can find the best fit for the calculated data points. In (18.3), w_i is the weight of the point on the line determined from the error bars in each isothermal-isobaric simulation. For the propagation of error, and in particular, by using the uncertainty in sums and differences and the uncertainty in products and quotients rules, the intersection of the lines, x, can be shown to be:

$$x = \frac{(b_i \pm \delta b_i) - (b_w \pm \delta b_w)}{m_w \pm \delta m_w - m_i \pm \delta m_i} \tag{18.4}$$

where b_i indicates the intercept of the ice free energy as a function of temperature and b_w is the intercept of the free energy as a function of temperature for the water; m_w is the slope of the free energy vs. temperature for the water and m_i is the slope of the free energy vs. temperature for the ice. The corresponding δb_w, δm_w, δm_w, and δm_i are the standard deviations for the respective b_w, m_w, m_w, and m_i variables from the weighted linear regression, determined in (18.3). By propagating the error through the slope and the intercept using the weighted linear regression, the error in the intersection point is determined accurately.

For the solutes, simple salt solutions were selected, as they would provide a basic understanding of how non-idealistic solute particles would disrupt the liquid phase, thereby requiring the temperature to be lowered to make the transition from one phase to the other. The simple salts selected were chosen to have no net charge on the simulations systems and the pure Ewald summation was selected as the water model was parameterized under these conditions [21]. The salt solutions studied include a selection for size to charge ratio and 1:1 salt and 1:2 salt comparisons; the salts studied included varying concentrations of NaCl, KCl, $CaCl_2$, and $MgCl_2$.

18.3 Results

18.3.1 Determination of Aqueous Freezing Points

Both the liquid and solid phase simulations were performed at five temperatures, ranging from 213 to 273 K by 15 K intervals for all of the selected water models in this study. For the TIP3P, an additional run was performed at 160 K, closer to the intersection point of the two lines, as the temperature range selected was outside of

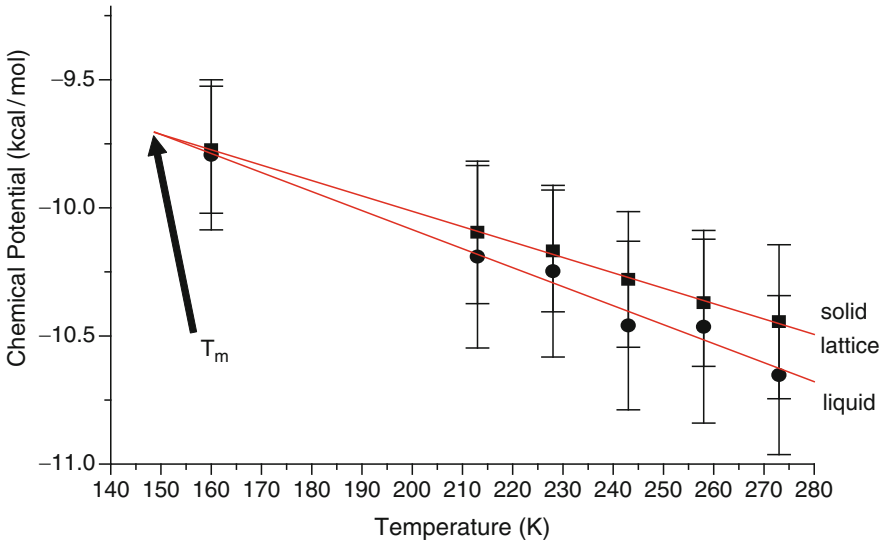

Fig. 18.1 Free energy vs. temperature for the liquid and solid phases using the TIP3P water model

both the calculated and literature values for the melting of the TIP3P water model. Figures 18.1 and 18.2 show the plots of free energy vs. temperature for both the liquid and solid phases for the TIP3P and TIP4P water models, respectively; the intersection of the two lines is the calculated melting temperature. From the graphs, the intersection of the lines from the two phases is very easy to observe, though the deviation in the melting temperature appears to be much larger than that of the actual value calculated through propagation of error.

From the intersection point on the graph in Fig. 18.1, the melting temperature of the TIP3P water model is determined to be 149.0 K$\pm$5.3 K. This is close to the reported melting temperature from free energy simulations of 145.6 K. Although the intersection point is outside of the available data points, the closest data point is within 12 K and is considered to be a test case for the TIP4P-Ew water model simulations, no more simulations were performed below the intersection point as they were time consuming and not as significant as the four-site model potential results. For the results from the TIP4P water model, the melting temperature was found to be 243.2 K$\pm$7.6 K. This is compared with literature values of 232.0 and 238 K, and the values for the free energy were comparable as well. Although these values are not within the error bars of the calculated melting temperature, both the TIP3P and TIP4P water model melting temperatures were within the 80% confidence limit of the literature values and were considered to be validation for the methodology for use in the calculation of the melting temperature for the TIP4P-Ew water model.

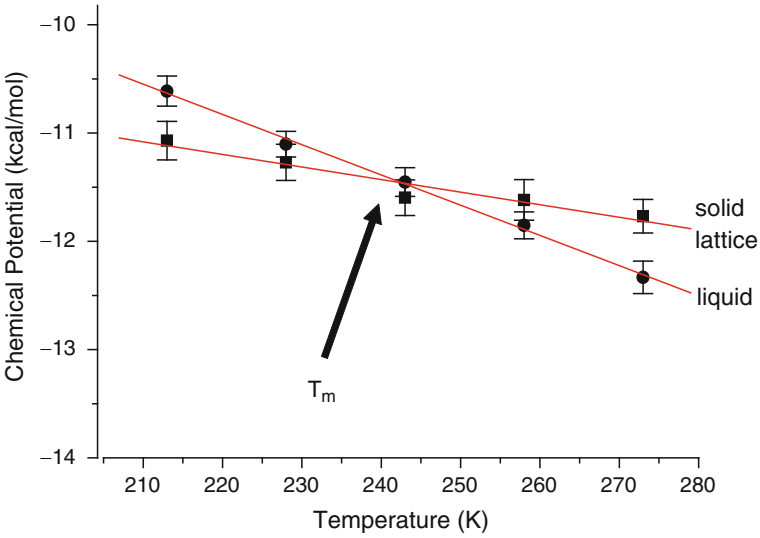

Fig. 18.2 Free energy vs. temperature for the liquid and solid phases using the TIP4P water model

The melting temperature for the TIP4P-Ew water model was determined to be 251.4 K ± 5.6 K, as compared with the literature value of 245.5 K. This is within the 85% confidence limit, and is, therefore, considered to be comparable to the literature value, as well as provide validation for the methodology. Both the liquid and solid phase simulations were extended to 400% of the original sampling steps at 263 K to ensure adequate sampling was achieved. From the extended simulation, it was observed that there was no improvement in the statistical certainty of the intersection, and thus, the simulation steps were concluded as being an adequate number of steps. The melting temperature simulations also provide a baseline for determining the amount of free energy required to move a molecule with solutes introduced into the simulation system (Fig. 18.3).

Figure 18.4 shows the free energy change for increasing NaCl concentrations as a function of temperature. Again, the intersection point of the solution and the solid phase provides the melting point of the solvent under those specific conditions. As the concentration of salt was increased, the free energy value at any set temperature decreased as expected. Similar trends are seen in the KCl, $CaCl_2$, and $MgCl_2$ salt solutions plots. A summary of all of the salt solution influences on the melting temperatures compared against the experiential deviation in melting temperatures can be viewed in Table 18.1. From the plot in Fig. 18.4, it can be seen that the increasing salt concentration shifts the y-intercept to a more negative value. For the individual salt solution simulations, the free energy lines are not parallel to each other, but are in fact very similar to one another.

For the KCl solutions, the same positive trend in comparison to the experimental deviation can be seen, although the actual deviations were slightly less than that of

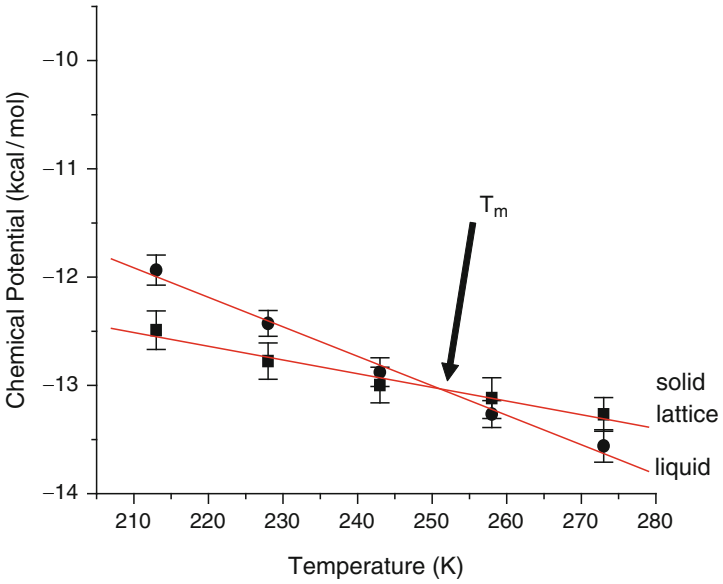

Fig. 18.3 Free energy vs. temperature for the liquid and solid phases using the TIP4P-Ew water model

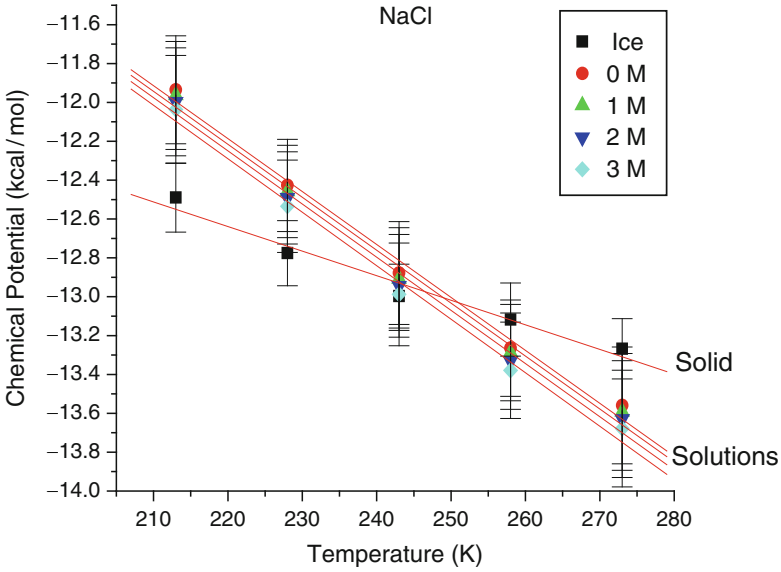

Fig. 18.4 Free energy vs. temperature for the solid phase and liquid phases, the latter containing increasing NaCl concentrations; the TIP4P-Ew water model was used as the solvent

Table 18.1 Values for the calculated freezing point depression (FPD) for NaCl, KCl, $CaCl_2$, and $MgCl_2$ salt solutions compared to the experimental values

Salt	Concentration (M)	Expt. ΔT_m (K)	Calc. ΔT_m (K)	St. Dev.	$\Delta\Delta T_m$, (Expt. – calc.) (K)
NaCl	1	1.9	2.9	4.5	1.0
	2	3.3	5.4	4.8	2.1
	3	5.9	9.1	4.8	3.2
KCl	1	1.6	2.3	4.3	0.7
	2	3.1	4.9	4.1	1.8
	3	5.1	7.9	4.9	2.8
$CaCl_2$	1	2.2	3.9	4.2	1.7
	2	5.0	5.6	4.2	0.6
	3	9.3	10.1	4.3	0.8
$MgCl_2$	1	2.3	3.9	4.2	1.6
	2	5.8	5.7	4.2	−0.1
	3	11.6	10.2	4.3	−1.4

the NaCl solutions. The reason for this phenomenon could be attributed to the size to charge ratio for K^+, which is larger than that of Na^+. Van't Hoff predictions are more closely related to the NaCl solutions than that of the other salt solutions studied in this work. Thus, the size to charge ratio could be considered to be an average salt size to charge ratio and deviations from this average size to charge ratio could be seen in the depression of the melting temperature. Further investigation into other salt influences, such as observing the trends in the 1:2 salt solutions, is needed before this idea can be substantiated.

Size to charge ratio influence is further reinforced in the di-anionic salt solution trends. The difference in depression of the freezing temperature is the reverse trend for all, but the highest $MgCl_2$ solutions. The deviation starts off as an underestimation of the depression value, crosses the difference in melting temperature for the experimental values, and then overestimates the depression value. Although this is a reverse trend to following the actual depression values, the absolute values of the freezing point depression (FPD) follow the experimental trend. There is what appears to be some multiplying factor that is salt type dependent that could match the FPD values to the experiment. Although the value for this factor is not important, it does re-iterate the point that salt type as well as concentration plays an important part in the depression of the freezing point of aqueous solutions.

The trends for the FPD follow what appears to be a size to charge ratio for the depression of the freezing point, deviating from an average salt size to charge ratio. This average salt size to charge ratio appears to be that for a NaCl solution with the larger size to charge ratio cations in the salt solutions depressing the freezing point less than the NaCl solutions, and the smaller size to charge ratio salts, such as the 1:2 salts, depressing the freezing point more. This trend is similar to that seen in the Hoffmeister series for the salting in/ out of proteins, for which different types and concentrations of salts are added to solutions already containing proteins and salt to change the protein's solubility. If more proteins can be added to the solution before solution saturation occurs, this is said to *salt in* the protein and if the protein falls out

of solutions when the salt is added, the salt is said to have *salted out* the protein. This trend seen in the FPD due to the salt addition to the solution can be seen as the NaCl salt being the average salt type as it follows the van't Hoff, or ideal solute trend more closely than any of the other salt solutions. As the salt size to charge ratio is increased, the depression of the freezing temperature deviates from the van't Hoff to the NaCl values more negatively for the larger size to charge ratios and more positively for the smaller size to charger ratios.

A structural explanation of the size to charge ratio is discussed frequently in the hydrophobic/ hydrophilic literature. Usually, this phenomenon is discussed in terms of two types of solute particles, known as cosmotropes and kaotropes, which are structure makers or structure breakers, respectively. When a solute can form a perfect shell of solvent around the molecule, it can then form the next solvation shell in succession, so that the molecules are in a uniformly repeating, tightly bound pattern. This forms the closest packed type of system which in turn, promotes a strong network of hydrogen bonds. In the other extreme, the solute particle has a radius in which the water molecules cannot form a perfect hydrogen bond network, thereby leaving irregularities in the first solvation shell. If the solute particle is also an ion, and there is a large size to charge ratio, the water molecules are not strongly attracted in the first place, and cannot form strong solvation shells. With the combinations of the disruption of hydrogen bond network, and the weakly bound solvation shells, the hydrogen bond network is weaker than that of pure water, and is thus, said to be a structure breaker. These structure makers and breakers would contribute to the solvent's ability to move from the solution, through the interfacial region, to attach to the solid phase increasing the lattice size. Structure makers could hold on to water molecules better than the kaotropes, and would be a contributing factor in the solution's ability to depress the freezing point. The radial distribution functions (RDFs) from the solution phase in the T_m simulations with the different salt solutions, show strong solvation peaks for the cosmotropes, while the kaotropes are shown to have weakly defined first and second solvation shells. This reinforces the idea that the salt influences in the solution play an important part in the amount of solvent that has the ability to transfer from the liquid phase to the solid phase at a certain temperature.

At the higher ion concentrations, the FPD values deviated more from the experimental values than at the lower concentrations. This concentration effect is speculated to have arisen due to the parameterizations process and sampling issues as well. These solutions are considered to be outside the normal conditions for most molecular simulations at the higher concentrations, which would in itself bring scrutiny to the simulation. In addition, the energetic, structural, and thermodynamic properties for which the ions were parameterized to reproduce were for infinite concentrations for the ions. Considering that these salt solutions are becoming saturated in the solution simulations, there would be ion–ion interactions for which the solvent was never intended to be used and would not be suitable for these types of effects. The other issue relating to the higher concentrations is the strength of the overall hydrogen bond network. For the strong cosmotropes, the solvent molecules could be strongly associated with more than one salt ion, making

its ability to traverse across the simulation system substantially less than that of a water molecule in a pure solvent situation. Sampling is hard at high concentrations as the ability to give up solvation shells reduces at a very high rate. These types of issues make the free energy values obtained for higher concentration salt solutions doubtful.

18.4 Conclusions

Salt solutions are known to depress the freezing point of aqueous solutions by disrupting the hydrogen bonding network that is naturally occurring the pure solvent. This phenomenon has been explained through the classical van't Hoff freezing point equation, where the solute concentration is the only factor that influences the depression of the freezing point. Through experiment, it is known that salt solutions, which do not form the ideal solutions for which the van't Hoff equation was intended, deviate drastically from the classical ideal solute particle predictions. For a more thorough understanding of how the different salts influence the FPD, a series of computational simulations were performed. These simulations show quantitative predictions of the FPD using a rigid four-site water model in simple salt solutions. On the basis of these simulations, a theory on how the different types and concentrations of salts influence the depression of the freezing point in aqueous solutions is proposed.

To first determine the influences of the salt upon the phase change of a solution, the understanding of the freezing of the pure solution is first needed. For this study, the TIP4P-Ew water model was used, and hence, the melting temperature, or the freezing temperature was needed to be obtained. To determine the melting temperature of the TIP4P-Ew water model, a series of molecular dynamics simulations was performed to study the melting of ice at various temperatures; each simulations was constructed using an ice lattice block encompassed on two ends with water. During the course of the simulations, the energetic, thermodynamic, structural, and time dependent properties were monitored, which included things, such as the RDFs, longitudinal bin counts of the oxygen atoms, and the self diffusion coefficients. From the methods used for these simulations, a value for the melting temperature, T_m, was determined to be between 263 and 258 K, but was considered to have an error of ± 5 K, due to the different criteria used for the melting temperature. Although these simulations provide somewhat of a reasonable value for the melting temperature, they did not provide any quantitative measurement of the freezing process, and could not be used in the determination of solute influences in the FPD in aqueous solutions.

For the quantitative understanding of the phase change process, a more robust method was used to determine the free energy contributions to the freezing process. The free energy as a function of temperature was determined for both the liquid and solid phases of the pure solvent using the lattice-coupling method and free energy perturbation. In this idea, the solid phase free energy is calculated by first coupling

the coordinate to a perfect Einstein lattice, and then isothermally expanding the lattice to an ideal gas state. To validate the method, the melting temperature for the TIP3P and TIP4P water models were first calculated. These models provided reasonable agreement with the reported literature value, so the TIP4P-Ew was evaluated as well. The freezing point of the TIP4P-Ew water model was determined to be 251.4 K $\pm$ 5.6 K; with the error, the calculated T_m was close to the value of the literature reported value of 245.5 K. Using the melting temperature and the free energy as a function of temperature, the salt influences were investigated.

Using the varied salt concentrations, the salts' influences on the FPD were compared to the Hoffmeister series for the salting in and out of proteins. The trends for the NaCl solutions appeared to follow the van't Hoff predictions and were considered to be an average salt size to charge ratio. The larger size to charge ratios for the cation, such as the potassium in the KCl solutions, broke up the hydrogen bonding in the solvent structure and allowed the waters to exit the solvation shell more easily than that of the bulk solvent. The smaller size to charge ratios formed a tight solvent structure around the ions, and thus, influenced the ability for the solvent to transition from the liquid to the solid phase. Other factors to consider for the simulations directed attention to the sampling around the smaller size to charge ratio salts at higher concentrations, although these influences were solved with more Monte Carlo steps. Our simulations tends to indicate that there may be issues with using higher ionic concentrations for sensitive thermodynamic quantities, such as the free energy, since the parameterizations for the ions are determined at infinite concentrations for the individual ions.

Acknowledgments This work was funded in part by the NSF (CHE-0723109, CHE-0321147, AB/PSC CHE-030008P); Department of Education (P116Z040100, P116Z050331, nd P116Z080180), NETL, Pittsburgh, PA; the Silicon Graphics Inc.; James River Technical, Inc.; Gaussian Corporations; the National Science Foundation under Grant No. CHE-0616674; co-funded by the Division of Chemistry; the Office of Polar Programs; and the EPSCoR Office.

References

1. J.J. Hoyt et al., Method for computing the anisotropy of the solid-liquid interfacial free energy. Phys. Rev. Lett. **86**, 5530–5533 (2001)
2. O.A. Karim et al., The ice/water interface: A molecular dynamics simulation using the simple point charge model. J. Chem. Phys. **92**, 4634–4635 (1990)
3. L.H. Seeley, G.T. Seidler, Two-dimensional nucleation of ice from supercooled water. Phys. Rev. Lett. **87**, 055702/1 (2001)
4. I.M. Svishchev, P.G. Kusalik, Crystallization of liquid water in a molecular dynamics simulation. Phys. Rev. Lett. **73**, 975–978 (1994)
5. G.W. Robinson, S.-B. Zhu, S. Singh, M.W. Evans, *Water in Biology, Chemistry and Physics* (World Scientific, Singapore, 1996)
6. O.B. Becker et al., *Computational Biochemistry and Biophysics* (Marcel Dekker, New York, 2001)
7. W. Jorgensen, C. Ravimohan, Monte Carlo simulation of differences in free energies of hydration. J. Chem. Phys. **83**, 3050–3054 (1985)

8. A. Leech, *Molecular Modeling Principles and Applications*, 2nd edn. (Prentice Hall, Harlow, 2001)
9. M. Pellegrini et al., Potentials of mean force for biomolecular simulations: Theory and test on alanine dipeptide. J. Chem. Phys. **104**, 8639–8648 (1996)
10. W.C. Swope, H.C. Andersen, A molecular dynamics method for calculating the solubility of gases in liquids and the hydrophobic hydration of inert-gas atoms in aqueous solution. J. Phys. Chem. **88**, 6548–6556 (1984)
11. D.A. Kofke, Direct evaluation of phase coexistence by molecular simulation via integration along the saturation line. J. Chem. Phys. **98**, 4149–4162 (1993)
12. D.A. Kofke, Gibbs-Duhem integration: A new method for direct evaluation of phase coexistence by molecular simulation. Mol. Phys. **78**, 1331–1336 (1993)
13. C. Vega et al., The fluid–solid equilibrium for a charged hard sphere model revisited. J. Chem. Phys. **119**, 964–971 (2003)
14. C.M. Vega et al., Radial distribution functions and densities for the SPC/E, TIP4P and TIP5P models for liquid water and ices I_h, I_c, II, III, IV, V, VI, VII, VIII, IX, XI and XII. Phys. Chem. Chem. Phys. **7**, 1450–1456 (2005)
15. C. Vega et al., Can simple models describe the phase diagram of water? J. Phys. Condens. Matter **17**, S3283–S3288 (2005)
16. D. Frenkel, B. Smit, *Understanding Molecular Simulation: From Algorithms to Applications* (Academic, San Diego, 1996)
17. L.A. Baez, P. Clancy, Phase equilibria in extended simple point charge ice-water systems. J. Chem. Phys. **103**, 9744–9755 (1995)
18. M.J. Vlot et al., Free energy calculations on systems of rigid molecules: An application to the TIP4P model of H_2O. J. Chem. Phys. **110**, 55–61 (1999)
19. N.J. English et al., Molecular-dynamics simulations of methane hydrate dissociation. J. Chem. Phys. **123**, 244503 (2005)
20. N.J. English, J.M.D. Macelroy, Structural and dynamical properties of methane clathrate hydrates. J. Comput. Chem. **24**, 1569–1581 (2003)
21. H.W. Horn et al., Development of an improved four-site water model for biomolecular simulations: TIP4P-Ew. J. Chem. Phys. **120**, 9665–9678 (2004)
22. T. Bryk, A.D.J. Haymet, Ice 1h/water interface of the SPC/E model: Molecular dynamics simulations of the equilibrium basal and prism interfaces. J. Chem. Phys. **117**, 10258–10268 (2002)

Chapter 19
The Potential Energy Shape for the Proton Motion in Protonated Naphthalene Proton Sponges (DMAN-s) and its Manifestations

Z. Latajka and L. Sobczyk

Abstract The problem of the low-barrier hydrogen bond in protonated naphthalene proton sponges is reviewed. Experimental data related to the infra-red and NMR spectra are presented, and the isotope effects are discussed. An unusual potential for the proton motion that leads to a reverse anharmonicity was shown: The potential energy curve becomes much steeper than in the case of the harmonic potential. The isotopic ratio, i.e., ν_H/ν_D (ν-stretching vibration frequency), reaches values above 2. The MP2 calculations reproduce the potential energy curve and the vibrational H/D levels quite well. A critical review of contemporary theoretical approaches to the barrier height for the proton transfer in the simplest homoconjugated ions is also presented.

19.1 Introduction

Since the first report on the synthesis and properties of 1,8-bis(dimethyloamino) naphthalene [1], it was commonly named as proton sponge [2]. As a number of strong bases classified as proton sponges was then synthesized, we started using the abbreviation DMAN as applied to naphthalene proton sponges in the wide meaning of its derivatives. Naphthalene proton sponges (DMAN-s) have been of particular interest as shown in reviews [3–7].

The importance of DMAN-s is due to its following characteristic features:

1. High basicity that can be modified by introducing various substituents.
2. After attraction of one proton hydrophobically isolated, stable intramolecular low-barrier $[NHN]^+$ bridges are formed.
3. The $[NHN]^+$ bridges are characterized by marked rigidity.

Z. Latajka (✉)
Faculty of Chemistry University of Wrocław, Joliot-Curie, 1450-383, Wrocław, Poland
e-mail: sobczyk@chem.uni.wroc

J. Leszczynski and M.K. Shukla (eds.), *Practical Aspects of Computational Chemistry*, 371
DOI: 10.1007/978-90-481-2687-3_19,

4. They are influenced by both external (solvent, crystalline lattice) and internal (substituents at positions 2 and 7) factors.

All these factors mean that DMAN-s can be treated as model compounds enabling to aid in understanding the various effects of modifying the physical properties of chemically symmetrical $[NHN]^+$ hydrogen bonds.

Protonated DMAN-s are, therefore, the subject of particular interest in this short review from the point of view of the potential for proton motion. In addition, this potential is reflected in various properties such as vibrational and NMR spectra and particularly the isotope $^1H/^2H$ effects connected with them.

General remarks are also presented on current trends in theoretical approaches to the potential energy shape of the proton motion in hydrogen bonded systems.

19.2 Main Properties of Protonated DMAN-s

19.2.1 Geometry of $[NHN]^+$ Hydrogen Bonds

The structures of ca. 50 DMAN·H^+ cations containing various substituents and counter-anions have been determined so far [8]. A non-symmetrical distribution of substituents affects the symmetry of the $[NHN]^+$ bridge, as does the position of counter-anions. However, the lower the symmetry, the longer is the bridge. This is not a rule because as in the case of the trimethoxymetane anion [9], the bridge is dynamically symmetrical, although it is rather long, which is probably caused by a free rotation of the counter-anion leading to dynamic averaging of the potential around the bridge.

The $[NHN]^+$ hydrogen bond length in protonated DMAN-s is remarkably shorter than what is expected for homoconjugated cations of freely linked amines as theoretical studies by Scheiner show [10]. These studies have also shown that in the free cation of conjugated amines, there is a double minimum of the potential with a relatively high barrier. For bridges with lengths characteristic of DMAN·H^+, one would expect a double minimum as well, but with a much lower barrier. From the analysis of data published in [11], it follows that bulky substituents at positions 2 and 7 exert some influence on the bridge length, which is called the buttressing effect. This effect can be analyzed in terms of the internal strain caused by a change in the bond angles of the di-methylamine group and some change in the charge distribution. One can discuss this problem also in terms of the softness of hydrogen bonds [12]. Examples of typical $[NHN]^+$ bridges in DMAN-s compared with other homoconjugated cations are presented in Table 19.1.

Symmetrical bridges in crystalline lattices of DMAN salts have been found, from the review in [8] and as cited in Table 19.1 for about 10 cases. One should remember of course that in the gas phase and solutions, all bridges are dynamically symmetrical if the base molecule is also symmetrical.

Table 19.1 Examples of $[NHN]^+$ hydrogen bonds

	Bridge length (Å)	References
Free $H_3NH^+NH_3$ cation (calculated)	2.73	[10]
Polycations of monoprotonated diazabicyclo[2.2.2]octane	2.84	[13]
4-Aminopyridine perchlorate	2.70	[14]
Homoconjugated cations of quinuclidin-3-one perchlorate	2.63	[15]
$DMANH^+$ for various salts	2.54–2.64	[8]
Protonated 1,6-diazabicyclo[4.4.4]tetradecane	2.526	[16]
$2,7\text{-}(CH_3O)_2\cdot DMAN\cdot H^+$	2.567	[17]
$2,7\text{-}Cl_2\cdot DMAN\cdot H^+$	2.561	[18]
$2,7\text{-}Br_2\cdot DMAN\cdot H^+$	2.547	[19]
$2,7\text{-}[(CH_3)_3Si]_2\cdot DMAN\cdot H^+$	2.530	[20]

Table 19.2 Geometrical parameters of the symmetrical $DMAN\cdot H^+$ cation with substituents in positions 2,7; the length of NHN^+ hydrogen bond R(N···N), linearity of the bridge expressed in ∠NHN; repulsion between the substituents in positions 2,7 and $N(CH_3)_2$ groups reflected in C(1)C(2)X angles

R	R(N···N) (Å)	∠NHN (°)	∠C(1)C(2)X (°)
OCH_3	2.567	160	116
Cl	2.561	165	123
Br	2.547	162	125
$Si(CH_3)_3$	2.530	161	133

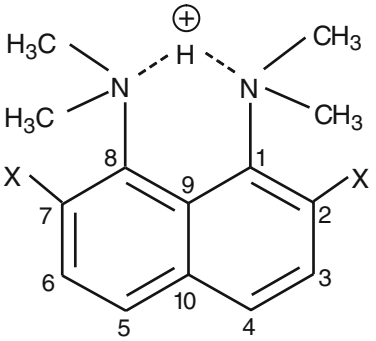

Scheme 19.1

Compared with the base molecules, their protonated forms are flattened to a large extent, i.e., the nitrogen atoms are located in the plane of the naphthalene ring. Let us remember that in DMAN molecules, a strong repulsion of lone electron pairs takes place that leads to a marked twisting of the $N(CH_3)_2$ groups and an inclination of the nitrogen atoms from the plane of the naphtyl ring. Let us compare the C(1)C(2)X angles (see Scheme 19.1) for the derivatives in which X denotes the atom bound with the carbon atom at position 2 (Table 19.2)

One should mention here that this is an informative parameter as the X-atoms, even in the case of the $Si(CH_3)_3$ substituent, are only slightly shifted from the naphthyl ring plane.

As shown in Table 19.2, most evident is the substituent effect upon the C(1)C(2) X angle and then on the bridge length. The linearity of the bridge is for all substituents, almost the same.

19.2.2 Infrared Spectra

Looking at the infrared spectra of NHN hydrogen bonded systems, one finds that the bridges in the DMAN·H^+ cation are characterized by a very low frequency of the asymmetric stretching ν(NHN) vibrations. Figure 19.1 can serve as an illustration wherein the evolution of the ν(NHN) band is presented passing from the weak bridges up to the strongest ones appearing in the DMAN·H^+ cation. Such peculiar behavior of the ν(NHN) band is manifested when the zero vibrational level is somewhat below the barrier for the so-called low-barrier hydrogen bonds. This problem will be one of the main topics of this review.

From limited data, as Table 19.3 shows, one can conclude that when the bridge length decreases, the ν(NHN) band undergoes a blue-shifting. On the other hand, as can be suspected based on the theoretical analysis (see section 19.3), we are dealing with the barrier height of the order of 220–250 cm^{-1}. Anyway, in the case of the single minimum potential, as found for protonated 1,6-diazabicyclo[4.4.4]tetradecane [16], a broad band centered at ca. 1,000 cm^{-1} appears. A similar situation is found when we are dealing with highly asymmetrical bridges. In such a case, a broad high-frequency wing appears [21, 22].

One of the most important parameters related to the potential shape for the proton motion is the isotope effect, defined by the isotopic ratio (ISR) ν(XH)/ν

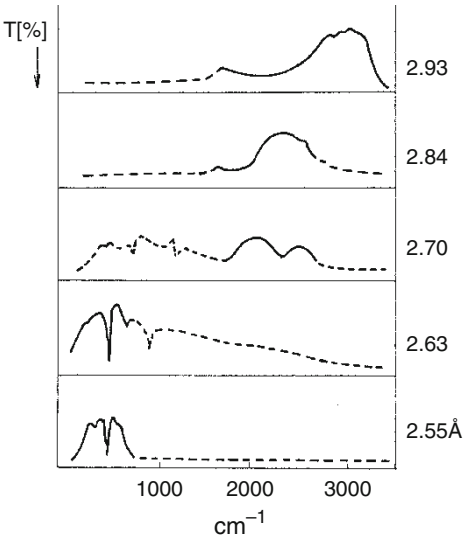

Fig. 19.1 The evolution of the ν(NHN) absorption band on shortening of the NHN bridge [24]

Table 19.3 Properties of protonated 2,7-R_2-DMAN-s [23]

R	R(N···N) (Å)	ν(NHN)(cm^{-1})	ISR	δppm	Δδ ppm
H	2.595[a]	490[a]	1.7–2.0[a]	18.65	0.69
OCH_3	2.567	488	2.08	19.54	0.31
Cl	2.561	530	1.80	20.10	0.30
Br	2.547	560	1.65	20.27	0.23
$Si(CH_3)_3$	2.530	610	1.6	20.63	0.14

[a]Average values for various salts of DMAN, markedly dependent on the counter-anion

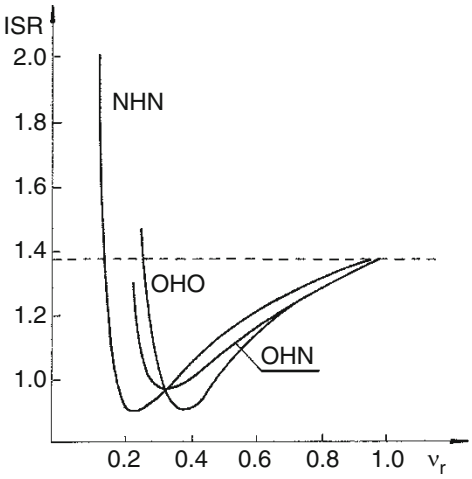

Fig. 19.2 Isotopic ratio ISR = ν(AH)/ν(AD) plotted versus relative frequency $\nu_r = \nu(XH)/\nu_0(XH)$ for three types of hydrogen bonding [25]

(XD). Due to the anharmonicity in usual hydrogen-bonded systems, the ISR value is less than $\sqrt{2}$. In the case of strong hydrogen bonds, it can even attain a value of less than 1. The run of the dependence of ISR on the relative frequency ν(XH)/ν_0(XH) is presented in Fig. 19.2 in which three types of hydrogen bonds, namely OHO, OHN and NHN, are compared. One can clearly see deep minima corresponding to low frequencies and then a fast increase in ISR to reach values exceeding $\sqrt{2}$. In the case of the OHO bridges, the maximum value of ISR does not exceed 1.5, while in the case of NHN bridges, the maximum value of ISR may be above 2. Such cases are only characteristic just of bridges in DMAN·H^+ cations. This problem can be discussed in terms of the reverse anharmonicity: the potential energy curves become steeper than they would be in harmonic potential.

19.2.3 NMR Spectra

Sensitive indicators of the potential energy shape for the proton motion in DMAN·H^+ cations are without doubts ^1H, ^2H, ^{13}C and ^{15}N NMR spectra. In the

DMAN·H^+ cation, the bridge proton is strongly deshielded and the greater this deshielding, the stronger and shorter the bridge. The maximum δ^1H value is naturally observed for the shortest bridges, exceeding 20 ppm. One should remember that high chemical shifts in DMAN·H^+ cations are additionally due to the diamagnetic ring current effect. For comparison, one can consider the extreme cases of 1,14-diaza[5]-helicene (1) and 1,6-diazabicycle[4.4.4]tetradecane (2).

For 1, the δ^1H value reaches 23.89 ppm, while for 2, it is only equal to 17.40 ppm, in spite of the fact that in the latter case, we are dealing with a single minimum potential, i.e., the maximum deshielding should be present. The second important parameter in the ^{1}H NMR spectra is the coupling constant of the bridge protons with methyl groups, which reflects the degree of asymmetrization of the bridge. In the case of dynamically symmetrical bridges, we do not observe a differentiation of splitting, i.e., both $N(CH_3)_2$ groups are equivalent. With asymmetry, when the bridge proton is located markedly close to one group, one observes larger coupling constants. This problem is illustrated by the data in Table 19.4.

Of great importance in analyzing the potential for the proton motion in protonated DMAN-s is the primary isotope effect $\Delta\delta(^1H/^2H)$. As already amply shown in the literature (see [27–29]), in cases of an asymmetric double-minimum potential, the isotope effect consists of intrinsic and equilibrium parts. For the symmetric bridges of DMAN-s cations, the intrinsic part predominates, which is related to the anharmonicity of the potential leading to a change in the hydrogen bond length and the position of the peak of the square wave function for ^{1}H and ^{2}H. This is illustrated in Fig. 19.3, showing the potential energy curves. One can see that after deuteration, the bridge becomes somewhat weaker, with greater separation of the minima.

As analysis performed by Matsushita and Matsubara shows, the largest isotope effect should be expected when the vigorous tunneling is present, i.e., when the zero-point energy approaches the top of the barrier [30].

Table 19.4 $^3J(NH,NCH_3)$ coupling constants for protonated DMAN derivatives in DMSO-d_6 [26]

R	$\delta(NH^+)$	$^3J_{NH,CH3}$		Degree of localization (%)	
		Position-1	Position-8	Position-1	Position-8
H	18.33	2.63	2.63	50	50
2,7-Cl_2	19.91	2.64	2.64	50	50
4,5-Cl_2	19.14	2.52	2.52	50	50
2,7-Br_2	20.09	2.41	2.41	50	50
4,5-Br_2	19.12	2.41	2.41	50	50
4-NH_2	18.26	3.23	1.21	73	27
4-NHAc	18.55	2.86	2.24	56	44
4-Cl	18.52	2.42	2.64	48	52
4-BR	18.56	2.31	2.53	48	52
4-CN	18.15	1.88	2.97	39	61
4-NO_2	18.50	1.72	3.19	35	65
2-Cl	18.02	0.77	4.06	16	84
2-Br	18.09	~0.5	3.45	11	89

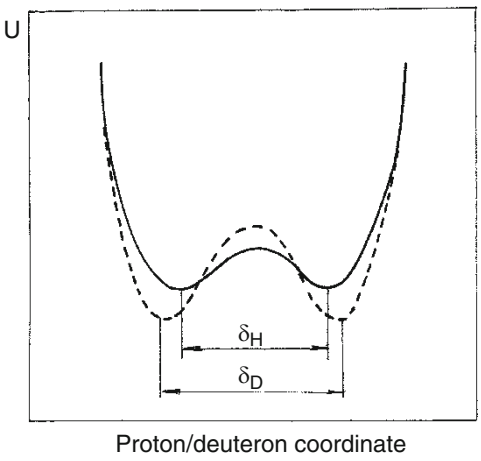

Fig. 19.3 The 1H/2H isotope effect on the distance between the potential energy minima for the symmetric low-barrier hydrogen bonds

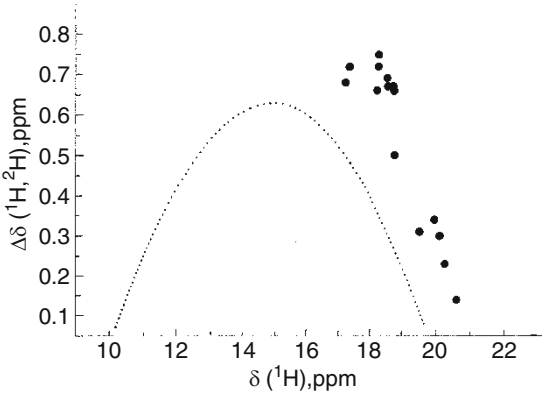

Fig. 19.4 Correlation between Δδ and δ(^{1}H) values for protonated DMAN-s against a background of similar relationship for OHO hydrogen bonded systems reported by Gunnarsson et al. [23, 32]

The results of studies on the primary NMR isotope effect performed with a set of protonated DMAN-s are illustrated in Fig. 19.4 which presents the relationships between the isotope effect and the ^{1}H chemical shift of non-deuterated compounds. The experimental points (full circles) come mainly from paper [23] and a few of them from [31]. The results collected for DMAN-s are compared with the corresponding relationship for OHO hydrogen-bonded systems [32]. The majority of the experimental points are in the region of $\Delta\delta \approx 0.6$–0.7 ppm and $\delta \approx 17.3$–18.8 ppm, i.e., close to data for non-substituted DMAN·H$^+$, for which $\delta = 18.65$ ppm and $\Delta\delta = 0.66$ ppm. One should mention here that asymmetry of the cation does not markedly affect either the δ or $\Delta\delta$ values. This is most probably due to similar electron density distributions on both nitrogen atoms and, consequently, similar populations of the two potential energy minima. Therefore, in our case, we can omit the contribution of the equilibrium effect on $\Delta\delta$ value. It seems that this effect is below 0.1 ppm.

Comparison of our results with the correlation curve for OHO bridges shows that the $[NHN]^+$ curve's maximum is shifted toward higher values of δ and the isotope effect is somewhat higher. The difference between OHO and NHN in DMAN·H^+ cations, reflected in Fig. 19.4, may result from two effects. The first, discussed by Scheiner [10, 33], is due to different covalent radii and a slightly different charge distribution. The second effect should be ascribed to the diamagnetic field of the naphthalene π-electron system.

19.2.4 ^{2}J(N,N) and J(N,H) Coupling Constants

The ^{2}J coupling constants can be estimated either directly by applying the ^{15}N isotope substituted compounds, or indirectly by using the data for ^{13}C NMR of carbon atoms at positions 1 and 8 [34–36]. The ^{2}J(N,N) values are usually less than 11 Hz. However, as follows from studies by Limbach et al. [37, 38], this coupling constant can achieve much higher values particularly in cases of anionic systems and when the π-electron delocalization takes place through nitrogen atoms. It has been estimated that ^{2}J(N,N) can reach 25 Hz when the N···N bridge length would be ca. 2.5 Å. However, as already mentioned, the shortest bridge in DMAN derivatives was found for the 2,7-di-Si$(CH_3)_3$ derivative, for which R(N···N) equals to 2.530 Å. Unfortunately, there are no data for this compound with respect to ^{2}J(N,N). Nevertheless, it should be much higher than 11 Hz.

There are no systematic results related to J(N,H) coupling constants, so we would like to present only the result obtained for the 4-NO_2 derivative with an asymmetric $[NHN]^+$ bridge. In this case, it was possible to compare the result with that obtained by using the ^{3}J(NH,CH_3) coupling constant. Both data enable an estimation of the population degrees for two N1 and N8 nitrogen atoms. The comparison is presented in Table 19.5.

As can be seen, there is good agreement between the data obtained using different coupling constants. From the results of Limbach et al. [36], it can be concluded that J(N1H) weakly decreases and J(N8H) weakly increases with δ^1H and that the sum of these quantities negligibly decreases with δ^1H. The δ^1H value generally expresses the strength of the [NHN] bridges. Finally, one should mention that δ^1H decreases, as a rule, with temperature. There is also a rule that δ^1H depends on the activity of the counter-anions expressed by their volume and the coordination strength.

Table 19.5 Population degrees derived from the ^{3}J(NH,CH_3) and J(NH) data for protonated 4-nitro derivative of DMAN

	^{3}J(N1H,CH_3)	^{3}J(N8H,CH_3)	J(N1H)	J(N8H)
	1.72	3.19	20.5	40.2 Hz
Occupation degrees (%)	35	65	34	66

19.3 Theoretical Treatment

The aim of the theoretical studies on the protonated DMAN-s was modeling of the potential energy curves for the proton motion and calculating the vibrational levels for the NHN^+ bridge. The object of analysis was 2,7-disubstituted DMAN-s. The substituents at positions 2 and 7, as shown, affect the bridge length and spectral characteristics. So far the 2,7-dibromo-, 2,7-dimethoxy and 2,7-di(trimethylsilyl) derivatives have been studied [17, 19, 20].

The first stage of modeling is optimization of the molecular structure by means of the standard procedure within the Gaussian program at the B3LYP and MP2 levels of theory with the double-ζ 6-31G(d,p) basis set. After optimization, the harmonic vibrational frequency calculations are performed to confirm the nature of the stationary point on the potential energy surface as a minimum. In the next stage, the potential energy is calculated step by step, changing the position of the bridge proton while preserving the remaining geometrical parameters found during the previous stage. The potential energy curves are obtained by scanning the potential energy surface along the NH coordinate with optimization of the NHN angle for each point. Such an approach allows taking into account the coupling of the NH stretching vibrations with the NHN bending one in modeling the adiabatic process. The adiabatic potential energy curve obtained in such a way allows one to reproduce the mode of the NH stretching vibrations. First, the ab initio energies are fitted with a sixth-order polynominal, V(r(NH)), and then the vibrational levels are calculated by solving a one-dimensional, vibrational, time-independent Schrödinger equation [39]. The vibrational Schrödinger equation is solved by the variational principle using a shifted Gaussian basis set.

The theoretical treatment is limited to the one-dimensional approach. The multi-dimensional procedure taking into account the coupling of the bridge stretching and bending modes is, at the moment, practically impossible for such large systems as DMAN-s derivatives.

The potential energy curve with vibrational energy levels for the NHN^+ bridge in protonated 2,6-dimethoxy derivative obtained by the MP2 method may serve as an example of calculations performed. It was shown that this method yields results with the best agreement with experimental data.

The results presented in Fig. 19.5 clearly show that we are dealing with a double-minimum potential and such a very low barrier that the zero-point energy level for the ν(NHN) vibrations is located slightly above the barrier's top (10 cm^{-1} for the MP2 method and 17 cm^{-1} for the DFT method). The zero-point energy level for the ν(NDN) vibrations is located somewhat below the barrier's top. In Fig. 19.5, an unusual anharmonic potential reversal to the typical anharmonicity taking place in stretching vibrations of hydrogen-bonded systems is well manifested. This is reflected in the pronounced increase in the distance between the successive overtone levels. Particularly meaningful in the spectroscopy of hydrogen bonds is the high value of the isotopic ratio νH/νD which is markedly higher than $\sqrt{2}$. In the case of the 2,6-dimethoxy derivative, the ISR

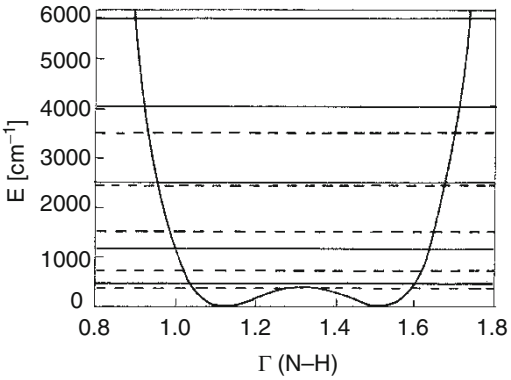

Fig. 19.5 MP2 anharmonic potential energy levels for $\nu(NHN)^+$ and $\nu(NDN)^+$, with solid lines for protonic and dashes ones for deuteronic motion. [17]

value reaches 2.08, the highest value reported in the literature till now for hydrogen-bonded systems. The calculated ISR values are in good agreement with experiment: by using the DFT method, one obtains 2.01, and using MP2, 1.97. It is not possible to compare the calculated transitions to higher vibrational levels because the overtones were not observed. In Table 19.3, experimental ISR values along with data related to the bridge lengths and NMR chemical shifts with isotope $^1H/^2H$ NMR effect are presented. From these data, it follows that the larger the chemical shift and the shorter the bridge, the smaller the isotopic ratio ISR in infra-red spectra. Unfortunately, we do not have enough theoretical data to confirm the trend of correlations among the quantities given in Table 19.3. In particular, there is a lack of precise calculations of the barrier height. Thus, for instance, the calculated barriers for the dimethoxy, dibromo, and di(trimethylsilyl) derivatives are equal to 220, 245 and 245 cm^{-1}, respectively, and it is not possible to draw any conclusion about correlations with other characteristics of NHN bridges in protonated DMANs.

19.4 General Remarks on the Accuracy of Ab Initio Calculations of Barrier Height for Proton Transfer

In connection with the problems discussed in section 3, it seemed justified to formulate some general aspects of theoretical pathways for proton transfer. The calculations of the potential energy shape for the proton motion have played important role in providing information about H-bonds not easily amenable to experimental research (for example, see [40, 41]). The accurate theoretical modeling of proton transfer processes is very challenging even today. Modeling proton transfer requires a reliable and accurate description of the potential energy surface that describes the ongoing formation and breaking of the molecular and hydrogen

Table 19.6 Calculated values of barrier height (kcal mol^{-1})

Method	$H_5O_2^+$		H_3O_2[c]	(FHF)[d]
HF	14.35[a]	9.90[b]	12.76	8.64
MP2	7.85	4.63	6.06	4.08
MP3		5.83	7.79	5.73
MP4(SDQ)		5.54	7.48	5.22
MP4(SDTQ)		4.86	6.68	4.21
QCISD				5.30
QCISD(T)	8.40			4.56
CCSD(T)	8.44		6.82	

[a]R(O. . .O)=2.8 Å, cc-pvTZ basis set, from [42]
[b]R(O. . .O)=2.74 Å, triple-zeta with two sets of polarization functions basis set, from [43]
[c]R(O. . .O)=2.74 Å, triple-zeta with two sets of polarization functions basis set, from [43]
[d]R(F. . .F)=2.6 Å , 6-311++G(3df, 3pd) basis set, from [44]

bonds involved in the transfer. The accuracy of quantum chemical calculations for hydrogen-bonded systems and proton-transfer phenomena depends on several factors, the most important of which are the theoretical level of the methods employed and the quality of the basis sets used.

Investigation of the potential energy surface for proton transfer requires calculations of electronic energy far from the equilibrium geometry, and, therefore, electron correlation becomes very important. As an illustration of this effect, selected examples of calculated barriers for simple model systems calculated by several methods are presented in Table 19.6. The barriers calculated at the Hartree-Fock (HF) level are greatly overestimated and the inclusion of the electron correlation leads to a dramatic reduction in the proton transfer barrier. Moreover, these barriers appear to converge as one progresses from one level of Moller-Plesset (MP2) theory to the next (i.e., MP4). The calculated electron correlation contributions to the barrier undergo alternation of sign and steadily decreasing magnitude. For this reason, the second order level of calculations (MP2) furnishes an excellent approximation of the full fourth-order calculation of the barrier height, and is a good alternative for larger systems wherein the full MP4 method is too time consuming. It is also interesting to note that triple (T) excitations have a fairly large contribution to the value of the barrier in comparison with single (S), double (D), and quadruple (Q) excitations. The Moller-Plesset calculations are in good agreement with coupled-cluster (CC) results. A particularly good agreement is noted between the MP4(SDTQ) and CCSDT. This means that it is recommended to use the full MP4 or a coupled cluster method, such as CCSDQ(T), to obtain very accurate results of the barrier height [45]. The difference in the geometrical structure between the MP2 and CCSD results is small, and thus, an accurate determination of the barrier heights requires MP2 geometry optimization and subsequent CCSDQ(T) or QCISDQ(T) energy estimation.

During the last few years, enormous progress has been made in the development of methods based on Density Functional Theory (DFT) to study molecular complexes [46–49]. The simplicity of DFT lies in the fact that it uses general functionals

of electron density to a model exchange and correlation. DFT methods show advantages of generality and accuracy in comparison with semi-empirical methods. In contrast to most advanced correlation methods, DFT consists of an inexpensive but rigorous approach to electron correlation if a proper correlation functional is applied. A great advantage of DFT methods is that they can be applied to fairly large molecular systems, since the need of computational resources in those methods formally scales as N3, where N is the number of basis functions, and the computer time is comparable to that of HF calculations. On the other hand, the more accurate MP4(SDTQ) method scales as N7, and the very accurate CCSDTQ approach scales as N8!.

In contrast to the many studies of the energetic, structural and vibrational properties of hydrogen bonded complexes, systematic studies of the applicability of various functionals to the description of the proton transfer barrier height have not been of major interest in DFT calculations. Until today, only a few papers have been published on this subject [42, 44, 50–55]. The form of the functional definitely plays a very important role in the determination of barrier heights. Local exchange-correlation functionals (as for example, SVWN) give barriers large improvement if the gradient-corrected (non-local) functionals are applied although the barrier heights are still underestimated. It should be added that all functionals with gradient-corrected exchange and correlation give values that are much better than the HF values. DFT methods with a portion of the Hartree-Fock exchange (so-called hybrid functionals) tend to produce results close to benchmark calculations. It is also worth noting that the accuracy of the calculated barrier depends strongly on the type of exchange functional used, and is less sensitive to the type of correlation functional.

The accuracy of the potential energy surfaces obtained by means of ab initio calculations is still governed by the limitations of the chosen basis set. The shape of the potential energy surface for molecular complexes is a result of the delicate balance between the various attractive and repulsive contributions. The basis set chosen for calculations should be versatile enough to describe efficiently all the different contributions to the interaction and the regions of chemical bonds as well as the regions for the nuclei (the region of transition state for proton transfer). In this respect, the most reliable are very extended and flexible basis sets with multiple sets of polarization functions and additional diffuse functions. For the study of proton transfer processes, very accurate barriers are obtained with recently developed basis, such as the correlation-consistent polarized valence (pVXZ, where X=T, Q, and 5) basis set augmented by diffuse functions (aug-cc-pVXZ), and are recommended as suitable basis sets if possible 45, 55.

Another aspect of the ab intio computation of molecular complexes is the basis set superposition error (BSSE). This is due to the use of an incomplete basis set for the description of molecular complexes. As a result, the basis set of one molecule provides a framework for artificial lowering the energy of its partner and vice versa. Consequently, the BSSE introduces a nonphysical attraction between two (or more) subunits which form a molecular complex. In another words, the BSSE decreases to zero as the atomic basis set used for the description of the molecular system becomes complete.

It is widely accepted that this artifact of calculations may be removed by the use of the Boys-Bernardi counterpoise (CP) scheme for the ab inito calculated interaction energy of complexes [56]. Because values of barrier heights are sensitive to the quality of the basis set used, one can also assume that the BSSE will influence the calculated values of the energy barriers. Although the effect of the BSSE upon the energetics of formation of the complex has been studied in some details in literature, little has been known about how this error affects the proton potential within the complex. It should be noted that the standard CP scheme is clearly defined for molecular systems in which the subunits can be considered as separate entities whose geometrical structure changes only slightly due to the interaction. This means that the application of the standard Boys-Bernardi CP scheme requires that each atom, and the basis set centered on it, should be assigned to either one subunit or the other. While such assignment is quite obvious for the equilibrium structure of the A–H. . ..B complex, it is not clear to which subunit the bridging proton in the transfer midpoint, A. . .H. . .B belongs, when it is equally distant from the two subunits. The simplest approach, presented in paper [57], is that the CP correction for the proton transfer midpoint (a transition state structure which corresponds to the barrier heights) is computed by considering the central hydrogen atom as a part of one subunit (donor center with elongated A–H bond). It has been found that although the BSSE can be fairly large for the interaction (stabilization) energy, it is comparable in magnitude to the minimum (A–H. . .B) structure and midpoint (A. . .H. . .B) for the proton transfer. As a final result, the BSSE has only little effect upon the barrier to proton transfer if the applied basis set is relatively large [57]. For poor-quality basis such as the split valence, double or triple zeta could be substantial, especially at the electron correlation level. Diffuse functions added to basis sets greatly reduce the value of BSSE for proton transfer. The procedure described above is approximated because only the so-called "intermolecular" part of BSSE is taken into account. However, one can suspect that the so-called "intramolecular" portion of the BSSE related to the stretching of the A–H bond, which is neglected, might not be negligible. In paper [58], alternative approaches to the calculations of the BSSE were described. One of the methods used was the so-called site-site function counterpoise (SSFC), originally proposed by Wells and Wilson [59]. It takes into account the superposition error between atoms involved in a covalent bond, is very time consuming and is not practical to use for larger system. The second method used in paper [58] was the so-called successive reaction counterpoise (SRCP) proposed by Martin et al. [60] and which takes a stepwise approach to the formation of polyatomic molecules. The SRCP approach is ambiguous in that one must specify a particular reaction pathway. An advantage is that it is free of many-body nonadditivity effects because it is defined in terms of two-body BSSE only. The analysis presented in paper [58] shows that the results from both methods are generally similar to those obtained with the standard Boys-Bernardi scheme. This means that the BSSE has only little effect on the barrier to proton transfer if the applied basis sets are of reasonable quality. Recently, Ponti and Mella applied the so-called three-fragment counterpoise procedure (3fCP) to study the influence of basis set superposition error on the shape of

proton transfer potential energy surfaces [61]. This method is similar to the SSFC in spirit. However, in our opinion, more work is needed to find a very reliable and efficient method of BSSE calculations for barrier heights.

Dedication This contribution is dedicated to Professor A.F. Pozharskii on the occasion of his 70th birthday.

References

1. R.W. Alder et al., The remarkable basicity of 1,8-bis(dimethylamino)naphthalene, J. Chem. Soc. Chem. Commun. 723–724 (1968)
2. Aldrich Chemicals, Sigma-Aldrich, Handbook of Fine Chemicals, 2007–2008
3. H.A. Staab, T. Saupe, Proton sponges and the geometry of hydrogen bonds: aromatic nitrogen bases with exceptional basicities. Angew. Chem. Int. Ed. Engl. **27**, 865–1008 (1988)
4. R.W. Alder, Strain effects on amine basicities. Chem. Rev. **69**, 1215–1233 (1985)
5. A.F. Pozharskii, Naphthalene proton sponges (naftalinovye protonnye gubki). Usp. Khim. **67**, 3–27 (1998)
6. F. Hibbert, J. Emsley, Hydrogen bonding and chemical reactivity. Adv. Phys. Org. Chem. **26**, 255–379 (1991)
7. A.L. Llamas-Saiz et al., Proton sponges. J. Mol. Struct. **328**, 297–323 (1994)
8. V.A. Ozeryanskii et al., X-ray diffraction and IR-spectroscopic studies on protonated 4-amino-1, 8-bis(dimethylamino) naphthalene. J. Mol. Struct. **607**, 1–8 (2002)
9. K. Woźniak et al., On consequences of protonation of diamines in the gas phase and the solid state. Isr. J. Chem. **39**, 245–252 (1999)
10. S. Scheiner, Proton transfers in hydrogen-bonded systems. 4. cationic dimers of NH_3 and OH_2 [1–3]. J. Phys. Chem. **86**, 376–382 (1982)
11. A.F. Pozharskii et al., Organometallic synthesis, molecular structure, and coloration of 2,7-disubstituted 1,8-bis(dimethylamino)naphthalenes. how significant is the influence of "buttressing effect" on their basicity? J. Org. Chem. **68**, 10109–10122 (2003)
12. L. Sobczyk, Softness of hydrogen bond interaction. Khim. Fiz. **24**, 1–8 (2005)
13. T. Głowiak et al., $[N\cdots H\cdots N]^+$ hydrogen bonding in homoconjugated polycations of triethylenediamine perchlorate. Chem. Phys. Lett. **36**, 106–107 (1975)
14. J. Roziere et al., A strong asymmetric N-H-N hydrogen bond: Neutron diffraction and IR spectroscopic studies of 4-aminopyridine hemiperchlorate. J. Chem. Phys. **72**, 6117–6122 (1980)
15. J. Roziere et al., A strong symmetrical N-H-N bond. A 120 Kneutron diffraction study of hydrogen diquinuclidinone perchlorate, J. Chem. Soc. Chem. Commun. 388–389 (1982)
16. R.W. Alder et al., Intrabridgehead hydrogen-bonded ions: spectroscopic characteristics and the question of single vs double minimum potentials, J. Chem. Soc. Chem. Commun. 1000–1003 (1983)
17. V.A. Ozeryanskii et al., $[NHN]^+$Hydrogen bonding in protonated 1,8- bis(dimethylamino)-2,7- dimethoxynaphthalene. x-ray diffraction, infrared, and theoretical ab initio and dft studies. J. Phys. Chem. A **109**, 1637–1642 (2005)
18. T. Głowiak et al., Structure and IR spectroscopic behaviour of 2,7-dichloro-1,8-bis(dimethylamino)naphthalene and its protonated form. J. Phys. Org. Chem. **12**, 895–900 (1999)
19. A.J. Bieńko et al., Low barrier hydrogen bond in protonated proton sponge. X-ray diffraction, infrared, and theoretical ab initio density functional theory studies. J. Chem. Phys. **119**, 4313–4319 (2003)

20. A.V. Degtyarev et al., 2,7-Disubstituted proton sponges as borderline systems for investigating barrier-free intramolecular hydrogen bonds. Protonated 2,7-bis(trimethylsilyl)-and 2,7-di (hydroxymethyl)-1,8-bis(dimethylamino)naphthalenes. Tetrahedron **64**, 6209–6224 (2008)
21. B. Brzezinski et al., Protonation of very strong bases by phenols in non-aqueous solutions, J. Chem. Res. (M) 1021–1040 (1997)
22. W. Sawka-Dobrowolska et al., NHN^+ hydrogen bonding in salts of bis(dimethylaminomethyl) naphthalene (DMAMN). J. Mol. Struct. **356**, 117–124 (1995)
23. P. Chmielewski et al., Primary 1H/2H isotope effect in the NMR chemical shift of $HClO_4$ salts of 1, 8-bis(dimethylamino) naphthalene derivatives. J. Phys. Org. Chem. **20**, 643–648 (2007)
24. G.S. Denisov et al., Potential energy shape for the proton motion in hydrogen bond reflected in infrared and NMR spectra, in *Hydrogen Bonding – New Insights*, ed. by S.J. Grabowski (Springer, Dordrecht, 2006), p. 377
25. Z. Mielke, L. Sobczyk, Vibrational isotope effects in hydrogen bonds, in *Isotope Effects in Chemistry and Biology*, ed. by A. Kohen, H.-H. Limbach (Taylor & Francis, Boca Raton, FL, 2006), pp. 281–304
26. A.F. Pozharskii, V.A. Ozeryanskii, Peri-Naphthylene-diamines 23 investigation of the intramolecular hydrogen bond in protonated 1, 8-bis(dimethylamino) naphthalenes by ^1H NMR spectroscopy. Russian Chem. Bull. **47**, 66–73 (1998)
27. P.E. Hansen, *Isotope Effects on Chemical Shifts as a Tool in Structural Studies* (Roskilde Univ. Press, Roskilde, 1996)
28. T. Dziembowska, Z. Rozwadowski, Application of the deuterium isotope effect on nmr chemical shift to study proton transfer equilibrium. Curr. Org. Chem. **5**, 289–313 (2001)
29. J. Emsley, The composition, structure and hydrogen bonding of the β-diketones. Struct. Bonding **57**, 147–191 (1984)
30. E. Matsushita, T. Matsubara, Note on isotope effect in hydrogen bonded crystals. Progr. Theoret. Phys. **67**, 1–19 (1982)
31. E. Grech et al., Deuterium isotope effects on ^{15}N, ^{13}C, and ^1H chemical shifts of proton sponges. J. Mol. Struct. **615**, 121–140 (2002)
32. G. Gunnarsson et al., Proton and deuterium NMR of hydrogen bonds: relationship between isotope effects and the hydrogen bond potential. Chem. Phys. Lett. **38**, 96–99 (1976)
33. S. Scheiner, Comparison of proton transfers in heterodimers and homodimers of NH_3 and OH_2. J. Chem. Phys. **77**, 4039–4050 (1982)
34. G.C. Lloyd-Jones et al., Scalar coupling between the ^{15}N centres in methylated 1, 8-Diaminonaphthalenes and 1, 6-Diazacyclodecane:To what extent is $^{2H}J_{NN}$ a reliable indicator of N-N distance? Chem. Eur. J. **9**, 4523–4535 (2003)
35. M. Pietrzak et al., ^{13}C detected scalar nitrogen-nitrogen couplings across the intramolecular symmetric NHN hydrogen bond of proton sponge. J. Am. Chem. Soc. **123**, 4338–4339 (2001)
36. M. Pietrzak et al., Counteranion and solvent effects on scalar couplings and hydrogen bond structures of protonated sponges, to be published
37. H. Benedict et al., Solid State ^{15}N NMR and theoretical studies of primary and secondary geometric h/d isotope effects on low-barrier nhn-hydrogen bonds. J. Am. Chem. Soc. **120**, 2939–2950 (1998)
38. M. Pietrzak et al., The largest ^{15}N–^{15}N coupling constant across an NHN hydrogen bond. Angew. Chem. Int. Ed. **47**, 1123–1126 (2008)
39. J. Stare, J. Mavri, Numerical solving of the vibrational time-independent Schroedinger equation in one and two dimensions using the variational method. J. Comput. Phys. Commun. **143**, 222–240 (2002)
40. P. Hobza, Theoretical studies of hydrogen bonding. Annu. Rep. Prog. Chem., Sec. C **100**, 3–27 (2004)
41. S.J. Grabowski, *Hydrogen Bonding–New Insights* (Springer Verlag, Berlin, 2006)
42. S. Sadhukhan et al., Predicting proton transfer barriers with density functional theory. Chem. Phys. Lett. **306**, 83–87 (1999)

43. Z. Latajka, S. Scheiner, Correlated proton transfer potentials. $(HO\text{-}H\text{-}OH)^-$ and $(H_2O\text{-}H\text{-}OH_2)^+$. J. Mol. Struct. (THEOCHEM) **234**, 373–385 (1991)
44. Z. Latajka et al., Critical assesment of density functional methods for study of proton transfer processes. $(FHF)^-$. Chem. Phys. Lett. **234**, 159–164 (1995)
45. K.Mierzwicki, Z.Latajka, to be published
46. W. Koch, M.C. Holthausen, *A Chemist's Guide to Density Functional Theory*, 2nd edn. (Wiley-VCH, Weinheim, 2002)
47. Z. Zhao, D.G. Truhlar, Benchmark databases for nonbonded interactions and their use to test density functional theory. J. Chem. Theory Comput. **1**, 415–432 (2005)
48. S.F. Sousa et al., General performance of density functionals. J. Phys. Chem. A **111**, 10439–10452 (2007)
49. Y. Zhao, D.G. Truhlar, Density functionals with broad applicability in chemistry. Acc. Chem. Res. **41**, 157–167 (2008)
50. C. Mijoule et al., Density functional theory applied to proton transfer systems: a numerical test. Chem. Phys. Lett. **208**, 364–368 (1993)
51. C. Lee, D. Vanderbilt, Proton transfer in ice. Chem. Phys. Lett. **210**, 279–284 (1993)
52. V. Barone et al., Proton transfer in model hydrogen-bonded systems by a density functional approach. Chem. Phys. Lett **231**, 295–300 (1994)
53. V. Termath, J. Sauer, Ab initio molecular dynamics simulation of $H_5O_2^+$ and $H_7O_3^+$ gas phase clusters based on density functional theory. Mol. Phys. **91**, 963–975 (1997)
54. I. Matanović et al., Exploring the potential energy surface for proton transfer in acetylacetone. Chem. Phys. **306**, 201–207 (2004)
55. S. Kawahara et al., Electron correlation and basis set effects on strong hydrogen bond behaviour: a case study on the hydrogen difluoride anion. Chem. Phys. **273**, 207–216 (2001)
56. S.F. Boys, F. Bernardi, The calculation of small molecular interactions by the difference of separate total energies. Some procedures with reduced errors. Mol. Phys. **19**, 553–566 (1970)
57. Z. Latajka et al., Basis set superposition error in proton transfer potentials. Chem. Phys. Lett. **196**, 384–389 (1992)
58. A.J. Abkowicz et al., Site-site function and successive reaction counterpoise calculation of basis set superposition error for proton transfer. J. Mol. Struct. (THEOCHEM) **342**, 53–159 (1995)
59. H. Wells, S. Wilson, Van der Waals interaction potentials: many-body basis set superposition effects. Chem. Phys. Lett. **101**, 429–434 (1983)
60. J.M.L. Martin et al., Combined bond-polarization basis sets for accurate determination of dissociation energies. Part 3. Basis set superposition error in polyatomic systems. Theor. Chim. Acta **76**, 195–209 (1989)
61. A. Ponti, M. Mella, Three-fragment counterpoise correction of potential energy curves for proton-transfer recations. J. Phys. Chem. A **107**, 7589–7596 (2003)

Chapter 20
Nucleic Acid Base Complexes: Elucidation of the Physical Origins of Their Stability

Żaneta Czyżnikowska, Robert Zaleśny, and Manthos G. Papadopoulos

Abstract Nucleic acids and proteins are biochemically important complexes responsible for heirdom and miscellaneous enzymatic cellular processes. Thus, the understanding of the physical origins of their stability, i.e., the nature of intermolecular interactions, is crucial for the interpretation of various biochemical processes. The intercalation of drugs into DNA may serve as an illuminating example. The most accurate and reliable framework for the analysis of intermolecular interactions is provided by the quantum mechanics. In general, two distinct approaches are usually used for the evaluation of interaction energies, namely the supermolecular approach and the perturbation theory. While the former explains the interaction energy as small difference between the values of the energy of the whole complex and the sum of energies of the monomers, the latter allows for direct calculation of contributions with a clear physical interpretation. Unfortunately, the majority of studies of the nucleic acid base complexes had either shown little concern for the elucidation of the nature of interactions or analyzed this aspect qualitatively. The present contribution is especially aimed at the compact and comprehensible presentation of the most important observations made on the physical origins of nucleic acid base pairs' stability. Throughout, we shall support the discussion by our own findings in this fascinating area.

20.1 Quantum–Chemical Approach to Evaluation of Noncovalent Interactions for Nucleic Acid Base Complexes: The Basics, the Pros, and the Cons

The stability of polynucleotide systems and the conformational variability of nucleic acids are governed, inter alia, by noncovalent interactions [1]. They lead to the

Ż. Czyżnikowska (✉), R. Zaleśny, and M.G. Papadopoulos
Institute of Organic and Pharmaceutical Chemistry, The National Hellenic Research Foundation, 48 Vas. Constantinou Avenue, 11635 Athens, Greece;
e-mail: zaneta.czyznikowska@gmail.com

J. Leszczynski and M.K. Shukla (eds.), *Practical Aspects of Computational Chemistry*,
DOI 10.1007/978-90-481-2687-3_20,

formation of molecular cluster in which a covalent bond is neither created nor broken. This term shall be carrying such a meaning throughout this article. Among the plethora of studied van der Waals systems, nucleic acid base complexes are of particular interest due to their biochemical significance. Two most commonly followed routes to study base stacking are molecular dynamics simulations and quantum-mechanical computations. We aim primarily to focus on the discussion of the results obtained within the latter approach. The most reliable and accurate variants of the wave-function theory are computationally most expensive [2]. Thus, the majority of advanced ab initio studies concerning interactions of nucleic acid bases were devoted to complexes formed by base pairs only. Intermolecular interaction energy can be evaluated theoretically either using supermolecular approach or on the basis of perturbation theory. Below, we shall briefly describe the two treatments.

20.1.1 Supermolecular Approach

Within the supermolecular approach, the total intermolecular interaction energy (ΔE) of a complex A$\cdots$B is evaluated as the difference between the energy of the complex ($E^{\mathrm{A}\cdots\mathrm{B}}$) and the sum of the energies of its subsystems (E^{A}, E^{B}):

$$\Delta E = E^{\mathrm{A}\cdots\mathrm{B}} - E^{\mathrm{A}} - E^{\mathrm{B}}. \tag{20.1}$$

The above equation is very conveniently used as the computation of the total energy is the standard quantum-chemical procedure. However, a purely theoretical problem arises when using monomer-centered basis set for evaluation of E^{A} and E^{B} according to (20.1): The intermolecular interaction energy will suffer from what is known as basis set superposition error (BSSE) [3]. In order to overcome this unphysical effect which usually manifests itself in too negative interaction energies, one frequently applies the so-called counterpoise correction [4].

During the last two decades, the total stabilization energies for over 100 nucleic acid base complexes were determined at the CCSD(T) level of theory applying supermolecular approach [5, 6]. These data are of unquestionable value for benchmarking purposes and also allow the comparison of the stabilities of different base pairs. Due to Moore's law, every 2 years, the speed of computers approximately doubles [7]. However, the scaling of electron correlation treatments with the number of so-called basis functions (N) is far from being linear, i.e., it usually scales as $O(N^t)$, where $t > 5$. This is the rationale for introducing various approximations. In this context, let us mention the CCSD(T) correlation correction commonly employed for the estimation of the stabilization energies of nucleic acid base complexes [8]:

$$\Delta E_{\mathrm{CBS}}^{\mathrm{CCSD(T)}} = \Delta E_{\mathrm{CBS}}^{\mathrm{MP2}} + (\Delta E^{\mathrm{CCSD(T)}} - \Delta E^{\mathrm{MP2}})|_{\text{medium-size basis set}}, \tag{20.2}$$

where the subscript "CBS" denotes the interaction energy evaluated in the so-called basis set limit. The supermolecular approach, although computationally much more

efficient than the perturbation theory, is still hardly applicable for complexes larger than 30 atoms using the CCSD(T) method with basis set of triple-ζ quality.

Because of the efficiency, the density functional theory also became an object of interest for the purpose of evaluation of intermolecular interaction energies for nucleic acid base complexes. Most standard functionals provide qualitatively a good picture of interactions in H-bonded nucleic acid base pairs. However, they completely fail for stacked complexes. This is due to the inability of current functionals to describe correctly the dispersion energy. Several routes were proposed to alleviate this deficiency with different rates of success [9–12].

20.1.2 Perturbation-Theory Approach

Contrary to the previously described supermolecular approach, perturbation theory treatment allows for the partition of the interaction energy into physically interpretable components. The most frequently used method for this purpose is symmetry-adapted perturbation theory (SAPT) [13]. More recently, great effort has also been invested in the development of DFT–SAPT [14–16]. In the present contribution, we use the variational-perturbational scheme [17–20]. In this approach, the intermolecular interaction energy components are determined based on the wave functions of the subsystems evaluated in the dimer-centered basis set. Thus, both interaction energy and its components are BSSE-free. More details about this scheme can be found elsewhere [21–23]. The total intermolecular interaction energy at the MP2 level of theory can be expressed as follows:

$$\Delta E^{\mathrm{MP2}} = \sum_{i=0}^{2} \Delta\varepsilon_{\mathrm{MP}}^{(i)} = \Delta E^{\mathrm{HF}} + \varepsilon_{\mathrm{MP}}^{(2)}. \tag{20.3}$$

ΔE^{HF} is further divided into Heitler-London (ΔE^{HL}) and delocalization term ($E_{\mathrm{del}}^{\mathrm{HF}}$):

$$\Delta E^{\mathrm{HF}} = \Delta E^{\mathrm{HL}} + \Delta E_{\mathrm{del}}^{\mathrm{HF}}, \tag{20.4}$$

where ΔE^{HL} is defined as a sum of first-order electrostatic interaction energy and Heitler–London exchange term:

$$\Delta E^{\mathrm{HL}} = \varepsilon_{\mathrm{ex}}^{\mathrm{HL}} + \varepsilon_{\mathrm{el}}^{(10)}. \tag{20.5}$$

It is noteworthy that the delocalization term, also referred to as the deformation component [20], contains charge transfer and polarization effects. The $\varepsilon_{\mathrm{MP}}^{(2)}$ term appearing in (20.3) comprises electron correlation corrections:

$$\varepsilon_{\mathrm{MP}}^{(2)} = \varepsilon_{\mathrm{el,r}}^{(12)} + \varepsilon_{\mathrm{disp}}^{(20)} + \Delta E_{\mathrm{ex-del}}^{(2)}, \tag{20.6}$$

where $\varepsilon_{\mathrm{el,r}}^{(12)}$ denotes the term arising due to the dispersion and correlation corrections to the first-order electrostatic interaction, $\varepsilon_{\mathrm{disp}}^{(20)}$ is the dispersion contribution, and $\Delta E_{\mathrm{ex-del}}^{(2)}$ is the exchange-delocalization component.

20.2 The Nature of Interactions in Nucleic Acid Base Complexes

As it was mentioned in the previous section, the supermolecular approach does not allow for the interpretation of the observed differences in stabilization energies in terms of physically interpretable components. The analysis of the nature of interactions in nucleic acid base complexes has only recently been settled on solid quantitative grounds [24–34]. In the next two sections, we will briefly summarize the results of calculations presented to date on this subject trying to grasp what is essential. Since stacking and H-bonding are *mainly* governed by different types of interactions, namely by London-forces and electrostatic interactions, respectively, we shall discuss the two types of systems separately. Before we proceed further, let us comment on the choice of geometries of nucleic acid base complexes. The most frequently adopted approaches to study base–base interactions (both stacked and H-bonded pairs) include the use of: (a) crystallographic structures; (b) geometries taken from molecular dynamics simulations; (c) structures optimized using quantum mechanical methods; and (d) structures with arbitrary conformations of monomers. Obviously, each of the above choices appears in many flavors making the possible comparisons between different studies difficult or even impossible. The situation is even worse when it comes to comparing the components of the intermolecular interaction energy calculated using different methods: One immediately finds the lack of systematic studies on this subject.

In this section, we shall support the discussion by the results of our own calculations. The interaction energy decomposition scheme we employ here, is the one described in Sect. 20.1.2. All calculations of energy components were done at the MP2/aug-cc-pVDZ level of theory using the modified version of the GAMESS US package [35]. Based on the set of parameters describing B-DNA [36] and the geometries of monomers optimized at the MP2/6-311++G(d,p) level of theory, the structures of nucleic acid pairs were generated to mimic those found in crystallographic database. More detailed description can be found elsewhere [32].

20.2.1 H-Bonded DNA Base Pairs

The most extensive analysis of the nature of intermolecular interaction components in hydrogen-bonded complexes of nucleic acid bases is that performed by Toczyłowski et al. [26]. The authors presented the results of calculations obtained on the basis of the intermolecular Møller–Plesset perturbation theory using

6-31G(d = 0.25) and aug-cc-pVDZ basis sets for numerous configurations of bases. Let us summarize the most important observations made by the authors. First, the largest component, in terms of magnitude, is the first-order electrostatic energy, $\varepsilon_{el}^{(10)}$. This is not a very surprising finding; however, the contribution of the dispersion term, $\varepsilon_{disp}^{(20)}$, is also very important [26, 28, 31]. Similar observation was reported by Hesselmann et al. on the basis of DFT–SAPT calculations for the hydrogen-bonded adenine–tymine and guanine–cytosine complexes [28]. Second it was found that the ε_{HL}^{exch} term is of similar importance (although smaller in magnitude) as first-order electrostatic interaction but of destabilizing character [26]. Congruent observation was reported by Guerra et al. for adenine–thymine complex [24]. Toczyłowski et al. also analyzed the directionality of interaction energy components in H-bonded bases complexes [26]. The results obtained by the authors, for in-plane $\pm$ 5° rotations of bases in the proximity of minimum, indicate that the total interaction energy does not vary significantly. Simultaneously, the individual components show more pronounced dependence, i.e., in the case of guanine–guanine complex, the change of $\varepsilon_{el}^{(10)}$ and $\varepsilon_{disp}^{(20)}$ upon in-plane rotation may be as large as 23 and 25%, respectively.

Another interesting aspect is the dependence of intermolecular interaction components for H-bonded systems on the quality of the employed basis set, despite a rather purely methodological character. The comparison of the data evaluated using 6-31G(d = 0.25) and aug-cc-pVDZ basis set reveals that although the agreement in the total interaction energies is very good, i.e., not exceeding 1 kcal/mol, the discrepancies for individual components are much more significant [26]. The absolute value of the dispersion energy may serve directly for the assessment purpose of the quality of the basis set. The difference in $\varepsilon_{disp}^{(20)}$ values for the two basis sets used by Toczyłowski et al. for the large majority of complexes exceeds 1 kcal/mol and reaches up to 1.6 kcal/mol for cytosine–guanine complex [26]. Similar conclusions regarding the quality of basis sets may be drawn based on the DFT–SAPT calculations of Hesselmann et al., which show that the difference in $\varepsilon_{disp}^{(20)}$ values between aug-cc-pVDZ and aug-cc-pVQZ is 1.7 and 2.3 kcal/mol for adenine–thymine and guanine–cytosine pairs, respectively. Surprisingly, the effect of basis set extension for the first-order electrostatic component was found to be negligible [28].

20.2.2 Stacked DNA Base Pairs

Contrary to H-bonded nucleic acid base pairs discussed in the previous section, the nature of intermolecular interactions in complexes of stacked bases was analyzed more extensively. The values of minimal, maximal, and average total stabilization energies, corrected for BSSE, for a set comprising over 80 stacked bases, are plotted in Fig. 20.1. In the case of guanine–adenine and adenine–cytosine complexes, the results are presented for two sequence contexts, i.e., A/G–G/A and A/C–C/A. The symbol AA denotes the 2-oxo-adenine – complexes of oxidized bases, and this

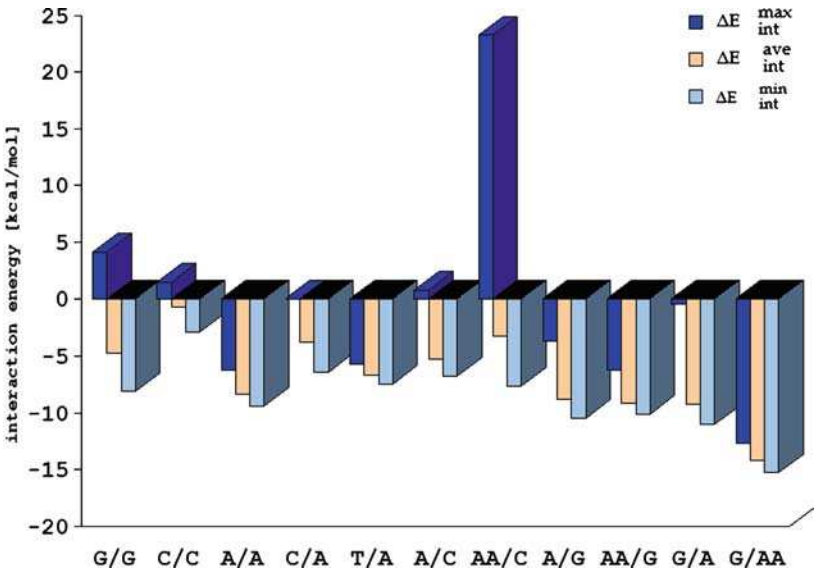

Fig. 20.1 The average, the maximal and the minimal values of intermolecular interaction energy for stacked nucleic acid base complexes calculated at the MP2/aug-cc-pVDZ level of theory

will be discussed in the further part of this section. The employed level of theory, namely MP2/aug-cc-pVDZ, makes the interaction energy decomposition feasible, yet is still adequate for reliable prediction of the stacking phenomenon. It was repeatedly pointed out that MP2 method tends to provide too large interaction energies for stacked base pairs in the so-called complete basis set limit [37, 38]. The split-valence double-ζ basis set, however, seems to cure the overshoot problem to a large extent [37]. As it is seen, the set of investigated complexes contains unstable base pairs. These were included in our calculations for the sake of demonstration that crystallographic structures of stacked base pairs considered in vacuo, may fall into the region of strong repulsion. Obviously, the total intermolecular energy of nucleobase pairs depends on the sequence context alignment. For the very same set of structures, the results of calculations of interaction energy components are plotted in Fig. 20.2. Only the stabilizing components were considered to illustrate their relative contributions to the total interaction energy. As expected, the $\varepsilon_{\mathrm{disp}}^{(20)}$ term is the foremost stabilizing component of interaction energy, as confirmed also by other authors [25, 27–34].

The first-order electrostatic interaction can also play an important role in base–base stacking. The $\varepsilon_{\mathrm{el}}^{(10)}$ term can, depending on the system and the configuration, stabilize or destabilize stacked nucleic acid complexes. In most cases, the ΔE^{HL} term is positive which indicates that the $\varepsilon_{\mathrm{el}}^{(10)}$ contribution is canceled out by the exchange component. Similar observations have also been reported recently [25,32]. In the case of guanine–guanine and cytosine–cytosine complexes, the electrostatic term has positive value. The average values of first-order electrostatic component

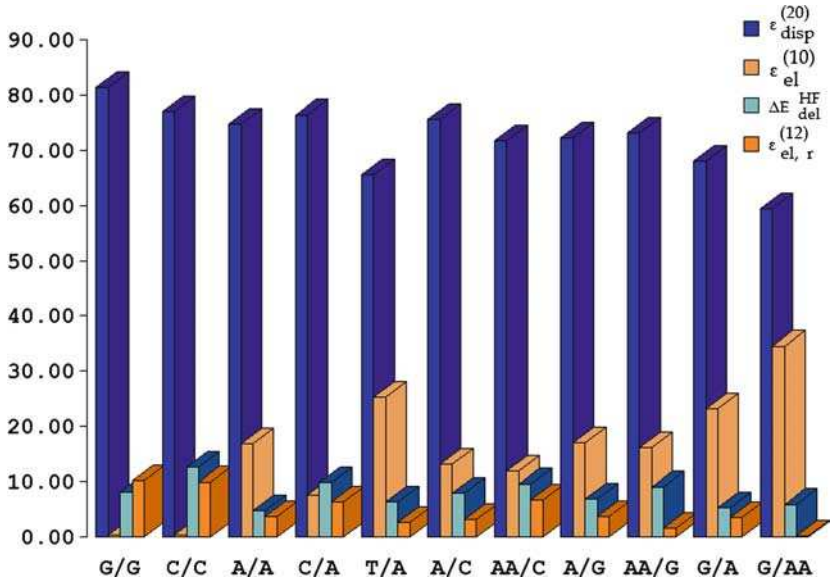

Fig. 20.2 Proportional representation of the intermolecular interaction energy components, calculated at the MP2/aug-cc-pVDZ level of theory, for stacked nucleic acid base complexes. Shown is the percentage contribution to the sum of all stabilizing terms

for these complexes are equal to 1.25 and 1.94 kcal/mol, respectively. In order to emphasize the importance of the choice of the geometry of base pairs, let us turn from the analysis of average values for the set of structures and inspect more closely the role of the electrostatics for the individual nucleic acid base pairs. For this purpose, we have plotted in Fig. 20.3 both $\varepsilon_{\mathrm{el}}^{(10)}$ and ΔE^{MP2} for the set of 54 crystallographic structures of guanine–adenine complex. Although the values of ΔE^{MP2} are approximately -10 kcal/mol for the majority of structures, the variations of $\varepsilon_{\mathrm{el}}^{(10)}$ are much more significant, and what is not shown on the plot, nonuniform with respect to base-step parameters describing the structure of the complexes. It is noteworthy, that the base pairs are also stabilized by the delocalization component, $\Delta E_{\mathrm{del}}^{\mathrm{HF}}$. The smallest contribution of $\Delta E_{\mathrm{del}}^{\mathrm{HF}}$ component to the total stabilization energy is observed for the adenine–adenine complex.

Another interesting topic, yet not well understood, is how the oxidation of nucleic acid bases influences the stability of DNA, and in particular, to what extent it changes the nature of intermolecular interactions. The biological consequences of damage to nucleic acids have been the subject of numerous experimental studies [39, 40]. DNA may be exposed in vivo to hydroxyl radicals produced during endogenic cellular processes [41, 42]. Increased concentration of modified nucleic acid base derivatives (i.e., 8-oxo-guanine, 2-oxo-adenine) in cancer cells has been observed. For this reason, the analysis of the influence of modification of nucleic acid bases by hydroxyl radical on the nature of intermolecular interactions seems to be very advisable. The results of calculations presented in Fig. 20.2 show that

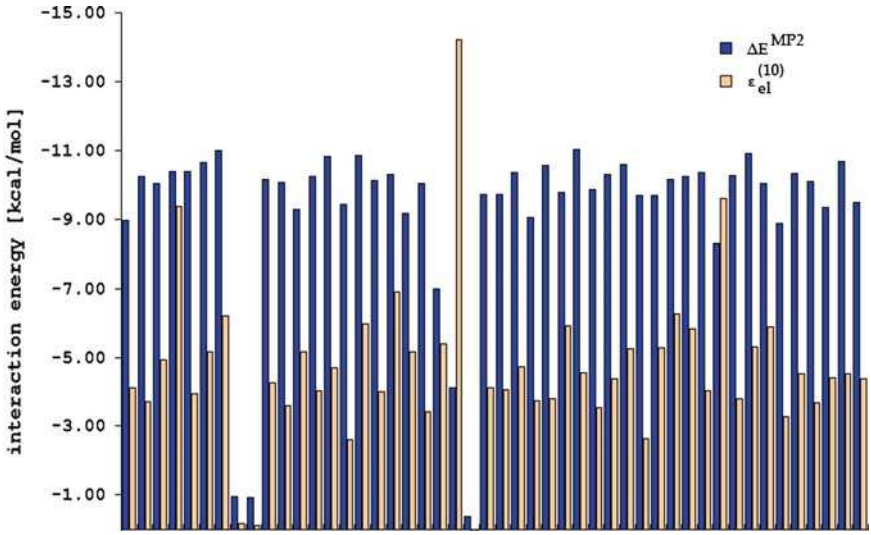

Fig. 20.3 The total intermolecular interaction energy and the first-order electrostatic interaction for 54 structures of guanine–adenine complex

in the case of adenine–guanine pair, the modification leads to larger stability of the complex in only one context alignment. Interestingly, this change in stabilization energy is also manifested in the change of electrostatic contribution to the total stabilization energy. However, more systematic studies for larger number of base pairs are necessary to arrive at general conclusions regarding the nature of interactions in complexes containing modified nucleobases.

Besides the above discussed aspects of the nature of base–base stacking, several studies have reported observations of different types. In this context, let us mention the statistical study of Hill et al. [25] and Langner et al. [29] who investigated the correlation between interaction energy components. A significant correlation was found, on the basis of calculations for 58 stacked nucleic acid dimers, between the Pauli exchange and dispersion [25]. A less strong relationship, with Spearman rank correlation coefficient equal to 0.85, between the first-order electrostatic interaction and the MP2 interaction energy was also noticed by these authors. Interestingly, Fiethen et al. came to the contradictory conclusions [33].

20.3 Summary and Outlook

In this article, we discussed several rigorous ab initio studies, including our own findings, which had recently put the discussion of the nature of intermolecular interactions in nucleic acid base complexes on quantitative basis. The results of computations summarized herein confirm that H-bonded and stacked base pairs are *mainly* stabilized by electrostatic/delocalization components and dispersion

interactions, respectively. However, in the case of both types of systems, the other components are also important. Particular attention has to be paid to the choice of geometry of nucleic acid base complexes. In certain cases, the influence of the structural parameters is found not on the total interaction energy, but rather on its components. More systematic studies are needed on this subject.

There are several areas in the field of base–base interactions, where the analysis of the nature of interactions may help to better understand undergoing processes, just to mention mispairing in the presence of modified forms of nucleobases [43] or intercalation of drugs into DNA [44]. The difficulty, however, still comes in establishing the nature of interactions in the complexes larger than base pairs. This is certainly due to the computational cost of the wave function theory approaches. DFT–SAPT seems to be very promising alternative to more advanced electron correlation treatments [20, 45–47]. It is still possible, however, to gain qualitative insight into the nature of interactions by applying empirical potentials [48–52].

Acknowledgments The authors are grateful to Dr. Robert W. Gora for the access to the modified version of the GAMESS US code. This work was supported by computational grants from WCSS (Wroclaw Centre for Networking and Supercomputing) and ACK Cyfronet. The allocation of computing time is greatly appreciated.

References

1. K. Müller-Dethlefs, P. Hobza, Noncovalent interactions: A challenge for experiment and theory. Chem. Rev. **100**, 143–167 (2000)
2. T. Helgaker, T.A. Ruden, P. Jørgensen, J. Olsen, W. Klopper, *A priori* calculation of molecular properties to chemical accuracy. J. Phys. Org. Chem. **17**, 913–933 (2004)
3. F.B. van Duijneveldt, J.G.C.M. van Duijneveldt-van de Rijdt, J.H. van Lenthe, State of the art in counterpoise theory. Chem. Rev. **94**, 1873–1885 (1994)
4. S.F. Boys, F. Bernardi, The calculation of small molecular interactions by the differences of separate total energies. Some procedures with reduced errors. Mol. Phys. **19**, 553–566 (1970)
5. P. Jurečka, J. Šponer, J. Černý, P. Hobza, Benchmark database of accurate (MP2 and CCSD(T) complete basis set limit) interaction energies of small model complexes, DNA base pairs, and amino acid pairs. Phys. Chem. Chem. Phys. **8**, 1985–1993 (2006)
6. I. Dąbkowska, H.V. Gonzales, P. Jurečka, P. Hobza, Stabilization energies of the hydrogen–bonded and stacked structures of nucleic acid base pairs in the crystal geometries of CG, AT, and AC DNA steps and in the NMR geometry of the 5′-d(GCGAAGC)-3′ hairpin: Complete basis set calculations at the MP2 and CCSD(T) levels. J. Phys. Chem. A **109**, 1131–1136 (2005)
7. G.E. Moore, Cramming more components onto integrated circuits, *Electronics* **38**, 114–117 (1965)
8. P. Hobza, Calculations of the stabilization energies of the building blocks of biomacromolecules. AIP Conf. Proc. **963**, 416–424 (2007)
9. M. Elstner, P. Hobza, T. Frauenheim, S. Suhai, E. Kaxiras, Hydrogen bonding and stacking interactions of nucleic acid base pairs: A density-functional-theory based treatment. J. Chem. Phys. **114**, 5149–5155 (2001)
10. P. Jurečka, P. Hobza, D.R. Salahub, Density functional theory augmented with an empirical dispersion term. Interaction energies and geometries of 80 noncovalent complexes compared with ab initio quantum mechanics calculations. J. Comput. Chem. **28**, 555–569 (2007)

11. J. Černý, P. Hobza, The X3LYP extended density functional accurately describes H-bonding but fails completely for stacking. Phys. Chem. Chem. Phys. **7**, 1624–1626 (2005)
12. S. Grimme, J. Antony, T. Schwabe, C. Mück-Lichtenfeld, Density functional theory with dispersion corrections for supramolecular structures, aggregates, and complexes of (bio)organic molecules. Org. Biomol. Chem. **5**, 741–758 (2007)
13. B. Jeziorski, R. Moszynski, K. Szalewicz, Perturbation theory approach to intermolecular potential energy surfaces of van der Waals complexes. Chem. Rev. **94**, 1887–1930 (1994)
14. A. Heßelmann, G. Jansen, M. Schütz, Density-functional theory-symmetry-adapted intermolecular perturbation theory with density fitting: A new efficient method to study intermolecular interaction energies. J. Chem. Phys. **122**, 014103 (2005)
15. R. Podeszwa, R. Bukowski, K. Szalewicz, Density-fitting method in symmetry-adapted perturbation theory based on Kohn–Sham description of monomers. J. Chem. Theory Comput. **2**, 400–412 (2006)
16. R. Podeszwa, K. Szalewicz, Physical origins of interactions in dimers of polycyclic aromatic hydrocarbons. Phys. Chem. Chem. Phys. **10**, 2735–2746 (2008)
17. G. Chałasiński, M. Szczęśniak, On the connection between the supermolecular Møller–Plesset treatment of the interaction energy and the perturbation theory of intermolecular forces. Mol. Phys. **63**, 205–224 (1988)
18. W.A. Sokalski, S. Roszak, K. Pecul, An efficient procedure for decomposition of the SCF interaction energy into components with reduced basis set dependence. Chem. Phys. Lett. **153**, 153–159 (1988)
19. W.A. Sokalski, S. Roszak, Efficient techniques for the decomposition of intermolecular interaction energy at SCF level and beyond. J. Mol. Struct. (Theochem.) **234**, 387–400 (1991)
20. S.M. Cybulski, G. Chałasiński, R. Moszyński, On decomposition of second-order Møller–Plesset supermolecular interaction energy and basis set effects. J. Chem. Phys. **92**, 4357–4363 (1990)
21. R.W. Gora, W. Bartkowiak, S. Roszak, J. Leszczynski, A new theoretical insight into the nature of intermolecular interactions in the molecular crystal of urea. J. Chem. Phys. **117**, 1031–1039 (2002)
22. R.W. Gora, W. Bartkowiak, S. Roszak, J. Leszczynski, Intermolecular interactions in solution: Elucidating the influence of the solvent. J. Chem. Phys. **120**, 2802–2813 (2004)
23. R.W. Gora, S.J. Grabowski, J. Leszczynski, Dimers of formic acid, acetic acid, formamide and pyrrole-2-carboxylic acid: An ab initio study. J. Phys. Chem. A **109**, 6397–6405 (2005)
24. C. Fonseca Guerra, F.M. Bickelhaupt, Orbital interactions in strong and weak hydrogen bonds are essential for DNA replication. Angew. Chem. Int. Ed. **41**, 2092–2095 (2002)
25. G. Hill, G. Forde, N. Hill, W.A. Lester Jr., W.A. Sokalski, J. Leszczynski, Interaction energies in stacked DNA bases? How important are electrostatics. Chem. Phys. Lett. **381**, 729–732 (2003)
26. R.R. Toczyłowski, S. Cybulski, An analysis of the interactions between nucleic acid bases: Hydrogen-bonded base pairs. J. Phys. Chem. A **107**, 418–426 (2003)
27. R.R. Toczyłowski, S. Cybulski, An analysis of the electrostatic interaction between nucleic acid bases. J. Chem. Phys. **123**, 154312 (2005)
28. A. Hesselmann, G. Jansen, M. Schütz, Interaction energy contributions of H-bonded and stacked structures of the AT and GC DNA base pairs from the combined density functional theory and intermolecular perturbation theory approach. J. Am. Chem. Soc. **128**, 11730–11731 (2006)
29. K.M. Langner, W.A. Sokalski, J. Leszczynski, Intriguing relations of interaction energy components in stacked nucleic acids. J. Chem. Phys. **127**, 111102 (2007)
30. Ż. Czyżnikowska, R. Zaleśny, M. Ziółkowski, R.W. Gora, P. Cysewski, The nature of interactions in uracil dimer: An *ab initio* study. Chem. Phys. Lett. **450**, 132–137 (2007)
31. R. Sedlák, P. Jurečka, P. Hobza, Density functional theory-symmetry adapted perturbation treatment energy decomposition of nucleic acid base pairs taken from DNA crystal geometry. J. Chem. Phys. **127**, 075104 (2007)

32. P. Cysewski, Ż. Czyżnikowska, R. Zaleśny, P. Czeleń, The post-SCF quantum chemistry characteristics of guanine–guanine stacking in B-DNA. Phys. Chem. Chem. Phys. **10**, 2665–2672 (2008)
33. A. Fiethen, G. Jansen, A. Hesselmann, M. Schütz, Stacking energies for average B-DNA structures from the combined density functional theory and symmetry-adapted perturbation theory approach. J. Am. Chem. Soc. **130**, 1802–1803 (2008)
34. Ż. Czyżnikowska, R. Zaleśny, P. Cysewski, Quantum chemical study of the nature of stacking interactions of 2-oxo-adenine with native B-DNA purine bases. Pol. J. Chem. **82**, 2269–2279 (2008)
35. M.W. Schmidt, K.K. Baldridge, J.A. Boatz, S.T. Elbert, M.S. Gordon, J.H. Jensen, S. Koseki, N. Matsunaga, K.A. Nguyen, S. Su, T.L. Windus, M. Dupuis, J.A. Montgomery, General atomic and molecular electronic structure system. J. Comput. Chem. **14**, 1347–1363 (1993)
36. H.M. Berman, W.K. Olson, D.L. Beveridge, J. Westbrook, A. Gelbin, T. Demeny, S.H. Hsieh, A.R. Srinivasan, B. Schneider, The nucleic-acid database – a comprehensive relational database of 3-dimensional structures of nucleic-acids. Biophys. J. **63**, 751–759 (1992)
37. K.E. Riley, P. Hobza, Assessment of the MP2 method, along with several basis sets, for the computation of interaction energies of biologically relevant hydrogen bonded and dispersion bound complexes. J. Phys. Chem. A **111**, 8257–8263 (2007)
38. J. Šponer, K.E. Riley, P. Hobza, Nature and magnitude of aromatic stacking of nucleic acid bases. Phys. Chem. Chem. Phys. **10**, 2595–2610 (2008)
39. S. Sentürker, B. Karahalil, M. Inal, H. Yilmaz, H. Müslümanoglu, G. Gedikoglu, M. Dizdaroglu, Oxidative DNA base damage and antioxidant enzyme levels in childhood acute lymphoblastic leukemia. FEBS Lett. **416**, 286–290 (1997)
40. Z.I. Alam, A. Jenner, S.E. Daniel, A.J. Lees, N. Cairns, C.D. Marsden, P. Jenner, B. Halliwell, Oxidative DNA damage in the parkinsonian brain: An apparent selective increase in 8-hydroxyguanine levels in substantia nigra. J. Neurochem. **69**, 1196–1203 (1997)
41. J.R. Wagner, C.C. Hu, B.N. Ames, Endogenous oxidative damage of deoxycytidine in DNA. Proc. Natl. Acad. Sci. **89**, 3380–3384 (1992)
42. J.A. Imlay, S. Linn, DNA damage and oxygen radical toxicity. Science **240**, 1302–1309 (1988)
43. D. Wang, D.A. Kreutzer, J.M. Essigmann, Mutagenicity and repair of oxidative DNA damage: insights from studies using defined lesions. Mutat. Res. **400**, 99–115 (1998)
44. D. Řeha, M. Kabeláč, F. Ryjaček, J. Šponer, M. Elstner, S. Suhai, P. Hobza, Intercalators. 1. Nature of stacking interactions between intercalators (ethidium, daunomycin, ellipticine, and 4,6-Diaminide-2-phenylindole) and DNA base pairs. *Ab initio* quantum chemical, density functional theory, and empirical potential study. J. Am. Chem. Soc. **124**, 3366–3376 (2002)
45. T. Korona, On the role of higher-order correlation effects on the induction interactions between closed-shell molecules. Phys. Chem. Chem. Phys. **9** 6004–6011 (2007)
46. T. Korona, B. Jeziorski, One-electron properties and electrostatic interaction energies from the expectation value expression and wave function of singles and doubles coupled cluster theory. J. Chem. Phys. **125**, 184109 (2006)
47. T. Korona, B. Jeziorski, Dispersion energy from denisty-fitted density susceptibilities of singles and doubles coupled cluster theory. J. Chem. Phys. **128**, 144107 (2008)
48. C.A. Hunter, X.-J. Lu, DNA Base-stacking interactions: A comparison of theoretical calculations with oligonucleotide X-ray crystal structures. J. Mol. Biol. **265**, 603–619 (1997)
49. J. Šponer, J. Leszczynski, P. Hobza, Nature of nucleic acid-base stacking: Nonempirical ab initio and empirical potential characterization of 10 stacked base dimers. Comparison of stacked and H-bonded base pairs. J. Phys. Chem. **100**, 5590–5596 (1996)
50. J. Šponer, H.A. Gabb, J. Leszczynski, P. Hobza, Base–Base and deoxyribose–base stacking interactions in B-DNA and Z-DNA: A quantum-chemical study. Biophys. J. **73**, 76–87 (1997)
51. J. Šponer, J. Leszczynski, P. Hobza, Electronic properties, hydrogen bonding, stacking, and cation binding of DNA and RNA bases. Biopolymers **61**, 3–31 (2002)
52. P. Mignon, S. Loverix, J. Steyaert, P. Geerlings, Influence of the π–π interaction on the hydrogen bonding capacity of stacked DNA/RNA bases. Nucleic Acids Res. **33**, 1779–1789 (2005)

Chapter 21
Conformational Flexibility of Pyrimidine Ring in Nucleic Acid Bases

Oleg V. Shishkin, Leonid Gorb, and Jerzy Leszczynski

Abstract Nucleic acid bases (NABs) have been considered for many years to be planar and conformationally rigid. However, recently, two possible sources of nucleobases nonplanarity have been found. Ab initio quantum-chemical calculations using large basis sets augmented by inclusion of electron correlation and recent experimental studies revealed that amino groups in isolated cytosine, guanine, and adenine adopt a nonplanar trigonal-pyramidal configuration. Since the values of amino group inversion barriers do not exceed approximately 1 kcal mol^{-1}, this group possesses rather flexible geometry. A different source of nonplanarity of nucleobases originates from the high deformability of the pyrimidine ring. Transition of such a ring in uracil, thymine, cytosine, and guanine molecules from a planar equilibrium conformation to a sofa configuration characterized by a relevant torsion angle of $\pm 20^{\circ}$ entails an increase of energy by less than 1.5 kcal mol^{-1}. Therefore, at room temperature, certain fraction of isolated DNA bases should possess nonplanar structure of the heterocyclic ring. This review summarizes recent theoretical studies on the flexibility of the NABs.

21.1 Introduction

It is well recognized that DNA macromolecules are very flexible and can easily change their conformation depending on solvation, concentration, nature of counterions, and temperature [1]. Conformational flexibility of these biomolecules also plays an

O.V. Shishkin[1,3], L. Gorb[1,2], and J. Leszczynski[1] (✉)
[1]NSF CREST Interdisciplinary Nanotoxicity Center, Department of Chemistry and Biochemistry, Jackson State University, P. O. Box 17910, 1325 Lynch str., Jackson, MS 39217, USA; [2]Department of Molecular Biophysics, Institute of Molecular Biology and Genetics, National Academy of Science of Ukraine, 150 Zabolotnogo St., Kyiv 03143, Ukraine; [3]STC "Institute for Single Crystals", National Academy of Science of Ukraine, 60 Lenina ave., Kharkiv 61001, Ukraine
e-mail: jerzy@icnanotox.org

J. Leszczynski and M.K. Shukla (eds.), *Practical Aspects of Computational Chemistry*, DOI: 10.1007/978-90-481-2687-3_21,

important role during interactions with proteins and drugs, creating the most favorable conditions for molecular recognition. Therefore, molecular mechanism of DNA flexibility is a focus of many studies.

Usually, conformational flexibility of these macromolecules is associated with easy conformational changes of backbone including rotation around the P-O bonds, change of ribose conformation, etc [2, 3]. Stacked nucleic acid bases are considered as quite rigid fragments of DNA playing the role of a rod for structure and dynamics of these biopolymers. In general, this is true because it was demonstrated that nucleotides are very flexible molecules with numerous minima on the potential energy surface [4–6]. However, in the case of nucleobases, commonly considered mechanism for deformation of stacked and hydrogen bonded base pairs involves, for example, flipping of bases accompanied by breaking of hydrogen bonds or stacking interactions [7–10].

On the other hand, during the last decade, it has been demonstrated that the nucleic acid bases (see Scheme 21.1 for structures and atomic numbering schemes) also should be considered as quite flexible moieties. In particular, this concerns the configuration and orientation of amino group in cytosine, guanine, and adenine, and conformational flexibility of pyrimidine ring in all bases. Such findings compel changes of the viewpoint on possible relaxation of DNA geometry during interactions with many drugs, metal ions, and proteins. In addition, this phenomenon also influences molecules which are able to intercalate between two adjacent pairs of bases. In such a case, high conformational flexibility of nucleobases can create the most suitable conditions for penetration of intercalators and stabilization of their complexes with DNA.

There is some imbalance in studying and describing those two phenomena. In spite of that, both of them were first predicted computationally [11, 12]; only nonplanarity of amino- group had been confirmed experimentally [13] and attracted considerable attention in the literature (see, for example [14, 15]). In case of conformational flexibility of DNA bases, only indirect experimental evidences have been revealed [16–18]. Therefore, in this review, we discuss in detail the current status of investigations on the ability of pyrimidine ring of DNA bases to fluctuate between planar and nonplanar states.

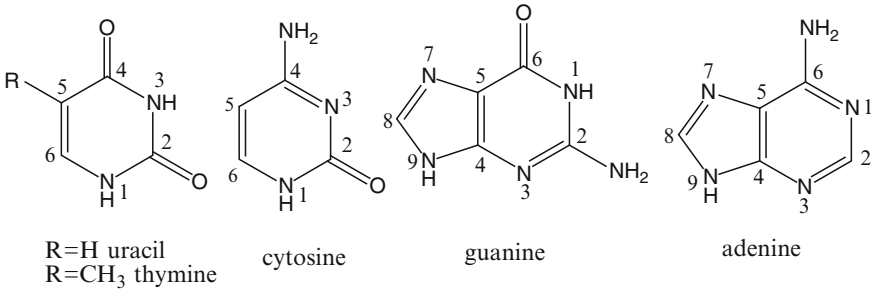

Scheme 21.1 Structure and atomic numbering of nucleic acid bases

21.2 Ab Initio Studies of Conformational Flexibility in Nucleic Acid Bases

The assumption about conformational flexibility of pyrimidine rings of nucleic acid bases proceeds from results of investigation of conformational properties of various dihydroaromatic rings [19]. Conformational flexibility of six-membered dihydrocycles containing saturated carbon atoms within ring is well-known for many years. For example, it is well recognized that 1,4-cyclohexadiene (Scheme 21.2) molecule may easily change planar equilibrium conformation to the boat one characterized by endocyclic torsion angles assuming values up to 30° [20]. Such transformation of ring is accompanied by rather small changes of energy – less than 2 kcal mol^{-1} [21]. The same feature was revealed for 1,4-dihydropyridine (Scheme 21.2) and 1,4-dihydropyrimidine rings [22–24], despite the presence of different substituents at the saturated carbon atoms [25]. High conformational flexibility of such rings was explained by a balance of two opposite factors influencing conformation of dihydrocycle [20]: (1) bending strain which is maximal at the planar geometry of ring and (2) 1,2-allylic strain which is minimal at the planar conformation. Therefore, transition of ring from planar to boat conformation results in simultaneous decrease of bending strain and increase of 1,2-allylic strain leading to very small changes of total energy of molecule for a large range of values of endocyclic torsion angles.

However, nonplanar geometry of dihydroaromatic rings was found also in compounds which do not contain saturated carbon atoms within ring (see for example [26]). More detailed analysis of potential energy surface of various 1,4- and 1,2-dihydroaromatic rings revealed that all these molecules possess high conformational flexibility [27–30]. A transition between planar equilibrium and nonplanar conformation (characterized by the values of endocyclic torsion angles up to 20°) results in molecular energy increase by less than 1.5 kcal mol^{-1}. It was concluded that conformational flexibility is a general property of all types of dihydroaromatic rings [19].

In the case of absence of the saturated carbon atoms, the bending and 1,2-allylic strains cannot be considered as the reasons for a flat potential energy surface around minimum. Therefore, it was suggested [27, 28] that the deviation of characteristics of cyclic conjugated systems from their aromatic features is responsible for conformational flexibility of such dihydroaromatic rings. In addition, it was demonstrated

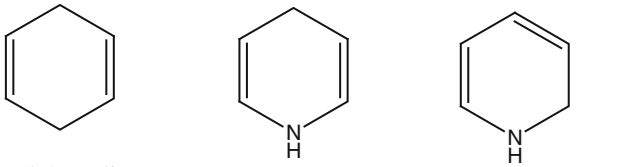

1,4-cyclohexadiene 1,4-dihydropyridine 1,2-dihydropyridine

Scheme 21.2 Structure of 1,4-cyclohexadiene, 1,4-dihydropyridine, and 1,2-dihydropyridine

that the decrease of polarity of exocyclic double bonds in para-benzoquinone accompanied by decrease of concentration of π-electrons within ring results in reduction of conformational flexibility of dihydrocycle due to enhancement of degree of aromaticity. The opposite trend was found for derivatives of 1,4-, 1,2-dihydropyridine containing formally nonaromatic 7-π-electron cyclic conjugated system. From general viewpoint, the pyrimidine rings in cytosine and guanine represent dihydroaromatic rings. Therefore, taking into account results of investigation of conformational flexibility of different types of dihydrocycles, it is possible to expect that these rings should also possess high conformational flexibility. The same conclusion should be derived for tetrahydroaromatic rings in uracil and thymine where cyclic conjugated system formally contains 8-π electrons and should be considered as anti-aromatic. It was demonstrated that anti-aromatic dihydrocycles are considerably more flexible than other dihydroaromatic rings [31].

The results of quantum-chemical studies using AM1 [12], HF [32], and MP2 [33] methods demonstrated that pyrimidine rings in uracil, thymine, cytosine, and guanine possess high conformational flexibility. A change of relevant endocyclic torsion angle within 20° results in energy increase by less than 1.5 kcal mol^{-1} (Fig. 21.1). The most flexible rings are in uracil, thymine, and cytosine, and the most rigid one is in guanine. This agrees well with general trends of conformational flexibility of six-membered rings without the saturated carbon atoms.

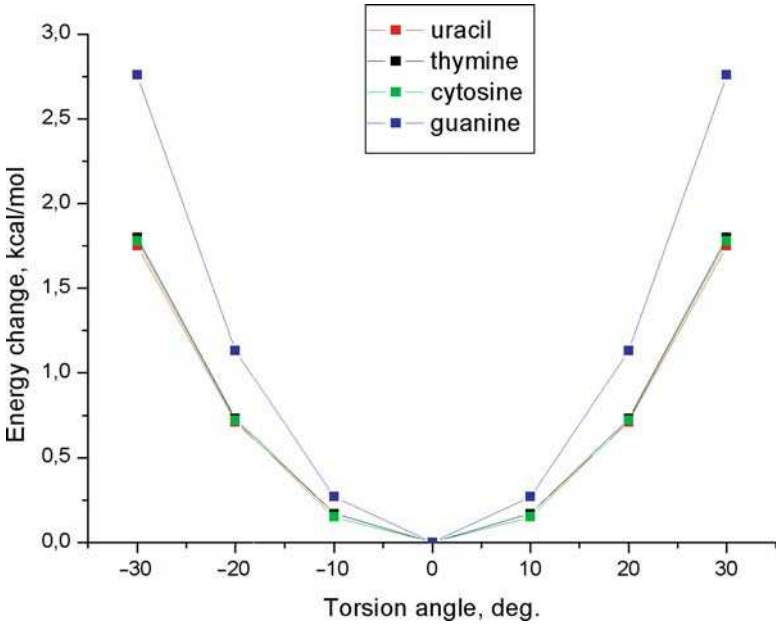

Fig. 21.1 Dependence of energy change on value of the N1-C2-N3-C4 torsion angle in uracil and thymine, the C6-N1-C2-N3 torsion angle in cytosine and C2-N1-C6-C5 torsion angle in guanine. The data are from the MP2/6-31G(d,p) level of calculations [32]

The main reason of high conformational flexibility of pyrimidine rings in nucleobases is the deviation of a character of cyclic conjugated system from genuine aromatic features. Replacement of exocyclic C=O bond by less polar C=NH and C=CH_2 fragments (Scheme 21.3) lead to increased concentration of π-electrons within conjugated system of pyrimidine ring. This results in enhancement of anti-aromatic (for uracil and thymine) or nonaromatic (for cytosine and guanine) character of cyclic conjugated system within heterocycle [32], accompanying by considerable increase of conformational flexibility of ring (Fig. 21.2).

High deformability of any molecular fragment usually results in existence of low-lying modes of normal vibrations [34]. A comparison of the easiest deformation modes resulted from scan of endocyclic torsion angle with a profile of ring out-of-plane normal vibrations demonstrates their remarkable agreement [33]. For example, in the case of uracil, it is possible to suggest two directions of ring out-of-plane deformations associated with out-of-plane motions of the N1 and N3 atoms. In terms of endocyclic torsion angles, these deformations may be described as change of the C6-N1-C2-N3 and C2-N3-C4-C5 torsion angles. Quantum-chemical calculations at different levels of theory [12, 26, 32] indicate that energy change revealed during scan for latter torsion angle is smaller (Table 21.1). This corresponds to lower vibrational frequency for out-of-plane-vibration of the N3 atom [26].

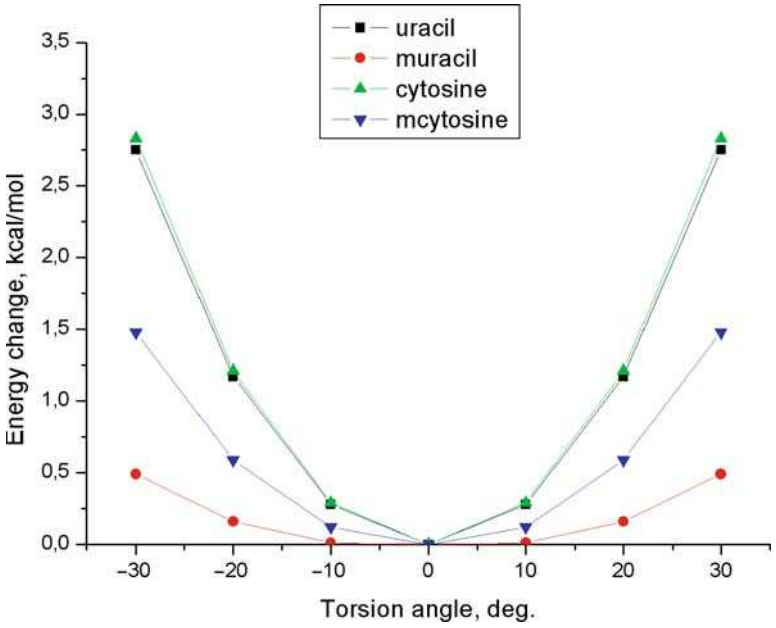

Fig. 21.2 Dependence of energy change on the value of the N1-C2-N3-C4 torsion angle in uracil and the C6-N1-C2-N3 torsion angle in cytosine and their methylene analogues predicted at the HF/6-31G(d,p) level of calculations [33]

Table 21.1 Frequencies of ring out-of-plane vibrations and change of energy during scans of the potential energy surface for nucleic acid bases calculated by MP2/6-31G(d,p) method [33]

Molecule	Frequency (cm^{-1})	Assignment	Torsion angle for scan	Value of torsion angle		
				10	20	30
Uracil	131	N(3) out-of-plane	N(1)-C(2)-N(3)-C(4)	0.17	0.71	1.75
	158	N(1) out-of-plane	C(6)-N(1)-C(2)-N(3)	0.22	0.94	2.31
Thymine	136	N(3) out-of-plane	N(1)-C(2)-N(3)-C(4)	0.17	0.73	1.80
	106	N(1) out-of-plane	C(6)-N(1)-C(2)-N(3)	0.22	0.93	2.31
Cytosine	127	N(1) out-of-plane	C(6)-N(1)-C(2)-N(3)	0.15	0.72	1.78
	202	NH2 wag.	C(2)-N(3)-C(4)-C(5)	0.41	1.79	4.26
Guanine	129	N(1) out-of-plane	C(2)-N(1)-C(6)-C(5)	0.27	1.13	2.76
	151	C=O wag.	C(4)-C(5)-C(6)-N(1)	0.39	1.63	4.04

Thus, high conformational flexibility of pyrimidine ring in nucleic acid bases may be confirmed by experimental investigation of low-lying normal vibrations of these molecules. A comparison of calculated values of vibrational frequencies of such vibrations with experimental data for uracil [35, 36], thymine [37, 38], and guanine [29] demonstrates good agreement between theory and experiment. This may be considered as experimental confirmation of high conformational flexibility of pyrimidine ring in nucleic acid bases.

Another experimental verification of theoretical data may be provided by the analysis of a range of variation of endocyclic torsion angles in crystal structures containing uracil and cytosine fragments. It was demonstrated [32] that range of variation of the N1-C2-N3-C4 torsion angle in uracil and the C6-N1-C2-N3 torsion angle in cytosine amounts to ± 12–13^{o}. For example, it was found that the value of the C6-N1-C2-N3 in the crystal of 5-bromo-2'-deoxycytidine is -7.1^{o}, -12.4^{o}, and -13.9^{o}, respectively, for three molecules in asymmetrical part of unit cell [39].

More detailed analysis of low-lying ring out-of-plane-vibrational modes in internal coordinates revealed several interesting features concerning conformational flexibility of heterocycles in nucleic acid bases. It was demonstrated that endocyclic torsion angle characterized by the smallest energy change during the potential energy surface scan has the maximal amplitude of changes related to the corresponding normal vibrations [33]. This allows suggesting simple method for determination of suitable torsion angle for scan in any cyclic system.

An analysis of low-lying normal vibrations in nucleic acid bases revealed existence of two vibrational modes including ring out-of-plane deformations. There are the N1 and N3 out-of-plane motions in uracil and thymine, wagging vibrations of amino group in cytosine and carbonyl oxygen in guanine including also considerable out-of-plane pyrimidine ring deformation. An investigation of potential energy surface for these modes of deformation demonstrates that both these modes are very soft. The values of ring deformation energy during scan along relevant endocyclic torsion angle (up to $\pm 20^{o}$) do not exceed 2 kcal mol^{-1}. It should be noted that deformation of pyrimidine ring during wagging vibrations of amino and carbonyl groups in cytosine and guanine results in considerable twist of

endocyclic double bonds. Nevertheless, the value of ring deformation energy remains rather small.

Taking into account a good agreement between values of calculated and experimental ring out-of-plane vibrational frequencies and shape, character, and also energy of ring out-of-plane deformations, it is possible to suggest that the values of vibrational frequencies may be considered as universal and experimentally verified indicators of conformational flexibility of pyrimidine rings. However, a comparison of vibrational frequencies and ring deformation energies for out-of-plane motions of the N1 and N3 atoms in uracil and thymine indicates that the vibrational characteristics should be used for these purposes with cautions. In the case of uracil, out-of-plane vibration of the N3 atom has lower values of both the frequency of normal vibration and ring deformation energy. It is difficult to assume that replacement of the hydrogen atom by methyl group in thymine should significantly influence intramolecular interactions within ring, and therefore, ring flexibility. In agreement with this expectation, ring deformation energy for out-of-plane motion of the N3 atom in thymine is smaller as compared to the N1 atom. However, the values of frequency of the corresponding vibrations have an opposite order. The frequency of out-of-plane-vibration related to the N1 atom becomes lower than the one belonging to N3 atom. Detailed analysis of character of this vibrational mode indicates that this vibration involves also out-of-plane motions of methyl group. Therefore, kinetic effects, namely, involvement of exocyclic substituent in molecular motions, result in decrease of vibrational frequency without considerable changes of the potential energy surface [33].

An analysis of character and frequencies of normal vibrations and scan of relaxed potential energy surface represents two complementary approaches to investigation of conformational flexibility of pyrimidine rings in nucleic acid bases. A combined application of these approaches allows estimating population of conformations with nonplanar rings for each molecule.

It is well-known that the position of maximum of probability density functions of low-lying levels of quantum mechanical harmonic oscillator strongly depends on a position of energy level [40]. For zero level, this maximum falls roughly in the center of minimum of the potential function for vibration (Fig. 21.3). However, for higher levels of harmonic oscillations, maxima of probability are located near potential wells. Therefore, molecules which populate these levels will possess geometry that differs considerably from the geometry of minimum of the potential energy.

In the case of discussed molecules, it means that for the nucleobase molecules populating zero vibrational level for every vibration, the planar or nearly planar geometry (Fig. 21.3) is the most probable. Molecules with considerably nonplanar conformation of pyrimidine ring will populate higher vibrational levels. Therefore, we can estimate a fraction of molecules with essentially nonplanar geometry based on population of vibrational levels characterized by number 1 and higher. Similar approach is used for analysis of structure and vibrational spectra of molecules with large amplitude motions [34].

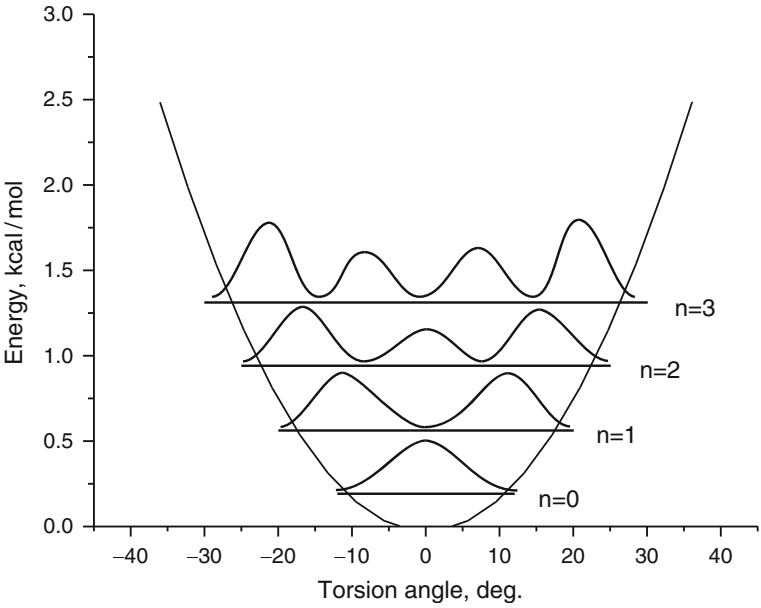

Fig. 21.3 Probability density function for different vibrational levels of normal vibrations. Dependence of energy change on the value of torsion angle corresponding to the out-of-plane deformation of pyrimidine ring in uracil. MP2/6-31G(d,p) level calculations

The population of harmonic vibrational levels for every out-of-plane ring vibration may be evaluated using Boltzmann distribution function. These values for nucleic acid bases are listed in Table 21.2. As can be seen, the population of the zero level for the lowest vibrations in molecules under study does not exceed 53%. Therefore, one can conclude that the remaining molecules have a nonplanar geometry of pyrimidine ring. The degree of ring deformation may be approximately estimated based on ring deformation energy (Table 21.1) and energy of populated levels (Table 21.2). For example, energy of the first vibrational level of the lowest vibration of uracil amounts to 0.56 kcal mol^{-1}. This corresponds to the ring deformation with the value of relevant torsion angle *ca.* $\pm 17^{o}$. Therefore, one can conclude that 25% of uracil molecules in every moment of time possess a nonplanar geometry of pyrimidine ring with the value of torsion angle about 17^{o}. The degree of ring nonplanarity increases with an increase of energy of the vibrational level. In uracil, for the third vibrational level (population 7%), the magnitude of relevant torsion angle is about 26^{o}.

Unlike in the case of uracil, thymine, cytosine, and guanine, the pyrimidine ring in adenine possesses clearly aromatic character. Therefore, it was expected that this ring should be conformationally rigid. However, an analysis of normal vibration of adenine demonstrated an existence of vibrational mode with frequency of only 166 cm^{-1} [41] corresponding to the wagging motion of amino group involving considerable pyrimidine ring out-of-plane deformation. A scan of relaxed potential energy surface for such deformation of six-membered ring in adenine indicates that

Table 21.2 Energy and population of harmonic vibrational levels for the lowest vibrational modes of nucleobases at 298 K

Molecule	Frequency (cm^{-1})	Level	Energy (kcal mol^{-1})	Population (%)
Uracil	131	0	0.19	47
		1	0.56	25
		2	0.94	13
		3 and higher	≥1.31	15
	158	0	0.23	53
		1	0.68	25
		2	1.13	12
		3 and higher	≥1.59	10
Thymine	136	0	0.20	48
		1	0.58	25
		2	0.97	13
		3 and higher	≥1.36	14
	145	0	0.21	50
		1	0.62	25
		2	1.04	12
		3 and higher	≥1.46	13
Cytosine	127	0	0.18	46
		1	0.55	25
		2	0.91	13
		3 and higher	≥1.27	16
	202	0	0.29	62
		1	0.87	23
		2	1.45	9
		3 and higher	≥2.03	6
Guanine	129	0	0.18	46
		1	0.55	25
		2	0.92	13
		3 and higher	≥1.29	16
	151	0	0.22	52
		1	0.65	25
		2	1.08	12
		3 and higher	≥1.52	11

The values of harmonic vibrational frequencies calculated at the MP2/6-31G(d,p) level of theory [33]

this heterocycle possesses notable degree of conformational flexibility despite of its aromatic character (Fig. 21.4). A change of value of endocyclic torsion angle (up to $\pm 20^{o}$) results in energy increase less than 2 kcal mol^{-1} [41].

An analysis of conformational flexibility of pyrimidine ring in related molecules (purine, aminopyrimidine, and unsubstituted pyrimidine (Scheme 21.4)) indicates that the flat character of the potential energy surface around minimum is a general property of pyrimidine ring. A presence of amino group and fused imidazole ring only promotes increase of conformational flexibility of heterocycle.

Estimation of population of the ground and excited vibrational levels for ring out-of-plane-vibrations demonstrate that even in the case of unsubstituted pyrimidine ring, 18% of molecules possess considerably nonplanar geometry of ring

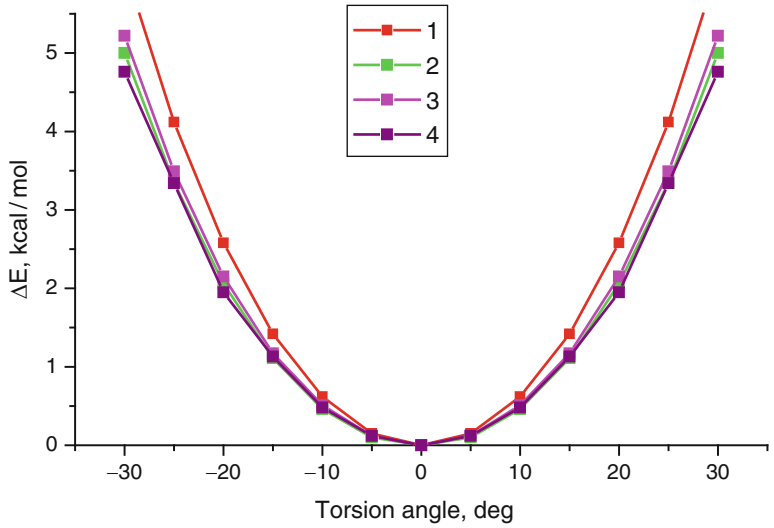

Fig. 21.4 Dependence of energy change on the value of the C4-C5-C6-N1 torsion angle in adenine (4) and aminopyrimidine (2), the N3-C4-C5-C6 torsion angle in pyrimidine (1) and purine (3). MP2/6-31G(d,p) level calculations

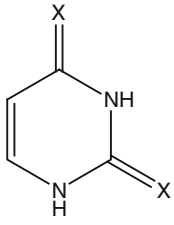

uracil X=O,
methyleneuracil X=CH_2

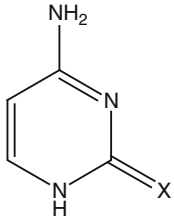

cytosine X=O,
methylenecytosine X=CH_2

Scheme 21.3 Structure of thymine, cytosine and their methlene analogues

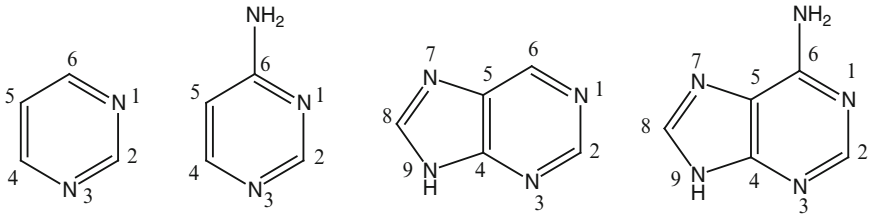

Scheme 21.4 Structure of adenine and related compounds

at every moment of time. In the case of adenine, the population of nonplanar conformations approaches almost 50% (Table 21.3).

Further investigation of conformational flexibility of aromatic rings indicates that this property is general for all molecules in this class including benzene [16, 42, 43]. The degree of conformational flexibility depends on the presence of heteroatoms, fused rings, or substituents. Moreover, it was found that the transition of the ring into nonplanar conformation with values of endocyclic torsion angles up to $\pm 30^{o}$ does not influence characteristics of electron density distribution [35] and aromaticity of benzene ring [44].

The most complete picture of conformational flexibility of pyrimidine rings in nucleic acid bases has been provided by molecular dynamics study of isolated molecules using ab initio Carr-Parinello method [45]. According to these studies, the population of planar conformation of heterocycle does not exceed 20% for thymine, cytosine, and guanine and amounts to about 30% for adenine (Table 21.4). These values are considerably smaller as compared to estimations based on vibrational frequencies mentioned above. Such difference is quite natural because in the case of vibrational analysis, only the lowest ring out-of-plane normal mode is considered. However, there are also smaller contributions of the other ring out-of-plane vibrations not included in this analysis. Therefore, such estimation should be considered as an upper limit for assessment of population of planar conformation of ring.

An analysis of conformational flexibility of imidazole rings in guanine and adenine indicates that these heterocycles are much more rigid (Table 21.4).

Table 21.3 Energy and population of harmonic vibrational levels for the lowest vibrational modes of adenine and related molecules at 298 K41]

		Pyrimidine	Aminopyrimidine	Purine	Adenine
Frequency (cm^{-1})		354	201	232	166
N=0	E (kcal mol^{-1})	0.51	0.29	0.33	0.24
	Population (%)	82	62	67	55
N=1	E (kcal mol^{-1})	1.52	0.86	1.00	0.71
	Population (%)	15	24	22	25
N=2	E (kcal mol^{-1})	2.54	1.44	1.66	1.19
	Population (%)	3	9	8	11
N=3	E (kcal mol^{-1})	3.65	2.02	2.33	1.67
	Population (%)	0	4	3	5

The values of harmonic vibrational frequencies calculated at the MP2/cc-pvdz level of theory

Table 21.4 Population of planar conformation of rings (with endocyclic torsion angles less than 10^{o}) in nucleic acid bases according to Carr-Parinello molecular dynamics simulations [45]

Molecule	Ring	Population (%)
Thymine	Pyrimidine	11.9
Cytosine	Pyrimidine	17.1
Guanine	Pyrimidine	17.8
Guanine	Imidazol	66.0
Adenine	Pyrimidine	30.3
Adenine	Imidazole	64.2

However, even in this case, more than 30% of molecules have also considerably nonplanar geometry of ring.

It should be noted that investigations of conformational flexibility of pyrimdine rings in nucleic acid bases had considered only isolated molecules. Therefore, a question how this property is affected by intermolecular interactions in solutions or DNA macromolecules should be independently addressed. An investigation of conformational flexibility of rings in Watson-Crick adenine-thymine and guanine-cytosine pairs of bases demonstrated [46] that the formation of hydrogen bonds between bases virtually does not influence energy of pyrimidine rings deformation. This establishes the possibility for effective relaxation of geometry of hydrogen bonded nucleobases with respect to different steric clashes. In particular, it was found that pyrimidine rings in stacked dimers of uracil, cytosine, and also adenine-uracil, and uracil-cytosine pairs possess considerable nonplanarity [47, 48]. However, a comparison of energy of interactions between planar and nonplanar stacked bases indicates rather small difference in their values (about 1 kcal mol^{-1}).

Therefore, it is possible to conclude that high conformational flexibility of pyrimidine rings does not significantly influence the energy of stacking interaction between bases in DNA macromolecules.

An investigation of structure of polyhydrated complexes of adenine [48] and guanine [49] demonstrates that asymmetric shape of hydrogen environment may lead to significant nonplanarity of the pyrimidine ring. High conformational flexibility allows adjustment of heterocycle conformations in order to provide conditions for maximal attraction between base and water. Therefore, it is possible that their conformational flexibility also remains in water solution despite the presence of numerous hydrogen bonds. This conforms well with the small changes of value of ring out-of-plane vibration frequency in complex of cytosine with 13 water molecules [4, 50].

A confirmation of the role of conformational flexibility of pyrimidine rings as efficient way for geometry relaxation was found during an investigation of conformational characteristics of canonical 2′-deoxyribonucleotides. It was demonstrated that formation of intramolecular hydrogen bonds between amino and phosphates groups of 2-deoxyriboadenosine monophosphate and 2′-deoxycytidine monophosphate results in significant out-of-plane deformation of pyrimidine ring [4, 5, 51]. The values of endocyclic torsion angles are up to 23° for cytosine and 13° for guanine. This allows for the creation of the most suitable conditions for formation of hydrogen bonds (Fig. 21.5). In addition to discussed theoretical studies, as it was already mentioned, there are also indirect experimental evidences of conformational flexibility of DNA bases and related molecular species [16, 17, 52].

21.3 Conclusions

Contrary to earlier beliefs, the recent computational studies have revealed that DNA bases are fairly flexible. There are two sources of conformational flexibility of nucleobases: nonplanarity of amino groups and high deformability of the

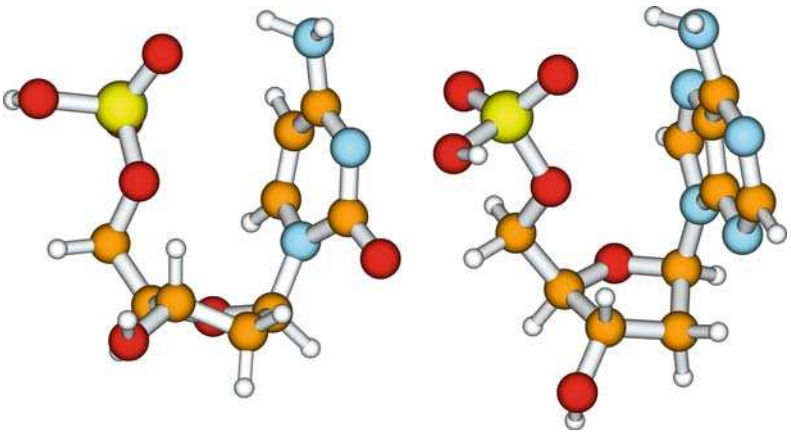

Fig. 21.5 Structure of orthogonal conformers of 2′-deoxyriboadenosine monophosphate (AMP) and 2′-deoxycytidine monophosphate (CMP) with nonplanar pyrimidine ring according to calculations at the B3LYP/aug-cc-pvdz level [4]

pyrimidine ring. The conformational flexibility of pyrimidine rings which is a topic of this review represents very important way for relaxation of molecular geometry as a response to intermolecular interactions or steric clashes. This is especially important for understanding the mechanisms of molecular recognition, for example, during intercalation process. In such a case, nucleic acid bases are able to easily change their conformation in order to maximize interactions with intercalating agent without considerable changes of electronic properties or intermolecular interactions with neighboring bases.

Acknowledgments This work was supported by NSF CREST Interdisciplinary Nanotoxicity Center (grant number HRD-0833178).

References

1. S. Niedle, *Principles of Nucleic Acid Structure* (Elsevier, New York, 2008)
2. D. Svozil et al., DNA conformations and their sequence preferences. Nucl. Acids Res. **36**, 3690–3706 (2008)
3. R.H. Sarma (ed), *Structure, Motion, Interaction and Expression of Biological Macromolecules* (Adenine Press, New York, 1998)
4. O.V. Shishkin et al., Conformational analysis of canonical 2-deoxyribonucleotides. 1. Pyrimidine nucleotides. J. Biomol. Struct. Dyn. **21**, 537–553 (2004)
5. O.V. Shishkin et al., Conformational analysis of canonical 2-deoxyribonucleotides. 2. Purine nucleotides. J. Biomol. Struct. Dyn. **22**, 227–243 (2004)
6. N. Foloppe et al., Intrinsic conformational energetics associated with the glycosyl torsion in DNA: A quantum mechanical study. Biophys. J. **82**, 1554–1569 (2002)

7. P. Hobza et al., Structure, energetics, and dynamics of the nucleic acid base pairs: Nonempirical ab initio calculations. Chem. Rev. **99**, 3247–3276 (1999)
8. R.E.A. Kelly et al., Homopairing possibilities of the DNA bases cytosine and guanine: An ab initio DFT study. J. Phys. Chem. B **109**, 22045–22052 (2005)
9. M. McCullagh et al., Effect of loop distortion on the stability and structural dynamics of DNA hairpin and dumbbell conjugates. J. Phys. Chem. B **112**, 11415–11421 (2008)
10. L.L. O'Neil et al., Base flipping of the thymine dimer in duplex DNA. J. Phys. Chem. B **111**, 11843–11849 (2007)
11. J. Leszczynski, Are the Amino Groups in the Nucleic Acid Bases Coplanar with the Molecular Rings? Ab Initio HF/6–31G* and MP2/6–31G* Studies. Int. J. Quantum Chem. **19**, 43–55 (1992)
12. O.V. Shishkin, Conformational flexibility of dihydropyrimidinone and tetrahydopyrimidin-2,4-dione rings in DNA bases, J. Chem. Soc.Chem.Commun , 1538 (1995).
13. F. Dong et al., Vibrational transition moment angles in isolated biomolecules: A structural tool. Science **298**, 1227–1230 (2002)
14. M.O. Ben Luis et al., On the potential role of the amino nitrogen atom as a hydrogen bond acceptor in macromolecules. J. Mol. Biol. **279**, 1123–1136 (1998)
15. Choi Myong Yong et al., Nonplanarity of adenine: Vibrational transition moment angle studies in helium nanodroplets. J. Phys. Chem. A **112**, 7185–7190 (2008)
16. O.V. Shishkin et al., Structural non-rigidity of six-membered aromatic rings. J. Mol. Struct. **616**, 159–166 (2002)
17. L.-L. Lai et al., 2,6-Bis(dimethylamino)-3,5-pyridine-dicarbaldehyde. Acta Crystallogr. **C 50**, 1931–1934 (1994)
18. D.A. Peters et al., Structures of 3-methoxypyrazine 1-oxide (1a) and 3-methoxy-5-methylpyrazine 1-oxide (1b). Acta Crystallogr. C **48**, 307–311 (1992)
19. O.V. Shishkin, Conformational flexibility of six-membered dihydrocycles. Russian Chem. Bull. **46**, 1981–1991 (1997)
20. P.W. Rabideau (ed), *Conformational analysis of cyclohexenes, cyclohexadienes and related hydroaromatic compounds* (VCH, New York, 1989)
21. K.B. Lipkowitz et al., Structure and conformation of 1,4-dihydrobenzene, 1,4-dihydronaphthalene, and 9,10-dihydroanthracene. A theoretical study. J. Org. Chem. **47**, 1002–1005 (1982)
22. Y.D. Wu et al., Theoretical study of conformational features of NAD+ and NADH analogs: protonated nicotinamide and 1,4-dihydronicotinamide. J. Org. Chem. **58**, 2043–2045 (1993)
23. O.V. Shishkin et al., Cycle mobility in 1,4-dihydropyridine and its monoalkyl and phenyl derivatives. Russ.Chem.Bull. **42**, 1160–1162 (1993)
24. O.V. Shishkin et al., The effect of substituents on the conformational mobility of the heterocycle in 1,4-dihydropyrimidine and its derivatives. Russ.Chem.Bull. **43**, 1320–1323 (1994)
25. O.V. Shishkin, Conformational flexibility of the 1, 4-dihydropyridine ring in calcium channel agonists and antagonists molecules. J. Mol. Struct. **385**, 209–214 (1996)
26. V.S. Bogdanov et al., The novel thermal rear-rangement in the pyrido[1,2-a]pyrimidine series: the transformation of 3-acetyl-4-phenylaminopy-rido[1,2-a]pyrimi-dine-4-on, Mendeleev Commun. , 106-107 (1995).
27. O.V. Shishkin, Conformational flexibility of six-membered 1, 4-dihydrocycles. J. Mol. Struct. **412**, 115–120 (1997)
28. O.V. Shishkin, Conformational flexibility of six-membered 1, 2-dihydrocycles and substituent electronic effects. J. Mol. Struct. **447**, 217–222 (1998)
29. O.V. Shishkin, Molecular structure and conformational flexibility of the 1, 3-cyclohexadiene carbonyl derivatives. J. Mol. Struct. **403**, 167–170 (1997)
30. O.V. Shishkin, Molecular, electronic structure and conformational flexibility of the 1, 6-dihydropyrimidine, 4, 5-dihydrofuro[2, 3-d]pyrimidine and their oxo, imino and methylene derivatives. J. Mol. Struct. **385**, 55–63 (1996)

31. O.Y. Borbulevych et al., Conformational flexibility of antiaromatic 1, 4 heterocyclic analogues of 1, 4-cyclohexadiene. J. Mol. Struct. **446**, 11–14 (1998)
32. O.V. Shishkin, Conformational flexibility of di- and tetrahydropyrimidine rings in nucleic acid bases. An ab initio HF/6-31G** study. J. Mol. Struct. **447**, 1–5 (1998)
33. O.V. Shishkinet al., Structural nonrigidity of nucleic acid bases. Post-Hartree-Fock ab initio study. Int. J. Quantum Chem. **80**, 1116–1124 (2000)
34. R.D. Brown, *Structure and Conformations of Non-Rigid Molecules*, ed. by M.D.J. Laane, B. van der Veken, H. Oberhammer (Kluwer Academic Publishers, Dordrecht, 1993)
35. A. Aamouche et al., Neutron inelastic scattering, optical spectroscopies and scaled quantum mechanical force fields for analyzing the vibrational dynamics of pyrimidine nucleic acid bases .1. Uracil. J. Phys. Chem. **100**, 5224–5234 (1996)
36. M.P. Gaigeot et al., Analysis of the structural and vibrational properties of RNA building blocks by means of neutron inelastic scattering and density functional theory calculations. Chem. Phys. **261**, 217–237 (2000)
37. A. Aamouche et al., Neutron inelastic scattering, optical spectroscopies, and scaled quantum mechanical force fields for analyzing the vibrational dynamics of pyrimidine nucleic acid bases. Thymine. J. Phys. Chem. A **101**, 1808–1817 (1997)
38. S.L. Zhang et al., Vibrational spectra and experimental assignments of thymine and nine of its isotopomers. J. Phys. Chem. A **102**, 461–470 (1998)
39. J.N. Low et al., Structure of 5-bromo-2′-deoxycytidine monohydrate. Cryst. Struct. Commun. **10**, 931–935 (1981)
40. C.E. Dykstra, *Quantum Chemistry and Molecular Spectroscopy* (Prentice Hall, Cliffs, NewJersey, 1992)
41. O.V. Shishkin, Conformational flexibility of pyrimidine ring in adenine and related compounds. Chem. Phys. Lett. **330**, 603–611 (2000)
42. M.V. Zhigalko et al., Out-of-plane deformability of aromatic systems in naphthalene, anthracene and phenanthrene. J. Mol. Struct. **693**, 153–159 (2004)
43. O.V. Shishkin et al., Aromaticity of monosubstituted derivatives of benzene. The application of out-of-plane ring deformation energy for a quantitative description of aromaticity. J. Mol. Struct. **791**, 158–164 (2006)
44. F. Feixaset al., Aromaticity of Distorted Benzene Rings: Exploring the Validity of Different Indicators of Aromaticity. J. Phys. Chem. A **111**, 4513–4521 (2007)
45. O. Isayev et al., Are isolated nucleic acid bases really planar? A Car-Parrinello molecular dynamics study. J. Phys. Chem. B **111**, 3476–3480 (2007)
46. O.V. Shishkin et al., Intramolecular flexibility of DNA bases in adenine-thymine and guanine-cytosine Watson-Crick base pairs. J. Mol. Struct. **477**, 15–21 (1999)
47. P. Hobza et al., Significant structural deformation of nucleic acid bases in stacked base pairs: an ab initio study beyond Hartree-Fock. Chem. Phys. Lett. **288**, 7–14 (1998)
48. O.S. Sukhanov et al., Molecular structure and hydrogen bonding in polyhydrated complexes of adenine: A DFT study. J. Phys. Chem. B **107**, 2846–2852 (2003)
49. O.S. Sukhanov et al., Structure and hydrogen bonding in polyhydrated complexes of guanine. Struct. Chem. **19**, 171–180 (2008)
50. O.V. Shishkin et al., Does the hydrated cytosine molecule retain the canonical structure? A DFT study. J. Phys. Chem. B **104**, 5357–5361 (2000)
51. O.V. Shishkin et al., Intramolecular Hydrogen Bonds in Canonical 2′-Deoxyribonucleotides: An Atoms in Molecules Study. J. Phys. Chem. B **110**, 4413–4422 (2006)
52. D.A. Peters et al., Structures of 3-methoxypyrazine 1-oxide (1*a*) and 3-methoxy-5-methylpyrazine 1-oxide (1*b*). Acta Crystallogr. C **48**, 307–309 (1992)

Chapter 22
DNA Lesions Caused by ROS and RNOS: A Review of Interactions and Reactions Involving Guanine

P.K. Shukla and P.C. Mishra

Abstract DNA is constantly attacked by a large number of endogenous and exogenous reactive oxygen species (ROS), reactive nitrogen oxide species (RNOS), and alkylating agents which produce a wide variety of modifications of its constituents, particularly the bases. Some of these modifications (lesions) are hazardous to normal cell functioning, and are implicated in several lethal conditions including chronic inflammatory diseases, atherosclerosis, aging, mutation, cancer, and neurodegenerative disorders, such as the Alzheimer's and Parkinson's diseases.

ROS and RNOS are present abundantly in living cells, and can oxidize and/or nitrate almost all the classes of biomolecules including DNA. Different ROS and RNOS primarily react with guanine in DNA to form 8-oxoguanine (8-oxoG) and 8-nitroguanine (8-nitroG) along with other mutagenic products. 8-OxoG readily mispairs with adenine during DNA replication to cause GC → AT transversion mutation. 8-OxoG and 8-nitroG are considered to be highly potent initiators of mutation and cancer.

Reactions of guanine and/or imidazole, the latter taken as a model for the five-membered ring of guanine, with different ROS and RNOS including the OH· radical, H_2O_2, H_2O_3, $ONOO^-$, $ONOOCO_2^-$, HOCl, and NO_2Cl, have been studied using quantum chemical methods. The present review brings out the main, interesting features of the results obtained in such studies.

22.1 Introduction

DNA (deoxyribonucleic acid), the biological hereditary material, is frequently attacked by a large number of endogenous and exogenous agents including the so-called reactive oxygen species (ROS) and reactive nitrogen oxide species

P.K. Shukla and P.C. Mishra (✉)
Department of Physics, Banaras Hindu University, Varanasi 221 005, India
e-mail: pcmishra_in@yahoo.com, pcmishra@bhu.ac.in

J. Leszczynski and M.K. Shukla (eds.), *Practical Aspects of Computational Chemistry*,
DOI: 10.1007/978-90-481-2687-3_22

(RNOS), alkylating agents, different free radicals, and pollutants [1–20]. Interaction of DNA with these agents, slow electrons, and high energy and ultraviolet radiations, can result in a wide variety of potentially mutagenic modifications of its constituents that act as DNA lesions [1–24]. Specific changes of the bases resulting from these interactions and reactions include their oxidation, nitration, halogenation, and alkylation [1–6, 8–12, 14, 16–20]. These changes can cause mispairing of the bases, single and double DNA strand breaks, inter- and intra-strand cross-links, and DNA-protein cross-links [1–4, 9–12, 17, 19–22, 25–33]. These lesions are hazardous to normal cell functioning, and are implicated in several lethal conditions including chronic inflammatory diseases, atherosclerosis, diabetes, aging, mutation, cancer, and neuro-degenerative disorders, such as the Alzheimer's and Parkinson's diseases [1–13, 16, 17, 27–31, 34–44]. Damages to DNA bases caused by ROS, RNOS and methylating agents are known to be the principal causes of the various deleterious consequences mentioned above [1–6, 11, 16, 17, 29, 31, 35, 36, 39–44]. Modifications in the sugar moiety of DNA can also cause lethal effects. The different aspects in this context have been reviewed recently [45].

DNA bases after being exposed to the ROS, RNOS, and methylating agents, undergo a multitude of modifications [1–4, 9–20, 25, 29, 35, 37, 45–49]. The ROS and RNOS can oxidize and/or nitrate different sites of the bases forming a myriad of oxidation and nitration products [1–5, 8–14, 37, 48–56]. It has been difficult to resolve the observed mutations in terms of contributions of the individual ROS and RNOS-induced modifications of DNA bases [2–5, 10, 11, 29, 35]. 8-Oxo and 8-nitro derivatives of guanine have been found to play important roles in mutation and cancer [2–6, 10, 11, 26, 27, 29, 30, 32, 35–41, 47–49, 51–54, 57–59]. Methylating agents can methylate the endocyclic nitrogen sites as well as exocyclic oxygen sites of the DNA bases forming several mutagenic products [16–20, 25, 28, 31, 33, 60–64]. The N7 site of guanine is the most favored site for alkylation [16, 19, 60–63], while O6-methylated guanine (O6-MeG) is the most important alkylated mutagenic modification of the base [16–18, 28, 31, 61, 62, 65, 66]. 8-OxoG and O6-MeG mispair with adenine and thymine, respectively, and cause GC → AT transversion mutation during DNA replication, which is believed to be one of the primary causes of the cancer [5, 16–18, 27–32, 35, 36, 38, 57–59, 65–70]. In the present review, we would focus our attention only on the DNA damage involving the guanine base of DNA caused by some of the important ROS and RNOS. Further, we have mainly considered the quantum chemical studies of interactions and reactions of the various ROS and RNOS with guanine and other related molecules, such as imidazole that serves as a model for the five-membered ring of guanine.

22.2 Basic Information About ROS and RNOS

ROS and RNOS are, in general, very reactive species that can damage almost all classes of biomolecules including DNA, RNA, proteins, and lipids [1–7, 9–12, 35, 36, 46, 71–75]. ROS is a term used collectively for oxygen-containing compounds that are

highly reactive free radicals or compounds that can readily be converted into very reactive oxygen free radicals in the cell. Examples of ROS include the superoxide radical anion ($O_2\cdot^-$), singlet oxygen ($^1O_2$), hydroxyl radical (OH·), hydrogen peroxide (H_2O_2), dihydrogen trioxide (H_2O_3), hypochlorous acid (HOCl), hydroperoxyl radical (HOO), alkoxyl radical (RO), alkylperoxyl radicals (ROO) (R=alkyl group), and carbonate radical anion ($CO_3\cdot^-$) [3, 5–7, 11, 12, 35, 36, 39, 46, 51, 53, 58, 76, 77]. Similarly, RNOS is a collective term used for compounds consisting of both nitrogen and oxygen atoms that cause oxidation and/or nitration of biomolecules, such as nitric oxide radical (NO), nitrogen dioxide radical ($NO_2\cdot$), peroxynitrite anion ($ONOO^-$), nitrous acid (HNO_2), dinitrogen trioxide (N_2O_3), nitrosoperoxycarbonate anion ($ONOOCO_2^-$), and nitryl chloride (NO_2Cl) [3, 11, 52, 54, 77, 78].

ROS and RNOS are generated constantly in living cells by endogenous as well as exogenous sources [1–7, 10–12, 35, 36, 44, 58, 77, 79–85]. The formation and specific property of some of the important ROS and RNOS are discussed below. The oxygen molecule in the ground state with triplet spin multiplicity ($^3O_2$), which is indispensable for human life, is dissolved in aqueous solutions and biological media. When the oxygen molecule combines with an electron produced by different mechanisms in living cells, it is transformed into the superoxide radical anion ($O_2\cdot^-$) [7, 12, 34, 50, 80–82]. Superoxide radical anion is abundantly produced during oxidative stress and damages the cells in a variety of ways [7, 12, 34, 50, 80–85]. Misiaszek et al. [50] have observed that reactions of $O_2\cdot^-$ with guanine radical result in the formation of 8-oxoG, along with other species. It has been further found that reactions of 8-oxoG with $O_2\cdot^-$ lead to the formation of diverse other products including dehydroguanidinohydantoin, oxaluric acid, and diastereomeric spiroiminodihydantoin [86]. Oxygen in its lowest singlet excited state ($^1O_2$), generally termed as singlet oxygen, is very reactive and can be produced in a number of ways, the most common being interaction of $^3O_2$ with a dye molecule (D) in its excited singlet state (^1D) [87–90]. $^1O_2$ can be detected using its fluorescence at 1,270 nm [91]. $^1O_2$ reacts with guanine out of the four bases of DNA and mainly forms 8-oxoG. [56, 87, 92]. In living cells, the enzyme superoxide dismutase catalyzes the conversion of $O_2\cdot^-$ into H_2O_2 and O_2 [7, 34, 36, 93–95]. H_2O_2 is also generated enzymatically as a major reaction product by a number of oxidases present in peroxisomes, mitochondria, and the endoplasmic reticulum [96–98].

H_2O_2 is not considered to be very reactive as such, but can generate the extremely reactive and devastating hydroxyl radicals (OH·) and other reactive oxygen species, e.g., HOCl [3, 5, 12, 34, 51, 76, 99]. Transition metals, e.g., Fe^{2+} and Cu^+, catalyze the formation of hydroxyl radicals by the non-enzymatic Fenton reaction [3, 5, 34, 51, 100, 101]. Hydroxyl radicals are also produced through a number of enzymatic and non-enzymatic mechanisms, including the Haber-Weiss reaction [3, 5, 34, 51, 102]. Hydroxyl radicals are one of the most studied and extremely potent species among the various ROS [1–7, 9, 10, 12, 15, 34–36, 40, 44, 51, 75, 100–112]. Hydroxyl radicals react strongly with a large number of molecules including biomolecules, such as DNA, proteins, and lipids [1–7, 9, 10, 12, 15, 34–36, 40, 44, 51]. It is involved in various addition, hydrogen abstraction, and

electron-transfer reactions [1, 3, 10, 51, 103–106, 111]. Reactions of DNA with hydroxyl radicals produce a plethora of modifications of DNA, including 8-oxoG [1–5, 9, 10, 12, 15, 29, 34, 35, 51]. Reactions of H_2O_2 with chloride anion (Cl^-), catalyzed by the heme enzyme myeloperoxidase released by phagocytic cells, lead to the formation of HOCl [5, 34, 74, 76, 99, 113]. Reactions of HOCl with different species in biological media produce other ROS, including the OH· radical and $^1O_2$ [12, 34, 76, 114]. While on one hand, HOCl is useful against microbial and bacterial infection [115], on the other, it is also hazardous because of its tremendous ability to alter DNA, RNA, proteins, and lipids [3, 71, 74, 76, 114, 116]. Reactions of HOCl with DNA can produce several oxidation and chlorination products, including 8-chloro-2′-deoxyguanosine (8-chlorodG) and 8-oxo-2′-deoxyguanosine (8-oxodG), the yield of the former being more than that of the latter [114].

Thermal reaction of H_2O_2 with singlet oxygen leads to the formation of dihydrogen trioxide (H_2O_3) in a significant amount [53, 117]. Ozonation of several compounds, such as 1,2-diphenylhydrazine, 2-ethylanthrahydroquinone, isopropyl alcohol, isopropyl methyl ether, and cumin, in various organic solvents at low temperatures, has been reported to produce H_2O_3 in large amounts [118]. Wentworth et al. [119] have shown that H_2O_3 is formed as an intermediate in the antibody catalyzed addition reactions of singlet oxygen and water. It has been detected by various spectroscopic methods, such as UV, IR, Raman, NMR, and Fourier transform microwave spectroscopy, and has been found to be far more stable than was previously believed [118, 120–123]. Thus, it may be present in significant amounts in the environment and in biological media [118, 119, 123]. H_2O_3 has widely been reported to be a reactive species that might be involved in various biological, atmospheric, and environmental oxidative processes [53, 117–119, 123, 124]. However, reactivity of H_2O_3 against various organic substrates and the role of environment in this context, e.g., that of water, are not yet properly understood. As H_2O_3 comes after H_2O_2 in the family of hydrogen oxides H_2O_n ($n = 1, 2, 3, 4\ldots$) [123, 125] and H_2O_2 oxidizes guanine to form 8-oxoG [51], it is expected that H_2O_3 can also oxidize guanine forming 8-oxoG.

Nitric oxide ($NO^{\cdot}$) radicals are synthesized from arginine by nitric oxide synthases in cells of the immune system, such as macrophages and neutrophils, endothelial cells, and in neuro-systems [11, 49, 77, 81, 83, 85]. It is also formed from nitrite (NO_2^-), which is naturally present in vertebrates [126]. Nitric oxide is essential for life and is also toxic [11, 49, 85, 127]. At low concentrations, it plays important roles in neurotransmission and vasodilation [49, 128]. While, at high concentrations, it combines with $O_2^{\cdot -}$ to form the highly toxic RNOS called peroxynitrite ($ONOO^-$), or with O_2 to form N_2O_3 [3, 11, 48, 49, 54, 83, 85, 127]. Peroxynitrite, due to its oxidizing and nitrating capability, has been reported to be a powerful cytotoxic and mutagenic agent in several bacterial and mammalian cell culture systems [3, 8, 49, 73, 83, 85, 127]. It has also been implicated in an increasing number of diseases, including atherosclerosis, inflammation, and neuro-degenerative diseases [3, 5, 11, 34, 37, 39, 48, 49]. Peroxynitrite can react with any of biomolecules, such as DNA, proteins, and lipids, under physiological conditions [3, 5, 11, 37, 47–49, 73, 85]. Reactions of DNA with

peroxynitrite lead to the formation of several products, including 8-oxoG and 8-nitroG [3, 5, 11, 37, 47–49, 52].

Rate constants, product yields, and product distribution of the reactions of $ONOO^-$ with different biomolecules including DNA, are found to be strongly affected by the presence of carbon dioxide or bicarbonate [54, 129–131]. The facts that concentration of CO_2 is very high in vivo [83] and the reaction of $ONOO^-$ with CO_2 is faster than any other reaction involving the former species, are of vital importance in this context [54, 83, 129–131]. It has been reported that $ONOO^-$ readily combines with CO_2 to form an intermediate species called nitrosoperoxycarbonate ($ONOOCO_2^-$) anion, which has a very high reactivity towards biological materials [48, 83, 130–134]. The reaction leading to the formation of $ONOOCO_2^-$ is found to be barrierless in gas phase, but it has a significant barrier energy (~12 kcal mol^{-1}) in aqueous media [133, 135]. The species $ONOOCO_2^-$ is a powerful oxidizing and nitrating agent [3, 11, 48, 54, 130–133]. $ONOOCO_2^-$ has been suggested to be a source of several reactive intermediates including the carbonate radical anion ($CO_3^{\cdot -}$) and nitrogen dioxide radical ($NO_2\cdot$), which may be formed via the homolysis of the peroxo O–O bond of $ONOOCO_2^-$ [14, 54, 83, 130–134]. The carbonate radical anion produced by the reaction between peroxynitrite and carbon dioxide has been detected in electron paramagnetic resonance (EPR) experiments [134]. The carbonate radical anion and nitrogen dioxide radicals are powerful ROS and RNOS, respectively [3, 11, 14, 54]. Nitryl chloride (NO_2Cl) is produced in biological media from reactions of HOCl and nitrite (NO_2^-) [71, 74, 78, 116]. NO_2Cl is the only member of the RNOS family that can serve as a potent nitrating, oxidizing as well as chlorinating agent [78, 116]. In certain studies of the reactions of DNA and proteins with a mixture of HOCl and NO_2^-, it has been observed that HOCl toxicity is increased, while in other studies, this finding is refuted [71, 72, 74, 116]. Thus, it is obvious that various ROS and RNOS present in living organisms have tremendous potential for modifying DNA as well as other biomolecules.

22.3 Reactions at the C8 Site of Guanine

Out of the four bases of DNA, guanine most readily reacts with ROS and RNOS which is usually attributed to the fact that it has the lowest ionization potential [136]. Reactions of ROS and RNOS with guanine produce 8-oxoguanine (8-oxoG), 8-nitroguanine (8-nitroG), 8-chloroguanine (8-chloroG), fapyguanine, spiroiminodihydantoin, guanidinohydantoin, 5-guanidino-4-nitroimidazole, xanthine, oxaluric acid, imidazolone, etc [1–7, 11, 12, 26, 27, 29, 30, 35–37, 47–54, 56, 58]. 8-OxoG is the most common modification of guanine in mammalian DNA, and is highly dangerous from the point of view of mutagenicity [2–5, 11, 12, 27, 30, 38, 40, 42, 43, 49, 57, 58, 67, 68, 103, 116]. The amount of 8-oxoG is found to be higher in mitochondrial DNA than in nuclear DNA [137]. It is estimated that 8-oxoG is formed in human cellular DNA as a byproduct of normal metabolic processes at the rate of about 178 residues/cell/day [138]. It has been reported that lungs of cigarette

smokers contain two to three times the amounts of 8-oxoG found in non-smokers [36]. It has been reported that elevated levels of 8-oxoG play a fundamental role in breast cancer [139]. The 6,8-diketo form of 8-oxoG is found to be most stable among its various possible tautomers at physiological pH [57, 140, 141]. The nucleoside of 8-oxoG can occur in both syn and anti conformations, similar to the standard nucleosides, produced by rotation about the glycosidic bond. Further, the syn conformer of 8-oxoG has been found to be more stable than the anti conformer [59, 142]. It has been reported that 8-oxoG and 8-nitroG are more reactive towards ROS and RNOS, e.g., the OH· radical, than guanine by several orders of magnitude, and their reactions lead to the formation of other highly mutagenic species [11, 29, 49, 86, 104, 143]. In view of a great importance of reactions of ROS and RNOS with DNA bases that can cause mutation and cancer, a major scientific effort has recently been directed towards understanding these reactions and the various related products. In such studies, the main aim is to elucidate the microscopic reaction mechanisms in terms of reaction barrier heights, and thus, to be able to explain the relative mutagenicities of the various ROS and RNOS.

22.3.1 Methods of Study

The experimental techniques employed in the measurement of DNA base damage induced by ROS, RNOS and other agents include: (a) high performance liquid chromatography-electrochemical detection (HPLC-ECD), (b) gas chromatography-mass spectrometry (GC-MS), (c) liquid chromatography-mass spectrometry (LC-MS), (d) HPLC or thin film layer chromatography (TLC)-^{32}P-postlabeling, (e) high performance liquid chromatography-electrospray-ionization tandem mass spectrometry (HPLC-MS/MS), (f) comet assay combined with use of repair enzymes (single cell electrophoretic method), and (g) alkaline elution techniques. Among these methods, the HPLC-MS/MS is considered to be the method of choice for measuring modified DNA bases [55]. Details about the working of these techniques can be obtained from the literature [3–5, 10, 55]

A chemical reaction is usually studied theoretically using quantum chemical ab-initio and density functional theoretic (DFT) methods, employing the concept of transition state theory (TST). TST is used for the determination of rate constants of reactions [144, 145]. According to TST, a simple one-step chemical reaction starts from a reactant complex (RC) and proceeds through a transitory structure called "activated complex" (commonly known as "transition state" (TS)) from where the product complex (PC) is formed. Thus, for a reaction to occur, the system would have to overcome the energy difference between the TS and the RC known as the "activation energy" or "barrier energy" (Fig. 22.1a). The barrier energy of a reaction can be obtained using the concept of potential energy surface (PES). On the PES, RC, and PC are minima that are characterized by all real vibrational frequencies, while TS is a maximum that is characterized by an imaginary vibrational frequency. Corresponding to each TS, there are two minima located

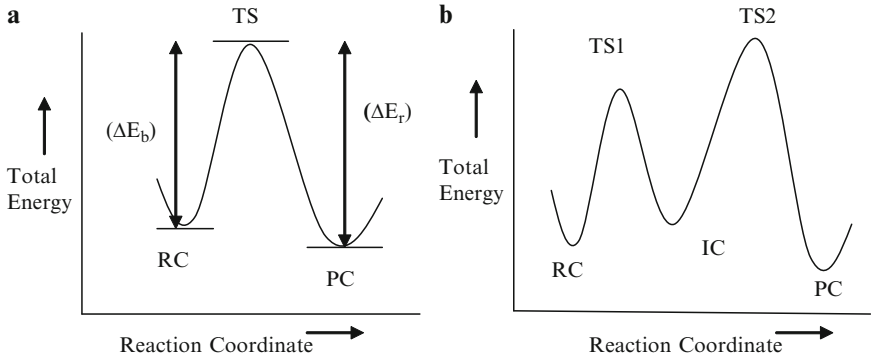

Fig. 22.1 Potential energy surfaces for a single-step reaction (a), and a two-step reaction (b)

on either side of it on the PES. In a complex, multi-step reaction, there may be several TS and minima other than the RC and PC, known as intermediate complexes (ICs) (Fig. 22.1b). An IC is a product in an elementary step and a reactant complex for a subsequent elementary step in a multi-step reaction. The structural changes that occur between the reactant complex and the final product complex, through the transition states and intermediate complexes, constitute a reaction mechanism. On the PES, the energy difference between the total energies (without any correction) of TS and RC is termed as the barrier energy (ΔE_b), and the difference in total energies of the TS and PC is termed as released energy (ΔE_r) (Fig. 22.1a). To be able to get energies that are appropriate for comparison with experiment, one applies zero-point energy (ZPE) correction and appropriate thermal energy correction to the calculated total energies. When ZPE-corrected total energies, and enthalpies or Gibbs free energies of RC and TS are used, the calculated barrier energies can be termed as ZPE-corrected barrier energies, and barrier enthalpies or Gibbs free barrier energies, respectively.

Once the barrier energy is obtained, the rate constant k of the reaction can be calculated using TST as follows [144, 146–148]:

$$k = \Gamma(T)\frac{k_B T}{h}\frac{Q_{\mathrm{TS}}}{Q_{\mathrm{RC}}}\mathrm{e}^{-\mathrm{E_b}/RT} \tag{22.1}$$

where $\Gamma(T)$ is the tunneling factor, k_B is the Boltzmann's constant, T is the absolute temperature, h is the Planck's constant, Q_{TS} is the partition function of the transition state, Q_{RC} is the partition function of the reactant complex, E_b is the barrier energy, and R is the ideal gas constant. The tunneling factor $\Gamma(T)$ can be obtained approximately using the Wigner transmission coefficient, $k^W(T)$ [147, 148]

$$\Gamma(T) \approx k^W(T) = 1 + \frac{1}{24}\left[\frac{h\omega^{\mathrm{TS}}}{2\pi k_B T}\right]^2 \tag{22.2}$$

where ω^{TS} is the imaginary frequency of the TS.

The calculation of barrier energies of a reaction is an important step for predicting its feasibility. By searching all the extrema on the PES of a reaction, one would get information about the structures of RC, ICs, PC, and TSs, including the reaction coordinate. In this way, one can easily get information about the favored mechanism of a reaction. Most quantum chemical calculations performed to study reactions involving biomolecules, are based on DFT. The B3LYP functional of DFT [149, 150] has been frequently used. The second order Møller-Plesset perturbation (MP2) theory [151, 152] is usually employed to obtain improved energies by single point energy calculations.

We employed the B3LYP functional of DFT in gas phase to obtain the structures of the RC, ICs, and PC, as well as TSs involved in the reactions of guanine with the OH· radical, H_2O_2, H_2O_3, $ONOO^-$, and $ONOOCO_2^-$, leading to the formation of 8-oxoG and/or 8-nitroG. The same approach was adopted to study reactions of imidazole (a model for the five-membered ring of guanine) with HOCl and NO_2Cl, leading to the formation of 2-oxoIm, 2-chloroIm, and 2-nitroIm corresponding to 8-oxoG, 8-chloroG, and 8-nitroG, respectively. The 6-31+G*, 6-31G** and AUG-cc-pVDZ basis sets were used. In these studies, either the 6-31+G* or 6-31G** basis set was used for initial calculations, while the AUG-cc-pVDZ basis set was used for final calculations. Some TSs involved in these reactions could be optimized only at the B3LYP/6-31+G*, B3LYP/6-31G** or B3LYP/6-311++G** level of theory. Therefore, for such TSs, single-point (SP) energy calculations were performed at the B3LYP/AUG-cc-pVDZ level of theory in gas phase using the B3LYP/6-31+G* or B3LYP/6-31G** optimized geometries. SP calculations in almost all the cases were also performed at the MP2/AUG-cc-pVDZ level of theory in gas phase using the B3LYP optimized geometries. In order to take into account the solvent effect of aqueous media on energetics of reactions, all the optimized species were solvated in aqueous media at the B3LYP/AUG-cc-pVDZ level of theory employing the polarizable continuum model (PCM) of the self-consistent reaction field (SCRF) theory [153].

Vibrational frequency analysis in gas phase was performed for all the B3LYP optimized geometries in order to ensure that each total energy minimum had all real frequencies and each transition state had only one imaginary frequency, and in order to obtain zero point energy (ZPE) and the thermal energy corrections to total energies. The genuineness of each calculated transition state was verified by visually examining the vibrational mode corresponding to the imaginary frequency, and applying the condition that it connected the reactant and product complexes properly. Where necessary, intrinsic reaction coordinate (IRC) [154] calculations in gas phase were also performed in order to further confirm the genuineness of calculated transition states. ZPE -corrections to total energies obtained at the B3LYP/AUG-cc-pVDZ level of theory in gas phase were also applied to the total energies obtained by single-point energy calculations at the same level of theory in aqueous media, and at the MP2/AUG-cc-pVDZ level of theory in gas phase and aqueous media.

22.3.2 Reaction of Guanine with OH· Radicals: Formation of 8-oxoG

Addition reactions of an OH· radical at the C2, C4, C5, and C8 sites of guanine lead to the formation of different guanine-OH· adducts (Gn-OH·, n = 2, 4, 5, and 8) [51]. When an OH· radical is added to the C2, C4 or C5 site of guanine, two types of structures are formed. First, where both the five- and six-membered rings remain closed, and second, where one of the rings gets opened. Addition of the OH· radical at the C8 position of guanine does not cause opening of its five-membered ring. The closed ring structures of the G4-OH· and G5-OH· adducts are more stable than their corresponding open ring structures, while the reverse is true for the G2-OH· adduct. If we consider only the more stable adduct in each case, the calculated ZPE-corrected binding energies of the adducts G2-OH·, G4-OH·, G5-OH·, and G8-OH· were found to be –36.3, –16.1, −12.1, and −30.4 kcal mol^{-1} respectively, at the B3LYP/AUG-cc-pVDZ level of theory in gas phase. Thus, the stability of adducts follows the order G2-OH· >G8-OH· >G4-OH· >G5-OH· [51]. The magnitudes of binding energies of the various adducts calculated at the MP2/AUG-cc-pVDZ(SP) level were are found to be smaller by 3-6 kcal mol^{-1} than those obtained at the B3LYP/AUG-cc-pVDZ level, but these also follow the same order as that followed by the binding energies obtained at the B3LYP/AUG-cc-pVDZ level [51].

The calculated barrier energies for addition of an OH· radical at the C2, C4, and C5 sites of guanine in gas phase are found to be 5.9, 5.3, and 1.5 kcal mol^{-1} respectively, at the B3LYP/AUG-cc-pVDZ level of theory [104]. The barrier energy for addition of an OH· radical at the C8 site of guanine was found to be too small to be computed. If we consider both the barrier and binding energies, we find that the formation of the adduct G8-OH· would be highly favored in comparison to those of the other Gn-OH· (n=2,4,5) adducts. The barrier energy for addition of an OH· radical at the C2 site of 5-methylimidazole, that corresponds to the C8 site of guanine was found to be 3 kcal mol^{-1} at the B3LYP/6-31G** level of theory in gas phase [51]. Llano et al. [106] have studied the reaction of an OH· radical with imidazole and found that the barrier energy for addition of an OH· radical at the C2 site of imidazole was 2.6 kcal mol^{-1} at the B3LYP/6-31G** level of theory in gas phase. Reactions of OH· radicals with other biomolecules, such as cytosine and 5-methylcytosine, have also been studied using quantum chemical methods [105, 107–112].

8-OxoG complexed with a water molecule can be formed from the reaction of an OH· radical with the adduct G8-OH· in two different ways (mechanisms 1 and 2) as depicted in Fig. 22.2 [51]. ZPE-corrected barrier energies involved at the different steps of mechanisms 1 and 2 of the reaction of an OH· radical with the adduct G8-OH·, and those involved in the different mechanisms of reactions of guanine with H_2O_2 [51], H_2O_3 [53], and (H_2O_3+H_2O) [53] obtained at the B3LYP/AUG-cc-pVDZ level of theory in gas phase and aqueous media are presented in Table 22.1.

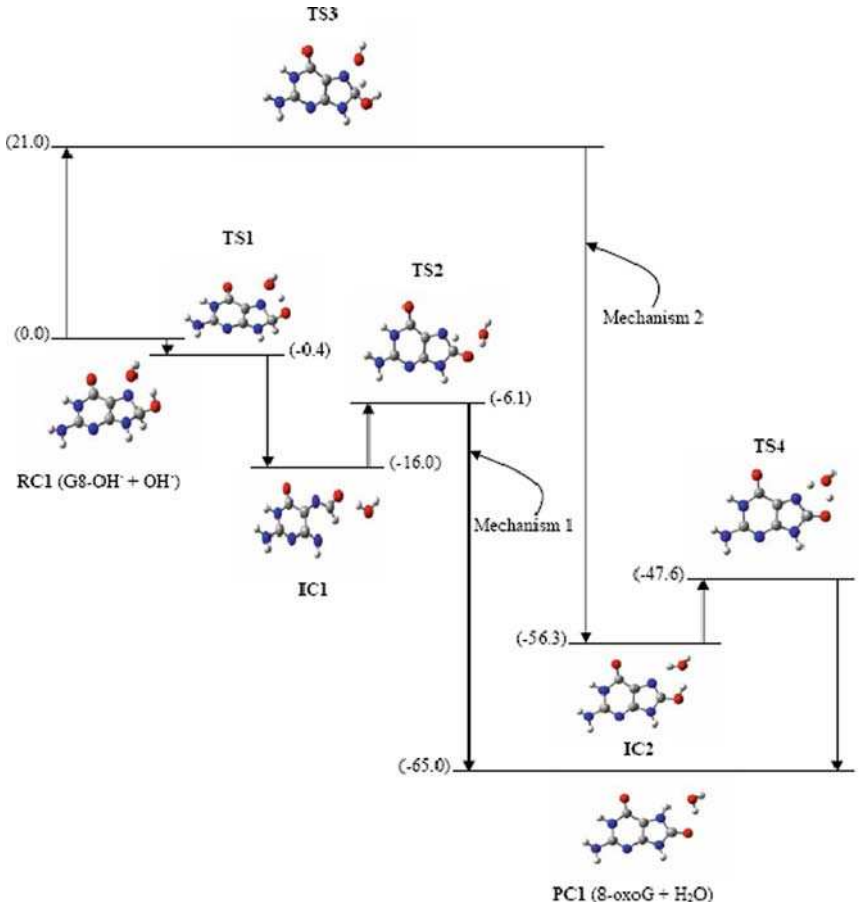

Fig. 22.2 Formation of product complex PC1 (8-oxoG + H_2O) starting from the reactant complex RC1 (G8-OH· + OH·) by two different mechanisms (1 and 2). ZPE-corrected relative total energies of the various species formed in the reaction, obtained at the B3LYP/AUG-cc-pVDZ level of theory in aqueous media, are given in parentheses. The adduct G8-OH· is formed barrierlessly by the addition of OH· at the C8 site of guanine

There are some common steps in the different reaction mechanisms. All the barrier energies, including those of the common steps, starting from the reactant complex to the product complex, are given in Tables 22.1–22.3. It is to be noted that only some of the important reaction mechanisms are shown in figures. Other reaction mechanisms (without numbering) are shown in figures elsewhere [51–54, 76, 78].

Mechanism 1 involves the reactant complex RC1 (a complex of OH· and G8-OH·), intermediate complex IC1, transition states TS1 and TS2 and product complex PC1, which is a complex of 8-oxoG and H_2O. Mechanism 2 shows how PC1 can be formed starting from RC1 through two other transition states TS3 and TS4

Table 22.1 ZPE-corrected barrier energies involved at various steps of different mechanisms of reactions of guanine with OH· radical, H_2O_2, H_2O_3, and ($H_2O_3 + H_2O$) leading to the formation of 8-oxoG obtained at the B3LYP/AUG-cc-pVDZ level of theory in gas phase and aqueous media

Reactive species and mechanism numbers[a]	Step number				
	I	II	III	IV	V
OH· radical					
1	6.3 (−0.4)	20.4 (9.9)			
2	27.5 (20.1)	7.0 (8.7)			
H_2O_2					
3	39.7 (39.9)	43.0 (42.6)			
4	64.3 (64.2)[b]	20.4 (9.9)			
H_2O_3					
5	33.8 (29.3)	4.0 (5.9)			
6	33.8 (29.3)	0.5 (−2.4)	7.8 (9.7)		
$H_2O_3 + H_2O$					
7	18.7 (19.0)	5.2 (−5.8)	−0.3 (5.9)	27.7 (15.3)	
8	18.7 (19.0)	5.2 (−5.8)	−0.3 (5.9)	14.3 (14.1)	19.7 (20.6)

[a]Energies obtained in aqueous media are given in parentheses. Mechanism numbers 1-6 are given in Figs. 2-4. Mechanisms 7 and 8 (not numbered) can be found in the literature [53]. [b]Calculated at the B3LYP/AUG-cc-pVDZ//B3LYP/6-311++G** level of theory in both gas phase and aqueous media.

and an intermediate complex IC2 (Fig. 22.2). Thus, mechanisms 1 and 2 involve two steps each. At the first step of mechanism 1, i.e., in going from RC1 to IC1 through TS1, the H-atom of the OH· group that is already attached to the C8 site of guanine in the G8-OH· adduct, moves and gets abstracted by the reacting OH· group, thus forming IC1, which is a complex of fapyguanine and a water molecule (Fig. 22.2). At the second step of mechanism 1, the complex IC1 undergoes a rearrangement and is converted into PC1. In going from RC1 to IC2 through TS3 (mechanism 2), the H-atom bonded to the C8 site of guanine in G8-OH· adduct moves and gets abstracted by the reacting OH· group forming 8-hydroxyguanine complexed with a water molecule (IC2), which, in the second step, tautomerizes to the final product complex PC1 (Fig. 22.2).

ZPE-corrected barrier energies at the first steps of the mechanisms 1 and 2 were found to be 6.3 and 27.5 kcal mol^{-1} at the B3LYP/AUG-cc-pVDZ level of theory in gas phase, respectively. In going from gas phase to aqueous media, the corresponding barrier energies are decreased substantially, the values being −0.4 and 20.1 kcal mol^{-1} respectively (Table 22.1). It shows that the first step of mechanism 1 would be barrierless in aqueous media. ZPE-corrected barrier energies at the second steps of the mechanisms 1 and 2 were found to be 20.4 and 7.0 kcal mol^{-1} , respectively, at the B3LYP/AUG-cc-pVDZ level of theory in gas phase, respectively. In going from gas phase to aqueous media, the barrier energy involved at the second step of mechanism 1 is drastically lowered down to almost half of its gas phase value (9.9 kcal mol^{-1}), while that of mechanism 2 is somewhat increased (8.7 kcal mol^{-1}) (Table 22.1). As the first step of

Table 22.2 ZPE-corrected barrier energies involved at various steps of different mechanisms of reactions of guanine with $ONOO^-$ and $ONOOCO_2^-$ leading to the formation of 8-oxoG and 8-nitroG obtained at the B3LYP/AUG-cc-pVDZ level of theory in gas phase and aqueous media

Reactive species, mechanism numbers and product[a]	Step number				
	I	II	III	IV	V
$ONOO^-$					
9 (8-oxoG)	51.5 (48.7)	49.0 (56.5)	27.4 (26.0)		
10 (8-oxoG)	53.9 (42.3)	35.2 (37.2)	42.1 (46.4)	49.0 (56.5)	27.4 (26.0)
11 (8-oxoG)	45.5 (37.0)	15.9 (6.0)			
12 (8-nitroG)	51.5 (48.7)	3.3 (10.0)			
13 (8-nitroG)	53.9 (42.3)	35.2 (37.2)	42.1 (46.4)	3.3 (10.0)	
14 (8-nitroG$^-$)	49.8 (43.4)	0.3 (−3.9)			
$ONOOCO_2^-$					
15 (8-nitroG$^-$)	29.9 (23.6)	−0.2 (−7.4)			
16 (8-oxoG$^-$)[b]	35.5 (18.9)	4.6 (10.2)			
17 (8-oxoG)	35.5 (18.9)	8.8 (17.4)	8.8 (18.5)		
18 (8-oxoG)	35.5 (18.9)	8.8 (17.4)	−0.5 (3.4)	−0.8 (−0.6)	
19 (8-oxoG)	52.3 (42.5)	8.8 (18.5)			

[a]Energies obtained in aqueous media are given in parentheses. Mechanism numbers 11, 14, 15, 16, and 18 are given in Figs. 5 and 6. Other mechanisms (not numbered) can be found in the literature [52, 54]. [b]8-OxoG anion where the H7 atom is absent from its site [8-oxoG$^-$ (-H7)].

mechanism 1 is barrierless and the barrier energies encountered at the second steps of mechanisms 1 and 2 are nearly equal in aqueous media, formation of 8-oxoG due to the reactions of guanine with OH· radical would preferentially occur following mechanism 1 [51].

22.3.3 Reaction of Guanine with H_2O_2: Formation of 8-oxoG

8-OxoG complexed with a water molecule, i.e., the product complex PC1, obtained in the reaction of an OH· radical with the G8-OH· adduct, can also be formed due to the reaction of guanine with H_2O_2 along with two alternative mechanisms, i.e., mechanisms 3 and 4 involving two steps each as shown in Fig. 22.3 [51]. Mechanism 3 involves the reactant complex RC2, which is a complex of guanine and H_2O_2, intermediate complex IC3, transition states TS5 and TS6, and the product complex PC1 (Fig. 22.3). Mechanism 4 shows how PC1 can be formed starting from RC2 through two other transition states, TS7 and TS2, and the intermediate complex IC1 (Fig. 22.3). In going from RC2 to IC3 through TS5 (mechanism 3), the following structural changes take place. At TS5, the H_2O_2 molecule is dissociated into an OOH group and an H atom, following which the H atom is attached to the N7 site of guanine, while the OOH group moves close to the C8 site and gets attached to it forming IC3 (Fig. 22.3). At the second step of mechanism 3, i.e., in going from IC3 to PC1 through TS6, the OO bond of the OOH group is ruptured and

Table 22.3 ZPE-corrected barrier energies involved at various steps of different mechanisms of reactions of imidazole with HOCl and NO_2Cl leading to the formation of 2-oxoIm, 2-chloroIm, and 2-nitroIm obtained at the B3LYP/AUG-cc-pVDZ level of theory in gas phase and aqueous media

Reactive species, mechanism numbers and product[a]		Step number			
		I	II	III	IV
HOCl					
20	(2-oxoIm)	59.5 (58.0)	28.6 (25.1)	36.6 (37.5)	
21	(2-oxoIm)	59.5 (58.0)	1.0 (1.0)	43.5 (40.1)	27.5 (18.1)
22	(2-chloroIm)	66.1 (64.0)	32.9 (32.1)		
23	(2-chloroIm)	29.4 (14.9)	36.9 (33.3)	32.9 (32.1)	
24	(2-chloroIm)	50.0 (53.1)	32.0 (28.5)		
NO_2Cl					
25	(2-oxoIm)	30.8 (20.5)	28.3 (29.7)		
26	(2-chloroIm)	33.4 (20.2)	19.5 (22.5)		
27	(2-chloroIm)	33.4 (20.2)	33.2 (30.4)		
28	(2-chloroIm)	33.4 (20.2)	30.7 (25.0)		
29	(2-nitroIm)	21.5 (14.3)	32.8 (27.8)		
30	(2-nitroIm)	21.5 (14.3)	34.4 (26.7)		

[a]Energies obtained in aqueous media are given in parentheses. Mechanism numbers 20–30 (not numbered) can be found from literature [76, 78].

the H atom attached to the C8 site moves toward the newly formed OH· group (Fig. 22.3). At the first step of mechanism 4, H_2O_2 is dissociated into two OH· groups at TS7, following which IC1 is formed. IC1 is also formed in the reaction of guanine with two OH· radicals, one after the other (Fig. 22.3). Thus, after IC1, mechanism 4 of the reaction of H_2O_2 with guanine is identical to mechanism 1 of the reaction of guanine with two successive OH· radicals.

The calculated barrier energies at the first and second steps of mechanism 3 were found to be 39.7 and 43.0 kcal mol^{-1} respectively, at the B3LYP/AUG-cc-pVDZ level of theory in gas phase (Table 22.1). In going from gas phase to aqueous media, these barrier energies are not changed significantly (Table 22.1). The barrier energy at the first step of mechanism 4 was found to be 64.3 kcal mol^{-1} at the B3LYP/AUG-cc-pVDZ//B3LYP/6-311++G** level of theory in gas phase. This barrier energy is not changed significantly in going from gas phase to aqueous media at the same level of theory (Table 22.1). Mechanism 3 may be a favored over mechanism 4 for the formation of 8-oxoG due to the reaction of H_2O_2 with guanine, as the barrier energy at the first step of mechanism 3 is lower than that of mechanism 4 [51].

22.3.4 Reaction of Guanine with H_2O_3: Formation of 8-oxoG

Starting from the reactant complex RC3 of guanine and H_2O_3, 8-oxoG complexed with H_2O_2 (PC2) can be formed in two different ways (mechanisms 5 and 6) as

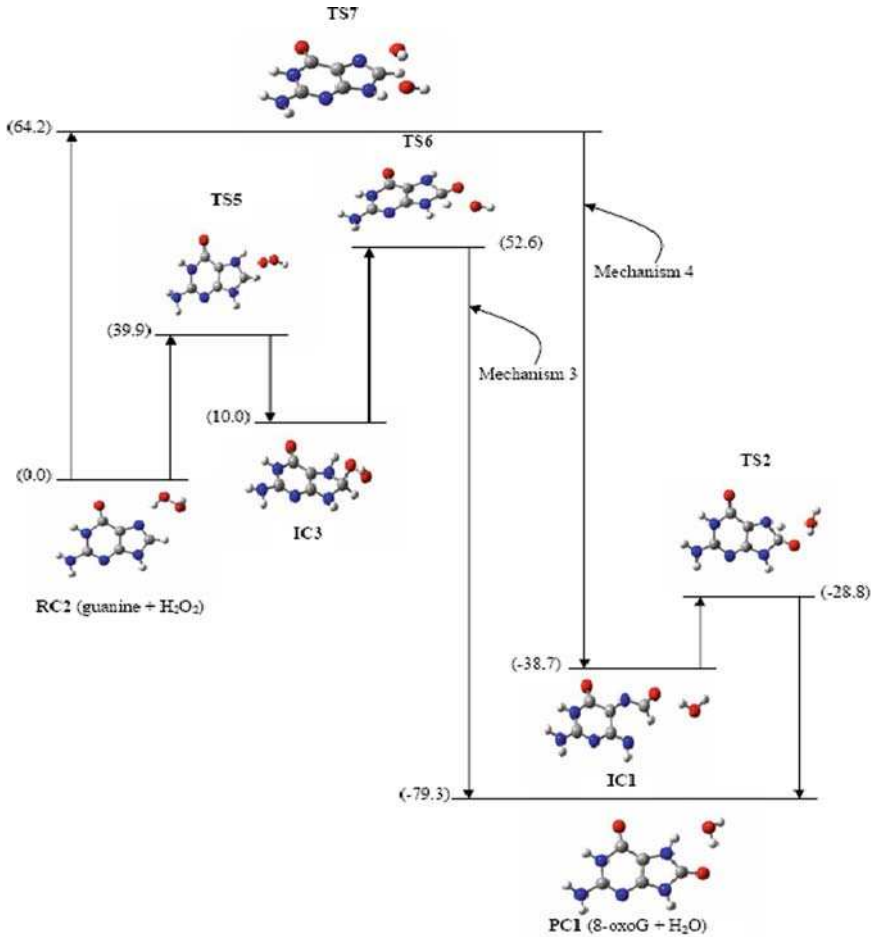

Fig. 22.3 Formation of product complex PC1 (8-oxoG + H_2O) starting from the reactant complex RC2 (guanine + H_2O_2) by two different mechanisms (3 and 4). ZPE-corrected relative total energies of the various species formed in the reaction, obtained at the B3LYP/AUG-cc-pVDZ level of theory in aqueous media, are given in parentheses

shown in Fig. 22.4 [53]. Mechanism 5 involves the reactant complex RC3, intermediate complex IC4, transition states TS8 and TS9, and the product complex PC2 (Fig. 22.4). Mechanism 6 shows how PC2 can be formed deviating from IC4 through two other transition states TS10 and TS11, and an intermediate complex IC5 (Fig. 22.4). Thus, the first step is common to both the mechanisms 5 and 6. At the first step of the reaction, i.e., in going from RC3 to IC4 through TS8, H_2O_3 is fragmented into an H atom, $^1O_2$, and an OH· group, following which the H atom is attached to the N7 site of guanine, and the OH· group moves close to the C8 site, eventually getting attached to it (Fig. 22.4). The mechanisms 5 and 6 are different

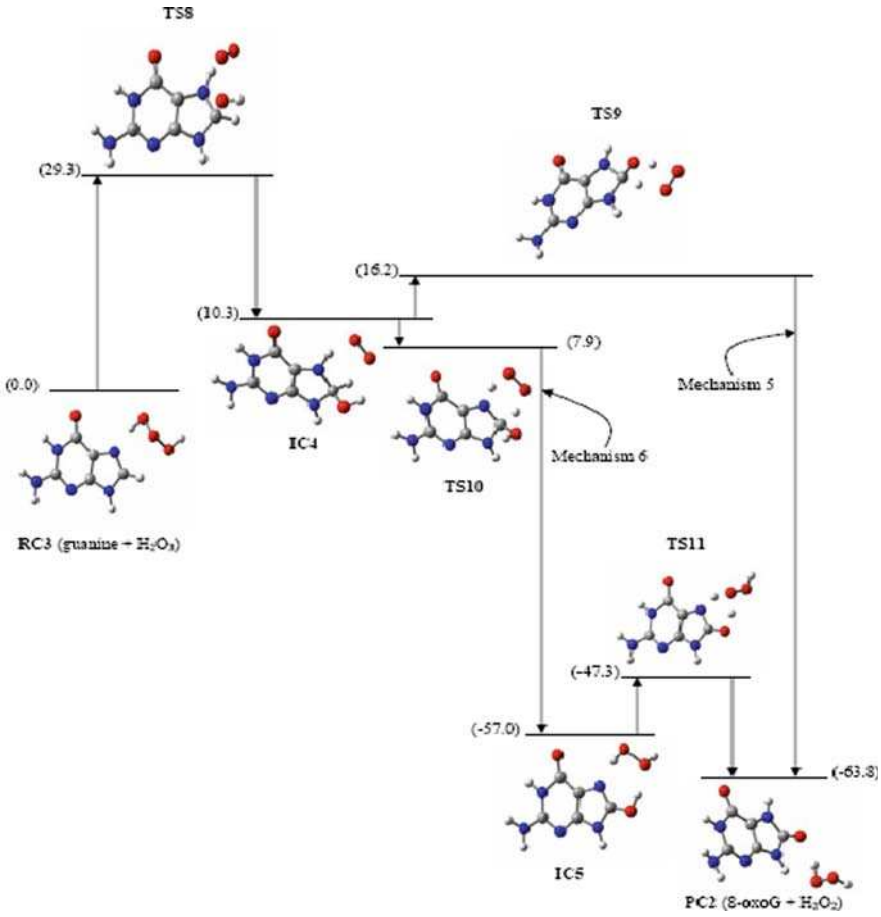

Fig. 22.4 Formation of product complex PC2 (8-oxoG + H_2O_2) starting from the reactant complex RC3 (guanine + H_2O_3) by two different mechanisms (5 and 6). ZPE-corrected relative total energies of the various species formed in the reaction, obtained at the B3LYP/AUG-cc-pVDZ level of theory in aqueous media, are given in parentheses

only in terms of the ways how two of the three hydrogen atoms of IC1 move to get bonded to the O_2 moiety to produce PC2. Mechanism 5 involves two steps, while mechanism 6 involves 3 steps (Fig. 22.4).

The ZPE-corrected barrier energy at the first step of the reaction of guanine with H_2O_3 was found to be 33.8 kcal mol^{-1} at the B3LYP/AUG-cc-pVDZ level of theory in gas phase. This barrier energy is reduced by 4.5 kcal mol^{-1} in going from gas phase to aqueous media at the same level of theory (Table 22.1) [53]. The barrier energies for the dissociation of H_2O_3 into $^1O_2$ and H_2O have been found to be 48.6 and 44.9 kcal mol^{-1} at the MP4//MP2/6-31++G* and at the B3LYP/cc-pVTZ//B3LYP/6-31G** levels of theory in gas phase, respectively [124, 155]. These barrier energies were reported to be reduced drastically when a specific

water molecule mediated the dissociation of H_2O_3 to 26.0 and 20.0 kcal mol^{-1} at the two levels of theory in gas phase, respectively [124, 155]. We found that 8-oxoG can be formed due to the reaction of guanine with (H_2O_3+H_2O) following two different mechanisms, labeled as mechanisms 7 and 8 involving 4 and 5 steps, respectively (Table 22.1) [53]. The first three steps are common to the mechanisms 7 and 8. The ZPE-corrected barrier energy at the first step of this reaction that corresponds to the dissociation H_2O_3 into $^1O_2$ and H_2O while interacting with guanine, was found to be 18.7 kcal mol^{-1} at the B3LYP/AUG-cc-pVDZ level of theory in gas phase. This barrier energy is not changed significantly in going from gas phase to aqueous media (Table 22.1) [53]. After this step, oxidation of guanine occurred mainly due to the singlet oxygen ($^1O_2$) formed by the dissociation of H_2O_3 [53]. Thus, involvement of a water molecule in the reaction of guanine with H_2O_3 leading to the formation of 8-oxoG, drastically reduces the first barrier energy [53].

The barrier energies involved in the dissociation of H_2O_2 while reacting with guanine into the H and OOH fragments (first step of mechanism 3) and into two OH· groups (first step of mechanism 4) were found to be 39.7 kcal mol^{-1} at the B3LYP/AUG-cc-pVDZ level and 64.3 kcal mol^{-1} at the B3LYP/AUG-cc-pVDZ//B3LYP/6-311++G** level in gas phase, respectively (Table 22.1) [51]. The experimentally measured barrier energy for the dissociation of H_2O_2 into two OH· groups has been found to be 51 kcal mol^{-1} [156], while the barrier energies for the dissociation of H_2O_2 into H and OOH groups, reported by two different experimental studies, have been found to be 87 and 90 kcal mol^{-1} respectively [156, 157]. Thus, the first barrier energy is decreased substantially in going from H_2O_2 to H_2O_3. It shows that H_2O_3 would be much more reactive than H_2O_2 in causing oxidation of guanine or other molecules. Therefore, broadly speaking, H_2O_3 can be considered as an effective reactive oxygen species (ROS) that causes mutagenic and carcinogenic lesions in DNA [53].

ZPE-corrected barrier energies at the second and third steps of mechanism 5, and at the second step of mechanism 6 were found to be 0.5 and 7.8, and 4.0 kcal mol^{-1} respectively, at the B3LYP/AUG-cc-pVDZ level of theory in gas phase (Table 22.1). In going from gas phase to aqueous media, the barrier energy at the second step of mechanism 5 is reduced and becomes negative (−2.4 kcal mol^{-1}) (barrier less step), while the barrier energies at the third step of mechanism 5 and at the second step of mechanism 6 are somewhat increased (Table 22.1). Thus, the barrier energies involved at the different steps of mechanisms 5 and 6 are low, which shows that formation of 8-oxoG due to the reaction of guanine with H_2O_3 would occur through both the mechanism efficiently.

22.3.5 Reaction of Guanine with $ONOO^-$: Formation of 8-oxoG and 8-nitroG

Reaction of guanine with $ONOO^-$ can lead to the formation of 8-oxoG, 8-nitroG, and 8-nitroG^- [52]. ZPE-corrected barrier energies involved in the different possible

reaction mechanisms leading to the formation of these products, and those involved in the reaction of guanine with $ONOOCO_2^-$ ($ONOO^- + CO_2$) leading to the formation of 8-oxoG and 8-nitroG[-] [54] at the B3LYP/AUG-cc-pVDZ level of theory in gas phase and aqueous media, are presented in Table 22.2.

The barrier energies given in Table 22.2 show that oxidation and nitration of guanine due to its reaction with $ONOO^-$ through the mechanisms 11 and 14, respectively, can occur more efficiently than through the other mechanisms. Further, the barrier energies involved at the different steps excluding those at a few steps of mechanisms 9–14 are quite high which suggests that as such, yields of the oxo- and nitro- products of guanine due to its reaction with $ONOO^-$ would be quite low [52]. A similar result was reported by Gogonea [158] who found the ZPE-corrected barrier energy at the first step of nitration of imidazole by peroxynitrite (ONOOH) at the B3LYP/6-31++G** level of theory to be too high, i.e., 84.1 and 94.6 kcal mol^{-1} in gas phase and aqueous media, respectively. Therefore, the involvement of some catalyst would be required for the production of these mutagenic products in significant amounts. Mechanisms 11 and 14 that correspond to the formation of the product complex PC3 which is a complex of 8-oxoG and NO_2^-, and the product complex PC4 which is a complex of 8-nitroG[-] and H_2O, respectively, starting from the reactant complex RC4 of guanine and $ONOO^-$ are shown in Fig. 22.5. At the first step of mechanism 11, $ONOO^-$ is dissociated into an O atom and the NO_2^- moiety, following which the intermediate complex IC6 is formed. IC6 is a complex of 8-hydroxyguanine and NO_2^-.

At the second step of mechanism 11, 8-hydroxyguanine tautomerizes through the involvement of NO_2^- to 8-oxoG, thus forming PC3. It is to be noted here that 8-hydroxyguanine was also obtained in the reaction of guanine with two successive OH· radicals as a precursor to 8-oxoG. In going from RC4 to IC7 through TS14 (mechanism 14), $ONOO^-$ is dissociated into NO· and $O_2{\cdot}^-$, following which the H8 atom of guanine is abstracted by $O_2{\cdot}^-$ forming the OOH group, and the NO· group is attached to the C8 site of guanine. At the second step of mechanism 14, the OOH group is dissociated into an O atom and an OH· group, following which the O atom moves near the N atom of the NO· group that is already bonded to the C8 site of guanine and gets attached to it, thus forming the product complex PC4 (Fig. 22.5).

ZPE-corrected barrier energies at the first and second steps of mechanism 11 were found to be 45.5 and 15.9 kcal mol^{-1} respectively, at the B3LYP/AUG-cc-pVDZ level of theory in gas phase. In going from gas phase to aqueous media, these barrier energies are reduced significantly, i.e., by 8.5 and 9.9 kcal mol^{-1} respectively (Table 22.2). Barrier energies at the first and second steps of mechanism 14 were found to be 49.8 and 0.3 kcal mol^{-1} respectively, at the B3LYP/AUG-cc-pVDZ level of theory in gas phase. These barrier energies are reduced appreciably to 43.4 and −3.9 kcal mol^{-1} respectively, in going from gas phase to aqueous media (Table 22.2). It shows that the second step of mechanism 14 would be barrierless in aqueous media. Relative total energies of the product complexes show that PC3 is more stable by 18.7 kcal mol^{-1} than PC4 (Fig. 22.5). Therefore,

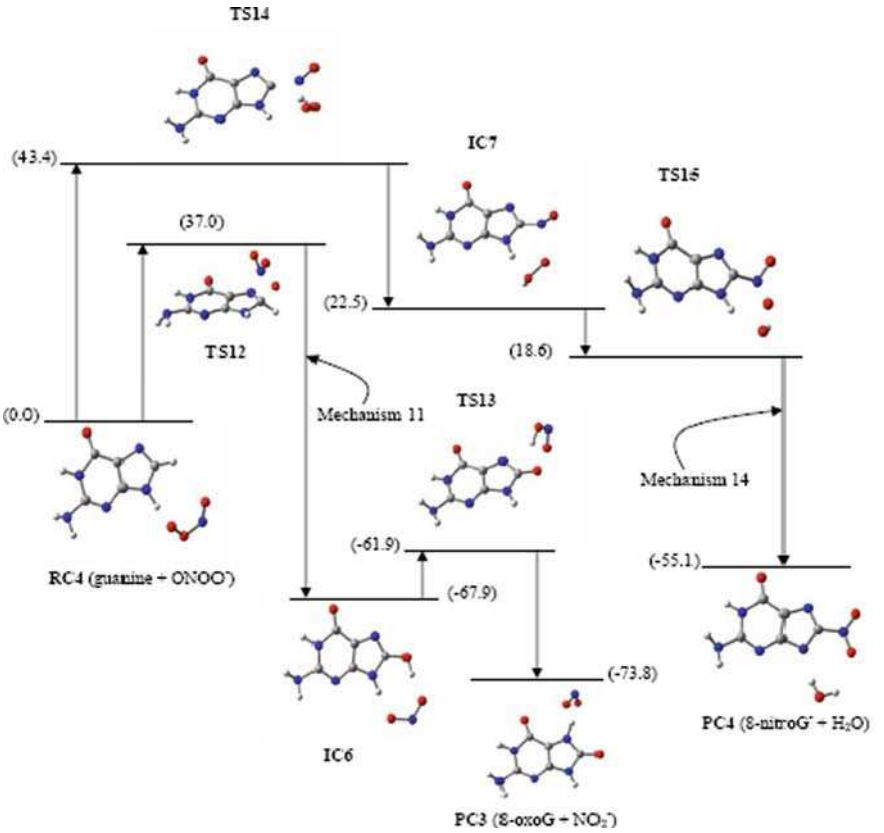

Fig. 22.5 Formation of product complexes PC3 (8-oxoG + NO_2^-) and PC4 (8-nitroG$^-$ + H_2O) starting from the reactant complex RC5 (guanine + $ONOO^-$) by two different mechanisms (11 and 14). ZPE-corrected relative total energies of the various species formed in the reactions, obtained at the B3LYP/AUG-cc-pVDZ level of theory in aqueous media, are given in parentheses. Mechanisms 9, 10, 12, and 13 are not shown

the yield of 8-oxoG would be expected to be more than that of 8-nitroG$^-$ produced due to the reaction between guanine and $ONOO^-$ [52].

22.3.6 *Reaction of Guanine with $ONOOCO_2^-$: Formation of 8-oxoG and 8-nitroG*

We studied the reaction of guanine with $ONOO^-$ producing 8-oxoG and 8-nitroG$^-$, including CO_2 as a catalyst [54]. The catalytic role of CO_2 was studied by considering the reaction of guanine with nitrosoperoxycarbonate anion ($ONOOCO_2^-$), which is a complex of $ONOO^-$ and CO_2 [54]. This reaction leads

to the formation of 8-oxoG or its anion by four different mechanisms, and 8-nitroG$^-$ by a single mechanism (Table 22.2) [54]. The barrier energy at the first step of mechanism 19 corresponding to the formation of 8-oxoG, is highest among all the barrier energies involved in different mechanisms, which suggests that this mechanism would not be a favored one (Table 22.2). The first step is common to the mechanisms 16–18, while the second step is common to the mechanisms 17 and 18 (Table 22.2). Mechanism 18 would be favored over mechanism 17 as the barrier energies after the second step in the former are smaller than those in the latter (Table 22.2). Mechanisms 15, 16, and 18 that lead to the formation of 8-nitroG$^-$, 8-oxoG$^-$ (-H7), and 8-oxoG, respectively, starting from the reactant complex RC5 of guanine and $ONOOCO_2^-$, are shown in Fig. 22.6. Mechanism 15 involves RC5, transition states TS16 and TS17, intermediate complex IC8, and the product complex PC5 of 8-nitroG$^-$ and H_2CO_3 (Fig. 22.6). Mechanism 16 shows formation of the product complex PC6, which is a complex of 8-oxoG anion where the H7 atom is absent from its site [8-oxoG$^-$ (-H7)], HNO_2, and CO_2, through the transition states TS18 and TS19, and an intermediate complex IC9 (Fig. 22.6). Mechanism 18 shows how the product complex PC7 of 8-oxoG, NO_2^-, and CO_2 can be formed deviating from the intermediate complex IC9 through three other transition states, TS20, TS21, and TS22, and three intermediate complexes, IC10, IC11, and IC12 (Fig. 22.6).

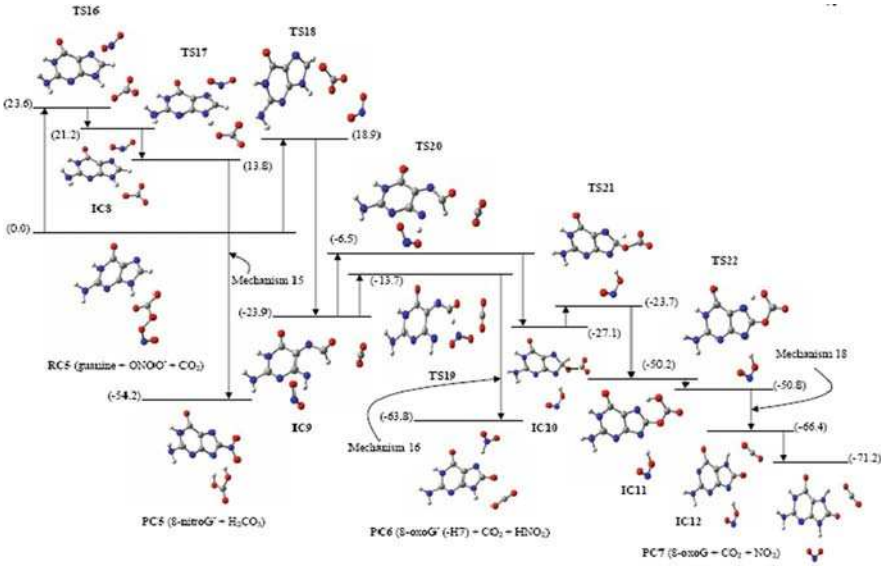

Fig. 22.6 Formation of product complexes PC5 (8-nitroG$^-$ + H_2CO_3), PC6 (8-oxoG$^-$ (-H7) + CO_2 + HNO_2) and PC7 (8-oxoG + CO_2 + NO_2) starting from the reactant complex RC5 (guanine + $ONOOCO_2^-$) by three different mechanisms (15, 16, and 18). ZPE-corrected relative total energies of the various species formed in the reaction, obtained at the B3LYP/AUG-cc-pVDZ level of theory in aqueous media, are presented in parentheses. Mechanisms 17 and 19 are not shown

At the first step of mechanism 15, i.e., in going from RC5 to IC8 through TS16, the OO bond of $ONOOCO_2^-$ is broken, following which the $NO_2^{\cdot}$ group moves above the plane of guanine near the C8 site, while the $CO_3^{\cdot -}$ group remains in the plane of guanine making a hydrogen bond with its H9 atom (Fig. 22.6). Thus, $ONOOCO_2^-$ is dissociated into the $NO_2\cdot$ and $CO_3^{\cdot -}$ groups, while reacting with guanine [54]. This finding supports the previous theoretical and experimental proposals, according to which homolysis of the OO bond of $ONOOCO_2^{\cdot -}$ leads to the formation of $CO_3^{\cdot -}$ and $NO_2^{\cdot}$ [14, 83, 130–134]. At the second step of mechanism 15, the $NO_2^{\cdot}$ group, located above the C8 site of guanine in IC8, gets attached to it and the H8 and H9 atoms move and get attached to the $CO_3^{\cdot -}$ group, thus forming PC5. In going from RC5 to IC9 through TS18 (first common step of mechanisms 16-18), the following structural changes take place. At TS18, the OO bond of $ONOOCO_2^-$ is ruptured, and thus, the $CO_3^{\cdot -}$ and $NO_2^{\cdot -}$ groups are ready to be formed, following which an O atom of the $CO_3^{\cdot -}$ group moves and gets attached to the C8 site of guanine forming the intermediate complex IC9 which is a complex of fapyguanine (FapyG), CO_2 and the NO_2^- (nitrite) group (Fig. 22.6). FapyG was also obtained in the reaction of guanine with two successive OH· groups (Fig. 22.2). It reveals again the fact that $ONOOCO_2^-$ is dissociated into the $CO_3^{\cdot -}$ and NO_2^- groups while reacting with guanine [14, 83, 130–134]. Thus we find that the first main step is the breaking of OO bond of $ONOOCO_2^-$ to form the $CO_3^{\cdot -}$ and $NO_2\cdot$ groups in both the oxidation and nitration reactions of guanine [54]. At the second step of mechanism 16, the H8 atom of FapyG in IC9 is abstracted by the N atom of the NO_2^- group forming the product complex PC6. At the second step of mechanism 18, the H9 atom of FapyG in IC9 moves and gets attached to one of the oxygen atoms of the NO_2^- group while CO_2 moves close to the O atom attached to the C8 site of FapyG, thus forming IC10. At the next step, IC10 tautomerizes to IC11 (Fig. 22.6). In going from IC11 to IC12 through TS22, the H atom of the HCO_3 group attached to the C8 site of guanine moves and gets attached to the N7 site of guanine. In this process, CO_2 is formed due to rupture of a CO bond (Fig. 22.6). IC12 is a complex of 8-oxoG$^-$ where the H9 atom is absent from its site [8-oxoG$^-$ (-H9)], CO_2, and HNO_2^-. IC12 is found to be less stable than PC7 by ~4.8 kcal mol^{-1} at the B3LYP/AUG-cc-pVDZ level of theory in aqueous media (Fig. 22.6). There is no barrier between IC12 and PC7. Therefore, IC12 would be readily converted into PC7.

ZPE-corrected barrier energies at the first and second steps of mechanism 15 were found to be 29.9 and −0.2 kcal mol^{-1}, respectively, at the B3LYP/AUG-cc-pVDZ level of theory in gas phase. In going from gas phase to aqueous media, these barrier energies are lowered down significantly to 23.6 and −7.4 kcal mol^{-1}, respectively (Table 22.2). This shows that the second step of mechanism 15 is barrierless in both gas phase and aqueous media. The ZPE-corrected barrier energy at the first step of the most favored nitration reaction of guanine with $ONOO^-$ (mechanism 14) was found to be 49.8 and 43.4 kcal mol^{-1} in gas phase and aqueous media, respectively, at the B3LYP/AUG-cc-pVDZ level of theory (Table 22.2). Thus, the barrier energy at the first step of nitration reaction of guanine is almost halved in going from $ONOO^-$ to $ONOOCO_2^-$ in both gas phase and aqueous

media. It shows that $ONOOCO_2^-$ would be a much better nitrating agent than $ONOO^-$ [54]. The barrier energy at the first step of oxidation reaction (mechanisms 16–18) was found to be 35.5 kcal mol^{-1} at the B3LYP/AUG-cc-pVDZ level of theory in gas phase (Table 22.2). In going from gas phase to aqueous media, this barrier energy is drastically lowered down to 18.9 kcal mol^{-1} (Table 22.2). The minimum ZPE-corrected barrier energy at the first step of oxidation reaction of guanine with $ONOO^-$ (mechanism 11) was found to be 45.5 and 37.0 kcal mol^{-1} in gas phase and aqueous media at the B3LYP/AUG-cc-pVDZ level of theory, respectively (Table 22.2). Thus, in going from $ONOO^-$ to $ONOOCO_2^-$, the barrier energy at the first step of oxidation reaction of guanine is decreased substantially in gas phase, while in aqueous media, it is drastically lowered down to almost half the barrier energy encountered at the first step of oxidation reaction of guanine with $ONOO^-$ (Table 22.2). Thus, on the whole, $ONOOCO_2^-$ is much more reactive than $ONOO^-$ with guanine [54].

Structures of the product complexes show that free CO_2 is liberated after the formation of 8-oxoG or its anion, while it is liberated in the form of H_2CO_3 after the formation of 8-nitroG$^-$ (Fig. 22.6). Thus, CO_2 acts as a catalyst for the reactions between guanine and $ONOO^-$. As already discussed, $ONOOCO_2^-$ is dissociated into the $CO_3\cdot^-$ and $NO_2\cdot$ while reacting with guanine. Thus, the primary cause of the catalytic action of CO_2 seems to be the occurrence or intermediacy of $CO_3\cdot^-$ and $NO_2\cdot$ [54]. Formation of 8-oxoG has been observed experimentally in the reaction of guanine with $CO_3\cdot^-$ [14, 159]. The relative total energies given in Fig. 22.6 show that all the transition states, intermediate complexes and product complexes involved in the oxidation of guanine, excepting the transition state TS18 (mechanisms 16, 18), have lower energies than that of RC5, and the oxidation products (PC6, PC7) are more stable than the nitration product (PC5). Thus, the yield of 8-oxoG would be more than that of the 8-nitroG in the reaction of guanine with $ONOOCO_2^-$. In other words, mutation would be caused by $ONOO^-$ in the presence of CO_2 mainly through the formation of 8-oxoG [54].

22.3.7 Reactions of Imidazole with HOCl and NO_2Cl

It has been found that ROS and RNOS while reacting with guanine, modify mainly its imidazole ring, and the results obtained by studying reactions of ROS and RNOS with guanine and with imidazole were found to be similar [51–53]. Therefore, reactions of imidazole, taken as models for those involving the five-membered ring of guanine, with HOCl [76] and NO_2Cl [78] were studied. It was found that reaction of imidazole with HOCl can lead to the formation of 2-oxoimidazole (2-oxoIm) in two different ways (mechanisms 20, 21) and 2-chloroimidazole (2-chloroIm) in three different ways (mechanisms 22–24) that correspond to the formation of 8-oxoG and 8-chloroG, respectively, due to the reaction of guanine with HOCl (Table 22.3) [76]. Reaction of imidazole with NO_2Cl can lead to the formation of 2-oxoIm (mechanism 25), 2-chloroIm (mechanisms 26-28), and 2-nitroG

(2-nitroimidazole) (mechanisms 29, 30) that correspond to the formation of 8-oxoG, 8-chloroG, and 8-nitroG, respectively, due to the reaction of guanine with NO_2Cl (Table 22.3) [78]. ZPE-corrected barrier energies involved in the different steps of these reactions obtained at the B3LYP/AUG-cc-pVDZ level of theory in gas phase and aqueous media, are presented in Table 22.3.

For the reaction involving HOCl, the ZPE-corrected barrier energy at the first step of chlorination reaction (mechanism 23) is almost half and $1/4^{th}$ of those at the first step of the oxidation reaction (mechanisms 20, 21) in gas phase and aqueous media, respectively, while the barrier energies at the subsequent steps of mechanism 23 for chlorination and mechanism 20 or 21 for oxidation are comparable in both gas phase and aqueous media at the B3LYP/AUG-cc-pVDZ level of theory (Table 22.3). It reveals that formation of 2-chloroIm would be favored over that of 2-oxoIm in the reaction of imidazole with HOCl. Thus, HOCl would be a better chlorinating agent than an oxidizing agent [76]. Further, most of the barrier energies at the different steps of the reaction of imidazole with HOCl are quite high in both gas phase and aqueous media (Table 22.3). There is no mechanism of reaction between imidazole and HOCl in which all the involved barrier energies are low. Therefore, the reaction of imidazole or guanine with HOCl as such, would be slow and some appropriate catalysts, e.g., metal cations and tertiary amines, would be needed to make the reaction efficient [76]. For reactions involving NO_2Cl, the barrier energies at the first steps of oxidation, chlorination, and nitration reactions were found to be 30.8, 33.4, and 21.5 kcal mol^{-1} respectively, at the B3LYP/AUG-cc-pVDZ level of theory in gas phase (Table 22.3). In going from gas phase to aqueous media, these barrier energies are lowered down significantly to 20.5, 20.2, and 14.3 kcal mol^{-1} respectively (Table 22.3). Thus, it appears that NO_2Cl would act as a more efficient nitrating agent than an oxidizing or chlorinating agent [78].

22.4 Conclusions

ROS and RNOS are present abundantly in living cells and can modify DNA in several ways, producing a plethora of mutagenic and carcinogenic lesions. Guanine among all the DNA bases is most readily modified by ROS and RNOS. Reactions of ROS and RNOS with guanine lead to the formation of 8-oxoG and 8-nitroG, along with other mutagenic products. 8-OxoG and 8-nitroG are considered to be highly potent initiators of mutation and cancer. The results obtained by quantum theoretical study of reactions of guanine and/or imidazole with OH· radicals, H_2O_2, H_2O_3, $ONOO^-$, $ONOOCO_2^-$, HOCl and NO_2Cl, reveal the following:

1. The calculated barrier energies in aqueous media show that the reaction of guanine with two OH· radicals, one after the other, would lead to the formation of 8-oxoG most efficiently. H_2O_2, H_2O_3, and HOCl also oxidize guanine through the formation of OH· radicals. Among these molecules, H_2O_3 would serve as the most efficient ROS, as in this case, the barrier energy required for the production of OH· radical is the lowest.

2. $ONOO^-$ as such, is not very reactive towards guanine to produce 8-oxoG and 8-nitroG, as in this case, the barrier energies are very high. However, $ONOO^-$ in the presence of CO_2 can oxidize and nitrate guanine efficiently through the formation of $ONOOCO_2^-$, where CO_2 acts as a catalyst. $ONOOCO_2^-$, while reacting with guanine, is easily dissociated into the highly reactive groups $CO_3^{\cdot -}$ and $NO_2^{\cdot}$, which is the principal cause of the catalytic action of CO_2.
3. HOCl would be a better chlorinating agent than an oxidizing agent towards imidazole or guanine. However, the calculated barrier energies reveal that reaction of imidazole or guanine with HOCl as such, would be slow and some suitable catalysts would be needed to make the reaction efficient. NO_2Cl would serve as a better nitrating agent than an oxidizing or chlorinating agent towards imidazole or guanine.

Acknowledgments The authors are thankful to the Council of Scientific and Industrial Research (New Delhi) and the University Grants Commission (New Delhi) for financial support. PKS gratefully acknowledges the research fellowships received from the University Grants Commission (New Delhi).

References

1. S. Steenken, Purine bases, nucleosides, and nucleotides: Aqueous solution redox chemistry and transformation reactions of their radical cations and e^- and $OH\cdot$ adducts. Chem. Rev. **89**, 503–520 (1989)
2. C.J. Burrows et al., Oxidative nucleobase modifications leading to strand scission. Chem. Rev. **98**, 1109–1151 (1998)
3. B. Halliwell, Oxygen and nitrogen are pro-carcinogens. Damage to DNA by reactive oxygen, chlorine and nitrogen species: measurement, mechanism and the effects of nutrition. Mutat. Res. **443**, 37–52 (1999)
4. J. Cadet et al., Oxidative damage to DNA: Formation, measurement and biochemical features. Mutat. Res. **531**, 5–23 (2003)
5. H. Wiseman et al., Damage to DNA by reactive oxygen and nitrogen species: Role in inflammatory disease and progression to cancer. Biochem. J. **313**, 17–29 (1996)
6. M.R. Bennett, Reactive oxygen species and death: Oxidative DNA damage in atherosclerosis. Circ. Res. **88**, 648–650 (2001)
7. S. Magder, Reactive oxygen species: toxic molecules or spark of life? Crit. Care **10**, 208 (2006)
8. J.P.E. Spencer et al., Nitrite-induced deamination and hypochlorite-induced oxidation of DNA in intact human respiratory tract epithelial cells. Free Radic. Biol. Med. **28**, 1039–1050 (2000)
9. J. Barciszewski et al., Some unusual nucleic acid bases are products of hydroxyl radical oxidation of DNA and RNA. Mol. Biol. Rep. **26**, 231–238 (1999)
10. J. Cadet et al., Hydroxyl radicals and DNA base damage. Mutat. Res. **424**, 9–21 (1999)
11. P.C. Dedon et al., Reactive nitrogen species in the chemical biology of inflammation. Arch. Biochem. Biophys. **423**, 12–22 (2004)
12. L.J. Marnett et al., Endogenous generation of reactive oxidants and electrophiles and their reactions with DNA and protein. J. Clin. Invest. **111**, 583–593 (2003)
13. T. Suzuki, DNA damage and mutation caused by vital biomolecules, water, nitric oxide and hypochlorous acid. Genes Environ. **28**, 48–55 (2006)

14. Y.A. Lee et al., Mechanisms of oxidation of guanine in DNA by carbonate radical anion, a decomposition product of nitrosoperoxycarbonate. Chem. Eur. J. **13**, 4571–4581 (2007)
15. Y. Wang et al., Bulky DNA lesions induced by reactive oxygen species. Chem. Res. Toxicol. **21**, 276–281 (2008)
16. Y. Mishina et al., Direct reversal of DNA alkylation damage. Chem. Rev. **106**, 215–232 (2006)
17. M.D. Wyatt et al., Methylating agents and DNA repair responses: Methylated bases and sorces of strand breaks. Chem. Res. Toxicol. **19**, 1580–1594 (2006)
18. P.K. Shukla et al., Reactions of guanine with methyl chloride and methyl bromide: O6-methylation versus charge transfer complex formation. Int. J. Quantum Chem. **107**, 1270–1283 (2007)
19. P.K. Shukla et al., Reactions of DNA bases with the anti-cancer nitrogen mustard mechlorethamine: A quantum chemical study. Chem. Phys. Lett. **449**, 323–328 (2007)
20. S. Shahin et al., Mitochondrial and nuclear DNA damage induced by sulphur mustard in keratinocytes. Chem. Biol. Interact. **138**, 231–245 (2001)
21. J. Simons, How do low energy (0.1-2 eV) electrons cause DNA strand breaks. Acc. Chem. Res **39**, 772–779 (2006)
22. J. Gu et al., Electron attachment-induced DNA single strand breaks: C3′-O3′ sigma-bond breaking of pyrimidine nucleotides predominates. J. Am. Chem. Soc. **128**, 9322–9323 (2006)
23. Z. Li et al., Low energy electron induced DNA damage: effects of terminal phosphate and base moieties on the distribution of damage. J. Am. Chem. Soc. **130**, 5612–5613 (2008)
24. Y. Zheng et al., DNA damage induced by low energy electrons: Electron transfer and diffraction. Phys. Rev. Lett. **96**, 208101 (2006)
25. M.R. Osborne et al., Alkylation of DNA by the nitrogen mustard bis(2-chloroethyl) methylamine. Chem. Res. Toxicol. **8**, 316–320 (1995)
26. D. Mu et al., Recognition and repair of compound DNA lesions (base damage and mismatch) by human mismatch repair and excision repair systems. Mol. Cell. Biol. **17**, 760–769 (1997)
27. A.P. Grollman et al., Mutagenesis by 8-oxoguanine: an enemy within. Trends Genet. **9**, 246–249 (1993)
28. M. Bignami et al., Unmasking a killer: DNA O^6-methylguanine and the cytotoxicity of methylating agents. Mutat. Res. **462**, 71–82 (2000)
29. W.L. Neeley et al., Mechanisms of formation, genotoxicity, and mutation of guanine oxidation products. Chem. Res. Toxicol. **19**, 491–505 (2006)
30. K.C. Cheng et al., 8-Hydroxyguanine, an abundant form of oxidative DNA damage, causes G→T and A→T substitutions. J. Biol. Chem. **267**, 166–172 (1992)
31. E.L. Loechler et al., In vivo mutagenesis by O6-methylguanine built into a unique site in a viral genome. Proc. Natl. Acad. Sci. U.S.A. **81**, 6271–6275 (1984)
32. A.K. Singh et al., Mismatch base pairing of the mutagen 8-oxoguanine and its derivatives with adenine: A theoretical search for possible antimutagenic agents. Int. J. Quantum Chem. **102**, 343–351 (2005)
33. G. Forde et al., Theoretical ab initio study of the effects of methylation on structure and stability of G:C Watson-Crick base pair. J. Biomol. Struct. Dyn. **20**, 811–818 (2003)
34. B. Halliwell et al., Role of free radicals and catalytic metal ions in human disease: An overview. Methods Enzymol. **186**, 1–85 (1990)
35. M.S. Cooke et al., Oxidative DNA damage: mechanisms, mutation, and disease. FASEB J. **17**, 1195–1214 (2003)
36. G. Waris et al., Reactive oxygen species: Role in the development of cancer and various chronic conditions. J. Carcinog. **5**, 14 (2006)
37. J. Tuo et al., Importance of guanine nitration and hydroxylation in DNA in vitro and in vivo. Free Radic. Biol. Med. **29**, 147–155 (2000)
38. S.D. Bruner et al., Structural basis for recognition and repair of the endogenous mutagen 8-oxoguanine in DNA. Nature **403**, 859 (2000)

39. M. Aslam et al., Reactive oxygen and nitrogen species in Alzheimer's disease. Curr. Alzheimer Res. **1**, 111–119 (2004)
40. T. Finkel et al., Oxidants, oxidative stress and the biology of aging. Nature **408**, 239–247 (2000)
41. J.E. Klaunig et al., The role of oxidative stress in carcinogenesis. Annu. Rev. Pharmacol. Toxicol. **44**, 239–267 (2004)
42. R. Olinski et al., Oxidative DNA damage: Assessment of the role in carcinogenesis, atherosclerosis, and acquired immunodeficiency syndrome. Free Radic. Biol. Med. **33**, 192–200 (2002)
43. A. Parihar et al., Oxidative stress and anti-oxidative mobilization in burn injury. Burns **34**, 6–17 (2008)
44. J.S. Beckman et al., Apparent hydroxyl radical production by peroxynitrite: Implications for endothelial injury from nitric oxide and superoxide. Proc. Natl. Acad. Sci. U S A **87**, 1620–1624 (1990)
45. P.C. Dedon, The chemical toxicology of 2-Deoxyribose oxidation in DNA. Chem. Res. Toxicol. **21**, 206–219 (2008)
46. B. Halliwell et al., Measuring reactive species and oxidative damage in vivo and in cell culture: How should you do it and what do the results mean. British J. Phramacol. **142**, 231–255 (2004)
47. V. Shafirovich et al., Photochemically catalyzed generation of site-specific 8-nitroguanine of long-lived neutral guanine radicals with nitrogen dioxide. Chem. Res. Toxicol. **15**, 591–597 (2002)
48. M. Dong et al., Development of enzymatic probes of oxidative and nitrosative DNA damage caused by reactive nitrogen species. Mutat. Res. **594**, 120–134 (2006)
49. J.C. Niles et al., Peroxynitrite-induced oxidation and nitration products of guanine and 8-oxoguanine: Structures and mechanisms of product formation. Nitric Oxide **14**, 109–121 (2006)
50. R. Misiaszek et al., Oxidative DNA damage associated with combination of guanine and superoxide radicals and repair of mechanisms via radical trapping. J. Biol. Chem. **279**, 32106–32115 (2004)
51. N.R. Jena et al., Mechanisms of formation of 8-oxoguanine due to reactions of one and two OH· radicals and the H_2O_2 molecule with guanine: A quantum computational study. J. Phys. Chem. B **109**, 14205–14218 (2005)
52. N.R. Jena et al., Formation of 8-nitroguanine and 8-oxoguanine due to reactions of peroxynitrite with guanine. J. Comput. Chem. **28**, 1321–1335 (2007)
53. P.K. Shukla et al., H_2O_3 as a reactive oxygen species: formation of 8-oxoguanine from its reaction with guanine. J. Phys. Chem. B **111**, 4603–4615 (2007)
54. P.K. Shukla et al., Catalytic involvement of CO_2 in the mutagenesis caused by reactions of ONOO- with guanine. J. Phys. Chem. B **112**, 4779–44789 (2008)
55. J. Cadet et al., Assessment of oxidative base damage to isolated and cellular DNA by HPLC-MS/MS measurement. Free Radic. Biol. Med. **33**, 441–449 (2002)
56. J.-L. Ravanat et al., Singlet oxygen oxidation of 2′-deoxyguanosine. Formation and mechanistic insights. Tetrahedron **62**, 10709–10715 (2006)
57. Y.H. Jang et al., First principle calculations of the tautomers and pKa values of 8-oxoguanine: Implications for mutagenicity and repair. Chem. Res. Toxicol. **15**, 1023–1035 (2002)
58. V.I. Bruskov et al., Heat-induced formation of reactive oxygen species and 8-oxoguanine, a biomarker of damage to DNA. Nucleic Acids Res. **30**, 1354–1363 (2002)
59. X. Cheng et al., Dynamic behavior of DNA base pairs containing 8-oxoguanine. J. Am. Chem. Soc. **127**, 13906–13918 (2005)
60. R. Saffhill et al., Mechanisms of carcinogenesis induced by alkylating agents. Biochim. Biophys. Acta **823**, 111–145 (1985)
61. D.T. Beranek, Distribution of methyl and ethyl adducts following alkylation with monofunctional alkylating agents. Mutat. Res. **231**, 11–30 (1990)

62. S.A. Kyrtopoulos et al., DNA adducts in humans after exposure to methylating agents. Mutat. Res. **405**, 135–143 (1998)
63. K.S. Ekanayake et al., Activation barriers for DNA alkylation by carcinogenic methane diazonium ions. J. Comput. Chem. **27**, 277–286 (2006)
64. G.K. Forde et al., Comprehensive study of the effects of methylation on tautomeric equilibria of nucleic acid bases. J. Phys. Chem. B **110**, 15564–15571 (2006)
65. A.C. Povey et al., Elevated levels of the pro-carcinogenic adduct, O6-methylguanine, in normal DNA from the cancer prone regions of the large bowel. Gut **47**, 362–365 (2000)
66. G.P. Margison et al., O6-alkylguanine-DNA alkyltransferase: Role in carcinogenesis and chemotherapy. Bioessays **24**, 255–266 (2002)
67. H.J. Helbock et al., 8-Hydroxydeoxyguanosine and 8-hydroxyguanine as biomarkers of oxidative DNA damag. Methods Enzymol. **300**, 155–166 (1999)
68. S. Shibutani et al., Insertion of specific bases during DNA synthesis past the oxidation-damaged base 8-oxodG. Nature **349**, 431–434 (1991)
69. H. Maki et al., MutT protein specifically hydrolyses a potent mutagenic substrate for DNA synthesis. Nature **355**, 273–275 (1992)
70. T.K. Hazra et al., Repair of hydantoins, one electron oxidation product of 8-oxoguanine by DNA glycosylases of Escherichia coli. Nucleic Acids Res. **29**, 1967–1974 (2001)
71. O.M. Panasenko et al., Oxidative modification and nitration of human low-density lipoproteins by the reaction of hypochlorous acid with nitrite. Arch. Biochem. Biophys. **343**, 254–259 (1997)
72. A.C. Carr et al., The nitric oxide congener nitrite inhibits myeloperoxidase/H2O2/Cl–mediated modification of low density lipoprotein. J. Biol. Chem. **276**, 1822–1828 (2001)
73. F. Yamakura et al., Modification of tryptophan and tryptophan residues in proteins by reactive nitrogen species. Nitric Oxide **14**, 152–161 (2006)
74. M. Whiteman et al., Lack of tyrosine nitration by hypochlorous acid in the presence of physiological concentration of nitrite. J. Biol. Chem. **278**, 8380–8384 (2003)
75. A.S. Ptolemy et al., Strategies for comprehensive analysis of amino acid biomarkers of oxidative stress. Amino Acids **33**, 3–18 (2007)
76. N.R. Jena et al., Reaction of hypochlorous acid with imidazole: Formation of 2-chloro- and 2-oxoimidazoles. J. Comput. Chem. **29**, 98–107 (2008)
77. O. Augusto et al., Nitrogen dioxide and carbonate radical anion: Two emerging radicals in biology. Free Radic. Biol. Med. **32**, 841–859 (2002)
78. P.K. Shukla et al., Reactions of NO_2Cl with imidazole: A model study for the corresponding reactions of guanine. J. Phys. Chem. B **112**, 7925–7936 (2008)
79. M.G. Bonini et al., Production of the carbonate radical anion during xanthine oxidase turnover in the presence of bicarbonate. J. Biol. Chem. **279**, 51836–51843 (2004)
80. J.F. Turrens, Mitochondrial formation of reactive oxygen species. J. Physiol. **552**, 335–344 (2003)
81. Y. Xia et al., Superoxide and peroxynitrite generation from inducible nitric oxide synthase in macrophages. Proc. Natl Acad. Sci. USA **94**, 6954–6958 (1997)
82. J.F. Torrens et al., Ubisemiquinone is the electron donor for superoxide formation by complex III of heart mito. Arch. Biochem. Biophys. **237**, 408–414 (1985)
83. G.L. Squadrito et al., Oxidative chemistry of nitric oxide: The roles of superoxide, peroxynitrite, and carbon dioxide. Free Radic. Biol. Med. **25**, 392–403 (1998)
84. J. Carlsson et al., Hydrogen peroxide and superoxide radical formation in anaerobic broth media exposed to atmospheric oxygen. Appl. Environ. Microbiol. **36**, 223–229 (1978)
85. W.A. Pryor et al., The chemistry of peroxynitrite: A product from the reaction of nitric oxide with superoxide. Am. J. Physiol. **268**, L699–L722 (1995)
86. R. Misiaszek et al., Combination reactions of superoxide with 8-oxoG radicals in DNA: kinetics and enol products. J. Biol. Chem. **280**, 6293–6300 (2005)
87. B. Epe, Genotoxicity of singlet O_2. Chem.-Biol. Intteract **80**, 239–260 (1992)

88. D.B. Min et al., Chemistry and reaction of singlet oxygen in foods. Compr. Rev. Food Sci. Food Safety **1**, 58–72 (2002)
89. F. Wilkinson et al., Quantum yields for the photosensitized formation of the lowest electronically excited singlet state of molecular oxygen in solution. J. Phys. Chem. Ref. Data **22**, 113–262 (1993)
90. P.F. Santos et al., Singlet oxygen generation ability of squarylium cyanine dyes. J. Photochem. Phtobiol. A **160**, 159–161 (2003)
91. E. Skovsen et al., Two-photon singlet oxygen microscopy: The challenges of working with single cells. Photochem. Photobiol. **73**, 1187–1197 (2006)
92. P.C. Mishra et al., Interaction of singlet oxygen and superoxide radical anion with guanine and formation of its mutagenic modification 8-oxoguanine. Int. J. Quantum Chem. **102**, 282–301 (2005)
93. J.M. McCord et al., Superoxide dismutase. An enzymatic function for erythrocuprein (hemocuprein). J. Biol. Chem **244**, 6049–6055 (1969)
94. I. Fridovich, Superoxide radical and superoxide dismutases. Annu. Rev. Biochem. **64**, 97–112 (1995)
95. H.G.D. Niekus et al., Superoxide dismutase and hydrogen peroxide formation in campylobacter sptorum subspecies bubulus. Arch. Microbiol. **119**, 37–42 (1978)
96. R. Kevin et al., Mechanism of superoxide and hydrogen peroxide formation by fumarate reductases, succinate dehydrogenase, aspartate oxidase. J. Biol. Chem. **277**, 42563–42571 (2002)
97. L. Brambilla et al., Mitochondrial formation of hydrogen peroxide is casually linked to the antimycin A-mediated prevention of tert- butylhydroperoxide- induced U937 cell death. FEBS Lett. **431**, 245–249 (1998)
98. R. Fritz et al., Compartment-dependent management of H_2O_2 by peroxisomes. Free Radic. Biol. Med. **42**, 1119–1129 (2007)
99. B.M. Babior, Phagocytes and oxidative stress. Am. J. Med. **109**, 33–44 (2000)
100. E. Graf et al., Iron-catalyzed hydroxyl radical formation. Stringent requirement for free iron coordination site. J. Biol. Chem **259**, 3620–3624 (1984)
101. H. Fickl et al., Vanadium promotes hydroxyl radical formation by activated human neutrophils. Free Radic. Biol. Med. **40**, 146–155 (2006)
102. J.P. Kehrer, The Haber-Weiss reaction and mechanisms of toxicity. Toxicology **149**, 43–50 (2000)
103. L.P. Candeias et al., Reaction of HO· with guanine derivatives in aqueous solution: Formation of two different redox active OH·-adduct radicals and their unimolecular transformation reactions. Properties of G(-H). Chem. Eur. J **6**, 475–484 (2000)
104. N.R. Jena et al., Addition and hydrogen abstraction reactions of an OH· radical with 8-oxoguanine. Chem. Phys. Lett. **422**, 417–423 (2006)
105. Y.J. Ji et al., Theoretical study of the OH· reaction with cytosine. J. Mol. Struct.: THEOCHEM **723**, 123–129 (2005)
106. J. Llano et al., Mechanism of hydroxyl radical addition to imidazole and subsequent water elimination. J. Phys. Chem. B **103**, 5598–5607 (1999)
107. W. Hiraoka et al., Free-radical reactions induced by OH·-radical attack on cytosine-related compounds: a study by a method combining ESR, spin trapping and HPLC. Nucleic Acids Res. **18**, 1217–1223 (1990)
108. Y. Wu et al., On the Mechanisms of OH· Radical Induced DNA-Base Damage: A Comparative Quantum Chemical and Car-Parrinello Molecular Dynamics Study. J. Phys. Chem. A **108**, 2922–2929 (2004)
109. P. Schyaman et al., Hydroxyl radical-thymine adduct induced DNA damage. Chem. Phys. Lett. **458**, 186–189 (2008)
110. S. Sun et al., Radical-mediated cytosine and S-methylcytosine hydrolytic deamination reactions. Int. J. Quantum Chem. **106**, 1878–1894 (2006)

111. A. Grand et al., H atom and OH· radical reactions with 5-methylcytosine. J. Phys. Chem. A **111**, 8968–8972 (2007)
112. B.G. Eatock et al., Ab intio SCF MO calculation on the reaction of hydroxyl radical with cytosine. Can. J. Chem. **64**, 914–919 (1986)
113. C.S. Foote et al., Assessment of chlorination by human neutrophills. Nature **301**, 715–716 (1983)
114. M. Masuda et al., Chlorination of guanosine and other nucleosides by hypochlorous acid and myeloperoxidase of activated human neutrophils. J. Biol. Chem. **276**, 40486–40496 (2001)
115. J. Marcinkiewicz et al., Antimicrobial and cytotoxic activity of hypochlorous acid: Interactions with taurine and nitrite. Inflamm. Res. **49**, 280–289 (2000)
116. M. Whiteman et al., Hypochlorous acid-induced DNA base modification: Potentiation by nitrite: Biomarkers of DNA damage by reactive oxygen species. Biochem. Biophys. Res. Commun. **257**, 572–576 (1999)
117. P.T. Nyffeller et al., Dihydrogen trioxide (HOOOH) is generated during the thermal reaction between hydrogen peroxide and ozone. Angew. Chem. Int. Ed. **43**, 4656–4659 (2004)
118. B. Plesničar, Progress in the chemistry of dihydrogen trioxide (HOOOH). Acta Chim. Slov. **52**, 1–12 (2005)
119. P. Wentworth et al., Antibody catalysis of the oxidation of water. Science **273**, 1806–1811 (2001)
120. B.H.J. Bielski et al., Absorption spectra and kinetics of hydrogen sesquioxide and the perhydroxyl radical. J. Phys. Chem. **72**, 3836–3841 (1968)
121. P.A. Giguere et al., Raman study of matrix isolated H_2O_2 and D_2O_2. Chem. Phys. Lett. **33**, 479–482 (1975)
122. A. Engdahl et al., Vibrational spectrum of H_2O_3. Science **295**, 482–483 (2002)
123. K. Suma et al., The rotational spectrum and structure of HOOOH. J. Am. Chem. Soc. **127**, 14998–14999 (2005)
124. X. Xu et al., The gas phase reaction of singlet oxygen with water: A water-catalyzed mechanism. Proc. Natl. Acad. Sci. U S A **99**, 3376–3381 (2002)
125. D.J. Mckay et al., How long can you make an oxygen chain. J. Am. Chem. Soc. **120**, 1003–1013 (1999)
126. F.B. Jensen, Nitric oxide formation from the reaction of nitrite with carp and rabit hemoglobin at intermediate oxygen saturations. FEBS J. **275**, 3375–3387 (2008)
127. H. Ischiropoulos, Biological tyrosine nitration: A pathophysiological function of nitric oxide and reactive oxygen species. Arch. Biochem. Biophys. **356**, 1–11 (1998)
128. J.P. Kiss, Role of nitric oxide in the regulation of monoaminergic neurotransmission. Brain Res. Bullet. **52**, 459–466 (2000)
129. S.V. Lymar et al., CO_2-catalyzed one-electron oxidations by peroxynitrite: Properties of the reactive intermediate. Inorg. Chem. **37**, 294–301 (1998)
130. R.M. Uppu et al., Acceleration of peroxynitrite oxidations by carbon dioxide. Arch. Biochem. Biophys. **327**, 335–343 (1996)
131. A. Denicola et al., Peroxynitrite reaction with carbon dioxide/ bicarbonate: Kinetics and influence on peroxynitrite-mediated oxidations. Arch. Biochem. Biophys. **333**, 49–58 (1996)
132. S. Goldstein et al., Formation of peroxynitrate from the reaction of peroxynitrite with CO_2: Evidence for carbonate radical production. J. Am. Chem. Soc. **120**, 3458–3463 (1998)
133. G.L. Squadrito et al., Mapping the reaction of peroxynitrite with CO_2: Energetics, reactive species, and biological implications. Chem. Res. Toxicol. **15**, 885–895 (2002)
134. M.G. Bonini et al., Direct EPR detection of the carbonate radical anion produced from peroxynitrite and carbon dioxide. J. Biol. Chem. **274**, 10802–10806 (1999)
135. M.C. González et al., QM-MM investigation of the reaction of peroxynitrite with carbon dioxide in water. J. Chem. Theory Comput. **3**, 1405–1411 (2007)
136. S. Steenken et al., How easily oxidizable is DNA? One-electron reduction potentials of adenosine and guanosine radicals in aqueous solution. J. Am. Chem. Soc. **119**, 617–618 (1997)

137. C. Richter et al., Normal oxidative damage to mitochondrial and nuclear DNA is extensive. Proc. Natl. Acad. Sci. U S A **85**, 6465–6467 (1988)
138. M.K. Shigenaga et al., Urinary 8-hydroxy-2′-deoxyguanosine as a biological marker of in vivo oxidative DNA damage. Proc. Natl. Acad. Sci. U S A **86**, 9697–9701 (1989)
139. D.C. Malins et al., Major alterations in the nucleotide structure of DNA in cancer of the female breast. Cancer Res. **51**, 30–32 (1991)
140. S.J. Culp et al., Structural and conformational analyses of 8-hydroxy-2′-deoxyguanosine. Chem. Res. Toxicol. **2**, 416–422 (1989)
141. D. Venkateswarlu et al., Tautomeric equilibria in 8-oxopurines: Implications for mutagenicity. J. Comput.-Aid. Mol. Design **12**, 373–382 (1998)
142. L.G. Brieba et al., Structural basis for the dual coding potential of 8-oxoguanosine by a high-fidelity DNA polymerase. EMBO J. **23**, 3452–3461 (2004)
143. N. Suzuki et al., Miscoding Events during DNA Synthesis Past the Nitration-Damaged Base 8-Nitroguanine. Biochemistry **44**, 9238–9245 (2005)
144. K.J. Laidler, *Chemical Kinetics*, third edn. (Pearson Education (Singapore) Pte. Ltd, Delhi, India, 2004)
145. I.N. Levine, *Quantum Chemistry*, fourth edn. (Prentice-Hall, Inc, Englewood Cliffs, N.J., U S A, 1994)
146. S. Olivella et al., Mechanisms for the reaction of hydroxyl radicals with acrolein: A theoretical study. J. Chem. Theory Comput. **4**, 941–950 (2008)
147. S.S. Ramalho et al., Theoretical rate constants for the reaction BF_2 + NF = BF_3 + N of importance in boron nitride chemistry. Chem. Phys. Lett. **413**, 151–156 (2005)
148. E. Henon et al., Comparative ab initio MO investigation on the reactivity of the three NH ($a^1\Delta$), NH(X^{3-}) and $NH_2(^2B_1)$ radical species in their bimolecular abstraction gas-phase reaction with the HN_3 molecule. J. Mol. Struct. (THEOCHEM) **531**, 283–299 (2000)
149. A.D. Becke, Density-functional thermochemistry. III. The role of exact exchange, *J*. Chem. Phys. **98**, 5648 (1993)
150. C. Lee et al., Development of the Colle-Salvetti correlation-energy formula into a functional of the electron density. Phys. Rev. B **37**, 785–789 (1988)
151. M.J. Frisch et al., A direct MP2 gradient method. Chem. Phys. Lett. **166**, 275–280 (1990)
152. M.J. Frisch et al., Semi-direct algorithms for the MP2 energy and gradient. Chem. Phys. Lett. **166**, 281–289 (1990)
153. B. Mennucci et al., Continuum solvation models: A new approach to the problem of solute's charge distribution and cavity boundaries. J. Chem. Phys. **106**, 5151 (1997)
154. C. Gonzalez et al., An improved algorithm for reaction path following. J. Chem. Phys. **90**, 2154 (1989)
155. J. Koller et al., Mechanism of the participation of water in the decomposition of hydrogen trioxide (HOOOH). A theoretical study. J. Am. Chem. Soc. **118**, 2470–2472 (1996)
156. J.A. Kerr, Bond dissociation energies by kinetics methods. Chem. Rev. **66**, 465–500 (1966)
157. M. Litorja et al., A photoionization study of the hydroperoxyl radical, HO_2, and hydrogen peroxide, H_2O_2. J. Electron Spectrosc. **97**, 131–146 (1998)
158. V. Gogonea, Potential energy surface of the reaction of imidazole with peroxynitrite: density functional theory study. Int. J. Quantum Chem. **104**, 342–353 (2005)
159. C. Crean et al., Oxidation of guanine and 8-oxo-7, 8-dihydroguanine by carbonate radical anions: Insight from oxygen-18 labeling experiments. Angew. Chem. Int. Ed. **44**, 5057–5060 (2005)

Chapter 23
Stability and Structures of the DNA Base Tetrads: A Role of Metal Ions

Jiande Gu, Jing Wang, and Jerzy Leszczynski

Abstract Nucleic acids can form complex structures that consist of multi-strands, which play a vital role in many biological processes. Quantum chemistry studies of the polyads of the nucleic acid bases (NABs) strongly suggest that all of them (NABs) can form stable tetrad structure in cyclic form through the H-bonding between the neighboring bases. All of the cyclic form tetrads possess the strong cooperativity of the hydrogen bonds. The cooperative effects should play a key role in the formation of stable tetraplexes. The existence of cation in the cavity of the tetrads greatly improves the stability of the tetraplexes. Metals can also replace the protons in the bases to form tetrads. This phenomenon could be extremely important in the construction of variety of newly designed nanomaterials. DNA bases are also able to form larger species. The studies of isoG quintet reveal that metal ions are crucial for regulating the strand association.

23.1 Introduction

Nucleic acids can form complex structures that consist of more than two strands. Recently, the interest in structures and functions of the DNA bases polyads has significantly increased. It has been shown that guanine tetrads are vital components of many biologically important processes.

The first experimental identification of the formation of guanine tetrad can be dated back to 1962 [1]. Since 1992, an increasing number of the X-ray crystal structure determinations of guanine tetrads has been reported [2–13]. The advances

J. Leszczynski (✉)
Department of Chemistry and Biochemistry, NSF CREST Interdisciplinary Nanotoxicity Center, Jackson State University, Jackson, MS 39217, USA
e-mail: jerzy@icnanotox.org

J. Leszczynski and M.K. Shukla (eds.), *Practical Aspects of Computational Chemistry*,
DOI: 10.1007/978-90-481-2687-3_23,

of the studies of the structure and the function of the DNA bases polyads have proposed that they might be relevant in areas ranging from biology to nanotechnology [14].

Computational studies could shed light on molecular structures and properties of such systems. A series of tetrads of DNA bases has been recently investigated in our laboratory. Ab initio, nonempirical quantum chemical method has been used in these studies. The considered structures reveal different conformational preferences of DNA bases. They have also one common feature: all tetrads are linked together by H-bonding patterns.

An additional series of calculations has been carried out for the complexes of the tetrads with the metal ions. It has been concluded that the stability of such tetrads is controlled by the presence of metal ions. In this presentation, we demonstrate that such cations dominate the H-bonding patterns that govern the structures of the DNA bases polyads.

23.2 Guanine Tetrad

At the HF/6-311G(d,p) level of theory, four guanines (G) have been found to form a stable tetrad through bifurcated H-bonding pattern even without the existence of cations [15]. Later studies [16, 17] based on the DFT approach reveal that the normal Hoogsteen H-bonded guanine tetrad is also the local minimum on the potential energy surface. However, using large basis set DFT calculations (B3LYP/6-311G(d,p) level) confirms that the bifurcated H-bonded conformer of G-tetrad is still more stable than the Hoogsteen H-bonded one. The stabilization energy of the G-tetrad amounts to 76.8 kcal mol^{-1} at the B3LYP/6-311G(d,p) level of theory [17]. The studies on G-tetrads have demonstrated that cooperativity plays a crucial role in the stabilization of the tetrads.

23.3 Isoguanine Tetrad

Isoguanine is an oxidized derivative of adenine. Like the guanine tetrad, the higher-order self-pairing of isoguanine has been recognized. On the other hand, unlike the guanine tetrad that adopts either the Hoogsteen bases-pair motif or the bifurcated hydrogen-bonding form, five different conformers have been located as the local minima on the potential energy surfaces at the B3LYP/6-311G(d,p) level of theory [18]. High stabilization energy has been revealed for these isoG tetrads. All cyclic isoG tetrads are more stable than guanine tetrads (the stabilization energy ranges from 80.4 to 87.9 kcal mol^{-1}). The most stable conformer adopts planar form and is held together through four pairs of normal and two pairs of bifurcated H-bonds. The conformer consisting of only bifurcated H-bond pattern has also been found

highly stabilized (85.2 kcal mol^{-1}). The difference in stabilization energy between the planar and non-planar conformers is basically negligible. As long as they can be stacked between layers of other tetrads, isoG tetrads should easily adopt a planar form.

IsoG has also been found to have strong tendency to form the near-planar form quintets [14, 19–21]. At the B3LYP/6-311G(d,p) level of theory, the stabilization energy of the isoG quintet amounts to 109.6 kcal mol^{-1} [21]. Experimental studies suggest that the isoG quintet-based DNA pentaplexes are of particular importance for the radonuclide ^{137}Cs separation due to their high selectivity for Cs^+ ions [14, 22, 23].

23.4 Tetrads Formed by Adenine, Cytosine, Thymine, and Uracil

Besides guanine and isoguanine, other nucleic acids bases are also found to be able to form the tetrad structures through H-bonds between the neighboring bases [24–27].

Depending on the H-bond pattern (N1···H(N6) or N7···H(N6)), adenine (A) can form two different tetrads through H-bonds [24]. The stabilization energy of the former amounts to 22.4 kcal mol^{-1}, about 5 kcal mol^{-1} less than the latter at the B3LYP/6-311G(d,p) level. Both conformers of A tetrad adopt the bowl-like structure with *C4* symmetry. Nevertheless, the energy difference between the planar and the bowl-like structure is small, suggesting a shallow minimum on the potential energy surface.

Thymine (T) and uracil (U) also form stable tetrads in the isolated form. Four O4···H(N3) H-bonds contribute 26.7 kcal mol^{-1} in T tetrad and 30.7 kcal mol^{-1} in U tetrad, respectively (B3LYP/6-311G(d,p) level) (Fig. 23.1) [24]. Although the T and U tetrads share similar bonding patterns, they have different nonplanar structures. The propeller structure in the T tetrad arises from the repulsion between the methyl group and the O2 atom, while with the bowl-like shape in the U tetrad suggests the O4–O4′ repulsion. However, the negligible energy difference (0.6 kcal mol^{-1}) between the planar and nonplanar forms of U tetrad implies a weak O4–O4′ repulsion.

The other tetrad formed through four H-bonds, cytosine (C) tetrad, is quite different from A, T, and U tetrads in both structure and stability. C tetrad adopts the planar form as the local minimum at the potential energy surface [25]. Without the presence of a cation, C tetrad has the conformation in which the four non-H-bonded amino protons point to the center of the tetrad. Significantly strong stabilization energy of 56.4 kcal mol^{-1} has been evaluated for this tetrad. This large binding energy is partly attributed to the zero electrostatic repulsion in the cavity of the tetrad as revealed by the electrostatic potential analysis.

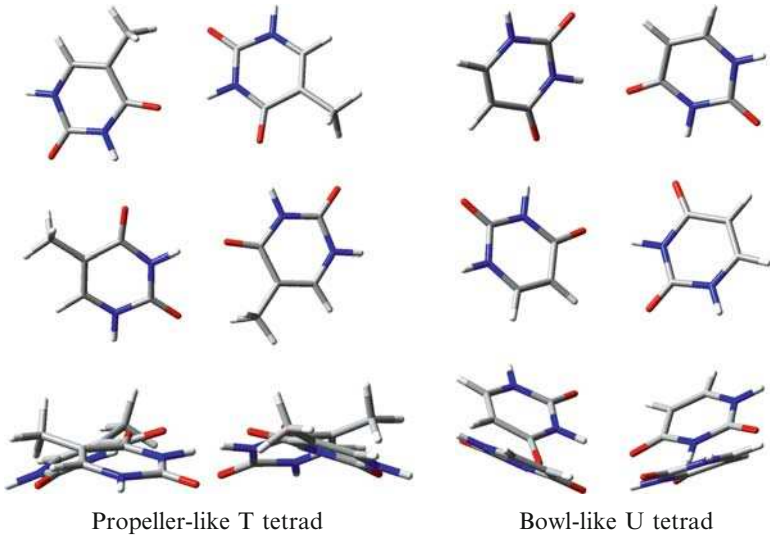

Fig. 23.1 Thymine and uracil tetrads

23.5 Tetrads with Mixed Bases

Challenging for both experimental and theoretical investigation is the tetrads form by different DNA basis. Among mixed DNA base tetrads studied are TATA, AGAG, GCGC, UAUA, and T^+AT^+A, where T^+ represents the 5-bromouracil.

Both Hoogsteen and Watson-Crick type TATA tetrads are stable in the isolated form in which the Hoogsteen type is more stable than the Waston-Crick type [28]. About 40 kcal mol^{-1} of stabilization energy suggests importance of such interactions in the formation of four stranded helices. AGAG tetrad seems to be less important than TATA due to its highly non-planar shape and low stabilization energy. TATA and AGAG tetrads adopt V-shape in the isolated form and are easy to decompose to separated TA and AG pairs since the binding energy between the pairs amounts only to 3.5 kcal mol^{-1} for AGAG and 7.6 kcal mol^{-1} for TATA tetrads.

Two highly stable conformers of GCGC tetrad have been predicted in the planar form [29]. The evaluated stabilization energy amounts to 83.9 and 82.0 kcal mol^{-1} at the B3LYP/6-311G(d,p) level of theory. The inter bases pair binding energy is estimated to be 19.1 and 17.2 kcal mol^{-1}, respectively. The H-bonding between the GC pairs in the tetrads is found to increase the intra base pair interactions by about 2 kcal mol^{-1}.

To understand the role of T^+AT^+A tetrads in the formation of the tetraplexes, the relative stability of different conformers of the tetrad and their bonding pattern have been studied [30]. The influence of bromine in the formation of the tetrads has been

revealed by the comparative studies of UAUA tetrad. Both T^+AT^+A and UAUA tetrads are in the planar form as the local minima on their potential energy surfaces. The stabilization energy of T^+AT^+A has been evaluated to be around 40 kcal mol^{-1}, compatible to those of TATA and UAUA. The role that Br plays in the stabilization of the tetrads is two folded: by improving the ability of proton-donating on its N3 position, it reinforces the H-bonding between A and T^+; and through electrostatic repulsion with N7 or N1 of A, it destabilizes the binding between the AT^+ pairs. The increase of the intra-base-pair binding energy compensates the decrease of the inter-base-pair interaction. It is the bifurcated H-bond consisting of Br(T^+), O4 (T^+), and H6′(A) that binds two AT^+ pairs to form the stable T^+AT^+A tetrads. This bifurcated H-bonding has been justified by the atoms in molecules (AIM) theory, the electron localization function (ELF) method, the electrostatic potential (ESP) description, and the electron density difference analysis.

23.6 Interaction Between Metal Ions and the NAB Tetrads

It has been recognized that the stabilization by interactions with metal ions is essential in the formation of tetraplex structures. Based on the electrostatic potential analysis of the tetrads, a number of tetrads are suggested as the possible hosts of cations. The interaction between the cation and the tetrads remarkably alter the bonding patterns of the tetrads.

Location of a potassium cation around the center of T tetrad leads to the elongation of the O4···H(N3) bonds by 0.5 Å, suggesting the reduction of the H-bonding interaction between the bases (Fig. 23.2) [24]. However, this destabilization effect has been compensated by the large cation-tetrad interactions, about 66.7 kcal mol^{-1} for the K^+–T tetrad complex. Location of the K^+ in the central area of U tetrad facilitates the conversion of the bowl-like U tetrad into planar form, as revealed in the DFT study. However, both T and U tetrads seem unlikely to host potassium cation in aqueous solutions because the hydration free energy of K^+ amounts to 80.6 kcal mol^{-1} [24].

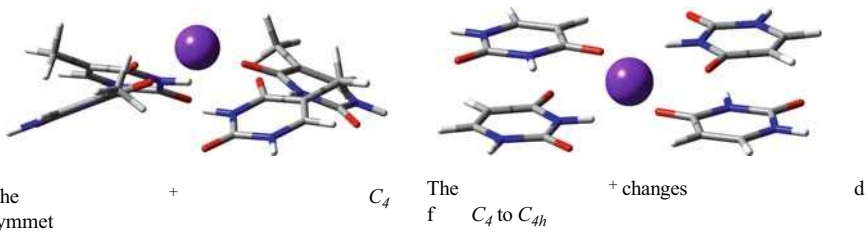

Fig. 23.2 Thymine and uracil tetrads stabilized by the K^+ cation

Complexes of mono-valence cations (Na^+, K^+) sandwiched between two T tetrads (also U tetrads) have been found to adopt an S_8-symmetry [31]. It is interesting to note that intercalating a cation between two T tetrads does not alter the propeller-like structure of T tetrad. Similarly, U tetrads in the cation sandwiched U tetrads complex adopt the bowl-like structure.

Although Na^+ and Li^+ have been found stable in the center of G tetrad, the results of high level of theoretical studies indicate that K^+ can only be stable when it is outside the tetrad plane, which explains the fact that potassium cations are usually located between the successive G tetrads. The interaction between a cation and G tetrad around the central area also changes the H-bonding pattern in the G tetrad. In the cation-G tetrad complex, bifurcated H-bonding pattern is replaced by the normal Hoogsteen H-bonding pattern [32].

To explore the origin of the cation selectivity of the G tetraplexes in water, the G tetrad–cation-G tetrad "sandwich" models, which consist of eight guanines and one cation, have been studied at both HF and DFT levels of theory [17]. Based on the fully optimized structures, these complexes reveal the binding energies in the order of $Na^+ > K^+ > Ru^+ > Cs^+$, which is the same as the recent solid-state NMR determination [33]. The binding energy difference between Na and K complexes evaluated at the B3LYP/6-311G(d,p) level of theory amounts to 15.2 kcal mol^{-1}, which is very close to the 15.7 kcal mol^{-1} of the experimental value. Including the hydration energy of the cations, this "sandwich" model reproduces the experimental results of the G tetraplex formation preference of K^+ over Na^+ by 2.42 kcal mol^{-1} (experimental values are 1.9 ± 0.4 [33] and 0.8 [34] kcal mol^{-1}). The theoretical studies clearly demonstrate that the preferred coordination of K^+ over Na^+ in the G tetraplexes is dominated by the relative energies of hydration.

It is interesting to note that in the presence of mono valence cations, such as K^+, Rb^+, and Cs^+, isoG can form a stable bowl-like tetrad structure [34]. Moreover, these bowl-like tetrads have been predicted to be able to form a ball-shape octamer complex through the H-bonding between the proton acceptor N7 and the proton donator H(N6) along the open edge of the isoG tetrads [34].

Metals can also replace the protons in the bases to form tetrads [35]. Our recent study of the platinated GCGC tetrad reveals a new insight into the H-bonding patterns in the metallated nucleobase complexes [36]. The influence of Pt on the intra GC base pair H-bonding has been found to reduce the intra base pair H-bonding of N4(C)···O6(G) in the platinated GCGC tetrad. The platinum in the GCGC tetrad facilitates the formation of the unique CH···N (H5(C)···N1(G)) hydrogen bond in the tetrad by offering improved geometric constrains rather than through changing the electronic properties around the H5 (C) and N1(G) sites. The electronic structure of the H5(C)···N1(G) H-bond is not affected by the chemical alternation or the electronic properties on the N site of the bases. The H-bonding energy of the C-H···N type H-bond is expected to be similar to that of N-H···N type. Platination at the N7 of guanine reduces the deprotonation energy considerably. The deprotonation energy of the di-valenced platinum complex (*trans*-$[(NH_3)_2Pt(G\text{-}N7)(C\text{-}N3)]^{2+}$) has been evaluated to be 9.01 eV.

23.7 Summary

Quantum chemistry studies of the polyads of the nucleic acid bases strongly suggest that all of the NABs can form stable tetrad structure in cyclic form through the H-bonding between the neighboring bases. One important phenomenon can be revealed from the tetrad studies: all of the planar or near planar cyclic form tetrads possess the strong cooperativity of the hydrogen bonds. The increase of the cooperative energy in isoG tetrads and in C tetrad is the most striking. The cooperative effects could play a key role in the formation of stable tetraplexes. The existence of cation in the cavity of the tetrads greatly improves the stability of the tetraplexes. In addition to the electrostatic interaction between the cation and the bases, metals can also replace the protons in the bases to form tetrads. This phenomenon could be extremely important in the construction of variety of newly designed nanomaterials.

DNA basis are also able to form larger species. Recent studies revealed molecular structure and properties of the stable isoG quintet. The comparison of the relative stability of the quintet with that of the tetrad indicates preferential formation of isoG tetrad in the absence of metal ions [29]. The entropy of the system governs this preference. Cooperative effects in H-bonding for the cyclic quintet of isoG system are substantial. The large interaction energy evaluated for the complexes of cations with isoG quintet suggests that metal ions are crucial for regulating the strand association. Theoretical study also provides the direct evidence for the orbital interaction between K^+ and the surrounding oxygen atoms in tetrad and quintet complexes [37].

Acknowledgment The authors are thankful for the financial assistance and support from the NSF CREST Interdisciplinary Nanotoxicity Center (grant no. HRD-0833178), NIH-RCMI grant no. G1 2RR13459, ONR grant no. N00034-03-1-0116, and NSF-EPSCoR grant no. 300423-190200-21000.

References

1. M. Gellert et al., Helix formation by guanylic acid. Proc. Natl. Acad. Sci. USA **48**, 2013–2018 (1962)
2. C. Kang et al., Crystal structure of four-stranded Oxytricha telomeric DNA. Nature **356**, 126–131 (1992)
3. K. Padmanabhan et al., The structure of alpha-thrombin inhibited by a 15-mer single-stranded DNA aptamer. J. Biol. Chem. **268**, 17651–17654 (1993)
4. G. Laughlan et al., The high-resolution crystal structure of a parallel-stranded guanine tetraplex. Science **265**, 520–524 (1994)
5. K. Padmanabhan, A. Tulinsky, An ambiguous structure of a DNA 15-mer thrombin complex. Acta. Crystallogr. Sect. D **52**, 272–282 (1996)
6. K. Phillips et al., The crystal structure of a parallel-stranded guanine tetraplex at 0.95 Å resolution. J. Mol. Biol. **273**, 171–182 (1997)

7. S.L. Forman et al., Toward artificial ion channels: a lipophilic g-quadruplex. J. Am. Chem. Soc. **122**, 4060–4067 (2000)
8. J.P. Deng et al., X-ray analysis of an RNA tetraplex (UGGGGU) 4 with divalent Sr^{2+} ions at subatomic resolution (0.61 Å). Proc. Natl. Acad. Sci. USA **98**, 13665–13670 (2001)
9. M.P. Horvath, S.C. Schultz, DNA G-quartets in a 1.86 Å resolution structure of an *Oxytricha nova* telomeric protein-DNA complex. J. Mol. Biol. **310**, 367–377 (2001)
10. G.N. Parkinson et al., Crystal structure of parallel quadruplexes from human telomeric DNA. Nature **417**, 876–880 (2002)
11. S. Haider et al., Crystal structure of the potassium form of an oxytricha nova g-quadruplex. J. Mol. Biol. **320**, 189–200 (2002)
12. S. Haider et al., Structure of a G-quadruplex–ligand complex. J. Mol. Biol. **326**, 117–125 (2003)
13. G.R. Cark et al., Structure of the first parallel DNA quadruplex-drug complex. J. Am. Chem. Soc. **125**, 4066–4067 (2003)
14. J.T. Davis, G-Quartets 40 years later: from 5′-gmp to molecular biology and supramolecular chemistry. Angew. Chem. Int. Ed. **43**, 668–698 (2004)
15. J. Gu et al., A new insight into the structure and stability of hoogsteen hydrogen bonded g-tetrad: an ab initio SCF study. Chem. Phys. Lett. **311**, 209–214 (1999)
16. M. Meyer et al., Are guanine tetrads stabilized by bifurcated hydrogen bonds? J. Phys. Chem. A. **105**, 8223–8225 (2001)
17. J. Gu, J. Leszczynski, Origin of Na^+/k^+ selectivity of the guanine tetraplexes in water: The theoretical rationale. J. Phys. Chem. A. **106**, 529–532 (2002)
18. J. Gu, J. Leszczynski, Isoguanine: From base pair to tetrad. J. Phys. Chem. A **107**, 9447–9455 (2003)
19. J.T. Davis et al., A self-assembled ionophore with remarkable Cs^+ selectivity. J. Am. Chem. Soc. **119**, 5271–5272 (1997)
20. J.C. Chaput, C. Switaer, A DNA pentaplex incorporating nucleobase quintets. Proc. Natl. Acad. Sci. USA **96**, 10614–10619 (1999)
21. J. Gu, J. Leszczynski, Isoguanine complexes: Quintet versus tetrad. J. Phys. Chem. B **107**, 6609–6613 (2003)
22. M. Cai et al., Binding cesium ions with nucleosides: Templated self-assembly of isoguanosine pentamers. Angew. Chem. Int. Ed. **39**, 1283–1285 (2000)
23. X.D. Shi et al., Enantiomeric self-recognition: Cation-templated formation of homochiral isoguanosine pentamers. Angew. Chem. Int. Ed. **39**, 3124–3127 (2000)
24. J. Gu, J. Leszczynski, A theoretical study of thymine and uracil tetrads: structures, properties, and interactions with the monovalent k^+ cation. J. Phys. Chem. A **105**, 10366–10371 (2001)
25. J. Gu, J. Leszczynski, The structure, stability, h-bonding pattern, and electrostatic potential of adenine tetrads. Chem. Phys. Lett. **335**, 465–474 (2001)
26. J. Suhnel, Beyond nucleic acid base pairs: From triads to heptads. Biopolymers **61**, 32–51 (2001)
27. M. Meyer, J. Suhnel, Biological significance, occurrence in three-dimensional experimental structures and computational studies, in *Computational Chemistry: Reviews of Current Trends*, ed. by J. Leszczynski (World Scientific Publishing, Singapore, 2003), pp. 161–208
28. J. Gu, J. Leszczynski, Structures and properties of mixed DNA bases tetrads: Nonempirical ab initio HF and DFT studies. J. Phys. Chem. A **104**, 1898–1904 (2000)
29. J. Gu, J. Leszczynski, Structures and properties of the planar G·C·G·C tetrads: Ab initio HF and DFT studies. J. Phys. Chem. A **104**, 7353–7358 (2000)
30. J. Gu et al., Hydrogen bonding in 5-bromouracil-adenine-5-bromouracil-adenine (T^+AT^+A) tetrads. J. Phys. Chem. B **108**, 9277–9286 (2004)
31. M. Meyer et al., Interaction of sodium and potassium ions with sandwiched cytosine-, guanine-, thymine-, and uracil-base tetrads. J. Comput. Chem. **26**, 352–364 (2005)

32. J. Gu, J. Leszczynski, A remarkable alteration in the bonding pattern: An HF and DFT study of the interactions between the metal cations and the hoogsteen hydrogen-bonded G-tetrad. J. Phys. Chem. A **104**, 6308–6313 (2000)
33. A. Wong, G. Wu, Selective binding of monovalent cations to the stacking G-quartet structure formed by guanosine 5′-monophosphate: a solid-state nmr study. J. Am. Chem. Soc. **125**, 13895–13905 (2003)
34. J. Gu et al., Isoguanine octamer: From bowl to ball. Chem. Phys. Lett. **445**, 243–245 (2007)
35. S. Metzger, B. Lippert, A metalated guanine,cytosine base quartet with a novel GC pairing pattern involving h(5) of c. J. Am. Chem. Soc. **118**, 12467–12468 (1996)
36. J. Gu et al., H-bonding patterns in the platinated guanine-cytosine base pair and guanine-cytosine-guanine-cytosine base tetrad: An electron density deformation analysis and aim study. J. Am. Chem. Soc. **126**, 12651–12660 (2004)
37. J. Gu et al., Iso-guanine quintet complexes coordinated by mono valent cations (Na^+, K^+, Rb^+, and Cs^+). J. Comput. Chem. **28**, 1790–1795 (2007)

Index